

**FRAGMENTATION- AND INFRARED SPECTROSCOPY
OF OXO-CENTERED
HOMO- AND HETEROTRIMETALLIC
CARBOXYLATE BRIDGED
TRANSITION METAL COMPLEXES**

vom Fachbereich Chemie der Universität Kaiserslautern zur Verleihung des
akademischen Grades 'Doktor der Naturwissenschaften' genehmigte

DISSERTATION

(D386)

vorgelegt von

Dipl.-Chem. JONATHAN RUBEN MEYER

Betreuer: Prof. Dr. Gereon Niedner-Schatteburg

Datum der wissenschaftlichen Aussprache: 20.12.2018

Promotionskommission

Vorsitzender

Prof. Dr. Werner Thiel

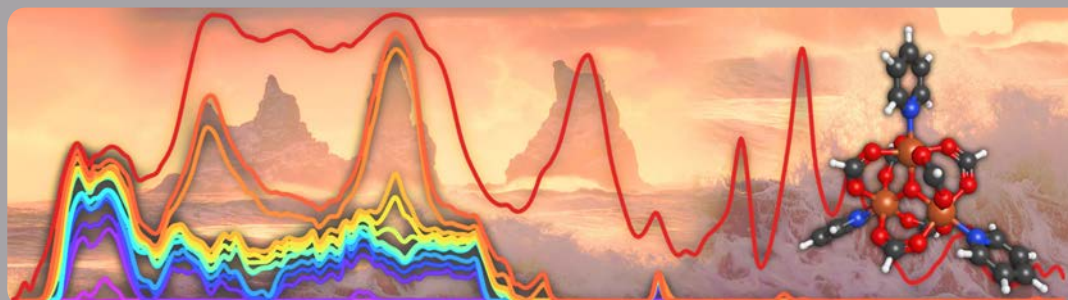
Erster Berichterstatter

Prof. Dr. Gereon Niedner-Schatteburg

Zweiter Berichterstatter

Prof. Dr. Markus Gerhards

Jonathan Ruben Meyer



Fragmentation- and Infrared Spectroscopy of Oxo-Centered Homo- and Heterotrimetallic Carboxylate Bridged Transition Metal Complexes

Fachbereich Chemie
Technische Universität Kaiserslautern
67653 Kaiserslautern
Telefon: + 49 631 205-2754
Telefax: + 49 631 205-2187
www.chemie.uni-kl.de

Dissertation
Fachrichtung Physikalische Chemie
Dezember 2018

Meiner Mutter und meiner Familie

'The mass spectrometer behaves at times in the most capricious and unaccountable manner... When by good fortune, all is well, the arrangement is capable of good performances. Thus, after a favorable setting of the apparatus, six elements were successfully analyzed in as many days. On the other hand, after dismantling became imperative and it had to be cleaned and rebuilt, exactly as before as far as one could tell, no results of any value were obtained during weeks of work.'

- Francis William Aston -

Der experimentelle Teil der vorliegenden Arbeit wurde im Zeitraum von Juni 2017 bis August 2018 im Fachbereich Chemie der Technischen Universität Kaiserslautern unter Betreuung von Herrn Prof. Dr. G. Niedner-Schatteburg durchgeführt.

Datum des Antrags auf Eröffnung des Promotionsverfahrens: 28.11.2018

Datum der wissenschaftlichen Aussprache: 20.12.2018

Promotionskommission

Vorsitzender

Prof. Dr. Werner Thiel

Erster Berichterstatter

Prof. Dr. Gereon Niedner-Schatteburg

Zweiter Berichterstatter

Prof. Dr. Markus Gerhards

Zusammenfassung

Die Infrarot Multiphotonen Dissoziation (IRMPD) Gasphasen-Spektren einer systematischen Gruppe trimetallischer oxo-zentrierter Übergangsmetall-Komplexe, mit Acetat und Formiat als Brückenliganden und Pyridin oder Wasser als endständigen Liganden, werden gezeigt und diskutiert.

Wie durch stossinduzierte Fragmentation (CID) im Vergleich mit geeigneten ab initio Simulationen gezeigt wird, kann die relative Stabilität der Komplexe zufriedenstellend erklärt werden. Die DFT Simulationen sagen das qualitative Verhalten der Aufspaltung der Carboxylat-Streckschwingungen erfolgreich vorher, können anharmonische Effekte im CH Streckschwingungsbereich des IRMPD Spektrums aber nicht erklären.

Zu diesem Zweck sind eine kurze Übersicht über Infrarot Spektren der verwendeten Brücken- und Axialliganden erstellt worden, die dort zusammengefassten Trends helfen bei der Interpretation der beobachteten Banden.

Eine neue Variante der IRMPD Spektroskopie wird vorgestellt und evaluiert. Zusätzlich zur traditionell gezeigten Gesamtfragmentationsausbeute wird die kumulative fragmentspezifische Ausbeute genutzt, um das wellenlängenabhängige Auftreten verschiedener Fragmentationsprodukte zu visualisieren.

Es wird gezeigt, dass in dieser Darstellungsweise wertvolle zusätzliche Informationen zu den angeregten Chromophoren und deren Kopplung mit verschiedenen Fragmentationskanälen enthalten sind.

Qualitativ hochwertige homo- und heterometallische IRMPD Spektren von bi- und trimetallischen, carboxylatverbrückten, oxo-zentrierten Komplexen von Chrom und Eisen werden auf die Einflüsse der Metallzentren, der verbrückenden Carboxylatliganden und der endständigen Liganden auf die Schwingungen der Carboxylatgruppe und auf die CH-Streckschwingungen der Brückenliganden untersucht.

Vor allem in den formiatverbrückten Komplexen treten Banden auf, die als Kombinationsbanden der symmetrischen und asymmetrischen Carboxylat-Streckschwingung und als eine Fermi Resonanz einer Kombinationsbande der asymmetrischen Streck- und der CH-Biegeschwingung mit der CH-Streckschwingung des Formiat-Brückenliganden identifiziert werden.

Bei den Wasseraddukten werden mögliche Hinweise auf eine partielle Hydrolyse der Carboxylat-Brückenbindung durch Wasser diskutiert.

Für alle Zuordnungen, die über eine direkte Erklärung hinausgehen, sei es durch ab initio Simulationen, die vorliegenden Messergebnisse oder durch Deuterierungsexperimente, werden geeignete Experimente vorgeschlagen, die zur Verifikation der gemachten Vorschläge dienen können.

Abstract

The gas phase infrared and fragmentation spectra of a systematic group of trimetallic oxo-centered transition metal complexes are shown and discussed, with formate and acetate bridging ligands and pyridine and water as axial ligands.

The stability of the complexes, as predicted by appropriate *ab initio* simulations, is demonstrated to agree with collision induced dissociation (CID) measurements.

A broad range of DFT calculations are shown. They are used to simulate the geometry, the bonding situation, relative stability and flexibility of the discussed complexes, and to specify the observed trends. These simulations correctly predict the trends in the band splitting of the symmetric and asymmetric carboxylate stretch modes, but fail to account for anharmonic effects observed specifically in the mid IR range.

The infrared spectra of the different ligands are introduced in a brief literature review. Their changes in different environments or different bonding situations are discussed and visualized, especially the interplay between fundamental-, overtone-, and combination bands, as well as Fermi resonances between them.

A new variation on the infrared multi photon dissociation (IRMPD) spectroscopy method is proposed and evaluated. In addition to the commonly considered total fragment yield, the cumulative fragment yield can be used to plot the wavelength dependent relative abundance of different fragmentation products. This is shown to include valuable additional information on the excited chromophors, and their coupling to specific fragmentation channels.

High quality homo- and heterometallic IRMPD spectra of oxo centered carboxylate complexes of chromium and iron show the impacts of the influencing factors: the metal centers, the bridging ligands, their carboxylate stretch modes and CH bend modes, and the terminal ligands.

In all four formate spectra, anharmonic effects are necessary to explain the observed spectra: combination bands of both carboxylate stretch modes and a Fermi resonance of the fundamental of the CH stretch mode, and a combination band of the asymmetric carboxylate stretch mode with the CH bend mode of the formate bridging ligand.

For the water adduct species, partial hydrolysis is proposed to account for the changes in the observed carboxylic stretch modes.

Appropriate experiments are suggested to verify the mode assignments that are not directly explained by the *ab initio* calculations, the available experimental results or other means like deuteration experiments.

Table of contents

1	Introduction to Trimetallic Carboxylate Bridged Transition Metal Complexes	1
1.1	Motivation for the Study of Transition Metal Complexes.....	1
1.2	Structural Motifs of Trimetallic Carboxylates.....	2
1.2.1	Nomenclature of Mixed Metal Coordinatively Unsaturated Complex Isomers (hom-L/H & het-L/H)	4
1.3	History of Trimetallic Carboxylate Complexes	5
1.4	Modern Developments and Applications of Trimetallic Carboxylates.....	7
1.4.1	Recent Magnetic Studies	7
1.4.2	Polymer-, Catalyst-, Nanoparticle-, and Biological Applications.....	8
1.4.3	Different Carboxylates/Metals/Coordination Centers	9
1.5	Cooperativity.....	10
1.6	References Chapter 1.....	11
2	Experimental and Computational Methods	22
2.1	Tunable IR Laser System for IRMPD Spectroscopy.....	22
2.2	The Electrospray Ionisation Process (ESI) for Mass Spectrometry.....	24
2.3	Paul Trap Mass Spectrometer	25
2.4	Collision Induced Dissociation (CID)	26
2.4.1	Sigmoidal Fit with Logistic Growth Curves.....	28
2.4.2	Multiple Component Sigmoidal (logistic) Fits of CID Curves.....	28
2.5	Infrared Multi Photon Dissociation (IRMPD) Spectroscopy	30
2.5.1	Fragment Mass Trace Specific IRMPD Spectroscopy	32
2.6	DFT ab initio Simulations of Transition Metal Complexes	32
2.6.1	DFT Simulations of Infrared Spectra	33
2.6.2	Basis Set Superposition Error Mitigation for CID Bond Energy Calculations	33
2.7	The Differential Many Body Cooperativity (DMBC) Formalism.....	34
2.8	References Chapter 2.....	36
3	Introduction to the Infrared Spectroscopy of Carboxylates and Other Ligands.....	40
3.1	Fundamental Vibrational Modes of the Formate Ion	40
3.2	Fermi Resonance, Combination Bands and Overtones	40
3.3	Fermi Resonance in Deuteroformyl Moieties.....	42
3.4	Formate Spectra	42
3.4.1	IR Signatures of Formate on Surfaces	44
3.4.2	Trends in the Formate Vibrational Modes.....	46
3.5	Acetate IR spectra.....	47
3.5.1	CO Stretch Modes	47
3.5.2	CH ₃ Stretch Modes	47
3.6	Pyridine Gas Phase IR Spectra.....	48
3.7	Water Adduct Spectra of Basic Acetates and Formates.....	49
3.8	References Chapter 3.....	50

4	DFT Simulations of Structures and Spectra of Carboxylate Complexes.....	56
4.1	Multiplicity of the $[\text{Fe}_{3-n}\text{Cr}_n\text{O}(\text{OAc})_6]^+$; $n = 0 - 3$ Series.....	57
4.2	Choice of Functional for $[\text{CrFe}_2\text{O}(\text{OAc})_6(\text{Py})_n]^+$ with $n = 2, 3$	58
4.3	Choice of Basis Set for $[\text{Fe}_3\text{O}(\text{OAc})_6(\text{Py})_n]^+$ with $n = 0 - 3$	59
4.4	Geometry Trends for Ligand and Metal Variation in Homo- and Hetero-metallic $[\text{Fe}_{3-n}\text{Cr}_n\text{O}(\text{Fo})_6\text{Py}_m]^+$ and $[\text{Fe}_{3-n}\text{Cr}_n\text{O}(\text{OAc})_6\text{Py}_m]^+$	60
4.4.1	Terminal- and Bridging Ligand Variation Induced Geometry Changes in Fe_3O Acetates and Formates	60
4.4.2	Metal Exchange Induced Geometry Changes in $[\text{Fe}_{3-n}\text{Cr}_n\text{O}(\text{Fo}/\text{OAc})_6\text{Py}_m]^+$ for $n, m = 0 - 3$ in the Formate and Acetate Complexes	61
4.5	Pyridine to Metal Bond Length Potential Energy Surface for $[\text{Fe}_{3-n}\text{Cr}_n\text{O}(\text{Fo})_6\text{Py}_m]^+$ and $[\text{Fe}_{3-n}\text{Cr}_n\text{O}(\text{OAc})_6\text{Py}_m]^+$ with $n = 0 - 3$ and $m = 1, 3$	66
4.6	Torsional Degrees of Freedom of the Pyridine Ligands.....	68
4.7	Differential Many Body Cooperativity of $\text{Fe}_{3-n}\text{Cr}_n\text{O}$ Acetates and Formates.....	70
4.8	References Chapter 4.....	72
5	Experimental Studies of the Basic Carboxylate Complexes	74
5.1	Synthesis of Trinuclear Carboxylate Complexes	74
5.1.1	Synthesis from the M^{III} Hydroxides	74
5.1.2	Direct Synthesis with $\text{M}^{\text{III}}\text{Cl}_3$ and Sodium Carboxylate.....	75
5.2	The Mass Spectra of the Complexes.....	75
5.3	Collision Induced Dissociation (CID) Experiments of Formate and Acetate Complexes.....	76
5.3.1	Correlation of the E_{com}^{50} Values Versus the Binding Energy and the Bond Distance.....	80
5.4	Fragment Specific IRMPD Spectroscopy.....	82
5.4.1	Foundations of Fragment Specific IRMPD Spectroscopy	82
5.4.2	Fragment Specific IRMPD of the Archetypal Iron Acetate Pyridine Complexes.....	83
5.4.3	Successive Fragmentation in the COO Stretch Modes of Iron Acetate Pyridine Complexes at Different Laser Fluences.....	86
5.4.4	Laser Power & Laser Shot Count Dependence of IRMPD Fragmentation Efficiency	88
5.5	Mode Specific Fragmentation in the CH Stretch Modes of Iron Acetate Pyridine Complexes.....	90
5.6	Isotope Exchange Effects of Iron Acetate Pyridine Complexes.....	92
5.6.1	Internal Vibrational Relaxation Processes Witnessed by Partial Isotopomerization	92
5.7	References Chapter 5.....	96
6	Systematic Study of the Carboxylate Stretch Modes in Chromium and Iron Complexes	98
6.1	Handling of the Accompanying Booklet.....	98
6.2	Ligand and Metal Induced Effects in the COO Stretch Modes of Homo- and Heterometallic Chromium and Iron Carboxylate Complexes with Pyridine	99
6.2.1	Formate Bridged Chromium and Iron Complexes.....	100
6.2.2	Acetate Bridged Complexes.....	106
6.3	Tentative Assignment of the hom/het Ligand/Hole Isomers of Partially Coordinated Mixed Metal Complexes.....	111
6.4	Trends in the Symmetric and Asymmetric COO Carboxylate Stretch Modes.....	114
6.5	Hints to Cooperative Effects in the Band Splitting of the Symmetric and Asymmetric Carboxylate Vibrations.....	120
6.6	References Chapter 6.....	121

7	Anharmonicity in the CH Stretch Modes of Acetate and Formate Pyridine Complexes	122
7.1	Formate Complexes in the Mid IR, a Curious Case	122
7.2	Acetate Complexes in the Mid IR, the Puzzle Continues	128
7.3	References Chapter 7	133
8	Other Ligands and Trivalent Metals: Water and Scandium	134
8.1	Carboxylate Stretch Modes of Chromium and Iron Water Complexes	134
8.2	Scandium Chromium Iron Oxo Acetate and Formate	138
8.3	References Chapter 8	141
9	Summary and Outlook	142
9.1	Summary	142
9.2	Outlook and Ongoing Work	143
9.2.1	Synthesis of Interesting Complexes	143
9.2.2	IR Measurements	144
9.2.3	Kinetics	145
9.2.4	UV-Vis	145
9.2.5	X-ray Magnetic Circular Dichroism (XMCD)	145
9.2.6	Future DFT Studies	145
9.2.7	Trapped Ion Mobility Spectrometry (TIMS)	146
9.3	References Chapter 9	147
10	Appendix A: Magnetostructural Correlation in Isolated Trinuclear Iron(III) Oxo Acetate Complexes	149
10.1	Preamble	149
10.2	Supporting Information to 'Magnetostructural Correlation in Isolated Trinuclear Iron(III) Oxo Acetate Complexes'	164
11	Appendix B: Additional Figures and Tables	188
11.1	DFT Simulated Geometries of Homo- and Heterometallic Carboxylate Complexes	188
11.1.1	Comparison of the $[\text{Fe}_3\text{O}(\text{RCOO})_6\text{Py}_m]^+$ ($m = 3, 2, 1, 0$; $\text{R} = \text{H}, \text{CH}_3$) Complexes	188
11.1.2	Homo- and Heterometallic Tri-pyridine Complexes	190
11.1.3	Dipyridine Complexes	191
11.1.4	Monopyridine Complexes	191
11.1.5	Bare Complexes	192
11.2	Geometry Changes on Metal or Ligand Exchange	194
11.3	Tables of Calculations for Differential Many Body Cooperativity (DMBC)	196
11.3.1	Acetate	196
11.3.2	Formate	198
11.4	Additional DFT Graphs to Chapter 4.2	200
11.5	Additional CID Graphs to Chapter 5.3	203
11.6	Additional IRMPD Graphs	207
11.6.1	Additional IRMPD Graphs of Acetate Pyridine Complexes	208
11.6.2	Additional IRMPD Spectra of the ScCrFe Acetate and Formate Complexes	238
11.7	Gaussian Fits on all Pyridine Spectra	239
11.8	Additional Tables of IR Band Position and the DMBC Formalism	240
11.9	UV VIS-, ATR Spectra of several $\text{Cr}_3\text{O}(\text{OAc})_6\text{L}_3$ Complexes	248
11.10	References for the Appendix B	248
11.11	Abbreviations	251

1 Introduction to Trimetallic Carboxylate Bridged Transition Metal Complexes

This thesis will focus on the study of homo- and heterometallic oxo-centered transition metal complexes, with three trivalent transition metal ions at their core; especially chromium or iron and either acetate or formate as the bridging ligands. This class of complexes is known as the basic carboxylates. They comprise a wide range of structures, as is discussed in detail in section 1.2.

They are archetypal examples of the class of inverse coordination complexes, as summarized by Haiduc et al.^{1,2} in a recent series of review articles. They are good cases to systematically study the interaction of oxo-bridged metal centers, the carboxo-bridging ligands, and the terminal ligands.

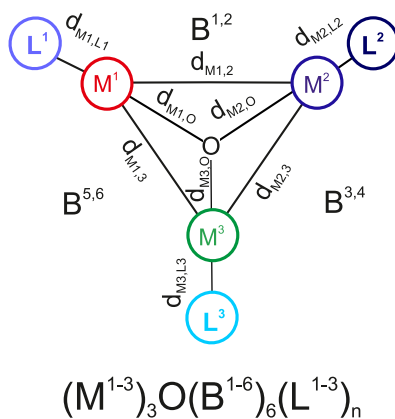


Figure 1 Highly simplified representation of the general structural motif of trimetallic oxo-centered carboxylate bridged complexes. Abridged sum formula: $(M^{1-3})_3O(B^{1-6})_6(L^{1-3})_n$. Important geometry parameters are labeled. For additional clarity, the two bridging carboxylate ligands between each metal pair are indicated by B^{1-6} and omitted.

The metal centers are gas phase model systems for the influence of metal surfaces, counterions, or complex partners on the bridging carboxylate ions. Specifically, for the formate ion, we will show how the ion and its infrared modes are influenced by their environment.

1.1 Motivation for the Study of Transition Metal Complexes

Coordination complexes of transition metals are very important for many aspects of chemistry. Fundamentally, to explore physical-chemical concepts; practically, for their chemical uses³ in catalysis⁴⁻⁷, as well as their unique magnetic⁸⁻¹² and optical^{8,13} properties. They come with exciting applications, for example in quantum computing^{10,14-18}.

We use the methods we have at our disposal on of this very interesting class of examples, to contribute to the understanding of basic carboxylates: infrared¹⁹, optical and x-ray spectroscopy²⁰⁻²² combined with ion trap^{23,24} mass spectrometry²⁵.

The electronic structure, stability, and spectral features of $[M_3O(O_2R)_6L_3]^+$ complexes (M = transition metal, $R = H, CH_3, \dots$, $L = Py, H_2O, \dots$) are very sensitive to intrinsic geometric distortions of the M_3O core¹⁹ induced by the involved metals; the bridging- and axial ligands; magnetic and electronic couplings; and the crystal lattice environment.

The majority of studies so far (section 1.3) have been performed in the condensed phase; in solution, or in crystal lattices. The resulting external effects such as crystal packing or the solvation environment were assumed to be of minor importance. We will see however, that the complexes often react very strongly to minute changes in environment. Therefore, to exclude those and other external effects, it is necessary or beneficial to investigate $[M_3O(O_2R)_6L_3]^+$ complexes as isolated species in the gas phase.

1.2 Structural Motifs of Trimetallic Carboxylates

The classic model system for oxo-centered trinuclear transition metal $(M^{III})_3O$ carboxylate complexes of the structural type $[M_3O(O_2CR)_6L_3]^+$ (L = axial ligands, O_2CR = carboxylate bridging ligand)^{9,13} is the archetypical $[Fe_3O(O_2CCH_3)_6Py_3]^+$. Three M^{III} ions coordinate around an O^{2-} center in a flat triangular arrangement (M_3O core). Each of the M metal centers achieve a pseudo-octahedral geometry through equatorial coordination with four carboxylate bridging ligands (O_2CR), and axial (or terminal) coordination with an extra monodentate ligand (L) and the μ -oxo center. This is shown in **Figure 1**.

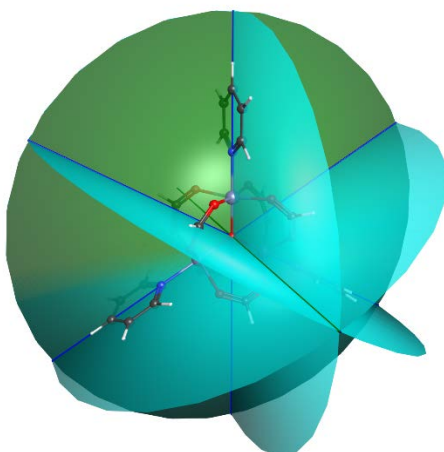


Figure 2 Example for a high symmetry complex, $[Cr_3O(Fo)_6Py_3]^+$. Symmetric axial ligands like pyridine in the right orientation can lead to an overall d_{3h} symmetry. Shown are also the symmetry elements; the d_3 and d_2 axes (blue lines) and mirror planes (teal and green).

Of course, the oxidation state is also important to the overall charge and the structure of the complex. Common are either a symmetric trivalent $(M^{III})_3O$ core with a net charge of +1, useful for mass spectrometry, or the mixed valence states $(M^{II}/M^{III})_2O$ ²⁶⁻³⁰, and more rarely $(M^{III}/M^{IV})_2O$ ³¹; where a phase change between localized and delocalized valence states can be observed at a critical temperature³².

Especially at low temperatures, depending on the electron configuration of the metal center, magnetic effects are possible, as each metal center can have an effective magnetic spin. In this triangular arrangement, the different metal centers cannot easily couple antiferromagnetically, leading to spin frustration^{33,34} and other interesting magnetic properties.

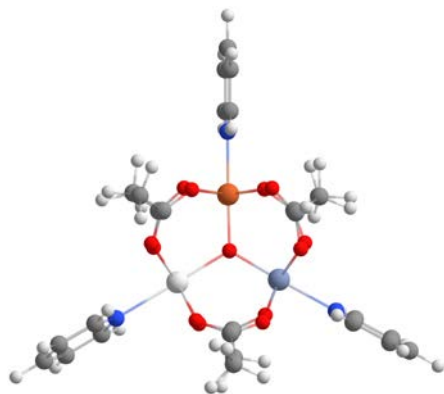


Figure 3 Structure of a $[\text{ScCrFeO}(\text{OAc})_6\text{Py}_3]^+$ complex to illustrate the general structural motif.

The next important factor are the bridging ligands^{35,36}: be it by their geometric constraints on the structure, the ligand strength (with formate being the strongest), their influence on the coupling between the metal centers³⁷, or a unique functionalization (e.g. ferrocene³⁶). Mixed ligand species³⁸⁻⁴⁰ are known but rare. Many examples of this are collected in section 1.4.3.

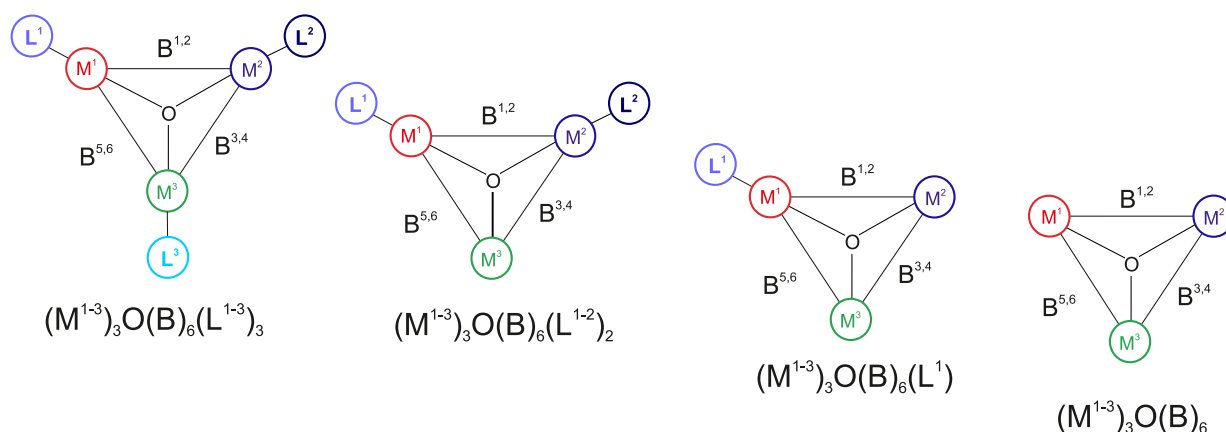


Figure 4 The four $(\text{M}^{1-3})_3\text{O}(\text{B}^{1-6})_6\text{L}_n$ combinations possible for $n = 3, 2, 1, 0$ axial ligands. Note that the metals $\text{M}_{1,3}$ can be permuted; leading to different energetically degenerate or distinct isomers. For further details, see **Figure 5**.

The third factor is the terminal or axial ligand. These can be a weakly coordinating ligand like N_2 ⁴¹; a strong ligand like the ubiquitous pyridine, water; or through a bidentate bridging ligand like formate⁴² or terephthalic acid⁴³⁻⁴⁵, even another coordinating metal^{34,42}. Each of them can have a strong influence on the geometry, stability, electronic structure, and the magnetic properties³⁴ of the complex.

Another less common factor could be a substitution of the central oxo-group, for example for a fluorine¹⁶, for two oxo-groups^{46,47}, or even to be left out all together^{12,48,49}. See section 1.4.3 for specific examples.

The last important tuning factor is the use of heterometals in the trimetallic M_3O core^{50,51}. This complicates the landscape of unique isomers, since now there are different binding sites for the axial ligands available. Counterintuitively, a complex with three different participating transition metals⁵² is simpler in respect to the location of subsequent axial ligand coordination, as there is usually a hierarchy

of bonding strengths between different transition metals. This leads to a more or less clear preference in the order of occupied coordination sites. The $[\text{ScCrFeO}(\text{OAc})_6\text{Py}_3]^+$ complex, to our knowledge first synthesized in the present work (see section 8.2), is shown in **Figure 3**; the observations and calculations suggest a M-Py bonding strength hierarchy of Sc being the lowest, followed by Fe, and then the strongest bonding metal, Cr.

All respective bridging ligands and axial ligands are usually kept the same in each comparison, unless otherwise noted. For a systematic look at the observed trends in geometry in homo- and heterometallic Cr/Fe complexes, see chapter 4.4.

1.2.1 Nomenclature of Mixed Metal Coordinatively Unsaturated Complex Isomers (hom-L/H & het-L/H)

For non-saturated heterobimetallic complexes with one or two axial ligands and two different metals, several energetically distinct regio-isomers are possible. To simplify the discussion, we propose a nomenclature of those types of isomers. There are two properties we have to specify here, that behave in a similar fashion.

For complexes with only one axial ligand and two dissimilar metal centers in the trimetallic core, it matters whether the ligand is coordinating to one or the other metal center type. This will leave the two additional uncoordinated axial binding positions to be either at dissimilar or the same metal type.

We choose to call those empty binding sites H for hole. For the former case of the ‘holes’ being at different metals, we call that the het-H type for heterogeneous hole position, the latter hom-H for homogenous hole positions. The difference in stability is easy to see here; if the metal, the ligand is coordinating to, is the stronger binding partner, the isomer will be the more stable one compared to the alternative.

In the inverse case of two axial ligands, the difference is between the location of those ligands in respect to the metal centers. If both coordinate to the same metal, we have the case we choose to call hom-L for homogenous ligand position, and if they coordinate on dissimilar metals, it is the het-L case respectively. The energetic ordering of the isomers is hom-L being the most favored one if the majority metal is the one with the strongest ligand-metal bond, otherwise the het-L isomer is the more stable one, leaving one weakly bound ligand position that should be clearly distinctive in its fragmentation behavior and stability.

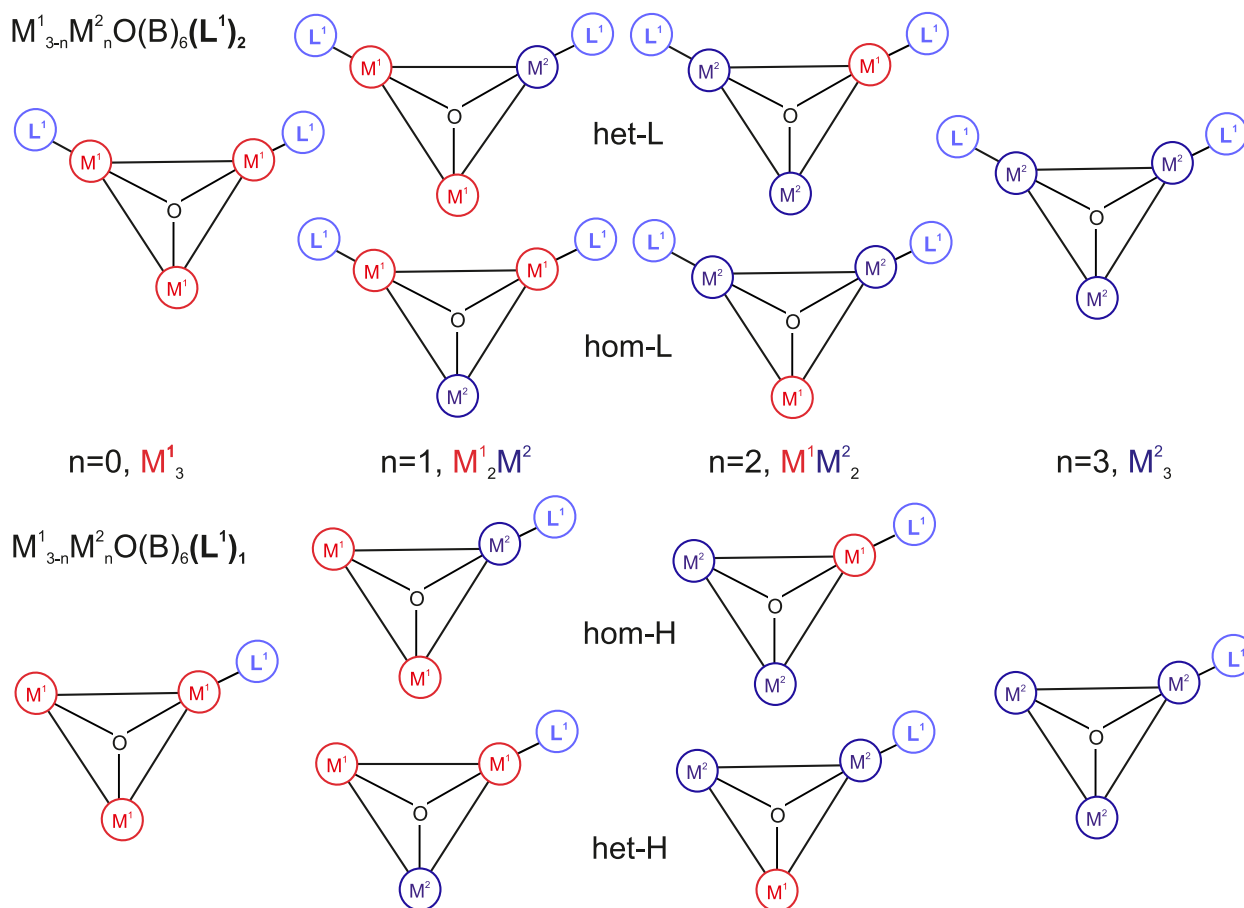


Figure 5 *hom-H*, *hom-L* stands for identical type unoccupied metal sites (H = hole) or occupied metal sites (L = ligand) respectively, *het-H* and *het-L* for different unoccupied and occupied metal positions. A practical application in the Fe/Cr mixed complexes is given in section 4.4, **Figure 25** and **Figure 26**.

1.3 History of Trimetallic Carboxylate Complexes

Mixed metal carboxylate bridged oxo-centered complexes have a rich history for over a century. They were first synthesized and recognized as such by Weinland et al.⁵³ in 1909, almost 110 years ago, described in his paper ‘Über Salze einer Acetato-ferribase und zweier Acetato-chromiferribasen’*. His and other groups, e.g. Werner et al.⁵⁴, soon also explored alternative carboxylate bridging ligands, specifically formate⁵⁵. A number of additional synthetic papers followed in the next decades^{53,55-59}.

They already recognized the extraordinary flexibility of this structure motif to incorporate an almost arbitrary number of different transition metals of the first row, and also incorporate different axial ligands and carboxylate bridging ligands, as their follow up work on iron nickel acetate complexes⁵⁶ shows.

The exact structure of the trinuclear complexes was unclear at first, at times linear configurations were suggested⁶⁰, until Orgel et al.⁶¹ suggested the correct structure. This was followed by efforts to confirm the triangular geometry by Kim⁶², and then finally through X-ray crystallography giving a definitive result, proving the highly symmetric triangular structure⁶³⁻⁶⁵.

* This translates to ‘About salts of an acetate iron base and two acetate chromate iron bases’

Different synthetic strategies for homo-^{64,66} and heterometallic complexes of iron and chromium^{63,67,68} were developed, although there are hints that the heterometallic complexes get often formed as mixtures⁶⁹. See section 5.1 for more, with details on the traditional synthesis and an alternative modern route.

This pairing of magnetically active metal ions with a large number of unpaired electrons was a fruitful ground for studies on their magnetic properties. At first, only the homometallic iron- and chromium complexes were considered⁷⁰, but Kambe et al. already included Cr₂Fe into their study on the thermomagnetism of hydrated metal acetates⁷¹. Further thermomagnetic studies on mixed chromium and iron acetates⁷² followed soon after. Additional numerous thermomagnetic and paramagnetic studies were conducted in Russia, Japan, and other countries^{29,51,64,65,72-84}. Further efforts on the Moessbauer spectra of iron acetate⁸⁵ and the study of exchange coupling and spin frustration in Cr^{III}₃⁸⁶ and other related structures^{27,78,87-89}, helped to improve the understanding of this substance class. In the following decades, several spectroscopic studies for various acetates of Cr, Fe, Ru etc. followed, using infrared⁹⁰, as well as UV-Vis^{74,91-93}, luminescence^{92,94,95}, and circular dichroism (CD)⁹⁶ spectra.

In 1988, a good summary of the progress in the study of the ‘Chemical and Physical Properties of Triangular Bridged Metal Complexes’, up until that point in time, can be found in the eponymous chapter of ‘Progress in Inorganic Chemistry’ by Cannon and White⁹⁷, as well as in further contemporary reviews on basic carboxylates by Catterick and Thornton³⁵; and by Miller, Cotton et al.⁹⁸

Special mention is necessary for the systematic work of Cannon et al.^{29,77-79,97,99-105} that culminated in a very interesting series of papers between 1982 to 1987: ‘Vibrational spectra of carboxylato complexes I-VI’^{99,101-105}. This series methodically studies the effects of ligand and metal variations on the condensed phase IR spectra of a wide class of metal carboxylates; also specifically the acetate and formate¹⁰³ chromium/iron homo- and heterometallic complexes¹⁰⁴ studied in this thesis.

A second systematic comparison of the IR spectra of all four (Fe/Cr)₃ acetates with water ligands has been done by Zhang et al.^{106,107}, already showing the systematic shift of the asymmetric COO stretch modes, although with a focus on the metal core. Another prolific researcher in this field is Vincent^{69,108-114}, who also focuses on bioinorganic and toxicologic aspects of chromium ions, among them the basic acetate variant, and their influence on glucose tolerance factor activity¹¹⁵ and catalyzing epoxidation reactions¹¹⁶.

Last but not least, a systematic UV-Vis spectroscopy and magnetic measurements of the Cr/Fe complex family and other heterometallic analogues has been done by Blake et al.^{52,74,117}. The UV-Vis spectra therein were my personal initial motivation to check the heterometallic analogues to the Cr and Fe homometallic acetates. For details, see **Figure 7a** of Ref⁷⁴ and the corresponding theory of the electronic structure¹¹⁸ of these complexes.

A good point to summarize the development of this field until 1989 is the excellent review by West⁵⁰.

1.4 Modern Developments and Applications of Trimetallic Carboxylates

Very recently, interest in this material class has increased again. There is a good review article by Haiduc et al.¹ on the structure motifs of inverse coordination complexes, which includes our basic carboxylates. It introduces a wealth of possible structures. There are fluorido centered complexes, with interesting applications as switchable-exchange molecular double qubits^{16,17} or spin-electric coupling devices^{18,119} for quantum computing; niobium dioxo-centered complexes with sulfate- or carboxylate bridging groups^{31,46}; molybdenum and tungsten complexes¹²⁰, beryllium¹⁰¹; and other variants found in more modern papers¹²¹⁻¹²⁵. Studies have been conducted on the biological breakdown pathway of chromium acetate¹²⁶, its hydrolysis¹¹², and use as catalyst¹²⁷. The water exchange dynamics on Cr^{III} acetate has been studied by neutron scattering^{128,129}. They are subject to intensive basic research for the last decades, and play an important role in understanding the nature of metal-metal interaction^{123,130,131}.

A crystal structure for the formate analogues has recently been published by Wang et al.¹³².

We would like to mention our own groups papers on iron and cobalt with N₂ and pyridine^{41,133,134} ligands, especially the work published in Johannes Lang's thesis¹³⁵, and our joint paper on the magnetostructural correlations of the basic iron(III) acetates¹³³, reprinted in chapter 10.

1.4.1 Recent Magnetic Studies

The magnetic properties of polynuclear transition metal complexes are inextricably correlated with their geometrical structure¹⁻⁵, their proper understanding helps in the design of molecular nanomagnets⁶ (SMM) and in the context of metalloenzymes³⁹.

Many studies have been conducted on trinuclear and even hexanuclear species with two coupled [Fe₃O]⁷⁺ cores¹⁴² as well as two covalently coupled mixed metal cores¹⁴³: on the pairwise distance to coupling correlations, through the central μ_3 oxo bridges⁸, or the bridging formate ligand¹³⁶; on the corresponding coupling constant determination^{137,139}, the interpretation of the exchange interaction¹⁴⁰, and on magnetoelectric coupling¹⁴¹.

Surface deposition of complexes acts as molecular magnets^{13,144,145} and polynuclear rings¹⁴⁶; showing antiferromagnetic coupling^{146,148}, 1-D metamagnetic spin chains³⁴ and dots⁴². This can be achieved by assembling pre-formed isolated magnetic frustrated polymetallic clusters into a correlated 1-D spin sequence. The triangular units are connected by coordinated bonds via spin centers, similar to the spin chains reported earlier¹³⁶. Furthermore, rectangular assemblies¹³⁶ are studied to learn about the intra-M₃O-core spin coupling¹⁰.

This is also observed by measurements of the total spin (S_T) in the cases of the symmetrically coordinated [Fe₃O(OAc)₆(H₂O)₃]NO₃¹⁴⁹, showing a S_T of 1/2 and the asymmetrically coordinated [Fe₃O(TIEO)₂(O₂CPh)₂Cl₃]⁺¹⁵⁰ with a S_T of 5/2.

A single metal core was modified with a tridentate oximate ligand by Christou et al.⁹. This combines the bridging and terminal ligands, inducing a structural distortion in the $[\text{Mn}^{\text{III}}_3\text{O}]^{7+}$ core, turning an antiferromagnetic coupling into a ferromagnetic one¹⁵¹, exhibiting spin coherence¹¹. Careful distortion¹⁵² of the triangular metal core seems to be the necessary strategy. These single molecular magnets (SMM) can even be covalently dimerized¹⁵³. Some complexes can potentially be modified with fluorescent chromophores to couple their magnetic state with their photoluminescence⁸.

The necessary group theoretical treatment on the homo and hetero-metallic systems has been done by Tsukerblat et al.³³, who pioneered in the magnetic studies (EPR)^{51,73} of this compound class much earlier. In further efforts he collaborated with Rakitin on the respective Jahn Teller effect and more^{82,154,155}.

As we can see, these complexes are popular model systems¹⁵⁶ for electronic coupling^{122,123,131,157} and magnetic effects^{78,88,158-161}.

1.4.2 Polymer-, Catalyst-, Nanoparticle-, and Biological Applications

The chemical and structural properties of the basic carboxylates can also be exploited. They find industrial use as linker for gels and polymers^{13,110,162-167}, along with some precursor variants^{88,139,168} to form coordination polymers; both with 1D, 2D, and 3D structures^{136,165,166}. They are used for nanoparticle¹⁶⁹ formation or as homochiral porous metal organic framework (MOF) material for enantioselective separation and catalysis¹⁷⁰. There are ionic crystals with iron or chromium formate complexes as macro-cations¹⁷¹⁻¹⁷³ in an organic zeolite type structure; for size selective heterogenous catalysis, formate structures as self-assembling Ag nano particle surfactants¹⁷⁴, conglomerates linked by phosphine groups¹⁷⁵, or other multidentate linkers like pyrazine¹⁷⁶.

According to the hard/soft acid/base (HSAB) principle, strong coordination bonds are formed between hard acid vs hard base, and soft acid vs soft base. Carboxylate-based ligands are regarded as hard bases; according to Feng et al.¹⁷⁷, water-stable MOFs can be formed together with hard acid metal ions such as Cr^{3+} , Al^{3+} , Fe^{3+} , and Zr^{4+} . In early works, some representative MOFs with remarkable stability in water include the MIL series (MIL stands for Material Institute Lavoisier, notable examples are MIL-53¹⁷⁸, MIL-100¹⁷⁹ and MIL-101⁴³).

The most notable example of this class of MOF with giant pores and internal windows of 12 to 15 Å is the Cr^{III} terephthalate MIL-101 (Cr), developed by Férey et al.^{43,44}, with over 2500 citations and countless industrial applications. The μ -oxo centered basic carboxylates form a trigonal basic building unit¹⁸⁰; especially when combined with other building blocks⁴⁵, the range of possibilities is enormous.

Another name of this class of structures is Porous Coordination Polymers (POP), based also on tri- (often $\text{Cr}_3^{\text{III}}\text{O}$) and tetrametallic (e.g. $\text{Zn}_4^{\text{II}}\text{O}$) μ -oxo complexes as their building blocks. An interesting study on the hydrolysis resistance of these substances was done by Low et al.¹⁸¹, with relevance to our

complexes; the Cr₃O acetate clusters (**Figure 65**) were used as models of the hydrolysis of metal organic frameworks¹⁸¹.

These MOFs are used as catalysts, for example: various oxidation reactions^{125,156,182}, oxidative couplings¹²⁷ by Fe₃ and Fe₂Co acetates deposited on a zeolite matrix, α -olefin polymerization¹⁸³, acetylene addition¹⁸⁴, C-H activation^{185,186}, and as catalyst intermediates¹⁸⁷. Also see the review by Lippard¹⁸⁸ ‘Oxo-Bridged Polyiron Centers in Biology and Chemistry’. Especially chromium(III) complexes are of interest as functional biomimetics^{113,114,116}, food supplements, or even of medical value^{113,114,189}; for example chromium(III) propionate^{112,190-192} seems to amplify insulin sensitivity and could have antiradical properties⁴⁰. The oxo-centered tri-nuclear iron complexes are even found as structural motifs in metal proteins³⁹.

The cobalt acetate complexes^{131,156,157,187,193-195} are another notable group, with the earliest mentions in this paper^{131,187}; on mixed iron cobalt complexes¹⁹⁴ and their chemistry^{157,182,196}. Our group also worked on this class of substances. Refer to Johannes Lang's paper and the bachelor thesis of Daniela Fries^{134,197,198}.

1.4.3 Different Carboxylates/Metals/Coordination Centers

The immense variety of related complexes is quite impressive. Some interesting examples are mentioned here in no particular order. There are beryllium¹⁰¹ and di-oxo centered niobium or osmium complexes^{31,46,199}, alkoxy centered (μ_3 -OH) nickel complexes²⁰⁰, heterometallic acetates^{194,201,202}, the first published heterotrimetallic complex with a Cr^{III}Fe^{III}Ni^{II} core⁵², complexes with molybdenum and iron¹⁴⁴ or In^{III}₂Ni^{II}²⁰³, as well as Iridium²⁰⁴. A route for creating different heterometallic or heterovalent complexes can be the direct exchange of single metal centers, as shown by Vrabel et al.²⁰⁵. Bigger softer ions like Uranium do not accommodate six bridging ligands anymore²⁰⁶; the tungstate complexes²⁰⁷ deviate from the hexa-carboxylato pattern as well.

On a side note, mixed valence complexes have phase transfers at around 200K between delocalized and localized states, as studied by thermography^{28,32} and xray²⁰⁸, showing the transition between low to high symmetry^{30,83,84,130,209}. Besides iron, ruthenium also forms mixed valence complexes²¹⁰, but cationic complexes are also studied²¹¹, as well as aryl coupled dimers displaying electron transfer behavior²¹².

The variety doesn't stop there. Notable examples are: mixed bridging ligand complexes with Schiff bases²¹³, oximes⁹, acrylic acid dimers and unsaturated carboxylic acids³⁸, biomolecules(flavonoid)⁴⁰, protein³⁹ or other mixed bridges³⁸ or even bridging several M₃O cores with multidentate bridging ligands¹⁴⁵; that can lead to coordination polymers¹³⁶. There many more examples of basic carboxylates: alkaline earth metal iron perchloroacetates¹⁶⁰, o-phthalate complexes^{214,215}, benzoic acid²¹⁶, p-chlorobenzoic acid²¹⁷, carboxylatopyridine²¹⁸, amino acids^{68,219,221}, propionate^{75,110,112,115,190,192,222} with pyazole¹⁹² ligands, with flavonoid ligand substitution⁴⁰, sulfate analogues²²³, thio-methyl groups¹⁷⁴,

trifluoroacetates^{89,158,224}, mercaptocarboxylic acids²²⁵, thiocarboxylates²²⁶, other examples²²⁷⁻²²⁹ of systematic carboxylate variation^{164,230,231}. Furthermore, there are helically ligated complexes^{232,233} (with Volker Schünemann et al.), chiral helices formed by TiMn_2 complex chains linked by formates²³⁴, and examples of metal to ligand charge transfer with Fe_3 and Cr_3 ferrocene functionalized carboxylates³⁶ (with Annie Powell et al.^{36,78,100,235,236}).

Last but not least, we would like to mention an example of a trinuclear carboxylate bridged complex without the central oxo-center: $\text{Pd}^{\text{II}}_3(\text{CH}_3\text{COO})_6$, first described by Wilkinson et al.⁴⁸. The triangular structure was only confirmed later by Skapski et al.⁴⁹. It has found considerable interest for its catalytic activity, e.g. in C-H activation reactions, recently studied by Roithova et al.²³⁷. The reaction seems to involve an opening and closing of the metal ring¹⁸⁵.

1.5 Cooperativity

Cooperativity is the concept at the heart of the 3MET research initiative, under which this work has been conducted. It has been summarized in a review by Niedner-Schatteburg et al.²³⁸.

An often-quoted definition states:

'When the total energy or another physical property of a many-body system is determined by more than pairwise contributions of its components, cooperativity or anti-cooperativity is involved.' - Lichtenfeld and Grimme²³⁹.

This cooperativity can also be quantified along many specific properties, often the total electronic energy, but also spectroscopic properties like infrared band positions or other optical transitions. For this, a many body expansion as formalized by Klopper et al.²⁴⁰ can be used. See section 2.7 for a definition of that formalism; section 4.7 for its application on our example of chromium and iron acetates and formates; and section 6.5 for an attempt on using it on the IRMPD band splitting $\Delta\nu$ between the symmetric and asymmetric COO vibrations of the same species.

There are also other examples on non-transition metal many body systems, such as carbohydrate networks, where structural cooperativity²⁴¹ can be observed.

1.6 References Chapter 1

1. Haiduc, I. Inverse coordination – An emerging new chemical concept. Oxygen and other chalcogens as coordination centers. *Coordination Chemistry Reviews* **338**, 1-26 (2017).
2. Haiduc, I. Inverse coordination – An emerging new chemical concept. II. Halogens as coordination centers. *Coordination Chemistry Reviews* **348**, 71-91 (2017).
3. Baker, A. T. & Livingstone, S. E. Historical Sketch. The early history of coordination chemistry in Australia. *Polyhedron* **4**, 1337-1351 (1985).
4. Beccalli, E. M., Broggin, G., Martinelli, M. & Sottocornola, S. C-C, C-O, C-N bond formation on sp² carbon by Pd(II)-catalyzed reactions involving oxidant agents. *Chemical Reviews* **107**, 5318-5365 (2007).
5. Lersch, M. & Tilset, M. Mechanistic aspects of C-H activation by Pt complexes. *Chemical Reviews* **105**, 2471-2526 (2005).
6. Labinger, J. A. & Bercaw, J. E. Understanding and exploiting C-H bond activation. *Nature* **417**, 507-514 (2002).
7. Ritleng, V., Sirlin, C. & Pfeffer, M. Ru-, Rh-, and Pd-catalyzed C-C bond formation involving C-H activation and addition on unsaturated substrates: Reactions and mechanistic aspects. *Chemical Reviews* **102**, 1731-1769 (2002).
8. Alexandropoulos, D. I. *et al.* Emissive molecular nanomagnets: introducing optical properties in triangular oximate {Mn III 3 } SMMs from the deliberate replacement of simple carboxylate ligands with their fluorescent analogues. *Dalton Trans.* **43**, 1965-1969 (2014).
9. Stamatatos, T. C. *et al.* Initial Example of a Triangular Single-Molecule Magnet from Ligand-Induced Structural Distortion of a [Mn III 3 O] 7+ Complex. *Journal of the American Chemical Society* **127**, 15380-15381 (2005).
10. Nguyen, T. N. *et al.* Supramolecular aggregates of single-molecule magnets: Exchange-biased quantum tunneling of magnetization in a rectangular [Mn3]4tetramer. *Chemical Science* **7**, 1156-1173 (2016).
11. Abeywardana, C., Mowson, A. M., Christou, G. & Takahashi, S. Spin coherence in a Mn 3 single-molecule magnet. *Applied Physics Letters* **108**, 042401 (2016).
12. Pakula, R. J. *et al.* Palladium Acetate Revisited: Unusual Ring-Current Effects, One-Electron Reduction, and Metal–Metal Bonding. *Inorganic Chemistry* **57**, 8046-8049 (2018).
13. Matsuse, R. *et al.* Metallopolymer Films Exhibiting Three-Color Electrochromism in the UV/Vis and Near-IR Region: Remarkable Utility of Trimetallic Clusters Bearing Thienyl Pendants and Their Mixed-Valent Charge Transfer Transitions. *Journal of Inorganic and Organometallic Polymers and Materials* **23**, 136-146 (2013).
14. Leuenberger, M. N. & Loss, D. Quantum computing in molecular magnets. *Nature* **410**, 789-793 (2001).
15. Aromí, G., Aguilà, D., Gamez, P., Luis, F. & Roubeau, O. Design of magnetic coordination complexes for quantum computing. *Chemical Society Reviews* **41**, 537-546 (2012).
16. Walsh, J. P. S. *et al.* Electronic Structure of a Mixed-Metal Fluoride-Centered Triangle Complex: A Potential Qubit Component. *Inorganic Chemistry* **54**, 12019-12026 (2015).
17. Ferrando-Soria, J. *et al.* Switchable Interaction in Molecular Double Qubits. *Chem* **1**, 727-752 (2016).
18. Trif, M., Troiani, F., Stepanenko, D. & Loss, D. Spin-Electric Coupling in Molecular Magnets. *Physical Review Letters* **101**, 217201 (2008).
19. Oomens, J., Sartakov, B. G., Meijer, G. & von Helden, G. Gas-phase infrared multiple photon dissociation spectroscopy of mass-selected molecular ions. *International Journal of Mass Spectrometry* **254**, 1-19 (2006).
20. Forbes, M., Talbot, F. & Jockusch, R. The Spectroscopy of Ions Stored in Trapping Mass Spectrometers. in *Practical Aspects of Trapped Ion Mass Spectrometry, Volume V* 239-290 (CRC Press, 2009). doi:10.1201/9781420083743-c9
21. Meyer, J., Tombers, M., Niedner-Schatteburg, G. & Lau, T. *Magnetic characterization of Single Molecular Magnets (SMM) of the [Fe4Ln2] type by X-ray Magnetic Circular Dichroism (XMCD)*. (2010).
22. Peredkov, S. *et al.* X-ray absorption spectroscopy of mass-selected transition metal clusters using a cyclotron ion trap: An experimental setup for measuring XMCD spectra of free clusters. *Journal of Electron Spectroscopy and Related Phenomena* **184**, 113-118 (2011).
23. Paul, W. Electromagnetic Traps for Charged and Neutral Particles(Nobel Lecture). *Angewandte Chemie International Edition in English* **29**, 739-748 (1990).

24. Paul, W. & Steinwedel, H. Ein neues Massenspektrometer ohne Magnetfeld. *Z. Naturforsch.* **8a**, 448-450 (1952).
25. Eyler, J. R. Infrared multiple photon dissociation spectroscopy of ions in Penning traps. *Mass Spectrometry Reviews* **28**, 448-467 (2009).
26. Poganiuch, P., Liu, S., Papaefthymiou, G. C. & Lippard, S. J. Trinuclear, oxo-centered mixed-valence iron complex with unprecedented carboxylate coordination: $[\text{Fe}_3\text{O}(\text{O}_2\text{CCH}_3)_6(\text{TACN})]\cdot 2\text{CHCl}_3$. *Journal of the American Chemical Society* **113**, 4645-4651 (1991).
27. Baca, S. G. *et al.* Synthesis, crystal structures and magnetic properties of trinuclear oxo-centered homo- and mixed-valence manganese pivalate complexes with imidazole (Im) and 1-methylimidazole (1-MeIm): and. *Polyhedron* **25**, 3617-3627 (2006).
28. Woehler, S. E. *et al.* Deuteron NMR study of lattice dynamics affecting the rate of intramolecular electron transfer in the iron acetato oxo pyridine mixed-valence complex $[\text{Fe}_3\text{O}(\text{O}_2\text{CCH}_3)_6(\text{py})_3](\text{py})$. *Journal of the American Chemical Society* **109**, 1063-1072 (1987).
29. White, R. P. *et al.* Electronic interactions in mixed-valence and mixed-metal ion clusters: inelastic neutron scattering spectra of the complexes $[\text{Fe}^{\text{III}}_2\text{M}^{\text{II}}\text{O}(\text{OOCMe})_6(\text{py})_3](\text{py})$, where M = manganese, nickel. *Journal of the American Chemical Society* **115**, 7778-7782 (1993).
30. Kambara, T., Hendrickson, D. N., Sorai, M. & Oh, S. M. Mechanism of phase transitions affecting intramolecular electron transfer in trinuclear mixed-valence transition-metal compounds. *The Journal of Chemical Physics* **85**, 2895-2909 (1986).
31. Bino, A. A trinuclear niobium cluster with six bridging sulfates and metal to metal bond order of 2/3. *Inorganic Chemistry* **21**, 1917-1920 (1982).
32. Sorai, M. Calorimetric investigations of phase transitions in which electrons are directly involved. *Journal of Chemical Thermodynamics* **34**, 1207-1253 (2002).
33. Tsukerblat, B. Group-theoretical approaches in molecular magnetism: Metal clusters. *Inorganica Chimica Acta* **361**, 3746-3760 (2008).
34. Wu, Q.-L. L. *et al.* Divalent metal ions modulated strong frustrated $\text{M}(\text{II})\text{-Fe}(\text{III})_3\text{O}$ (M = Fe, Mn, Mg) chains with metamagnetism only in a mixed valence iron complex. *Chemical Communications* **51**, 15336-15339 (2015).
35. Catterick, J. & Thornton, P. Structures and Physical Properties of Polynuclear Carboxylates. in *Advances in Inorganic Chemistry and Radiochemistry* **20**, 291-362 (1977).
36. Mereacre, V. *et al.* Unusual metal-ligand charge transfer in ferrocene functionalized $\mu_3\text{-O}$ iron carboxylates observed with Mössbauer spectroscopy. *Journal of Magnetism and Magnetic Materials* **407**, 87-91 (2016).
37. Long, G. J., Robinson, W. T., Tappmeyer, W. P. & Bridges, D. L. The magnetic, electronic, and Mössbauer spectral properties of several trinuclear iron(III) carboxylate complexes. *J. Chem. Soc., Dalton Trans.* 573-579 (1973). doi:10.1039/DT9730000573
38. Yazdanbakhsh, M., Alizadeh, M. H., Khorramdel, H. Z. & Frank, W. Synthesis, Characterization and Crystal Structure of Novel Mixed Bridged Trinuclear Oxo-Centered Iron(III), Chromium(III) Complexes Containing Terminal Unsaturated Carboxylato and Acrylic Acid Dimer Anion Ligands. *Zeitschrift für anorganische und allgemeine Chemie* **633**, 1193-1198 (2007).
39. Högbom, M. & Nordlund, P. A protein carboxylate coordinated oxo-centered tri-nuclear iron complex with possible implications for ferritin mineralization. *FEBS Letters* **567**, 179-182 (2004).
40. Alexiou, A. *et al.* A Trinuclear Oxo-Chromium(III) Complex Containing the Natural Flavonoid Primuletin: Synthesis, Characterization, and Antiradical Properties. *Molecules* **20**, 6310-6318 (2015).
41. Lang, J., Mohrbach, J., Dillinger, S., Hewer, J. M. & Niedner-Schatteburg, G. Vibrational blue shift of coordinated N_2 in $[\text{Fe}_3\text{O}(\text{OAc})_6(\text{N}_2)_n]^+$: “non-classical” dinitrogen complexes. *Chemical Communications* **53**, 420-423 (2017).
42. Ciupa, A., Trzebiatowska-Gusowska, M. & Ptak, M. Vibrational properties of the mixed-valence iron oxo-complex. *Vibrational Spectroscopy* **86**, 218-222 (2016).
43. Ferey, G. A Chromium Terephthalate-Based Solid with Unusually Large Pore Volumes and Surface Area. *Science* **309**, 2040-2042 (2005).
44. Hong, K., Bak, W., Moon, D. & Chun, H. Bistable and porous metal-organic frameworks with charge-neutral acs net based on heterometallic $\text{M}_3\text{O}(\text{CO}_2)_6$ building blocks. *Crystal Growth and Design* **13**,

- 4066-4070 (2013).
45. Yaghi, O. M. *et al.* Reticular synthesis and the design of new materials. *Nature* **423**, 705-714 (2003).
46. Cotton, F. A., Duraj, S. A. & Roth, W. J. New bi-oxo-capped triangular trinuclear cluster compounds of niobium. *Journal of the American Chemical Society* **106**, 3527-3531 (1984).
47. Pineda, K. A., Fettingner, J. C. & Houston, J. R. Synthesis, structure, and substitution reactivity of a new bi-oxo capped molybdenum cluster: $[\text{Mo}_3(\mu_3\text{-O})_2(\mu\text{-O})_2\text{CCH}_2\text{Cl}]_6(\text{H}_2\text{O})_2(\text{OH})^+$. *Inorganic Chemistry Communications* **48**, 90-93 (2014).
48. Stephenson, T. A., Morehouse, S. M., Powell, A. R., Heffer, J. P. & Wilkinson, G. 667. Carboxylates of palladium, platinum, and rhodium, and their adducts. *Journal of the Chemical Society (Resumed)* 3632 (1965). doi:10.1039/jr9650003632
49. Skapski, A. C. & Smart, M. L. The Crystal Structure of Trimeric Palladium(II) Acetate. *Chemical Communications* 658-259 (1970).
50. West, B. O. Homonuclear and heteronuclear oxo-bridged compounds of the transition elements. *Polyhedron* **8**, 219-247 (1989).
51. Tsukerblat, B. S., Kuyavskaya, B. Y., Fainzilberg, V. E. & Belinskii, M. I. ESR spectra of trimeric heteronuclear clusters. II. Paramagnetic resonance of heteronuclear chromium and iron carboxylates. *Chemical Physics* **90**, 373-386 (1984).
52. Blake, A. B., Sinn, E., Yavari, A., Murray, K. S. & Moubaraki, B. Oxo-centred trinuclear acetate complexes containing mixed-metal clusters. Crystal structure of a chromium(III)iron(III)nickel(II) complex and magnetic properties of a dichromium(III)magnesium(II) complex ‡. *Journal of the Chemical Society, Dalton Transactions* 45-50 (1998). doi:10.1039/a705778d
53. Weinland, R. & Gussmann, E. Über Salze einer Acetatoferribase und zweier Acetatochromiferribasen. III. *Berichte der deutschen chemischen Gesellschaft* **42**, 3881-3894 (1909).
54. Werner, A. Zur Kenntnis der organischen Metallsalze. I. Mitteilung. Über ameisensaure und essigsäure Salze des Chroms. *Berichte der deutschen chemischen Gesellschaft* **41**, 3447-3465 (1908).
55. Weinland, R. & Engel, L. Über pyridinhaltige Ferriformiate. (Nebst einem Anhang über ein Ferrichlorid=(bromid=) Formiat. *Archiv der Pharmazie* **264**, 33-45 (1926).
56. Weinland, R. & Holtmeier, H. Über Ferri-nickel- usw. -acetate und über ein sehr basisches kristallisiertes Ferriacetat. *Zeitschrift für anorganische Chemie* **173**, 49-62 (1928).
57. Weinland, R. & Gußmann, E. Über eine Acetato-Pyridin-Eisenbase und über ein sehr basisches, pyridinhaltiges Ferriacetat. *Berichte der deutschen chemischen Gesellschaft* **43**, 2144-2149 (1910).
58. Weinland, R. F. & Gussmann, E. Über Salze einer Hexaacetato-tripyridin-trichrombase. *Zeitschrift für anorganische Chemie* **67**, 167-182 (1910).
59. Weinland, R. F. & Beck, C. Über komplexe, pyridinhaltige Acetato-ferri-Basen. *Zeitschrift für anorganische Chemie* **80**, 402-447 (1913).
60. Starke, K. Remarks on the trinuclear acetato complexes of iron(III), chromium(III) and aluminium. *Journal of Inorganic and Nuclear Chemistry* **13**, 254-260 (1960).
61. Orgel, L. E. Structure of the Trinuclear Basic Acetates. *Nature* **187**, 504-505 (1960).
62. Kim, Y. H. Basic iron (III) alkanoate complexes. (Missouri University, 1967).
63. Głowiak, T., Kubiak, M., Szymańska-Buzar, T. & Jezowska-Trzebiatowska, B. Crystal and molecular structure of the trinuclear chromium(III) and iron(III) complex, $[\text{Cr}_2\text{FeO}(\text{CH}_3\text{COO})_6(\text{H}_2\text{O})_3][\text{NO}_3]\cdot\text{CH}_3\text{COOH}$. *Acta Crystallographica Section B Structural Crystallography and Crystal Chemistry* **33**, 3106-3109 (1977).
64. Figgis, B. N. & Robertson, G. B. Crystal-Molecular Structure and Magnetic Properties of $\text{Cr}_3(\text{CH}_3\text{COO})_6\text{OCl}\cdot 5\text{H}_2\text{O}$. *Nature* **205**, 694-695 (1965).
65. Earnshaw, A., Figgis, B. N. & Lewis, J. Chemistry of polynuclear compounds. Part VI. Magnetic properties of trimeric chromium and iron carboxylates. *Journal of the Chemical Society A: Inorganic, Physical, Theoretical* 1656 (1966). doi:10.1039/j19660001656
66. Chang, S. C. & Jeffrey, G. A. The crystal structure of a basic chromium acetate compound, $[\text{OCr}_3(\text{CH}_3\text{COO})_6\cdot 3\text{H}_2\text{O}]\cdot\text{Cl}\cdot 6\text{H}_2\text{O}$, having feeble paramagnetism. *Acta Crystallographica Section B Structural Crystallography and Crystal Chemistry* **26**, 673-683 (1970).
67. Clegg, W., Lam, O. M. & Straughan, B. P. Crystal Structure of $[\text{FeCr}_2(\mu_3\text{-O})(\text{CH}_3\text{COO})_6(\text{H}_2\text{O})_3][\text{FeCl}_4]\cdot 2(\text{CH}_3)_2\text{CO}\cdot\text{CH}_3\text{OH}$. *Inorganica Chimica Acta* **90**, 75-76 (1984).
68. Clegg, W., Lam, O. M. & Straughan, B. P. Structure of a Novel m_3 -Oxo- $\text{Fe}^{\text{II}}\text{Cr}^{\text{III}}$ -Glycine Complex.

- Angew. Chem. Int. Ed. Engl.* **23**, 434-435 (1984).
69. Vincent, J. B. Heterotrimeric Carboxylates of Chromium(III) and Iron(III): Mixtures or Pure Compounds? *Inorganic Chemistry* **33**, 5604-5606 (1994).
 70. Welo, L. A. XLIX. Magnetic studies on salts, with particular reference to those with complex ions. *The London, Edinburgh, and Dublin Philosophical Magazine and Journal of Science* **6**, 481-509 (1928).
 71. Kambe, K. On the Paramagnetic Susceptibilities of Some Polynuclear Complex Salts. *Journal of the Physical Society of Japan* **5**, 48-51 (1950).
 72. Gijsman, H. M., Karantassis, T. & Wucher, J. Propriétés thermomagnétiques de l'acétate complexe mixte $[\text{Cr}_2\text{Fe}(\text{CH}_3\text{COO})_6(\text{OH})_2]\text{Cl}\cdot 6\text{H}_2\text{O}$. *Physica* **20**, 367-371 (1954).
 73. Belinskii, M. I., Tsukerblat, B. S. & Ablov, A. V. E.S.R. spectra and hyperfine structure of symmetric trinuclear clusters. *Molecular Physics* **28**, 283-291 (1974).
 74. Blake, A. B., Yavari, A., Hatfield, W. E. & Sethulekshmi, C. N. Magnetic and spectroscopic properties of some heterotrimeric basic acetates of chromium(III), iron(III), and divalent metal ions. *Journal of the Chemical Society, Dalton Transactions* 2509 (1985). doi:10.1039/dt9850002509
 75. Honda, M., Morita, M. & Date, M. Electron Spin Resonance in Cr-Trimer Complexes. *Journal of the Physical Society of Japan* **61**, 3773-3785 (1992).
 76. Honda, M. Effect of Dzyaloshinsky-Moriya Interaction on the High Field Magnetization of Cr-Trimer Complexes. *Journal of the Physical Society of Japan* **62**, 1818-1818 (1993).
 77. Jayasooriya, U. A. *et al.* Exchange interactions in trinuclear basic chromium(III) clusters: Direct observation of the magnetic spectrum by inelastic neutron scattering. *The Journal of Chemical Physics* **98**, 9303-9310 (1993).
 78. Sowrey, F. E. *et al.* Spin frustration and concealed asymmetry: structure and magnetic spectrum of $[\text{Fe}_3\text{O}(\text{O}_2\text{CPh})_6(\text{py})_3]\text{ClO}_4\cdot\text{py}$. *Journal of the Chemical Society, Dalton Transactions* **6**, 862-866 (2001).
 79. Cannon, R. D. *et al.* Spin Frustration in High-Spin Triiron(III) Complexes: An Inelastic Neutron Scattering Study. *Journal of the American Chemical Society* **116**, 11869-11874 (1994).
 80. Yablokov, Gaponenko, V. A., Eremin, M. V., Zelentsov, V. V. & Zhemchuzhnikova, T. A. Paramagnetic Resonance of Mixed Triads of Chromium and Iron. *JETP Letters* **17**, 146 (1973).
 81. Yabloko, Y. V., Gaponenko, V. A., Eremin, M. V., Zelentsov, V. V. & Zhemchuzhnikova, T. A. Paramagnetic resonance of mixed chromium and iron triads. *Sov. Phys.-JETP* **38**, 988-990 (1983).
 82. Rakitin, Y. V., Zhemchuzhnikova, T. A. & Zelentsov, V. V. Magnetic susceptibility of trinuclear chromium(III) and iron(III) monochloroacetates in the temperature range 1.6 to 300 °K. *Inorganica Chimica Acta* **23**, 145-148 (1977).
 83. Nakano, M., Wakamatsu, T., Sorai, M. & Suga, H. Cluster pairing in the paramagnetic trinuclear complex compound $[\text{Cr}_3\text{O}(\text{CH}_3\text{COO})_6(\text{H}_2\text{O})_3]\text{Cl}\cdot 6\text{H}_2\text{O}$: Calorimetric study at very low temperatures. *Journal of Physics and Chemistry of Solids* **49**, 987-992 (1988).
 84. Sorai, M., Tachiki, M., Suga, H. & Seki, S. Magnetic and Thermal Properties of Crystals Including Isolated Clusters. I. Heat Capacity and Infrared Spectrum of $[\text{Cr}_3\text{O}(\text{CH}_3\text{COO})_6(\text{H}_2\text{O})_3]\text{Cl}\cdot 6\text{H}_2\text{O}$ Crystal between 1.5 and 280 K. *Journal of the Physical Society of Japan* **30**, 750-759 (1971).
 85. Yoshimasa, T., Yasuyuki, T., Takashima, Y. & Tateishi, Y. Mossbauer Spectra of Various Organic Iron Chelates. *Bulletin of the Chemical Society of Japan* **38**, 1688-1693 (1965).
 86. Bates, C. A. & Jasper, R. F. The properties of exchange-coupled triads of Cr³⁺ ions in ruby. *Journal of Physics C: Solid State Physics* **4**, 2330-2340 (1971).
 87. Qi, X.-Y. *et al.* Crystal Structure and Spin Frustration Behavior of an Oxo-centered Trinuclear Chromium(III) Complex. *Journal of the Chinese Chemical Society* **63**, 985-990 (2016).
 88. Figuerola, A. *et al.* Synthesis, crystal structure, and magnetic studies of oxo-centered trinuclear chromium(III) complexes: $[\text{Cr}_3(\mu_3\text{-O})(\mu_2\text{-PhCOO})_6(\text{H}_2\text{O})_3]\text{NO}_3\cdot 4\text{H}_2\text{O}\cdot 2\text{CH}_3\text{OH}$, a case of spin-frustrated system, and... *Inorganic Chemistry* **46**, 11017-11024 (2007).
 89. Gavrilenko, K. S., Addison, A., Thompson, L. & Pavlishchuk, V. V. Magnetic Characteristics of Trinuclear Complexes $[\text{M}_3\text{O}(\text{CH}_3\text{COO})_6(\text{pz})_3] + (\text{M} = \text{Fe}, \text{Cr}; \text{pz} = \text{Pyrazine})$. *Theoretical and Experimental Chemistry* **40**, 214-219 (2004).
 90. Griffith, W. P. Tri- and tetra-nuclear oxy-complexes. *Journal of the Chemical Society A: Inorganic, Physical, Theoretical* 2270 (1969). doi:10.1039/j19690002270
 91. Straughan, B. P. & Lam, O. M. Preparations and structures of some Tris(aquo)-hexa- μ -glycinato- μ_3 -oxo complexes, $[\text{Cr}_3\text{Fe}_{3-n}(\mu_3\text{-O})(\text{glycine})_6(\text{H}_2\text{O})_3](\text{NO}_3)_7\cdot x\text{H}_2\text{O}$. *Inorganica Chimica Acta* **98**, 7-10

- (1985).
92. Dubicki, L. & Martin, R. The ligand field spectra of trinuclear chromium(III) and iron(III) basic acetates. *Australian Journal of Chemistry* **22**, 701 (1969).
93. Ferguson, J. & Güdel, H. U. Spectroscopic study of the trinuclear complex salt $[\text{Cr}_3\text{O}(\text{CH}_3\text{COO})_6(\text{H}_2\text{O})_3]\text{Cl}\cdot 6\text{H}_2\text{O}$. *Chemical Physics Letters* **17**, 547-550 (1972).
94. Dubicki, L. & Day, P. Electronic spectrum of trinuclear chromium(III) acetate. *Inorganic Chemistry* **11**, 1868-1875 (1972).
95. Morita, M. & Kato, Y. N₂ Laser excited luminescence of antiferromagnetically coupled trinuclear chromium(III) complexes. *International Journal of Quantum Chemistry* **18**, 625-631 (1980).
96. Purl, R. N., Asplund, R. O. & Tucker, W. F. The CD Spectra of Tri-1 3 -0x0-Triaquohexakis (Perchlorates G Amino Acid) triiron (III). *Sciences-New York* **66**, 7-11 (1982).
97. Cannon, R. D. & White, R. P. Chemical and Physical Properties of Triangular Bridged Metal Complexes. in *Progress in Inorganic Chemistry* (ed. Lippard, S. J.) **36**, 195-298 (John Wiley & Sons, Inc., 1988).
98. Müller, A., Jostes, R. & Cotton, F. A. Trinuclear Clusters of the Early Transition Elements. *Angewandte Chemie International Edition in English* **19**, 875-882 (1980).
99. Meesuk, L., Jayasooriya, U. A. & Cannon, R. D. Vibrational spectra of carboxylato complexes—VI. Isotopic substitution in the mixed-metal trinuclear complexes $[\text{Fe}^{\text{III}}_2\text{Ni}^{\text{II}}\text{O}(\text{OOCCH}_3)_6\text{L}_3]$. *Spectrochimica Acta Part A: Molecular Spectroscopy* **43**, 687-692 (1987).
100. Anson, C. E. *et al.* Crystal structures of the isomorphous prototypic oxo-centered trinuclear complexes $[\text{Cr}_3\text{O}(\text{OOCCH}_3)_6(\text{H}_2\text{O})_3]\text{Cl}$ center dot $6\text{H}_2\text{O}$ and $[\text{Fe}_3\text{O}(\text{OOCCH}_3)_6(\text{H}_2\text{O})_3]\text{Cl}$ center dot $6\text{H}_2\text{O}$. *Inorganic Chemistry* **36**, 1265- (1997).
101. Johnson, M. K., Powell, D. B. & Cannon, R. D. Vibrational spectra of carboxylato complexes—I. Infrared and Raman spectra of beryllium(II) acetate and formate and of zinc(II) acetate and zinc(II) acetate dihydrate. *Spectrochimica Acta Part A: Molecular Spectroscopy* **37**, 899-904 (1981).
102. Johnson, M. K., Powell, D. B. & Cannon, R. D. Vibrational spectra of carboxylato complexes—II. Some oxo-tetranuclear complexes. *Spectrochimica Acta Part A: Molecular Spectroscopy* **38**, 125-131 (1982).
103. Johnson, M. K., Powell, D. B. & Cannon, R. D. Vibrational spectra of carboxylato complexes—III. Trinuclear 'basic' acetates and formates of chromium(III), iron(III) and other transition metals. *Spectrochimica Acta Part A: Molecular Spectroscopy* **37**, 995-1006 (1981).
104. Johnson, M. K., Cannon, R. D. & Powell, D. B. Vibrational spectra of carboxylato complexes—IV. Mixed-metal and mixed-valence oxo-trinuclear complexes. *Spectrochimica Acta Part A: Molecular Spectroscopy* **38**, 307-315 (1982).
105. Montri, L. & Cannon, R. D. Vibrational spectra of carboxylato complexes—V. Vibrations of the bridging oxide ion in the trinuclear complex $[\text{Fe}_3\text{O}(\text{OOCCH}_3)_6(\text{C}_5\text{H}_5\text{N})_3]^+$. *Spectrochimica Acta Part A: Molecular Spectroscopy* **41**, 643-646 (1985).
106. Lin, F., Zhang, Z., Zheng, L. & Jiang, A. 含 $\mu_3\text{-O}$ 三核混合铁锤醋酸配合物的骨架振动和简正坐标分析. *Acta Chimica Sinica* **49**, 1078-1084 (1991).
107. Zhang, L.-N., Liu, Z.-P., He, L.-J., Cai, S.-H. & Jian, F.-Y. Infrared spectra and normal coordinate analysis of trinuclear $\mu_3\text{-oxoacetato}$ complexes of chromium and iron. *Acta Chimica Sinica* **7**, 219-228 (1989).
108. Ellis, T. *et al.* Synthetic Models for Low-Molecular-Weight Chromium-Binding Substance: Synthesis and Characterization of Oxo-Bridged Tetranuclear Chromium(III) Assemblies. *Inorganic Chemistry* **33**, 5522-5527 (1994).
109. Harton, A. *et al.* Synthesis and characterization of symmetric and unsymmetric oxo-bridged trinuclear chromium benzoate complexes: Crystal and molecular structure of $[\text{Cr}_3\text{O}(\text{O}_2\text{CPh})_6(\text{py})_3]\text{ClO}_4$. *Inorganica Chimica Acta* **217**, 171-179 (1994).
110. Tadros, A. M. *et al.* Aminopyridine complexes of Cr(III) basic carboxylates as potential polymer precursors: Synthesis, characterization, and crystal structure of $[\text{Cr}_3\text{O}(\text{propionate})_6(\text{X-aminopyridine})_3]^+$ (X=3 or 4). *Polyhedron* **100**, 17-27 (2015).
111. Schloter, K., Nagel, U. & Beck, W. Paramagnetic ¹⁹F NMR and electrospray ionization mass spectrometric studies of substituted pyridine complexes of chromium(III): Models for potential use of ¹⁹F NMR to probe Cr(III)–nucleotide interaction. *Chemische Berichte* **113**, 3775-3782 (1980).
112. Royer, A. C., Russell, K., Belmore, K. & Vincent, J. B. Formation of oxo-centered trinuclear chromium

- carboxylate complexes and hydrolysis of Cr³⁺ as established by paramagnetic ²H NMR spectroscopy. *Journal of Inorganic Biochemistry* **131**, 12-20 (2014).
113. Sun, Y., Mallya, K., Ramirez, J. & Vincent, J. B. The biomimetic [Cr₃O(O₂CCH₂CH₃)₆(H₂O)₃]⁺ decreases plasma cholesterol and triglycerides in rats: towards chromium-containing therapeutics. *JBIC Journal of Biological Inorganic Chemistry* **4**, 838-845 (1999).
 114. Vincent, J. B. Elucidating a Biological Role for Chromium at a Molecular Level. *Accounts of Chemical Research* **33**, 503-510 (2000).
 115. Botezat, O. *et al.* Synthesis, crystal structure, and properties of a μ₃-oxo-trichromium(III) propionate cluster with pyrazole. *Journal of Coordination Chemistry* **69**, 72-80 (2016).
 116. Ito, S., Inoue, K. & Mastumoto, M. [Fe₃O(OCOR)₆L₃]⁺-catalyzed epoxidation of olefinic alcohol acetates by molecular oxygen. *Journal of the American Chemical Society* **104**, 6450-6452 (1982).
 117. Blake, A. B. & Yavari, A. Heterotrinnuclear basic acetates containing chromium(III), iron(III), and a divalent metal: spectroscopic consequences of Metal–Metal interactions. *J. Chem. Soc., Chem. Commun.* 1247-1249 (1982). doi:10.1039/C39820001247
 118. Jiang, Y., Tang, A., Hoffmann, R., Huang, J. & Lu, J. Trinuclear Clusters of Early Transition Metals: Jahn-Teller Distortions and Electronic Structure. *Organometallics* **4**, 27-34 (1985).
 119. Choi, K.-Y. *et al.* Observation of a half step magnetization in the {Cu₃}-type triangular spin ring. *Physical Review Letters* **96**, 107202 (2006).
 120. Powell, G. & Richens, D. T. Complex formation and water exchange on the trinuclear dioxo-capped complexes [M₃(μ₃-O)₂(μ₂-CH₃CO₂)₆(OH₂)₃]²⁺ (M = molybdenum, tungsten) and monooxo-capped complex [W₃(μ₃-O)(μ₂-CH₃CO₂)₆(OH₂)₃]²⁺. *Inorganic Chemistry* **32**, 4021-4029 (1993).
 121. Kiana, S., Yazdanbakhsh, M., Jamialahmadi, M. & Tayyari, S. F. Vibrational assignment and structure of trinuclear oxo-centered of basic formate iron(III) and chromium(III) complexes: A density functional theory study. *Spectrochimica Acta Part A: Molecular and Biomolecular Spectroscopy* **130**, 287-294 (2014).
 122. Yazdanbakhsh, M., Lotfian, N., Tavakkoli, H. & Boese, R. Synthesis, characterization and crystal structure analysis of a novel oxo-centered mixed-metal complex containing unsaturated bridging carboxylates. *Open Chemistry* **9**, 585-589 (2011).
 123. Yazdanbakhsh, M., Khosravi, I. & Tavakkoli, H. Synthesis and characterization of novel oxo-bridged, trinuclear mixed-metal complexes of Cr(III) and Fe(III). *Journal of the Serbian Chemical Society* **74**, 401-406 (2009).
 124. Yazdanbakhsh, M., Tavakkoli, H., Taherzadeh, M. & Boese, R. Synthesis, X-ray crystal structure and spectroscopic characterization of heterotrinnuclear oxo-centered complex [Fe₂NiO(CH₃CH₂COO)₆(H₂O)₃]. *Journal of Molecular Structure* **982**, 176-180 (2010).
 125. Yazdanbakhsh, M., Lotfian, N. & Tavakkoli, H. Synthesis and characterization of two novel trinuclear oxo-centered, of chromium and iron complexes containing unsaturated carboxylate bridging ligand. *Bulletin of the Chemical Society of Ethiopia* **23**, 463-466 (2009).
 126. Chaudhary, S. & Van Horn, J. D. Breakdown kinetics of the tri-chromium(III) oxo acetate cluster ([Cr₃O(OAc)₆]⁺) with some ligands of biological interest. *Journal of Inorganic Biochemistry* **101**, 329-335 (2007).
 127. Das, S. K., Mahanta, S. P. & Bania, K. K. Oxidative coupling of 2-naphthol by zeolite-Y supported homo and heterometallic trinuclear acetate clusters. *RSC Adv.* **4**, 51496-51509 (2014).
 128. Stride, J. A., Jayasooriya, U. A. & Eckert, J. Dynamics of Ligated Water Molecules in Oxo-Centered Trinuclear Carboxylates: An Incoherent Inelastic Neutron Scattering Study. *Angewandte Chemie International Edition* **38**, 116-121 (1999).
 129. Lutz, H. D. Dynamik von Liganden-Wassermolekülen in dreikernigen Carboxylatkomplexen. *Angewandte Chemie* **111**, 3855-3855 (1999).
 130. McCusker, J. K., Jang, H. G., Wang, S., Christou, G. & Hendrickson, D. N. Ground-state variability in μ₃-oxide trinuclear mixed-valence manganese complexes: spin frustration. *Inorganic Chemistry* **31**, 1874-1880 (1992).
 131. Sumner, C. E. & Steinmetz, G. R. Isolation of oxo-centered cobalt(III) clusters and their role in the cobalt bromide catalyzed autoxidation of aromatic hydrocarbons. *Journal of the American Chemical Society* **107**, 6124-6126 (1985).
 132. Wang, J. *et al.* Syntheses and structure of three 2D polyoxometalates derived from macrocation [Cr₃O(COOH)₆(H₂O)₃]⁺ and α-Keggin-type polyoxomolybdate anions. *Journal of Molecular Structure*

- 1011**, 1-7 (2012).
133. Lang, J. *et al.* Magnetostructural correlation in isolated trinuclear iron(III) oxo acetate complexes. *Physical Chemistry Chemical Physics* **20**, 16673-16685 (2018).
 134. Lang, J., Fries, D. V. & Niedner-Schatteburg, G. Characterization of Trinuclear Oxo Bridged Cobalt Complexes in Isolation. *Zeitschrift für Physikalische Chemie* **232**, 649-669 (2018).
 135. Lang, J. Characterization of Structures Fragmentation Pathways and Magnetism of Mononuclear and Oligonuclear Transition Metal Complexes in Isolation. (TU Kaiserslautern, 2017).
 136. Yutkin, M. P. *et al.* Synthesis, structure and magnetic behavior of new 1D metal-organic coordination polymer with Fe₃O core. *Inorganica Chimica Acta* **365**, 513-516 (2011).
 137. Ruiz, E., Cano, J., Alvarez, S. & Alemany, P. Broken symmetry approach to calculation of exchange coupling constants for homobinuclear and heterobinuclear transition metal complexes. *Journal of Computational Chemistry* **20**, 1391-1400 (1999).
 138. Psycharis, V. *et al.* Syntheses, Structural, and Physical Studies of Basic Cr(III) and Fe(III) Benzilates and Benzoates: Evidence of Antisymmetric Exchange and Distributions of Isotropic and Antisymmetric Exchange Parameters. *European Journal of Inorganic Chemistry* **2006**, 3710-3723 (2006).
 139. Vlachos, A. *et al.* A nearly symmetric trinuclear chromium(III) oxo carboxylate assembly: preparation, molecular and crystal structure, and magnetic properties of [Cr₃O(O₂CPh)₆(MeOH)₃](NO₃)·2MeOH. *Inorganica Chimica Acta* **357**, 3162-3172 (2004).
 140. Sanakis, Y., Boudalis, A. K. & Tuchagues, J.-P. J-strain and antisymmetric exchange in a polynuclear compound containing the {Fe₃O}⁷⁺ core. *Comptes Rendus Chimie* **10**, 116-124 (2007).
 141. Boudalis, A., Robert, J. & Turek, P. First Demonstration of Magnetoelectric Coupling in a Polynuclear Molecular Nanomagnet: Single-Crystal EPR studies of [Fe₃O(O₂CPh)₆(py)₃](ClO₄)*py under static electric fields. *Chemistry - A European Journal* 1-6 (2018). doi:10.1002/chem.201803038
 142. Boudalis, A. K., Sanakis, Y., Dahan, F., Hendrich, M. & Tuchagues, J. P. An octanuclear complex containing the [Fe₃O]⁷⁺ metal core: structural, magnetic, Mossbauer, and electron paramagnetic resonance studies. *Inorg Chem* **45**, 443-453 (2006).
 143. Alborés, P., Plenck, C. & Rentschler, E. Tailoring the exchange interaction in covalently linked basic carboxylate clusters through bridging ligand selection. *Inorganic Chemistry* **51**, 8373-8384 (2012).
 144. Frock, L. R. Synthesis and Electrodeposition of Mixed Metal Trinuclear Clusters of Molybdenum and Chromium in Ionic Liquid onto a Platinum Electrode. (Wright State University, 2013).
 145. Corradini, V. *et al.* Oxo-centered carboxylate-bridged trinuclear complexes deposited on Au(111) by a mass-selective electrospray. *New Journal of Chemistry* **35**, 1683 (2011).
 146. Eshel, M. *et al.* Polynuclear Chromium(III) Carboxylates. 1. Synthesis, Structure, and Magnetic Properties of an Octanuclear Complex with a Ring Structure. *Inorganic Chemistry* **39**, 1376-1380 (2000).
 147. Eshel, M. & Bino, A. Polynuclear chromium(III) carboxylates. *Inorganica Chimica Acta* **320**, 127-132 (2001).
 148. Eshel, M. & Bino, A. Polynuclear chromium(III) carboxylates. 3. Cyclic and cubane type hexachromium acetates. *Inorganica Chimica Acta* **329**, 45-50 (2002).
 149. Filoti, G. *et al.* Intermediate frustration in [Fe₃O(CH₃COO)₆(H₂O)₃] NO₃ · 4(H₂O) trinuclear cluster. *Journal of Magnetism and Magnetic Materials* **196-197**, 561-563 (1999).
 150. Gorun, S. M., Papaefthymiou, G. C., Frankel, R. B. & Lippard, S. J. Synthesis, structure, and magnetic and Moessbauer properties of mononuclear and asymmetric, oxo-bridged trinuclear iron(III) complexes of a new polyimidazole ligand. *Journal of the American Chemical Society* **109**, 4244-4255 (1987).
 151. Stamatatos, T. C. *et al.* "Switching On" the Properties of Single-Molecule Magnetism in Triangular Manganese(III) Complexes. *Journal of the American Chemical Society* **129**, 9484-9499 (2007).
 152. Inglis, R., Milios, C. J., Jones, L. F., Piligkos, S. & Brechin, E. K. Twisted molecular magnets. *Chem. Commun.* **48**, 181-190 (2012).
 153. Nguyen, T. N. *et al.* Covalently Linked Dimer of Mn 3 Single-Molecule Magnets and Retention of Its Structure and Quantum Properties in Solution. *Journal of the American Chemical Society* **137**, 7160-7168 (2015).
 154. Rakitin, Y. V., Kalinnikov, V. T. & Novotortsev, V. M. Jahn-Teller effect in trigonal μ-oxoclusters. *Russian Chemical Bulletin* **53**, 2478-2484 (2004).
 155. Rakitin, Y. ., Yablokov, Y. . & Zelentsov, V. . EPR spectra of trigonal clusters. *Journal of Magnetic Resonance (1969)* **43**, 288-301 (1981).

156. Fischer, A. I., Panina, N. S. & Belyaev, A. N. The structural organization of oligonuclear cobalt(II, III) and cobalt(III) carboxylates. *Russian Journal of Coordination Chemistry* **42**, 635-646 (2016).
157. Fisher, A. I. *et al.* The first example of cobalt(III) μ -oxoacetate with water molecules in apical positions. *Russian Journal of General Chemistry* **78**, 2006-2012 (2008).
158. Gavrilenko, K. S. *et al.* Synthesis, Magnetochemistry, and Spectroscopy of Heterometallic Trinuclear Basic Trifluoroacetates $[\text{Fe}_2\text{M}(\mu_3\text{-O})(\text{CF}_3\text{COO})_6(\text{H}_2\text{O})_3] \cdot \text{H}_2\text{O}$ (M = Mn, Co, Ni). *European Journal of Inorganic Chemistry* **2002**, 3347-3355 (2002).
159. Kochur, A. G. *et al.* Effect of the Structure of Carboxylate Ligands on the X-Ray Photoelectron Spectral Parameters of Trinuclear Heterometallic Complexes $[\text{Fe}_2\text{MO}(\text{O}_2\text{CR})_6(\text{H}_2\text{O})_3](\text{H}_2\text{O})_3$ (M = Co, Ni; R = CH₃, CCl₃). *Theoretical and Experimental Chemistry* **52**, 252-258 (2016).
160. Schloter, K., Nagel, U. & Beck, W. Synthesis, structure and properties of heterotrinuclear carboxylate complexes $[\text{Fe}_2\text{M}(\text{Ca}, \text{Sr}, \text{Ba})\text{O}(\text{CCl}_3\text{COO})_6(\text{THF})_n]$. *Chemische Berichte* **113**, 3775-3782 (1980).
161. Dong, J., Liu, B. & Yang, B. Synthesis, crystal structure and magnetic properties of trinuclear chromium(III) basic carboxylate assembly: $[\text{Cr}_3\text{O}(\text{salH})_7(\text{H}_2\text{O})_2]$ (salH₂=salicylic acid), a new member of $[\text{Cr}_3\text{O}]$ family. *Journal of Molecular Structure* **1116**, 311-316 (2016).
162. Tackett, J. E. Hydrolyzed Polyacrylamide/Chromium(III) Acetate Gel Chemistry. *Applied Spectroscopy* **45**, 1674-1678 (1991).
163. Vargas-Vasquez, S. M. & Romero-Zerón, L. B. A Review of the Partly Hydrolyzed Polyacrylamide Cr(III) Acetate Polymer Gels. *Petroleum Science and Technology* **26**, 481-498 (2008).
164. Kapoor, R., Kapoor, P. & Sharma, R. Reactions of Chromyl Chloride with Carboxylic Acids and Carboxylic Acid Anhydrides. *Zeitschrift für Naturforschung B* **40**, 247-250 (1985).
165. Sotnik, S. A. *et al.* Heterometallic Coordination Polymers Assembled from Trigonal Trinuclear Fe 2 Ni-Pivalate Blocks and Polypyridine Spacers: Topological Diversity, Sorption, and Catalytic Properties. *Inorganic Chemistry* **54**, 5169-5181 (2015).
166. Kongpatpanich, K. *et al.* Synthesis and Porous Properties of Chromium Azolate Porous Coordination Polymers. *Inorganic Chemistry* **53**, 9870-9875 (2014).
167. Vargas-Vasquez, S. M., Romero-Zerón, L. B. & MacMillan, B. Characterization of Cr(II) and Cr(III) Acetate Aqueous Solutions Using UV-vis Spectrophotometry and ¹H NMR. *Chemical Engineering Communications* **197**, 491-505 (2009).
168. Laurikėnas, A. *et al.* Formation peculiarities of iron (III) acetate: potential precursor for iron metal-organic frameworks (MOFs). *Lithuanian Journal of Physics* **56**, 35-41 (2016).
169. Kluchova, K. *et al.* Superparamagnetic maghemite nanoparticles from solid-state synthesis – Their functionalization towards peroral MRI contrast agent and magnetic carrier for trypsin immobilization. *Biomaterials* **30**, 2855-2863 (2009).
170. Seo, J. S. *et al.* A homochiral metal-organic porous material for enantioselective separation and catalysis. *Nature* **404**, 982-986 (2000).
171. Uchida, S. & Mizuno, N. Selective Adsorption of Water. *Journal of the American Chemical Society* **126**, 1602-1603 (2004).
172. Uchida, S., Hashimoto, M. & Mizuno, N. A Breathing Ionic Crystal Displaying Selective Binding of Small Alcohols and Nitriles: $\text{K}_3[\text{Cr}_3\text{O}(\text{OOCH})_6(\text{H}_2\text{O})_3][\text{-SiW}_{12}\text{O}_{40}] \cdot 16 \text{H}_2\text{O}$. *Angewandte Chemie International Edition* **41**, 2814-2817 (2002).
173. Uchida, S. & Mizuno, N. Unique Guest-Inclusion Properties of a Breathing Ionic Crystal of $\text{K}_3[\text{Cr}_3\text{O}(\text{OOCH})_6(\text{H}_2\text{O})_3][\alpha\text{-SiW}_{12}\text{O}_{40}] \cdot 16 \text{H}_2\text{O}$. *Chemistry - A European Journal* **9**, 5850-5857 (2003).
174. Lu, M. *et al.* A new μ_3 -oxo-centered tri-nuclear carboxyl bridged iron (III) complex with thio-methyl groups in the periphery: Structural, spectroscopic and electrochemical studies. *Journal of Molecular Structure* **1060**, 131-137 (2014).
175. Chen, J.-L., Zhang, L.-Y., Shi, L.-X., Ye, H.-Y. & Chen, Z.-N. Syntheses, characterization and redox properties of di- and poly-phosphine linked oligomeric complexes of oxo-centered triruthenium clusters. *Inorganica Chimica Acta* **359**, 1531-1540 (2006).
176. Wilson, S. T., Bondurant, R. F., Meyer, T. J. & Salmon, D. J. Oxidation state properties of delocalized, ligand-bridged metal complexes. $[\text{Ru}_3\text{O}(\text{CH}_3\text{CO}_2)_6\text{L}_3]^{n+}$ and the pyrazine-bridged, cluster-cluster dimer, $[\text{Ru}_3\text{O}(\text{CH}_3\text{CO}_2)_6(\text{py})_2]_2\text{pyzm}^+$. *Journal of the American Chemical Society* **97**, 2285-2287 (1975).
177. Feng, M., Zhang, P., Zhou, H. C. & Sharma, V. K. Water-stable metal-organic frameworks for aqueous

- removal of heavy metals and radionuclides: A review. *Chemosphere* **209**, 783-800 (2018).
178. Férey, G. *et al.* Hydrogen adsorption in the nanoporous metal-benzenedicarboxylate $M(OH)(O_2C-C_6H_4-CO_2)$ ($M = Al^{3+}, Cr^{3+}$), MIL-53. *Chemical Communications* **9**, 2976-2977 (2003).
179. Férey, G. *et al.* A hybrid solid with giant pores prepared by a combination of targeted chemistry, simulation, and powder diffraction. *Angewandte Chemie - International Edition* **43**, 6296-6301 (2004).
180. Hupp, J. T. CHEMISTRY: Enhanced: Better Living Through Nanopore Chemistry. *Science* **309**, 2008-2009 (2005).
181. Low, J. J., Jakubczak, P., Abrahamian, J. F., Faheem, S. A. & Willis, R. R. Virtual High Throughput Screening Confirmed Experimentally: Porous Coordination Polymer Hydration. 15834-15842 (2009). doi:10.1021/ja9061344
182. Sumner, C. E., Little, J., Howard, A. S. & Liang, W. C. Thermal Decomposition of Pyridine-Substituted Cobaltic Acetate in Acetic Acid. *Inorganic Chemistry* **49**, 4606-4610 (2010).
183. Gan, S. Modified chromium(III) acetate used in the polymerization of α -olefins. *Journal of Catalysis* **105**, 249-253 (1987).
184. Weiwen, X. *et al.* In Situ IR Study of the Reaction Behavior of $[Cr_3(\mu_3-O)(\mu-O)_2(CH)_6(H_2O)_2(O_2CH)] \cdot xH_2O$ and its Active Fragments for the Addition Reaction of Acetylene. *Applied Spectroscopy* **47**, 1183-1186 (1993).
185. Váňa, J., Hanusek, J. & Sedlák, M. Bi and trinuclear complexes in palladium carboxylate-assisted C-H activation reactions. *Dalton Transactions* **47**, 1378-1382 (2018).
186. Carole, W. A. & Colacot, T. J. Understanding Palladium Acetate from a User Perspective. *Chemistry - A European Journal* **22**, 7686-7695 (2016).
187. Sumner, C. E. & Steinmetz, G. R. Synthesis and reactivity of alkoxide-bridged cobaltic acetates. *Inorganic Chemistry* **28**, 4290-4294 (1989).
188. Lippard, S. J. Oxo-Bridged Polyiron Centers in Biology and Chemistry. *Angewandte Chemie International Edition in English* **27**, 344-361 (1988).
189. Vincent, J. B. Beneficial Effects of Chromium(III) and Vanadium Supplements in Diabetes. in *Nutritional and Therapeutic Interventions for Diabetes and Metabolic Syndrome* 365-374 (Elsevier, 2018). doi:10.1016/B978-0-12-812019-4.00029-5
190. Davis, C. M., Royer, A. C. & Vincent, J. B. Synthetic Multinuclear Chromium Assembly Activates Insulin Receptor Kinase Activity: Functional Model for Low-Molecular-Weight Chromium-Binding Substance. *Inorganic Chemistry* **36**, 5316-5320 (1997).
191. Jiang, L., Vincent, J. B. & Bailey, M. M. $[Cr_3O(O_2CCH_2CH_3)_6(H_2O)_3]NO_3 \cdot H_2O$ (Cr_3) Toxicity Potential in Bacterial and Mammalian Cells. *Biological Trace Element Research* **183**, 342-350 (2018).
192. Botezat, O. *et al.* Synthesis, crystal structure, and properties of a 3-oxo-trichromium(III) propionate cluster with pyrazole. *Journal of Coordination Chemistry* **69**, 72-80 (2016).
193. Langenberg, A. *et al.* Spin and orbital magnetic moments of size-selected iron, cobalt, and nickel clusters. *Physical Review B* **90**, 184420 (2014).
194. Sato, T. & Ambe, F. An Oxo-Centered Trinuclear Cobalt(II)-Diron(III) Acetate-Aqua Complex. *Acta Crystallographica Section C Crystal Structure Communications* **52**, 3005-3007 (1996).
195. Sumner, C. E. Interconversion of dinuclear and oxo-centered trinuclear cobaltic acetates. *Inorganic Chemistry* **27**, 1320-1327 (1988).
196. Beattie, J. K., Klepetko, J. A., Masters, A. F. & Turner, P. The chemistry of cobalt acetate. VIII. New members of the family of oxo-centred trimers, $[Co_3(\mu_3-O)(\mu-O_2CCH_3)_5-p(\mu-OR)pL_5]^{2+}$ ($R=H$, alkyl, L =ligand, $p=0-4$). The preparation and characterisation of the trimeric tetrakis(μ -acetato)-(μ -hydroxo)- μ_3 -oxo-pentaki. *Polyhedron* **22**, 947-965 (2003).
197. Fries, D. V. & Lang, J. Synthesis & gas phase-characterization of trinuclear, oxo centered Cobaltacetate-complexes. (TU Kaisersautern, 2016).
198. Fries, D. V. Synthese & Gasphasen-Charakterisierung von trinuklearen, oxozentrierten Cobaltacetat-Komplexen. (2016).
199. D'Alessandro, D. M. & Keene, F. R. Intervalence Charge Transfer (IVCT) in Trinuclear and Tetranuclear Complexes of Iron, Ruthenium, and Osmium. *Chemical Reviews* **106**, 2270-2298 (2006).
200. Esteban, J., Ruiz, E., Font-Bardia, M., Calvet, T. & Escuer, A. Triangular Nickel Complexes Derived from 2-Pyridylcyanoxime: An Approach to the Magnetic Properties of the $[Ni_3(\mu_3-$

- OH){pyC(R)NO}3]2+ Core. *Chemistry - A European Journal* **18**, 3637-3648 (2012).
201. Rafizadeh, M., Tayebee, R. & Amani, V. Synthesis of Isomorphous Prototypic [CrFe 2 O (AcO) 6 (TEP) 3] Cl and [CrFe 2 O (AcO) 6 (TMP) 3] Cl As Oxo-Centered Hetero Tri-Nuclear Carboxylate Complexes. *Turk J Chem* **29**, 385-390 (2005).
202. Nakata, K., Nagasawa, A., Soyama, N., Sasaki, Y. & Ito, T. Kinetic studies on the terminal-ligand-substitution reactions of acetate-bridged trinuclear molybdenum and tungsten cluster complexes, [Mo3(μ₃-CCH3)(μ₃-O)(μ₃-CH3COO)6(L)3]⁺ (L = H₂O or pyridine) and [W3(μ₃-O)(μ₃-CH3COO)6(H₂O)3]2⁺. *Inorganic Chemistry* **30**, 1575-1579 (1991).
203. Sañudo, E. C. *et al.* Al, Ga and in heterometallic wheels and their by-products. *Chemical Communications* 801-803 (2007). doi:10.1039/b613877b
204. Uemura, S., Spencer, A. & Wilkinson, G. μ₃-Oxotrimetal acetato-complexes of chromium, manganese, iron, cobalt, rhodium, and iridium. *J. Chem. Soc., Dalton Trans.* 2565-2571 (1973). doi:10.1039/DT9730002565
205. Vrubel, H., Hasegawa, T., De Oliveira, E. & Nunes, F. S. A new facile high yield preparative route for mixed-trinuclear acetate clusters. *Inorganic Chemistry Communications* **9**, 208-211 (2006).
206. Klepov, V. V., Peresykina, E. V., Serezhkina, L. B., Virovets, A. V. & Serezhkin, V. N. Synthesis and structure of [Cr3O(CH3COO)6(H2O)3][UO2 (CH3COO)3] · 3H2O. *Russian Journal of Inorganic Chemistry* **57**, 1341-1347 (2012).
207. Schloter, K., Nagel, U. & Beck, W. Starke metallorganische Lewis-Säuren, II. Reaktion von (η⁵-C₅H₅)(OC)₃MoBF₄ mit Wasser. Struktur eines Tris(metallo)oxonium-Kations {[η⁵-C₅H₅)(OC)₂Mo]3O}⁺. *Chemische Berichte* **113**, 3775-3782 (1980).
208. Wilson, C. *et al.* Multi-Temperature Crystallographic Studies of Mixed-Valence Polynuclear Complexes; Valence Trapping Process in the Trinuclear Oxo-Bridged Iron Compound, [Fe 3 O(O 2 CC(CH 3) 3) 6 (C 5 H 5 N) 3]. *Journal of the American Chemical Society* **122**, 11370-11379 (2000).
209. Jang, H. G. *et al.* Highly cooperative valence detrapping of mixed-valence manganese complex [Mn3O(O₂CCH₃)₆(py)₃](py) in the solid state. *Journal of the American Chemical Society* **111**, 7778-7784 (1989).
210. Dikhtiarenko, A., Khainakov, S., García, J. R. & Gimeno, J. Mixed-valence μ₃-oxo-centered triruthenium cluster [Ru₃(II,III,III)(μ₃-O)(μ-CH₃CO₂)₆(H₂O)₃]·2H₂O: Synthesis, structural characterization, valence-state delocalization and catalytic behavior. *Inorganica Chimica Acta* **454**, 107-116 (2017).
211. Tauchman, J., Paul, L. E. H., Furrer, J., Therrien, B. & Süß-Fink, G. Cationic triruthenium(III) oxo complexes of the type [Ru₃O(OAc)₆L₃]+containing imidazole, pyrazole, thiazole and oxazole ligands: Synthesis, molecular structure, and cytotoxicity. *Inorganica Chimica Acta* **423**, 16-20 (2014).
212. Glover, S. D., Goeltz, J. C., Lear, B. J. & Kubiak, C. P. Inter- or intramolecular electron transfer between triruthenium clusters: we'll cross that bridge when we come to it. *Coordination Chemistry Reviews* **254**, 331-345 (2010).
213. Singh, A. K. & Singh, A. K. Synthesis and spectral characterization of trinuclear, oxo-centered, carboxylate-bridged, mixed-valence iron complexes with Schiff bases. *Spectrochimica Acta Part A: Molecular and Biomolecular Spectroscopy* **96**, 986-991 (2012).
214. Hanzel, D. *et al.* A study of trinuclear iron(III) O-phthalates. *Hyperfine Interactions* **53**, 339-343 (1990).
215. Vančina, V. *et al.* Thermal behaviour and characterization of some novel iron(III)-o-phthalates. *Thermochimica Acta* **246**, 199-212 (1994).
216. Degang, F., Guoxiong, W., Wenxia, T. & Kaibei, Y. The structure and magnetic properties of μ₃-oxotriiron(III) complex [Fe₃O(OBZ)₆(CH₃OH)₃] (NO₃)(CH₃OH)₂ (HOBZ = benzoic acid). *Polyhedron* **12**, 2459-2463 (1993).
217. Khosravi, I. & Yazdanbakhsh, M. Preparation and characterization of novel oxo-centered basic p-chlorobenzoic bridging trinuclear complexes. *Journal of the Serbian Chemical Society* **75**, 929-934 (2010).
218. Bradshaw, J. E., Grossie, D. A., Mullica, D. F. & Pennington, D. E. Preparations and characterizations of μ₃-oxo-hexakis(μ₂-carboxylatopyridine-O,O)triaquatrichromium(III) perchlorates. *Inorganica Chimica Acta* **141**, 41-47 (1988).
219. Holt, L. *et al.* Preparation and Properties of Fe³⁺-Amino Acid Complexes. *Archives of Biochemistry and Biophysics* 433-438 (1975). doi:10.1016/0003-9861(75)90406-3
220. Holt, E. M., Holt, S. L., Tucker, W. F., Asplund, R. O. & Watson, K. J. Preparation and properties of

- iron(III)-amino acid complexes. Iron(III)-alanine, a possible ferritin analog. *Journal of the American Chemical Society* **96**, 2621-2623 (1974).
221. Clegg, W., Mi Lam, O. & Straughan, B. P. Struktur eines neuen μ_3 -Oxo-FeIII₂CrIII-Glycin-Komplexes. *Angewandte Chemie* **96**, 424-425 (1984).
222. Mukherjee, R. *et al.* Structural and Spectroscopic Evidence for the Formation of Trinuclear and Tetranuclear Vanadium(III)/Carboxylate Complexes of Acetate and Related Derivatives in Aqueous Solution. *Inorganic Chemistry* **46**, 1575-1585 (2007).
223. Thich, J. A., Toby, B. H., Powers, D. A., Potenza, J. A. & Schugar, H. J. Magnetic properties of K₅[(H₂O)₃(SO₄)₆Fe₃O].6H₂O, a sulfate analog of the trimeric basic iron(III) carboxylates. *Inorganic Chemistry* **20**, 3314-3317 (1981).
224. Puri, M. & Verma, R. D. Trinuclear metal(III) trifluoroacetates. *Monatshefte für Chemie Chemical Monthly* **115**, 533-539 (1984).
225. Pandey, A. K., Gupta, T. & Baranwal, B. P. Trinuclear, oxo-bridged, mixed-valence iron mercaptocarboxylates. 370-375 (2004).
226. Baranwal, B. P. & Gupta, T. Synthesis and spectral characterization of some oxo-centered, trinuclear mixed-valence iron thiocarboxylates. *Spectrochimica Acta - Part A: Molecular and Biomolecular Spectroscopy* **59**, 859-865 (2003).
227. Hatop, H. *et al.* Lightest Member of the Basic Carboxylate Structural Pattern: [Al₃(μ_3 -O)(μ_2 -O₂CCF₃)₆(THF)₃][(Me₃Si)₃CAI(O₂CCF₃)₃] \cdot C₇H₈. *Inorganic Chemistry* **41**, 1022-1025 (2002).
228. Baranwal, B. P., Fatma, T. & Varma, A. Synthesis, spectral and thermal characterization of nano-sized, oxo-centered, trinuclear carboxylate-bridged chromium(III) complexes of hydroxycarboxylic acids. *Journal of Molecular Structure* **920**, 472-477 (2009).
229. Pali, S. P. *et al.* Mixed-terminal-ligand oxo-centered carboxylate-bridged trinuclear complexes: gas phase generation by means of electrospray ionization FT-ICR MS, condensed phase synthesis, and X-ray. *Inorganica Chimica Acta* **319**, 23-42 (2001).
230. Paul, R. C., Kapoor, P., Baidya, . B. & Kapoor, R. Basic Chromium(III) Formate: Reaction of Chromium(III) Chloride with Formic Acid. *Zeitschrift für Naturforschung B* **34**, 160-162 (1979).
231. Kapoor, R. Basic Chromium(III) Carboxylates: Reactions of Chromium(III) Chloride with Some Carboxylic Acids. *Zeitschrift für Naturforschung B* **34**, 247-250 (1979).
232. Saalfrank, R. W. *et al.* A Neutral, Triple-Helical, Trinuclear, Oxo-Centered Mixed-Valence Iron Complex. *Angewandte Chemie International Edition in English* **35**, 2206-2208 (1996).
233. Saalfrank, R. W. *et al.* Ein neutraler, tripelhelicaler, gemischtvalenter μ_3 -Oxotri Eisen-Komplex. *Angewandte Chemie* **108**, 2350-2352 (1996).
234. Chen, S., Narayanam, N., Zhang, L. & Zhang, J. Hydrogen bond-assisted homochiral lattice packing between inorganic helices built from heterometallic units. *Dalton Transactions* **47**, 2134-2137 (2018).
235. Novitchi, G., Helm, L., Anson, C., Powell, A. K. & Merbach, A. E. NMR Study of Ligand Exchange and Electron Self-Exchange between Oxo-Centered Trinuclear Clusters [Fe₃(μ_3 -O)(μ_2 -O₂CR)₆(4-R'py)₃]⁺⁰. *Inorganic Chemistry* **50**, 10402-10416 (2011).
236. Wu, R. *et al.* Electron Localization and Delocalization in Mixed-Valence Transition Metal Clusters: Structural and Spectroscopic Studies of Oxo-Centered Trinuclear Complexes [Fe₃O(OOCCMe₃)₆(py)₃]⁺⁰ and [Mn₃O(OOCCMe₃)₆(py)₃]⁺⁰. *Inorganic Chemistry* **37**, 1913-1921 (1998).
237. Váña, J. *et al.* The role of trinuclear species in a palladium acetate/trifluoroacetic acid catalytic system. *Dalton Transactions* **46**, 16269-16275 (2017).
238. Niedner-Schatteburg, G. Cooperative Effects in Clusters and Oligonuclear Complexes of Transition Metals in Isolation. in *Structure and Bonding* **119**, 1-40 (2016).
239. Mück-Lichtenfeld, C. & Grimme, S. Theoretical analysis of cooperative effects of small molecule activation by frustrated Lewis pairs. *Dalton Transactions* **41**, 9111 (2012).
240. Chmela, J. *et al.* Differential Many-Body Cooperativity in Electronic Spectra of Oligonuclear Transition-Metal Complexes. *ChemPhysChem* **17**, 37-45 (2016).
241. Çarçabal, P. *et al.* Hydrogen bonding and cooperativity in isolated and hydrated sugars: Mannose, galactose, glucose, and lactose. *Journal of the American Chemical Society* **127**, 11414-11425 (2005).

2 Experimental and Computational Methods

2.1 Tunable IR Laser System for IRMPD Spectroscopy

We are using a pulsed tunable table top IR laser^{1,2} system, powered by an injection seeded NdYAG laser (Continuum-PL 8000; 10 Hz, 540 - 560 mJ/pulse). It is made tunable by an optical parametrical oscillator/amplifier (OPO/OPA)^{3,4} system. It is also specified again in the method section in our paper⁵ reprinted in chapter 10.

As shown schematically in **Figure 7**, the laser system works as follows: intense laser pulses of the fundamental pump laser at $\omega = 1064 \text{ nm}$ (9394 cm^{-1}) with a pulse length of $\sim 7 \text{ ns}$ pump the OPO/OPA system. A beam splitter guides one third of the ω photons to a potassium titanyl phosphate crystal (KTP) for second harmonic generation (SHG) at 2ω . This 2ω laser pulse (2ω , 532 nm , 18789 cm^{-1}) undergoes wavelength conversion in a system of non linear optical crystals using second order non linear optical interaction⁶. An optical resonator (or oscillator) consisting of two mirrors (optical gratings can be used to improve the spectral resolution) and a non-linear optical KTP crystal is used to tune the frequency (λ) of these photons by changing the incident angle on the surface of the KTP crystal.

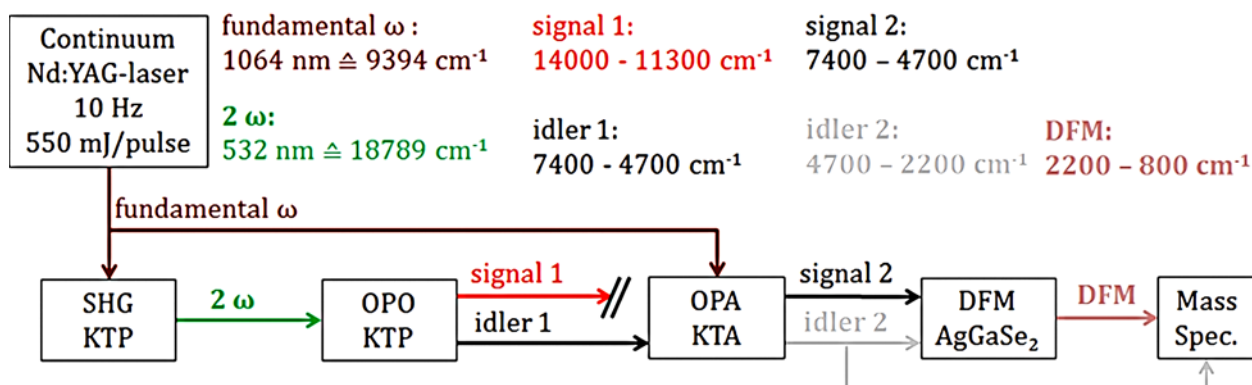


Figure 6 Nonlinear optical processes in the Dean Guyer Laser Vision OPO/OPA laser system: potassium titanyl phosphate (KTP) crystals for second harmonic generation (SHG), and the optical parametric oscillator (OPO); potassium titanyl arsenate (KTA) crystals as optical parametrical amplifier (OPA) and AgGaSe₂ crystals for difference frequency mixing (DFM)⁷.

The OPO creates two photons from one 2ω pump photon: a signal 1 and an idler 1 photon, where the frequency of the signal photon is higher than the frequency of the idler photon. The frequency ratio depends on the incident angle of the pump laser to the crystal axis. The photon energies of the sum of the signal and the idler photon have to observe energy conservation and equal the photon energy of the 2ω pump photon.

The next step is an OPA; an optical parametrical amplifier, where the idler photons of the OPO stage can be amplified and split into signal 2 and idler 2 by using the remaining $2/3$ of the fundamental

beam ω . Here too the sum of the signal and the idler photon has to equal the incoming beam ω , while the idler 2 wavelength is determined by idler 1. For power adjustment, the fundamental can be attenuated by turning a $\lambda/2$ wave plate (OPA attenuator angle). The effects of that can be seen in **Figure 7**.

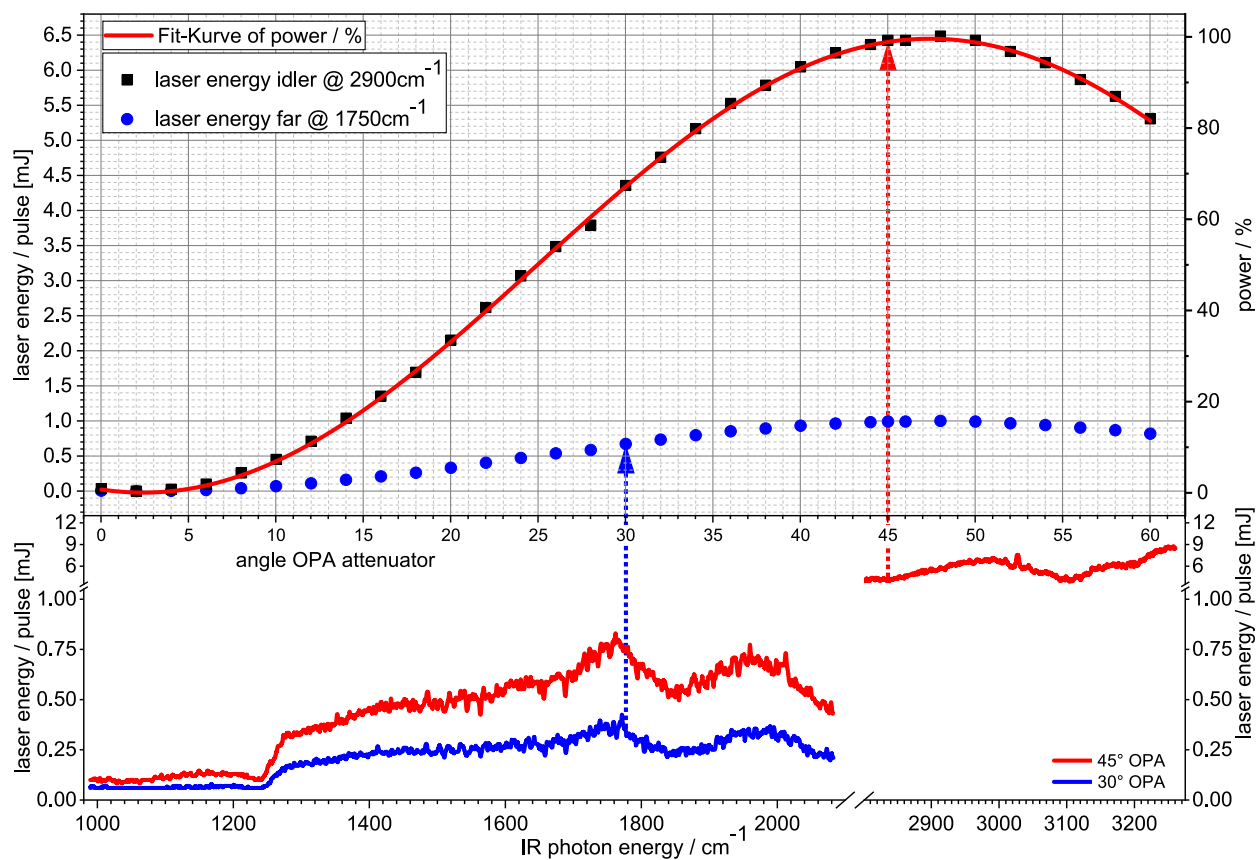


Figure 7 Laser power curves in dependence of the OPA angle (top graph) and for two angles (45° and 30°) at different wavelengths (bottom graph), both in the far IR region (1000 - 2000 cm^{-1}) and idler region (2500 - 3500 cm^{-1}).

For IRMPD spectroscopy, we either use the idler 1 beam, or we combine idler 2 and signal 2 in a difference frequency mixing stage using an AgGaSe_2 crystal⁸; yielding photons in the 4700 - 2000 cm^{-1} and 2400 - 1000 cm^{-1} range. The resulting power curves at minimum OPA power attenuation (max power) are shown in red in **Figure 7**, in the bottom graph. More on this in section 5.4.4.

2.2 The Electrospray Ionisation Process (ESI) for Mass Spectrometry

Electrospray ionization²⁰⁻²² (ESI) is an ionization method that allows the transfer of ions from a solution into the gas-phase. It is known as a relatively soft way of getting fragile ions into the gas-phase, and into the vacuum environment of a mass spectrometer with minimal fragmentation.

Its invention and the resulting applications in the analytics of proteins, biomolecules, and other organic substances, has earned John Fenn the Nobel prize. In his Nobel lecture⁹ ‘Flying Elephants’ and in later reviews¹⁰⁻¹², he details the working principle and application of this method. For its role to study the transition metal (TM) complexes in this thesis, see section 5.2

The ESI process, as shown in **Figure 8**, is based on an analyte solution flowing through an ESI capillary under a high voltage gradient. The strong electrostatic fields applied to the solution lead to the formation of a Taylor cone^{13,14}, and to the liberation of charged droplets, when the coulomb repulsion grows stronger than surface tension of the solvent.

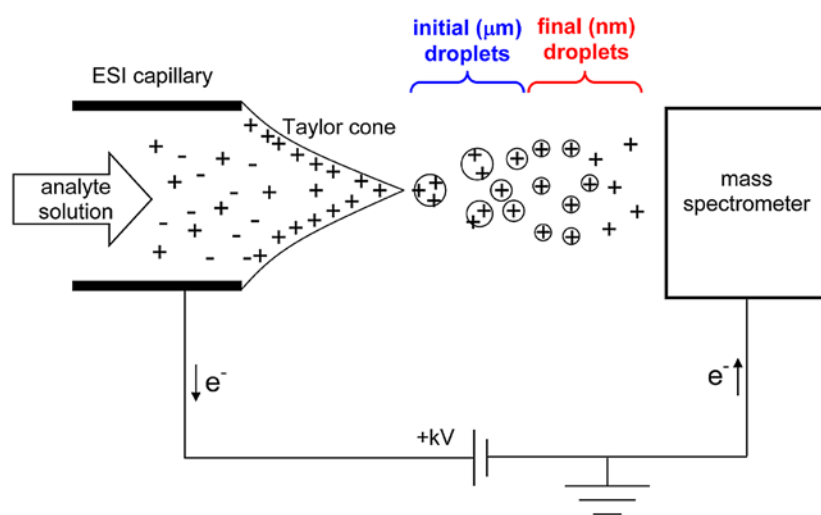


Figure 8 Release of ions and analyte solution by the Electrospray Ionisation (ESI) process¹⁵.

In a warm stream of a drying gas, often nitrogen, aided by thermally induced desolvation; the droplets reach the Rayleigh limit¹⁶, where the electrostatic repulsion of the accumulated charges increases with decreasing droplet size and grows stronger than the surface tension. This leads to a Coulomb explosion, ultimately resulting in bare free molecular ions¹⁵.

These ions are then guided by an electric field through a glass capillary into the vacuum system of the mass spectrometer. The ionization is discussed using two competing mechanisms: the Charge Residue (CR-) Model¹⁷ and the Ion Evaporation (IE-) Model¹⁸. The ESI Mechanism¹⁹⁻²¹ depends on the combination of analytes and solvents used. Polar solvents with low boiling points suit the ESI process best, since they stabilize ions well and facilitate the desolvation process.

A Bruker Apollo II ESI source (**Figure 9**) is used in this work, in combination with both a Bruker Amazon SL^{22,23} (for IRMPD) and Amazon ETD mass spectrometer (for CID).

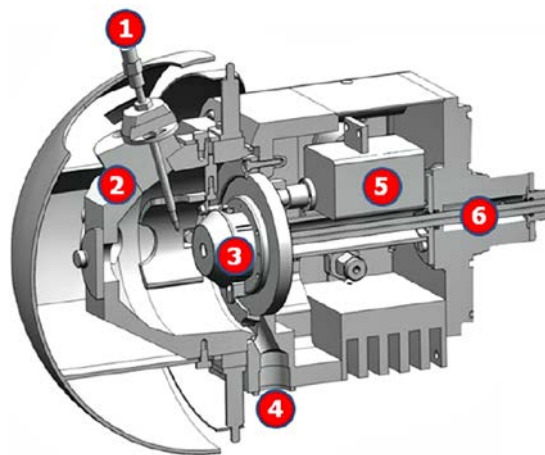


Figure 9 3D-model of the Apollo II ESI ion source²².

The ESI Sprayer ① houses the spray needle. A HamiltonTM gas tight syringe injects the sample solution into the spray needle through a peek capillary (inner diameter = 0.13 mm). A syringe pump provides a constant solution flow rate of $\sim 2 \mu\text{l}/\text{min}$. A constant flow of nitrogen gas ($\sim 400 \text{ mbar}$; flowrate $\sim 2.5 \text{ L}/\text{min}$) alongside the spray needle helps with nebulizing the solution in the Spray Chamber ②. An electrostatic field is generated by applying a high voltage (4.5 kV - 3.5 kV) on the Spray Shield ③ and grounding of the spray needle. The Glass Capillary ⑥ serves as the entrance to the mass spectrometer, limiting the inflow of gas. It is metal coated on both ends with platinum. Nitrogen gas heated by the Dry Gas Heater ⑤ (gas temperature $\sim 220 \text{ }^\circ\text{C}$) flows in the opposite direction of the droplet stream (4 - 6 L/min) and supports ion desolvation. The gas flow is guided away by a hose connection ④. An additional electrostatic potential between the Spray Shield ③ and the Glass Capillary ⑥ focuses the ion to the capillary entrance. An electrostatic gradient between entrance and exit of the Glass Capillary ⑥ guides the charged particles into the ion optics and guides of the mass spectrometer.

2.3 Paul Trap Mass Spectrometer

The utilized mass spectrometers are an ‘amazon ETD’ (for a schematic overview see **Figure 10**) and an ‘amazon SL’ instrument from Bruker Daltonics^{24,25}. They are commercial mass spectrometers that are capable of the tandem mass spectrometry necessary for the infra red multiple photon dissociation²³⁻²⁵ (IRMPD, see section 2.5) and collision induced dissociation²⁶⁻²⁸ (CID, see section 2.4) methods we utilize to gain information on the molecular structure and vibration modes.

The used ion trap, a Paul trap^{26,27}, consists of a ring electrode and two end caps forming a nearly hyperbolic inner profile. See **Figure 11** and **Figure 14** for higher detailed cross-section schematics of the used ion traps. The ions enter and exit the trap through pinholes in the end caps. A high voltage RF (radio frequency) potential (781 kHz) is applied to the ring electrode, while the end caps are grounded. The resulting oscillating quadrupolar electric field allows for the trapping of the ions within the volume between the three electrodes. Depending on the amplitude of the RF voltage, the field

traps ions within a wide mass range. An auxiliary dipolar voltage is fed to either the exit cap or both end-caps, for subsequent ion isolation and fragmentation. A proportional integral derivative (PID) gas controller maintains a partial helium buffer gas pressure of ca. 10^{-3} mbar inside the trap.

As explained in **Figure 14** in section 2.5, the Amazon SL instrument has been modified by adding a pair of mirrors and holes in the trap ring, giving access for an IR laser beam to be overlapped with the ion cloud in the ion trap.

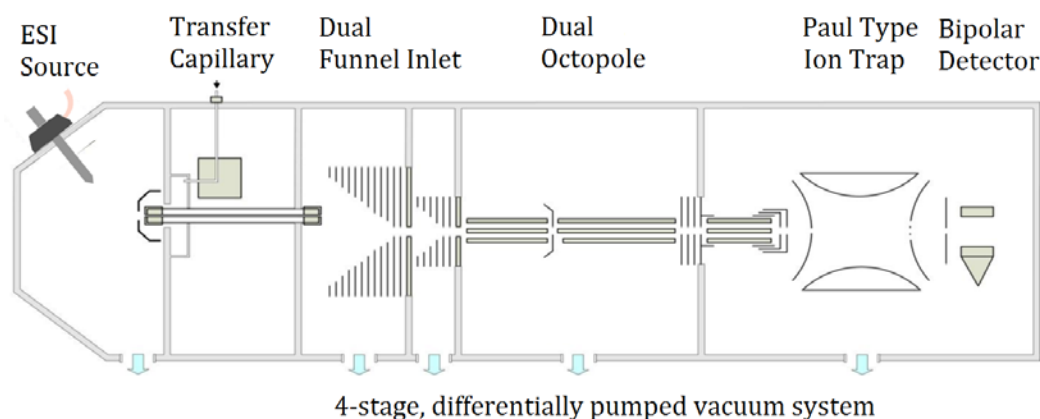


Figure 10 Schematic cross section of an Amazon ETD mass spectrometer²³.

The mass spectrometer itself, as shown in **Figure 10**, consists of several differentially pumped vacuum chambers. Gaseous ions exit the ESI ion source from transfer capillary and enter the first vacuum stage (pressure ~ 1 mbar). A double arrangement of ion lenses with decreasing inner diameters form a dual ion funnel^{28,29}.

The ion funnel focuses the ion cloud by combining radio RF and direct current (DC) voltages. The dual ion funnel is fitted ‘off axis’, in relation to the exit of the transfer capillary to deflect direct neutral gas flow from the ESI source, thereby improving the vacuum gradient.

In the next vacuum stage, two linear RF octupoles guide the ions to the Paul type ion trap, where the ions are accumulated and m/z determination and isolation takes place.

2.4 Collision Induced Dissociation (CID)

The CID method^{24,30-35} is based on the collisional activation of ions³⁶, leading to the molecular fragmentation, as shown schematically in **Figure 11**. CID is a standard tandem mass spectrometry method to analyse the structures of organic molecules and transition metal complexes³⁷. The masses of the ionic fragments³⁸ reveal information about the precursor ion and its structure. In combination with IRMPD (section 2.5), it can be a powerful tool³⁹. See also the method section in our paper⁵ reprinted in chapter 10.

DC voltages (in addition to the trapping potentials) accelerate the mass-selected precursor ions. This increases the kinetic energy by inelastic collisions. Kinetic energy accumulates⁴⁰ in intramolecular

degrees of freedom by ‘slow multi collision heating’^{44,45}, until the ion dissociates⁴¹. The necessary collisional energy is related to available intramolecular fragmentation pathways⁴², ligand binding energies⁴³, or other intramolecular fragmentation processes⁴⁴. It helps to understand the structure of the molecule, especially when combined with appropriate DFT calculations. See section 2.4 and 5.3 for more on that.

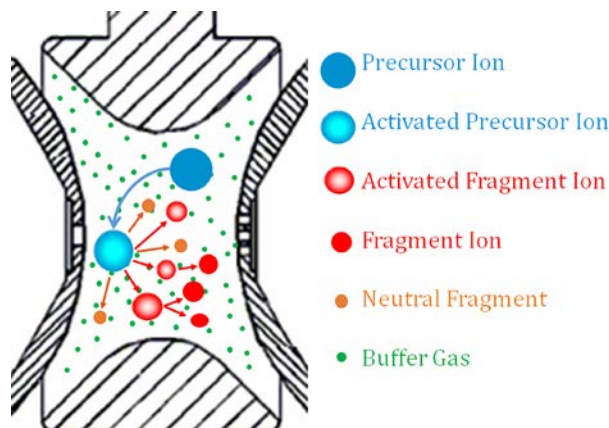


Figure 11 CID process in a Paul trap: precursor ions are activated by applying an acceleration voltage and subsequent buffer gas collisions, neutral and activated ionic fragments are formed, which then decelerate by collisional cooling⁷.

The exact energy transferred to the ions is difficult to quantify, as CID is more of a relative method depending on many variables. It can be approximated by using so called thermometer ions^{44,45} with well-known fragmentation energies. It is often used for peptides³², also previously on iron acetates⁴⁶ and cobalt acetates³⁵, and for the differentiation of metal binding sites²⁴

The CID intensity for a specific fragment ion is normalized by the sum of all ions in the ion trap after isolation and fragmentation.

$$I_{tot}^{fr}(E_{lab}) = \left(\frac{\sum_i I_i^{fr}(E_{lab})}{\sum_i I_i^{fr}(E_{lab}) + \sum_i I_i^p(E_{lab})} \right) \quad \text{I}$$

The collisional energy has to be converted from the applied collision voltage by a centre of mass transformation, to account for the mass dependant energy transfer efficiency from the background helium gas atoms to the the accelerated analyte ions.

$$E_{com} = \left(\frac{m_{He}}{m_{He} + m_{ion}} \right) \cdot E_{lab} \quad \text{II}$$

The DC excitation amplitude is slowly raised step by step while the mass spectrum is recorded. From this mass spectrum, the signal of the precursor ion and the sum of the resulting fragments is derived and plotted according to the following equation:

$$Y(CID) = \left(\frac{\sum_i I_i^{fr}(E_{com})}{\sum_i I_i^{fr}(E_{com}) + \sum_i I_i^p(E_{com})} \right) \quad \text{III}$$

2.4.1 Sigmoidal Fit with Logistic Growth Curves

The resulting E_{com} values are modelled and fitted by sigmoidal logistic functions using a least square criterion

$$I_{fit}^{fr}(E_{com}) = \left(\frac{A}{1 + e^{(E_{com}^{50} - E_{com}) \cdot C_A}} \right) + D \quad \text{IV}$$

Here the E_{com}^{50} fit parameter is the excitation amplitude, at which the sigmoid function is at half its maximum value, whereas C_A describes the slope of the sigmoid curve. A is the amplitude of the sigmoid curve. D describes an offset at the beginning, for example to account for auto fragmentation of a non-excited complex. Often it can be set to zero.

2.4.2 Multiple Component Sigmoidal (logistic) Fits of CID Curves

In case of multiple competing fragmentation channels of different characteristic fragmentation energies, the data can be fitted with a bi-logistic or tri-logistic growth model. A mathematical model and explanation for the deconvolution of bi-logistic curves can be found in the paper by Meyer et al.^{47,48} (see **Figure 12**). We used a slightly altered version of the logistic curve function, as introduced in the previous section; more in line with Lipovetsky⁴⁹, rearranged into a more readable yet equivalent form.

The multiple growth pulses logistic functions are the sum of two or more mono logistic growth pulses. Analogous to the mono-logistic function in equation IV, the $E_{com}^{50}{}_{A,B,C}$ fit parameter in equations V and VI correspond to the excitation amplitude, at which the respective sigmoid logistic function is at half maximum value, whereas C_A , C_B and C_C describe the slope of their sigmoid curve. A , B and C are the amplitude of the respective sigmoid curve. D describes the offset at the beginning to account for auto fragmentation of a non-excited complex, as observed for some weakly bound iron complexes.

This gives the following fit curve equations:

Bi-logistic growth

$$I_{fit}^{fr}(E_{com}) = \left(\frac{A}{1 + e^{(E_{com}^{50}{}_A - E_{com}) \cdot C_A}} \right) + \left(\frac{B}{1 + e^{(E_{com}^{50}{}_B - E_{com}) \cdot C_B}} \right) + D \quad \text{V}$$

Tri-logistic growth

$$I_{fit}^{fr}(E_{com}) = \left(\frac{A}{1 + e^{(E_{com}^{50}{}_A - E_{com}) \cdot C_A}} \right) + \left(\frac{B}{1 + e^{(E_{com}^{50}{}_B - E_{com}) \cdot C_B}} \right) + \left(\frac{C}{1 + e^{(E_{com}^{50}{}_C - E_{com}) \cdot C_C}} \right) + D \quad \text{VI}$$

For further examples for a bi-logistic behaviour, see **Figure 35** and **Figure 34** in section 5.3, as well as in the appendix, section 11.5, **Figure 72**; the latter also gives an example of tri-logistic growth.

The interpretation of this multi component behaviour is discussed in section 5.3 and in Jonas Krüger's bachelor thesis⁵⁰.

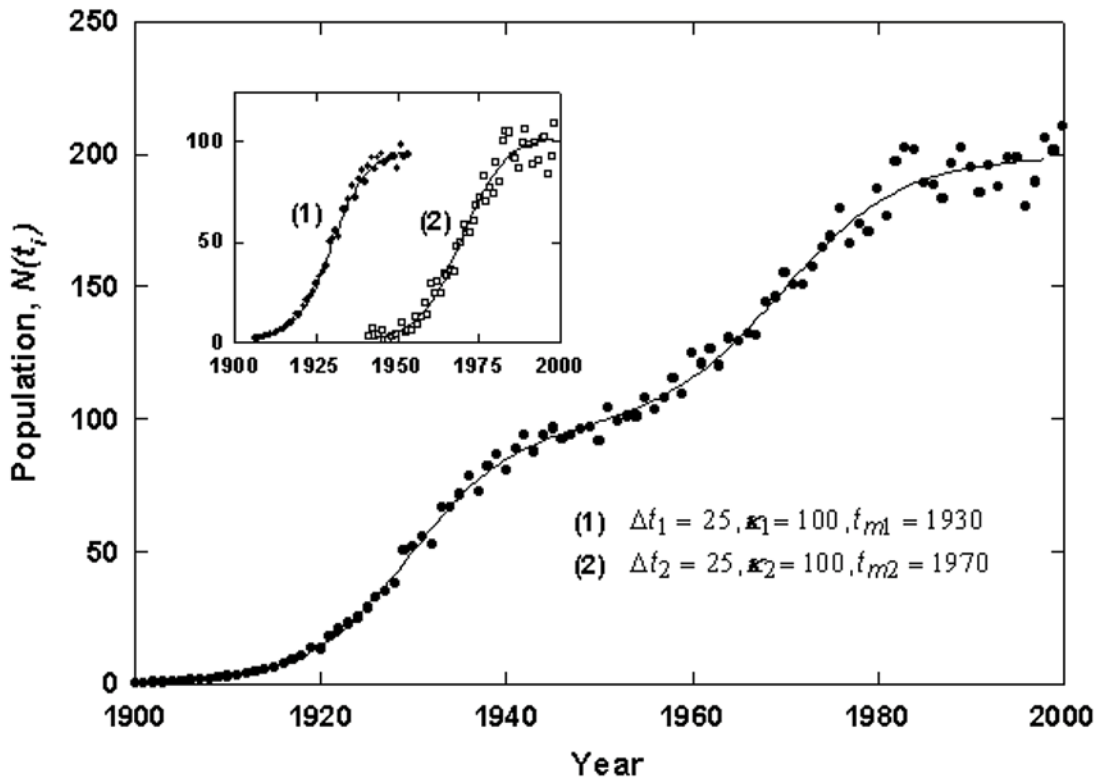


Figure 12 Example of a bi-logistic growth curve generated with 3% relative gaussian error. The inset shows the component growth curves. Reproduced from 'Bi-logistic growth'^{247,48} with kind permission of the author, P. Meyer.

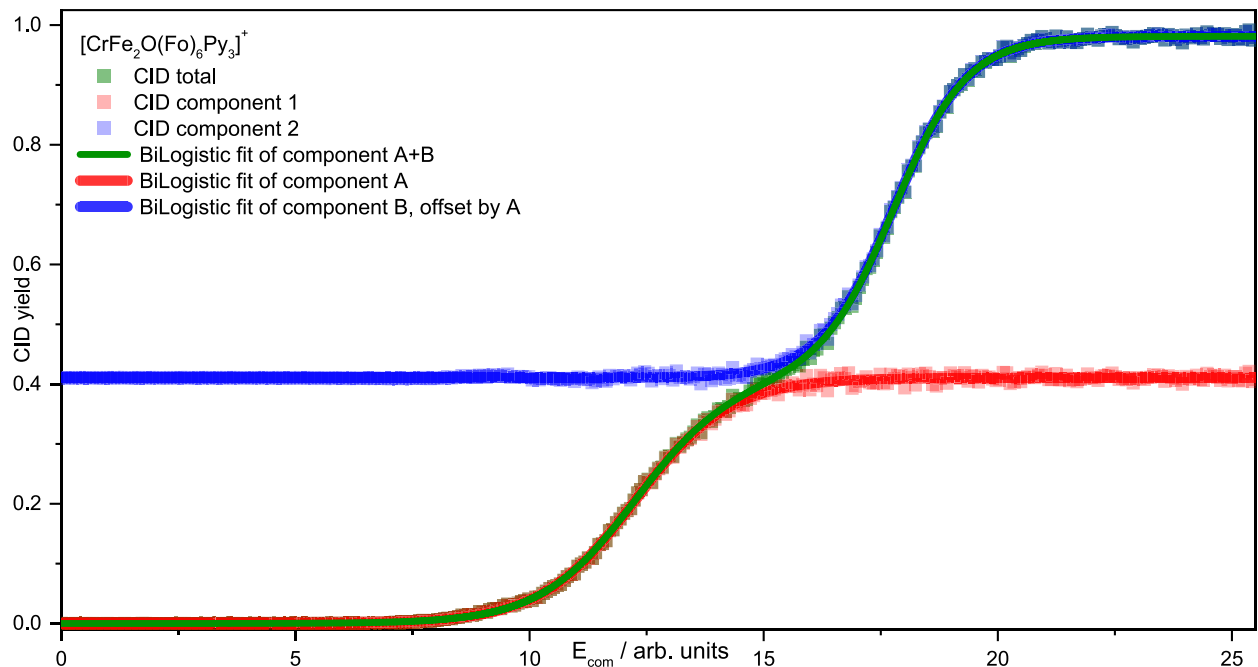


Figure 13 CID of $[\text{CrFe}_2\text{O}(\text{Fo})_6\text{Py}_3]^+$, an example of a CID curve (green, in background) with two separate logistic components. The deconvoluted curves of those two logistic components (in red and blue) are shown, with the blue curve being offset by the amplitude of the red curve.

2.5 Infrared Multi Photon Dissociation (IRMPD) Spectroscopy

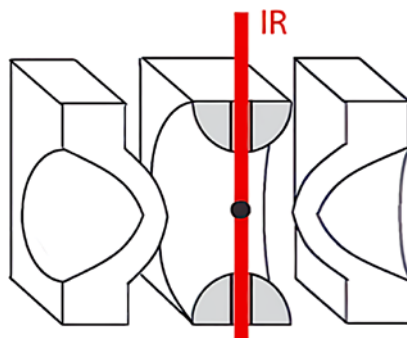


Figure 14 Cross section of a Paul trap for IRMPD spectroscopy with optical access on the ion cloud in the middle for an IR laser beam.

The infrared multi photon dissociation (IRMPD) is a method for recording IR spectra of ions in the gas phase. The vibrational fingerprint of a molecule provides vital information to understand its structure and reactivity, achieving this on isolated molecular ions enables their investigation without any solvent influences. The issue is the low ion density in the gas phase, preventing the use of absorption spectroscopy. Therefore, we use an ‘action spectroscopy’ mechanism, where the incoherent absorption of a single or multiple IR photons^{36, 37} results in a fragmentation (which can be observed by a change of the m/z ratio) of the isolated ion.

Absorption occurs when the photon frequency is in resonance with a molecular energy transition. This is demonstrated in

Figure 15. The energy of a single IR photon is in the range of 10 - 50 kJ/mol (800 - 4000 cm^{-1}), which makes it possible to break noncovalent bonds; e.g. hydrogen bonds or messenger tags. Stronger (covalent) bonds requires multiple IR photons to accumulate.

In the non-coherent IRMPD model, internal vibrational redistribution (IVR)⁵¹ leads to the rapid dissipation of the additional energy into available molecular vibrational degrees of freedom^{52,53} and the heating of the isolated molecular ion. The original oscillation mode is thereby able to absorb additional IR photons. This process repeats until the molecular dissociation threshold is exceeded and fragmentation occurs.

The technique was first reported by Woodlin⁵⁴ and discussed in good detail by Bagratashvil et al.⁵⁵, and more recently by Roithová et al.⁵⁶. It is the subject of regular review articles^{56,58} and book chapters^{59,60}. See also the method section in our paper on iron acetate⁵, reprinted in chapter 10. Additional information can be found in the tutorial review article by Polfer et al.⁶¹ and is frequently used on biomolecules^{64,65}, on organometallic ions⁶²; especially their cations⁶³.

A possible problem for the IRMPD method can be the phenomenon of dark bands that are not visible in the fragmentation response, or are far weaker than expected. This can be caused by so called IVR bottlenecks. They can be caused by high dissociation thresholds and/or an inefficient IVR process.

This may prevent fragmentation within one or even multiple laser pulses, leading to ‘dark’ vibrational bands. Inefficient IVR can be caused by low densities of vibrational states, inhibiting molecular dissociation. In previous investigations we applied two color IRMPD schemes^{66,67} to overcome such IVR bottlenecks³⁸. This could also be applied to future measurements, as discussed in the outlook section 9.2.

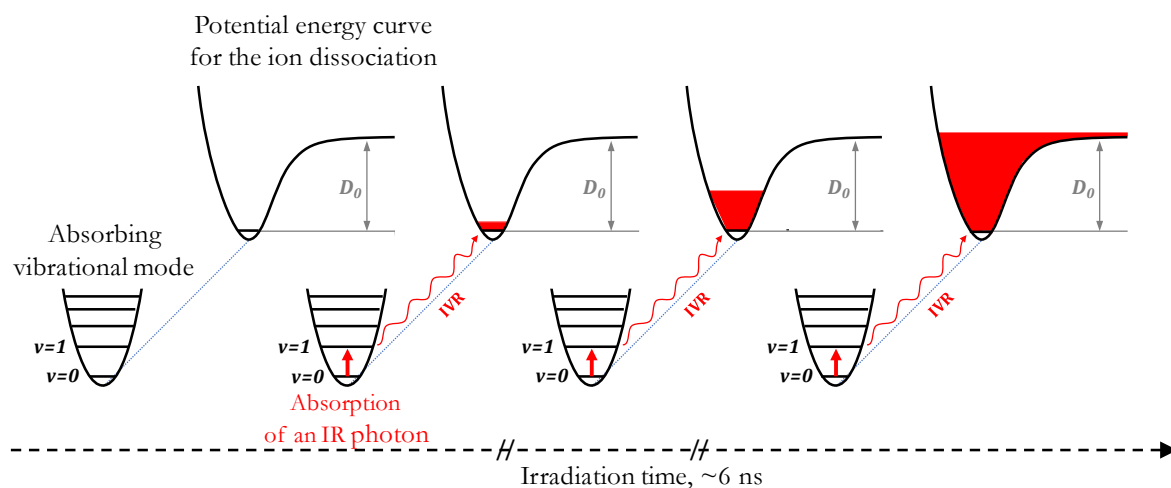


Figure 15 Representation of the non-coherent IRMPD process⁵⁶: A resonant IR photon is absorbed by the isolated ion. The additional energy is redistributed within the ion by internal vibrational redistribution (IVR). This process repeats until the dissociation limit of the ion is exceeded and it fragments. The irradiation time is ~7 ns (a single IR laser pulse). Multiple laser pulses can be used. Adapted from ‘Characterization of reaction intermediates by ion spectroscopy’ by Rhoitova et al.⁵⁶.

The weakest bond of the ion can be broken, even if it has not been excited directly by the IR laser, since the absorbed energy is stored in the entire molecular ion and can be distributed between modes.

The IRMPD fragmentation yield is defined by equation:

$$Y(v)_i = \left(\frac{\sum_i I_i^{fr}(v)}{\sum_i I_i^{fr}(v) + \sum_i I_i^p(v)} \right) \quad VII$$

with I_i^{fr} fragment ions, I_i^p parent/precursor ions, v laser frequency.

The experimental IRMPD spectrum is the plot of the fragmentation efficiency as a function of the laser frequency (v).

IRMPD, in tandem with quantum chemical calculations of sufficient quality, can give valuable structural information by comparing calculated linear absorption spectra of geometry optimized energy minimum structures with the observed IRMPD spectrum. Here the intensities may not be linearly dependent on the laser fluence and the absorption intensity of the oscillation mode due to the multi photon process⁶⁶.

2.5.1 Fragment Mass Trace Specific IRMPD Spectroscopy

As we will motivate in section 5.4 and as already detailed in the bachelor thesis of Jonas Schuchmann⁶⁸, observing the wavelength dependent abundance of specific fragment channels can be very helpful to observe unique mode specific fragmentation behavior. This can point to the presence of several overlapping modes, or hint at the identity of the chromophore or specific IVR coupling pathways (section 5.6.1) and more.

We slightly modify equation VII to give the fragment mass trace specific IRMPD yield:

$$Y(\nu)_i^{fr} = \left(\frac{I_i^{fr}(\nu)}{\sum_i I_i^{fr}(\nu) + \sum_i I_i^p(\nu)} \right) \quad \text{VII}$$

As shown and discussed in section 5.4, it is beneficial to plot the cumulative IRMPD yield, which is the intensity of the current fragment trace plus the sum of all previous mass traces:

$$Y(\nu)_i^{cum} = \sum_0^i Y(\nu)_i^{fr} \quad \text{IX}$$

There is a number of examples in the literature where the behavior of specific fragment channels is important: chromophore specific fragmentation pattern^{69,71}, for example in NH_4^+ and H_2O complexes⁷²; in disaccharides⁷³; in the differentiation of isomers⁶⁹ or anomers⁷³; in identifying different mode-specific fragmentation channels⁷⁴; sequential or competing fragmentation channels^{75,76}; fragment mode specific anharmonicities⁷⁷, as well as fragmentation channels unique to IRMPD⁵⁷; and other mass resolved IRMPD spectra^{74,76}. Reversely, IRMPD spectra of fragments⁷⁸, are also known. This is discussed in the IRMPD review⁶¹ and paper on adamantyl cations⁷⁹ by Polfer et al.

2.6 DFT ab initio Simulations of Transition Metal Complexes

Density functional theory is a computational quantum mechanical modelling method to approximate the electronic structure of atoms and molecules. The basic idea of DFT, developed by Thomas⁸⁰ and Fermi⁸¹, is that all information needed to calculate the energy of a molecule is given by the electron density of the molecule. In contrast to other ab initio methods, the molecular energy is not calculated by addition of the individual atomic energies. It has to be said though, that the initial implementations of the DFT model were not adequate to characterize chemical bonds and were over all too imprecise to be of practical use^{80,81}.

Then in the 1960's, Hohenberg and W. Kohn proved the fundamental correctness of the theory; developing the 1st Hohenberg-Kohn-Theorem⁸². For further information see literature^{83,84}.

Methodical advancements and improvements throughout the years have established DFT as a standard tool for quantum chemical calculations. It is routinely used by scientists in various fields of research. For a good introduction, the 'Chemists Guide to DFT'⁸⁵ is recommended. See also the

method section in our paper⁵ ‘Magnetostructural Correlation in Isolated Trinuclear Iron(III) Oxo Acetate Complexes’ reprinted in chapter 10.

2.6.1 DFT Simulations of Infrared Spectra

To simulate the vibrational frequencies observed in an infrared spectrum, an optimization of the molecular geometry provides structures located at stationary minimum points of the potential energy surface.

The second derivatives of those structures are transformed to mass-weighted coordinates, and $3N$ eigenvectors/eigenvalues are determined. Rotational and translational motions of the molecule are sorted out and $3N-6$ vibrational modes emerge ($3N-5$ for linear molecules).

Vibrational frequencies are calculated for these modes. Minima structures exhibit no negative frequencies, as per definition their second derivatives are all positive. Transition state structures exhibit exactly one negative frequency. This imaginary vibration corresponds to a force constant associated to a motion along the reaction coordinate.

In the present work, all geometry optimizations and frequency calculations have been performed using the Gaussian 09^{83,86} program package, through the WebMO interface.

The used basis sets and functionals and the reasoning behind their choices are addressed individually in the corresponding chapters, specifically in section 4.2 and 4.3.

2.6.2 Basis Set Superposition Error Mitigation for CID Bond Energy Calculations

The concept and importance of the basis set superposition error (BSSE) was introduced by Liu et al.⁸⁷. When calculations refer to molecules that undergo fragmentation, the bond strength is determined by the energy difference between the complex and the fragments. The addition of extra accessible basis functions for monomers, at shorter intermolecular distances, stabilizes the complex. Therefore the energy of the complex is not equal to the sum of the monomers⁸⁸.

This can be corrected by either using sufficiently large basis sets, which can potentially be prohibitively computationally expensive, or by suitable pairwise calculations of the parent molecule and the fragments. We used the treatment by Boys and Bernadi⁸⁹, implemented in the routine invoked by the ‘counterpoise’ keyword in Gaussian 09.

You can see the principle in action in section 4.5, **Figure 29**, where a more complete basis set, designed to account for dispersion interaction, better approximates the long distance interaction.

2.7 The Differential Many Body Cooperativity (DMBC) Formalism

In the 3MET research initiative, the cooperativity between several (usually three) transition metals in a molecular unit is investigated. For a definition of cooperativity, please refer to section 1.5. The specific interaction of these metal centers in respect to their combined properties, be it chemical, optical, magnetic, or otherwise, is the focus of that initiative.

As shown by Klopper et al.⁹⁰ in section 2.3 of their paper, a many-body expansion can be formulated to define one, two, and many body terms of interaction effects.

They write: ‘The one-body terms $\Delta E_k^{(1)}$ consist of deformation (or relaxation) energies of the subsystems, the two-body terms $\Delta E_{kl}^{(2)}$ consist of pair-interaction energies, and the terms starting with the three-body terms $\Delta E_{klm}^{(3)}$ contain all contributions beyond pair interactions’.

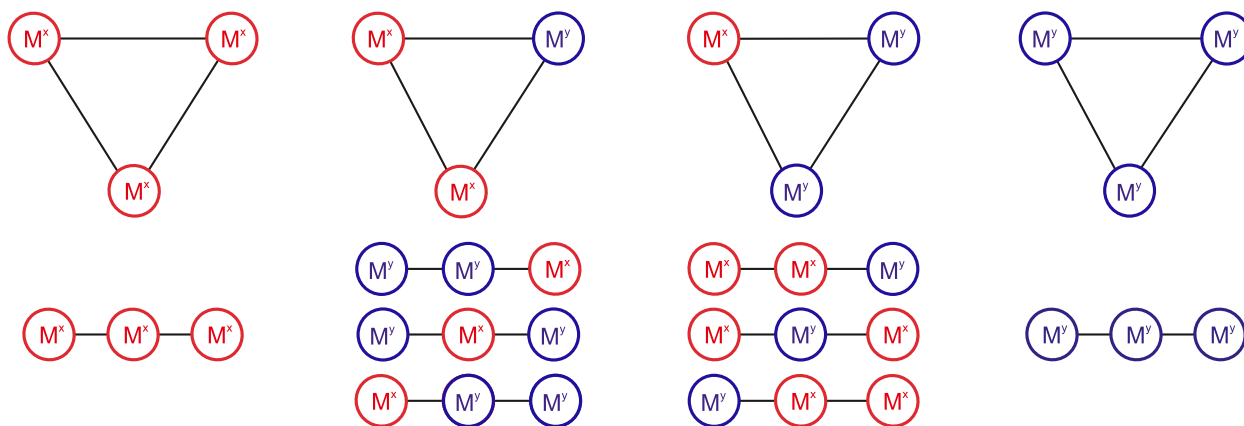


Figure 16 The different permutations for triangular and for linear trimetallic complexes. Depending on the rest of the molecule, the different permutations can be degenerate in respect to the observed property. For equally (un-)coordinated triangular structures, only one of the three possible rotamers is shown.

For the total energy (E) or any other property (P) of a system, the formalism gives the following terms:

$$\Delta P = \sum_k \Delta P_k^{(1)} + \sum_{k<l} \Delta P_{kl}^{(2)} + \sum_{k<l<m} \Delta P_{klm}^{(3)} + \dots \quad \text{X}$$

$$\Delta P^{(1)} = \sum_{k=1}^3 \Delta P_k^{(1)} \quad \text{XI}$$

Here, $\Delta P^{(yxx)}$ is the property of the complex with the metals x and y , and $\Delta P^{(xxx)}$ is the property of the homometallic parent complex. With the different permutations that gives the three one body terms:

$$\Delta P_1^{(1)} = P(yxx) - P(xxx)$$

$$\Delta P_2^{(1)} = P(xyx) - P(xxx)$$

$$\Delta P_3^{(1)} = P(xxy) - P(xxx)$$

But both yxx and xxx contain n -body interactions and thus, $\Delta P^{(1)}$ has to be a sum of all of the differences between the possible permutations of the systems yxx and xxx .

This of course applies to $\Delta P^{(2)}$ and $\Delta P^{(3)}$ as well. Furthermore, the two-body term is:

$$\Delta P^{(2)} = \sum_{l=2}^3 \sum_{k=1}^{l-1} \Delta P_{kl}^{(2)} \quad \text{XII}$$

With:

$$\Delta P_{12}^{(2)} = P(yyx) - P(xxx) - \Delta P_1^{(1)} - \Delta P_2^{(1)}$$

$$\Delta P_{13}^{(2)} = P(yxy) - P(xxx) - \Delta P_1^{(1)} - \Delta P_3^{(1)}$$

$$\Delta P_{23}^{(2)} = P(xyy) - P(xxx) - \Delta P_2^{(1)} - \Delta P_3^{(1)}$$

And finally, the three-body term is:

$$\Delta P^{(3)} = P(yyy) - P(xxx) - \Delta P^{(2)} - \Delta P^{(1)} \quad \text{XIII}$$

This formalism has been applied on the $\text{Cr}_n\text{Fe}_{3-n}\text{O}(\text{Fo}/\text{OAc})_6(\text{Py})_m$ system, the total electronic energy in section 2.7, and the band splitting between the symmetric and asymmetric carboxylate stretch mode in section 6.5. For symmetric examples, the different permutations can be degenerate in respect to the relevant property P , e.g. in their total electronic energy (see **Figure 16**). For triangular complexes, all three mixed metal permutations are energetically degenerate, provided that the axial positions are equally populated or empty. In linear complexes, the two permutations with the heterometal in the terminal position can be degenerate. If that is not the case, all permutations have to be considered separately.

2.8 References Chapter 2

1. Eichler, J. & Eichler, H.-J. *Laser. Laser* (Springer Berlin Heidelberg, 2010). doi:10.1007/978-3-642-10462-6
2. Inutan, E. & Trimpin, S. Laserspray ionization (LSI) ion mobility spectrometry (IMS) mass spectrometry. *Journal of the American Society for Mass Spectrometry* **21**, 1260-1264 (2010).
3. Franken, P. A., Hill, A. E., Peters, C. W. & Weinreich, G. Generation of Optical Harmonics. *Physical Review Letters* **7**, 118-119 (1961).
4. Baxter, G. W. *et al.* Spectroscopic diagnostics of chemical processes: applications of tunable optical parametric oscillators. *Applied Physics B* **71**, 651-663 (2000).
5. Lang, J. *et al.* Magnetostructural correlation in isolated trinuclear iron(III) oxo acetate complexes. *Physical Chemistry Chemical Physics* **20**, 16673-16685 (2018).
6. Bakker, J. M., Besson, T., Lemaire, J., Scuderi, D. & Maitre, P. Gas-Phase Structure of a π -Allyl-Palladium Complex: Efficient Infrared Spectroscopy in a 7 T Fourier Transform Mass Spectrometer. *The Journal of Physical Chemistry A* **111**, 13415-13424 (2007).
7. Lang, J. Characterization of Structures Fragmentation Pathways and Magnetism of Mononuclear and Oligonuclear Transition Metal Complexes in Isolation. (TU Kaiserslautern, 2017).
8. Gerhards, M. High energy and narrow bandwidth mid IR nanosecond laser system. *Optics Communications* **241**, 493-497 (2004).
9. Fenn, J. B. Electrospray wings for molecular elephants (Nobel lecture). *Angewandte Chemie - International Edition* **42**, 3871-3894 (2003).
10. Fenn, J. B., Mann, M., Meng, C. K., Wong, S. F. & Whitehouse, C. M. Electrospray ionization—principles and practice. *Mass Spectrometry Reviews* **9**, 37-70 (1990).
11. Yamashita, M. & Fenn, B. J. Negative ion production with the electrospray ion source. *J Phys.Chem.* **88**, 4671-4675 (1984).
12. Yamashita, M. & Fenn, J. B. Electrospray ion source. Another variation on the free-jet theme. *Journal of Physical Chemistry* **88**, 4451-4459 (1984).
13. Taylor, G. Disintegration of Water Drops in an Electric Field. *Proceedings of the Royal Society A: Mathematical, Physical and Engineering Sciences* **280**, 383-397 (1964).
14. Chen, H. K., Chang, C. K., Wu, C. C., Huang, M. C. & Wang, Y. S. Synchronized Dual-Polarity Electrospray Ionization Mass Spectrometry. *Journal of the American Society for Mass Spectrometry* **20**, 2254-2257 (2009).
15. Konermann, L., Ahadi, E., Rodriguez, A. D. & Vahidi, S. Unraveling the Mechanism of Electrospray Ionization. *Analytical Chemistry* **85**, 2-9 (2013).
16. Rayleigh, Lord. XX. On the equilibrium of liquid conducting masses charged with electricity. *The London, Edinburgh, and Dublin Philosophical Magazine and Journal of Science* **14**, 184-186 (1882).
17. Schmelzeisen-Redeker, G., Bütfering, L. & Röllgen, F. W. W. Desolvation of ions and molecules in thermospray mass spectrometry. *International Journal of Mass Spectrometry and Ion Processes* **90**, 139-150 (1989).
18. Thomson, B. A. & Iribarne, J. V. Field induced ion evaporation from liquid surfaces at atmospheric pressure. *The Journal of Chemical Physics* **71**, 4451-4463 (1979).
19. Wang, G. & Cole, R. B. Charged residue versus ion evaporation for formation of alkali metal halide cluster ions in ESI. *Analytica Chimica Acta* **406**, 53-65 (2000).
20. Gross, J. H. *Massenspektrometrie - Ein Lehrbuch.* (2013). doi:10.1007/978-3-8274-2981
21. Menges, F. *et al.* *ESI-MS and IR-MPD studies on mono-, di- and trimetallic transition metal complexes.* (2013).
22. Daltonics, B. amaZon SL Series. *User Manual*
23. Bruker Daltonics amaZon SL Series User Manual.
24. Lang, J. *et al.* Intermetallic Competition in the Fragmentation of Trimetallic Au-Zn-Alkali Complexes. *Chemistry - A European Journal* **22**, 2345-2355 (2016).
25. Gaffga, M. *et al.* Multistate-Mediated Rearrangements and FeCl₂ Elimination in Dinuclear FePd Complexes. *The Journal of Physical Chemistry A* **119**, 12587-12598 (2015).
26. Paul, W. Electromagnetic Traps for Charged and Neutral Particles(Nobel Lecture). *Angewandte Chemie*

- International Edition in English* **29**, 739-748 (1990).
27. Paul, W. & Steinwedel, H. Ein neues Massenspektrometer ohne Magnetfeld. *Z. Naturforsch.* **8a**, 448-450 (1952).
 28. Kelly, R. T., Tolmachev, A. V., Page, J. S., Tang, K. & Smith, R. D. The ion funnel: Theory, implementations, and applications. *Mass Spectrometry Reviews* **29**, n/a-n/a (2009).
 29. Julian, R. R., Mabbett, S. R. & Jarrold, M. F. Ion funnels for the masses: Experiments and simulations with a simplified ion funnel. *Journal of the American Society for Mass Spectrometry* **16**, 1708-1712 (2005).
 30. Becker, C. *et al.* A novel approach to collision-induced dissociation (CID) for ion mobility-mass spectrometry experiments. *Journal of the American Society for Mass Spectrometry* **20**, 907-914 (2009).
 31. Xie, Y. & Lebrilla, C. B. Infrared multiphoton dissociation of alkali metal-coordinated oligosaccharides. *Analytical Chemistry* **75**, 1590-1598 (2003).
 32. Collin, O. L., Beier, M. & Jackson, G. P. Dynamic Collision-Induced Dissociation of Peptides in a Quadrupole Ion Trap Mass Spectrometer. *Analytical Chemistry* **79**, 5468-5473 (2007).
 33. Gray, A., Tsybizova, A. & Roithova, J. Carboxylate-assisted C-H activation of phenylpyridines with copper, palladium and ruthenium: A mass spectrometry and DFT study. *Chemical Science* **6**, 5544-5553 (2015).
 34. Zhang, X. G., Liyanage, R. & Armentrout, P. B. Potential energy surface for activation of methane by Pt⁺: A combined guided ion beam and DFT study. *Journal of the American Chemical Society* **123**, 5563-5575 (2001).
 35. Lang, J., Fries, D. V. & Niedner-Schatteburg, G. Characterization of Trinuclear Oxo Bridged Cobalt Complexes in Isolation. *Zeitschrift für Physikalische Chemie* **232**, 649-669 (2018).
 36. James D. Dill, Camel L. Fischer, and F. W. M. Collisional Activation and Theoretical Studies of Gaseous COH₃⁺ Ions. *Journal of the American Chemical Society* **1**, 6531-6534 (1979).
 37. Sleno, L. & Volmer, D. A. Ion activation methods for tandem mass spectrometry. *Journal of Mass Spectrometry* **39**, 1091-1112 (2004).
 38. Levsen, K. & Schwarz, H. Collisional Activation Mass Spectrometry—A New Probe for Determining the Structure of Ions in the Gas Phase. *Angewandte Chemie International Edition in English* **15**, 509-519 (1976).
 39. Škriba, A., Schulz, J. & Roithová, J. Monitoring of Reaction Intermediates in the Gas Phase: Ruthenium-Catalyzed C–C Coupling. *Organometallics* **33**, 6868-6878 (2014).
 40. Gabelica, V. & Pauw, E. De. Internal energy and fragmentation of ions produced in electrospray sources. *Mass Spectrometry Reviews* **24**, 566-587 (2005).
 41. Shukla, A. K. & Futrell, J. H. Tandem mass spectrometry: Dissociation of ions by collisional activation. *Journal of Mass Spectrometry* **35**, 1069-1090 (2000).
 42. Laskin, J., Kong, R. P. W. W., Song, T. & Chu, I. K. Effect of the basic residue on the energetics and dynamics of dissociation of phosphopeptides. *International Journal of Mass Spectrometry* **330-332**, 295-301 (2012).
 43. Falvo, F. *et al.* Fragmentation reactions of thiourea- and urea-compounds examined by tandem MS-, energy-resolved CID experiments, and theory. *International Journal of Mass Spectrometry* **330-332**, 124-133 (2012).
 44. Zins, E.-L. *et al.* Investigations of the fragmentation pathways of benzylpyridinium ions under ESI/MS conditions. *Journal of Mass Spectrometry* **44**, n/a-n/a (2009).
 45. Barylyuk, K. V., Chingin, K., Balabin, R. M. & Zenobi, R. Fragmentation of benzylpyridinium “thermometer” ions and its effect on the accuracy of internal energy calibration. *Journal of the American Society for Mass Spectrometry* **21**, 172-177 (2010).
 46. Kaczorowska, M. A. & Cooper, H. J. Electron induced dissociation: A mass spectrometry technique for the structural analysis of trinuclear oxo-centred carboxylate-bridged iron complexes. *Journal of the American Society for Mass Spectrometry* **21**, 1398-1403 (2010).
 47. Meyer, P. Bi-logistic growth. *Technological Forecasting and Social Change* **47**, 89-102 (1994).
 48. Meyer, P. S., Yung, J. W. & Ausubel, J. H. A Primer on Logistic Growth and Substitution. *Technological Forecasting and Social Change* **61**, 247-271 (1999).
 49. Lipovetsky, S. Double logistic curve in regression modeling. *Journal of Applied Statistics* **37**, 1785-1793 (2010).

50. Krüger, J. S. Regioselective fragmentation of trimeric iron and chromium carboxylates. (TU Kaiserslautern, 2018).
51. Nesbitt, D. J. & Field, R. W. Vibrational Energy Flow in Highly Excited Molecules: Role of Intramolecular Vibrational Redistribution. *The Journal of Physical Chemistry* **100**, 12735-12756 (1996).
52. Gruebele, M. & Wolynes, P. G. Vibrational Energy Flow and Chemical Reactions. *Accounts of Chemical Research* **37**, 261-267 (2004).
53. Wong, V. & Gruebele, M. How does vibrational energy flow fill the molecular state space? *Journal of Physical Chemistry A* **103**, 10083-10092 (1999).
54. Woodin, R. L., Bomse, D. S. & Beauchamp, J. L. Multiphoton dissociation of molecules with low power continuous wave infrared laser radiation. *Journal of the American Chemical Society* **100**, 3248-3250 (1978).
55. Bagratashvili, V. N., Letokhov, V. S., Makarov, A. A. & Ryabov, E. A. Multiple Photon IR Laser Photophysics and Photochemistry. V. *Laser Chemistry* **5**, 53-105 (1984).
56. Roithová, J. Characterization of reaction intermediates by ion spectroscopy. *Chem. Soc. Rev.* **41**, 547-559 (2012).
57. Brodbelt, J. S. & Wilson, J. J. Infrared multiphoton dissociation in quadrupole ion traps. *Mass Spectrometry Reviews* **28**, 390-424 (2009).
58. Eyler, J. R. Infrared multiple photon dissociation spectroscopy of ions in Penning traps. *Mass Spectrometry Reviews* **28**, 448-467 (2009).
59. Forbes, M., Talbot, F. & Jockusch, R. The Spectroscopy of Ions Stored in Trapping Mass Spectrometers. in *Practical Aspects of Trapped Ion Mass Spectrometry, Volume V* 239-290 (CRC Press, 2009). doi:10.1201/9781420083743-c9
60. Nakamoto, K. *Infrared and Raman Spectra of Inorganic and Coordination Compounds. Handbook of Vibrational Spectroscopy* (John Wiley & Sons, Inc., 2008). doi:10.1002/9780470405840
61. Polfer, N. C. Infrared multiple photon dissociation spectroscopy of trapped ions. *Chemical Society Reviews* **40**, 2211 (2011).
62. MacAleese, L. & Maître, P. Infrared spectroscopy of organometallic ions in the gas phase: From model to real world complexes. *Mass Spectrometry Reviews* **26**, 583-605 (2007).
63. Fridgen, T. D. Infrared consequence spectroscopy of gaseous protonated and metal ion cationized complexes. *Mass Spectrometry Reviews* **28**, 586-607 (2009).
64. Polfer, N. C. & Oomens, J. Vibrational spectroscopy of bare and solvated ionic complexes of biological relevance. *Mass Spectrometry Reviews* **28**, 468-494 (2009).
65. Polfer, N. C., Oomens, J. & Dunbar, R. C. Alkali Metal Complexes of the Dipeptides PheAla and AlaPhe: IRMPD Spectroscopy. *ChemPhysChem* **9**, 579-589 (2008).
66. Hewer, J. M. Magnetic and Structural Characterization of Isolated Gaseous Ions by XMCD and IRMPD Spectroscopy. (TU Kaiserslautern, 2017).
67. Lang, J., Mohrbach, J., Dillinger, S., Hewer, J. M. & Niedner-Schatteburg, G. Vibrational blue shift of coordinated N₂ in [Fe₃O(OAc)₆(N₂)_n]⁺: “non-classical” dinitrogen complexes. *Chemical Communications* **53**, 420-423 (2017).
68. Schuchmann, J. P. Modifikation von Analysemethoden für die differenzierte Interpretation von fragmentspezifischen IRMPD Spektren: Anwendung auf trinukleare oxo- zentrierte Eisenkomplexe. (TU Kaiserslautern, 2018).
69. Polfer, N. C. *et al.* Differentiation of Isomers by Wavelength-Tunable Infrared Multiple-Photon Dissociation-Mass Spectrometry: Application to Glucose-Containing Disaccharides. *Analytical Chemistry* **78**, 670-679 (2006).
70. Scott Hopkins, W., Marta, R. A., Steinmetz, V. & McMahon, T. B. Mode-specific fragmentation of amino acid-containing clusters. *Physical Chemistry Chemical Physics* **17**, 28548-28555 (2015).
71. Lemaire, J. *et al.* Gas Phase Infrared Spectroscopy of Selectively Prepared Ions. *Physical Review Letters* **89**, 273002 (2002).
72. Pankewitz, T., Lagutschenkov, A., Niedner-Schatteburg, G., Xantheas, S. S. & Lee, Y. T. Infrared spectrum of NH₄⁺(H₂O): Evidence for mode specific fragmentation. *Journal of Chemical Physics* **126**, 074307 (2007).
73. Stefan, S. E. & Eyler, J. R. Differentiation of glucose-containing disaccharides by infrared multiple photon dissociation with a tunable CO₂ laser and Fourier transform ion cyclotron resonance mass

- spectrometry. *International Journal of Mass Spectrometry* **297**, 96-101 (2010).
74. Ortiz, D. *et al.* Radiolysis as a solution for accelerated ageing studies of electrolytes in Lithium-ion batteries. *Nature Communications* **6**, 6950 (2015).
 75. Oomens, J., Sartakov, B. G., Meijer, G. & von Helden, G. Gas-phase infrared multiple photon dissociation spectroscopy of mass-selected molecular ions. *International Journal of Mass Spectrometry* **254**, 1-19 (2006).
 76. Maître, P. *et al.* Ultrasensitive spectroscopy of ionic reactive intermediates in the gas phase performed with the first coupling of an IR FEL with an FTICR-MS. *Nuclear Instruments and Methods in Physics Research Section A: Accelerators, Spectrometers, Detectors and Associated Equipment* **507**, 541-546 (2003).
 77. Oomens, J., Moore, D. T., Meijer, G. & Helden, G. Von. Infrared multiple photon dynamics and spectroscopy of cationic PABA and its dehydroxylated fragment ion. *Physical Chemistry Chemical Physics* **6**, 710 (2004).
 78. Martens, J., Grzetic, J., Berden, G. & Oomens, J. Structural identification of electron transfer dissociation products in mass spectrometry using infrared ion spectroscopy. *Nature Communications* **7**, 11754 (2016).
 79. Polfer, N., Sartakov, B. G. & Oomens, J. The infrared spectrum of the adamantyl cation. *Chemical Physics Letters* **400**, 201-205 (2004).
 80. Thomas, L. H. The calculation of atomic fields. *Mathematical Proceedings of the Cambridge Philosophical Society* **23**, 542 (1927).
 81. Fermi, E. Eine statistische Methode zur Bestimmung einiger Eigenschaften des Atoms und ihre Anwendung auf die Theorie des periodischen Systems der Elemente. *Zeitschrift für Physik* **48**, 73-79 (1928).
 82. Rajagopal, A. K. & Callaway, J. Inhomogeneous Electron Gas. *Physical Review B* **7**, 1912-1919 (1973).
 83. Andzelm, J. DGauss: Density Functional — Gaussian Approach. Implementation and Applications. in *Density Functional Methods in Chemistry* 155-174 (Springer New York, 1991). doi:10.1007/978-1-4612-3136-3_11
 84. Holthausen, M. C., Heinemann, C., Cornehl, H. H., Koch, W. & Schwarz, H. The performance of density-functional/Hartree–Fock hybrid methods: Cationic transition-metal methyl complexes MCH + 3 (M=Sc–Cu,La,Hf–Au). *The Journal of Chemical Physics* **102**, 4931-4941 (1995).
 85. Koch, W. & Holthausen, M. C. *A Chemist's Guide to Density Functional Theory*. (Wiley-VCH Verlag GmbH, 2001). doi:10.1002/3527600043
 86. M. J. Frisch, G. W. Trucks, H. B. Schlegel, G. E. Scuseria, M. A. Robb, J. R. Cheeseman, G. Scalmani, V. Barone, G. A. Petersson, H. Nakatsuji, X. Li, M. Caricato, A. Marenich, J. Bloino, B. G. Janesko, R. Gomperts, B. Mennucci, H. P. Hratchian, J. V. Ort, and D. J. F. *Gaussian 09 Revision A.02*. Gaussian, Inc. (2016).
 87. Liu, B. & McLean, A. D. Accurate calculation of the attractive interaction of two ground state helium atoms. *The Journal of Chemical Physics* **59**, 4557-4558 (1973).
 88. Sherrill, C. Counterpoise Correction and Basis Set Superposition Error. *Vergil.Chemistry.Gatech.Edu* 1-5 (2010). Available at: <http://vergil.chemistry.gatech.edu/notes/cp.pdf>.
 89. Boys, S. F. & Bernardi, F. The calculation of small molecular interactions by the differences of separate total energies. Some procedures with reduced errors. *Molecular Physics* **19**, 553-566 (1970).
 90. Chmela, J. *et al.* Differential Many-Body Cooperativity in Electronic Spectra of Oligonuclear Transition-Metal Complexes. *ChemPhysChem* **17**, 37-45 (2016).

3 Introduction to the Infrared Spectroscopy of Carboxylates and Other Ligands

In the discussion of infrared spectra, several abbreviations for different infrared modes are commonly used: ν , stretching modes; δ , deformation; ρ , rocking; oop, out-of-plane; ip, in-plane; s, symmetric; and as, asymmetric. Some common applications of these abbreviations are: symmetric carboxylate stretch mode $\nu(\text{COO})_s$; asymmetric carboxylate stretch mode $\nu(\text{COO})_{as}$; methyl bend mode $\delta(\text{CH}_3)$; out of plane $\delta_{oop}(\text{CH})$ and in plane CH bend mode $\delta_{ip}(\text{CH})$; C-C stretch mode $\nu(\text{C}-\text{C})$; carboxylate bend mode $\delta(\text{COO})$; or carboxylate out of plane rocking mode $\rho_{oop}(\text{COO})$.

3.1 Fundamental Vibrational Modes of the Formate Ion

For the formate anion, the simplest ion discussed in this work, there are six fundamental vibrational modes of relevance. They are shown in **Figure 17**. These modes stay consistent, even when the environment of the ion changes, e.g. by being a bridging ligand between two metal centers; although their respective energies are shifted and new modes in combination with the rest of the molecule or ion occur.

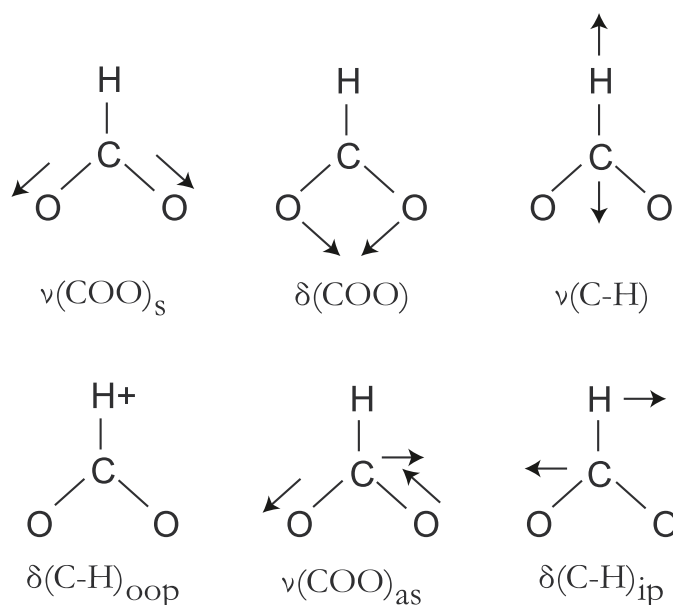


Figure 17 The six normal modes of vibration of the free formate ion HCO_2^- . The + symbol implies motion out of the plane of the diagram. Adapted from Fig. 6.13 in ‘Characterizing Molecules and Molecular Interactions on Surfaces’ by Woodruff et al.¹

3.2 Fermi Resonance, Combination Bands and Overtones

Normally in a polyatomic molecule behaving like a harmonic oscillator, each vibrational normal mode at best has one spectroscopically active transition from the ground state ($\nu = 1 \leftarrow \nu = 0$) associated with it. If anharmonicity is present and the harmonic approximation is not good enough anymore, weak new bands involving overtone and combination transitions can appear in the spectrum².

Fermi resonance can occur in the accidental case that the frequency of an overtone or combination band has nearly the same value as the frequency of another fundamental.

In the example of two interacting bands, two relatively strong bands are measured, where only one strong band for the fundamental was expected. Fermi resonance results in a quantum-mechanical mixing of the overtone and fundamental.

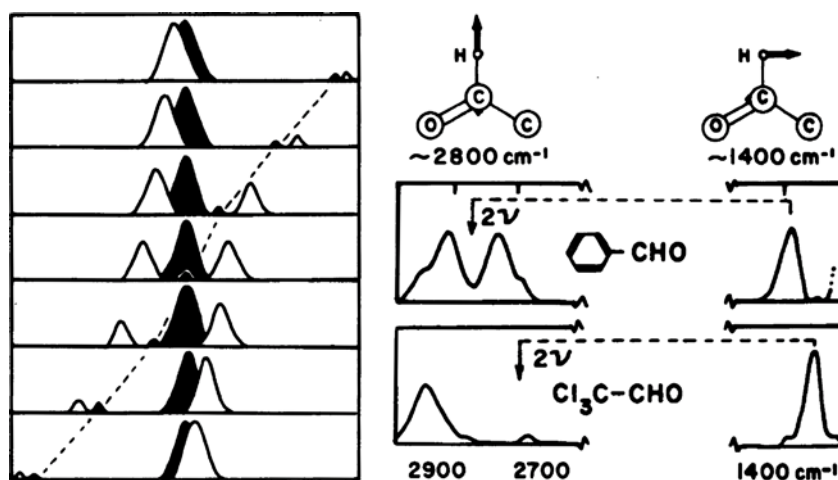


Figure 18 Fermi resonance is strongly involved in the splitting of the C-H stretch band in benzaldehyde. On the left the theoretical unperturbed bands are shaded and the observed bands are unshaded. On the right 2ν marks the expected position of the unperturbed overtone of the C-H bending vibration in two aldehydes. Adapted from Fig. 1.14. in 'Introduction to infrared and Raman spectroscopy' by Colthup et al.³

The Fermi resonance bands are observed at somewhat higher and lower frequencies than the expected unperturbed positions of the fundamental and the overtone mode. Both bands involve the fundamental and the overtone.

In the classical case of benzaldehyde^{3,4}, the $\nu = 1$ level of the CH stretch vibration at 2800 cm^{-1} , is close in energy to the first overtone $\nu = 2$ level of the perpendicular CH bend vibration near 1400 cm^{-1} . These levels can interact quantum-mechanically because of anharmonic terms in the potential energy. When the energy difference between the two unperturbed levels involved is small, the anharmonic terms may cause a significant perturbation. If the two bands coincide, they are symmetrically displaced around the unperturbed position (as seen in **Figure 18**, middle left). In the spectrum of chloroacetaldehyde, the two modes do not coincide well. In result, the two bands near 2800 cm^{-1} are not symmetrically placed around the expected position for the overtone, and the intensities differ strongly.

Relative intensity changes in the two bands in a related series of spectra are caused by small shifts in the position of the overtone relative to the fundamental before mixing.

3.3 Fermi Resonance in Deuteroformyl Moieties

An observation by Spinner et al.⁵ is perhaps of interest in the interpretation of the bare heterometallic formate species (section 6.2.1.3). An apparent doubling of the infrared carbonyl stretching band seen there could be connected to the first overtone of the CD out of plane bending ($2 \times \text{CD op be}$) being in Fermi resonance with the CO stretching mode.

3.4 Formate Spectra

The asymmetric (ν_4) and symmetric carboxylate stretching mode (ν_2) of formate (in itself of C_{2v} symmetry) are observed in the range 1657 - 1567 cm^{-1} and 1366 - 1336 cm^{-1} ⁶⁻⁸. See Nakamoto's 'Infrared and Raman Spectra of Inorganic and Coordination Compounds'⁹ for an excellent introduction.

In their comparisons of the $\nu(\text{COO})_{s/as}$ vibrational modes, Catterick et al.¹⁰ and Deacon et al.¹¹ stress the importance of the band splitting of $\Delta\nu(\text{COO})$. They state that the carboxylate coordination motif can be identified through the frequency difference $\Delta\nu = (\nu_{as} - \nu_s)$ between the two CO stretching vibrations (for monodentate formates $\approx 300 \text{ cm}^{-1}$, bridging formates $\approx 200 \text{ cm}^{-1}$ and bidentate formates $\approx 80 \text{ cm}^{-1}$). This becomes apparent in **Figure 19** and **Figure 20**.

The $\Delta\nu$ values for bridging complexes are greater than those of chelating (bidentate) complexes, and are close to the ionic values. Very small values for unidentate carboxylates are known for complexes with additional water molecules creating a pseudo-bridge¹¹ by hydrogen bonding to the free oxygen of the monodentate carboxylate. This might be apparent in section 8.1. This has been seen for axial formate salt crystals with crystal water, as reported by Cannon et al.¹².

On free formate anions, Thompson et al.¹³ remark that the spectrum of $\text{HCOO}^- \cdot \text{Ar}$ features two prominent bands at 1617 cm^{-1} and 1314 cm^{-1} . This is consistent with earlier photodissociation spectroscopy data by Johnson et al.¹⁴, and can be assigned to the asymmetric and symmetric C-O stretching modes, respectively. The presence of the hydrogen atom results in a red-shift of the asymmetric COO stretching frequency, compared to the value obtained for CO_2^- , along with a corresponding blue-shift of the symmetric COO stretch.

First attempts to assign the vibrational spectra of formate were attempted by Edsall¹⁵ and Fonteyne¹⁶, and additionally for Raman spectra by Newman et al.¹⁷. A broader study for formate, acetate, and oxalate by Ito and Bernstein¹⁸ further refined those findings. There are also several studies of the inorganic formates¹⁹⁻²¹ and the influence of different metal ions on the IR spectra of formate salts. To confirm these assignments, Hammaker¹⁶ used IR and Raman spectroscopy of ^{13}C enriched sodium formate. The results of those and newer studies can be found summarized in **Table 28**, in the appendix; selected examples are plotted in **Figure 20**.

Harvey et al. did a systematic study of main group¹⁹ and especially sodium formates²², along with Heyns et al.^{23,25} on the polymorphism of formate salt crystals, followed by works on copper²⁶ and other inorganic formates¹⁹. Curiously, a number of studies has also been done on the actinide formates^{25,27-29} and rare earth formates³⁰. The thorium formates²⁵ exhibit similar overtone and combination bands to the results in the present work, this will be discussed later in chapter 7. See **Figure 20** in section 3.4.2, based on the literary values of **Table 26** in the appendix for more.

Other heavy elements induce similar behavior, a somewhat recent example being $\text{Y}(\text{HCOO})_3 \cdot 2 \text{H}_2\text{O}$ ³¹, along with a whole series of rare earth formates (La, Pr, Nd, Gd, Tb and Y)³². Formates of lighter metals can do so as well, especially at lower temperatures: $\text{Mg}(\text{HCOO})_3$ ^{33,34}, $\text{Cu}_x\text{M}_{1-x}(\text{HCOO})_2 \cdot \text{H}_2\text{O}$ with (M = Mn, Co, Ni, Zn, and Cd)³⁴ and $\text{Cu}(\text{II})$ ^{26,35}.

Spinner et al.³⁶, having several decades of previous work on formate vibrational spectroscopy^{5,37-39}, took the identification of the formate bands a good bit further; by not only employing H/D isotopomerization but also ¹⁸O/¹⁶O and ¹²C/¹⁴C exchange. They observe that for polarized bands, p usually changes only by a small amount on isotopic substitution. CH and CD stretch modes are exceptions, and the CH stretch mode is highly polarized. An even greater corresponding difference is found between the overtones of the $2\delta(\text{CH/D})_{\text{ip}}$ in plane bend.

These overtones derive most of their intensity by Fermi resonance with the CH and CD stretch modes. In addition, the fact that $\delta(\text{CH})_{\text{ip}}$ is much more highly polarized than $\delta(\text{CD})_{\text{ip}}$ is reflected in the polarizability of their overtones. This is one more hint at the nature of the overtone bands for non-coordinated formate ions.

Bartholomew et al.^{40,41} looked at the temperature and pressure dependence of the Fermi doublet involving the CH stretch mode of formate in aqueous solution. They observe a strong temperature and pressure dependence for the Fermi resonance, which also matches the observation of Saxon et al.⁴²; the intensity ratio of the two $\nu(\text{CH})$ components at 2840 and 2910 cm^{-1} is reversed after cooling.

Krekeler, Botschwina et al.⁴³ did a full anharmonic theoretical study for the gas-phase formate and deuterio-formate anions $\text{HCO}_2^-/\text{DCO}_2^-$, that match well to gas-phase studies. This is the result of Botschwina's long series of works on the nature of the anharmonicity of the formate anion⁴⁴.

For the free formate anion, excellent Ar tagged spectra were obtained by Mark Johnson and Geradi et al.^{14,45}. They observe: *'One complication that is well documented in HCO_2^- spectroscopy^{23,38-40} is the relatively strong Fermi-type interaction between the in-plane CH bending $\nu = 2$ level ($2\nu_{\text{IP}} \text{H}$) and the $\nu = 1$ level of the CH stretch vibration. The anharmonic theoretical treatment reported in Krekeler et al.⁴³ accurately predicted this $2\nu_{\text{IP}} \text{H}$ transition energy at 2677 cm^{-1} , and it is observed here for the first time in the slightly perturbed, argon tagged ion. A second weak transition in the HCO_2^- spectrum occurs at 2928 cm^{-1} , which is quite close to the expected location of a combination band involving simultaneous excitation of the symmetric and asymmetric CO stretches ($\nu_{\text{CO}_s} + \nu_{\text{CO}_a}$). That transition is anticipated to occur at 2936 cm^{-1} based on the simple sum of the experimental fundamentals.'*

In their review on CO₂ activation, Dodson et al.⁴⁶ put this into perspective. The $\nu_s + \nu_{as}$ combination band was observed by Gerardi et al.¹⁴ at 2928 cm⁻¹ in the gas phase. The C-H stretching mode in HCO₂⁻ is highly anharmonic, with a fundamental energy that is anomalously low, both in the gas phase¹⁴ and in rare gas matrices⁴⁷. It has a calculated C-H bond distance of 113 pm and a measured gas-phase vibration at 2449 cm⁻¹.

Upon solvation with just one water molecule, which binds to the COO⁻ group, the ν_{CH} vibration blue-shifts by more than 100 cm⁻¹, bringing this mode much closer to the bulk value.

This can be seen very well in **Figure 20** in section 3.4.2. In both aqueous and polycrystalline NaHCO₂, the $\nu(CH)$ vibration is in the range of 2800 - 2830 cm⁻¹^{40,48}. Georges et al. extended this study to the formic acid dimer, resulting into even more combination bands⁴⁹.

The fluoroformate anion⁵⁰⁻⁵² is another hint at the resilience of the anharmonic behavior in formate ions to drastic changes in their environment or constituents. It also shows coupling between C-F modes and COO modes. It is the carboxylate ion with the widest splitting between the symmetric and asymmetric COO vibration of over 520 cm⁻¹. Stewart et al.⁵³ also observe strong evidence for such anharmonicity in IR fluorescence experiments in methyl formate.

3.4.1 IR Signatures of Formate on Surfaces

Further literature research by Calatayud et al.^{66,68} shows that the spectral features of formate survive a wide range of conditions. Besides the metal complexes, surface bound carboxylates (especially formate) are important intermediates in industry and synthesis. As discussed previously in section 3.4, they still preserve many of the spectral features of the carboxylates in solution, in solid phase or gas phase.

Formate is an important intermediate in the activation of CO₂ and in the synthesis of important feed stock chemicals like methanol. Formate on surfaces is an important intermediate in water gas shift catalysis⁷⁴; on Ru surfaces⁷⁵ (Ru(001); K-Ru) during CO/H₂ catalysis; on Al(111)⁷⁶; and other metal oxide surfaces⁵⁴ (see table 8 therein). This explains the enormous number of publication on the topic^{54,55,64-73,56-63}, as compiled e.g. by Calatayud et al.^{66,68}.

Formate on Cu SiO surfaces⁷⁷ also shows two bands in the CH region, as do formates on Cu surfaces^{42,78,79} (with a weak wiggle at about 3000 cm⁻¹) and on CeO₂⁸⁰, where those bands are used to observe the catalytic formation of formate under heating of CO on CeO₂ surfaces at over 400 K.

Al^{III} behaves in a similar fashion, as Donaldson et al.²⁰ note. With a few exceptions, all the formates studied show all six fundamental bands, as shown in **Figure 17**. In many cases, ν_5 , ν_2 , and ν_3 are split, and occasionally ν_4 and ν_6 appear as doublets. A number of overtones and combinations are also found.

Busca et al.⁷³ remark that in the $\nu(CH)$ frequency region, which is very useful to identify the adsorbed species, the spectra of formate ions are complex; due to the Fermi resonances between the $\nu(CH)$

fundamental and combinations or overtones of the bands. This seems to extend to silver surfaces too; McQuillan et al.⁸¹ measured acetate and formate on silver, their Raman spectra also show three bands at 3000 cm^{-1} for formate. Morrow et al.¹⁹ argue that the assignment of $\nu_{\text{comb}} = \nu(\text{COO})_{\text{as}} + \delta(\text{CH})$ is problematic; on the grounds of symmetry selection rules for single, highly symmetric surface formate species, and the strict selection rules of infrared reflection-absorption spectroscopy (IRAS).

In contrast, weaker selection rules in the IR studies of sodium formate may make that assignment more likely. Similar ambiguities exist in the assignment of $2\delta(\text{CH})$, but in view of the weak fundamental, it is surprising that the overtone is observed at all.

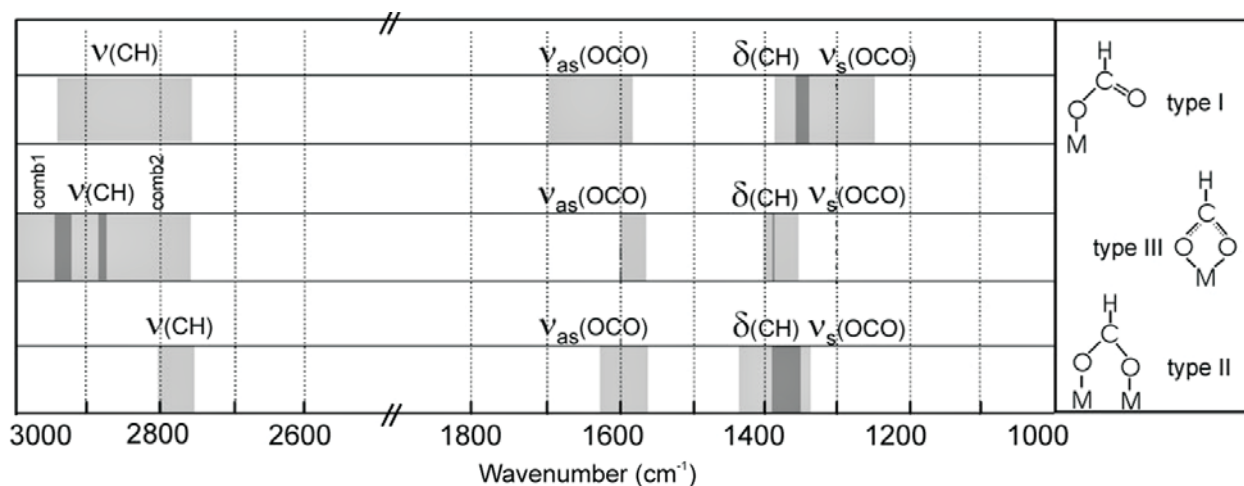


Figure 19 Experimental IR vibrational frequency correlation chart of different types of formate species over several metal oxides and organometallic complexes [comb 1 stands for $\nu(\text{COO})_{\text{as}} + \delta(\text{CH})$ and comb 2 stands for $\nu(\text{COO})_{\text{s}} + \delta(\text{CH})$]. The compiled data corresponds to monodentate (type I), bridged (type II), and bidentate (type III) formate species⁵⁴⁻⁷³. The light-grey regions indicate the range for the reported vibrational frequencies, while the dark-grey regions correspond to the overlapping between two neighboring light-grey regions, that is, between two vibrational modes of the same type of formate. Reproduced with permission from *Phys. Chem. Chem. Phys.*, 2009, **11**, 1397 - 1405⁶⁸.

Morrow et al.¹⁹ argue that in every case this difference must be the result of Fermi resonance with the fundamental $\nu(\text{CH})$, also rationalizing the variations in the difference between the observed and calculated frequency values of $2\delta(\text{CH})$. This matches the observations by Toomes⁸² and Weisel^{75,83}, arguing against COO mode involvement, based on ^{13}C isotope exchange studies for Pt and K doped Co(100) surfaces.

However, Dubois et al.⁸⁴ disagree and insist the feature at 2930 cm^{-1} to be the combination of the asymmetric O-C-O stretch and the in-plane C-H bending mode. This band has been observed in the vibrational spectra of the formate anion, both in aqueous solution⁸⁵ and in the solid state⁸⁵; as well as formates formed by the chemisorption of formic acid on Cu(110) by Hayden et al.^{86,87}. Further agreement comes from Nakano⁸⁸ over Cu(111); together with Bowker^{78,89} on Cu(110); Busca et al.^{54,73,90} on V/Ti oxide catalysts; Penner et al.⁹¹ on Y_2O_3 , YSZ-8, and ZrO_2 ; Catalyund et al.^{67,68} on Ga oxide; and finally Jones et al.^{92,93} on GaAs and Ni(110)⁹³.

3.4.2 Trends in the Formate Vibrational Modes

The position of the vibrational bands of a selected number of formates is shown in **Figure 20**. It nicely shows the range of values the different formate modes can have; depending on their environment, conditions, and bonding partners. The CH stretch mode (black box) shows a very strong dependence on the environment, especially in the switch from the free ions; be it in Ne matrix or with an Ar tag, to adding a single water, and then to an aqueous solution. Following the band shifts from the free Ar tagged ion [1]⁹⁴, the Ar tagged ion with one water adduct [1]⁹⁴, to the ion in aqueous solution [3]²³, shows a nice progression of all relevant or significant modes towards their position in the coordinated state. This is most notable in the behavior of the CH stretch mode and the first overtone CH bend mode (light blue triangle). Likewise, the oxoFeFe [20]⁶ species introduced in section 1.4.1 is a nice example case showing all fundamental modes, combination, and overtones related to the formate ion. This will be very helpful for our discussion in section 7.1., where the 2500 - 3500 cm⁻¹ region of this graph is compared against our observed band positions (see **Figure 61**).

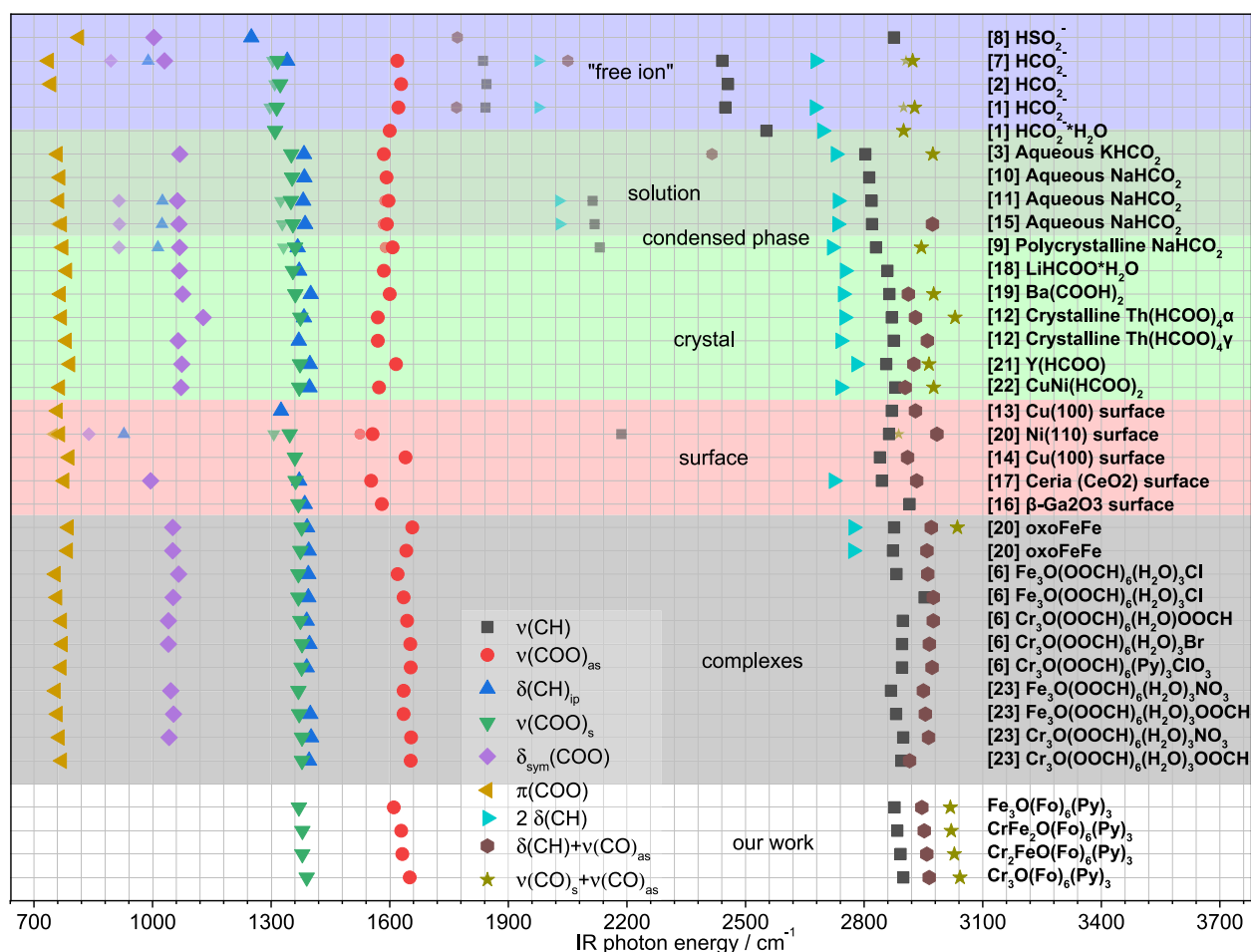


Figure 20 Overview of the spectra of several selected formate species as free ion, in solution, in crystals, on surfaces and finally on trimetallic basic formate complexes and our own results introduced in chapter 6 and chapter 7. For the raw values and references refer to **Table 26** and **Table 27** in the appendix.

3.5 Acetate IR spectra

3.5.1 CO Stretch Modes

The dependence of the $\nu(\text{COO})_{\text{as/s}}$ splitting is characterized by Deacon et al.¹¹ in his review article on the relationships between the carbon-oxygen stretching frequencies of carboxylato complexes and the type of carboxylate coordination. Tackett et al.⁹⁵ also classify the IR spectra of metal acetates: ionic, unidentate, bidentate, and bridging acetate. This is in tradition with early works of Edwards et al.⁹⁶ on transition metal acetates in solid state IR and previously Donaldson et al.^{20,21} on main group acetates. Nara et al.⁹⁷ also worked on a theoretical treatment of this phenomenon in their paper ‘Correlation between the Vibrational Frequencies of the Carboxylate Group and the Types of Its Coordination to a Metal Ion: An ab Initio Molecular Orbital Study’. Sutton et al.⁸ follow up with ‘Modeling the IR Spectra of Aqueous Metal Carboxylate Complexes: Correlation between Bonding Geometry and Stretching Mode Wavenumber Shifts’.

Cotton et al.^{12,98} also conducted systematic studies of bridging ligand permutations⁹⁹⁻¹⁰¹. Heyns et al.^{23,26,102} worked on surface spectroscopy of cold Cu^{II} formate and acetates, along with Frost et al.¹⁰³ with more cold IR studies. Very recently, Oomens et al.^{104,105} measured the gas phase IR electron detachment spectrum of free acetate, under exclusion of bulk, solution, tag, or counter ion influences; using the free electron laser (FEL) at the FELIX facility. Here the symmetric $\nu(\text{COO})_{\text{s}}$ mode is considerably more redshifted than in acetates bonding to a metal.

A systematic comparison of the IR spectra of all basic $(\text{Fe/Cr})_3$ acetates was done by Zhang et al.^{106,107}, already showing the systematic shift of the asymmetric COO and the small shift of the symmetric COO stretch in their paper: ‘Infrared spectra of four trinuclear μ_3 -oxo-acetato complexes of chromium and iron and empirical assignment of $\nu(\text{Cr-L})$ ’.

Amani et al.¹⁰⁸ summarize the literature, stating that the IR spectra of the carboxylate complexes are usually dominated by two strong bands between 1350 and 1650 cm^{-1} arising from the carbon-oxygen stretching vibrations. The frequency difference $\Delta\nu$ ($\Delta\nu = \nu(\text{COO})_{\text{as}} - \nu(\text{COO})_{\text{s}}$) is correlated with the coordination mode of the carboxylate ligand. The $\Delta\nu$ value is smaller for a bidentate bridging mode of the acetate ligand than those of NaO_2CCH_3 (164 cm^{-1}), as is anticipated^{9,11,98,109}. According to Deacon et al.¹¹, monodentate carboxylates show a bigger splitting of the two modes instead.

3.5.2 CH₃ Stretch Modes

As previously seen for the formate ion, the methyl group is not free of spectroscopic surprises. Barnes et al.¹¹⁰ comments on CH_3 overtones/Fermi resonances in methanol: ‘*The band at 2848 cm^{-1} , is clearly the symmetric stretch; the bands at 3005 and 2962 cm^{-1} , each of which shifts by about 10 cm^{-1} on ^{13}C substitution, while the 2956 cm^{-1} band is not affected, must be the asymmetric stretches. The remaining absorptions are due to overtones and combinations of the CH_3 deformation modes, in Fermi resonance with the CH stretches (thus making the A^1 stretch the higher frequency band)*’.

This phenomenon is explored in detail on methyl groups on aromatic systems by Zwier et al.¹¹¹, in conjunction with extended high level ab initio calculations. They also observe the bands between 2930 and 2980 cm^{-1} , and below 2900 cm^{-1} . These bands are assigned to Fermi resonances with combination and overtones of the $\delta(\text{CH}_3)$ modes. This confirms previous assignments of Lavalley et al.¹¹² and McKean et al.¹¹³ for a broad variety of methyl halogens and other species.

This rough pattern of three primary modes and a combination mode below is also applicable for the acetates. Myshakin et al.¹¹⁴ observe three pronounced, sharp bands between 2900 and 3000 cm^{-1} in gas-phase Ar-tagged action spectroscopy of $\text{CH}_3\text{CO}_2^-\cdot(\text{H}_2\text{O})$. According to them they can be assigned with confidence to the CH stretch vibrations. Similar to Zwier et al.¹¹¹, they also use cubic force field calculations for the CH_3 stretch modes to successfully improve on harmonic calculations and to approximate their experimental spectra. Their calculations give an overall splitting for the CH stretch vibrations in closer agreement with experiment than found in the harmonic approximation. Unfortunately, the expected $2\delta(\text{CH}_3)$ overtone is right outside the observed area. Follow up work by Johnson et al.¹¹⁵ on acetate plus water with an Ar tag give the following frequencies for CH_3COOH : 2961, 2997, 3048 cm^{-1} , and 2878 cm^{-1} (assigned as $2\delta(\text{CH}_3)_{\text{as}}$; in agreement with Wilmhurst et al.¹¹⁶); for CH_3CO_2^- , 2902, 2941, 2953, and 2967 cm^{-1} ; and for $\text{CH}_3\text{CO}_2^-\cdot\text{H}_2\text{O}$ 2912, 2953, and 2980 cm^{-1} .

Surface spectra reported by Gao et al.¹¹⁷ for vibrational HREEL studies of CH_3COOH , CH_3COOD and $^{13}\text{CD}_3\text{COOH(D)}$ adsorption on Pt(111) and their references for Cu(100)⁴², Al(111)⁷⁶, often only show one broad unresolved band for the CH_3 modes. For solvated acetate La/Na acetate by Rudolph et al.^{118,121} (see their supplement¹²¹ for the $\nu(\text{CH}_3)$ bands), the band shape is very reminiscent of the ones we observed for Fe_3 acetate in section 7.2.

This pattern persists for other complexes of acetate, as Edwards et al.¹²² observe on Fe^{II} acetate; the stretching vibrations of the CH_3 group are seen along with a number of combination bands in the infrared. The bands at 3024, 2984, 2947, and 2858 cm^{-1} (IR), as well as 3019 and 2945 cm^{-1} (Raman), are assigned to modes of the CH_3 group. Still, no analogy is seen in the literature for the broad feature observed in our experiments, even for deuterated acetates (see **Figure 63**). So far, it seems exclusive to basic carboxylates in the gas phase.

3.6 Pyridine Gas Phase IR Spectra

The IR and Raman spectroscopy of pyridine and his isotopomers has a long history^{123,126} and is still a topic of current interest^{127,128}. Like the formate anion, it is a C_{2v} molecule that shows a high degree of anharmonicity and a plethora of overtones and combination bands. As one relevant example, that will be of interest in chapter 7, Bernstein et al.¹²⁵ show a high quality vapor IR spectrum of the relevant CH stretch bands in the 2900 - 3200 cm^{-1} range; that also shows the same satellite bands we observe later in the formate (**Figure 59**) and acetate (**Figure 62**) spectra of our pyridine coordinated species.

3.7 Water Adduct Spectra of Basic Acetates and Formates

The water adducts are often one of the species directly created in the synthesis of the basic metal carboxylates; as the most widely used synthesis route creates them from the metal hydroxides, which are formed by neutralization of the metal(III) chlorides with sodium hydroxide. This will leave enough water in the solution to make it the most abundant axial ligand, although monodentate formate coordination is also known for the formates⁹⁸. Cannon et al.¹² and Zhang et al.^{106,107,129} both study the trends of successive metal substitution in the chromium and iron acetate complexes. Their analysis both focuses on the skeletal vibrations of the M_3O core, with Zhang et al.^{106,107} doing a normal coordinate analysis to derive the associated force constants. Only Cannon et al. show the formate spectrum including the COO stretch modes for the Fe, Cr_2Fe , and Cr_3 formates with water. They¹² remark that the differences in carboxylate band location and shape in their spectra are too unclear for differentiation. Likewise, Zhang et al.¹⁰⁷ only give a range for the shift in the carboxylate modes, with a small window of only 5 cm^{-1} for the symmetrical, and a wider range of 25 cm^{-1} for the asymmetric acetate carboxylate stretch mode. Big differences are shown and discussed on the M_3O core. Both of their results will be useful to compare with eventual IR measurements including the respective skeletal modes. Unfortunately, that is outside the range of our available gas-phase methods. There are studies by Fujihara et al.¹³⁰ of the hydrolysis of bimetallic chromium(III) complexes, where the carboxylate band split $\Delta\nu(\text{COO})$ is one diagnostic tool, among optical and $^1\text{H-NMR}$ spectroscopy, to observe the hydrolysis of carboxylate bridges. First a hydroxide is inserted on one side, and then the carboxylate group is fully cleaved. Similar processes are observed in reverse during the synthesis of the trinuclear oxo-centered carboxylates, as well as during its hydrolysis in physiological tissue, as reported by Vincent et al.¹³¹, using $^2\text{H-NMR}$.

One important intermediate compound in the formation and hydrolysis of the basic carboxylates is the dicarboxylate hex aqua dichromium(III) complex. It is characterized by Lippard et al.¹³² for the formate, along with its diiron(III) counterpart; antiferromagnetic coupling is observed.

The acetate version of these dichromium complexes is characterized by Brudenell et al.¹³³ with a $\Delta\nu(\text{COO})$ of 109 cm^{-1} .

3.8 References Chapter 3

1. Woodruff, D. P. & Delchar, T. A. *Modern Techniques of Surface Science*. (1994). doi:10.1017/CBO9780511623172
2. Holmes, A. Combination Bands, Overtones and Fermi Resonances. *Chemistry LibreTexts* **1**, 1-7 (2013).
3. Colthup, N. B., Daly, L. H. & Wiberley, S. E. *Introduction to infrared and Raman spectroscopy*. Academic Press **1**, (1990).
4. Lin-Vien, D., Colthup, N. B., Fateley, W. G. & Grasselli, J. G. *The Handbook of Infrared and Raman Characteristic Frequencies of Organic Molecules*. Academic Press **1**, (1991).
5. Rowe, J. E. & Spinner, E. Interaction between CO Stretching and Overtone of CD Out-of-plane Bending Observed in the Infrared Spectra of Deuterioformyl Compounds. *Applied Spectroscopy* **33**, 639-640 (1979).
6. Ciupa, A., Trzebiatowska-Gusowska, M. & Ptak, M. Vibrational properties of the mixed-valence iron oxo-complex. *Vibrational Spectroscopy* **86**, 218-222 (2016).
7. Sutton, C. C. R., Franks, G. V. & da Silva, G. Modeling the antisymmetric and symmetric stretching vibrational modes of aqueous carboxylate anions. *Spectrochimica Acta Part A: Molecular and Biomolecular Spectroscopy* **134**, 535-542 (2015).
8. Sutton, C. C. R., da Silva, G. & Franks, G. V. Modeling the IR Spectra of Aqueous Metal Carboxylate Complexes: Correlation between Bonding Geometry and Stretching Mode Wavenumber Shifts. *Chemistry - A European Journal* **21**, 6801-6805 (2015).
9. Nakamoto, K. *Infrared and Raman Spectra of Inorganic and Coordination Compounds*. *Handbook of Vibrational Spectroscopy* (John Wiley & Sons, Inc., 2008). doi:10.1002/9780470405840
10. Catterick, J. & Thornton, P. Structures and Physical Properties of Polynuclear Carboxylates. in *Advances in Inorganic Chemistry and Radiochemistry* **20**, 291-362 (1977).
11. Deacon, G. & Phillips, R. J. Relationships between the carbon-oxygen stretching frequencies of carboxylato complexes and the type of carboxylate coordination. *Coordination Chemistry Reviews* **33**, 227-250 (1980).
12. Johnson, M. K., Cannon, R. D. & Powell, D. B. Vibrational spectra of carboxylato complexes—IV. Mixed-metal and mixed-valence oxo-trinuclear complexes. *Spectrochimica Acta Part A: Molecular Spectroscopy* **38**, 307-315 (1982).
13. Thompson, M. C. & Weber, J. M. Enhancement of infrared activity by moving electrons through bonds – The case of CO₂ anion and carboxylate. *Chemical Physics Letters* **683**, 586-590 (2017).
14. Gerardi, H. K. *et al.* Supporting information to “Unraveling the Anomalous Solvatochromic Response of the Formate Ion Vibrational Spectrum: An Infrared, Ar-Tagging Study of the HCO²⁻, DCO²⁻, and HCO²⁻·H₂O Ions.” *The Journal of Physical Chemistry Letters* **2**, 2437-2441 (2011).
15. Garfinkel, D. & Edsall, J. T. Raman Spectra of Amino Acids and Related Compounds. XI. The Ionization of Cysteine. *Journal of the American Chemical Society* **80**, 3823-3826 (1958).
16. Hammaker, R. M. & Walters, J. P. The infrared spectra of C-13 enriched sodium formate. *Spectrochimica Acta* **20**, 1311-1317 (1964).
17. Newman, R. Polarized Infrared Spectrum of Sodium Nitrite. *The Journal of Chemical Physics* **20**, 444-446 (1952).
18. Ito, K. & Bernstein, H. J. The vibrational spectra of the formate, acetate and oxalate ions. *Canadian Journal of Chemistry* **34**, 170-178 (1956).
19. Harvey, K. B., Morrow, B. a. & Shurvell, H. F. The infrared absorption if some crystalline inorganic formates. *Canadian Journal of Chemistry* **41**, 1181-1187 (1963).
20. Donaldson, J. D., Knifton, J. F. & Ross, S. D. The fundamental vibrational spectra of the formates of the main group elements. *Spectrochimica Acta* **20**, 847-851 (1964).
21. Donaldson, J. D., Knifton, J. F. & Ross, S. D. The effect of the lone pair on the infra-red spectra of some main group acetates. *Spectrochimica Acta* **21**, 275-277 (1965).
22. Charlton, T. L. & Harvey, K. B. Infrared absorption of single crystals of anhydrous sodium formate. *Canadian Journal of Chemistry* **44**, 2717-2727 (1966).
23. Heyns, A. M., Range, K.-J. & Müller, K. The polymorphism of alkali metal formates. Part 4. A Raman study of the phase transition in KHCOO. *Canadian Journal of Chemistry* **69**, 1774-1780 (1991).

24. Mentzen, B. F. & Comel, C. Study of the polymorphism of strontium and calcium formates by infrared spectroscopy. *Spectrochimica Acta Part A: Molecular Spectroscopy* **30**, 1263-1270 (1974).
25. Mentzen, B. F. The infrared absorption of crystalline thorium tetraformates. I. Characterization of thorium tetraformates in the solid state by infrared spectroscopy. *Journal of Solid State Chemistry* **3**, 12-19 (1971).
26. Heyns, A. M. The vibrational spectra of the copper(II) formates. *Journal of Molecular Structure* **18**, 471-485 (1973).
27. Greis, O., Bohres, E. W. & Schwochau, K. Darstellung, Infrarotspektren und röntgenographische Untersuchungen der Tetraformiate von Thorium, Protactinium, Uran und Neptunium. *Zeitschrift für anorganische und allgemeine Chemie* **433**, 111-118 (1977).
28. Schwochau, K. & Drożdżyński, J. Synthesis and properties of neptunium(III) formate. *Inorganic and Nuclear Chemistry Letters* **16**, 423-426 (1980).
29. Bagnall, K. W. Thorium Formiate. in *Gmelin Handbook of Inorganic Chemistry* (ed. Fluck, E.) 37-40 doi:10.1007/978-3-662-08315-6
30. Kartha, V. B. & Venkateswaran, S. Vibrational spectra and normal vibrations of rare earth formates. *Spectrochimica Acta Part A: Molecular Spectroscopy* **37**, 927-934 (1981).
31. Maczka, M., Hanuza, J. & Kaminskii, A. A. Polarized IR, spontaneous and stimulated Raman spectra of Y(HCOO) 3·2H2O single crystal - A new Raman laser material. *Journal of Raman Spectroscopy* **37**, 1257-1264 (2006).
32. Silva, E. N. *et al.* Vibrational modes of rare-earth formates. *Journal of Raman Spectroscopy* **40**, 954-957 (2009).
33. Mączka, M., Pietraszko, A., Macalik, B. & Hermanowicz, K. Structure, Phonon Properties, and Order-Disorder Transition in the Metal Formate Framework of [NH 4][Mg(HCOO) 3]. *Inorganic Chemistry* **53**, 787-794 (2014).
34. Moura, M. R. *et al.* Phonons in isostructural compounds CuxM1-x(HCOO)2*2H2O (M = Mn, Co, Ni, Zn, and Cd): a Raman scattering study. *Journal of Raman Spectroscopy* **33**, 273-277 (2002).
35. Carter, R. O., Poindexter, B. D. & Weber, W. H. Vibrational spectra of copper formate tetrahydrate, copper formate dihydrate and three anhydrous forms of copper formate. *Vibrational Spectroscopy* **2**, 125-134 (1991).
36. Spinner, E. Further Studies of Depolarization Ratios in the Raman Spectrum of Aqueous Formate Ion. *Australian Journal of Chemistry* **38**, 47 (1985).
37. Spinner, E. The effect of disc pressing on the infrared spectrum of potassium formate. Two modifications of HCO2K and DCO2K. *Spectrochimica Acta Part A: Molecular Spectroscopy* **31**, 1545-1546 (1975).
38. Spinner, E. 812. The vibration spectra of some substituted acetate ions. *Journal of the Chemical Society (Resumed)* 4217 (1964). doi:10.1039/jr9640004217
39. Spinner, E. Vibration-spectral studies of carboxylate ions. Part III. Sodium formate, HCO2Na and DCO2Na; Raman-spectral depolarisation ratios in aqueous solution, and band splitting in the solid-state infrared spectrum. *Journal of the Chemical Society B: Physical Organic* 879 (1967). doi:10.1039/j29670000879
40. Bartholomew, R. J. & Irish, D. E. Raman spectral studies of solutions at elevated temperatures and pressures.13. Sodium formate – water. *Canadian Journal of Chemistry* **71**, 1728-1733 (1993).
41. Bartholomew, R. J., Stevenson, W. J. & Irish, D. E. A Raman spectral study of the kinetics of deuterium-hydrogen exchange on the formate anion at elevated temperatures and pressures. *Spectrochimica Acta Part A: Molecular and Biomolecular Spectroscopy* **52**, 1695-1701 (1996).
42. Sexton, B. A. Observation of formate species on a copper (100) surface by high resolution electron energy loss spectroscopy. *Surface Science* **88**, 319-330 (1979).
43. Krekeler, C., Mladenovic, M. & Botschwina, P. A theoretical investigation of the vibrational states of HCO2- and its isotopomers. *Physical Chemistry Chemical Physics* **7**, 882 (2005).
44. Botschwina, P. Structures and spectroscopic properties of small negative molecular ions - theory and experiment. in *Structure / Reactivity and Thermochemistry of Ions* (eds. Ausloos, P. & Lias, S. G.) (NATO ASI Advanced Science Institutes, 1986).
45. Gerardi, H. K. *et al.* Structural characterization of electron-induced proton transfer in the formic acid dimer anion, (HCOOH) 2 – , with vibrational and photoelectron spectroscopies. *The Journal of Chemical*

- Physics* **136**, 134318 (2012).
46. Dodson, L. G., Thompson, M. C. & Weber, J. M. Characterization of Intermediate Oxidation States in CO₂ Activation. *Annual Review of Physical Chemistry* **69**, 231-252 (2018).
 47. Forney, D., Jacox, M. E. & Thompson, W. E. Infrared spectra of trans -HOCO, HCOOH⁺, and HCO₂⁻ trapped in solid neon. *The Journal of Chemical Physics* **119**, 10814-10823 (2003).
 48. Kidd, K. G. & Mantsch, H. H. Formate anion: The physical force field. *Journal of Molecular Spectroscopy* **85**, 375-389 (1981).
 49. Georges, R. *et al.* Jet-cooled and room temperature FTIR spectra of the dimer of formic acid in the gas phase. *Chemical Physics* **305**, 187-196 (2004).
 50. Ault, B. S. Matrix isolation investigation of the fluoroformate anion. *Inorganic Chemistry* **21**, 756-759 (1982).
 51. Schloter, K., Nagel, U. & Beck, W. Structure, stability and vibrational spectrum of the fluoroformate anion. *Chemische Berichte* **113**, 3775-3782 (1980).
 52. Thomas, D. A. *et al.* Vibrational Spectroscopy of Fluoroformate, FCO₂⁻, Trapped in Helium Nanodroplets. *The Journal of Physical Chemistry Letters* **9**, 2305-2310 (2018).
 53. Stewart, G. M., Ensminger, M. D., Kulp, T. J., Ruoff, R. S. & McDonald, J. D. Intramolecular vibrational energy transfer in methyl formate. *The Journal of Chemical Physics* **79**, 3190-3200 (1983).
 54. Busca, G. & Lorenzelli, V. Infrared spectroscopic identification of species arising from reactive adsorption of carbon oxides on metal oxide surfaces. *Materials Chemistry* **7**, 89-126 (1982).
 55. Pokrovski, K., Jung, K. T. & Bell, A. T. Investigation of CO and CO₂ Adsorption on Tetragonal and Monoclinic Zirconia. *Langmuir* **17**, 4297-4303 (2001).
 56. Clarke, D. B. & Bell, A. T. An Infrared Study of Methanol Synthesis from CO₂ on Clean and Potassium-Promoted Cu/SiO₂. *Journal of Catalysis* **154**, 314-328 (1995).
 57. Fornika, R., Dinjus, E., Görls, H. & Leitner, W. Structure and reactivity of dimeric rhodium(i) formate complexes: X-ray crystal structure analysis of $[(\text{cod})\text{rh}(\mu\text{-}\eta^2\text{O},\text{o}'\text{-hco}_2)]_2$ and phosphane-induced hydride transfer to give an η^3 -cyclooctenyl complex. *Journal of Organometallic Chemistry* **511**, 145-155 (1996).
 58. Gibson, D. H. Carbon dioxide coordination chemistry: metal complexes and surface-bound species. What relationships? *Coordination Chemistry Reviews* **185-186**, 335-355 (1999).
 59. Gopal, P. G., Schneider, R. L. & Watters, K. L. Evidence for production of surface formate upon direct reaction of CO with alumina and magnesia. *Journal of Catalysis* **105**, 366-372 (1987).
 60. Grushin, V. V., Bensimon, C. & Alper, H. The First Isolable Organopalladium Formate Complexes: Synthesis, Characterization, and X-ray Structure. Facile and Convenient Thermal Generation of Coordinatively Unsaturated Palladium(0) Species. *Organometallics* **14**, 3259-3263 (1995).
 61. Guglielminotti, E. *et al.* Elementary Steps in CO Hydrogenation on Rh Catalysts Supported on ZrO₂ and Mo/ZrO₂. *Journal of Catalysis* **146**, 422-436 (1994).
 62. Haneda, M. *et al.* In situ Fourier transform infrared study of the selective reduction of NO with propene over Ga₂O₃-Al₂O₃. *Journal of Catalysis* **206**, 114-124 (2002).
 63. Hara, M., Kawamura, M., Kondo, J. N., Domen, K. & Maruya, K. Thermal conversion of methoxy species on dimethyl ether adsorbed CeO₂. *Journal of Physical Chemistry* **100**, 14462-14467 (1996).
 64. Le Peltier, F., Chaumette, P., Saussey, J., Bettahar, M. M. & Lavalley, J. C. In-situ FT-IR spectroscopy and kinetic study of methanol synthesis from CO/H₂ over ZnAl₂O₄ and Cu-ZnAl₂O₄ catalysts. *Journal of Molecular Catalysis A: Chemical* **122**, 131-139 (1997).
 65. Mugniery, X., Chafik, T., Primet, M. & Bianchi, D. Characterization of the sites involved in the adsorption of CO on ZrO₂ and ZnO/ZrO₂ methanol synthesis aerogel catalysts. *Catalysis Today* **52**, 15-22 (1999).
 66. Korhonen, S. T., Calatayud, M. & Krause, A. O. I. Stability of hydroxylated (111) and (101) surfaces of monoclinic zirconia: A combined study by DFT and infrared spectroscopy. *Journal of Physical Chemistry C* **112**, 6469-6476 (2008).
 67. Collins, S., Baltanas, M. & Bonivardi, A. An infrared study of the intermediates of methanol synthesis from carbon dioxide over Pd/-GaO. *Journal of Catalysis* **226**, 410-421 (2004).
 68. Calatayud, M., Collins, S. E., Baltanás, M. A. & Bonivardi, A. L. Stability of formate species on β -Ga₂O₃. *Physical Chemistry Chemical Physics* **11**, 1397 (2009).
 69. Bandara, A., Kubota, J., Wada, A., Domen, K. & Hirose, C. Adsorption and reactions of formic acid

- on (2x2)-NiO(111)/Ni(111) surface. 2. IRAS study under catalytic steady-state conditions. *Journal of Physical Chemistry B* **101**, 361-368 (1997).
70. Bando, K. K., Sayama, K., Kusama, H., Okabe, K. & Arakawa, H. In-situ FT-IR study on CO₂ hydrogenation over Cu catalysts supported on SiO₂, Al₂O₃, and TiO₂. *Applied Catalysis A: General* **165**, 391-409 (1997).
71. Boiadjiev, V. & Tysoe, W. T. Infrared Study of the Surface Species Formed by Sequential Chemical Vapor Deposition of Trimethylaluminum and Methanol on a Hydroxylated Alumina Surface. *Chemistry of Materials* **10**, 334-344 (1998).
72. Millar, G. J., Rochester, C. H. & Waugh, K. C. An FTIR study of the adsorption of formic acid and formaldehyde on potassium-promoted Cu/SiO₂ catalysts. *Journal of Catalysis* **155**, 52-58 (1995).
73. Busca, G., Lamotte, J., Lavalley, J. C. ciaude & Lorenzelli, V. FT-IR study of the adsorption and transformation of formaldehyde on oxide surfaces. *Journal of the American Chemical Society* **109**, 5197-5202 (1987).
74. Kobl, K. *et al.* In situ infrared study of formate reactivity on water-gas shift and methanol synthesis catalysts. *Comptes Rendus Chimie* **18**, 302-314 (2015).
75. Weisel, M. D., Chen, J. G., Hoffmann, F. M., Sun, Y. -K. & Weinberg, W. H. A Fourier transform-infrared reflection absorption spectroscopy study of the formation and decomposition of chemisorbed formate on clean and potassium-modified Ru(001). *The Journal of Chemical Physics* **97**, 9396-9411 (1992).
76. Crowell, J. E., Chen, J. G. & Yates, J. T. A vibrational study of the adsorption and decomposition of formic acid and surface formate on Al(111). *The Journal of Chemical Physics* **85**, 3111-3122 (1986).
77. Millar, G. J., Rochester, C. H. & Waugh, K. C. Infrared study of the adsorption of formic acid on silica-supported copper and oxidised copper catalysts. *Journal of the Chemical Society, Faraday Transactions* **87**, 1491-1496 (1991).
78. Bowker, M. & Waugh, K. C. From surface science to catalysis: The importance of methoxy and formate species on Cu single crystals and industrial catalysts. *Surface Science* **650**, 93-102 (2016).
79. Sexton, B. A. Summary Abstract: Vibrational spectra of formate and acetate species on copper (100). *Journal of Vacuum Science and Technology* **17**, 141-142 (1980).
80. Li, C. *et al.* Adsorption of carbon monoxide and carbon dioxide on cerium oxide studied by Fourier-transform infrared spectroscopy. Part 2.—Formation of formate species on partially reduced CeO₂ at room temperature. *Journal of the Chemical Society, Faraday Transactions 1: Physical Chemistry in Condensed Phases* **85**, 1451 (1989).
81. J. Mcquillan, A. & Pope, C. G. Raman spectra of formate and acetate ions adsorbed on silver particles in aqueous solutions. *Chemical Physics Letters* **71**, 349-352 (1980).
82. Toomes, R. L. & King, D. A. Potassium-promoted synthesis of surface formate and reactions of formic acid on Co{100}. *Surface Science* **349**, 43-64 (1996).
83. Hoffmann, F. M. & Weisel, M. D. In situ observation of a formate intermediate during CO hydrogenation over alkali-promoted Ru(001) at high pressures. *Surface Science Letters* **253**, L402-L406 (1991).
84. Dubois, L. H., Ellis, T. H., Zegarski, B. R. & Kevan, S. D. New insights into the kinetics of formic acid decomposition on copper surfaces. *Surface Science* **172**, 385-397 (1986).
85. Ito, K. & Bernstein, H. J. The vibrational spectra of the formate, acetate, and oxalate ions. *Canadian Journal of Chemistry* **34**, 170-178 (1956).
86. Hayden, B. E., Prince, K., Woodruff, D. P. & Bradshaw, A. M. An iras study of formic acid and surface formate adsorbed on Cu(110). *Surface Science* **133**, 589-604 (1983).
87. Hayden, B. E., Prince, K., Woodruff, D. P. & Bradshaw, A. M. Infrared-Active Combination Band in a Surface Formate Species. *Physical Review Letters* **51**, 475-478 (1983).
88. Nakano, H., Nakamura, I., Fujitani, T. & Nakamura, J. Structure-Dependent Kinetics for Synthesis and Decomposition of Formate Species over Cu(111) and Cu(110) Model Catalysts. *The Journal of Physical Chemistry B* **105**, 1355-1365 (2001).
89. Bowker, M. *et al.* Spectroscopic and kinetic studies of formic acid adsorption on Cu(110). *Journal of the Chemical Society, Faraday Transactions* **92**, 4683 (1996).
90. Busca, G., Elmi, A. S. & Forzatti, P. Mechanism of selective methanol oxidation over vanadium oxide-titanium oxide catalysts: a FT-IR and flow reactor study. *The Journal of Physical Chemistry* **91**, 5263-5269 (1987).

91. Köck, E.-M., Kogler, M., Bielz, T., Klötzer, B. & Penner, S. In Situ FT-IR Spectroscopic Study of CO₂ and CO Adsorption on Y₂O₃, ZrO₂, and Ytria-Stabilized ZrO₂. *The Journal of Physical Chemistry C* **117**, 17666-17673 (2013).
92. Aquino, A. A. & Jones, T. S. Strong mode-selective resonant vibrational excitation in chemisorbed molecules: an electron energy loss spectroscopy study of HCOO/GaAs (100). *Surface Science* **322**, 301-306 (1995).
93. Jones, T. S., Ashton, M. R. & Richardson, N. V. An electron energy loss study of the surface formate species chemisorbed on Ni(110): Dipole, impact, and resonance scattering for adsorbate covered surfaces. *The Journal of Chemical Physics* **90**, 7564-7576 (1989).
94. Gerardi, H. K. *et al.* Unraveling the Anomalous Solvatochromic Response of the Formate Ion Vibrational Spectrum: An Infrared, Ar-Tagging Study of the HCO₂⁻, DCO₂⁻, and HCO₂⁻·H₂O Ions. *The Journal of Physical Chemistry Letters* **2**, 2437-2441 (2011).
95. Tackett, J. E. FT-IR Characterization of Metal Acetates in Aqueous Solution. *Applied Spectroscopy* **43**, 483-489 (1989).
96. Edwards, D. a. & Hayward, R. N. Transition metal acetates. *Canadian Journal of Chemistry* **46**, 3443-3446 (1968).
97. Nara, M., Torii, H. & Tasumi, M. Correlation between the Vibrational Frequencies of the Carboxylate Group and the Types of Its Coordination to a Metal Ion: An ab Initio Molecular Orbital Study. *The Journal of Physical Chemistry* **100**, 19812-19817 (1996).
98. Johnson, M. K., Powell, D. B. & Cannon, R. D. Vibrational spectra of carboxylato complexes—III. Trinuclear ‘basic’ acetates and formates of chromium(III), iron(III) and other transition metals. *Spectrochimica Acta Part A: Molecular Spectroscopy* **37**, 995-1006 (1981).
99. Kapoor, R., Kapoor, P. & Sharma, R. Reactions of Chromyl Chloride with Carboxylic Acids and Carboxylic Acid Anhydrides. *Zeitschrift für Naturforschung B* **40**, 247-250 (1985).
100. Paul, R. C., Kapoor, P., Baidya, . B. & Kapoor, R. Basic Chromium(III) Formate: Reaction of Chromium(III) Chloride with Formic Acid. *Zeitschrift für Naturforschung B* **34**, 160-162 (1979).
101. Kapoor, R. Basic Chromium(III) Carboxylates: Reactions of Chromium(III) Chloride with Some Carboxylic Acids. *Zeitschrift für Naturforschung B* **34**, 247-250 (1979).
102. Heyns, A. M. The low-temperature infrared spectra of the copper(II)acetates. *Journal of Molecular Structure* **11**, 93-103 (1972).
103. Frost, R. . & Klopogge, J. . Raman spectroscopy of the acetates of sodium, potassium and magnesium at liquid nitrogen temperature. *Journal of Molecular Structure* **526**, 131-141 (2000).
104. Steill, J. D. & Oomens, J. Action Spectroscopy of Gas-Phase Carboxylate Anions by Multiple Photon IR Electron Detachment/Attachment. *The Journal of Physical Chemistry A* **113**, 4941-4946 (2009).
105. Steill, J. D. & Oomens, J. Supplementary information to “Action spectroscopy of gas-phase carboxylate anions by multiple photon IR electron detachment/attachment.” *Journal of Physical Chemistry A* **113**, 4941-4946 (2009).
106. Lin, F., Zhang, Z., Zheng, L. & Jiang, A. 含 μ₃-O 三核混合铁钨醋酸配合物的骨架振动和简正坐标分析. *Acta Chimica Sinica* **49**, 1078-1084 (1991).
107. Zhang, L.-N., Liu, Z.-P., He, L.-J., Cai, S.-H. & Jian, F.-Y. Infrared spectra and normal coordinate analysis of trinuclear μ₃-oxoacetato complexes of chromium and iron. *Acta Chimica Sinica* **7**, 219-228 (1989).
108. Amani, V., Safari, N. & Khavasi, H. R. Solution and solid state characterization of oxo-centered trinuclear iron(III) acetate complexes [Fe₃(μ₃-O)(μ-OAc)₆(L)₃]⁺. *Spectrochimica Acta - Part A: Molecular and Biomolecular Spectroscopy* **85**, 17-24 (2012).
109. Fernandes, C., Stadler, E., Drago, V., Jorge da Cunha, C. & Hiroko Kuwabara, I. Mössbauer, vibrational and electronic spectroscopy of trinuclear μ-oxo iron(III) acetate clusters with pyridine and derivatives as ligands. *Spectrochimica Acta Part A: Molecular and Biomolecular Spectroscopy* **52**, 1815-1821 (1996).
110. Barnes, a. J., Evans, M. L. & Hallam, H. E. Infrared cryogenic studies. *Journal of Molecular Structure* **99**, 235-245 (1983).
111. Sibert, E. L., Tabor, D. P., Kidwell, N. M., Dean, J. C. & Zwier, T. S. Fermi Resonance Effects in the Vibrational Spectroscopy of Methyl and Methoxy Groups. *The Journal of Physical Chemistry A* **118**, 11272-11281 (2014).

112. Lavalley, J. C. & Sheppard, N. Anharmonicity of CH₃ deformation vibrations and Fermi resonance between the symmetrical CH₃ stretching mode and overtones of CH₃ deformation vibrations. *Spectrochimica Acta Part A: Molecular Spectroscopy* **28**, 2091-2101 (1972).
113. McKean, D. C. CHD₂ spectra and Fermi resonance effects in the CH₃ and CD₃ stretching regions. Symmetrical CH₃ groups. *Spectrochimica Acta Part A: Molecular Spectroscopy* **29**, 1559-1574 (1973).
114. Myshakin, E. M., Jordan, K. D., Sibert, E. L. & Johnson, M. A. Large anharmonic effects in the infrared spectra of the symmetrical CH₃NO₂·(H₂O) and CH₃CO₂·(H₂O) complexes. *The Journal of Chemical Physics* **119**, 10138-10145 (2003).
115. Robertson, W. H. *et al.* Infrared Signatures of a Water Molecule Attached to Triatomic Domains of Molecular Anions: Evolution of the H-bonding Configuration with Domain Length. *The Journal of Physical Chemistry A* **107**, 6527-6532 (2003).
116. Wilmshurst, J. K. Infrared Investigation of Acetic Acid and Acetic Acid-d-Vapors and a Vibrational Assignment for the Monomeric Acids. *The Journal of Chemical Physics* **25**, 1171-1173 (1956).
117. Gao, Q. & Hemminger, J. C. A vibrational spectroscopy study of CH₃COOH, CH₃COOD and ¹³CD₃COOH(D) adsorption on Pt(111). *Surface Science* **248**, 45-56 (1991).
118. Rudolph, W. W. & Irmer, G. A Raman Spectroscopic Study of Aqueous La(CH₃CO₂)₃ Solutions and La(CH₃CO₂)₃·1.5 H₂O(cr). *Journal of Solution Chemistry* **46**, 190-214 (2017).
119. Rudolph, W. W. & Irmer, G. Raman spectroscopic studies and DFT calculations on NaCH₃CO₂ and NaCD₃CO₂ solutions in water and heavy water. *RSC Advances* **5**, 21897-21908 (2015).
120. Rudolph, W. W., Fischer, D. & Irmer, G. Vibrational spectroscopic studies and DFT calculations on NaCH₃CO₂ (aq) and CH₃COOH(aq). *Dalton Trans.* **43**, 3174-3185 (2014).
121. Rudolph, W. W., Fischer, D. & Irmer, G. Supplementary Material "Vibrational spectroscopic studies and DFT calculations on NaCH₃CO₂(aq) and CH₃COOH(aq)." *Dalton Trans.* **568**, 1-4 (2015).
122. Edwards, H. G. M. & Lewis, I. R. Vibrational spectroscopic studies of iron(II) acetate. *Journal of Molecular Structure* **296**, 15-20 (1993).
123. Kline, C. H. & Turkevich, J. The Vibrational Spectrum of Pyridine and the Thermodynamic Properties of Pyridine Vapors. *The Journal of Chemical Physics* **12**, 300-309 (1944).
124. Corrsin, L., Fax, B. J. & Lord, R. C. The Vibrational Spectra of Pyridine and Pyridine- d 5. *The Journal of Chemical Physics* **21**, 1170-1176 (1953).
125. Wilmshurst, J. K. & Bernstein, H. J. The vibrational spectra of pyridine, pyridine-4-d, pyridine-2,6-d₂, and pyridine-3,5-d₂. *Canadian Journal of Chemistry* **35**, 1183-1194 (1957).
126. Parry, E. An infrared study of pyridine adsorbed on acidic solids. Characterization of surface acidity. *Journal of Catalysis* **2**, 371-379 (1963).
127. Ureña, F. P., Gómez, M. F., González, J. J. L. & Torres, E. M. A new insight into the vibrational analysis of pyridine. *Spectrochimica Acta Part A: Molecular and Biomolecular Spectroscopy* **59**, 2815-2839 (2003).
128. Omidvar, B. A., Tayyari, S. F., Vakili, M. & Nekoei, A. Normal coordinate analysis of pyridine and its C 2v 2 H-isotopomers. A new approach. *Journal of Molecular Structure* **1151**, 236-244 (2018).
129. Weiwen, X. *et al.* In Situ IR Study of the Reaction Behavior of [Cr₃(μ₃-O)(μ-O₂CH)₆(H₂O)₂(O₂CH)]·xH₂O and its Active Fragments for the Addition Reaction of Acetylene. *Applied Spectroscopy* **47**, 1183-1186 (1993).
130. Fujihara, T., Abe, Y. & Kaizaki, S. Base hydrolysis in homometallic dinuclear chromium(III) complexes bridged by hydroxide and carboxylate. *Journal of the Chemical Society, Dalton Transactions* 1823-1831 (1995). doi:10.1039/DT9950001823
131. Royer, A. C., Russell, K., Belmore, K. & Vincent, J. B. Formation of oxo-centered trinuclear chromium carboxylate complexes and hydrolysis of Cr₃ as established by paramagnetic ²H NMR spectroscopy. *Journal of Inorganic Biochemistry* **131**, 12-20 (2014).
132. Turowski, P. N., Bino, A. & Lippard, S. J. μ-Hydroxobis(μ-formato)hexaaquadichromium(III), an Intermediate in the Formation of Basic Chromium Carboxylates. *Angewandte Chemie International Edition in English* **29**, 811-812 (1990).
133. Brudenell, S. J. *et al.* Binuclear chromium(III) complexes bridged by hydroxide and acetate groups. *Inorganica Chimica Acta* **247**, 35-41 (1996).

4 DFT Simulations of Structures and Spectra of Carboxylate Complexes

For the interpretation of the experimental data from the CID and IRMPD experiments, molecular properties like binding energies and minimum energy geometric structures were determined using DFT (density functional theory) calculations. All calculations have been done in the Gaussian 09¹ quantum chemistry software package through the WebMO interface. We used the Elwetritsch computing cluster at the University of Technology, Kaiserslautern. For our calculations, the B3LYP^{50,51} functional and cc-pVTZ basis sets⁵² (C, H, N, O) in combination with the ecp-10-mdf effective core potential^{2,3} (for Fe, Cr, Sc). The reasoning for the respective choices is given and motivated in the following sections.

Available crystal structure data of $[\text{Fe}_3\text{O}(\text{OAc})_6(\text{Py})_3](\text{FeBr}_4)^{11}$ serves as a starting point to calculate minimum energy structures and linear IR absorption spectra of free $[\text{M}_3\text{O}(\text{B})_6(\text{L})_n]^+$ ($n = 0, 1, 2, 3$) complexes.

We decided against using the broken symmetry approach used in our previous Fe_3 studies⁴ on antiferromagnetic couplings between the metal centres. As shown in scheme 2 of our paper⁴ found in chapter 10, considering the broken symmetry configuration would open up another degree of freedom for the matrix of $[\text{M}^1\text{M}^2\text{M}^3\text{O}(\text{B})_6\text{L}_n]^+$ with $n = 0 - 3$. While the broken symmetry calculations will be important to the interpretation of our planned XMCD measurements (see section 9.2.5), for the systematic study of the IR spectra, structures, and stabilities of the $\text{Fe}_n\text{Cr}_{3-n}$ system; not taking them into account narrowed the number of necessary isomers to consider. Due to the high number of relevant species we will need to take a more selective approach to choose the appropriate cases for our calculations.

It can be shown that for the sake of discussing the stability of each molecular ion (for CID experiments, see chapter 5.3) and the predicted IR spectra (relevant for our IRMPD studies discussed in chapter 6 ff.) the influence of antiferromagnetic coupling is relatively small. It is probable that they rapidly interchange at our experimental conditions and are averaged over time. Therefore, it is presumably acceptable to disregard their effect in the scope of this work. A detailed comparison of the change in the IR spectra with the respective coupling scheme has been given in **Figure S7- S10** in the supplement⁵ (section 10.2) of our paper⁴ on iron acetate in chapter 10. The changes due to magnetic effects are below the resolution of our room temperature IRMPD experiment and would be thermally averaged, therefore it seems like an acceptable approximation to neglect these effects at this stage. Additionally, to reduce the computational effort needed to simulate transition metals, effective core potentials are used to approximate the inner electron shells of the transition metals, that don't participate significantly in chemical interactions. We use the Stuttgart ECP parameter set as published by the universities of Cologne and Stuttgart⁶ for the Sc, Cr and Fe metal centers⁷⁻⁹.

4.1 Multiplicity of the $[\text{Fe}_{3-n}\text{Cr}_n\text{O}(\text{OAc})_6]^+$; $n = 0 - 3$ Series

As a first step, we do unrestricted DFT calculations for the bare core complex without any axial ligands. We assume 1 - 10 unpaired alpha electrons, yielding spin multiplicities $2S + 1$ of 2 (doublet) to 20 (20tet). As shown in **Figure S11** in the supplemental information⁵ of our paper⁴, reprinted in section 10.2, the influence of the axial ligands on the multiplicity is very minor, therefore we are confident in not including them in this series of calculations.

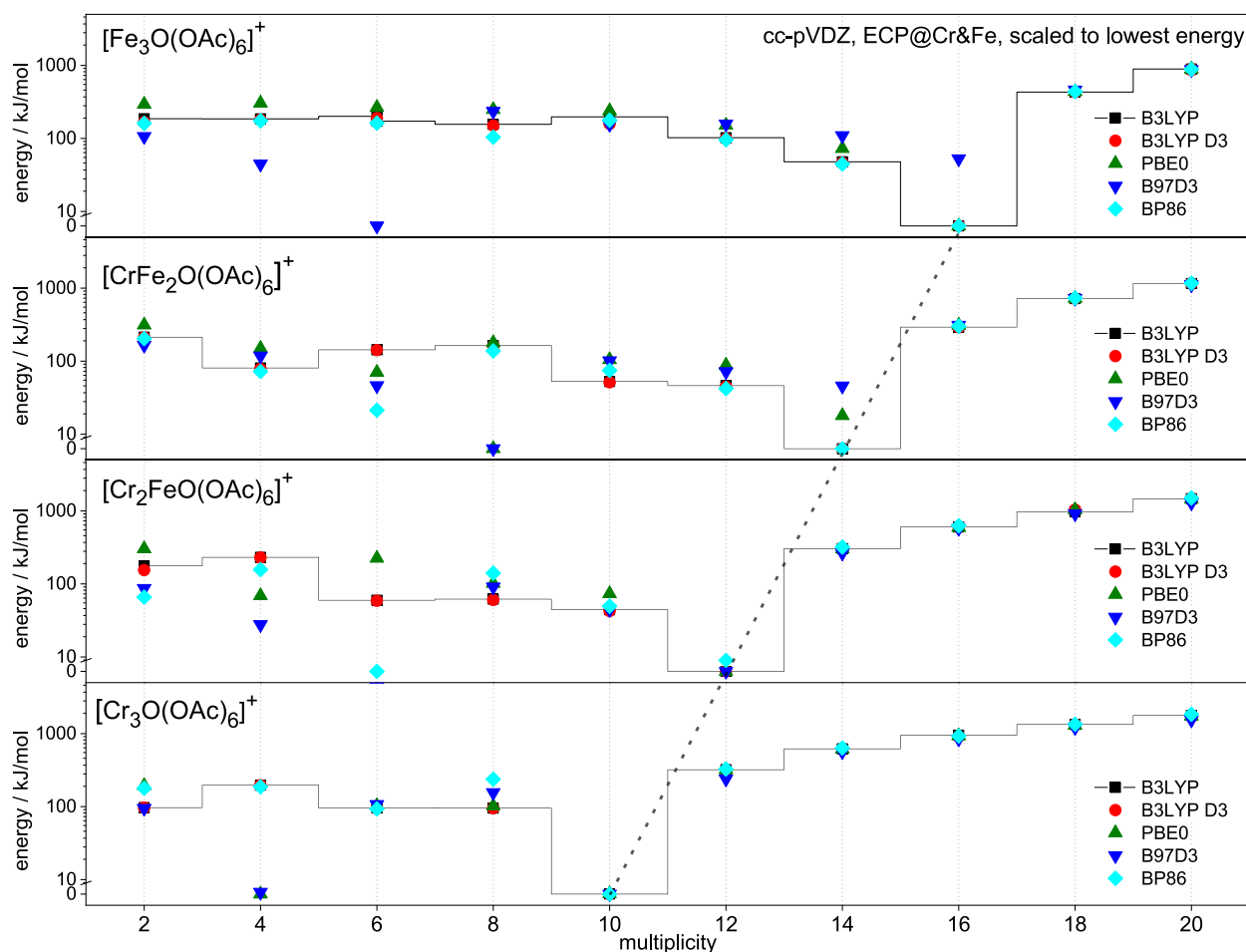


Figure 21 Preferred multiplicity of the bare complexes of the different Fe/Cr combinations in dependence on different DFT functionals. The results for Fe_3 match nicely with the results in Figure S11, section 10.2. The values for B3LYP have been connected to guide the eye. A semilogarithmic energy scale is used.

The overall preferred multiplicity of the different complexes have been determined by the energy minimum, comparing a variety of different basis sets, B3LYP, B3LYP-D3^{2,10}, PBE0, B97D3 and BP86. In general, there is good agreement in the results for the different functionals used, with some exceptions. B97D3 and PBE0 seem to underestimate the multiplicity and deviate the most from the rest, giving additional minima at multiplicities of 6, 8, 6, and 4 respectively. The overall minima we will use in our calculations are 16-tett for Fe_3 , 14-tett for Cr_2Fe , 12-tett for CrFe_2 , and 10-tett for Cr_3 . This would indicate three high spin centers (d^5 for Fe^{III} , d^3 for Cr^{III}). The results are shown in **Figure 21**.

4.2 Choice of Functional for $[\text{CrFe}_2\text{O}(\text{OAc})_6(\text{Py})_n]^+$ with $n = 2, 3$

We used some of our IRMPD spectra as benchmarks to compare the performance of the basis sets and of different functionals. The different functionals coupled with a cc-pVDZ basis sets show disagreements, especially in the band of the asymmetric stretch mode of the carboxylate group at around 1600 cm^{-1} . While B97D3 predicts the band with a red shift relative to the recorded spectra, even in the unscaled state and with a bigger splitting than observed, PBE0 and BP86 predict the bands at higher wavelengths than observed and with an asymmetric splitting, not agreeing well with the recorded spectra.

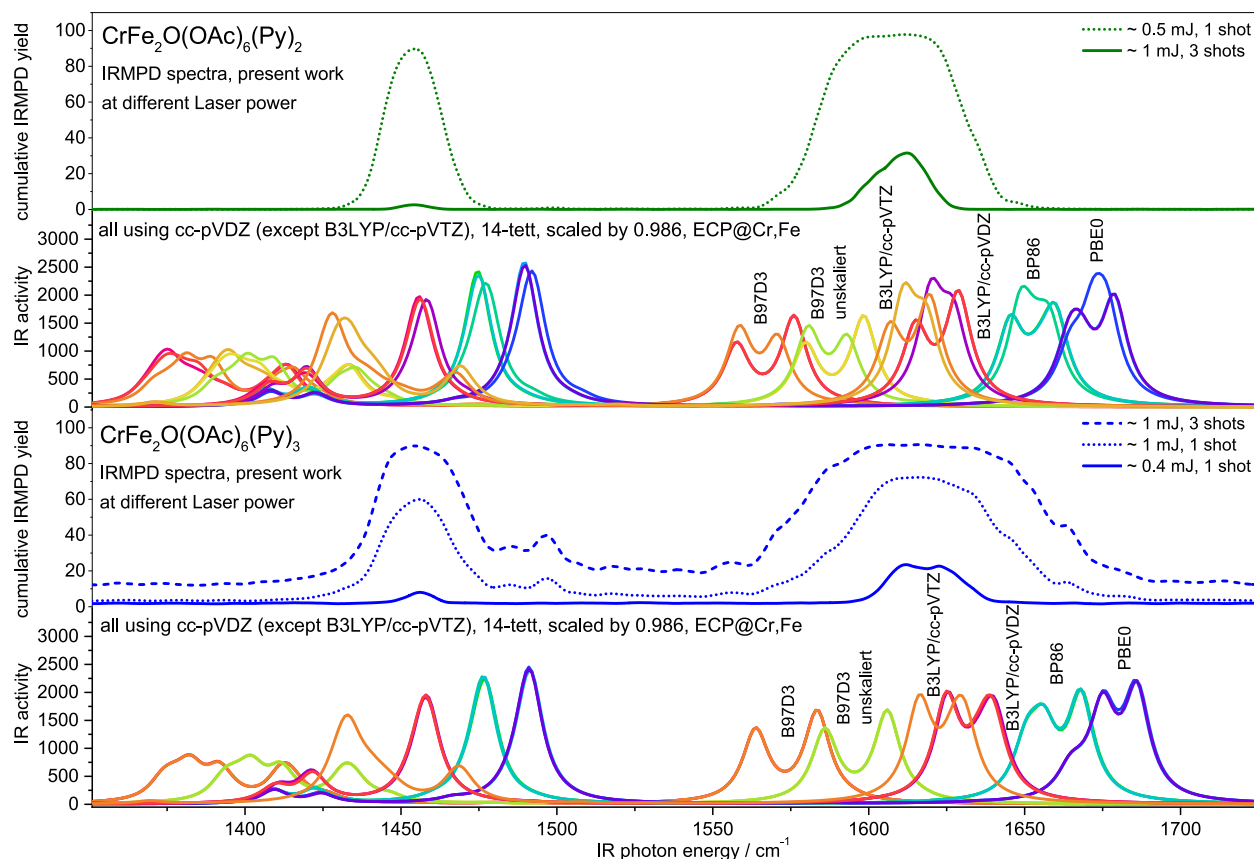


Figure 22 Comparison of the predicted IR spectra for $[\text{CrFe}_2\text{O}(\text{OAc})_6(\text{Py})_2]^+$. Different DFT functionals are used, all with the cc-pVDZ basis set, except for the otherwise labeled B3LYP/cc-pVTZ example (shown in yellow/orange).

It was determined that B3LYP is the best functional to approximate the experimental IRMPD spectra. For more comparisons refer to **Figure 69** and **Figure 70** in the appendix.

As further discussed in the next section (4.3), using a better basis set (cc-pVTZ instead of cc-pVDZ) further improves the results, although at high computational cost, especially considering the number of relevant complexes. Therefore, we conclude that the functional already used for the homometallic cases (Fe_3 and Co_3), B3LYP, also seems to be the best choice for the heterometallic case CrFe_2 and Cr_2Fe . This agrees with the literature, where B3LYP has also been found to perform well for organometallic ions (see Maitre et al.¹¹ and others), as well as our own groups considerations in N_2 coordinated iron acetate complexes¹².

4.3 Choice of Basis Set for $[\text{Fe}_3\text{O}(\text{OAc})_6(\text{Py})_n]^+$ with $n = 0 - 3$

We use some of our IRMPD spectra of $[\text{Fe}_3\text{O}(\text{OAc})_6(\text{Py})_n]^+$, $n = 0 - 3$ as benchmarks against our frequency calculations with the B3LYP functional. The calculations were repeated twice, using both cc-pVDZ and the computationally more expensive cc-pVTZ basis set. As seen in **Figure 23**, a triple zeta basis set, like cc-pVTZ or better, is needed for a reliable approximation of the theoretical spectra to real ones. The cc-pVQZ basis set has also been considered, but only resulted in a minor improvement of the predicted IR spectra over cc-pVTZ and has therefore not been applied systematically, as the jump in computational cost is too high.

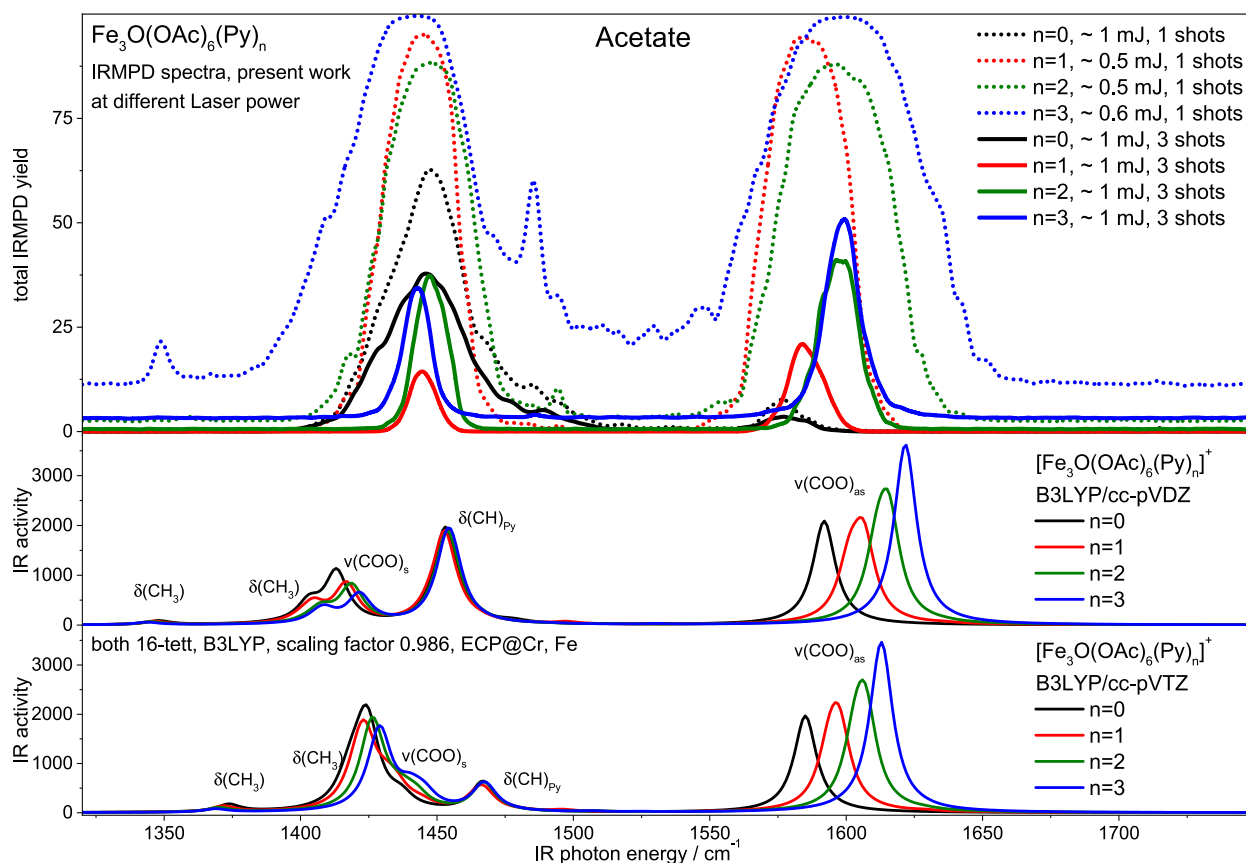


Figure 23 Basis set comparison cc-pVDZ versus cc-pVTZ on the predicted IR spectra for $[\text{Fe}_3\text{O}(\text{OAc})_6(\text{Py})_n]^+$ for $n = 0 - 3$, compared against the gas phase IRMPD spectra of the same species. The B3LYP functional is used.

This is both supported by the splitting of the symmetric and asymmetric CO stretch bands observed at $\sim 1450 \text{ cm}^{-1}$ and $\sim 1600 \text{ cm}^{-1}$ and the position and split between the former symmetric CO band and the $\delta(\text{Py-CH})$ band at a bit under 1500 cm^{-1} .

Harmonic vibrational frequencies are scaled with 0.986 to account for anharmonicity and broadened with gaussian envelope curves (usually 10 cm^{-1} FWHM). The scaling factor was determined by matching the calculated asymmetric carboxylate stretching vibration frequency of $[\text{Fe}_3\text{O}(\text{OAc})_6]^+$ to the corresponding band position in the IRMPD spectrum. To keep the results in line with each other, this scaling factor has not been changed for the formates and for the CH stretch modes, even if there are certain systematic deviations for the predicted band positions as compared to our observed results.

4.4 Geometry Trends for Ligand and Metal Variation in Homo- and Hetero-metallic $[\text{Fe}_{3-n}\text{Cr}_n\text{O}(\text{Fo})_6\text{Py}_m]^+$ and $[\text{Fe}_{3-n}\text{Cr}_n\text{O}(\text{OAc})_6\text{Py}_m]^+$

For a better understanding of the experimental results, it is beneficial to compare them to ab initio calculations. This can help to better understand their structure and intrinsic properties of their binding motifs^{39,42} and other properties.

Previously⁴³, $[\text{Fe}_3\text{O}(\text{OAc})_6(\text{N}_2)_n]^+$ complexes ($n = 1, 2, 3$) revealed a slight distortion of the triangular Fe_3O core geometry by stepwise N_2 coordination to the Fe centers. This effect is enhanced by using strongly binding pyridine (Py) ligands⁴. The stepwise coordination of 1 - 3 axial pyridine ligands induces significant geometrical distortion of the Fe_3O core. Using our gas phase approach, we can exclude bulk or crystal packing effects and also enable the isolation of under-coordinated molecular ions (e.g. $[\text{Fe}_3\text{O}(\text{OAc}/\text{Fo})_6(\text{Py})_{0-2}]^+$), which would not be accessible in the condensed phase.

4.4.1 Terminal- and Bridging Ligand Variation Induced Geometry Changes in Fe_3O Acetates and Formates

In Scheme 4 of our paper⁴, reprinted in chapter 10, we reported antiferromagnetic coupling of spins (UUD coupling), leading to slight changes of geometry in the cases of $n = 0, 1, 3$ in $[\text{Fe}_3\text{O}(\text{OAc})_6\text{Py}_n]^+$. The $n = 2$ case showed a different coupling scheme (DUU) and a symmetric structure.

We choose to disregard the effects of magnetic couplings in the present work. The conditions of the experiments in this work are slightly elevated temperatures, relative to ambient, and frequent collisions. Analogous to mixed valence complexes^{14,15}, the slight geometry distortions introduced by the distinct antiferromagnetic coupling schemes are thermally averaged over the three equivalent metal cores. Determining the critical temperature for this decoupling process is one of the objectives of the XMCD experiments discussed in the outlook section 9.2.5.

That said, the effect of pyridine coordination leads to an elongation of the M-O bond and therefore to a distortion of the originally almost equilateral M_3 triangle of the bare M_3O core. Upon saturation of all axial binding sites with three pyridines, the equilateral d_3 symmetry is restored; albeit at a longer M-M' distance. We plotted the corresponding bond length changes in **Figure 27** in section 4.4.

New here is the inclusion of the formate analogues to the acetate species considered previously. The formate carboxylate ligands lack the -I effect of the methyl group in the acetate, leading to a stronger partial charge in the metal centers. This leads to a slight elongation of the Fe-O bond and a widening of the Fe_3 triangle, which in turn leads to shorter metal to pyridine bonds and matches the observed higher CID energies necessary to cause the ligand bond to be severed. The trends of these bond elongations upon ligand exchange are visualized in **Figure 27**.

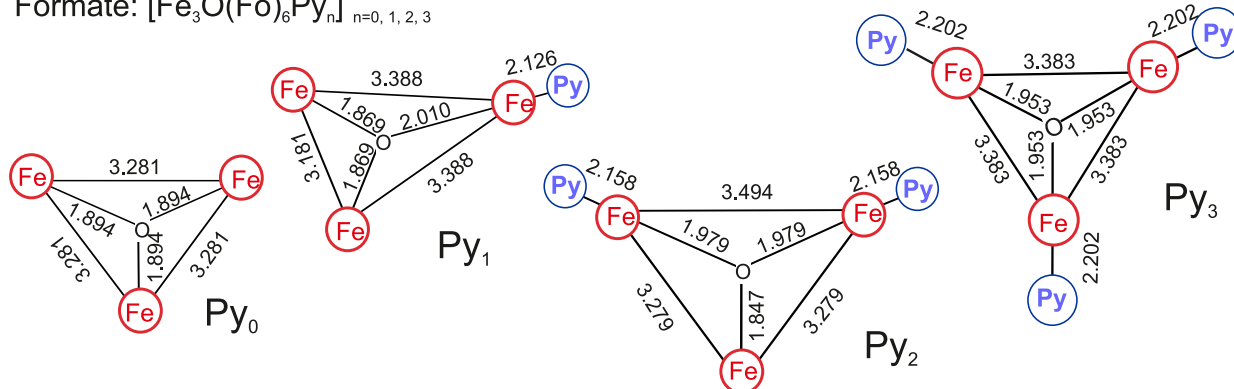
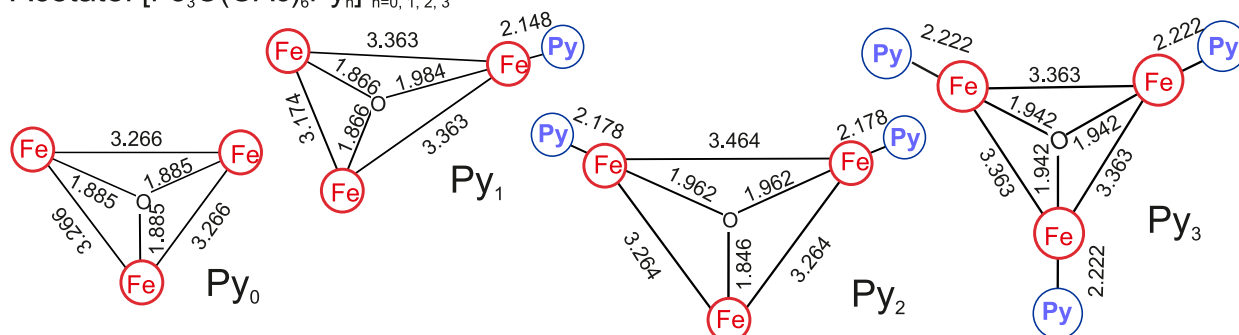
Formate: $[\text{Fe}_3\text{O}(\text{Fo})_6\text{Py}_n]^+$ $n=0, 1, 2, 3$ Acetate: $[\text{Fe}_3\text{O}(\text{OAc})_6\text{Py}_n]^+$ $n=0, 1, 2, 3$ 

Figure 24 Ligand induced geometry changes in $[\text{Fe}_3\text{O}(\text{OAc}/\text{Fo})_6\text{Py}_n]^+$ as given by B3LYP DFT calculations. Using the cc-pVTZ basis set and ECPs¹³ for Fe, see 11.1.1.

4.4.2 Metal Exchange Induced Geometry Changes in $[\text{Fe}_{3-n}\text{Cr}_n\text{O}(\text{Fo}/\text{OAc})_6\text{Py}_m]^+$ for $n, m = 0 - 3$ in the Formate and Acetate Complexes

Not only bridging and terminal ligand changes have an influence on the geometry of the basic carboxylate complexes. Exchanging a chromium(III) center with an iron(III) center has a contracting effect on the M-Py distance and an elongating effect on both the M-O and the M-M distances.

To compare the simplest case of the bare formate and acetate complexes (**Figure 25** and **Figure 26**, bottom row respectively), replacing a chromium(III) center with an iron(III) leads to a bigger elongation of the Cr-Cr distance than the Fe-Cr distance. Conversely, introducing a chromium(III) ion both reduces the Fe-Cr and the Fe-Fe distance and interestingly has the stronger influence on the Fe-Fe distance.

Therefore, the heterometal influence of iron in a chromium system and of chromium in an iron system is reversed. The chromium increases the iron-iron interaction, and the iron decreases it for the chromium-chromium pair. This might have an effect as well on other properties like magnetic exchange couplings or spectroscopic properties.

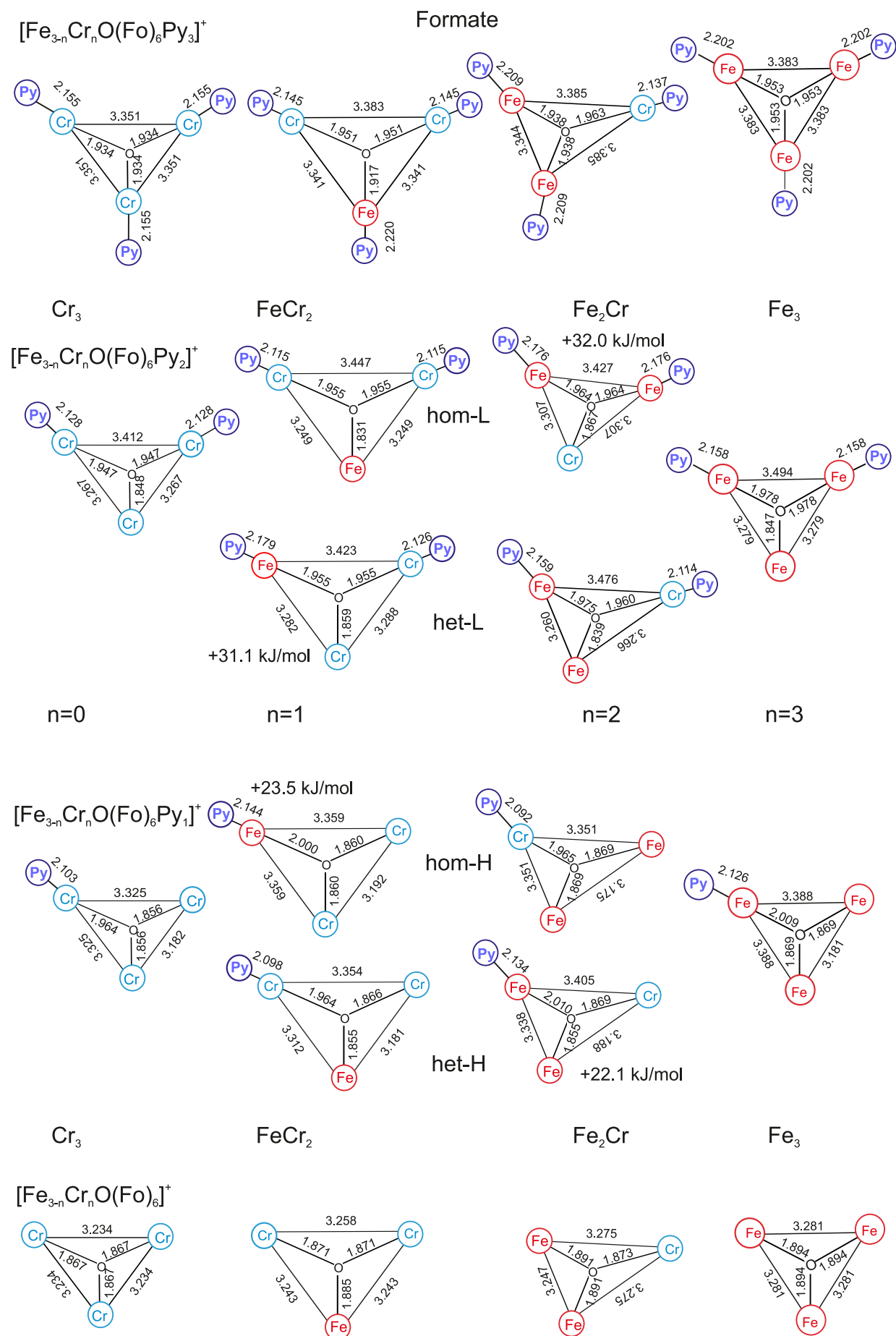


Figure 25 Metal and ligand substitution induced geometry changes in $[\text{Fe}_{3-n}\text{Cr}_n\text{O}(\text{Fo})_6\text{Py}_m]^+$, ($n, m = 0, 1, 2, 3$) as given by B3LYP DFT calculations with a cc-pVTZ basis set and ECP¹³ for Fe, see section 11.1 for tables of the values. For a visualization of the trends, see **Figure 27**.

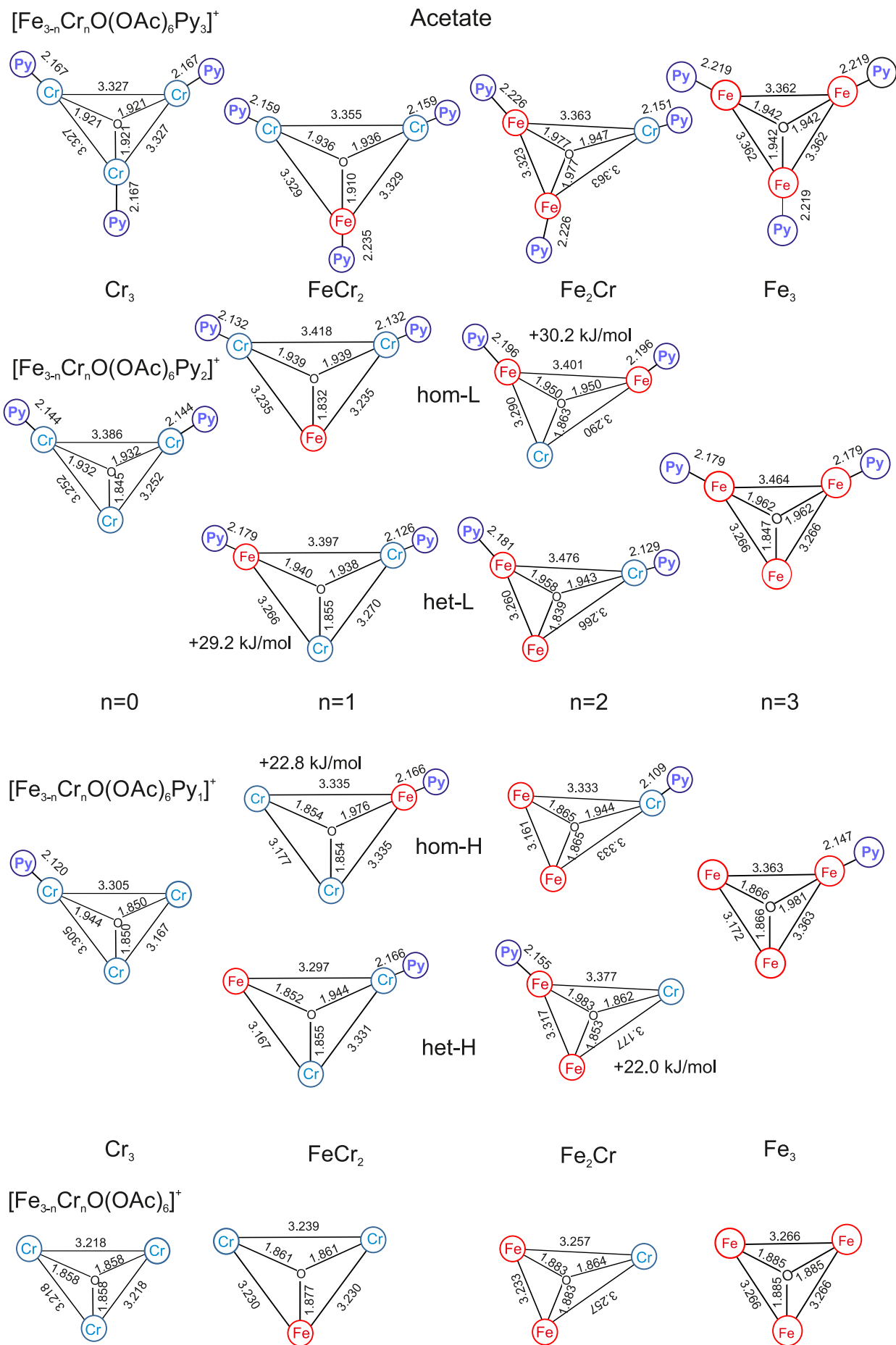


Figure 26 Metal and ligand substitution induced geometry changes in $[\text{Fe}_{3-n}\text{Cr}_n\text{O}(\text{OAc})_6\text{Py}_m]^+$, ($n, m = 0, 1, 2, 3$) as given by B3LYP DFT calculations with a cc-pVTZ basis set and ECP¹³ for Fe, see section 11.1 for tables of the values. For a visualization of the trends, see **Figure 27**.

This effect also survives in the pyridine coordinated species, the Cr-Cr bond gets longer with Cr to Fe substitution and the Fe-Fe bond gets shorter for Fe to Cr substitution. Likewise, the M-O bond has to follow this trend, with the Cr-O distance getting longer with increasing Fe count and vice versa.

Both sets of graphs, for acetate and formate respectively in **Figure 27** basically contain the same information, ordered by metal variation locally and by ligand variation between sets and vice versa. This way the competing trends around the occupied and unoccupied coordination sites become clear.

The same trend can be seen for the M-Py bond length, shortening for Cr-Py with increasing iron count and for Fe-Py, also along with increasing iron count. Keeping the core metal centers identical, the distorting effect of increasing the pyridine ligand number is slightly larger than the effect introduced by subsequent Cr to Fe exchange while keeping the pyridine count fixed, as previously discussed. This can be seen in the apparent slopes of the trends; black dots for pyridine ligands on iron, and red dots for pyridine on chromium. This is most apparent in the first row of graphs in **Figure 27**. For successive metal substitution, a moderate bond shortening is seen, as opposed to the second row of graphs with successively lower pyridine count, showing a pretty drastic bond length shortening upon removal of other pyridine ligands.

The metal-metal distances are not plotted in this graph, but can be seen in **Figure 25** and **Figure 26**. There are too many possible combinations of iron to chromium, with or without pyridine, especially in the partially coordinated mixed metal cases. Separately plotting those would rather confuse than help.

As can be seen in **Figure 25** and **Figure 26**, the metal-metal distances are closely correlated to the M-O distances of those two metal centers, and the angles of the M-O bonds relative to each other do not vary too strongly. Therefore, the Cr-O/Fe-O distances with and without pyridine are good proxy values to observe the trends.

In general, these trends are very linear with successive ligand coordination or metal exchange, although slightly perturbed by the different pyridine regioisomers in the mixed metal/mixed ligand cases. However, there is a strong hierarchy in the magnitude of the influence of switching between the two major isomers possible for each species. The direct influence of the ligand bonding to a metal center is an M-O bond elongation of about 0.2 Å. The indirect effect of the ligand coordination on the respective other metal centers one position over, is diminished by a factor of ten, to roughly 0.02 Å, about a percent of the total bond length. This small secondary effect is responsible for the biggest observed deviations from the linear trend, and is presumably biased in the direction of the filled circles, predicted to be the more stable isomers by about 20 - 30 kJ/mol, caused by the chromium ligand bond being stronger by a similar amount as compared to the iron to ligand bond.

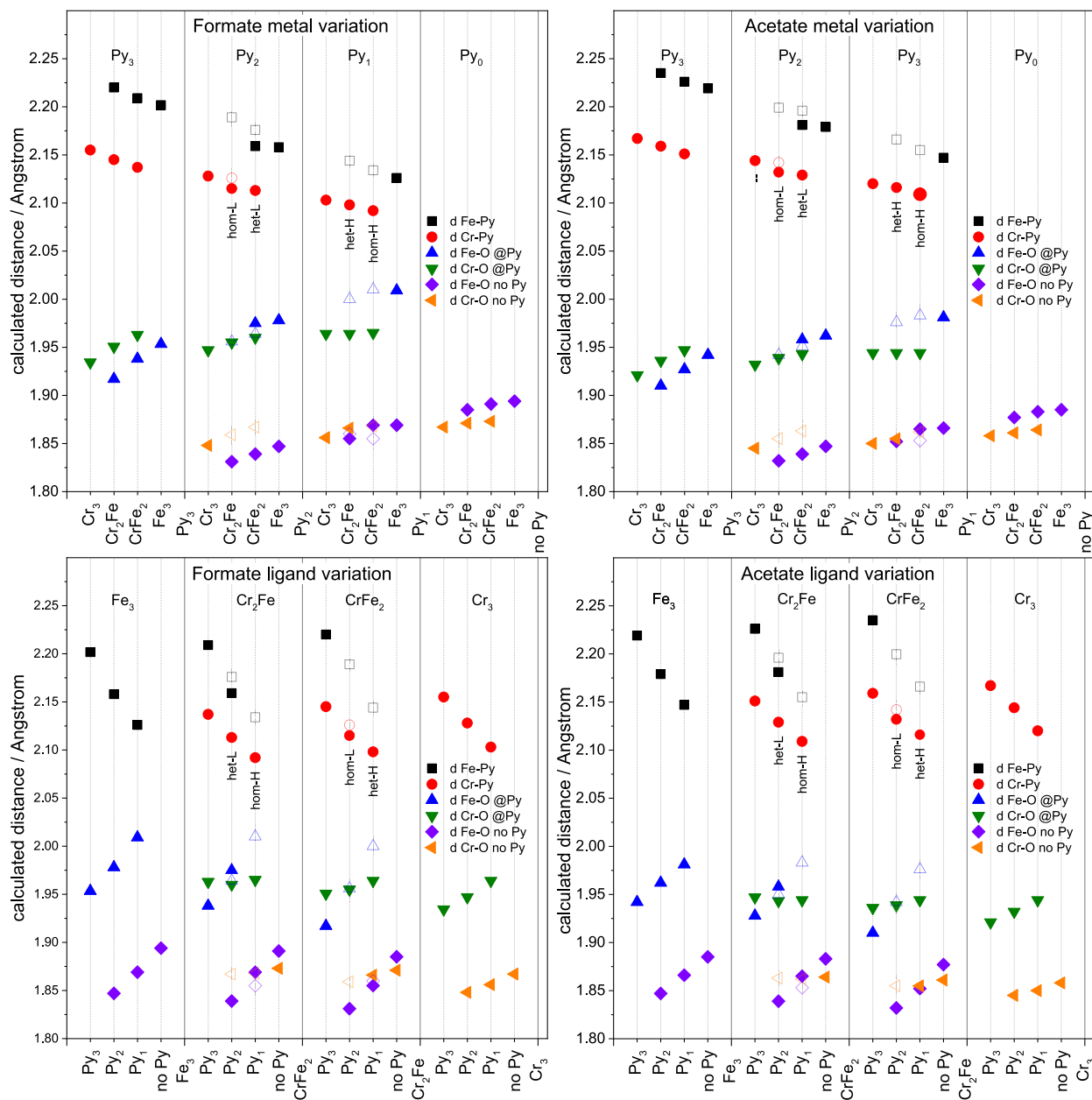


Figure 27 Geometry variations upon successive metal substitution and ligand coordination. See section 11 for **Table 14** and **Table 17**. Filled symbols are the energetically more favorable isomer, their type (hom/het-H or hom/het-L, see section 1.2.1) is noted at the Cr-Py distance marker. The unfilled symbols show the more unfavored isomer. They are of the opposite type respectively.

As we will show in section 5.3.1, **Figure 36**, the bond length is highly correlated with the bond strength. A tight correlation of the CID E_{com}^{50} values with both of those values can be demonstrated. This is also corroborated by the observed IRMPD spectra, as we argue in section 6.3. In the partially coordinated mixed metal formate complexes, a correspondence can be seen between the predicted and observed spectra of the more stable isomer, agreeing with the assumptions made in this section.

4.5 Pyridine to Metal Bond Length Potential Energy Surface for $[\text{Fe}_{3-n}\text{Cr}_n\text{O}(\text{Fo})_6\text{Py}_m]^+$ and $[\text{Fe}_{3-n}\text{Cr}_n\text{O}(\text{OAc})_6\text{Py}_m]^+$ with $n = 0 - 3$ and $m = 1, 3$

As we are trying to show in **Figure 29**, there are only very small differences in both the equilibrium geometries and the potential total electronic energy surface (PES) between calculations using either cc-pVDZ or cc-pVTZ basis sets, especially around the equilibrium geometry. This is very good to know, as cc-pVTZ is computationally quite expensive for acetate calculations.

The relative energy values given for the $R(\text{M-Py1N}) = \infty$ data point are taking the basis set superposition error (BSSE) energy correction¹⁶ into account by using a counterpoise calculation as detailed in section 2.6.2. The deviation from that value is about 30 kJ/mol for the B3LYP functional.

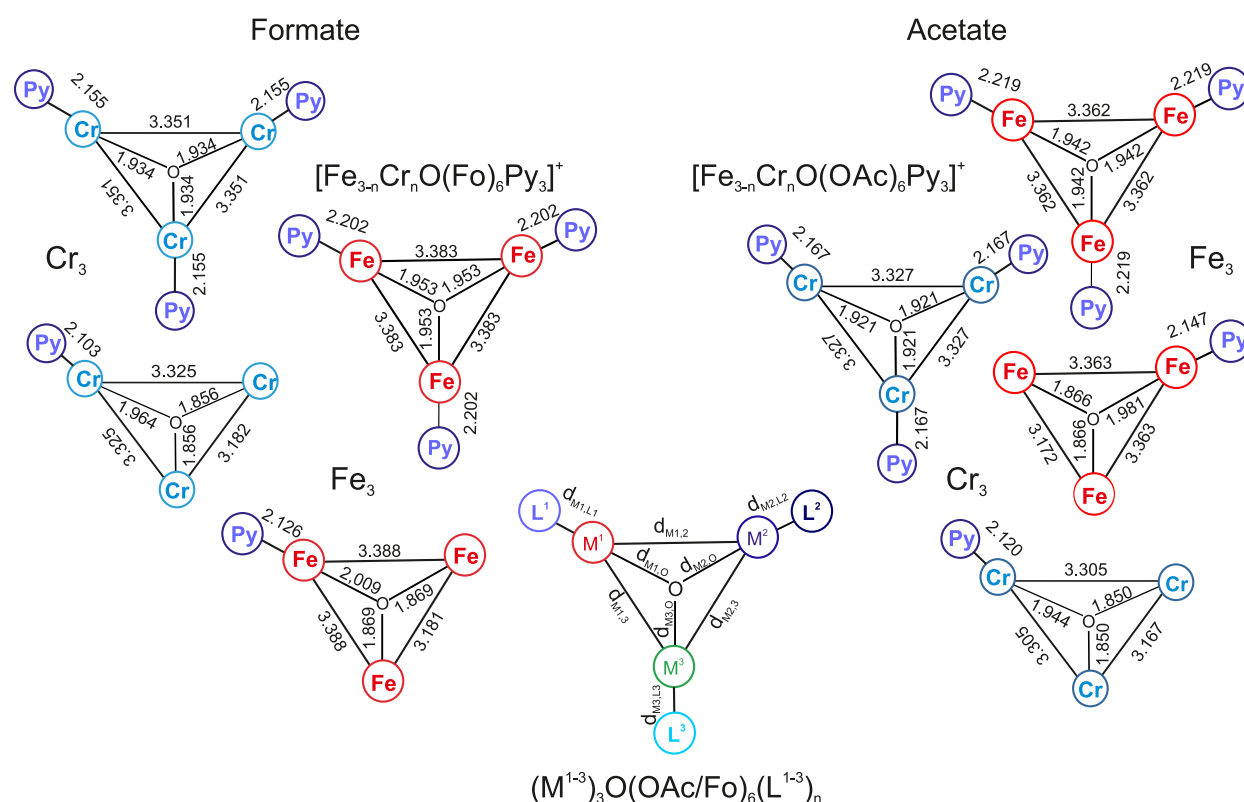


Figure 28 Equilibrium distances for the species shown in **Figure 29** as well as the naming convention for the geometry parameters, as shown in **Figure 1** previously.

This deviation can be mitigated considerably by using the B3LYP-D3^{2,10,17} functional, which accounts for long range interaction, especially dispersion interaction. However, this functional leads to inconsistencies at shorter distances at around 2 Angstrom, as seen in the geometry parameters $R(\text{M1-O})$ in **Figure 29**, middle row.

B3LYP does exhibit some deviation for longer distances, but gives more consistent results around the equilibrium geometry. Therefore, it seems to be a good choice for the geometry calculations for our class of species. The exact equilibrium geometries of the discussed species are given in **Figure 28**.

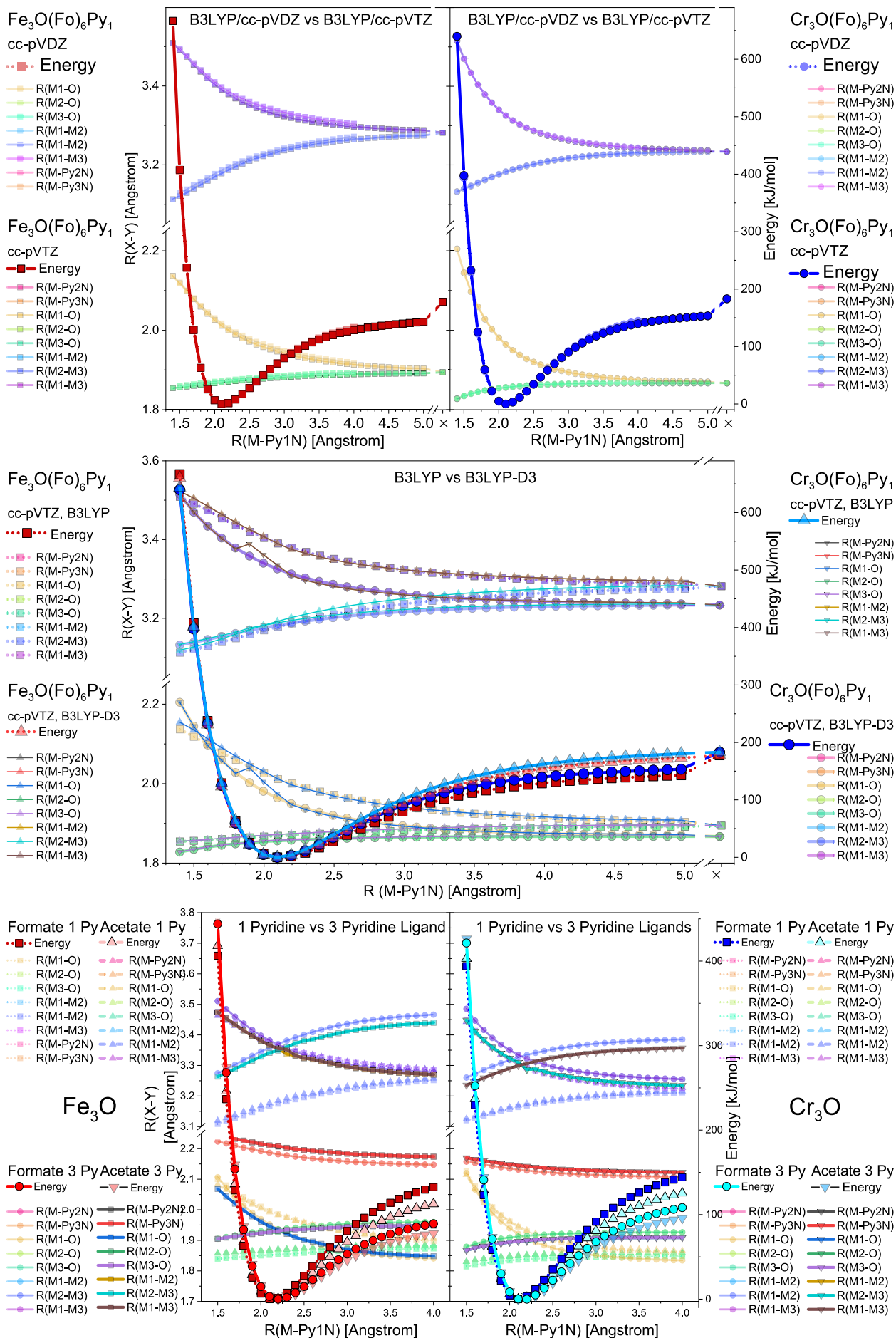


Figure 29 Potential energy surfaces (PES) and geometry parameters of the pyridine bond length variation on $\text{Fe}_3/\text{Cr}_3 \text{Py}_{1,3}$ Acetate/Formate complexes. For the used distance parameter naming convention and the equilibrium distances, refer to **Figure 28**.

Looking at the potential energy surfaces for iron and chromium with no other or two further pyridine ligands, we see the potential being tighter for the single pyridine, with differences already for short distances from the equilibrium distance.

Comparing acetate and formate of the same metal and terminal ligand type, differences only become apparent at longer bond distances. For short length deviations the potentials along the bond axis are very similar. This matches the observations made in section 4.5 in **Figure 27** on the equilibrium geometries.

4.6 Torsional Degrees of Freedom of the Pyridine Ligands

We also calculated the total energy profile along the torsional degree of freedom of pyridine in the $[M_3O(OAc)_6(Py)_1]^+$ complexes. This coordinate is defined by rotation of the pyridine ligand around the axis coinciding with the N-M coordination bond. In **Figure 30**, the total energy profile of the plane given by the pyridine ligand relatively to the plane created by the three metal atoms in the complex is plotted.

For the homometallic complexes, we observe a preference of the pyridine ligands to orient perpendicular to the plane of the M_3O core. There is a second minimum with the pyridine and M_3 planes being parallel, although it is much shallower and less stable. For PES calculations of Fe_3O , especially when using cc-pVTZ, it is almost flat.

This second minimum with both planes being parallel is higher for both complexes, by about 5 kJ/mol in the iron and around 7 kJ/mol in the chromium coordinated pyridine. The torsional barriers are very low for the iron complex and higher by ~ 3 kJ/mol in the chromium complex. This barrier height is easily overcome by the thermal energy available at our experimental conditions.

The energy barrier for an unhindered torsion of the pyridine is dependent on the ligating metal, for the homometallic case it follows the bond strength trends of CID and our DFT calculations, with only small effect by the surrounding methyl groups for the acetate case as compared to the formate species. The heterotrimetallic case of ScCrFeO is deviating considerably from that trend. pyridine ligands on iron centers have the highest barrier of almost 12 kJ/mol and the deepest secondary minimum at 5 kJ/mol, with a relative barrier height of almost 7 kJ/mol. We also see a double minimum for the Sc coordination site.

Probably none of the torsional barriers is low enough for fully unhindered pyridine rotation. Nevertheless, there is a strong dependence of the potential energy surface on the other metals in the system. At room temperature – and upon CID excitation at ion temperatures much above – the hindered pyridine torsion of the complexes, especially Fe_3 , can easily be excited, and may freely rotate, only slightly less so for Cr_3 or Fe and Cr in the ScCrFe mixed complex.

In the case of ScCrFeO with Py at Fe and at Cr, at the local minima at 0° , with the pyridine plane parallel to the plane of the M_3O core; metastable isomers with a torsional barrier of about 7 kJ/mol might be possible. These could possibly be discriminated for by TIMS, as discussed in section 9.2.7.

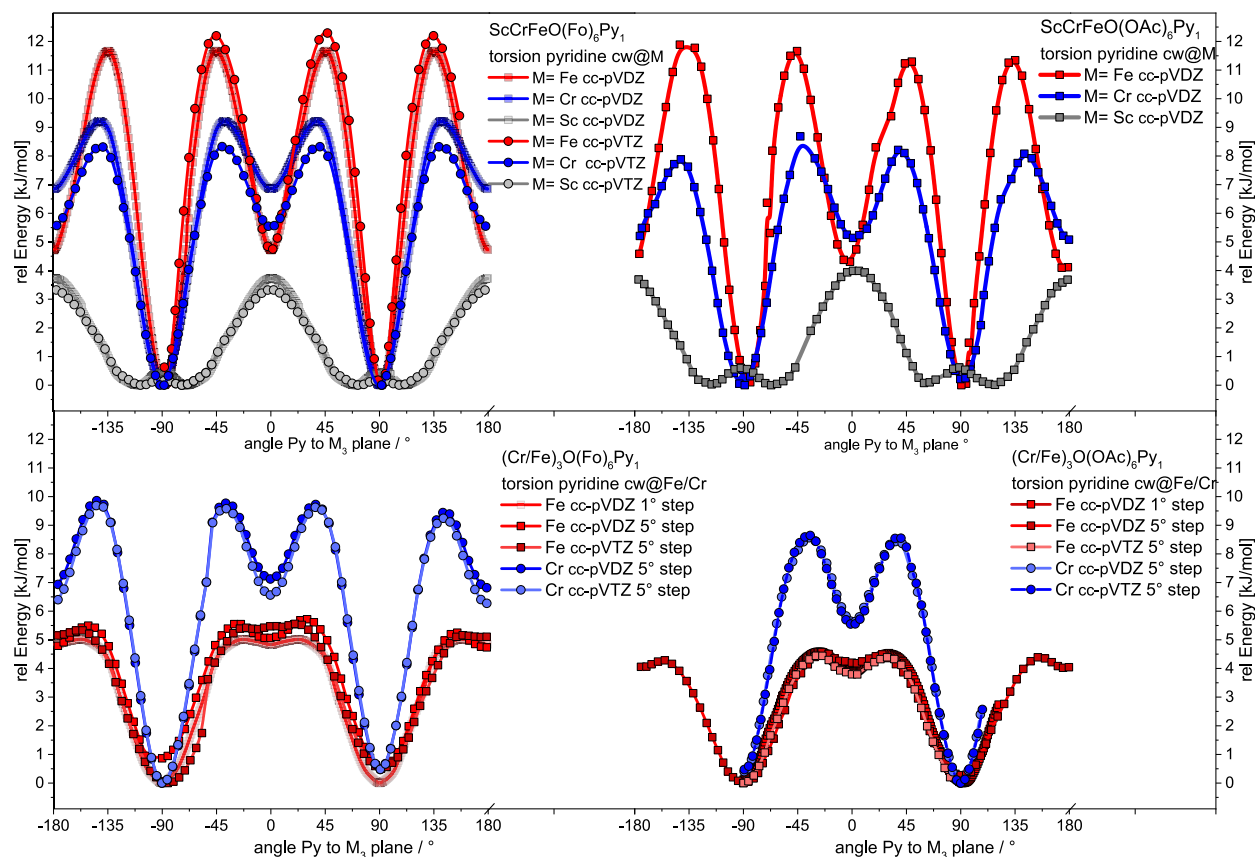


Figure 30 Torsions of pyridine ligands on several metal binding sites. The abbreviations VDZ/VTZ indicate the use of the cc-pVDZ or cc-pVTZ basis set, all calculations use B3LYP.

First calculations of Collisional Cross Sections of $\text{ScCrFeO}(\text{Fo})_6\text{Py}_3$ were done with the kind help of Erik Schneider, KIT. With two torsional isomers of the pyridine coordinating to the iron center, one angled perpendicular (90°) and one parallel (0°) to the metal plane, the results suggest that an observation of the presence of the isomers should be possible, although a full separation of the isomers might be difficult. The perpendicular position has only a slightly bigger cross-section ($163 \text{ \AA}^2/228 \text{ \AA}^2$) than the parallel one ($164 \text{ \AA}^2/224 \text{ \AA}^2$), according to projection approximation or the trajectory method respectively.

The energy profile for the internal CH_3 rotation of the isolated acetate, propionate, and benzoate ions has been calculated by Oomens et al.¹⁸. The results can be found in the supplemental material thereof¹⁹. For benzoate, a barrier of around 17 kJ/mol for the benzyl torsion has been observed. As for acetate, the barrier for the internal rotation of the CH_3 moiety was found to be around 0.012 kJ/mol.

In crystal structures the Py orientation in some complexes is parallel to the Fe_3 plane, e.g. for the Fe_3 mixed valence case²⁰⁻²⁴. This is caused by Py-Py interactions through aromatic π -interactions. Perpendicular orientations are also known²⁵, as well as mixed orientations, for example in some Co_3 ²⁶ and Fe_3 ²⁷ complexes.

4.7 Differential Many Body Cooperativity of $\text{Fe}_{3-n}\text{Cr}_n\text{O}$ Acetates and Formates

As introduced in section 2.7, using the formalism introduced by Klopper et al.²⁸, it is possible to determine the non additive nature of any given property in a three body system, in which each body is consecutively replaced by a second similar alternative body.

We applied this formalism to the $\text{Fe}_{3-n}\text{Cr}_n\text{O}$ system. We considered two different bridging ligands, formate and acetate. For each of them we look at the cases with three axial pyridine ligands and also the bare complexes. Furthermore, the formalism was applied on the homometallic Fe_3O system for systematic coordination of pyridine ligands. The actual tables for all values needed for the calculation can be found in the appendix, section 11.3. The energies for the Fe to Cr exchange with three pyridine ligands are calculated both with individual geometry optimization, and for a common fixed geometry originally optimized for Fe_3O . In contrast to the literature case of Pd to Pt, where the results of applying individual geometry optimizations or keeping the same fixed geometry are different, in our case the change in the three-body term for our complexes is surprisingly small. There is no obvious reason why this should be the case, it is probably by chance. Still, in the following discussion we focus on the respective geometry optimized cases.

Looking at the results, there are much smaller changes in the one body term for the Fe to Cr series than for the zero pyridine to three pyridine series. This also holds for the inverse cases. As is especially apparent in the ligand to no ligand exchange case, this one body term is the sum of the energy difference between each single ligand addition, or exchange of a metal in each position of the complex M_3O core. The addition/subtraction of a whole moiety comprises a much larger change in total energy than the mere exchange of a metal center. This term is a measure of the energy difference and of no big interest in the context of cooperativity.

The two-body terms are negative for all Fe to Cr exchanges and of similar value as in the Pd to Pt exchange case, especially in the bare complexes. Looking at the equation in 2.7, the two-body term quantifies the change of the considered property (total electronic energy) in dependence of double exchange of Fe to Cr or no pyridine ligand to pyridine ligand, corrected by the corresponding one body terms. They seem to have moderate influence on each other and notice the presence of the corresponding second change.

The three-body term for all three pyridine cases, in turn, is of similar magnitude as for the geometry optimized Pd to Pt case, while it is considerably larger for the bare complex. The cooperativity seems to rely strongly on the geometry of the complexes, short metal distances promote higher values, likewise stronger bridging ligands (at least in the case of formate) also lead to a longer metal distance; giving higher results. Similar to the Rh to Ir exchange where there is a considerable distance between the metal centers, the pyridine ligand exchange is giving smaller three body terms, witnessing the smaller influence the distant pyridine ligands have on each other.

A good example to bridge the gap between the Pd/Pt example²⁸⁻³² to our species would be to study the Pd^{II}(OAc)₆ system³³⁻³⁸, lacking a central μ -oxo O²⁻ atom. The heterometal could be platinum. The non-ionic nature of the native complex would make gas phase studies with mass spectrometry difficult. It is encouraging though, as observed by Pakulas et al.³⁷, that the Pd₃ acetate complex can be reduced by one electron reduction to a structurally similar monoanionic complex containing an isolated Pd^I ion. This species has stronger Pd-Pd bonds than Pd^{II}(OAc)₆ and appears to be relevant as an intermediate along the pathway toward Pd nanoparticle formation. Details for this anion, together with calculated structures, can be found in the supplementary information³⁸ of Pakulas paper³⁷.

Besides applying the DMBC formalism to the total electronic energy, we also attempted to use it on a key spectroscopic feature in the IRMPD spectra we measured for the mixed metal complexes; the band splitting between the symmetric and asymmetric carboxylate stretch mode. There seems to also be a small but relevant cooperative term. More on this in section 6.5, **Table 2** and **Table 3**.

Table 1 Many-body decomposition of the total electronic energy (in kJ mol⁻¹). For the derivation, please refer to the description of the formalism in 2.7 and appendix chapter 11.3.

Complex ^{II}		Geometry ^{III}	$\Delta P^{(1)}/10^3$	$\Delta P^{(2)}$	$\Delta P^{(3)}$
Pd Pt ^{IV}		Fixed	67.40	6.84	0.14
Pd Pt ^{III}		Optimized	67.40	7.41	1.29
Rh Ir ^V		Fixed	48.80	Negl. ^{VI}	Negl. ^V
Rh Ir ^{IV}		Optimized	48.90	-0.21	-0.004
Fe ₃ to Cr ₃ Acetate	Py ₃	Fixed	2903.15	-4.85	1.38
Fe ₃ to Cr ₃ Formate	Py ₃	Fixed	2902.70	-3.91	1.17
Fe ₃ to Cr ₃ Acetate	Py ₃	Optimized	2902.95	-5.07	1.28
Fe ₃ to Cr ₃ Formate	Py ₃	Optimized	2902.91	-3.44	1.08
Fe ₃ to Cr ₃ Acetate	No Py	Optimized	2903.41	-8.03	6.17
Fe ₃ to Cr ₃ Formate	No Py	Optimized	2903.39	-6.82	4.69
Fe ₃ Acetate	Py ₃ to Py ₀	Optimized	19565.79	68.71	0.20
Fe ₃ Formate	Py ₃ to Py ₀	Optimized	19566.22	83.89	0.53
Inverse order DMBC					
Cr ₃ to Fe ₃ Acetate	Py ₃	Fixed	-2903.10	-0.70	-1.38
Cr ₃ to Fe ₃ Formate	Py ₃	Fixed	-2902.65	-0.41	-1.17
Cr ₃ to Fe ₃ Acetate	Py ₃	Optimized	-2902.88	-1.24	-1.28
Cr ₃ to Fe ₃ Formate	Py ₃	Optimized	-2902.88	-0.20	-1.08
Cr ₃ to Fe ₃ Acetate	No Py	Optimized	-2903.43	10.50	-6.17
Cr ₃ to Fe ₃ Formate	No Py	Optimized	-2903.40	7.23	-4.69
Fe ₃ Acetate	Py ₀ to Py ₃	Optimized	-19567.17	69.31	-0.20
Fe ₃ Formate	Py ₀ to Py ₃	Optimized	-19567.91	85.49	-0.53

^{II} Target complex

^{III} One fixed geometry for all complexes or individually optimized for each of the complexes involved.

^{IV} Homo-trinuclear Pd/Pt complex [(Pd/Pt)₃{Si(mt^{Me})₃}₂] (mt^{Me} = methimazole)^{28,29,31,39,40}

^V Pd and Pt⁷ tritopic triphenylene-based N-heterocyclic carbene Rh complex⁴¹⁻⁴⁴

^{VI} Negligible (<0.5 J mol⁻¹)

4.8 References Chapter 4

1. M. J. Frisch, G. W. Trucks, H. B. Schlegel, G. E. Scuseria, M. A. Robb, J. R. Cheeseman, G. Scalmani, V. Barone, G. A. Petersson, H. Nakatsuji, X. Li, M. Caricato, A. Marenich, J. Bloino, B. G. Janesko, R. Gomperts, B. Mennucci, H. P. Hratchian, J. V. Ort, and D. J. F. *Gaussian 09 Revision A.02. Gaussian, Inc.* (2016).
2. Hujo, W. & Grimme, S. Comparison of the performance of dispersion-corrected density functional theory for weak hydrogen bonds. *Physical Chemistry Chemical Physics* **13**, 13942 (2011).
3. Holthausen, M. C., Heinemann, C., Cornehl, H. H., Koch, W. & Schwarz, H. The performance of density-functional/Hartree–Fock hybrid methods: Cationic transition-metal methyl complexes MCH + 3 (M=Sc–Cu,La,Hf–Au). *The Journal of Chemical Physics* **102**, 4931-4941 (1995).
4. Lang, J. *et al.* Magnetostructural correlation in isolated trinuclear iron(III) oxo acetate complexes. *Physical Chemistry Chemical Physics* **20**, 16673-16685 (2018).
5. Lang, J. *et al.* Supporting Information to “Magnetostructural correlation in isolated trinuclear iron(III) oxo acetate complexes.” *Phys. Chem. Chem. Phys.* **20**, 16673-16685 (2018).
6. Cologne, U. of. Energy-consistent Pseudopotentials of the Stuttgart/Cologne Group. <http://www.tc.uni-koeln.de/> 0-0 Available at: <http://www.tc.uni-koeln.de/PP/clickpse.en.html>. (Accessed: 19th October 2018)
7. Andrae, D., Häußermann, U., Dolg, M., Stoll, H. & Preuß, H. Energy-adjusted ab initio pseudopotentials for the second and third row transition elements. *Theoretica Chimica Acta* **77**, 123-141 (1990).
8. Dolg, M., Wedig, U., Stoll, H. & Preuss, H. Energy-adjusted ab initio pseudopotentials for the first row transition elements. *The Journal of Chemical Physics* **86**, 866-872 (1987).
9. Martin, J. M. L. & Sundermann, A. Correlation consistent valence basis sets for use with the Stuttgart–Dresden–Bonn relativistic effective core potentials: The atoms Ga–Kr and In–Xe. *The Journal of Chemical Physics* **114**, 3408-3420 (2001).
10. Grimme, S., Antony, J., Ehrlich, S. & Krieg, H. A consistent and accurate ab initio parametrization of density functional dispersion correction (DFT-D) for the 94 elements H–Pu. *Journal of Chemical Physics* **132**, (2010).
11. MacAleese, L. & Maître, P. Infrared spectroscopy of organometallic ions in the gas phase: From model to real world complexes. *Mass Spectrometry Reviews* **26**, 583-605 (2007).
12. Lang, J., Mohrbach, J., Dillinger, S., Hewer, J. M. & Niedner-Schatteburg, G. Vibrational blue shift of coordinated N₂ in [Fe₃O(OAc)₆(N₂)_n]⁺: “non-classical” dinitrogen complexes. *Chemical Communications* **53**, 420-423 (2017).
13. Mains, G. J. & White, J. M. All-electron and relativistic effective core potential study of rhodium compounds. *Journal of Physical Chemistry* **95**, 112-118 (1991).
14. Stratt, R. M. & Adachi, S. H. On the origin of the phase transitions in a class of mixed valence compounds. *The Journal of Chemical Physics* **86**, 7156-7163 (1987).
15. Jang, H. G. *et al.* Highly cooperative valence detrapping of mixed-valence manganese complex [Mn₃O(O₂CCH₃)₆(py)₃](py) in the solid state. *Journal of the American Chemical Society* **111**, 7778-7784 (1989).
16. Sherrill, C. Counterpoise Correction and Basis Set Superposition Error. *Vergil.Chemistry.Gatech.Edu* 1-5 (2010). Available at: <http://vergil.chemistry.gatech.edu/notes/cp.pdf>.
17. Mück-Lichtenfeld, C. & Grimme, S. Theoretical analysis of cooperative effects of small molecule activation by frustrated Lewis pairs. *Dalton Transactions* **41**, 9111 (2012).
18. Steill, J. D. & Oomens, J. Action Spectroscopy of Gas-Phase Carboxylate Anions by Multiple Photon IR Electron Detachment/Attachment. *The Journal of Physical Chemistry A* **113**, 4941-4946 (2009).
19. Steill, J. D. & Oomens, J. Supplementary information to “Action spectroscopy of gas-phase carboxylate anions by multiple photon IR electron detachment/attachment.” *Journal of Physical Chemistry A* **113**, 4941-4946 (2009).
20. Woehler, S. E. *et al.* Deuteron NMR study of lattice dynamics affecting the rate of intramolecular electron transfer in the iron acetato oxo pyridine mixed-valence complex [Fe₃O(O₂CCH₃)₆(py)₃](py). *Journal of the American Chemical Society* **109**, 1063-1072 (1987).
21. Kambara, T., Hendrickson, D. N., Sorai, M. & Oh, S. M. Mechanism of phase transitions affecting intramolecular electron transfer in trinuclear mixed-valence transition-metal compounds. *The Journal of*

- Chemical Physics* **85**, 2895-2909 (1986).
22. Nakano, M., Wakamatsu, T., Sorai, M. & Suga, H. Cluster pairing in the paramagnetic trinuclear complex compound $[\text{Cr}_3\text{O}(\text{CH}_3\text{COO})_6(\text{H}_2\text{O})_3]\text{Cl} \cdot 6\text{H}_2\text{O}$: Calorimetric study at very low temperatures. *Journal of Physics and Chemistry of Solids* **49**, 987-992 (1988).
 23. Sorai, M., Tachiki, M., Suga, H. & Seki, S. Magnetic and Thermal Properties of Crystals Including Isolated Clusters. I. Heat Capacity and Infrared Spectrum of $[\text{Cr}_3\text{O}(\text{CH}_3\text{COO})_6(\text{H}_2\text{O})_3]\text{Cl} \cdot 6\text{H}_2\text{O}$ Crystal between 1.5 and 280 K. *Journal of the Physical Society of Japan* **30**, 750-759 (1971).
 24. Wu, R. W. *et al.* Electron Transfer Rates in a Trinuclear Mixed-Valence Iron(III,III,II) Molecule: A Variable-Temperature Infrared Spectroscopic Study. *Journal of the Chemical Society-Chemical Communications* **30**, 1657-1658 (1994).
 25. Sowrey, F. E. *et al.* Spin frustration and concealed asymmetry: structure and magnetic spectrum of $[\text{Fe}_3\text{O}(\text{O}_2\text{CPh})_6(\text{py})_3]\text{ClO}_4 \cdot \text{py} \cdot \dagger$. *Journal of the Chemical Society, Dalton Transactions* **6**, 862-866 (2001).
 26. Sumner, C. E. & Steinmetz, G. R. Isolation of oxo-centered cobalt(III) clusters and their role in the cobalt bromide catalyzed autoxidation of aromatic hydrocarbons. *Journal of the American Chemical Society* **107**, 6124-6126 (1985).
 27. Wu, R. *et al.* Electron Localization and Delocalization in Mixed-Valence Transition Metal Clusters: Structural and Spectroscopic Studies of Oxo-Centered Trinuclear Complexes $[\text{Fe}_3\text{O}(\text{OCCMe}_3)_6(\text{py})_3]^{+0}$ and $[\text{Mn}_3\text{O}(\text{OCCMe}_3)_6(\text{py})_3]^{+0}$. *Inorganic Chemistry* **37**, 1913-1921 (1998).
 28. Chmela, J. *et al.* Differential Many-Body Cooperativity in Electronic Spectra of Oligonuclear Transition-Metal Complexes. *ChemPhysChem* **17**, 37-45 (2016).
 29. Zimmer, M. *et al.* Time-resolved IR spectroscopy of a trinuclear palladium complex in solution. *Physical Chemistry Chemical Physics* **17**, 14138-14144 (2015).
 30. Willersinn, S. Studienarbeit: Massenspektrometrische Untersuchung einer Palladium- katalysierten Kupplungsreaktion.
 31. Schmitt, Y. *et al.* In-depth exploration of the photophysics of a trinuclear palladium complex. *Phys. Chem. Chem. Phys.* **16**, 8332-8338 (2014).
 32. Bakker, J. M., Besson, T., Lemaire, J., Scuderi, D. & Maître, P. Gas-Phase Structure of a π -Allyl-Palladium Complex: Efficient Infrared Spectroscopy in a 7 T Fourier Transform Mass Spectrometer. *The Journal of Physical Chemistry A* **111**, 13415-13424 (2007).
 33. Stephenson, T. A., Morehouse, S. M., Powell, A. R., Heffer, J. P. & Wilkinson, G. 667. Carboxylates of palladium, platinum, and rhodium, and their adducts. *Journal of the Chemical Society (Resumed)* 3632 (1965). doi:10.1039/jr9650003632
 34. Skapski, A. C. & Smart, M. L. The Crystal Structure of Trimeric Palladium(II) Acetate. *Chemical Communications* 658-259 (1970).
 35. Váňa, J. *et al.* The role of trinuclear species in a palladium acetate/trifluoroacetic acid catalytic system. *Dalton Transactions* **46**, 16269-16275 (2017).
 36. Carole, W. A. & Colacot, T. J. Understanding Palladium Acetate from a User Perspective. *Chemistry - A European Journal* **22**, 7686-7695 (2016).
 37. Pakula, R. J. *et al.* Palladium Acetate Revisited: Unusual Ring-Current Effects, One-Electron Reduction, and Metal-Metal Bonding. *Inorganic Chemistry* **57**, 8046-8049 (2018).
 38. Pakula, R. J. *et al.* Supporting Information for "Palladium Acetate Revisited: Unusual Ring-Current Effects, One-Electron Reduction, and Metal-Metal Bonding." *Inorganic Chemistry* **57**, 8046-8049 (2018).
 39. Armbruster, F. *et al.* A triangulopalladium cluster consisting of μ_3 -capping silyl ligands. *Chem. Commun.* **47**, 221-223 (2011).
 40. Kuzu, I., Krummenacher, I., Meyer, J., Armbruster, F. & Breher, F. Multidentate ligand systems featuring dual functionality. *Dalton Transactions* 5836 (2008). doi:10.1039/b808347a
 41. de Frémont, P., Marion, N. & Nolan, S. P. Carbenes: Synthesis, properties, and organometallic chemistry. *Coordination Chemistry Reviews* **253**, 862-892 (2009).
 42. Vignolle, J., Cattoën, X. & Bourissou, D. Stable Noncyclic Singlet Carbenes. *Chemical Reviews* **109**, 3333-3384 (2009).
 43. Herrmann, W. a. N-Heterocyclic Carbenes: A New Concept in Organometallic Catalysis. *Angewandte Chemie International Edition* **41**, 1290-1309 (2002).
 44. Bourissou, D., Guerret, O., Gabbai, F. P. & Bertrand, G. Stable Carbenes. *Chemical Reviews* **100**, 39-92 (2000).

5 Experimental Studies of the Basic Carboxylate Complexes

5.1 Synthesis of Trinuclear Carboxylate Complexes

While the iron and chromium acetate complexes are easily available commercially, any mixed metal and other carboxylate complexes must be synthesized in house. The synthesis is relatively straightforward and seems to be easily modified for different transition metals and bridging ligands, as long as equivalent starting materials can be found. We utilized two different synthetic routes, from the M^{III} hydroxides and straight from the M^{III} chlorides, reacting them with the sodium carboxylates or the carboxylate acid respectively. Both routes were met with good success, at least to have sufficient material for ESI mass spectrometry. The second variant, being a one pot reaction (section 5.1.2), seems to be a bit simpler, with the sodium chloride salt formation being a strong driver. There is a third variant directly from the respective metals, e.g. using iron and an acetic acid/hydrogen peroxide mix. The formation mechanism of that reaction was investigated by Laurikenas et al.¹. We didn't attempt this synthesis variant ourselves yet. We want to thank Marko Leist and the Thiel group to give us the opportunity and valuable help to synthesize the complexes in their lab.



Figure 31 Picture of several metal carboxylate complexes after synthesis using the classical method.

5.1.1 Synthesis from the M^{III} Hydroxides

This synthesis route was used in the initial discovery of the basic carboxylates by Weinland²⁻⁷ and is used frequently, for example by Johnson et al.⁸.

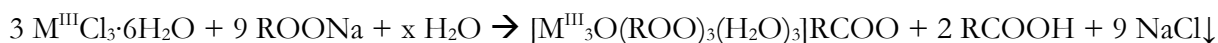
The $M^{III}Cl_3$ salt is first turned into the respective hydroxide by reacting it with sodium hydroxide. In this step it is important to pay attention to the pH of the solution to successfully precipitate the hydroxide, as the hydroxide is soluble again in overly basic solutions. The metal hydroxide gets separated by filtration or centrifugation. It is then reacted with an excess of the respective carboxylate acid, in our case formic or acetic acid. After refluxing the reaction mixture for a few hours, the trimetallic hexacarboxylate complex is formed.



Once a solution of the respective trimetallic carboxylate in its carboxylate acid is obtained, it can be crystallized by evaporating the acid. This can be difficult, especially for formate, which occurs as a strongly bound dimer and starts to decompose around its boiling point.

5.1.2 Direct Synthesis with $M^{III}Cl_3$ and Sodium Carboxylate

Clegg^{9,10}, Wilkinson¹¹, Earnshaw¹², and Weinland et al.¹³ are using a very elegant alternative. They use the metal(III) chloride and the sodium salt of the carboxylic acid, with the formation of sodium chloride salt as the driver of the reaction. See Max Luczak's master thesis (in preparation) for details.



This shortens the reaction to a single step, while still giving acceptable yield and quality for the use in our ESI experiments.

5.2 The Mass Spectra of the Complexes

CID and IRMPD measurements were performed using a modified Paul-type quadrupole ion trap instrument (Amazon ETD and Amazon SL, respectively, both by Bruker Daltonics). Typical settings are given in the ESI introduction in section 2.2.

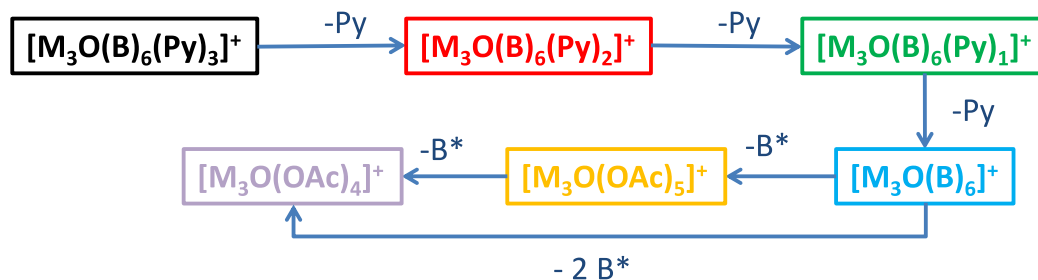


Figure 32 Fragmentation scheme behind the mass spectra in **Figure 33**, adapted from **Scheme 3** in chapter 10. B stands for the bridging ligand, as previously introduced in **Figure 1**.

A representative example of the mass spectra obtained in this work will be the case of $[Fe_3O(OAc)_6(Py)_n]^+$. This case has also been discussed in depth in our paper¹⁴ (chapter 10), with additional mass spectra shown in the supporting material¹⁵ (section 10.2). We obtain a series of isotopic peaks, in the example of $[Fe_3O(OAc)_6(Py)_n]^+$ ($n = 0, 1, 2, 3$) at $m/z = 538, 617, 696,$ and 775 . They match convincingly with simulated isotopic patterns of $[Fe_3O(OAc)_6(Py)_n]^+$ ($n = 0, 1, 2, 3$), as shown in the insets in **Figure 34**. In a solution of acetonitrile and pyridine, the axial H_2O ligands of the precursor ion $[Fe_3O(OAc)_6(H_2O)_3]^+$ exchange with the stronger binding pyridine ligand (Py, C_5H_5N), especially when they are first dissolved in pyridine and then diluted with acetonitrile.

Note, the intensity of the $n = 3$ mass peak is significantly lower than that of $n = 2$, as the tri pyridine coordinated complex is the weakest bound species (see CID) and shows autofragmentation at isolation conditions in the ion trap or during resonance ejection for mass analysis.

The satellite peaks at $m/z = 524, 603, 682,$ and 761 arise from complexes with a formate bridging ligand instead of an acetate, probably by impurities of the commercial sample material in the case of $[\text{Fe}_3\text{O}(\text{OAc})_6]^+$.

In the formate or heterometallic case, this scheme still holds, although relative fragmentation energies differ, as shown in the CID results discussed in section 5.3. This can promote or inhibit the occurrence of a specific step; due to the higher water affinity of the formates and chromium containing complexes. This affinity additionally enhances the post fragmentation pre-detection adduction of water, which is always present in trace amounts in the trap. This happens especially often in the case of free chromium binding sites in complexes with few axial ligands and has been exploited in the case of the acetate and formate water complexes discussed in section 8.1. They have been sprayed from an acetonitrile/ethanol mix, which contains sufficient trace amounts of water. This can lead to high water adducts, up to six, as can be seen in the spectra shown in the appendix in **Figure 87**. This also explains the decreased resolution of the isotope mass peaks of $[\text{Fe}_3\text{O}(\text{OAc})_6(\text{Py})_3]^+$ at $m/z = 775$ (shown in the inset for $n = 3$ in grey). We observe further weak mass peaks around 556, which we assigned to the water adduct $[\text{Fe}_3\text{O}(\text{OAc})_6(\text{H}_2\text{O})]^+$.

5.3 Collision Induced Dissociation (CID) Experiments of Formate and Acetate Complexes

Credit to a good part of these measurements go to the work of Jonas Krüger, which he describes in his bachelor thesis¹⁶ ‘Regioselective fragmentation of trimeric iron and chromium carboxylates’. He took a good part of the measurements shown here and worked on correlating the calculated bond breakage energy to the CID E_{com}^{50} values. The discussion of the CID curves themselves is therefore intentionally kept short and mostly a summary of his conclusions. His results are correlated in **Figure 36** with the pyridine metal bond lengths, using data from section 4.4, as those results had not yet been compiled from the DFT calculation before the submission of his thesis.

One focus in his thesis is looking at the bi- and trilogistic behavior of the fragment appearance curves in the mixed metal complexes. Looking at the fragmentation patterns, the first curve can be correlated with cleavage of the pyridine ligand from the weakest available metal pyridine bond, while the second component depends strongly on the specific complex, where competition is possible between single pyridine cleavage from the stronger coordination site or sequential pyridine cleavage, if available.

The details can be seen in **Figure 73**, where the fragment channels for all CID-appearance and breakdown curves of $[\text{Cr}_n\text{Fe}_{3-n}\text{O}(\text{B})_6(\text{Py})_m]^+$ ($n = 0, 1, 2, 3$; $m = 1, 2, 3$; $\text{B} = \text{formate, acetate}$) are shown. The CID spectra were recorded in the Amazon ETD spectrometer with varying excitation amplitudes (0.0 V to 1.5 V), which determine the internal energy scale (E_{lab} in Volt).

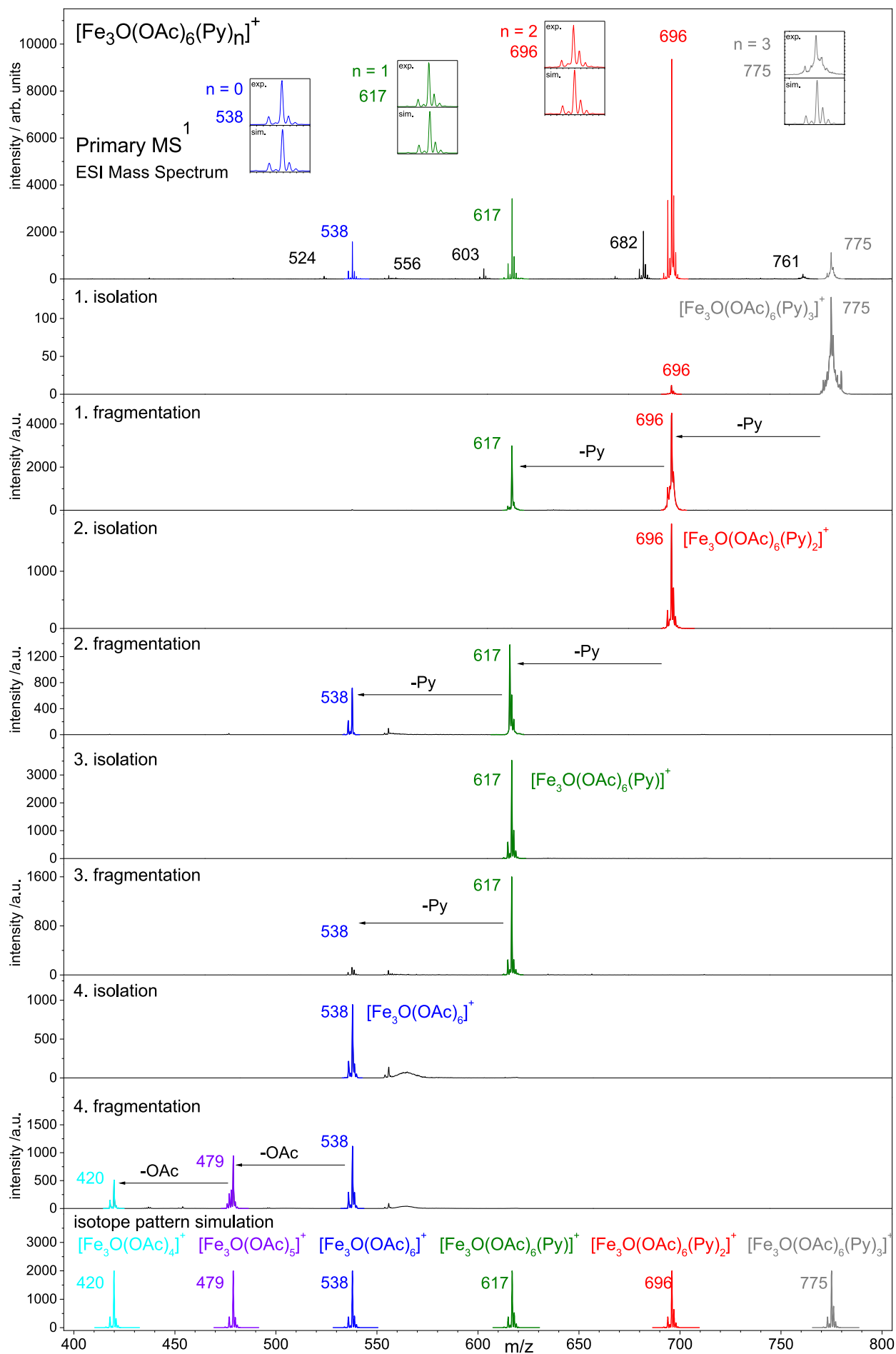


Figure 33 Mass spectra of all $[\text{Fe}_3\text{O}(\text{OAc})_6(\text{Py})_n]^+$ species and the MS^5 mass spectra with successive isolation and fragmentation steps for $n = 3 - 0$. Adapted and expanded from Figure 1 in our paper¹⁴, as shown in chapter 10 and Figure S1 - S6 in section 10.2.

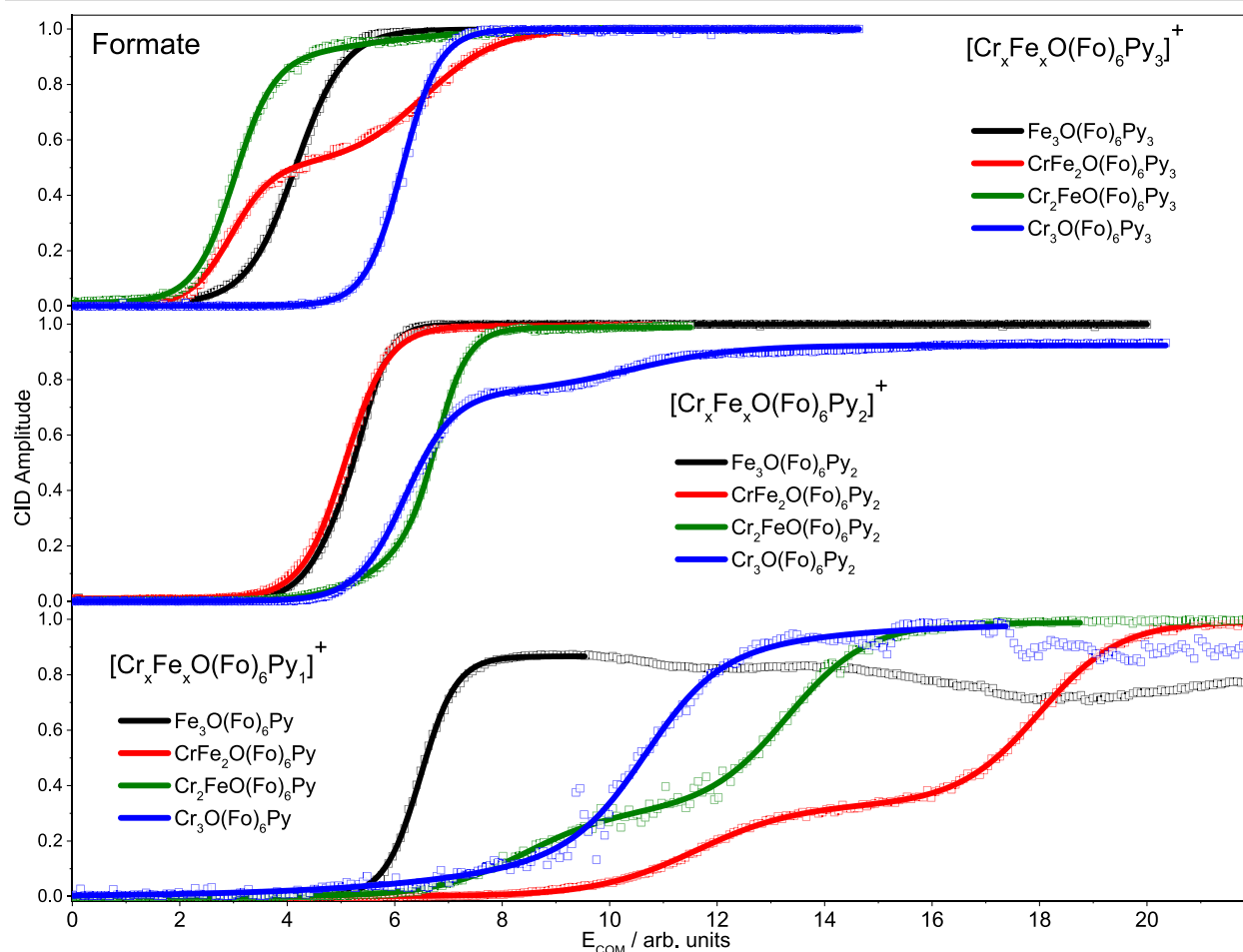


Figure 34 CID of $[\text{Cr}_n\text{Fe}_{3-n}\text{O}(\text{Fo})_6\text{Py}_m]^+$ for $n, m = 0 - 3$, see **Table 23** in the appendix for the extracted E_{com}^{50} values and the corresponding calculated fragmentation energies.

The CID spectra were recorded in the Amazon ETD spectrometer with varying excitation amplitudes (0.0 V to 1.5 V), which determine the internal energy scale (E_{lab} in Volt). Relative abundances were calculated according to equation I. Center of mass corrected fragmentation amplitudes (E_{com}) were calculated from the internal amplitudes (E_{lab}) by using equation II.

The CID spectra were modeled and fitted by sigmoid functions of the type defined in section 2.4.1, equation IV for mono-, and section 2.4.2, equation V for bi-, and VI for cases of tri-logistic fragmentation behaviors, using a least-squares criterion.

The initial fragment appearance curves can be associated to the relative stability of the lowest energy fragmentation channel available in the parent complexes⁴⁶⁻⁴⁹. We have to keep in mind the multi collision environment in a room temperature Paul ion trap and the relative nature of CID measurements, limiting us to a qualitative interpretation. The corresponding fragment mass traces for all discussed species are shown in the appendix in **Figure 73**. Single pyridine elimination usually dominates the initial sigmoid rise of the fragment appearance curves; only later additional fragments arise. Weak mass peaks at $m + 18$ u are often observed as well.

This is assigned to water attachment within the ion trap to the available coordination sites of the fragment ion, which is therefore a daughter product of the initial fragment population.

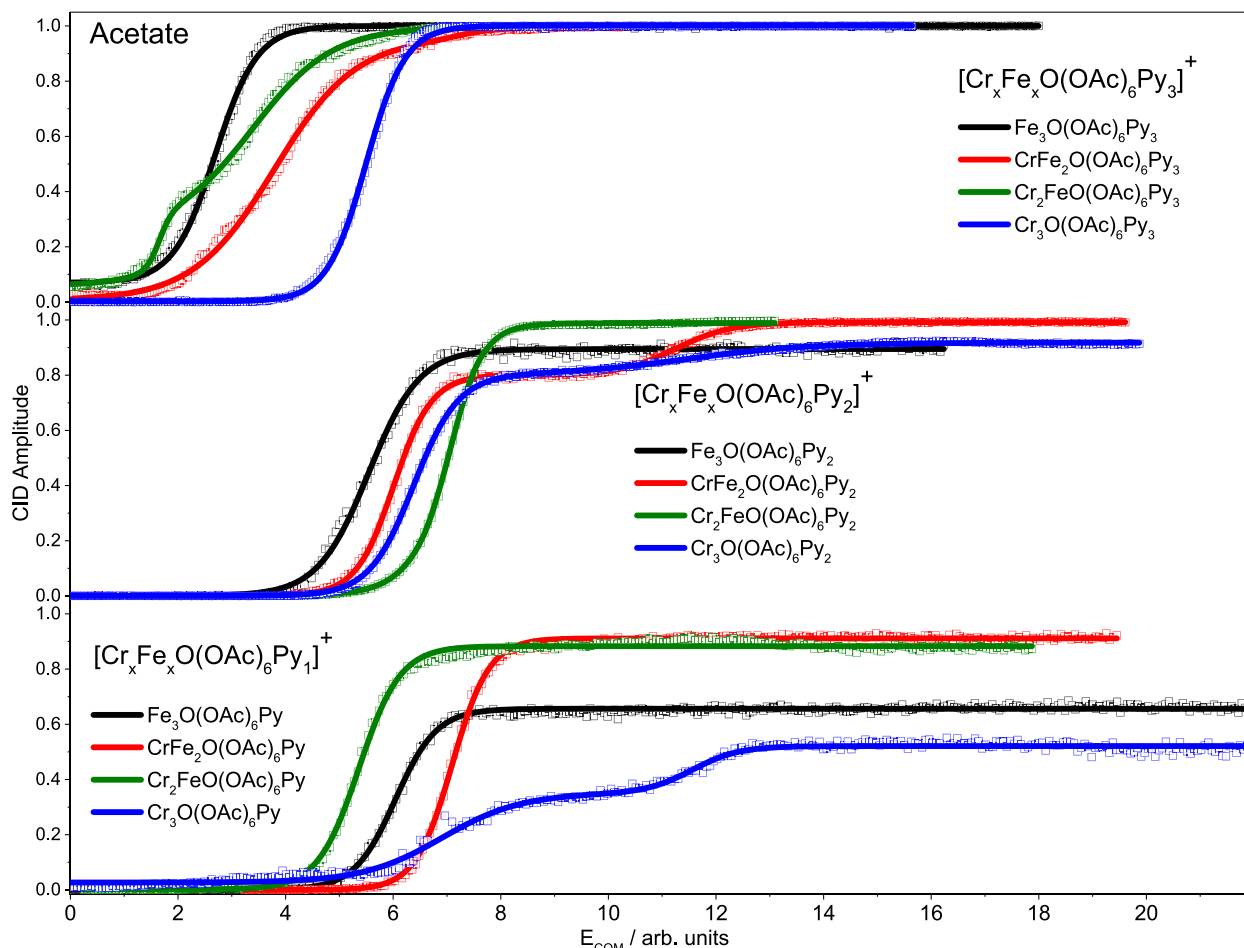


Figure 35 CID of $[\text{Cr}_n\text{Fe}_{3-n}\text{O}(\text{OAc})_6\text{Py}_m]^+$ for $n, m = 0 - 3$, see **Table 22** in the appendix for the extracted E_{com}^{50} values and the corresponding calculated fragmentation energies.

The intensity of these adducts were therefore summed into the total intensity of the corresponding fragment channel. We observe cleavage of neutral carboxy radicals when no pyridine ligands are available. The observed mass spectra are well represented by the spectra shown in section 5.2.

The relative stability of $[\text{M}_3\text{O}(\text{OAc})_6(\text{Py})_n]^+$ ($n = 0, 1, 2, 3$) was determined by recording the CID appearance curves of the associated fragments as shown in **Figure 35** for acetate and **Figure 34** for formate.

When comparing the formate with the acetate bridging ligands, we have to differentiate between the different pyridine species with three, two, or one pyridine ligands. Starting with three pyridine ligands and a therefore fully saturated complex, we see the mixed metal formates to be even less stable than the pure iron complex. As we have seen with the calculated bond lengths in **Figure 27** and later in **Figure 36**, this matches well with the expected order, as the chromium(III) center has a weakening effect on the iron(III) centers, while being a very strongly coordinating center itself. This effect is a bit lessened in the acetate complexes, where only the Cr_2Fe species fragment at energies below the Fe_3 fragmentation threshold.

Overall, as the next section shows, at least the first fragmentation energies matches very well with the dissociation energies predicted by BSSE corrected DFT calculations.

5.3.1 Correlation of the E_{com}^{50} Values Versus the Binding Energy and the Bond Distance

As discussed in our paper¹⁴ (chapter 10), it is possible to compare the experimental E_{com}^{50} to the respective calculated fragmentation energies determined by the following simple formula:

$$\Delta_{fr}E_n = \{[E([M_3O(B)_6(Py)_{n-1}]^+) + E(Py)] - E([M_3O(B)_6(Py)_n]^+)\} \quad XIV$$

Like introduced in section 2.6.2, we used the BSSE corrected fragmentation energies to account for basis set superposition error. This simple energy difference is of course a simplification of the actual fragmentation process.

Besides the adiabatic binding (free) energies, we would actually need to consider the presence of molecular fragmentation activation barriers and the relative energies of transition state structures to evaluate the E_{com}^{50} values, rather than just the mere endothermicity of bond breaking^{64, 65}.

In the present case, as shown in section 4.5 in **Figure 29**, the pyridine being removed from the ligating metal shows a simple potential energy surface without transition states. This energy surface is dominated by the endothermicity of bond breaking^{67,68}. As a general trend, the binding energies^{41,49,66} of pyridine ligands decrease with the number of pyridine ligands coordinated to the $[M_3O(OAc)_6]^+$ core. When plotting the dissociation energy against the E_{com}^{50} value (see **Figure 36**, right column, based on the values in **Table 22** and **Table 23**), there seems to be a significant linear correlation between them.

Similarly, using the values from the previous section 4.4, it also correlates with the length change of the bond between the ligating metal and the pyridine ligand or the metal center and the oxide center atom (again **Figure 36**, left column).

The correspondence of the observed initial CID fragmentation curve to the expected energetically favored regioisomer is further indication that they make up a majority fraction of the complex population. For a more detailed discussion on this, please refer to Jonas Krüger's bachelor thesis¹⁷ on the 'Regioselective fragmentation of trimeric iron and chromium carboxylates'.

In turn, the dissociation energy and the bond length also are directly correlated with each other. A stronger bond, as measured by its fragmentation energy, is shorter and a weaker bond longer, respectively. This makes sense in an intuitive way, but is good to see confirmed directly. It is valuable confirmation of the assumption, that the geometry trends discussed in section 4.4 can be applied directly to the discussion of the IRMPD spectra in later chapters.

This will help with assigning the correct isomer to the respective IR spectra. More on this in section 6.3 and in **Figure 54 D**.

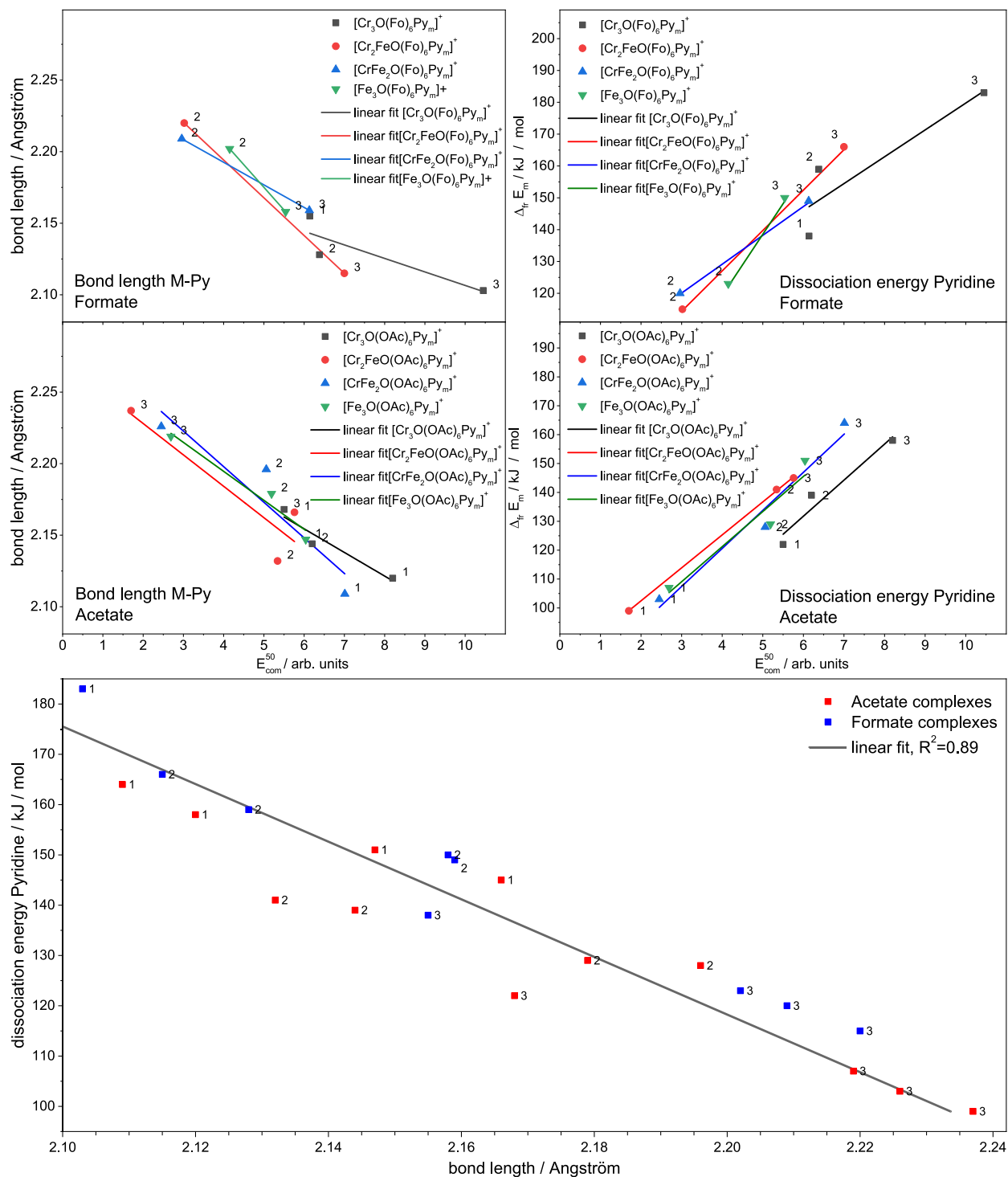


Figure 36 Correlation diagram of the E_{com}^{50} values versus the fragmentation energy and the bond distance. Based on the values given in **Table 22** and **Table 23**, as compiled in cooperation with Jonas Krüger, described in his bachelor thesis¹⁶.

5.4 Fragment Specific IRMPD Spectroscopy

5.4.1 Foundations of Fragment Specific IRMPD Spectroscopy

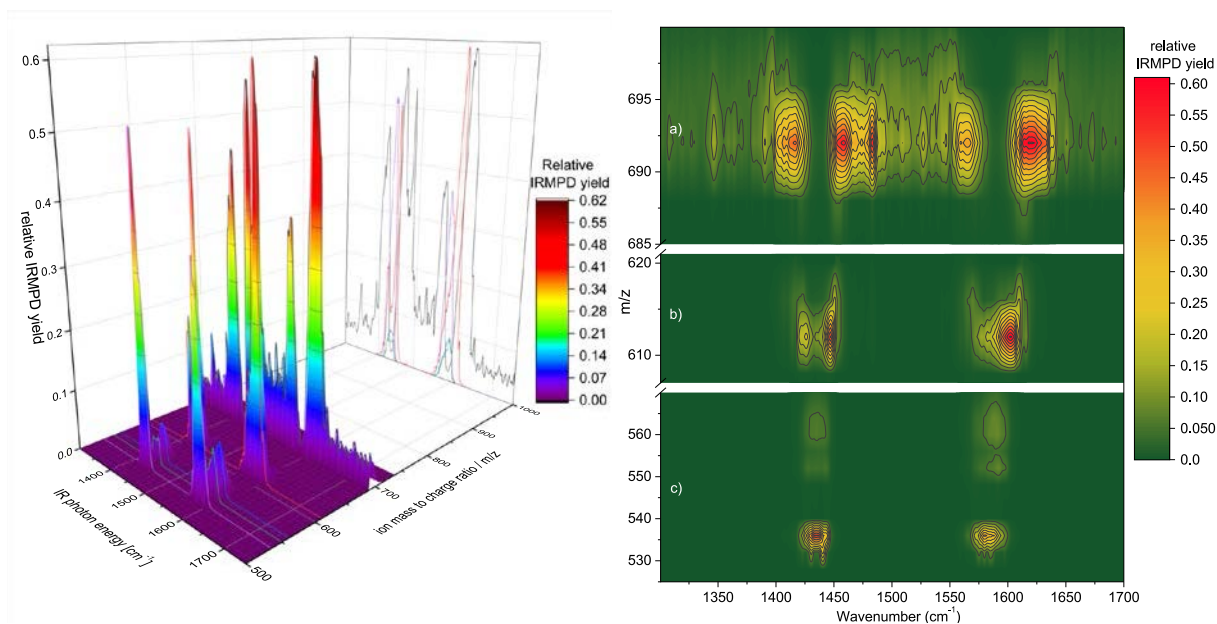


Figure 37 Different ways of visualizing the data stream of a wavelength dependent IRMPD mass spectrum of iron acetate with three pyridine ligands, adapted from Jonas Schuchmann's bachelor thesis¹⁶. Ultimately the cumulative IRMPD plot proved best (see section 5.4.2).

An experimental IRMPD spectrum arises from a plot of the fragmentation efficiency as a function of laser frequency (ν), or as labeled here, the IR photon energy in cm^{-1} , as defined in equation III in section 2.5. Like introduced in section 2.5.1, it is beneficial to not only determine the total IRMPD yield of a given IRMPD measurement, but to also pay attention to the separate fragment mass traces.

The necessary data processing legwork to extract the IRMPD fragment mass traces from the recorded mass spectra has been done in cooperation with the bachelor student Jonas Schuchmann in his bachelor thesis¹⁶ *‘Modifikation von Analysemethoden für die differenzierte Interpretation von fragmentspezifischen IRMPD Spektren: Anwendung auf trinukleare oxo-zentrierte Eisenkomplexe’*.

His work makes it possible to condense the three-dimensional data stream recorded using the Amazon SL mass spectrometer by the TrapControl software (by Bruker Daltonics): time (with a constant laser scan rate of 0,03 nm/s directly correlated with the wavelength); the mass to charge ratio (m/z); and the corresponding ion intensity value. At first it is important to find a good representation of that data. Some possible visualizations of this data set are shown in **Figure 37**. This information is extracted by a Visual Basic Script (VBS)¹⁸ in the Compass Data Analysis Software Version 4.2 by Bruker. It is then written into a text file in the correct data format to be imported semi-automatically into a specially set up Origin (by Origin Labs) worksheet. To improve the signal to noise ratio, multiple repetitions of the same measurement can be automatically concatenated, averaged, and smoothed at this step. This worksheet then relays this data into a series of relevant plots, on which the IRMPD spectra plots are based in the following chapters.

The information we obtain from a typical data analysis of a set of measurements not only contains the wavenumber, the total IRMPD yield, a record of the laser intensity behind the trap exit, but also the normalized fragment mass traces we defined in the data analysis script. How to best use this additional information is the focus of the following section.

5.4.2 Fragment Specific IRMPD of the Archetypal Iron Acetate Pyridine Complexes

We choose to demonstrate the value and behavior of this method by using the example of the archetypal iron acetate complex. Without going too deep into the specific interpretation of the iron acetate IR spectra, done in depth in chapter 6 and previously in our paper¹⁴ (chapter 10), we can observe a good deal of useful information in the fragment mass traces. The fragment traces in this section are slightly simplified, minor complications like post-fragmentation pre-detection adduction of water in the ion trap have been summed into the primary fragment mass trace. However, this does not change the overall behavior, as can be seen in **Figure 42** and in the full spectrum shown later in **Figure 51 B**.

First, as shown in **Figure 38 a**), increasing the laser power and shot count does not affect the peak position and only leads to a broadening of the band. This is expected, given that only one mode dominates the apparent peak. This applies at least in the cases of the symmetric and asymmetric $\nu(\text{COO})$ bands observed here. Even more interesting is the behavior of the fragment traces of $[\text{Fe}_3\text{O}(\text{OAc})_6\text{Py}_n]^+$ in relation to the total IRMPD yield. The fragment traces themselves are informative, but their behavior does not follow the observed and predicted spectra well, as seen in **Figure 38 b**). This way of plotting non summed fragment mass traces was done previously by Maitre et al.¹⁹. This might be acceptable for spectra with only a few relevant traces, but breaks down quickly for more complicated spectra.

It is necessary to plot the cumulative sum of channels (**Figure 38 c**); also **Figure 41** and **Figure 42**, top graphs). All fragment channels are summed with all previous channels, up to the total IRMPD limit; as defined in equation IX in section 2.5.1. When plotting the cumulative sum of the fragment traces, the IRMPD spectra for $[\text{Fe}_3\text{O}(\text{OAc})_6\text{Py}_n]^+$ with $n - m$ for $m = 0$ to $n - 1$ appears to be contained in the mass traces for the respective parent species with n pyridine ligands. This becomes clear from **Figure 39 c**) and **d**). The fragment species band positions are quantified with the gaussian fits in **Figure 39 e**) and are shown in **Figure 38 b**), compared there to the actual classical IRMPD band position of the species equivalent to the one in the fragment trace. They show very similar behavior to the species not obtained through IRMPD fragmentation, but with some caveats.

There seems to be a small shift in wavenumber compared to the species of $[\text{Fe}_3\text{O}(\text{OAc})_6\text{Py}_n]^+$ directly isolated from the population generated by the ESI ion source. A possible explanation for that would be that the ions of the $n - m$ species are freshly formed by IRMPD fragmentation from the $n = m + 1$ species, as isolated in the ion trap. They are not yet fully annealed by collisional cooling to their respective ambient ground state and are still considerably heated from leftover energy originating from the absorbed IR photons.

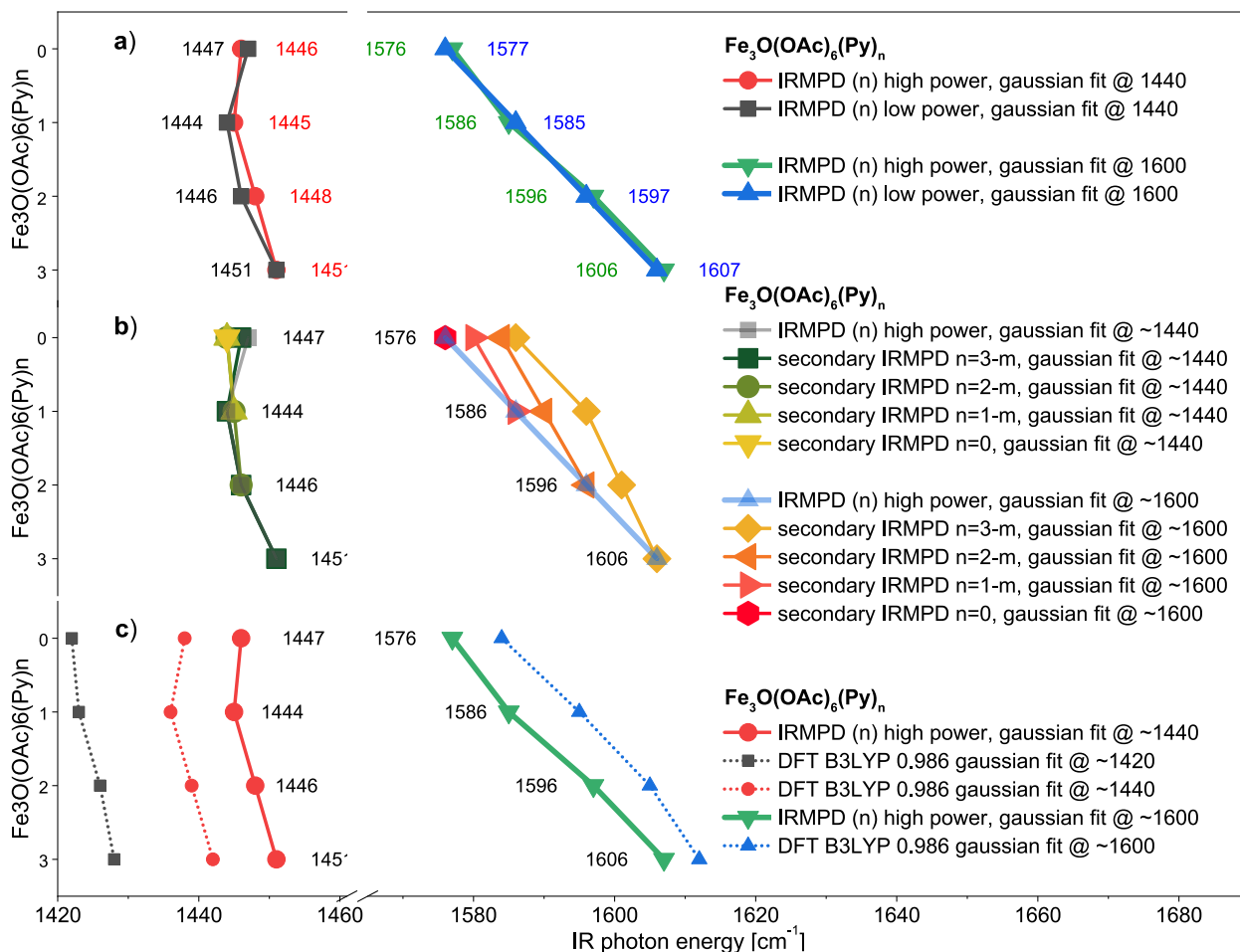


Figure 38 a) band position at low and high laser fluence (from **Figure 39 a)** b) the general trend of the primary and secondary IRMPD spectra (as determined by the gaussian fits in **Figure 39 e)** c) Comparison between predicted and observed band position in the $[\text{Fe}_3\text{O}(\text{OAc})_6\text{Py}_{0-3}]^+$ complexes.

Therefore, the apparent peak positions of the $n - 1$ species in the fragment mass traces cannot fully replace a dedicated measurement of the respective IRMPD spectrum. Nevertheless, for screening purposes or in cases where that species is hard to obtain directly from the original ESI ion population, it still gives a valuable hint on the IRMPD spectrum of the respective species. The predicted IR spectrum shown in **Figure 40** matches reasonably well to the observed IRMPD spectra in **Figure 39**, as shown in the comparison in **Figure 38 c)**. The band splitting $\Delta\nu$ of $\nu(\text{COO})_s$ and $\nu(\text{COO})_{as}$ is slightly overestimated, and the predicted strong $\delta(\text{CH})$ band at around 1424 cm^{-1} does not result in a high observed IRMPD yield. This is a common effect in IRMPD spectroscopy due to inefficient IVR processes, where the energy absorbed by that chromophore is not efficiently transferred into the available fragmentation channels. Dark bands are ‘observed’ as well in the CH region of the iron acetate spectrum, as discussed later in section 5.5. The trends of the symmetric and asymmetric $\nu(\text{COO})$ vibration in iron acetate complexes, together with those of the mixed metal acetates and the respective formates, are discussed in detail in chapter 7. In conclusion, together with the alternative plot variants shown in section 5.4.3, it is obviously useful to not discard the additional information contained in an IRMPD mass spectrum with the relative abundances of the different fragmentation channels.

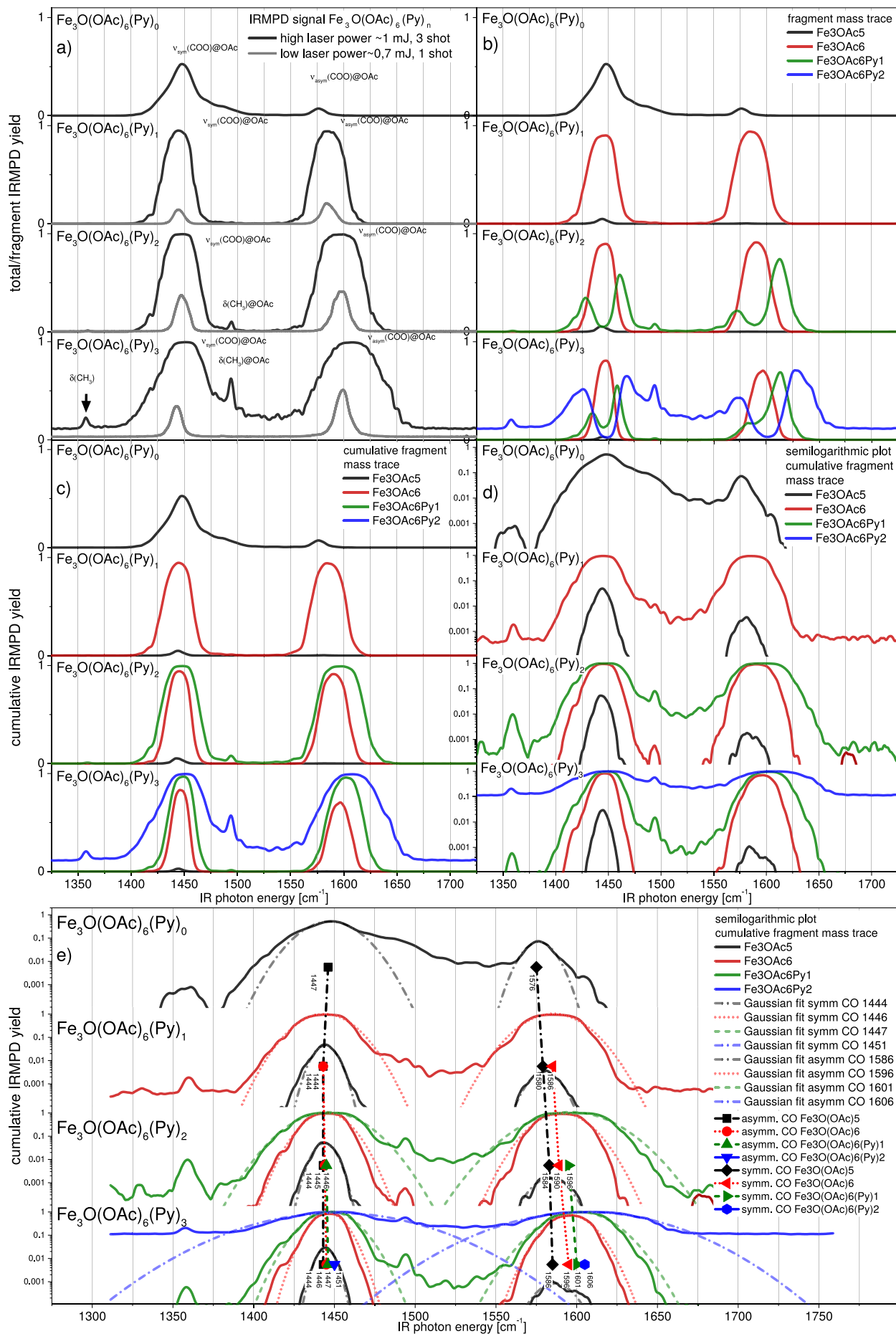


Figure 39 a) the $Y(v)$ spectra at low and high laser power, b) non-cumulative fragment mass traces $Y(v)_i^{fr}$, c) the cumulative fragment mass trace (cumulative IRMPD $Y(v)_i^{cum}$), providing improved readability, d) semi logarithmic plot of c), all $[\text{Fe}_3\text{O}(\text{OAc})_6\text{Py}_{0-3}]^+$ show the $\nu(\text{COO})$ s and $\nu(\text{COO})$ as bands for all fragment traces, e) gaussian peak fit for each mass trace (results are shown in **Figure 38 b**).

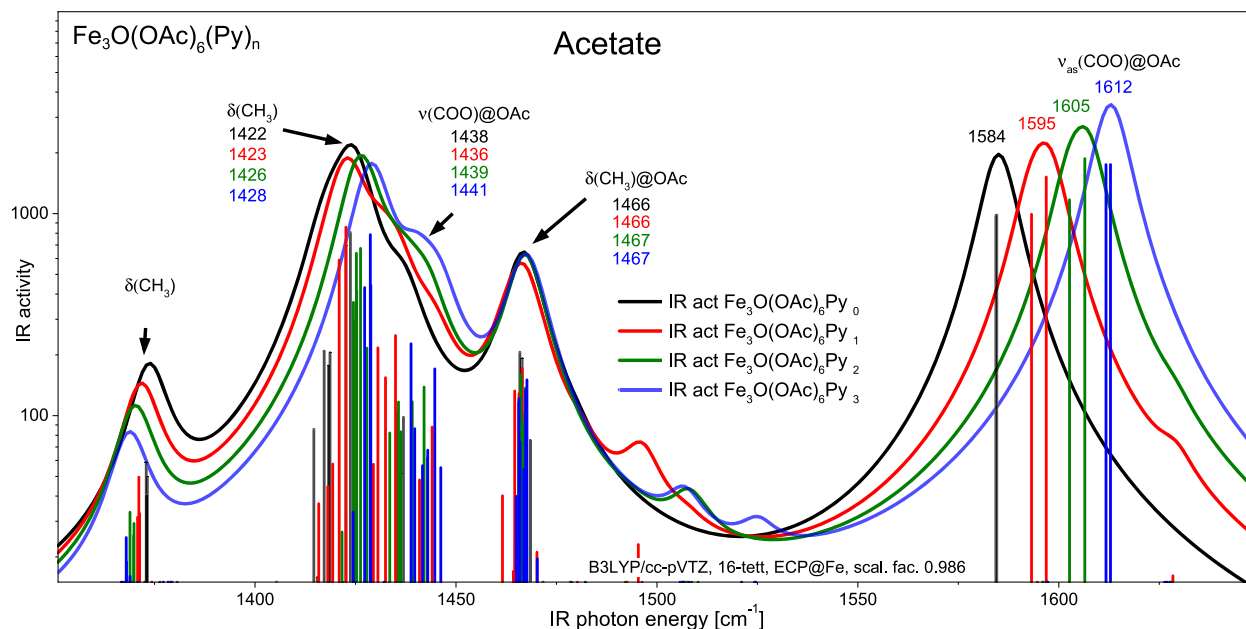


Figure 40 DFT simulation of the linear IR spectra of $[\text{Fe}_3\text{O}(\text{OAc})_6\text{Py}_{0-3}]^+$.

5.4.3 Successive Fragmentation in the COO Stretch Modes of Iron Acetate Pyridine Complexes at Different Laser Fluences

Successive fragmentation and competing fragmentation channels in IRMPD spectroscopy at high laser fluences are well known phenomena, but are often ignored when considering the overall spectrum itself. There have been previous works on sequential vs. competitive fragmentation²⁰, especially at the very high laser fluences possible in FEL laser systems. Lemaire et al.²¹ show a linear dependence of fragmentation efficiency with the number of laser pulses. Incidentally, they also observed a wavelength dependent second fragmentation channel. Maitre et al.¹⁹⁻²¹ highlighted the phenomenon before as well, describing wavelength dependent fragmentation channels in $\text{Fe}(\text{DME})_2^+$ ions. Competing fragmentation channels are often discussed for CID experiments, which Surya et al.²² also did for their IRMPD experiment.

With low laser power, only the lowest energy fragmentation channels are active. In the case of iron acetate with three pyridine ligands, that would be the dissociation of a single pyridine. This fragmentation channel is shown in mid blue in **Figure 41**. Other channels only play minor roles. Plot **c**) in **Figure 41** and **Figure 42** matches what Maitre et al.¹⁹ showed for $\text{Fe}(\text{DME})_2^+$ (Figure 4 in their paper). However, they didn't study a system with as many available consecutive dissociation steps as found in $[\text{Fe}_3\text{O}(\text{OAc})_6\text{Py}_3]^+$, provided sufficiently high laser fluence is available (see **Figure 42**). Therefore, they only plotted the total IRMPD yield and not the cumulative IRMPD yield as seen in plot **a**). What was previously (**Figure 39**, section 5.4.2) abbreviated into a single combined mass trace is explicitly shown here. The post fragmentation pre-detection water coordination in the ion trap at high laser fluences and with longer trapping times starts to become noticeable, as seen in **Figure 42 a**) and **b**). Here the acetate species fragment channel with a single pyridine ligand at 537 m/z coordinates water, adding up to 556 m/z .

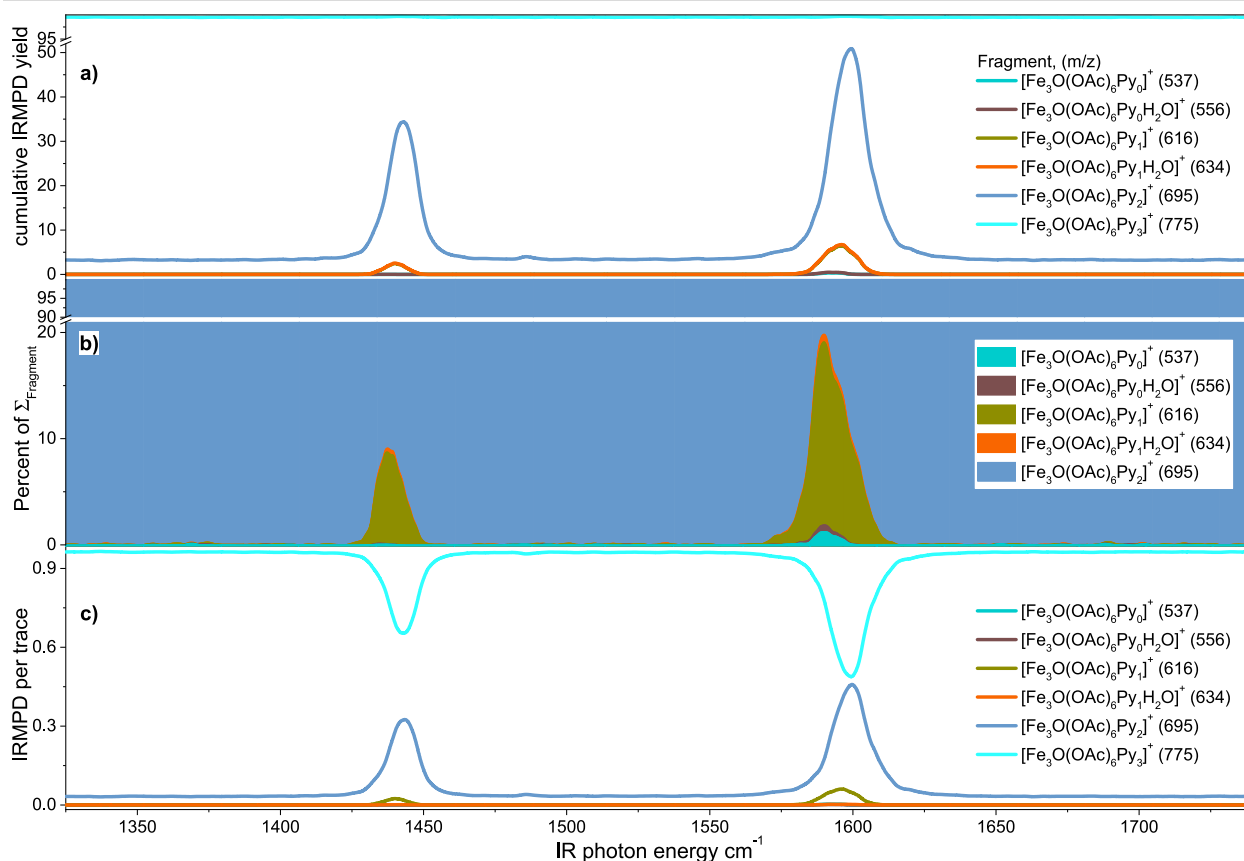


Figure 41 IRMPD spectrum of $[\text{Fe}_3\text{O}(\text{OAc})_6\text{Py}_3]^+$ at low laser fluence and an attempted assignment of the respective fragment traces. **a)** cumulative fragment yield; **b)** relative fragment yield normalized by total fragment yield; **c)** relative (non-cumulative) fragment yield.

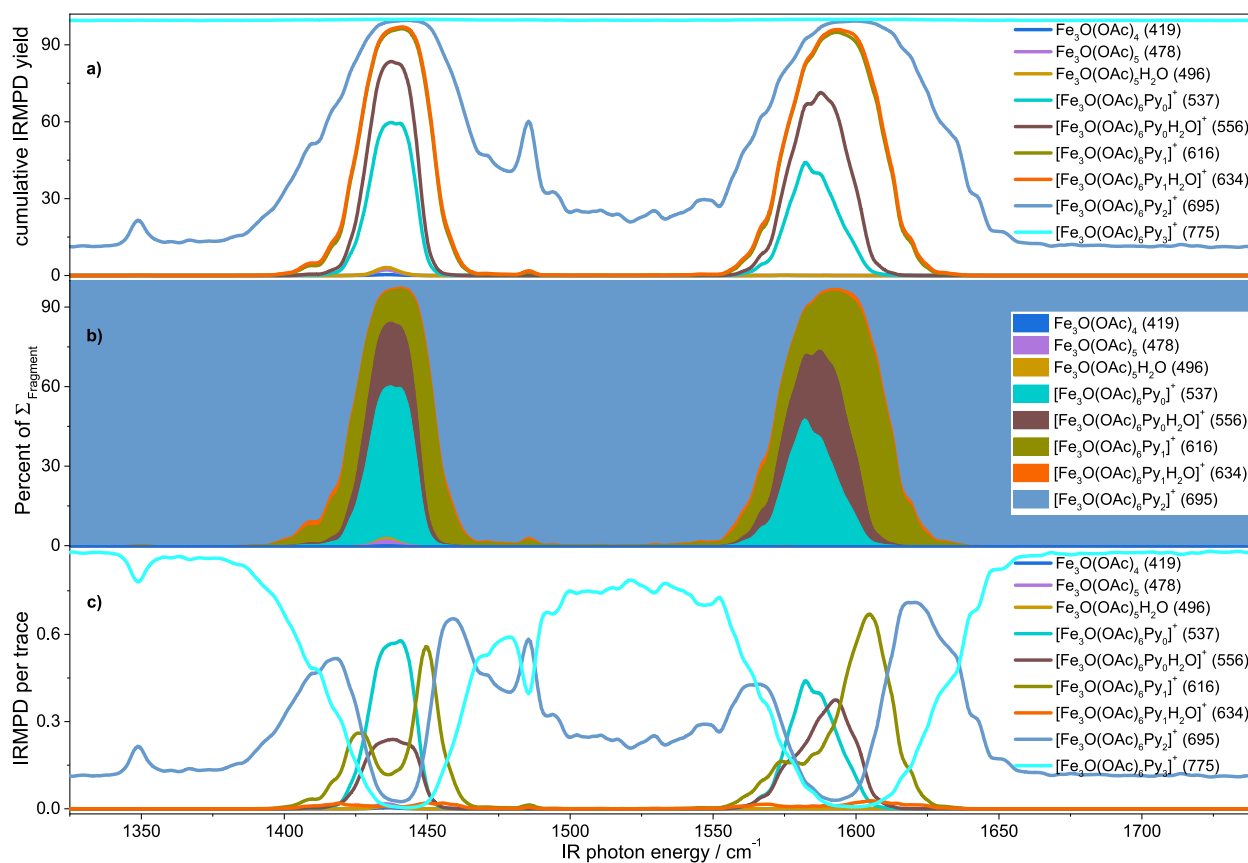


Figure 42 IRMPD spectrum of $[\text{Fe}_3\text{O}(\text{OAc})_6\text{Py}_3]^+$ at high laser fluence and an attempted assignment of the respective fragment traces. **a)** cumulative fragment yield; **b)** relative fragment yield normalized by total fragment yield; **c)** relative (non-cumulative) fragment yield.

In **Figure 42 c)** the concurring behavior of the water adducts is not that apparent, as the relative abundance and the peak appearance is strongly dependent on the behavior of the rest of the fragment channels. Only when we either plot the cumulative percentage each fragment has of the total fragment population, or if we use the previously introduced cumulative plot; the strong correlation between a fragment and the post fragmentation formation of its respective water adduct becomes apparent. This matches well with the post fragmentation behavior of the CID spectra and the isolation/fragmentation experiments shown in **Figure 33** in section 5.2.

In conclusion, all relevant information about the fragmentation behavior of an IRMPD spectrum is contained in the cumulative IRMPD plot; therefore, we propose this as the primary plot to show our results. However, sometimes it becomes useful to plot this with the semilogarithmic cumulative IRMPD yield to highlight small effects in the fragment traces, as shown in **Figure 60** in section 7.1.

5.4.4 Laser Power & Laser Shot Count Dependence of IRMPD Fragmentation Efficiency

For comparisons, such as in the previous section or in chapter 6, the following questions might arise: is it fair to compare spectra taken at different laser fluences and different number of successive laser shots per IRMPD data point? How much does that influence the fragmentation yield as well as the relative fragment abundances?

To answer this question, the following experiments were done. The laser was tuned to 1600 cm^{-1} , the wavelength of the highest fragmentation of the asymmetric $\nu(\text{COO})_{\text{as}}$ vibration of $[\text{Fe}_3\text{O}(\text{OAc})_6\text{Py}_3]^+$. For all three laser shot-counts commonly used in this work (a single laser shot, three sequential shots and nine sequential shots), the OPA attenuator angle was tuned from 0° (full attenuation) to the maximum transmission at around 45° , for the highest available laser power. See **Figure 7** for the corresponding laser power curve. Here we plotted the fragment yield, as is customary for CID spectra, and not the cumulative yield as previously done in this chapter. The observed fragmentation patterns are very familiar. They very much resemble the CID curves discussed in section 5.3 and in our paper¹⁴. They also match the isolation/fragmentation experiments of section 5.2, although successive dissociations occur much earlier, with smaller relative energy differences between their consecutive appearances.

This can have at least two possible reasons. The IRMPD process heats up the whole molecule, leaving considerable energy in its internal modes, even after causing the first fragmentation. The leftover energy can either be sufficient to directly lead to additional fragmentations, or the hot fragment ion can absorb further photons, given that the corresponding $\nu(\text{COO})_{\text{as}}$ mode of the fragment ion has not shifted too far and can still absorb energy at that wavelength. This subsequent photon absorption induced fragmentation process can happen either during a single laser shot, or by several successive laser shots. This suggests an incomplete thermalization of the ion population between laser shots, which are placed 100 ms apart. The nature of the fragmentation process does not seem to depend on the number of laser shots. Still, the corresponding fragments occur at lower laser energies.

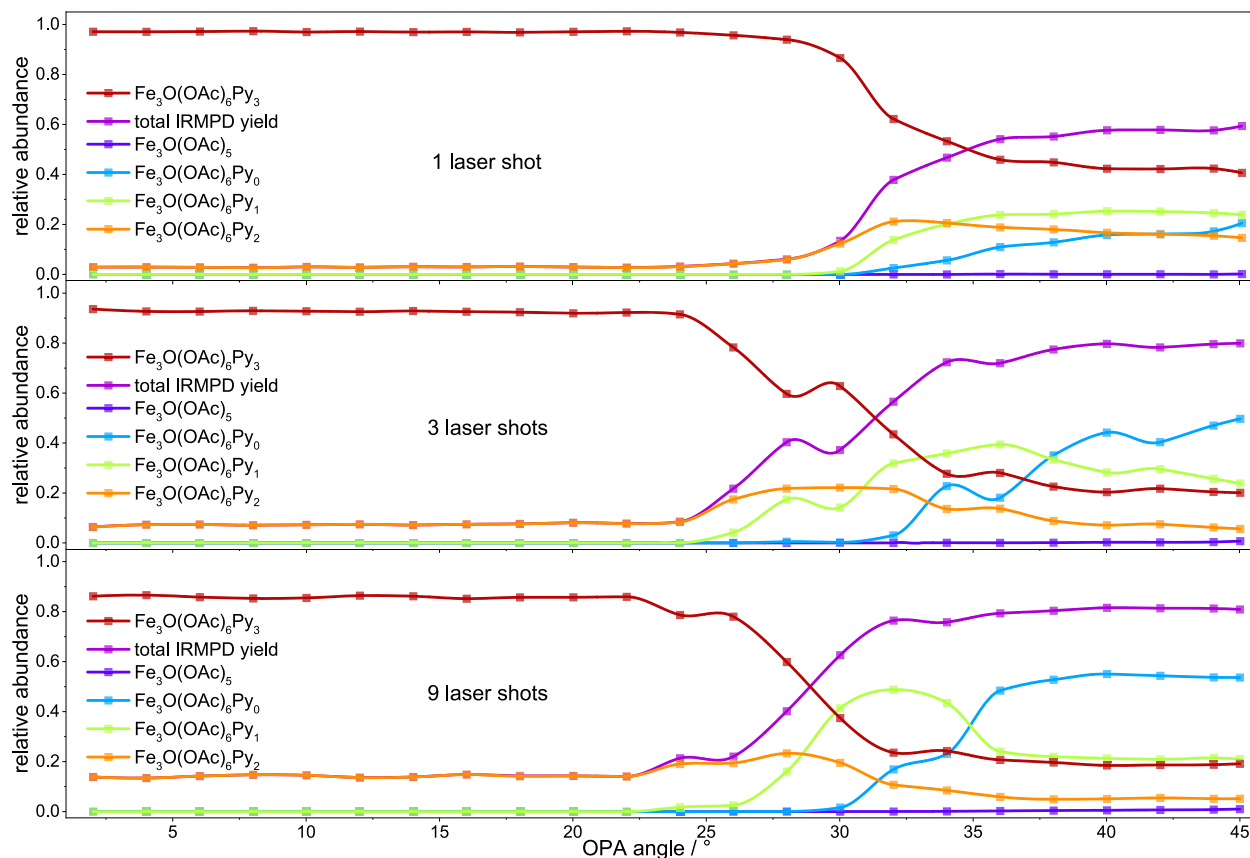


Figure 43 Laser power variation by attenuator (OPA) angle adjustment (see **Figure 7**) and the resulting relative abundances of fragments of $[\text{Fe}_3\text{O}(\text{OAc})_6\text{Py}_3]^+$ for 1, 3 and 9 laser shots.

Therefore, with multiple shots, the fragmentation seems to behave as if the IR laser had more energy than possible with a single laser pulse of our table top system.

In a CID experiment on the other hand, each ion population starts at the same baseline energy before the parent ion is excited selectively and made to collide with the buffer gas.

We conclude that it seems fair to compare spectra at different laser powers and laser shot counts. Therefore, we are using the combination that achieves the best species dependent fragmentation rate, suitable to either weakly absorbing fragmenting modes or strongly absorbing modes. Both variables seem to have a comparable effect on the overall IRMP fragmentation pattern. Furthermore, as shown in **Figure 38**, there seems to be little power shifting of the band position between using low or high laser fluences and/or shot counts. This also seems to hold for the other acetate complexes, as seen in **Figure 106** in the appendix.

5.5 Mode Specific Fragmentation in the CH Stretch Modes of Iron Acetate Pyridine Complexes

The phenomenon of chromophore specific fragmentation pattern^{21,23}, IR wavelength dependent competing fragmentation pathways^{19,24}, and fragment mode specific anharmonicity²⁵ have all been observed previously. We think our data suggests similar effects in our cases. This is also discussed by Jonas Schuchmann in his bachelor thesis¹⁶ on the method development of fragment specific IRMPD plots and their interpretation.



Infrared induced dissociation of specific bands can give rise to new fragmentation channels (as compared to CID)^{22,26} by exciting mode specific fragmentation pathways. A similar effect has been seen in the spectra of NH_4^+ and H_2O complexes²⁷.

An obvious benefit of plotting the cumulative fragment IRMPD yield is that mode specific fragmentation behavior becomes apparent immediately and intuitively. This can be seen in **Figure 44**. There the cumulative fragment yield IRMPD spectrum of $[\text{Fe}_3\text{O}(\text{OAc})_6\text{Py}_3]^+$ in the 2800 - 3200 cm^{-1} region is shown. We see two main group of bands, first a group of relatively broad bands between 2850 and 3000 cm^{-1} . Second, we see another triplet of comparatively narrow bands between 3060 and 3125 cm^{-1} , which have been identified previously¹⁴ as the aromatic pyridine $\nu(\text{CH})$ stretch modes. Looking at the fragment pattern, a big difference in the occurring mass traces becomes apparent immediately. To discuss those species in more detail, the averaged mass spectra of the green and blue regions in **Figure 44** are plotted in **Figure 45**.

The mass spectra show the stark difference in the fragmentation behavior just as clearly. The mass spectrum for the pyridine $\nu(\text{Py-CH})$ bands around 3100 cm^{-1} , as marked in blue in **Figure 45**, was integrated from the blue area of the IRMPD spectrum in **Figure 44**. It is comparatively simple and only shows two fragments; primarily the single dissociation of pyridine ligands, with the double dissociation occurring only in trace amounts. This largely agrees with the observations made in our CID experiments discussed previously (section 5.3). This first case of IR absorption by pyridine $\nu(\text{Py-CH})$ seems to have a very small pool of available fragmentation pathways; the cleavage of the excited pyridine ligands.

In contrast to that, the mass spectrum for the bands between 2925 and 2945 cm^{-1} is much more involved. It is marked in light green; both in the IRMPD graph in **Figure 44**, and the corresponding mass spectrum in **Figure 45**. Calculations using a harmonic approximation to simulate the IR spectrum only predict CH_3 stretch modes in this spectral range. The fragmentation pattern observed here does not match with CH_3 chromophore excitation observed elsewhere.

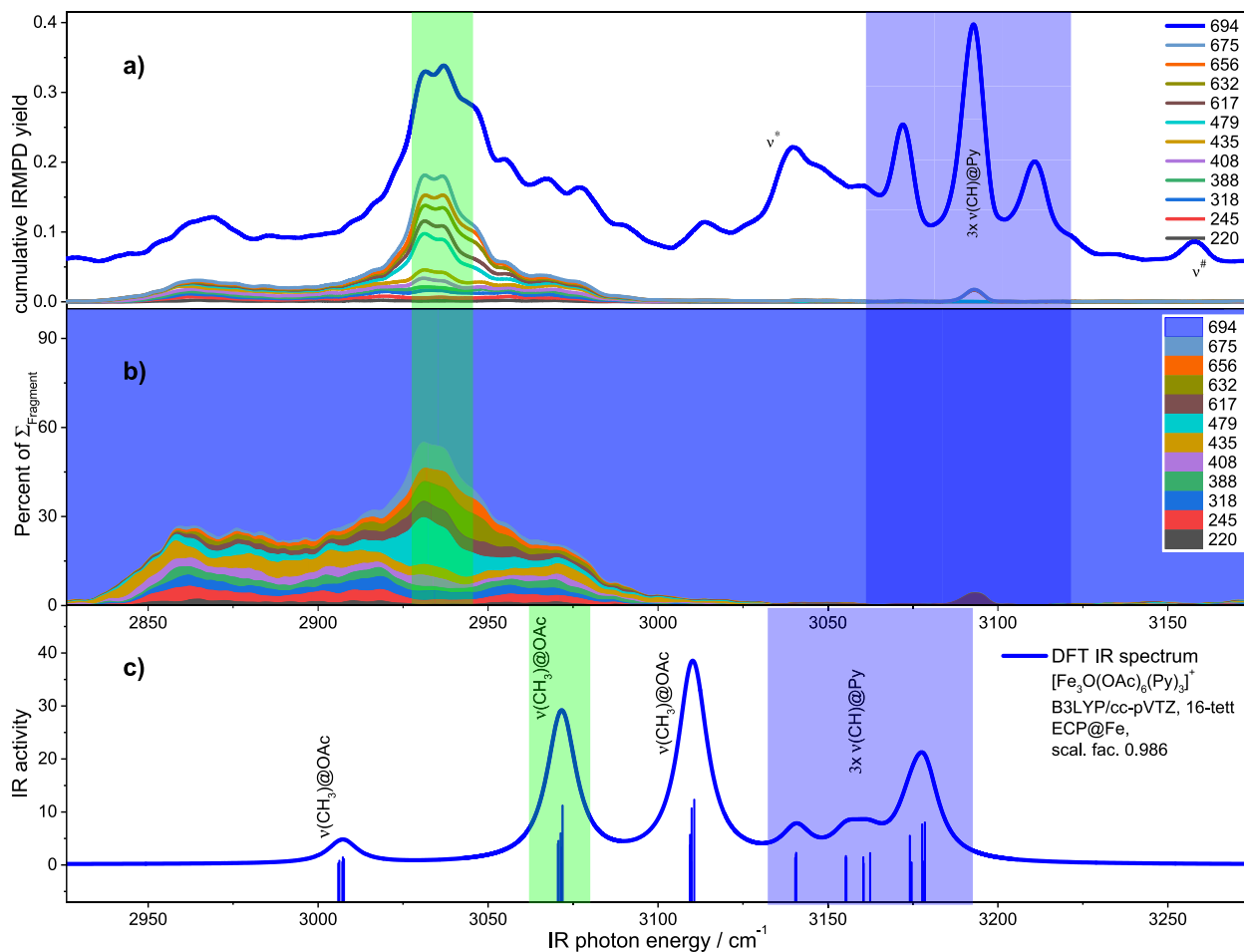


Figure 44 Mode specific fragmentation patterns in IRMPD spectrum of $[\text{Fe}_3\text{O}(\text{OAc})_6\text{Py}_3]^+$ for $\nu(\text{CH}_3)$ and $\nu(\text{Py-CH})$ bands respectively in the 2800 - 3200 cm^{-1} region. **a)** cumulative fragment yield; **b)** relative fragment yield normalized by total fragment yield, **c)** the simulated IR spectrum broadened with a gaussian of a FWHM of 10 cm^{-1} . The y range of graph c) has been adjusted for best match with a) and b), the same scaling factor 0.986 from the COO spectra is used. Adapted from **Abb. 21** in Jonas Schuchmann's bachelor thesis¹⁶. Shown fragment trace labels are given in m/z .

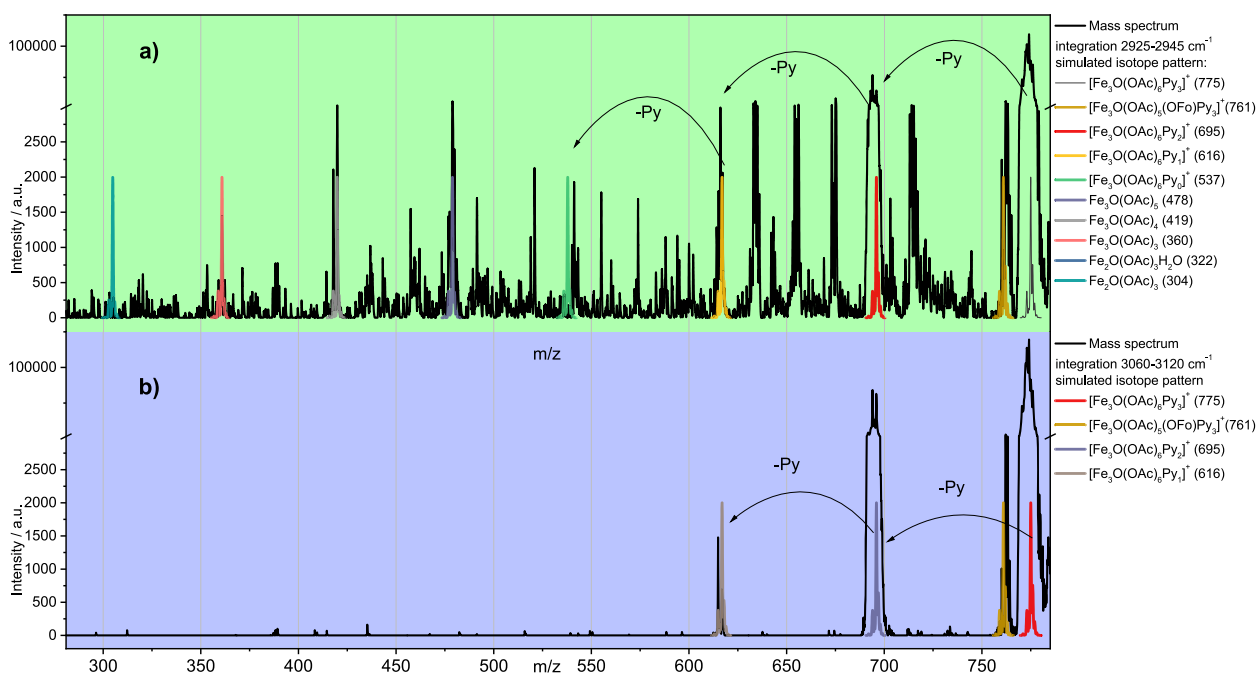


Figure 45 Mode specific fragmentation patterns for the CH_3 and Py-CH bands respectively. **a)** corresponds to the green area marked in **Figure 44**, **b)** to the blue area, respectively. Transparently superimposed are simulated mass spectra to identify the fragment mass peaks. Adapted from **Abb. 21** in Jonas Schuchmann's bachelor thesis¹⁶.

IR absorption by these bands seems to couple really well with the rest of the molecule, as the absorbed energy leads to the partial and total cleavage of many different bonds; that of axial pyridine ligands, bridging acetate ligands, and possibly core iron ions. This leads to the rearrangement of the molecule, as is witnessed by the many, often difficult to identify, fragments and post-fragmentation adducts observed in the mass spectrum of **Figure 45 a**).

Many of these mass peaks, especially a series of three peaks between the masses corresponding to the first and second pyridine loss at 695 m/z and 616 m/z , are separated by 18 masses; typical of post fragmentation water adducts. We take the presence of these bands as indication of a rearrangement of the molecular ion in a way that exposes many newly available coordination sites, possibly by breaking open the triangular metal core or the partial cleavage of the bridging acetate.

The identity of the broad band leading to this behavior is not clearly identified yet. The band between 2850 and 3000 cm^{-1} was originally tentatively assigned as the CH_3 stretch vibrations, as we motivate in our paper in chapter 10. Experiments both with deuterated acetate (**Figure 85**) and the spectra of the formate species in **Figure 63** suggest the presence of additional chromophors. To further narrow down the possibilities, we compare the iron acetate with the other Cr/Fe combinations, the formate bridged complexes, and with a series of isotope exchange experiments. This is discussed in chapter 7, especially section 7.2.

5.6 Isotope Exchange Effects of Iron Acetate Pyridine Complexes

When substituting some atoms in a molecule or ion by different isotopes of the same element, the mass change influences the reduced mass in the corresponding normal mode and therefore its vibrational frequency. This will lead to a shift in the observed band position. We conducted IRMPD studies of $[\text{Fe}_3\text{O}(\text{OAcD}_3)_6(\text{Py})_3]^+$, $[\text{Fe}_3\text{O}(\text{OAc})_6(\text{D}_5\text{Py})_3]^+$, and $[\text{Fe}_3\text{O}(\text{D}_3\text{OAc})_6(\text{D}_5\text{Py})_3]^+$ complexes as summarized in the supplement¹⁵ of our paper (cf. Fig. S18, section 10.2).

In the case of $[\text{Fe}_3\text{O}(\text{OAc})_6(\text{D}_5\text{Py})_3]^+$, as visible in **Figure 46**, the three sharp IRMPD bands at 3085, 3107, and 3124 cm^{-1} vanish from our observation windows and presumably shift below 2800 cm^{-1} . Meanwhile the broad bands at 2880, 2948, and 3050 cm^{-1} persist in $[\text{Fe}_3\text{O}(\text{OAc})_6(\text{D}_5\text{Py})_3]^+$, except for minor changes in their shape. This supports the assignment of these bands as sharp pyridine CH stretching bands. These bands display an interesting behavior upon successive substitution of normal pyridine ligands with perdeuterated **D₅ pyridine**.

5.6.1 Internal Vibrational Relaxation Processes Witnessed by Partial Isotopomerization

If we assume a perfect internal vibrational relaxation (IVR) process, it should lead to an equal energy distribution in an iron acetate complex with three axial pyridine ligands, energy absorbed by one pyridine ligand should also affect the dissociation of the others.

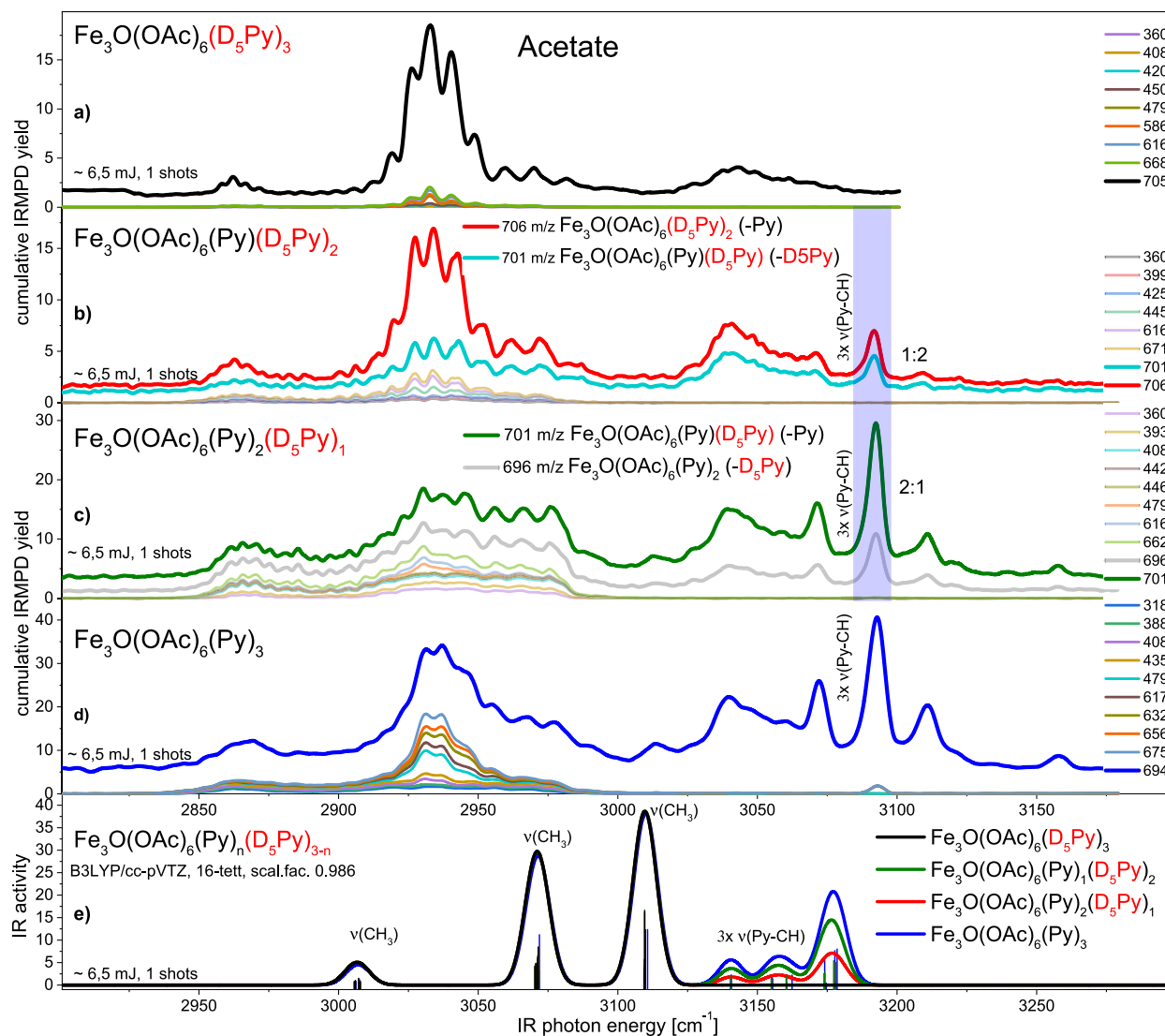


Figure 46 Mixed pyridine/ D_5 pyridine coordination in the CH region; $[\text{Fe}_3\text{O}(\text{OAc})_6(\text{Py})_n(\text{D}_5\text{Py})_{3-n}]^+$, $n = 0 - 3$. **a) - d)** cumulative IRMPD yield of the respective complex, cumulative fragment trace labels in m/z , **e)** simulated IR spectrum. The mass spectrum of the blue marked area is shown in **Figure 47**.

For equivalent pyridine ligands, that would be indistinguishable, as the chance for any single ligand to absorb an IR photon of the appropriate wavelength is equal and the fragmentation channels are identical to each other as well. This degeneracy of fragment mass and absorption wavelength breaks down with partial deuteration. The strength of isotope substitution here is the ability to not only shift the wavelength of IR absorption bands by changing the reduced mass of a vibrational mode, but also to mass label the fragments.

If we introduce a mix of deuterated and protonated pyridine ligands to a $[\text{M}_3\text{O}(\text{B})_6(\text{Py})_n(\text{D}_5\text{Py})_{3-n}]$ complex, both the parent and fragment masses change. Furthermore, the vibrational band position of the deuterated pyridine ligand, compared to the protonated pyridines, is shifted to lower wavenumbers. In the case of the $\nu(\text{Py-CH})$ stretch modes of non-deuterated pyridine, they shift from around $3090 - 3100 \text{ cm}^{-1}$ to below the observed region. This means we can observe an intensity shift of the total IRMPD yield by modifying the number of chromophors. In **Figure 46**, in the Py-CH bands in the region between 3090 and 3100 cm^{-1} , the predicted and observed IR activity scales with the number of undeuterated pyridine from $n = 0 - 3$, as they are the only chromophors absorbing

IR photons at that wavelength. This is reflected in the total IRMPD yield by the respective ion species, as seen in **Figure 46**.

We can also deduce by the fragment mass whether a deuterated or protonated pyridine was dissociated. For the series of $[M_3O(B)_6(Py)_n(D_5Py)_{3-n}]^+$, the two mixed ligand cases of $n = 1$ and $n = 2$ are especially interesting, as can be seen in the mass spectra shown in **Figure 47**. It is integrated from the blue area between 3090 to 3100 cm^{-1} in **Figure 46**, corresponding to the strongest observed $\nu(Py-CH)$ stretch mode of non-deuterated pyridine.

The mass difference for the cleavage of D_5Py is 5 u higher than that of the dissociation of ordinary pyridine, so the fragment is lighter by that mass. This is apparent in the first two fragmentation channels and the mass peaks in the corresponding mass spectrum (**Figure 47**).

We observe very clearly in **Figure 47** for $[Fe_3O(OAc)_6(Py)_n(D_5Py)_{3-n}]^+$ that the relative fragment channel yields mirror their statistical abundance in the parent ion of 1:2 for $n = 1$, and of 2:1 for $n = 2$. This points very clearly to an efficient energy transfer between all three axial pyridine ligands, irrespective of their isotopomerization. We appear to find a fully ergodic randomization of localized excitations prior to fragmentation. Otherwise a higher relative abundance of the heavier fragment would be expected, which is corresponding to non-deuterated pyridine loss.

Equivalent behavior is seen in **Figure 48** for the $\delta(D_5Py-CD)$ mode in $Fe_3O(FO)_6(D_5Py/Py)_3$. There, the band observed at about 1590 cm^{-1} appears with successive D_5 -pyridine substitution, with the total IRMPD yield increasing correspondingly with the number of deuterated chromophors.

The relative fragment channel yields show the same relative abundances as seen for the $\nu(Py-CH)$ modes. Energy is transferred from IR photons absorbed by deuterated pyridine to the normal pyridine, which does not absorb at the wavelength of about 1590 cm^{-1} . Good IVR and an efficient energy transfer seems possible, both from D_5 -pyridine to undeuterated pyridine ligands and vice versa.

Unfortunately, the series is incomplete for the equivalent acetate species in the CO region, as seen in **Figure 83** in the appendix. So far, we only have measured the $Py_2D_5Py_1$ case, but the expected 2:1 fragment yield is observed there as well. However, additional fragment channels complicate the situation further.

It would be interesting to extend this experiment to the mixed metal complexes, to see if the dissimilar metals have an influence on the efficiency of the IVR process.

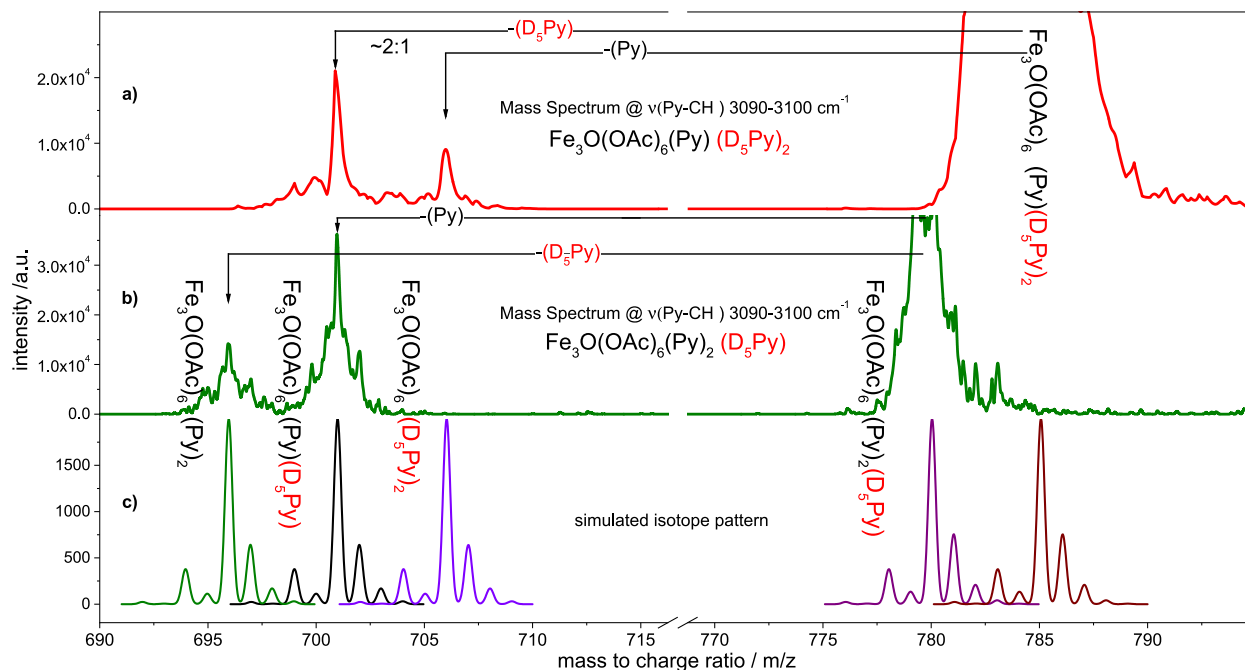


Figure 47 Mixed pyridine/ D_5 -pyridine coordination on $[\text{Fe}_3\text{O}(\text{OAc})_6(\text{Py})_n(\text{D}_5\text{Py})_{3-n}]^+$, $n = 1, 2$. **a)** fragmentation mass spectrum of the $\text{Py D}_5\text{Py}_2$ complex, **b)** fragmentation mass spectrum of the $\text{Py}_2 \text{D}_5\text{Py}$ complex and **c)** simulated isotope pattern for all relevant ions.

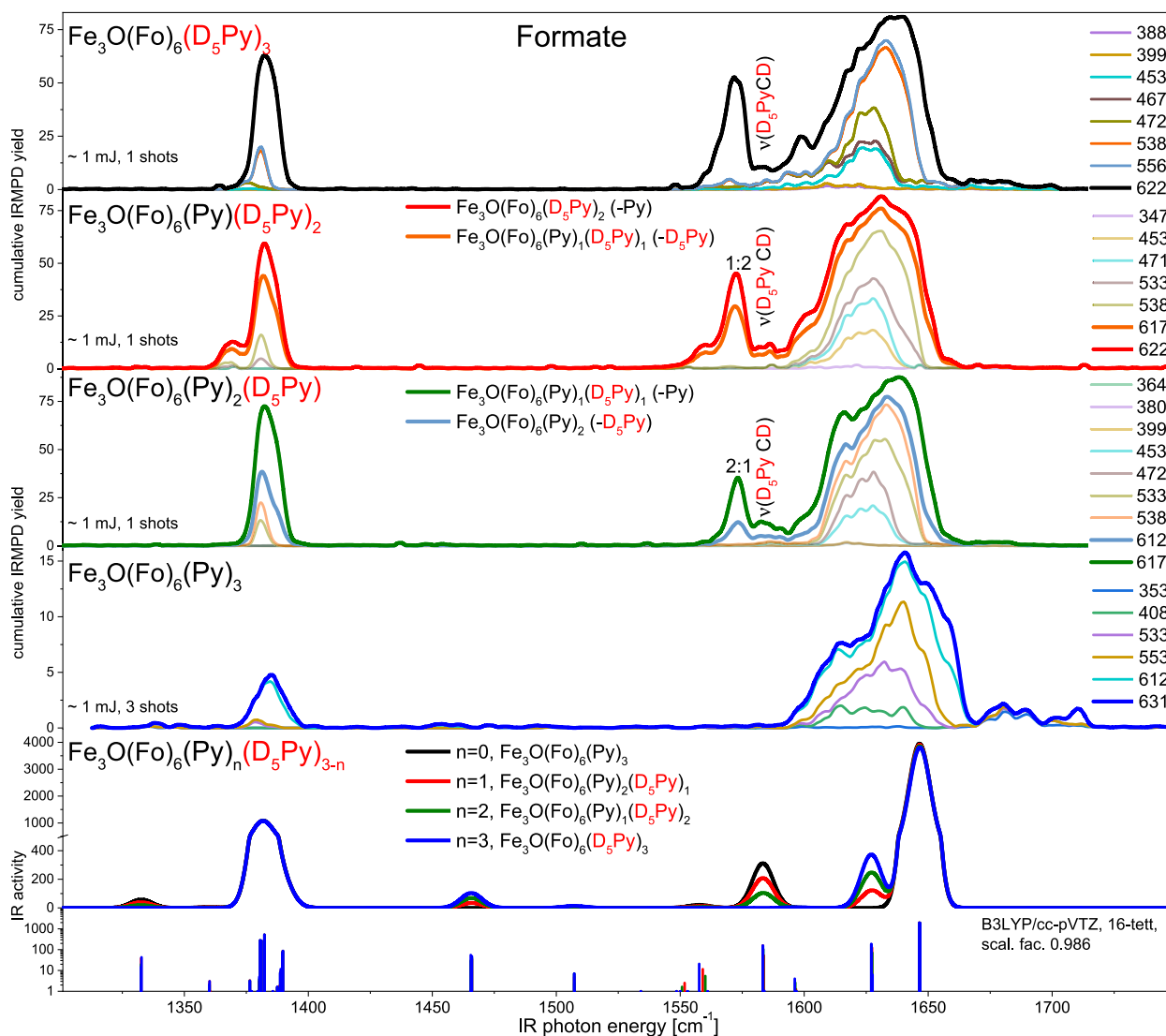


Figure 48 Mixed pyridine/ D_5 -pyridine coordination on formate bridged $[\text{Fe}_3\text{O}(\text{Fo})(\text{Py})_n(\text{D}_5\text{Py})_{3-n}]^+$, $n = 1, 2$ in the CO spectral region. The mass spectrum is not shown. Cumulative fragment trace labels in m/z .

5.7 References Chapter 5

1. Laurikėnas, A. *et al.* Formation peculiarities of iron (III) acetate: potential precursor for iron metal-organic frameworks (MOFs). *Lithuanian Journal of Physics* **56**, 35-41 (2016).
2. Weinland, R. & Holtmeier, H. Über Ferri-nickel- usw. -acetate und über ein sehr basisches kristallisiertes Ferriacetat. *Zeitschrift für anorganische Chemie* **173**, 49-62 (1928).
3. Weinland, R. & Gußmann, E. Über eine Acetato-Pyridin-Eisenbase und über ein sehr basisches, pyridinhaltiges Ferriacetat. *Berichte der deutschen chemischen Gesellschaft* **43**, 2144-2149 (1910).
4. Weinland, R. F. & Gussmann, E. Über Salze einer Hexaacetato-tripyridin-trichrombase. *Zeitschrift für anorganische Chemie* **67**, 167-182 (1910).
5. Weinland, R. F. & Beck, C. Über komplexe, pyridinhaltige Acetato-ferri-Basen. *Zeitschrift für anorganische Chemie* **80**, 402-447 (1913).
6. Weinland, R. & Gussmann, E. Über Salze einer Acetatoferribase und zweier Acetatochromiferribasen. III. *Berichte der deutschen chemischen Gesellschaft* **42**, 3881-3894 (1909).
7. Weinland, R. & Engel, L. Über pyridinhaltige Ferriformiate. (Nebst einem Anhang über ein Ferrichlorid=(bromid=) Formiat. *Archiv der Pharmazie* **264**, 33-45 (1926).
8. Johnson, M. K., Cannon, R. D. & Powell, D. B. Vibrational spectra of carboxylato complexes—IV. Mixed-metal and mixed-valence oxo-trinuclear complexes. *Spectrochimica Acta Part A: Molecular Spectroscopy* **38**, 307-315 (1982).
9. Clegg, W., Lam, O. M. & Straughan, B. P. Crystal Structure of [FeCr₂(μ₃-O)(CH₃COO)₆(H₂O)₃][FeCl₄]*2(CH₃)₂CO*CH₃O. *Inorganica Chimica Acta* **90**, 75-76 (1984).
10. Clegg, W., Mi Lam, O. & Straughan, B. P. Struktur eines neuen μ₃-Oxo-FeIII₂CrIII-Glycin-Komplexes. *Angewandte Chemie* **96**, 424-425 (1984).
11. Uemura, S., Spencer, A. & Wilkinson, G. μ₃-Oxotrimetal acetato-complexes of chromium, manganese, iron, cobalt, rhodium, and iridium. *J. Chem. Soc., Dalton Trans.* 2565-2571 (1973). doi:10.1039/DT9730002565
12. Earnshaw, A., Figgis, B. N. & Lewis, J. Chemistry of polynuclear compounds. Part VI. Magnetic properties of trimeric chromium and iron carboxylates. *Journal of the Chemical Society A: Inorganic, Physical, Theoretical* 1656 (1966). doi:10.1039/j19660001656
13. Weinland, R. F. & Gussmann, E. Über Ferriacetate und über die Essigsäurereaktion mit Eisenchlorid, sowie über die "basische Fällung." *Zeitschrift für anorganische Chemie* **66**, 157-168 (1910).
14. Lang, J. *et al.* Magnetostructural correlation in isolated trinuclear iron(III) oxo acetate complexes. *Physical Chemistry Chemical Physics* **20**, 16673-16685 (2018).
15. Lang, J. *et al.* Supporting Information to "Magnetostructural correlation in isolated trinuclear iron(III) oxo acetate complexes." *Phys. Chem. Chem. Phys.* **20**, 16673-16685 (2018).
16. Schuchmann, J. P. Modifikation von Analysemethoden für die differenzierte Interpretation von fragmentspezifischen IRMPD Spektren: Anwendung auf trinukleare oxo- zentrierte Eisenkomplexe. (TU Kaiserslautern, 2018).
17. Krüger, J. S. Regioselective fragmentation of trimeric iron and chromium carboxylates. (TU Kaiserslautern, 2018).
18. Daltonics, B. DataAnalysis Help. **Version 4.**
19. Maître, P. *et al.* Ultrasensitive spectroscopy of ionic reactive intermediates in the gas phase performed with the first coupling of an IR FEL with an FTICR-MS. *Nuclear Instruments and Methods in Physics Research Section A: Accelerators, Spectrometers, Detectors and Associated Equipment* **507**, 541-546 (2003).
20. MacAleese, L. & Maître, P. Infrared spectroscopy of organometallic ions in the gas phase: From model to real world complexes. *Mass Spectrometry Reviews* **26**, 583-605 (2007).
21. Lemaire, J. *et al.* Gas Phase Infrared Spectroscopy of Selectively Prepared Ions. *Physical Review Letters* **89**, 273002 (2002).
22. Surya, P. I., Roth, L. M., Ranatunga, D. R. A. & Freiser, B. S. Infrared Multiphoton Dissociation of Transition Metal Containing Ions: MC_nH_{2n} + (M=Fe, Co, Ni; n=2-5). *Journal of the American Chemical Society* **118**, 1118-1125 (1996).
23. Polfer, N. C. *et al.* Differentiation of Isomers by Wavelength-Tunable Infrared Multiple-Photon Dissociation-Mass Spectrometry: Application to Glucose-Containing Disaccharides. *Analytical Chemistry* **78**, 670-679 (2006).

24. Oomens, J., Sartakov, B. G., Meijer, G. & von Helden, G. Gas-phase infrared multiple photon dissociation spectroscopy of mass-selected molecular ions. *International Journal of Mass Spectrometry* **254**, 1-19 (2006).
25. Oomens, J., Moore, D. T., Meijer, G. & Helden, G. Von. Infrared multiple photon dynamics and spectroscopy of cationic PABA and its dehydroxylated fragment ion. *Physical Chemistry Chemical Physics* **6**, 710 (2004).
26. Brodbelt, J. S. & Wilson, J. J. Infrared multiphoton dissociation in quadrupole ion traps. *Mass Spectrometry Reviews* **28**, 390-424 (2009).
27. Pankewitz, T., Lagutschenkov, A., Niedner-Schatteburg, G., Xantheas, S. S. & Lee, Y. T. Infrared spectrum of $\text{NH}_4^+(\text{H}_2\text{O})$: Evidence for mode specific fragmentation. *Journal of Chemical Physics* **126**, 074307 (2007).

6 Systematic Study of the Carboxylate Stretch Modes in Chromium and Iron Complexes

As discussed in section 3.4, there have been quite a few studies on the effect of different metals on the IR spectra, and by proxy the structure of different trimetallic oxo-centered carboxylates. A systematic variation of both the number of axial ligands and the central metal ions by themselves have only been done in some select studies, and never both in a systematic comparative fashion. As examples for axial ligand variation, our groups efforts by Johannes Lang et al. on Iron¹ and Cobalt² acetate complexes should be highlighted. For systematic metal variations, especially the Cr_nFe_{3-n}O case covered here, there are classical papers by Cannon et al.³ and an IR study on the Cr_nFe_{3-n}O(OAc)₆(H₂O)₃, n = 0 - 3 complexes with axial water ligands by Zhang et al.^{4,5}. Either of these are limited in the covered wavelengths, in showing both $\nu(\text{CO})$ and $\nu(\text{CH})$ vibrations, the inherent limitations of non gas-phase methods, and the available theoretical methods at the time to do calculations of sufficient quality. Both Cannon and Zhang, however, cover the important skeletal vibrations in the area 100 - 900 cm⁻¹, which is not accessible by the range of our laser system, but might be considered in future work (see section 9.2.4). Additionally Blake et al.⁶⁻⁸ worked on the optical spectra of the heterotrimetallic complexes, which could be of interest in future gas phase studies.

6.1 Handling of the Accompanying Booklet

For the convenience of the reader to follow the arguments in this chapter, a fold out booklet is included with this thesis. Hopefully, this booklet helps with the numerous cross references necessary. It is intended to aid in showing the different trends and connections that emerge from systematic comparisons; the influence of exchanging the transition metal, the bridging ligand, and the number of terminal pyridine ligands; in the iron-, chromium- as well as the acetate- and formate complexes.

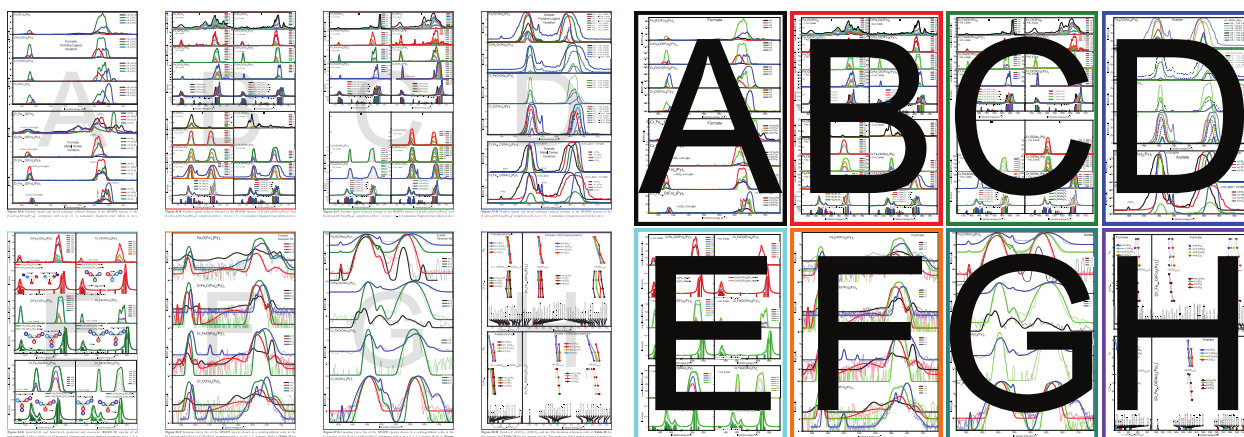


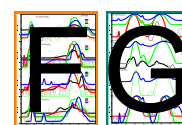
Figure 49 The front (first row) and back (second row) sides of the accompanying booklet, both as the original (left) in miniature, and their respective thumbnail (right). They are comprised of selected graphs showing the total (A,D) and cumulative (B,C) IRMPD yields of all measured acetate and formate species in the CO region, all species able to exhibit hom/het L/H isomerism (E), a semilogarithmic summary of the gaussian fits of the spectra (F,G), and the extracted peak positions and their trends (H).

The graphs themselves are still included in this thesis. In the booklet, they can be viewed side by side and next to the text, as needed. They are color coded and marked by transparent gray letters in their backgrounds; for easier visual recognition of both the graph and the corresponding thumbnail. This gives the advantage to the reader, so they can easily compare the referenced spectra while following along with the argument given in the text. They can also be arranged in different combinations, by folding the booklet in suitable ways. Throughout the text we refer to these graphs not only by their number, but also by including their thumbnail in the margin. The eight chosen graphs are a handpicked subset of the full range of spectra recorded, the full range of which is given in the appendix, section 11.

The graphs in the booklet and in the following section are optimized to show the relative differences of the IRMPD spectra upon ligand or metal variation. This is done by either plotting the total IRMPD yield of a ligand- or metal variation series on top of each other, or by stacking a series of cumulative IRMPD plots in one column. These combinations of plots hopefully help the reader to follow the behavior of the spectra, as we can see important details and trends both in the band shifts of the total IRMPD yield, as well as in the specific fragment patterns; which can differ with each single band or with metal or ligand variation.

6.2 Ligand and Metal Induced Effects in the COO Stretch Modes of Homo- and Heterometallic Chromium and Iron Carboxylate Complexes with Pyridine

The shifts and band splits that are seen in the symmetric and asymmetric carboxylate vibrations of the iron acetate (as discussed in section 5.4.2) upon successive pyridine coordination at the axial binding sites can also be measured for the acetate and formate complexes of iron, chromium, and chromium/iron mixed metal complexes. The trends of these shifts and splits are quantified and discussed in detail in section 6.4., based on a series of gaussian fits shown in **Figure 56 F** and **Figure 57 G**.



We also give a quick recapitulation (in section 6.2.2.1) for the results on iron acetate; which has been discussed in chapter 5, our publication¹ on iron acetate (chapter 10), and the supporting information⁹ for that paper (section 10.2). For the bands in the spectral region from 1000 - 2000 cm^{-1} (referenced here as the CO spectral region), we agree with the assignments given there. In contrast, in the spectral region 2500 - 3500 cm^{-1} (referenced here as the CH spectral region), we believe that by using fragment specific IRMPD, additional information given by the formate species, as well as by further deuteration experiments, we can elaborate on the given assignment. This will be done in chapter 7. Therefore, this section focuses on the quantitative discussion of the nature of the observed bands and their changes according to the ligand and metal variations shown.

Several of the early measurements were done together with lab student Kevin Weffling.

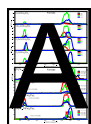
6.2.1 Formate Bridged Chromium and Iron Complexes

The simplest carboxylate bidentate bridging ligand possible is formate. It is a stronger and stiffer ligand than other carboxylates. Even stronger are only fluoro-formate and maybe other halogen analogs, although only data on the sodiumfluoroformate¹⁰ and the free anion¹¹ is known. On the other hand, this leads to a slight increase in the size of the metal triangle as compared to acetate. This is both seen in crystal structures of basic formate complexes¹² and the calculated structure trends discussed in section 4.4, especially in **Figure 27**. Formate also leads to higher band splitting $\Delta\nu$ and sharper bands, which hints to less conformational flexibility in the observed species.

As proven by the behavior exhibited in the CH spectral region (discussed in chapter 7) and in the free anion¹³, formate is known for strong anharmonic behavior¹⁴ (introduced in chapter 3). Especially for the bare complexes; knowing those anharmonic contributions can help to understand the behavior of the spectra. Compared to the acetate spectra from section 6.2.2, formate bands are less strong, narrower, and have a more discernable fine structure. This aids in an improved correlation of the observed spectra with the DFT simulations. In section 6.3, we will try to use the information from the spectra, the CID measurement of section 5.3, and the aforementioned DFT simulations of chapter 4, to assign the hom/het H/L regio-isomers (introduced in section 1.2.1) we expect to observe.

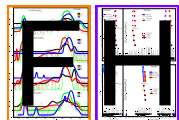
6.2.1.1 Tri Pyridine Coordinated Formate Complex Spectra

The best example to identify the types of bands in the formate spectra in the 1000 - 2000 cm^{-1} spectral

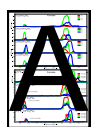


region is the Cr_3 formate with three axial pyridine ligands. We see it as the blue line in **Figure 50 A**, bottom graph. It has the advantage that the $\Delta\nu = \nu(\text{COO})_{\text{as}} - \nu(\text{COO})_{\text{s}}$ band split is especially large and the $\delta(\text{Py-CH})$ is therefore clearly separated from the $\nu(\text{COO})_{\text{as}}$ band. It

can be positively identified as the $\delta(\text{Py-CH})$ band by replacing the pyridine with perdeuterated pyridine. This is shown in the appendix in **Figure 92**. There the pyridine mode at 1610 cm^{-1} is the only visible band to shift to the red. The other two bands in this spectral region are clearly the formate carboxylate stretch modes. The heterometallic species of Cr_2Fe or CrFe_2 are especially interesting, because they show the specific differences of the different binding motifs bidentate formate ligands can have in a heterotrimetallic complex. The possibilities are bridging positions of the formate between the Cr-Cr, Fe-Cr, or Fe-Fe metal pair combinations. It therefore makes sense that we can see three overall bands in the two mixed metal species, with CrFe_2 in red and Cr_2Fe in green. The specific



trends will be quantified and discussed in chapter 6.4, **Figure 58 H** and are based on a series of gaussian fits of the respective bands as shown in **Figure 58 F**.



There are also very faint additional bands in the Cr_3 and Cr_2Fe spectra that are too weak to be visible in the linear plot of **Figure 50 A**, but become more apparent and rise above the noise floor in the semilogarithmic plot of **Figure 56 F**. The bands in question are seen, one at $\sim 1450 \text{ cm}^{-1}$, for both Cr_3 and Cr_2Fe , and an even fainter band in the Cr_2Fe case at almost 1500 cm^{-1} .

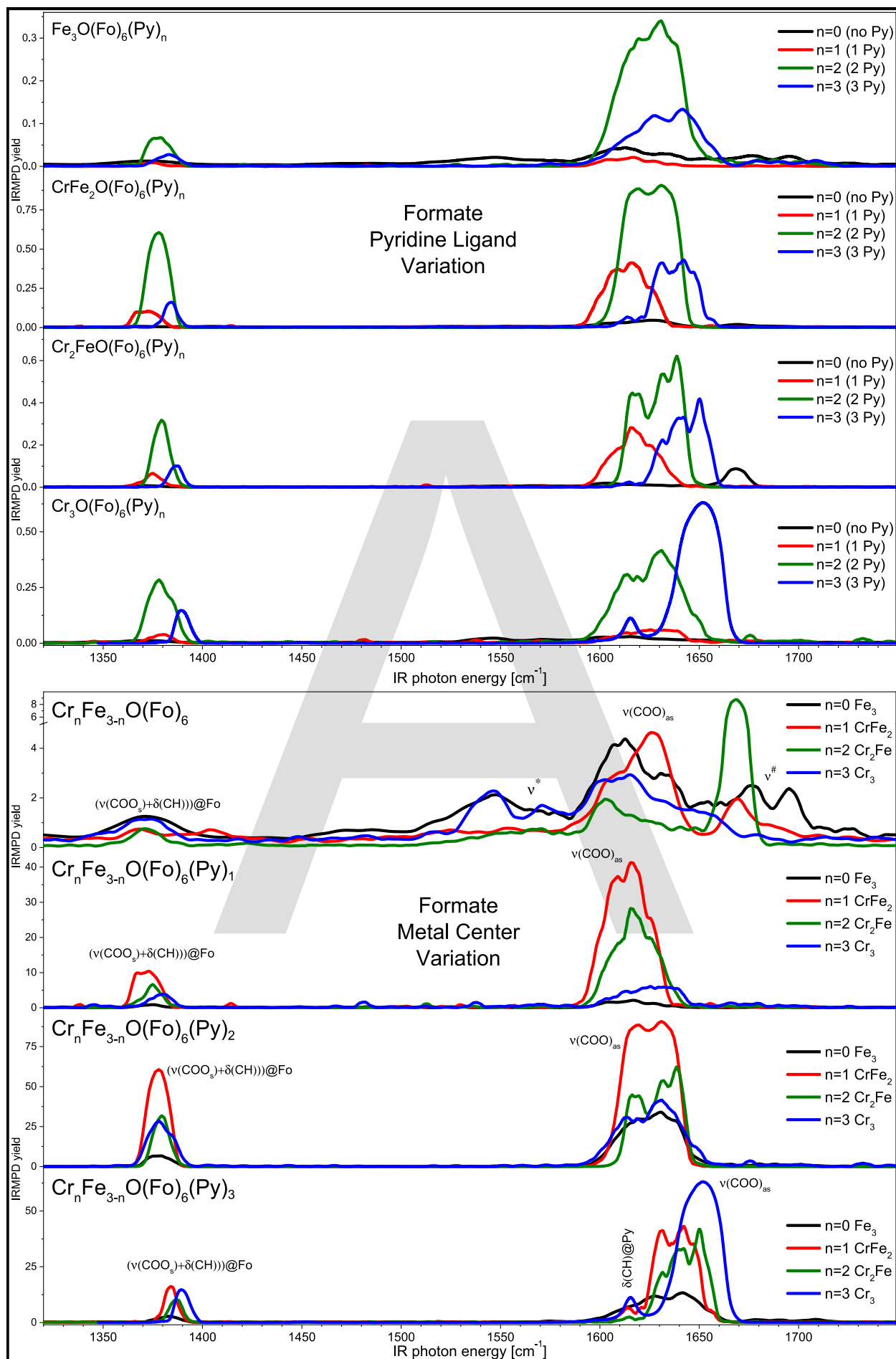
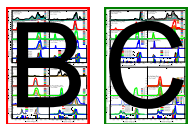


Figure 50 A Pyridine ligand and metal exchange induced changes in the IRMPD spectrum of the $[\text{Cr}_n\text{Fe}_{3-n}\text{O}(\text{Fo})_6(\text{Py})_m]^+$ complexes with $n, m = 0 - 3$, cumulative fragment trace labels in m/z .



These two weak bands are matching up with the expected positions of two $\delta(\text{Py-CH})$ modes, as can be seen in the simulated spectra shown in the fifth row of **Figure 51 B** and **Figure 52 C**. These bands are not observed in the other spectra.

CH bend modes are often not seen in IRMPD spectra, similar to the CH_3 bend modes in the acetate spectra. This phenomenon of dark modes is discussed in section 5.4.2 for the iron acetate. However, both bands are visible in the ScCrFe formate spectra (section 8.2, **Figure 67**), although only at the highest possible laser shot count of 9 shots. This is triple the standard count, giving us the best possible chance at making faint bands visible, as can be seen when comparing the 9 shot example of **Figure 67** to the series of 9, 3, and 1 laser shot spectra of the same ion in **Figure 105**, in the appendix.

6.2.1.2 Bi and Mono Pyridine Coordinated Formate Complex Spectra

The four heterometallic bi and mono pyridine coordinated formate complexes, shown in green and red respectively, are discussed in section 6.3, **Figure 54 E**. There, the observed spectra are correlated with the respective hom/het L/H isomers and their predicted IR spectra. Compared to the homometallic iron and chromium formates, they seem to be more IRMPD active. This might coincide with the distorted M_3O core described in section 4.4, positively influencing energy transfer efficiency into specific fragmentation modes.

6.2.1.3 Bare Formate Complex Spectra

The bare formate spectra are displaying the most deviance from the simulated spectra. They are best seen in **Figure 50 A** and **Figure 56 F**. It is important to note that the ion yield of the parent complex and the IRMPD fragmentation efficiency is very low due to their high stability. It is experimentally challenging to record spectra of such unsaturated complexes, compounded by their tendency to attach background water vapor always present in the ion trap mass spectrometer. Therefore, it cannot be excluded that bands are behaving differently than expected due to these experimental difficulties.

As can be seen in the CID spectra of the mono pyridine coordinated acetates and formates in section 5.3 and in **Figure 73**, the undersaturated complexes often show the most unexpected behavior. The unadulterated properties of the metal core are most dominant here. In section 4.7 and 6.5, when applying the DMBC formalism, they also display the biggest three body terms, a measure for cooperativity.

Therefore, it will be important to also repeat the experiments shown here in a mass spectrometer with a better vacuum environment, such as an FT-ICR instrument. This should make it possible to improve the ion yield and reduce interferences. Additionally, our Cryo-setup allows measurements at reduced temperatures, that can help to improve the spectral resolution.

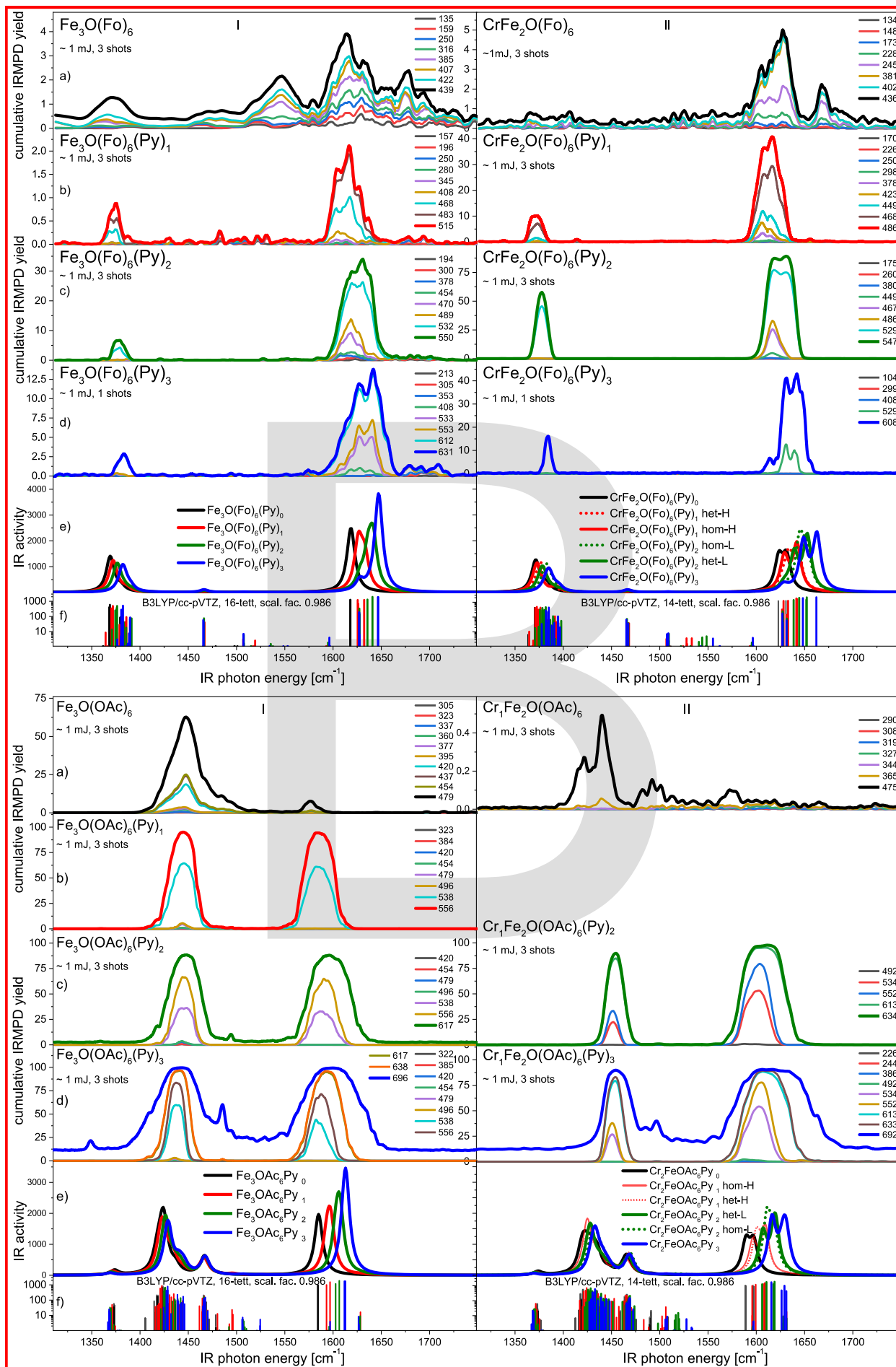


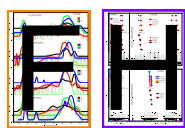
Figure 51 B Pyridine ligand induced changes in the IRMPD spectrum of $[\text{Cr}_n\text{Fe}_{3-n}\text{O}(\text{Fo})_6(\text{Py})_m]^+$ and $[\text{Cr}_n\text{Fe}_{3-n}\text{O}(\text{OAc})_6(\text{Py})_m]^+$ complexes with $n = 0, 1$, $m = 0 - 3$. Cumulative fragment trace labels in m/z.

Furthermore, utilizing a second infrared laser can help to improve fragmentation efficiency, often in a selective way, by adding additional energy into specific modes associated with suitable chromophors. This is discussed further in the outlook in section 9.2.2.

In the recorded spectra, two groups of vibrational modes are observed that are not expected based on the simulated DFT spectra. These are denoted in **Figure 50 A** with ν^* and $\nu^\#$. Bands in the ν^* range are not completely new in the IR of formate complexes. As Cannon et al.¹⁵ conclude, the weak band doublet at approximately 1560 and 1550 cm^{-1} , denoted with ν' in their paper, is frequently observed in the spectra of trinuclear basic formates. They assign them as a Fermi resonance-enhanced overtone of $\delta(\text{OCO})$.

As we still lack the IR spectra of isolated basic formates in the spectral region of 100 - 1000 cm^{-1} , it is difficult to independently confirm that conclusion, as we are not able to observe the fundamentals associated with these suggested overtones directly, due to the technical limitations of our laser system.

Based on the broad literature review of different formate spectra in section 3.4 and the observed range for the different normal modes associated with bridging formate ions, we concur that Cannon's assignment is a reasonable candidate for the first band group. However, it does not account for the second group of bands denoted with $\nu^\#$.



As evident from **Figure 56 F** and the trends of the band positions shown in **Figure 58 H**, the mixed metal complexes, incidentally those with the strongest observed $\nu^\#$ bands, simultaneously stand out by slightly red-shifted position of the $\nu(\text{COO})_{\text{as}}$ bands and a blue shift of the $\nu^\#$ mode relative to the common trend. This slight shift of adjacent bands and strong changes in their relative band strengths is a telltale sign for Fermi resonances.

We can only make guesses at the nature of the band in apparent Fermi resonance with at least some of the $\nu(\text{COO})_{\text{as}}$ modes. The asymmetric carboxylate modes here are slightly split, as witnessed by the bi- and mono pyridine complexes in section 6.2.1.2, due to the symmetry breaking caused by the presence of the heterometal. This shifting of bands only happens for modes involving formates bonding to the heterometal, exaggerating the degeneracy breaking in this subgroup of carboxylate modes. Since Fermi resonances are highly sensitive to the exact nature and position of the interacting bands as shown in section 3.2, **Figure 18**, it is not difficult to hypothesize that only some of the observed bands are of the appropriate band position and symmetry to effectively be in Fermi resonance. As to the nature of the second component participating in the Fermi resonance, it is around 100 cm^{-1} above the $\nu^\#$ band.

At around 150 cm^{-1} , the first skeletal vibrations, involving the M_3O core of the fully coordinated formates, are observed¹⁶, additional $\delta(\text{OMO})$ modes are seen at around 230 cm^{-1} and 283 cm^{-1} , the latter could perhaps create a combination band with the symmetric carboxylate stretch vibration.

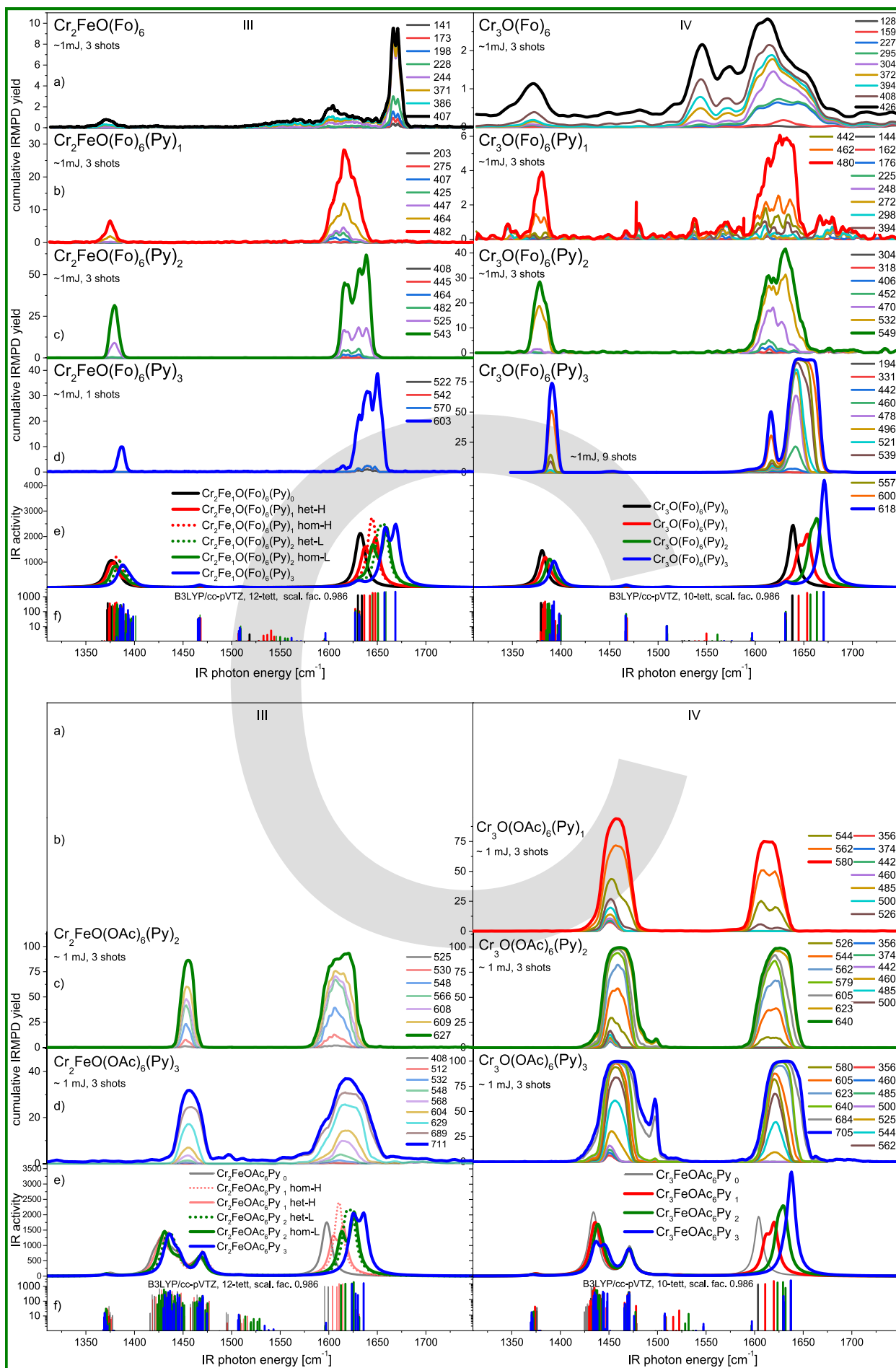


Figure 52 C Pyridine ligand induced changes in the IRMPD spectra of $[\text{Cr}_n\text{Fe}_{3-n}\text{O}(\text{Fo})_6(\text{Py})_m]^+$ and $[\text{Cr}_n\text{Fe}_{3-n}\text{O}(\text{OAc})_6(\text{Py})_m]^+$ complexes with $n = 2$ and 3 , $m = 0 - 3$, cumulative fragment trace labels in m/z .

Involving a skeletal mode into this set of interacting bands would fit into the observation of similar core fragmentation patterns in the cumulative fragmentation yields, plotted in **Figure 51 B** and **Figure 52 C**. In any case, this assignment is only conjecture at this point and would necessitate additional experiments; similar to the combination bands observed in the CH stretch modes, as discussed in section 7.1.

In upcoming two-color experiments, we would have the option to pump IR energy into one of the hypothesized components of the combination band, and observe the probe response of the band. It would be interesting to see if we can observe an increase or decrease in the strength of the combination band when scanning the probe laser over its wavelength.

An alternative explanation, in line with the arguments from Palacios et al.¹⁷, would be partial dissociation of the bare complex. This changes both the environment of the formates coordinating to a specific metal center and introduces a new, easily dissociated chromophore of the $\nu(\text{C}=\text{O})$ of a monodentate formate without water bonding to it, which would be expected at or above 1700 cm^{-1} , as shown in section 8.1.

6.2.2 Acetate Bridged Complexes

It gets consecutively more difficult to measure the bare or undercoordinated complexes with successive chromium count in our acetate species. This explains the lack of those spectra in **Figure 51 B** and **Figure 52 C**. Those complexes are very eager to bind to any trace water molecules still present in the quadrupole ion trap, especially at the prolonged trapping times necessary for achieving sufficient fragmentation efficiencies, by using several laser pulses (section 5.4.4). This water coordination can influence the resulting IRMPD spectrum quite strongly, as is shown for mixed pyridine/water coordination in **Figure 66**. We observe both blue and red shifts with growing water count. We are proposing two explanations to that in section 8.1. In summary, the preferred explanation is partial hydrolysis of the carboxylate bridges. This explains why we struggled to measure IRMPD spectra of sufficient quality for the bare and single pyridine coordinated hetero- and homometallic chromium complexes. Therefore, spectra of all four metal combinations were obtained only for the bi- and tri pyridine coordinated complexes.

A remedy for that is discussed in the outlook. There we suggest measurements in our FT-ICR instrument, at much improved vacuum pressures and at potentially colder temperatures, which reduces the partial pressure of water and improves spectral resolution. See section 9.2.2.1 for more details on that.

6.2.2.1 Recapitulation of the Iron Acetate Spectra

To summarize, the iron acetate spectra (**Figure 52 C**, bottom left; **Figure 42**) are a good archetypical example on the bands we generally observe in the CO spectral region. As is typical for the carboxylate

spectra, shown in chapter 3, they are dominated by the two CO bands; the symmetric COO stretch vibration at around 1400 cm^{-1} , and the asymmetric COO stretch at around 1600 cm^{-1} . Additional bands appear with additional chromophors introduced either by the carboxylate bridging ligand, e.g. the CH or CH_3 bend modes of formate or acetate, or the CH bend modes of axial pyridine ligands, which are coincidental with the asymmetric COO mode of the acetates.

Those additional chromophors don't show a strong wavelength dependence on the presence of other ligands. Often, they are relatively weak and depend on the complex to have both a high number of chromophors, and relatively low energy fragmentation pathways available. This is usually the single cleavage of the first axial pyridine. On the other hand, the carboxylate vibrations show a very strong absorption and couple to a number of fragmentation channels. Sufficient laser fluence can cause successive pyridine cleavage; in extreme cases even the dissociation of bridging ligands.

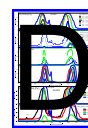
Often the IRMPD spectrum of those bands reaches saturation, with complete fragmentation of the parent mass at the available laser fluence. This usually occurs when tuning the system to maximum fragmentation to best detect weak bands. As discussed in our paper¹ reprinted in chapter 10, the spectra follow a trend of increased band splitting $\Delta\nu$ upon increased pyridine coordination.

In chapter 5, we observe that the fragmentation channel appearance wavelengths approximate the IR spectrum of the respective fragment species, albeit with a slightly higher $\Delta\nu$, shifted towards the band position of the respective parent ion.

This strongly hints at a successive fragmentation mechanism, with leftover energy and incomplete annealing of the complex structure to a thermal equilibrium in between each consecutive fragmentation step.

6.2.2.2 Tri Pyridine Coordinated Acetate Complex Spectra

The total IRMPD yield of all tri- pyridine coordinated acetate species can be found in **Figure 53 D**, bottom graph. Comparing the homometallic cases Fe_3 to Cr_3 , we see a number of changes in the spectrum. The considerable auto fragmentation of iron acetate (black) and also the CrFe_2 (red) case is almost nonexistent for chromium acetate (blue) and Cr_2Fe (green).

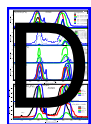


The asymmetric $\nu(\text{COO})_{\text{as}}$ vibration band of CrFe_2 is very wide, hinting at a very strong bond of the single chromium metal center on the acetate bridging ligands. There are two types of distinct bridging ligand binding motifs of acetate in this complex: one with two ligands exclusively bonding to iron, and the other with four ligands bonding to both a chromium and iron center. This asymmetric binding motif seems to couple strongly to the fragmentation channels available.

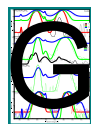
The symmetric $\delta(\text{CH}_3)$ bend vibration at around 1350 cm^{-1} is barely visible in the Cr_3 complex, probably due to the stronger bonds and more compact nature of the complex, as is apparent from the geometry trends discussed in section 4.5 and CID measurements in chapter 5.3.

The calculations and literature spectra also locate another asymmetric $\delta(\text{CH}_3)$ bend vibration at around 1425 cm^{-1} . However, this mode is not observed, neither at higher laser power nor at low power, as can be seen in the appendix in **Figure 87 ff**. This mode seems to have very bad energy transfer to the available fragmentation channels. Even if it were weakly active in the IRMPD spectrum by itself, at the necessary higher laser power it would be overlapped by the broad symmetric carboxylate stretch mode adjacent to it. We perhaps see it in **Figure 51 B**, bottom left graph, as a weak shoulder or asymmetry for the iron acetate at around 1400 cm^{-1} . If present at all, it only impacts the first fragment trace; single pyridine cleavage. Just like the other CH bend modes, it does not register on successive fragmentation traces.

On the other hand, the asymmetric $\delta(\text{CH}_3)$ bend vibration at around 1490 cm^{-1} in the chromium acetate is even more pronounced and is blue-shifted by about 5 cm^{-1} , as compared to the iron acetate. This blue shift and slight increase in band activity is also seen for the heterometallic case in the spectrum of CrFe_2 and Cr_2Fe , although the general fragmentation efficiency is relatively low there.

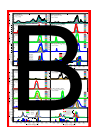


In the CrFe_2 trace (red) in **Figure 53 D**, bottom graph, we might even be able to see two distinct $\delta(\text{CH}_3)_{\text{as}}$ bands, but the left band is hard to differentiate from residual fragmentation in between the two adjacent high intensity bands. In the gaussian fits shown in **Figure 57 G**, we did not explicitly use a separate gaussian to fit that band. The results of the fits are listed in **Table 31** in the appendix.

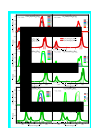


Considering the cumulative IRMPD yields, chromium acetate (**Figure 52 C**, bottom right) shows a stronger CO band splitting and some general blue shift, but it very much mirrors the behavior of the homometallic iron species. Again, the Py_3 species shows successive pyridine cleavage, with little band shifting in the symmetric CO band at about 1460 cm^{-1} and considerable red shift for the successive fragment species, albeit with slightly increased water coordination compared to the iron case.

6.2.2.3 Bi- and Mono- Pyridine Coordinated Acetate Complex Spectra



The bi-pyridine series in **Figure 53 B**, in the second graph from the bottom, is similar to the tri-pyridine case at a first glance, but reveals a few key differences at a closer look. It is the only acetate complex series where the hom/het L isomer distinction in the heterometallic species (as defined in section 1.2.1) has to be considered. This will be discussed specifically in tandem with the formate cases in section 6.3. Unfortunately, the band splitting differences in the asymmetric $\nu(\text{COO})_{\text{as}}$ vibration modes predicted by our calculations (detailed in **Figure 54 E**) are not distinct enough to easily discern between the different isomers, at least at the conditions of our experiment.



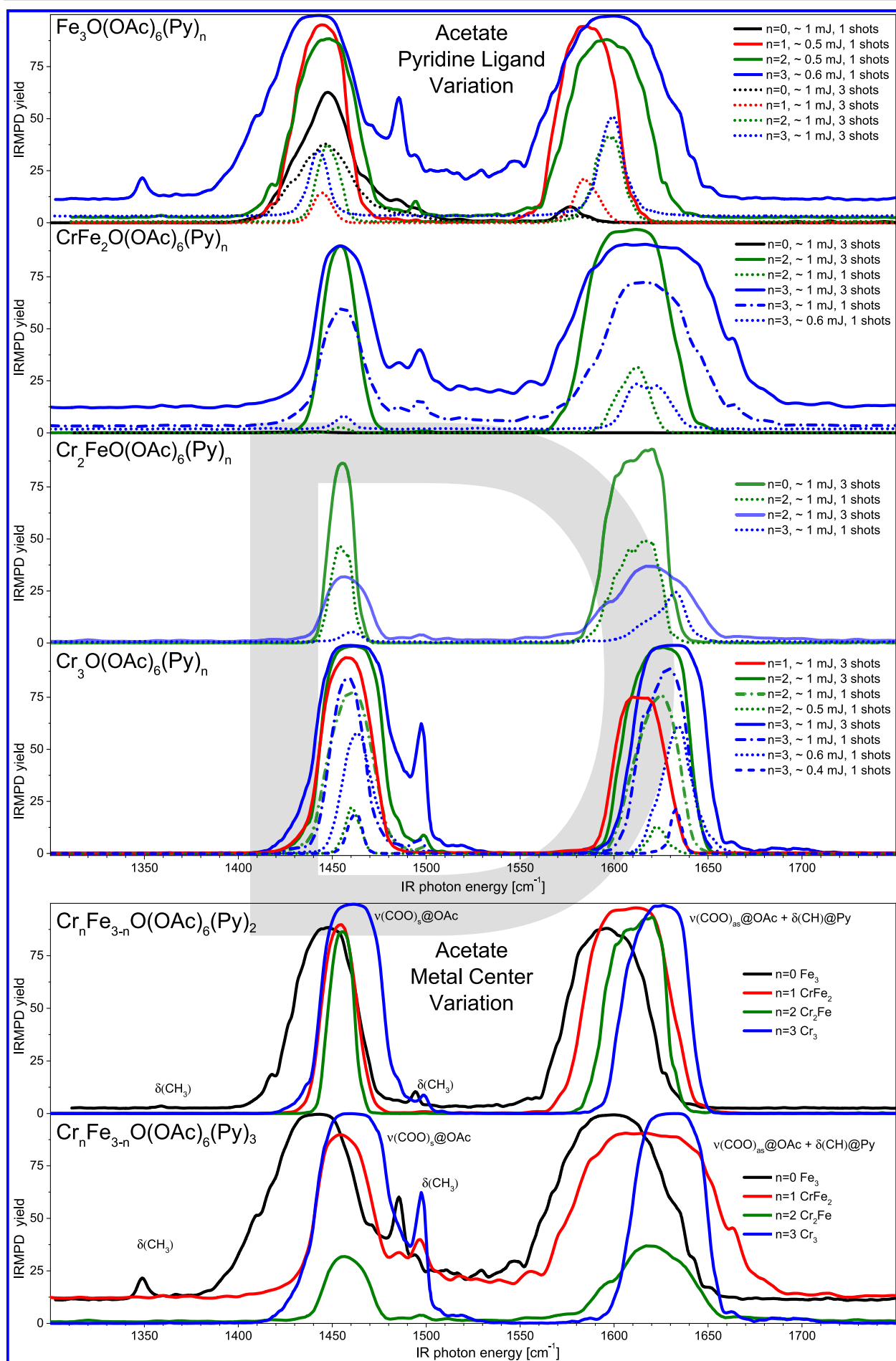
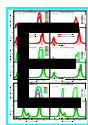


Figure 53 D Pyridine ligand and metal exchange induced changes in the IRMPD spectra of the $[\text{Cr}_n\text{Fe}_{3-n}\text{O}(\text{OAc})_6(\text{Py})_m]^+$ complexes with $n, m = 0 - 3$, cumulative fragment trace labels in m/z .

However, a few general observations can still be made. The symmetric $\nu(\text{COO}_s)$ vibration modes for the heterometallic species are surprisingly sharp and even less shifted in respect to each other than usual. This might be the case because of the combination of two factors. The theoretically more favorable isomer for both species would be the one with the highest number of pyridine ligands bound to a chromium metal center, hence leading to the het-L case for CrFe_2 and hom-L for Cr_2Fe as shown in **Figure 54 E**.



Contrary to that, a number of observations all hint at a slightly more complicated picture: the surprisingly similar CID dissociation energy, the trends in the band shape with longer trap times and multiple laser shots (as seen in **Figure 76** and **Figure 77**), and the band position similarity. The energetically disfavored isomers still seem to be populated as well, at least at longer trap times and under multiple laser shot conditions. It might be assumed, that for the less stiff and weaker bound acetate complexes, an interconversion between isomers might be possible. In CID experiments not included in this thesis, we have seen tantalizing hints at possible interconversions, but the results have not been easy to interpret and would need further efforts to clear up.

If we assume the presence of iron coordinated pyridine species for both heterometallic acetates, with pyridine being most readily dissociated from that metal center, the very similar IRMPD spectrum could be explained. In both cases, the most active chromophore would be an acetate ligand bridging an iron and chromium metal center. The fragmentation channel activated by that would be the dissociation of the pyridine from the neighboring iron center. This would also match the similar $\nu(\text{COO})_s$ band positions for the hom-L case for CrFe_2 and het-L for Cr_2Fe , as compared to the predicted wavelengths for the respective isomers.

6.2.2.4 Bare Acetate Complex Spectra

We only manage to obtain spectra of the acetate metal core without terminal ligands for the Fe_3 and CrFe_2 acetates. The iron acetate spectra very much lines up with expectations, as discussed in section 5.4.3. On the other hand, the CrFe_2 acetate is more similar to the formate spectra. The fragmentation efficiency is extremely low, so when plotted in graphs scaled for the other complexes, only the semilogarithmic plot shows any details, as can be seen in **Figure 57 G**. The high red shift of the asymmetric carboxylate stretch mode from its expected position, which can be seen in **Figure 58 H**, is probably due to a Fermi resonance, as discussed in section 6.2.1.3. The second component of that resonance could be the band blue-shifted to 1660 cm^{-1} . The same argument as in the bare formate case probably applies here as well, like we argued in section 6.2.1.3.

6.3 Tentative Assignment of the hom/het Ligand/Hole Isomers of Partially Coordinated Mixed Metal Complexes

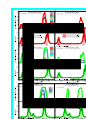
As introduced in section 1.2.1, **Figure 5**, non-saturated heterotrimetallic complexes like $M_nM'_{3-n}O(B)_6L_m$ with $m, n = 1, 2$, display two types of regio-isomerism, which we dubbed het/hom L/H for heterogenous/homogenous ligand/hole coordination patterns. The respective hom isomer has the occupied (L, ligand) or unoccupied (H, hole) axial binding site at the same metal and the het isomer has them at dissimilar metals.

Typically, different metals have different bond strengths to the axial ligands. This is further modified by the bridging ligands and axial ligands influence. In general, the different isomers should still show a preference to the stronger binding metal, in our case of iron and chromium, pyridine-chromium bonds are preferred. This has been shown in the CID results, as discussed in chapter 5.3.1, in **Figure 35** and **Figure 34** and the geometry trends in the pyridine metal bond shown in section 4.4 in **Figure 27**.

While this energy difference should favor a specific isomer by approximately 40 kJ/mol or less, it is considerably lower than the total bond breaking energy necessary for cleaving a typical first-of-three pyridine metal bond, with energies of 150 - 190 kJ/mol for the formates and 150 - 170 kJ/mol for the acetates (see **Figure 36**). Under typical bond cleavage conditions there is more than enough energy present to overcome this isomer energy difference. If such a process was possible, it could hypothetically enable a dynamic process where the complex has enough energy to move the pyridine over any transition states to the respectively less stable isomer. This isomer in turn would require less energy to undergo fragmentation. This could act like a virtual catalyst by offering a lower energy path of stepwise isomer interconversion and then ligand bond cleavage from the weaker coordinating metal, especially under long trapping times and multiple laser shot conditions.

Furthermore, in preliminary efforts together with Jonas Krüger, not included in this thesis, we saw hints in CID spectra that the ratio of the different isomers can depend on the history of the complex. Although the reaction product might be of different stability, pyridine coordination in solution is a random process, presumably leading to a stochastic ratio of the different regioisomers. The isomer ratio, as measured by CID, by isolating the $Cr_nFe_{3-n}O(B)_6Py_m$, $m, n = 1, 2$ species straight out of solution, is different than when creating the complexes by collisional excitation of a higher coordinated $m = x+1$ species to create the desired $m = x$ species. We recommend careful further studies in a better controlled environment. This would ideally be under temperature control, to exploit the better resolution at those conditions and possibly with a second laser pulse of a different color, to selectively pump energy in a specific isomer.

In **Figure 54 E**, bottom row, the cumulative IRMPD spectra of the bi-pyridine coordinated heterometallic acetates are plotted. In trap water coordination made taking spectra of the mono-pyridine species difficult, no data of sufficient quality is available yet.



The two bands we do observe, already discussed in 6.2.2.3, are relatively narrow for the $\nu(\text{COO})_s$ vibration at $\sim 1450\text{ cm}^{-1}$ but the $\nu(\text{COO})_{as}$ is just as wide as seen in the homometallic spectra. This can either be natural band broadening or because the sum spectra of both possible isomers are contributing. To disambiguate this, IRMPD spectra under cold conditions with improved spectral resolution would help.

If we take the observation from the CID spectra, CrFe_2 exists as an 80/20 mix of pyridine coordinated to an iron position as compared to chromium coordinated pyridine. Unfortunately, this is difficult to uniquely attribute to the existence of the hom-L species, as the more stable het-L species has a strong energetic preference for the weaker Fe-Py bond to be broken first. Still, the broad, unresolved nature of the $\nu(\text{COO})_{as}$ bands might suggest at least some part of the energetically disfavored isomer to be present.

On the other hand, the formate species are a bit easier to discuss, as the spectra are much more defined here. The simpler, stiffer complex displays less thermal band broadening, also the energy difference between isomers is slightly higher, maybe leading to a clearer distribution.

For the bi pyridine coordinated case this is also supported by the CID spectra, showing a first fragmentation in the case of CrFe_2 almost identical in energy to Fe_3 , hinting at a strong preference for bond cleavage from iron. This observation alone cannot differentiate between the hom or het-L case. Cr_2Fe on the other hand is a bit simpler. Its first CID fragmentation channel is very similar in its fragmentation behavior to the Cr_3 species, the second fragmentation matches that of mono-pyridine Cr_3 . This hints at a strong preference for the hom-L isomer. The IRMPD spectrum for the bi pyridine coordinated complex of CrFe_2 shows a slightly split $\nu(\text{COO})_{as}$ mode, matching at least a situation where a good part of the energetically favored het-L isomer being present in the ion population. The presence of some of the disfavored isomer cannot be excluded by the band shape, but would only give a small contribution.

Cr_2Fe with two pyridine ligands on the other hand is not as obvious. We see a triplet of bands for the $\nu(\text{COO})_{as}$ modes. The first band at 1620 cm^{-1} might be slightly boosted by overlapping with the $\delta(\text{Py-CH})$ bend mode, but the split in the other two bands speaks for at least some meaningful contribution of the het-L isomer. Here again it will be interesting to investigate further, especially by selectively creating the hom-L isomer from the tri-pyridine. The CID spectrum suggests this should be relatively easy, as the $\text{Cr}_2\text{Fe Py}_3$ species selectively cleaves pyridine from the Fe position species when only applying a low fragmentation energy. This should favor the more stable isomer to be formed as the dominant fragmentation product.

For mono pyridine coordinated formates both spectra look quite similar, a not clearly resolved triplet of bands, each hinting at a mix of both isomers being present, but the resolution is not sufficient to determine the exact ratio. Here again, better resolved spectra at lower temperatures would be helpful.

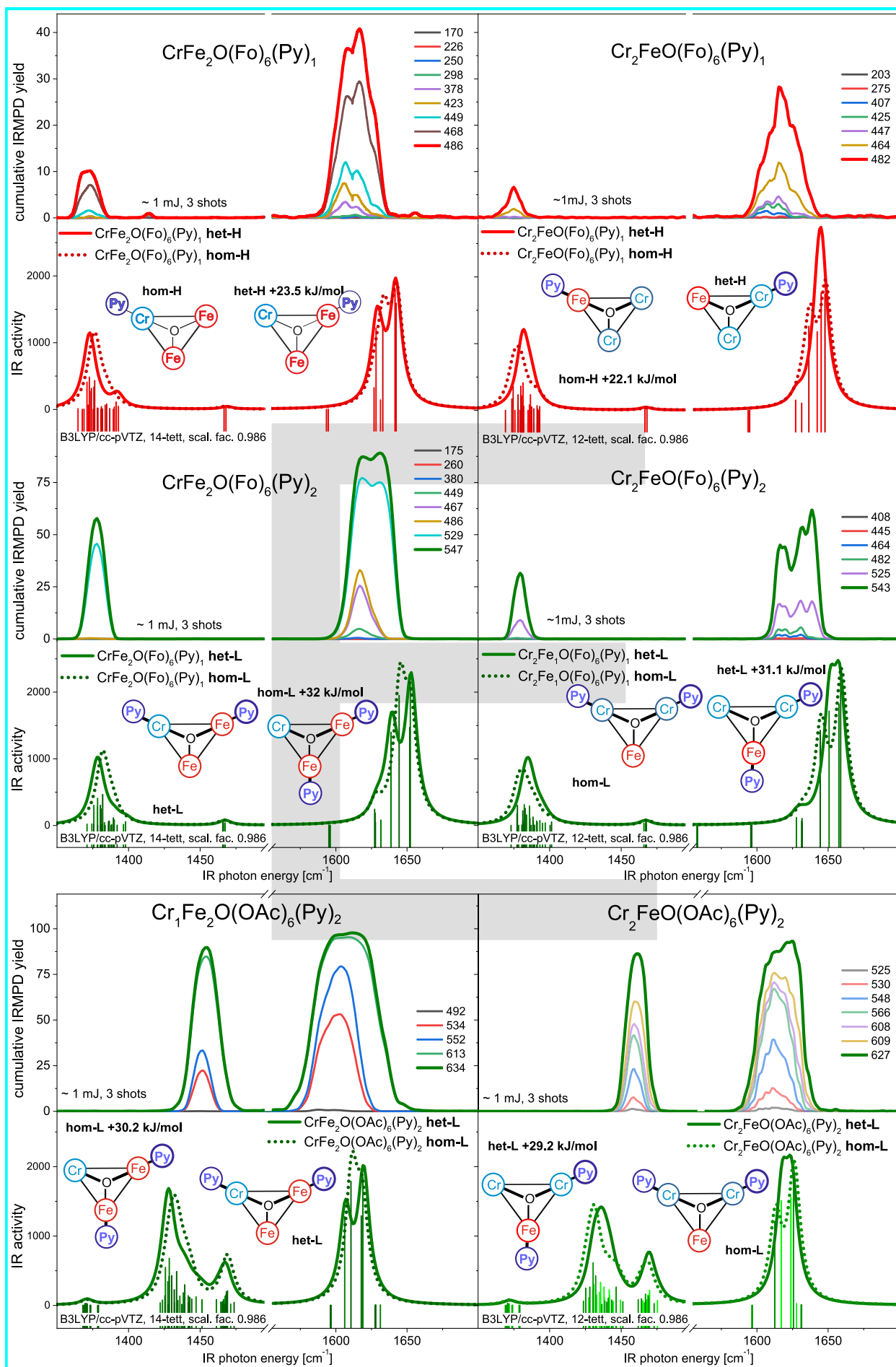
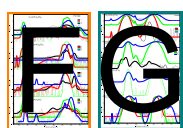


Figure 54 E hom/het-H and hom/het-L predicted and measured IRMPD/IR spectra of all heterometallic $\text{Cr}_n\text{Fe}_{3-n}$ species of all measured formate and acetate bridged complexes for $n = 1, 2$, cumulative fragment trace labels in m/z .

6.4 Trends in the Symmetric and Asymmetric COO Carboxylate Stretch Modes

The qualitative discussion of the bands observed in the COO stretch mode region in the previous chapters is only one half of the story. As introduced in chapter 3; on the spectra of the formates and acetates in isolation, on surfaces and on metal complexes, and as mono- and bidentate ligands; the band splitting $\Delta\nu = \nu(\text{COO})_{\text{as}} - \nu(\text{COO})_{\text{as}}$ and the specific band shifts for both carboxylate bands are important factors in categorizing the properties of the carboxylate and its bonding situation.

To be able to do a quantitative comparison of the bands and their ligand and metal induced shifts, we need to specify the band position in a reproducible way. We therefore fitted all spectra with a series



of gaussian fit functions. The used fits can be seen in a semilogarithmic plot in **Figure 56 F** and **Figure 57 G**. We chose to apply some assumptions and simplifications. Especially for the formate spectra the whole band assigned to the symmetric and asymmetric COO stretch modes respectively, was fitted with a single gaussian function.

Fitting separate fit functions to the band splitting by the different metal to bridging ligand bonds and the achieved spectral resolution would greatly complicate the discussion and a clear disambiguation is not always straightforward or even possible. For the formate spectra especially, this introduces a certain ambiguity, as we bunched all $\nu(\text{COO})_{\text{as}}$ bands of the different bridging modes into the same gaussian function, only deconvoluting the part assigned to the pyridine bend modes. This of course oversimplifies the situation. Occasionally the band shape of the somewhat resolved $\nu(\text{COO})_{\text{as}}$ bands also displays a poor fit with a gaussian function.

Where there is a shoulder clearly belonging to a different chromophore, we tried to approximate that by a separate gaussian, in some cases this introduces a bit of variability. For example, deconvoluting the $\nu(\text{COO})_{\text{as}}$ bands and the $\delta(\text{Py-CH})$ bend mode is not always easily possible. While it is distinctly visible for at least the highly coordinated formate species, cases like the iron formates (see **Figure**) necessitated a somewhat arbitrary weighting of how much band intensity should be assigned to this band.



Keep this in mind when judging the resulting band shifts. Refer to **Figure 56** for the fitted formate spectra in a semilogarithmic plot and **Table 30** for a list of the formate peak positions **Figure 58 H** is based on.

Here the fully coordinated formates with three pyridine ligands show a very linear dependence on the metal variation, as necessarily all terminal positions are occupied and no directing influence of the metal pyridine bond strength can be exerted. The total effect of the metal combination is therefore averaged over all bridging ligand positions.

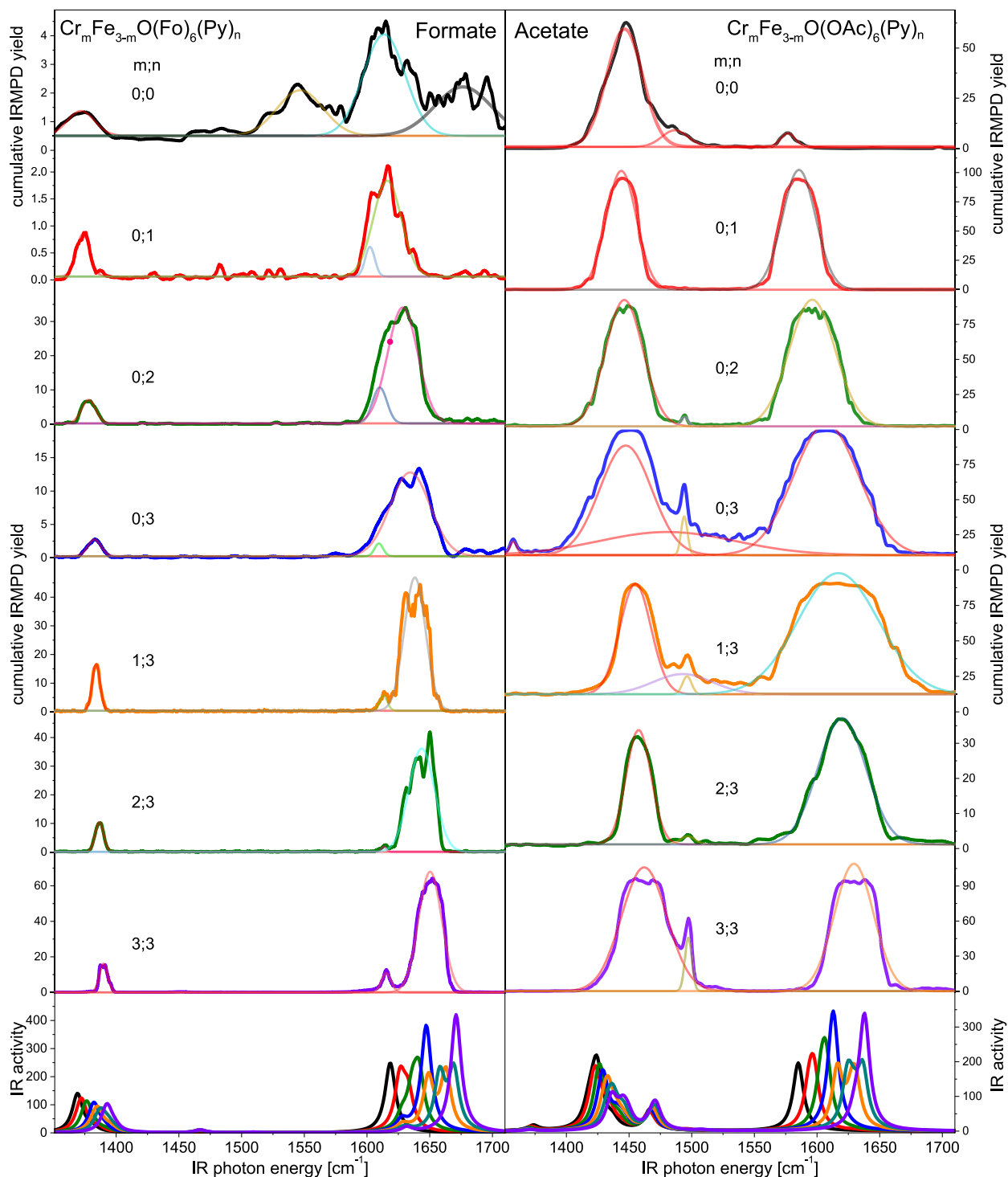


Figure 55 Gaussian curve fits of the IRMPD spectra in the CO region of the $[\text{Fe}_n\text{Cr}_{3-n}\text{O}(\text{OAc}/\text{Fo})_6\text{Py}_m]^+$ complexes with $n, m = 0, 1, 2, 3$ species.

This changes for the doubly pyridine coordinated formates. Suddenly the hom/het L isomers are energetically distinct, as the Cr-Py bond is stronger and therefore favored. This leads to isomers with formates overwhelmingly in bridging position between a chromium with a pyridine and an iron without, as can be concluded from the isomer structures shown in **Figure 54 E**.



The mono pyridine coordinated and bare formates are somewhat red shifted for the heterometallic complexes relative to the expected position based on a linear extrapolation of the homometallic formates.

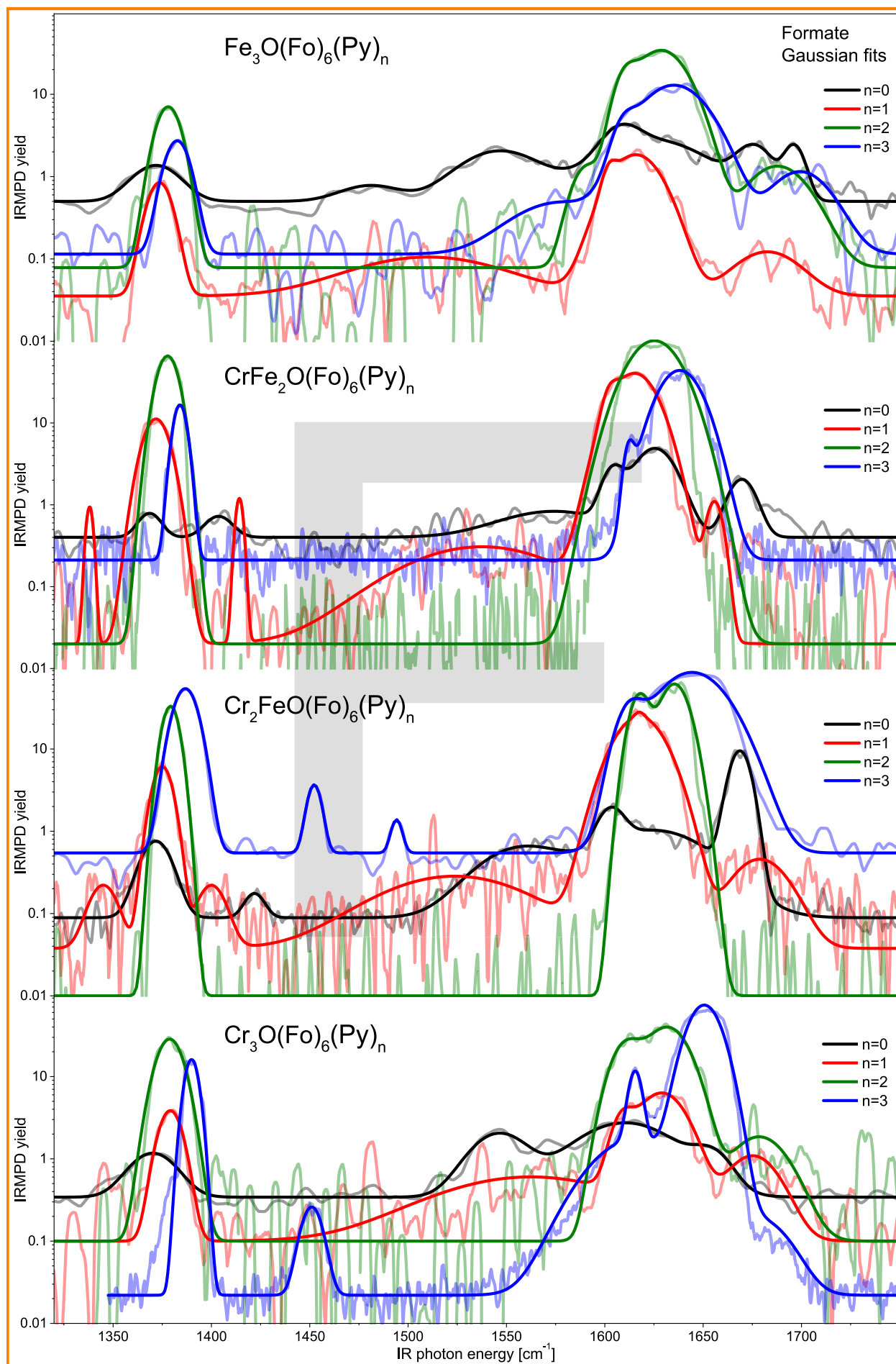


Figure 56 F Gaussian curve fits of the IRMPD spectra shown in a semilogarithmic scale in the CO region of the $[\text{Fe}_n\text{Cr}_{3-n}\text{O}(\text{Fo})_6\text{Py}_m]^+$ complexes with $n, m=0, 1, 2, 3$ species. Refer to **Table 31** for the formate band positions determined by the fits.

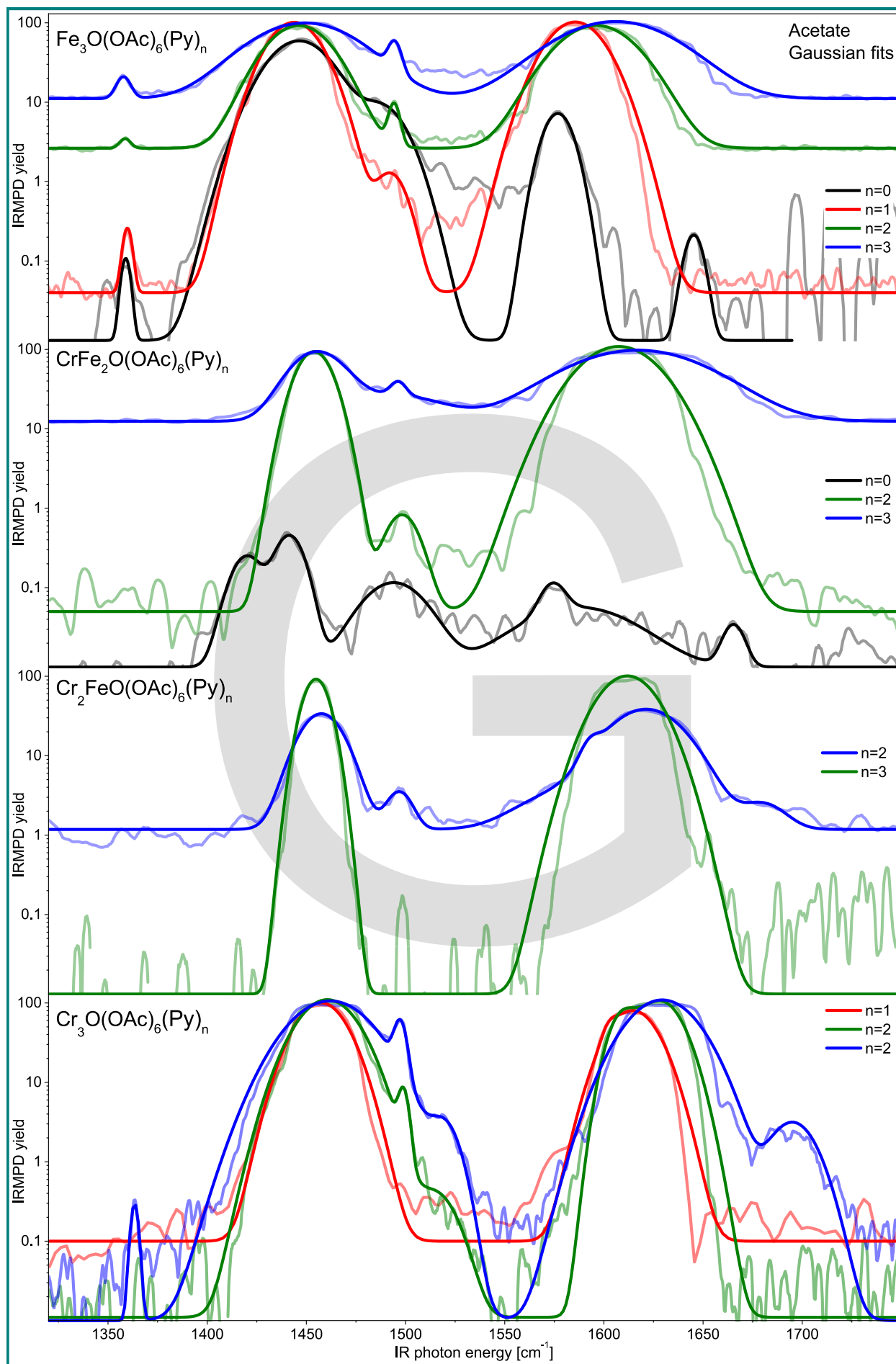


Figure 57 G Gaussian curve fits of the IRMPD spectra shown in a semilogarithmic scale in the CO region of the $[\text{Fe}_n\text{Cr}_{3-n}\text{O}(\text{OAc})_6\text{Py}_m]^+$ complexes with $n, m = 0, 1, 2, 3$ species. Refer to **Figure 106** for all Gaussian fits and **Table 31** for the acetate band positions determined by the fits.

This is discussed for the bare formate spectra in section 6.2.1.3: the $n = 0$, $m = 1, 2$ asymmetric COO stretch modes are especially shifted to the red, presumably because of a Fermi resonance with a band slightly above, which could be a combination band of a OMO bend mode and the symmetric COO stretch. This remains to be corroborated.

In the case of the acetates, we often had several spectra taken at multiple laser powers and shot counts, we fitted all available spectra and took an average of the resulting band positions, this averaged out some small random spread of the resulting band positions. These fits are shown in **Figure 106**, with the cumulative sum of all gaussian fit, **Table 31** for the acetate band positions and **Table 32** for the averaged band positions. For the acetates we had fewer data points to follow the trends, all metal variations are only available for the bi and tri pyridine coordinated acetates. Interestingly while the tri pyridine species again show an almost linear dependence on the metal variations, as discussed above for the formates, the bi pyridine coordinated acetates are a bit more interesting.

The two heterometallic acetates with two pyridine ligands appear at almost exactly the same band positions, differently from the behavior seen in the formates. While it is not explicitly apparent from the band shapes, their broad appearance, as discussed in section 6.3, could speak for an hom het-L isomer mixture. This may be due to a lower interconversion transition barrier or a stochastic isomer mix originating from the solution, which survives ESI ionization and transfer into the Paul trap. This would help motivate the almost identical peak position.

For carboxylates, the band split between the symmetric and asymmetric COO stretch vibrations is a common diagnostic value to characterize the binding motif of the carboxylate group; free, mono- and bidentate. In section 3 we gave some background on that. A selection of band positions and the associated band splits of a number of carboxylate species from the literature has been plotted into **Figure 58 H**.



Similar as seen in the trends in the observed band position of the species discussed in this thesis, the symmetric COO stretch mode is relatively insensitive to the environment of the carboxylate group, safe for $\text{Br}_3\text{OAc}^{-18}$. Still, the free or solvated acetate and formate anions are redshifted in comparison to metal coordinated carboxylates. The asymmetric COO stretch mode is much more sensitive to changes in its bonding partners. Especially the halogenated basic acetates are far blue shifted, especially for $\text{M}_3\text{O}(\text{F}_3\text{OAc})_6^{19}$ with $\text{M} = \text{Cr}, \text{Mn}$ and the aforementioned $\text{Br}_3\text{OAc}^{-18}$.

These shifts and of course the absence of CH modes in those complexes might be good candidates to study the nature of the broad feature at below 3000 cm^{-1} from chapter 7. The band positions of our set of species are observed very close to the band positions of the respective similar basic carboxylate complexes from literature and especially for the bare complexes, almost similar to the bare or solvated carboxylate ion. It seems like our complexes are a good tunable facsimile of different metal surfaces, perhaps they can serve as model systems for the behavior of carboxylates on metal surfaces.

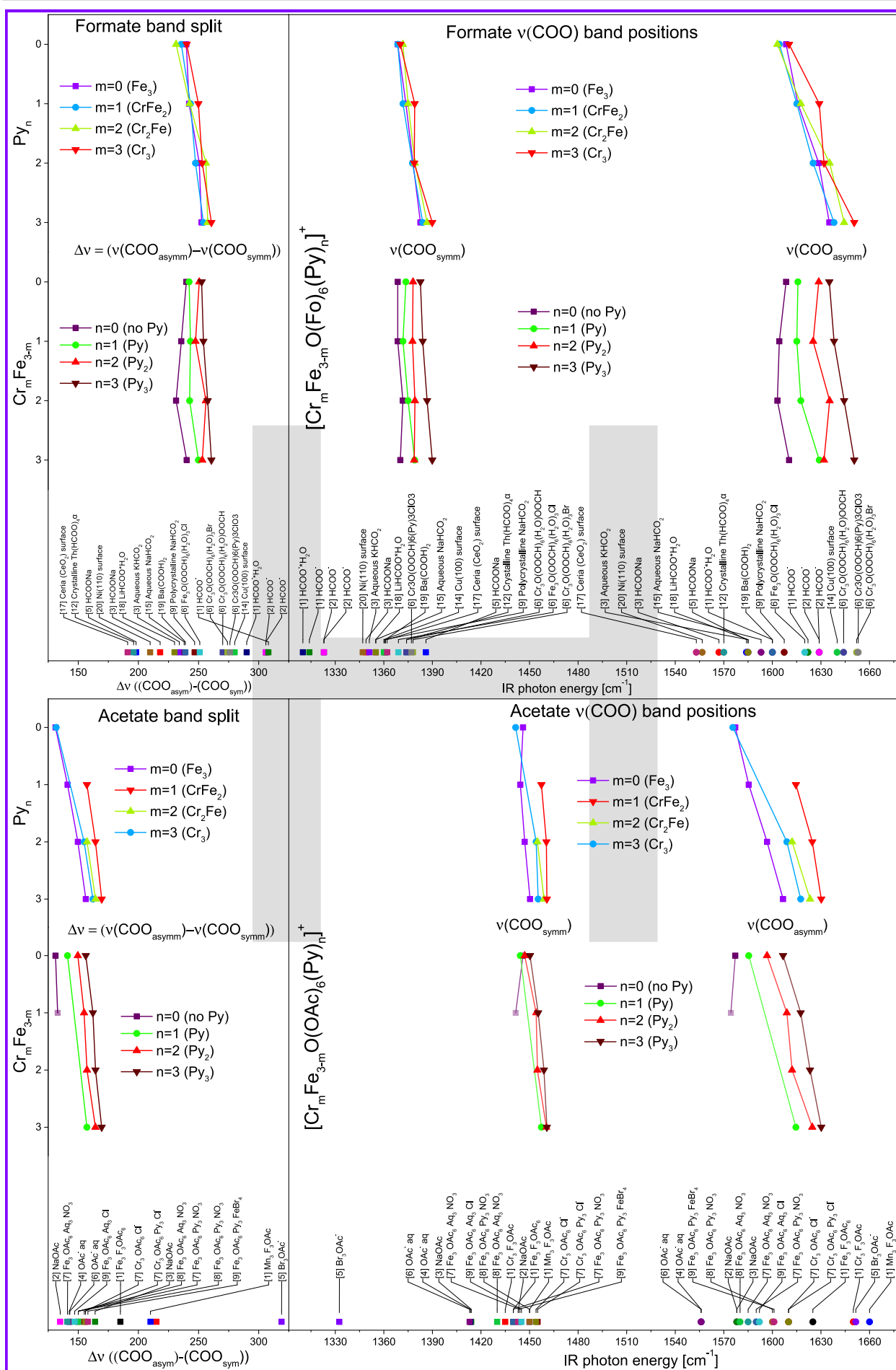


Figure 58 H Trends of $\nu(\text{COO})_s$, $\nu(\text{COO})_{as}$ and $\Delta\nu$. The literature references refer to **Table 28** for the formate and **Table 29** for the acetate species. The peaks are fitted with a gaussian function as shown in **Figure 56 F** and **Figure 106**.

6.5 Hints to Cooperative Effects in the Band Splitting of the Symmetric and Asymmetric Carboxylate Vibrations

The different $\text{Cr}_n\text{Fe}_{3-n}\text{O}(\text{B})_6\text{Py}_m$; $m, n = 0 - 3$ complexes with the bridging ligand $\text{B} = \text{formate}$ or acetate; each show different trends in the carboxylate band positions and band splitting. This can be seen clearly in **Figure 58 H**. The differential many body cooperativity (DMBC) formalism (defined in section 2.7) requires a single value or property to track with consecutive metal/moiety exchange to be able to quantify the cooperative effect. The band splitting of the carboxylate stretch vibrations is one of the properties that can be put into the formalism. We have done so, as detailed in **Table 33** and **Table 34** (appendix), and are showing the results in **Table 2** and **Table 3**.

The results mirror the DMBC observations made already in section 4.7, based on the total electronic energy from DFT calculations. The three-body term change that is induced by changing the pyridine ligands is relatively small at only 2 cm^{-1} . Such small terms are observed in systems where the points of change are widely separated and only interact indirectly with each other. For an iron to chromium exchange in the bare formates, the effect is almost five times bigger, as the metals are in close proximity and can therefore interact strongly. Interestingly, the fully coordinated tri-pyridine species for both formate and acetate behave quite differently. The formates only show a very small, almost vanishing, three-body term and the acetates display a much bigger effect of over 8 cm^{-1} . It is conceivable, that for the formates the interaction of the other metal centers with the changed metal and the changes induced in the pyridine bond on that metal accidentally cancel out.

Still, to our knowledge, this is the first time that this formalism has been applied to a characteristic change in the experimental spectra of a bimetallic trinuclear system with systematic metal exchange. The comparison with further systems will help with interpreting the results in a more systematic fashion. Please see the outlook section 9.2.6 on the Pd acetate system²⁰ as a potential candidate.

Table 2 DMBC values for the band splitting $\Delta\nu$ for successive Fe to Cr metal or no ligand to pyridine ligand exchanges/coordination as determined by the DMBC formalism (see section 2.7), for details see **Table 33**.

DMBC; changes, species	$\Delta\nu_1$	$\Delta\nu_2$	$\Delta\nu_3$
Fe -> Cr, bare Formate	-2.9	24.0	-11.8
Fe -> Cr, Py ₃ Formate	9.1	1.1	-0.8
Fe -> Cr, Py ₃ Acetate	17.5	-13.2	8.3
no Py -> 3 Py, Acetate, Fe ₃	30.1	-2.8	-2.0
no Py -> 3 Py, Formate, Fe ₃	-8.3	4.6	2.0

Table 3 DMBC values for the band splitting $\Delta\nu$ for successive Cr to Fe metal or pyridine ligand to no ligand exchanges/coordination in reverse order relative to **Table 2** as determined by the DMBC formalism (see section 2.7), for details see **Table 34**.

reverse DMBC; changes, species	$\Delta\nu_1$	$\Delta\nu_2$	$\Delta\nu_3$
Cr -> Fe, bare Formate	-9.4	-11.5	11.8
Cr -> Fe, Py ₃ Formate	-8.9	-1.3	0.8
Cr -> Fe Py ₃ Acetate	-16.1	11.8	-8.3
3 Py -> no Py Acetate, Fe ₃	-18.3	-8.9	2.0
3 Py -> no Py, Formate, Fe ₃	-7.0	10.7	-2.0

6.6 References Chapter 6

- Lang, J. *et al.* Magnetostructural correlation in isolated trinuclear iron(III) oxo acetate complexes. *Physical Chemistry Chemical Physics* **20**, 16673-16685 (2018).
- Lang, J., Fries, D. V. & Niedner-Schatteburg, G. Characterization of Trinuclear Oxo Bridged Cobalt Complexes in Isolation. *Zeitschrift für Physikalische Chemie* **232**, 649-669 (2018).
- Johnson, M. K., Cannon, R. D. & Powell, D. B. Vibrational spectra of carboxylato complexes—IV. Mixed-metal and mixed-valence oxo-trinuclear complexes. *Spectrochimica Acta Part A: Molecular Spectroscopy* **38**, 307-315 (1982).
- Zhang, L.-N., Liu, Z.-P., He, L.-J., Cai, S.-H. & Jian, F.-Y. Infrared spectra and normal coordinate analysis of trinuclear μ_3 -oxoacetato complexes of chromium and iron. *Acta Chimica Sinica* **7**, 219-228 (1989).
- Lin, F., Zhang, Z., Zheng, L. & Jiang, A. 含 μ_3 -O 三核混合铁钨醋酸配合物的骨架振动和简正坐标分析. *Acta Chimica Sinica* **49**, 1078-1084 (1991).
- Blake, A. B., Yavari, A. & Kubicki, H. Exchange interactions in a series of novel heteronuclear basic carboxylate complexes containing two iron(III) ions and a divalent metal ion. *Journal of the Chemical Society, Chemical Communications* 796-797 (1981). doi:10.1039/C39810000796
- Blake, A. B. & Yavari, A. Heterotrimeric basic acetates containing chromium(III), iron(III), and a divalent metal: spectroscopic consequences of Metal–Metal interactions. *J. Chem. Soc., Chem. Commun.* 1247-1249 (1982). doi:10.1039/C39820001247
- Blake, A. B., Sinn, E., Yavari, A., Murray, K. S. & Moubaraki, B. Oxo-centred trinuclear acetate complexes containing mixed-metal clusters. Crystal structure of a chromium(III)iron(III)nickel(II) complex and magnetic properties of a dichromium(III)magnesium(II) complex ‡. *Journal of the Chemical Society, Dalton Transactions* 45-50 (1998). doi:10.1039/a705778d
- Lang, J. *et al.* Supporting Information to “Magnetostructural correlation in isolated trinuclear iron(III) oxo acetate complexes.” *Phys. Chem. Chem. Phys.* **20**, 16673-16685 (2018).
- Ault, B. S. Matrix isolation investigation of the fluoroformate anion. *Inorganic Chemistry* **21**, 756-759 (1982).
- Thomas, D. A. *et al.* Vibrational Spectroscopy of Fluoroformate, FCO⁻, Trapped in Helium Nanodroplets. *The Journal of Physical Chemistry Letters* **9**, 2305-2310 (2018).
- Wang, J. *et al.* Syntheses and structure of three 2D polyoxometalates derived from macrocation [Cr₃O(COOH)₆(H₂O)₃]⁺ and α -Keggin-type polyoxomolybdate anions. *Journal of Molecular Structure* **1011**, 1-7 (2012).
- Gerardi, H. K. *et al.* Unraveling the Anomalous Solvatochromic Response of the Formate Ion Vibrational Spectrum: An Infrared, Ar-Tagging Study of the HCO₂⁻, DCO₂⁻, and HCO₂⁻·H₂O Ions. *The Journal of Physical Chemistry Letters* **2**, 2437-2441 (2011).
- Krekeler, C., Mladenovic, M. & Botschwina, P. A theoretical investigation of the vibrational states of HCO₂⁻ and its isotopomers. *Physical Chemistry Chemical Physics* **7**, 882 (2005).
- Powell, D. B. & Cannon, R. D. Vibrational spectra of carboxylato complexes- III. Trinuclear ‘basic’ acetates and formates of chromium(III), iron(III) and other transition metals*. *East* **37**, 995-1006 (1981).
- Johnson, M. K., Powell, D. B. & Cannon, R. D. Vibrational spectra of carboxylato complexes—III. Trinuclear ‘basic’ acetates and formates of chromium(III), iron(III) and other transition metals. *Spectrochimica Acta Part A: Molecular Spectroscopy* **37**, 995-1006 (1981).
- Palacios, E. G., Juárez-López, G. & Monhemius, A. J. Infrared spectroscopy of metal carboxylates: II. Analysis of Fe(III), Ni and Zn carboxylate solutions. *Hydrometallurgy* **72**, 139-148 (2004).
- Rudolph, W. W. & Irmer, G. Raman spectroscopic studies and DFT calculations on tribromoacetic acid and tribromoacetic acid-d. *Spectrochimica Acta - Part A: Molecular and Biomolecular Spectroscopy* **90**, 165-172 (2012).
- Puri, M. & Verma, R. D. Trinuclear metal(III) trifluoroacetates. *Monatshefte für Chemie Chemical Monthly* **115**, 533-539 (1984).
- Carole, W. A. & Colacot, T. J. Understanding Palladium Acetate from a User Perspective. *Chemistry - A European Journal* **22**, 7686-7695 (2016).

7 Anharmonicity in the CH Stretch Modes of Acetate and Formate Pyridine Complexes

7.1 Formate Complexes in the Mid IR, a Curious Case

As introduced in the literary review on carboxylate IR spectra in chapter 3, the formate group exhibits a number of different anharmonic behaviors such as Fermi resonances, overtones, and combination bands. This behavior is not only present in the spectra of the free formate ion^{1,2} (section 3.4), but also persists in solution, in crystal lattices, for surface bound formate ions (section 3.4.1), and also for formate metal complexes. Following the trends through this progression of different environments (section 3.4.2) helps us to understand the spectra presented here. Max Luczak also helped with some of the experimental efforts presented here, as part of his current master thesis.

At least two examples of anharmonic behavior become evident: the apparent band doubling of the CH stretch vibration, and a combination band slightly above 3000 cm⁻¹.

The band positions of this doublet and other important bands were approximated by a series of gaussian curves fitted to their peak shape. The extracted positions are shown both as connected dots in **Figure 59**, and their values are given directly next to the data points.

As visualized in **Figure 59**, the peak positions of the doublet of bands between 2875 and 2965 cm⁻¹ shift at about 7 cm⁻¹ for each consecutive Fe to Cr exchange, with an almost constant but slightly decreasing offset of around 67 cm⁻¹.

Although the absolute peak position and the anharmonic peaks are not well approximated by our DFT calculations, the shift of the $\nu(\text{CH})$ bands is pretty well predicted there. This mismatch between the harmonic prediction of the band position and the observed location is taken into account by an intentional shift in the shown spectral window. The x axis of the predicted IR spectra is shifted by 100 cm⁻¹ while the interval width is kept constant. This choice is made to keep the observed and predicted bands somewhat aligned with each other, while not introducing additional scaling factors, besides the universally applied factor of 0.986, as motivated in section 4.3. This makes it easier to see the systematic mismatch of the harmonic predictions with the actual spectrum.

Building on this pretty empirical description, the nature of this doublet can now be investigated. It seems apparent that there seems to be a pretty strong correlation throughout the spectra. As already shown in **Figure 20**, the CH stretching modes that are predicted and observed with a pretty strong band strength, often couple with bands of the correct type. These bands need to be close enough in wavelength to interact with them. It will be very important to complete the formate set of spectra with measurements of the deuterated formate complexes; as to further supplement evidence to confirm the identity of the broad bands in the 2800 - 3000 cm⁻¹ range.

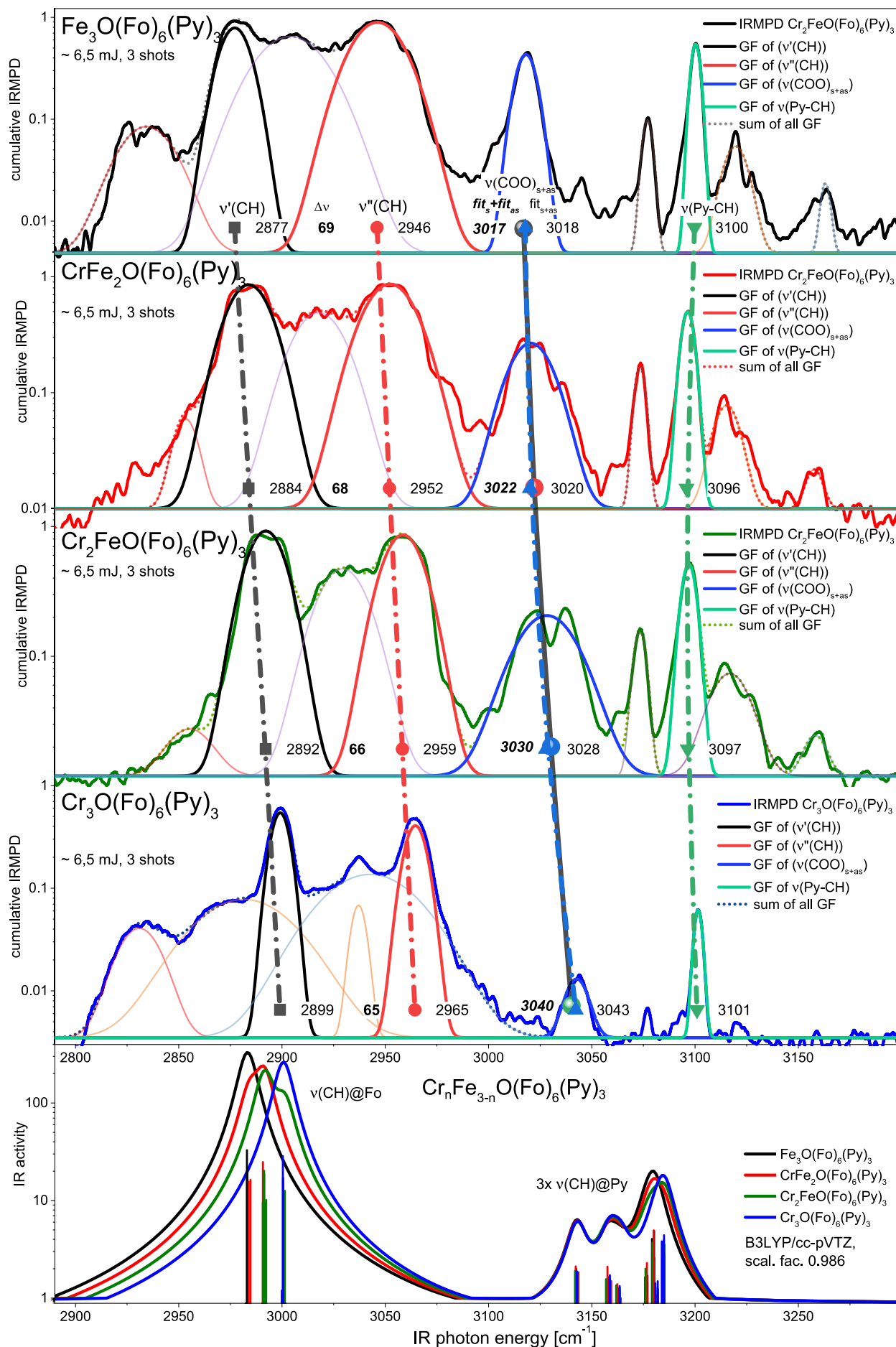


Figure 59 IRMPD spectra of formate $[\text{Cr}_n\text{Fe}_{3-n}\text{O}(\text{Fo})_6(\text{Py})_3]^+$ complexes, with $n = 0 - 3$, in the CH spectral region, with gaussian fit curves and their peak positions plotted, also the sum of $v(\text{COO})_s + v(\text{COO})_{as}$ are shown, as taken from **Figure 61**, section 6.4. Cumulative fragment trace labels in m/z .

As the literature review of formate IR signatures in chapter 3 shows, the different vibrational modes react very differently on the changing environment encountered by a formate ion in isolation, in solution, in salt crystals, on surfaces, and on complexes. This is shown in more detail in the lower half of **Figure 61**. Coordination of the formate ion to massive bonding partners lead to a reordering of the different formate modes; as seen with heavy metals, metal surfaces, as well as multimetallic complexes.

The strongest reaction to the change in environment is shown by the CH stretch mode. When the formate is interacting with sufficiently heavy partners, this mode blue-shifts considerably. The bend mode and its overtone do not react quite as strongly compared to the stretch mode, although a moderate blue-shift is also observed. This moves the position of the CH stretch relative to the CH bend mode and other modes, so that the ordering is inverted.

When the formate ion is interacting with heavy metal ions, for example actinides such as thorium³⁻⁵, rare earth elements like yttrium^{6,7}, or on metal surfaces⁸⁻¹⁰, the CH stretch mode is strongly blue-shifted. It now becomes more likely to interact with the combination mode of the asymmetric COO stretch mode at about 1600 cm^{-1} combined with the CH in plane bend mode at around 1350 cm^{-1} . This observation is discussed in depth in section 3.4.2.

In tri-metallic complexes like basic iron¹¹ or chromium formate, the first overtone of the CH in plane bend mode is too low in wavenumber to account for the Fermi resonance band observed here. Therefore, the mode in Fermi resonance with the CH band is proposed to be the aforementioned combination band of $\nu(\text{COO})_{\text{as}} + \delta(\text{CH})_{\text{ip}}$, leading to the pair of bands at about 2890 and 2960 cm^{-1} .

Unfortunately, we cannot independently verify the position of the $\delta(\text{CH})_{\text{ip}}$ mode ourselves. In the spectra shown in this thesis, it either overlaps with the symmetric $\nu(\text{COO})_{\text{s}}$ mode or has insufficient energy transfer into the available fragmentation modes to be observed directly. An important test would be a deuteration experiment, by synthesizing the deuterio-formate complexes. This is very high on the list of experiments for the near future, as discussed in the outlook, section 9.2.1.

A simple disappearance of both bands will not be sufficient proof for this band assignment, as the CD stretch mode might shift to the blind area of our IR laser system at around 2000 cm^{-1} . In this spectral region, neither the idler nor the far mode of our OPO/OPA laser system provides sufficient laser power, as seen in the laser power curve in **Figure 7**. Without the relatively strong CH absorber nearby to add band strength, the combination mode on its own might not be strong enough to still be visible. An appearance of a line pair near the expected CD mode position would give credence to the CH $\nu + 2\delta$ hypothesis, as both should be influenced by the isotopomerization in a similar fashion. This could be achieved by using another tunable IR source or spectroscopic method, like KBr disk FT-IR or ATR IR. As a side note, a third band often appears between the two main bands of this doublet. It seems to shift relative to the two main bands and primarily shows IRMPD activity in the fragment mass trace assigned to pyridine cleavage. It has not been identified so far.

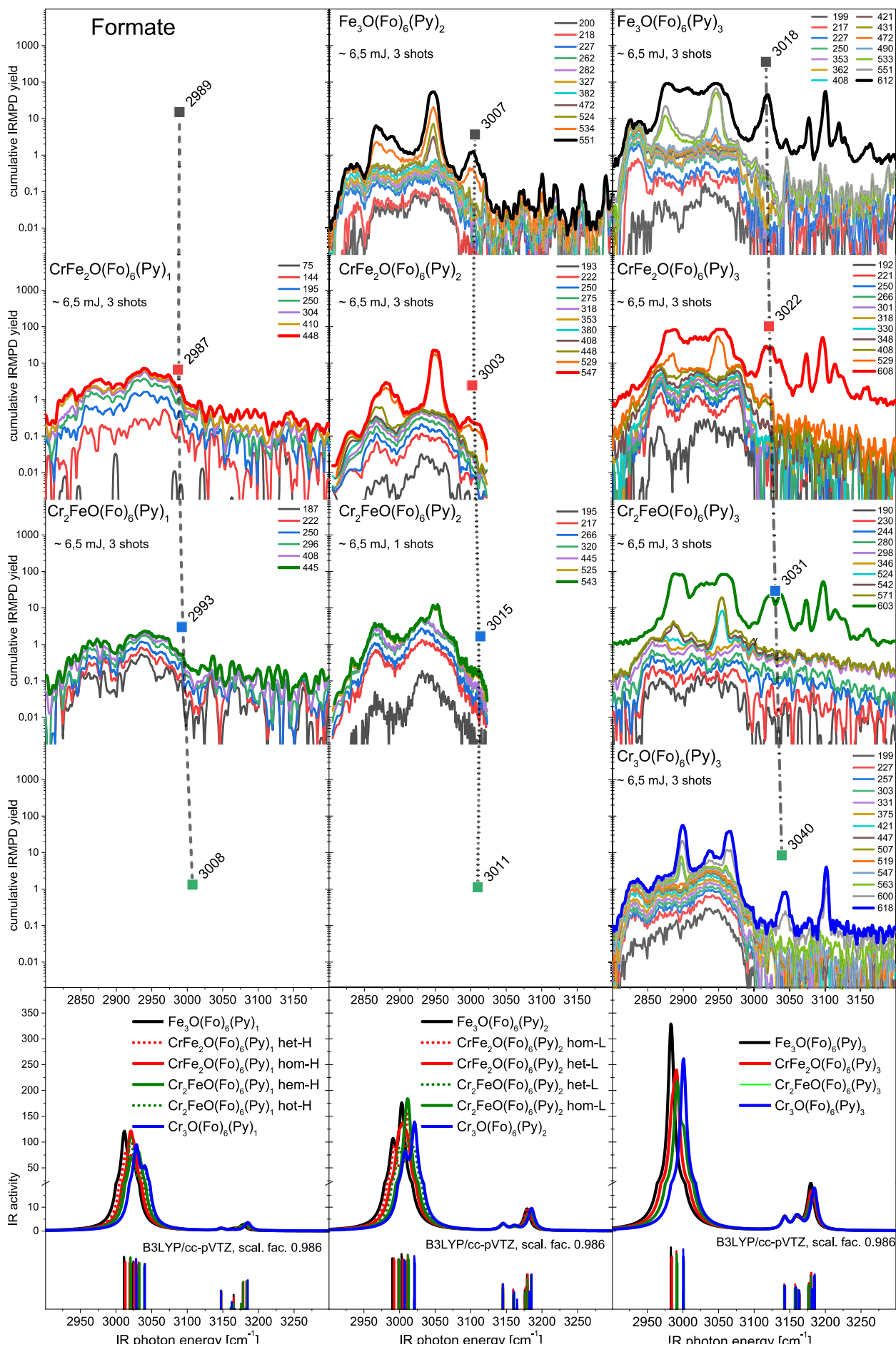
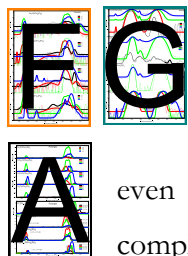


Figure 60 Semi-logarithmic plot of the CH region IRMPD spectra of $[\text{Cr}_m\text{Fe}_{3-m}\text{O}(\text{Fo})_6(\text{Py})_n]^+$ with $n = 0 - 3$ and $m = 1 - 3$, with the sum of $\nu(\text{COO})_s + \nu(\text{COO})_{as}$ plotted, as taken from **Figure 61**.

The next unexpected feature is the series of bands between 3018 and 3043 cm^{-1} , as shown for the tri-pyridine complexes in **Figure 59**, and additionally for the bi- and mono-pyridine coordinated formates in **Figure 60**. For the assignment of this band, the free formate anion^{12,13} provides the relevant analogy as well.

In the free formate ion, a faint band is assigned^{1,2} to the combination mode of both the symmetric and asymmetric carboxylate stretch mode. The sum of the experimental values we obtained for those



modes, as derived by the gaussian fits given in **Figure 56 F** and **Figure 57 G**, fits the observed band positions exceedingly well. This can be seen by the impressive overlap of both line graphs superimposed on each other in **Figure 59**. The peaks of this band even match the observed band splitting of the heterometallic CrFe_2 and Cr_2Fe formate complexes with three pyridine ligands, as shown in **Figure 50 A**.

The series of the sums of the carboxylates stretch modes continues to match the bi- and mono-pyridine coordinated formates. They still show increasingly faint matching bands of pyridine fragmentation in the Fe_3 , CrFe_2 and Cr_2Fe spectra, as seen in the middle and left column of graphs in **Figure 60**.

To additionally complicate the situation, between 2800 and 3000 cm^{-1} , a broad set of bands is observed which exhibits a peculiar pattern of fragmentation channels. This has already been noted in the method section on the example of iron acetate, as shown in **Figure 44** in section 5.5. So far, the nature of this band has not been possible to narrow down. It is characterized by broad areas of fragmentation patterns that correspond to mass spectra markedly different from the one known from successive ligand cleavage; as seen in the introduction to fragmentation mass spectrometry (**Figure 33**, section 5.2), and the CID measurements (section 5.3).

These bands also occur in the acetates, as becomes apparent from **Figure 62** and **Figure 63** (section 7.2). Their possible origins are discussed there as well. Upon the metal exchange, they shift slightly, but in general they are surprisingly resilient to changes of the terminal ligand or the end group (H vs. CH_3) of the bridging carboxylate. This can best be seen in **Figure 60**, **Figure 63**, and **Figure 62**. This has already puzzled us in the iron acetate spectra discussed in section 5.5.

Lastly, as shown in **Figure 61** and **Figure 60**, we observe three well resolved peaks of the axial pyridine ligands (3080 - 3130 cm^{-1}), similar to those in **Figure 44**. They match the DFT calculations, which predict a triplet of bands, as well as the IR spectra of isolated pyridine¹⁴ that display a corresponding series of bands in this spectral range, as we have introduced in section 3.6. Furthermore, for the acetate complexes, we verified their identity with deuteration experiments, as can be seen in **Figure 63** and **Figure 86** in the appendix. Besides this band triplet, we see two satellite peaks at around 3050 and 3160 cm^{-1} , unless they are overlapped by other bands. Due to better fragmentation efficiencies and less interference of the acetate CH spectra in that spectral region, these will be discussed in section 7.2.

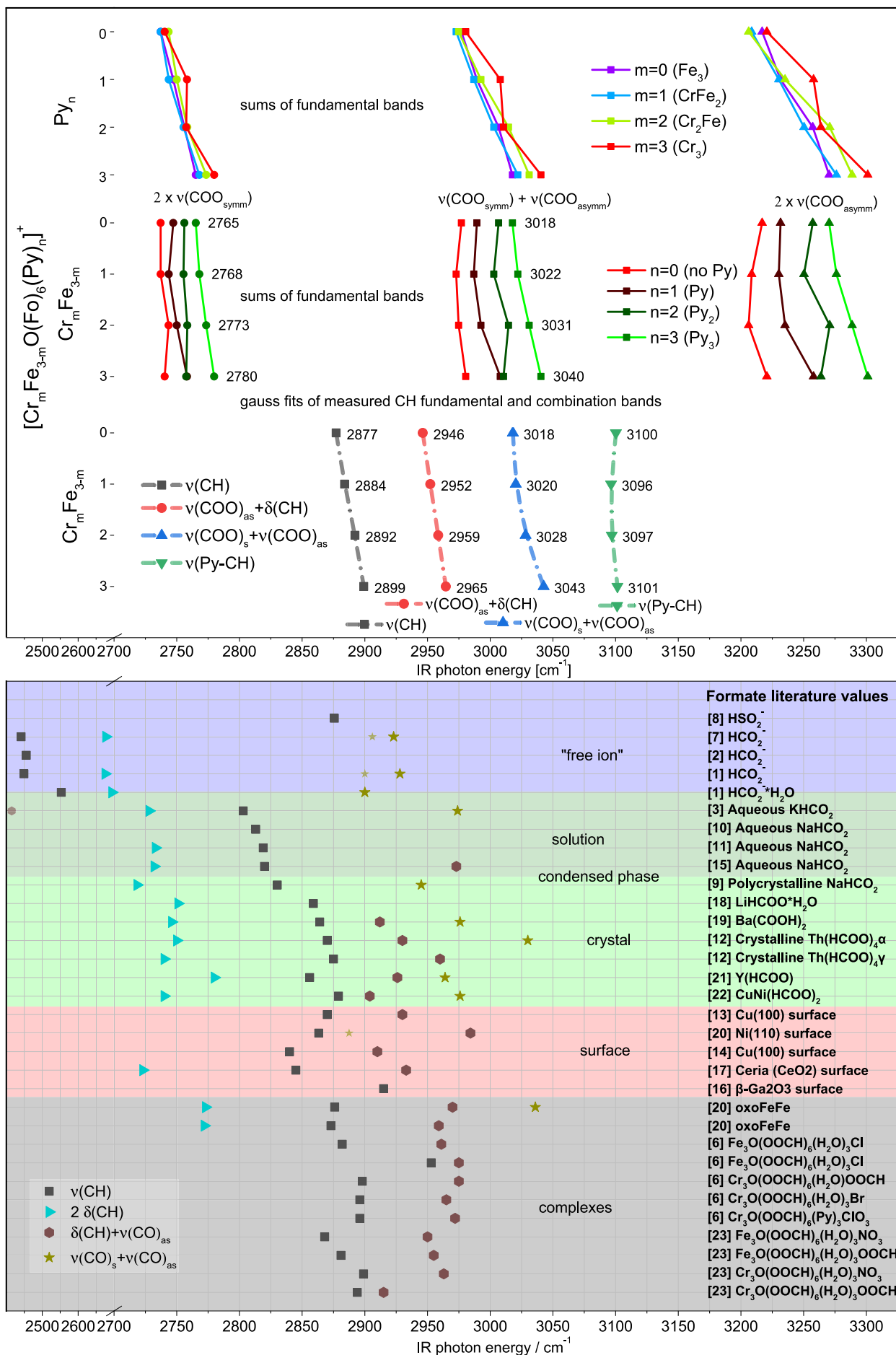


Figure 61 Top: The trends of the formate $2\nu(\text{COO})_s$ and $2\nu(\text{COO})_{as}$ as well as $(\nu(\text{COO})_s + \nu(\text{COO})_{as})$, based on the experimental values determined in Figure 58 H. Bottom: Detailed view of CH stretch vibration region and other overtones and combination bands found in the literature, as given in Figure 20, for all values and sources refer to Table 26 and Table 27.

7.2 Acetate Complexes in the Mid IR, the Puzzle Continues

The acetate IRMPD spectra in the spectral range between 2800 to 3200 cm^{-1} , also called idler, are similarly challenging to interpret. This applies for the homo- and the heterometallic basic acetate complexes of iron and chromium with axial pyridine ligands as well as previously for the formates. Even though this spectral range has much higher laser powers available than the CO region, fragmentation yields of the bands observed here are much lower than measured in the far IR range of the COO stretch modes. The available laser fluence of both spectral regions is shown in **Figure 7**, section 2.1.

For some metals such as the homometallic chromium acetate (**Figure 62**) and cobalt acetate^{15,16}, the only prominent bands visible in the region between 3040 and 3150 cm^{-1} are those of the pyridine ligands, with the most prominent peak at about 3100 cm^{-1} . These bands exhibit only minor changes in band position with changing metal core^{15,16}, or with different bridging ligands, such as formate (**Figure 59**). This matches very well with the discussion in the previous section. Only faint traces of the broad feature below 3000 cm^{-1} remain in the spectra of strongly coordinating metals.

Of the three expected CH_3 stretch modes, one symmetric and two asymmetric groups of stretches seen in the simulated spectrum shown in **Figure 62**, it is tempting to simply assign the CH_3 modes to the broad feature between 2850 and 3000 cm^{-1} . With only the iron acetate data to base our conclusions on, we have tentatively done that. Confer to section 3.2 of our paper¹⁷, reprinted in chapter 10.

In the deuteration experiments shown in **Figure 63** as well as the formate spectra in **Figure 60**, the feature is still present. As mentioned in section 5.5, the observed mass traces hint at fragmentation and an opening of the complex involving the metal core. This exposes a number of coordination sites to which water from the trap background can coordinate to. For example, this can be seen in the IRMPD spectrum (**Figure 44**) and the corresponding mass spectra (**Figure 45**) of iron acetate, as discussed in section 5.5.

We still think the CH_3 modes contribute to the fragmentation pattern here, especially to the feature at 2940 cm^{-1} and also to the band at 2860 cm^{-1} . This is a bit more apparent in the spectrum of iron acetate with 5 laser shots (**Figure 63**, fourth graph). The fragmentation pattern, especially for the strongest part of the feature at around 2940 cm^{-1} , witnesses a baseline fragmentation level by the broad feature and additional energy added by IR absorption through the CH_3 modes of the acetate methyl group.

The same can be said about the weaker mode at around 2865 cm^{-1} . The band width is considerably broader than is observed for the pyridine modes; probably caused by the higher flexibility of the methyl group (such as its almost unhindered rotation with a barrier of about 0.01 kJ/mol ^{18,19}), and the increased ion temperature by energy absorption through the additional broad mode present.

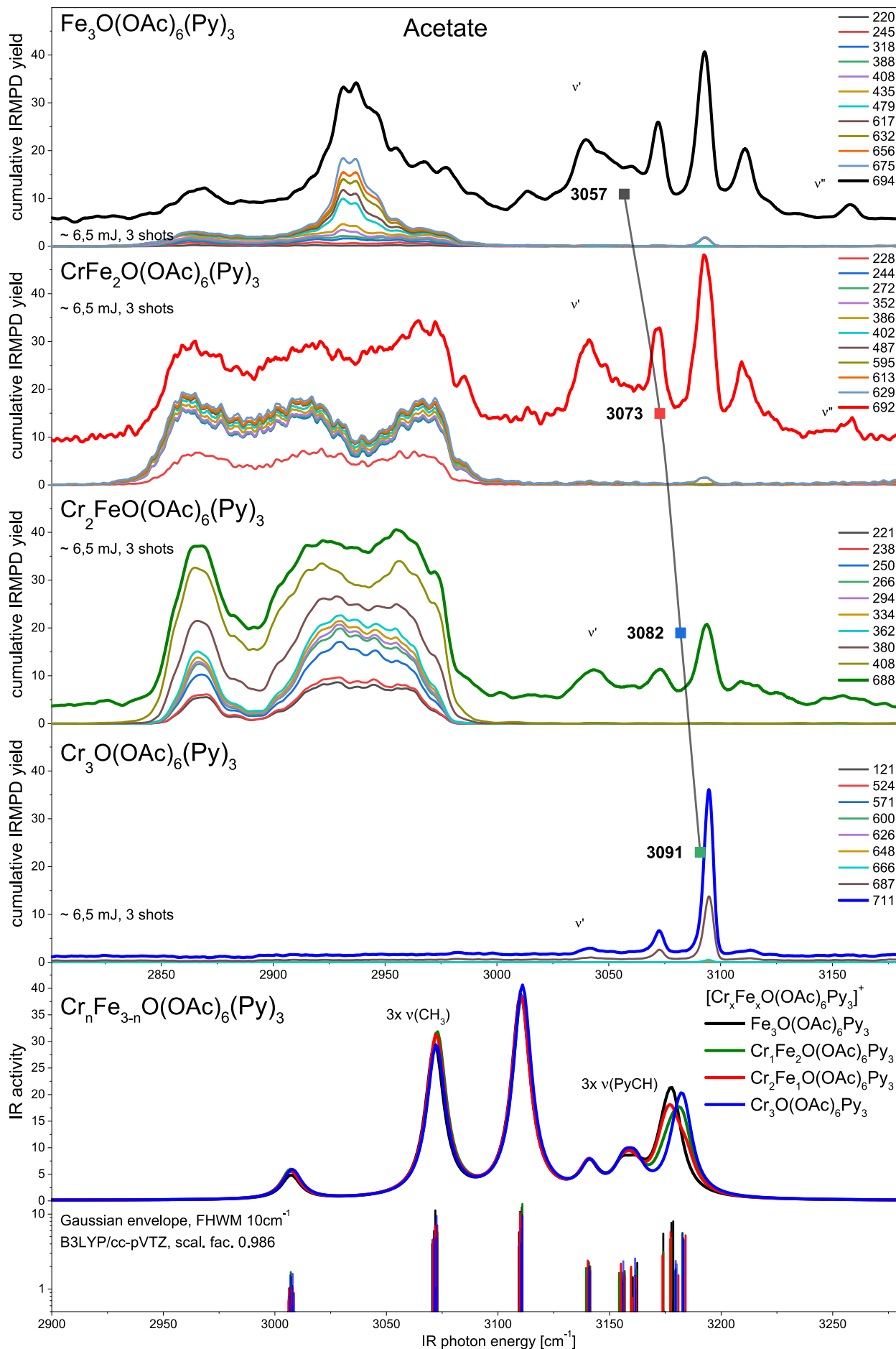


Figure 62 IRMPD spectra in the CH region of the $[\text{Fe}_n\text{Cr}_{3-n}\text{O}(\text{OAc})_6\text{Py}_3]^+$ species. The sums of $\nu(\text{COO})_s + \nu(\text{COO})_{as}$ are plotted, as taken from **Figure 57**, but no corresponding modes are found. Cumulative fragment trace labels in m/z .

Finally, the combination band of the symmetric and asymmetric COO stretch modes, that we prominently observed in the formate spectra, is absent or alternatively covered under the pyridine modes and too weak to be seen. The sum of the symmetric and asymmetric COO stretch modes, as determined in the gaussian fits shown in **Figure 57**, is plotted in **Figure 62**. At least in the spectra shown here, no corresponding combination modes are observed. Maybe two-color experiments could improve the band strength by additionally exciting one of the constituent modes of the suspected combination band. However, the existence of such a two-color effect would first have to be demonstrated in the formate example, where the combination band is naturally visible.

The behavior of the iron acetate upon selective deuteration of the pyridine or acetate hydrogens is very interesting, as shown in **Figure 63** and **Figure 86**. Deuteration of the pyridine ligand fully suppresses the bands associated with its Py-CH modes. Simultaneously, the auto fragmentation that causes a constant weak fragmentation signal is not present anymore; save the broad feature between 2850 and 3000 cm^{-1} , the baseline fragmentation is almost zero. This matches CID measurements (**Figure 74**) we have taken of deuterated pyridine on iron acetate, showing a higher stability of **D₅-pyridine** coordinated to the same core complex. When fragmentation occurs, the fragment pattern is different, not matching the initial pyridine cleavage usually seen (**Figure 33**). This too points to a different chromophore coupling to different fragmentation channels. Here it could maybe interact with the unobserved overtone of the symmetric carboxylate stretch mode. This is not yet a satisfying assignment.

In the inverse case, with deuterated **D₃-acetate**, the pyridine associated modes reappear, but the broad feature also stays, almost unchanged. This is another strong indication that the CH₃ modes alone cannot account for this spectral feature. We also measured the fully deuterated spectrum, but like the standard iron acetate spectrum measured that day (**Figure 86**, bottom left and right plot, in the appendix), the unsatisfactory adjustment of the laser lead to very different fragmentation behavior than usual. The results will have to be repeated, before reliable conclusions can be made.

Interestingly, the heterometallic species (CrFe₂ and Cr₂Fe) give almost identical spectra to the iron acetate complex with **deuterated acetate**, without the CH₃ stretch modes clearly impacting the fragmentation pattern, as is seen in the iron acetate case (**Figure 63**). For chromium acetate, only the pyridine CH stretch modes remain active, similar to the cobalt acetate spectra published previously^{16,20}. The chromium complex is too stable to show fragmentation of the core, or too stiff to efficiently transfer energy to the terminal pyridine ligands.

Overall, the broad feature found in all formate-, the heterometallic acetate-, as well as the partially deuterated iron acetate complexes, is still a challenge for our understanding of the spectra. The leading candidate would be some property that is common to all basic carboxylates; perhaps the interaction of the μ -oxo bridged metal triangle with the bridging ligand motion.

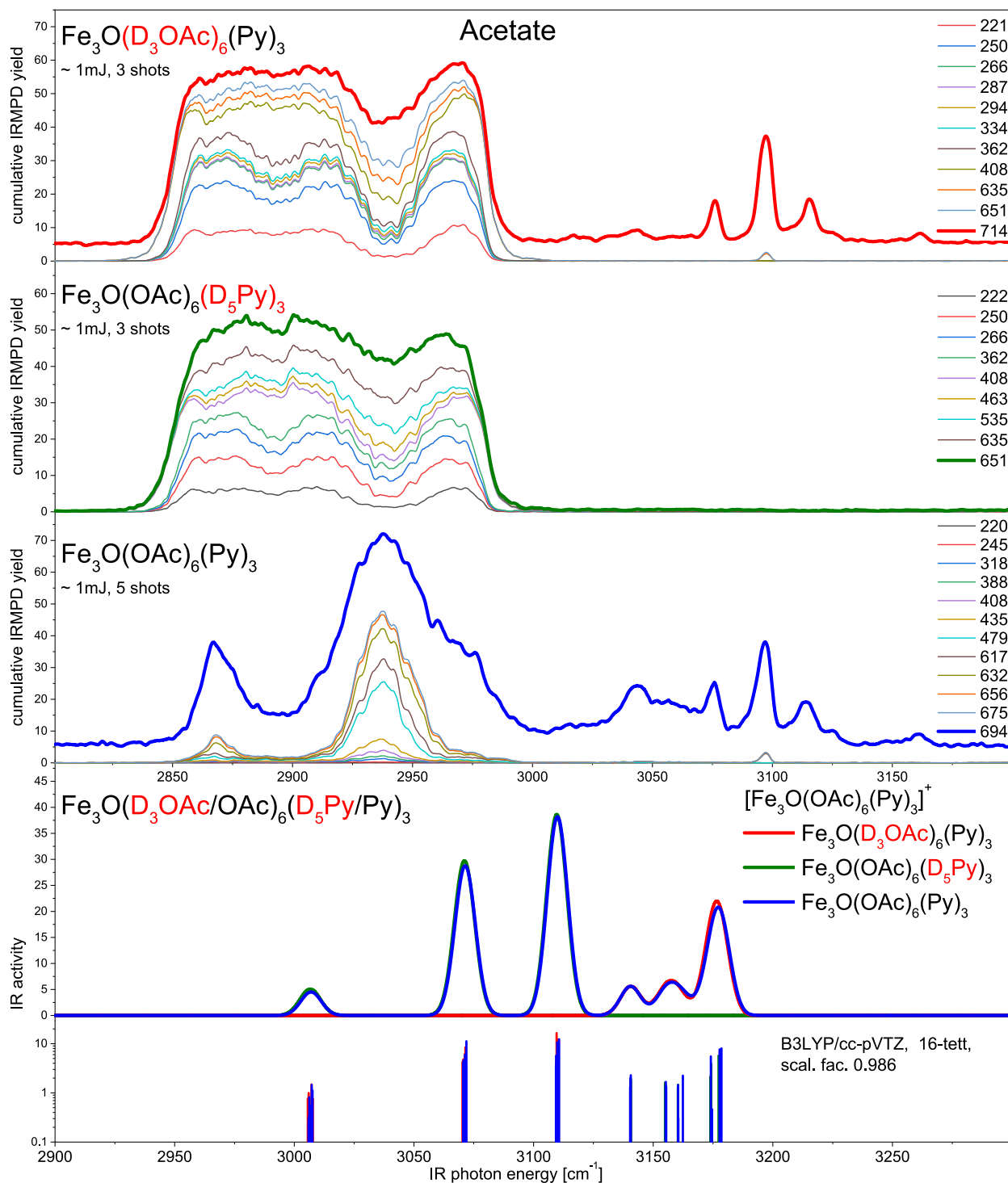


Figure 63 $[\text{Fe}_3\text{O}(\text{OAc}(\text{D}_3\text{OAc})_6(\text{Py}/\text{D}_5\text{Py})_3)]^+$ in the CH region, together with a simulated IR spectrum (bottom graphs), cumulative fragment trace labels in m/z .

This might be a combination of a $\delta(\text{MOM})$ mode with the symmetric carboxylate stretch, as previously proposed for the hypothetical Fermi resonance with the asymmetric carboxylate stretch; both in the bare formates and the bare CrFe_2 acetate.

Another observation about this band, further strengthening the prevailing assumption that the CH_3 stretch modes are not the only significant part of this broad feature, are the spectra of the tri-, bi-pyridine, and the bare acetate complexes shown in **Figure 81**, in the appendix. With fewer pyridine ligands, the fragmentation efficiency drops precipitously, to almost zero for the naked acetates. Still, the broad feature persists.

For the under- and unsaturated complexes, it even changes its pattern, matching even less to the predicted acetate pattern seen in the calculated spectra. This is not behavior normally expected from a CH₃ chromophore, but rather matches that of a mode involving the metal core. Further experiments are planned to finally get a good identification of the second component contributing to this feature, as detailed in the outlook, section 9.2.2.

7.3 References Chapter 7

- Kidd, K. G. & Mantsch, H. H. Formate anion: The physical force field. *Journal of Molecular Spectroscopy* **85**, 375-389 (1981).
- Krekeler, C., Mladenovic, M. & Botschwina, P. A theoretical investigation of the vibrational states of HCO₂⁻ and its isotopomers. *Physical Chemistry Chemical Physics* **7**, 882 (2005).
- Mentzen, B. F. The infrared absorption of crystalline thorium tetraformates. I. Characterization of thorium tetraformates in the solid state by infrared spectroscopy. *Journal of Solid State Chemistry* **3**, 12-19 (1971).
- Bagnall, K. W. Thorium Formiate. in *Gmelin Handbook of Inorganic Chemistry* (ed. Fluck, E.) 37-40 doi:10.1007/978-3-662-08315-6
- Greis, O., Bohres, E. W. & Schwochau, K. Darstellung, Infrarotspektren und röntgenographische Untersuchungen der Tetraformiate von Thorium, Protactinium, Uran und Neptunium. *Zeitschrift für anorganische und allgemeine Chemie* **433**, 111-118 (1977).
- Maczka, M., Hanuza, J. & Kaminskii, A. A. Polarized IR, spontaneous and stimulated Raman spectra of Y(HCOO) 3·2H₂O single crystal - A new Raman laser material. *Journal of Raman Spectroscopy* **37**, 1257-1264 (2006).
- Köck, E.-M., Kogler, M., Bielz, T., Klötzer, B. & Penner, S. In Situ FT-IR Spectroscopic Study of CO₂ and CO Adsorption on Y₂O₃, ZrO₂, and Ytria-Stabilized ZrO₂. *The Journal of Physical Chemistry C* **117**, 17666-17673 (2013).
- Sexton, B. A. Observation of formate species on a copper (100) surface by high resolution electron energy loss spectroscopy. *Surface Science* **88**, 319-330 (1979).
- Hayden, B. E., Prince, K., Woodruff, D. P. & Bradshaw, A. M. An iras study of formic acid and surface formate adsorbed on Cu(110). *Surface Science* **133**, 589-604 (1983).
- Woodruff, P. Characterising Molecules and Molecular Interactions on Surfaces. in *Modern Techniques of Surface Science* **5**, 383-467 (Cambridge University Press, 2017).
- Ciupa, A., Trzebiatowska-Gusowska, M. & Ptak, M. Vibrational properties of the mixed-valence iron oxo-complex. *Vibrational Spectroscopy* **86**, 218-222 (2016).
- Gerardi, H. K. *et al.* Unraveling the Anomalous Solvatochromic Response of the Formate Ion Vibrational Spectrum: An Infrared, Ar-Tagging Study of the HCO₂⁻, DCO₂⁻, and HCO₂⁻·H₂O Ions. *The Journal of Physical Chemistry Letters* **2**, 2437-2441 (2011).
- Gerardi, H. K. *et al.* Supporting information to “Unraveling the Anomalous Solvatochromic Response of the Formate Ion Vibrational Spectrum: An Infrared, Ar-Tagging Study of the HCO₂⁻, DCO₂⁻, and HCO₂⁻·H₂O Ions.” *The Journal of Physical Chemistry Letters* **2**, 2437-2441 (2011).
- Wilmshurst, J. K. & Bernstein, H. J. The vibrational spectra of pyridine, pyridine-4-d, pyridine-2,6-d₂, and pyridine-3,5-d₂. *Canadian Journal of Chemistry* **35**, 1183-1194 (1957).
- Fries, D. V. Synthese & Gasphasen-Charakterisierung von trinuklearen, oxozentrierten Cobaltacetat-Komplexen. (2016).
- Lang, J., Fries, D. V. & Niedner-Schatteburg, G. Characterization of Trinuclear Oxo Bridged Cobalt Complexes in Isolation. *Zeitschrift für Physikalische Chemie* **232**, 649-669 (2018).
- Lang, J. *et al.* Magnetostructural correlation in isolated trinuclear iron(III) oxo acetate complexes. *Physical Chemistry Chemical Physics* **20**, 16673-16685 (2018).
- Rudolph, W. W., Fischer, D. & Irmer, G. Supplementary Material “Vibrational spectroscopic studies and DFT calculations on NaCH₃CO₂(aq) and CH₃COOH(aq).” *Dalton Trans.* **568**, 1-4 (2015).
- Steill, J. D. & Oomens, J. Supplementary information to “Action spectroscopy of gas-phase carboxylate anions by multiple photon IR electron detachment/attachment.” *Journal of Physical Chemistry A* **113**, 4941-4946 (2009).
- Fries, D. V. & Lang, J. Synthesis & gas phase-characterization of trinuclear, oxo centered Cobaltacetate-complexes. (TU Kaisersautern, 2016).

8 Other Ligands and Trivalent Metals: Water and Scandium

8.1 Carboxylate Stretch Modes of Chromium and Iron Water Complexes

Fragmentation efficiency in the $\nu(\text{COO})_s/\nu(\text{COO})_{as}$ modes of the acetate shows the opposite ratio to pyridine, with the symmetric bands resulting in a stronger fragmentation signal than the asymmetric modes. As seen in the right column of **Figure 64** for the formates, the band strength ratios change strongly as well, with a weak symmetric band in the Fe_3 complex and successively higher activities in the series towards the Cr_3 species. The peak doubling specifically of the CrFe_2 complex has already been observed for the respective bare formate (**Figure 56**).

At the same time, with an opposite trend, the strong shoulder at 1570 cm^{-1} starts out as the dominant band in the Fe_3 spectra and gets successively weaker towards the Cr_3 complex. Cannon et al.¹ also observe this band as a weak shoulder in their spectra, with it being almost absent in the Cr_3 case; matching our data. They do not assign it to any specific molecular vibrational mode. Our DFT calculations predict the water bend mode at a slightly higher wavenumber, but with that assumption, it would be difficult to explain the strong core fragmentation observed in conjunction with these bands. This is not so easily explained with energy absorbed by an axial ligand, as previously seen for pyridine coordination. It might be possible that hydrogen back bonds of some water ligands can lead to a coupling with core modes. This does not match with the isomers considered in our calculations. The minimum energy structures found so far all have the water ligand coordinate to the metal using its free electron pairs of the oxygen, with the hydrogen pointing away from the complex. Additional calculations of further isomers might result in different minimum structures, especially some with hydrogen bonded water networks around the coordination sites, with hydrogen back bonding to the carboxylate oxygens. This is a case where a deuteration experiment, using heavy water, may also yield valuable experimental indication of the bonding situation.

Another hint for the hypothesized water network are the spectra of mixed ligand complexes, with two terminal metal coordination sites already saturated with pyridine ligands (**Figure 66**). This presumably directs the water ligands to the one free metal. They still show similar behavior as is shown in the formates, with strong bands roughly 60 cm^{-1} below the asymmetric carboxylate stretch mode. This is most apparent for the species with two water molecules, also yielding the same general fragmentation pattern as seen in the formates. This even extends to a tri-pyridine species with three water molecules, leading to a weak band between 1550 and 1600 cm^{-1} . Here, only the carboxylate oxygens offer good places for hydrogen bonds to attach. Again, more data is needed for a positive identification of the actual bonding situation.

Iron acetate and other basic carboxylates are known for slow hydrolysis in solution²⁻⁵, with formates reacting even faster⁶⁻⁸, leading to a monodentate acetate and two water molecules bonding to the now coordinatively unsaturated iron center. One of these waters can potentially form a hydrogen bridge with the carboxylate ligand. Chromium centers are not typically known for this behavior.

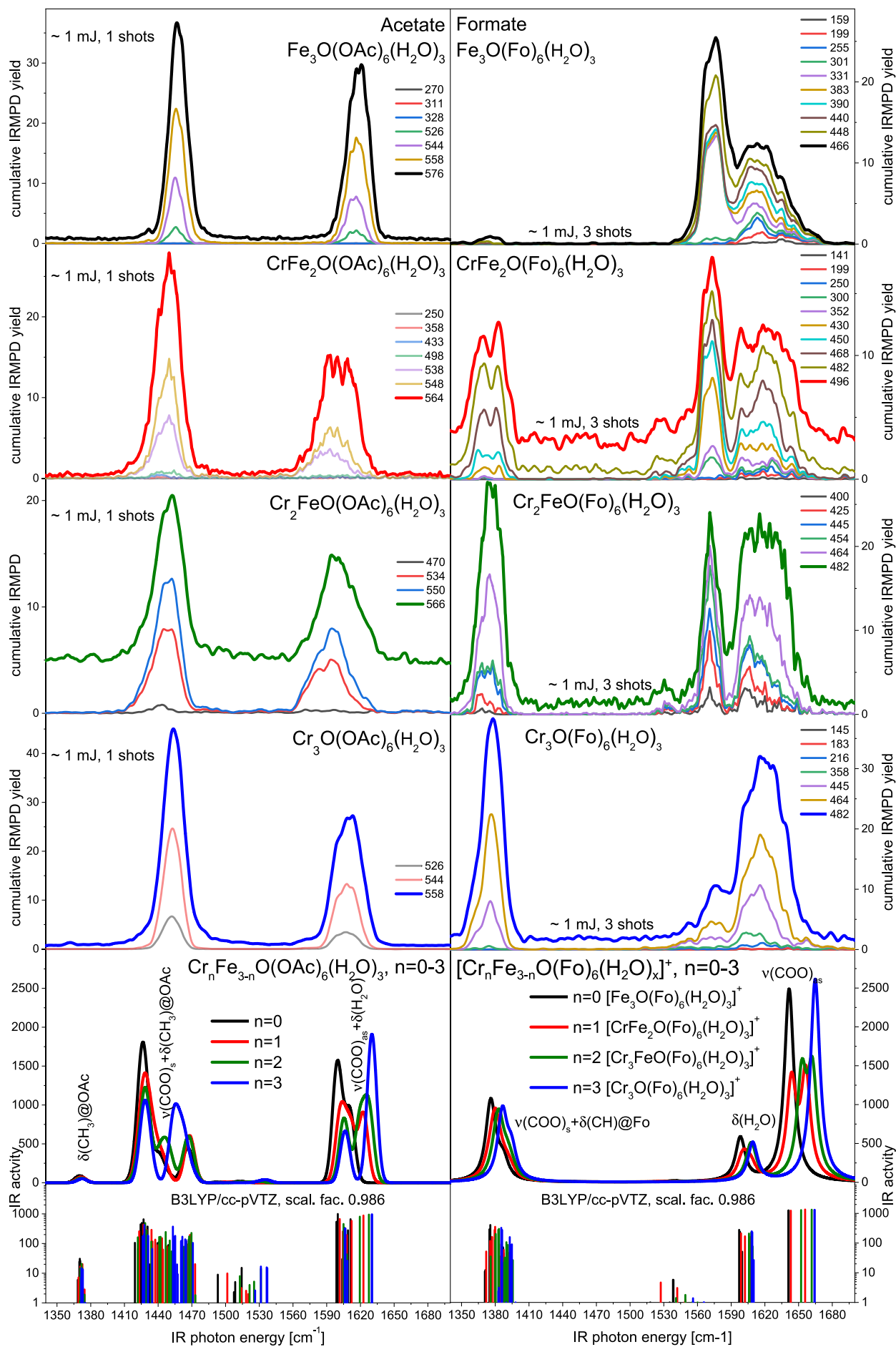


Figure 64 IRMPD spectra in the CO region of the $[\text{Fe}_n\text{Cr}_{3-n}\text{O}(\text{OAc})_6(\text{H}_2\text{O})_3]^+$, $n = 0 - 3$ species, cumulative fragment trace labels in m/z .

This is a second hypothesis to explain the striking change in the observed bands with the different metals. This applies for the formates and also for the mixed ligand acetate spectra in **Figure 66**. The originally very stable Cr_3 acetate behaves as if it is much more susceptible to hydrolysis after two or three pyridines are coordinated to it. These pyridines elongate the metal cores to a more formate like structure, as can be seen from the geometry trends discussed in section 4.4.

The relatively high susceptibility of the formates to hydrolysis is the reason we spray our water adduct species from ethanol, relying on trace water to form the water complexes, as explained in section 5.2. We know the pyridine ligands probably change the acetate bonding strength, just like we see in the CID measurements. Other pyridine bonds, and presumably other coordination bonds to the metal centers, are weakened and elongated upon successive pyridine coordination. The hydrolysis hypothesis also fits to the observed behavior of the formates and the fragmentation behavior displayed there (see **Figure 64**). The band splitting and intensity ratio for the suspected monodentate formate at around 1600 cm^{-1} match the reported values⁹ for monodentate formate on surfaces, with the asymmetric stretch mode at 1610 cm^{-1} . There a very weak symmetric mode is found, matching our observations.

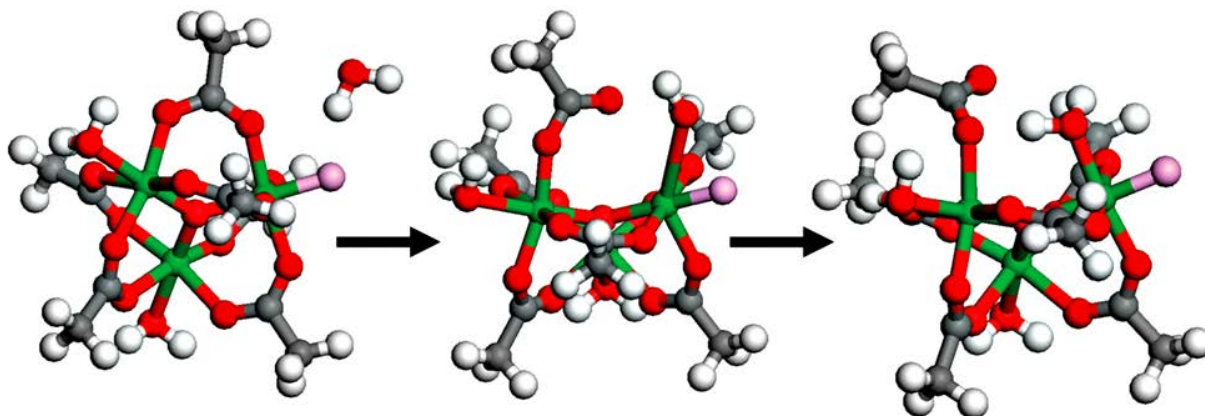


Figure 65 Ligand displacement reaction of MIL-101¹¹. Structures represent reactant, transition state, and hydrolysis product clusters. Color scheme: gray, C; red, O; white, H; dark green, Cr; pink, F; Adapted with permission from Figure 1 of J. Am. Chem. Soc. 2009, 131, 43, 15834-15842, Copyright 2009, American Chemical Society¹².

Monodentate carboxylates in complexes have very low band splitting when they form a ‘pseudo bridged’ structure with a water molecule¹⁰. This is noted in section 3.4 and 6.2.1.3. For the Cr_3 formate complex, as reported by Cannon et al.¹, the $\nu(\text{COO})_{\text{as}}$ mode of monodentate formates is seen at around 1570 cm^{-1} , while bridging formates have them at 1644 cm^{-1} . However, in Cannon’s case the formate in question is a terminal ligand and simultaneously the counter ion, with crystal water bonding to it. If this analogy holds, it could explain the band doubling for the CrFe_2 formate species in **Figure 64** at 1380 cm^{-1} , where two symmetric carboxylate bands and two asymmetric bands are visible, one of each for the bridging and the monodentate binding motif, respectively.

This hypothesis matches the shoulder seen in the second spectrum of **Figure 66** at 1460 cm^{-1} . The Fe_3 symmetric mode is already blue-shifted and weak, with the presumptive monodentate asymmetric carboxylate stretch mode being the dominant band, as expected for that binding motif, according to the literature⁹.

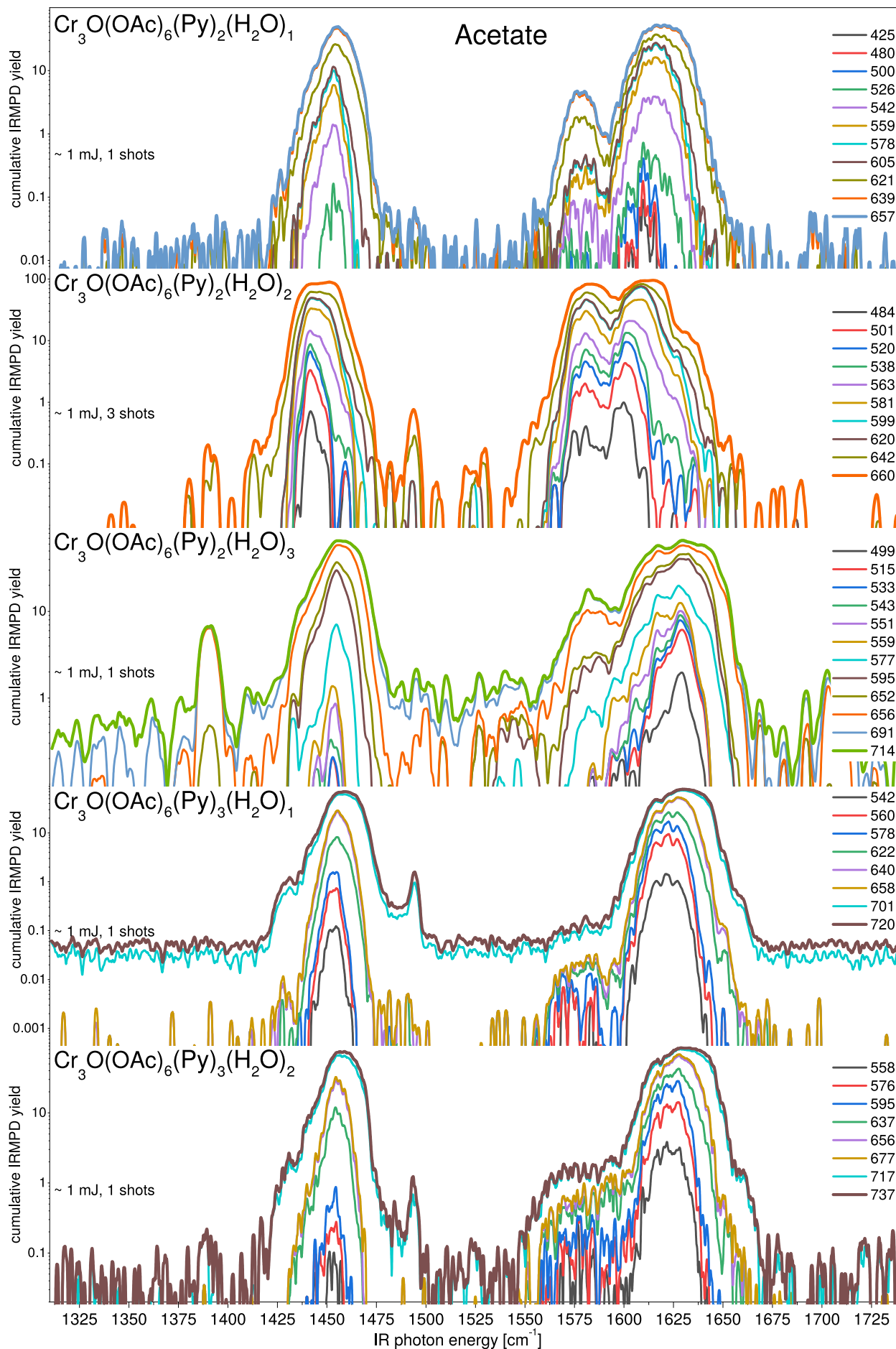


Figure 66 IRMPD spectra of acetate $[\text{Cr}_3\text{O}(\text{OAc})_6(\text{Py})_n(\text{H}_2\text{O})_m]^+$ with $n = 2, 3$ and $m = 1, 2$ in the CO spectral region, hinting at water networks interacting with the acetates. Cumulative fragment trace labels in m/z .

In the appendix, in **Figure 87** to **Figure 90** for the acetates, and **Figure 101** to **Figure 104** for the formates, we show the IRMPD spectra for additional water coordinated complexes of all four Cr/Fe metal combinations. They corroborate the observations in the tri-aqua coordinated species shown in **Figure 64** and display even more rapid changes in their spectra. Given the occasional erratic behavior, a full discussion of those results is beyond the scope of this thesis. Careful additional measurements and calculations will be necessary; with the high number of possible isomers making this challenging. To check this hypothesis, a few new experiments are suggested, both for the formates and the mixed ligand acetates. It will be interesting to check for a time dependence of the relative band ratios with increasing trapping time, and to check for significant changes with a trap saturated with heavy water.

The modification of susceptibility to hydrolysis^{12,13}, in dependence on the used transition metal; the bridging ligands; and terminal ligands, is of considerable interest to the MOF/PCP community. They are investing considerable efforts trying to modify the activity or stability of nano porous designed materials^{2,11,12,14,15}, as introduced briefly in section 1.4.2.

8.2 Scandium Chromium Iron Oxo Acetate and Formate

Following the same strategy used to synthesize the mixed Cr/Fe metal formates and acetates (section 5.1.1), ScCl_3 is used as an additional starting material and mixed in a 1:1:1 ratio with the respective iron and chromium chlorides. After reacting them to their hydroxides, concentrated formic and acetic acid are used to obtain the respective formate and acetate complexes. The resulting product is a mixture of several different metal complexes; among them, in sufficient abundance, is the trimetallic ScCrFe complex. This is confirmed by the ESI mass spectrum, the isotope pattern, and its fragmentation products. IRMPD spectra are recorded to see the effect of three distinct metals on the different vibrational modes of the molecular ion.

All measured $\text{ScCrFeO}(\text{Fo}/\text{OAc})_6\text{Py}_3$ IRMPD spectra, also recorded at lower laser power and lower shot counts, are plotted in **Figure 105** in the appendix. They corroborate the observations shown in **Figure 67**.

The formate pyridine- and deuterio-pyridine spectra are a good demonstration case for many of the conclusions and observations made previously about the acetate and formate bridged complexes of chromium(III) and iron(III): In general, there is a good match of the calculated spectra to experimental observations. Again, the $\delta(\text{CH}_3)$ and $\delta(\text{CH})$ vibrations are strongly underreported in the IRMPD spectrum of all three species, hinting at a low IVR efficiency for energy absorbed in this type of normal mode. The acetate species especially lacks the strong predicted band at slightly under 1440 cm^{-1} . This is already well known from the other acetate species, as seen clearly in **Figure 23** and **Figure 40**, although the bands were not so clearly separated in the simulated spectra there. For the formate, we observe the $\nu(\text{Py-CH})$ and $\nu(\text{COO})_{\text{as}}$ closely together, and at high laser fluence they merge to a very broad asymmetric peak from $1550 - 1680\text{ cm}^{-1}$.

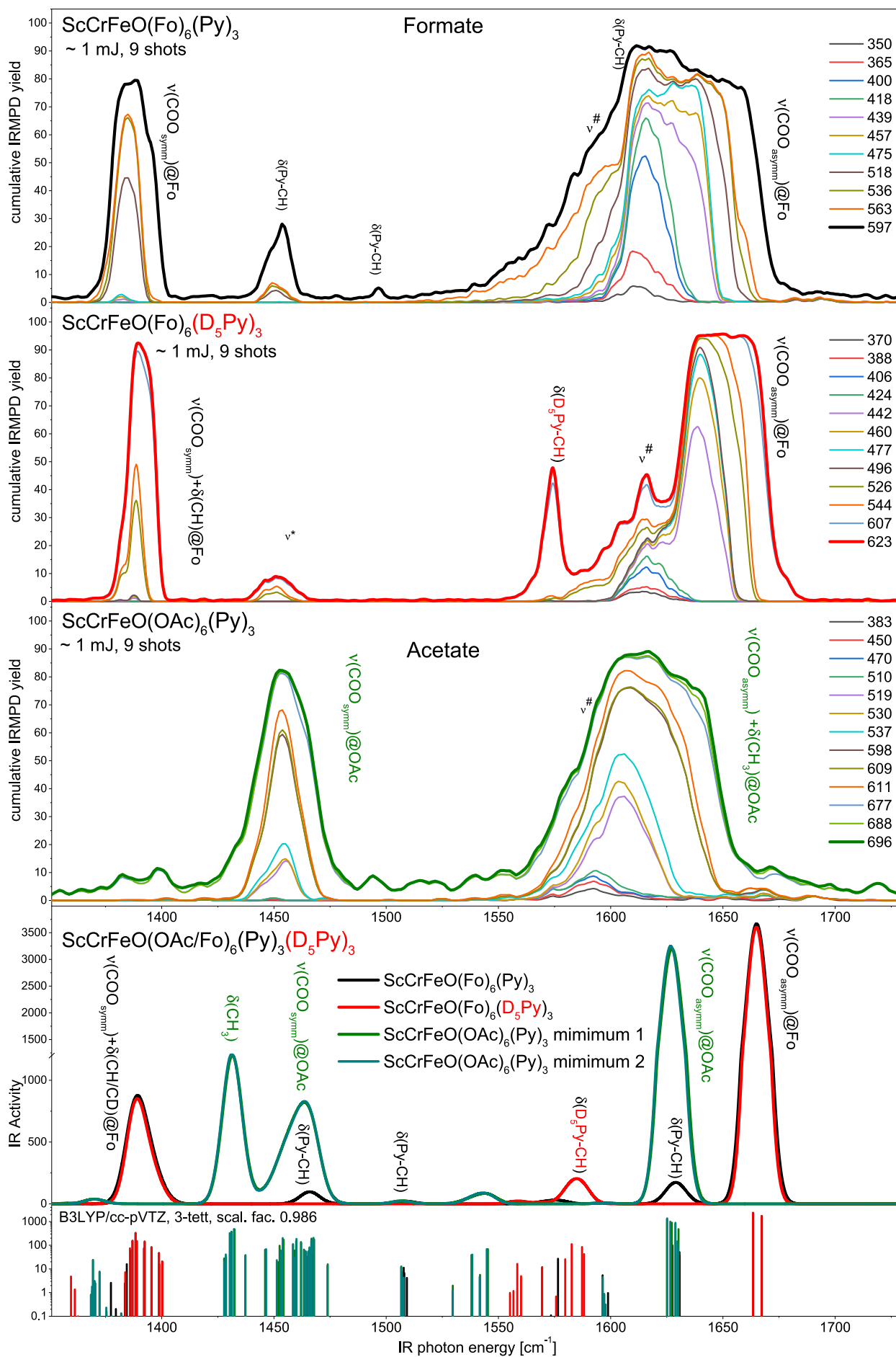


Figure 67 Bridging ligand induced changes in the IRMPD spectrum of $[\text{ScCrFeO}(\text{Fo})_6(\text{Py})_3]^+$, $[\text{ScCrFeO}(\text{Fo})_6(\text{D}_5\text{Py})_3]^+$ and $[\text{ScCrFeO}(\text{OAc})_6(\text{Py})_3]^+$. Cumulative fragment trace labels in m/z .

At low laser power and single shot conditions (**Figure 105**, appendix), the peak is much better resolved. Overall there seems to be more than just the $\delta(\text{Py-CH})$ and $\nu(\text{COO})_{\text{as}}$ peaks present, especially the peak marked with $\delta(\text{Py-CH})$ is broader than typical for a solitary peak of its kind, for example as seen in the perdeuterated pyridine formate spectrum, at about 1570 cm^{-1} .

The formate species with deuterated formates is an interesting case. The band shows good resolution, even at maximum laser power and the maximum possible number of consecutive laser shots. This matches the slightly higher stability of **D₅-pyridine** as observed by CID (see **Figure 74**). However, a band marked ν^* still remains for the deuterated pyridine at the former $\delta(\text{Py-CH})$ position.

The fragment mass traces are of help once more in understanding this situation. In a relatively narrow region around 1630 cm^{-1} , fragmentation into lower mass fragments is greatly enhanced. This, in one possible explanation, is interpreted as the combination of IR absorption by the pyridine chromophores and additionally a much broader hot band. This hot band shows curious behavior in the case of deuterated pyridine (see **Figure 105**), where it can be seen without overlap with the now red shifted **D₅-pyridine** band. Its exact nature is still to be determined, but one candidate may be an overtone of the $\delta(\text{COO})$ mode. This is probably intensified by the asymmetric situation of the metal core, as caused by the heterotrimetallic structure motif.

An alternative explanation would be partial hydrolysis by water molecules attaching to the excited molecule in the trap, as discussed in section 8.1. This may be supported by the successive development of this spectral feature with increasing laser power and shot count (**Figure 105**). Presumably, it is the same feature we already know from the water adducts and the bare formates. This would be along the lines of the arguments given in section 8.1, indicating a general susceptibility of formates; and as pertinent here, pyridine coordinated carboxylates; to hydrolysis by in-trap water adduction. Even after isolating the correct ion mass in the ion trap; during the 100ms - 1s the IRMPD experiment takes place in, water can still attach to the molecular ion and then lead to enhanced partial hydrolysis. This is sensitizing the ion to fragmentation by IR photons of the appropriate wavelength, by creating semi-detached monodentate carboxylate groups that readily pump energy in an already partially weakened ion core.

For the acetate $\text{ScCrFeO}(\text{OAc})_6\text{Py}_3$, both torsional minima of the pyridine orientation on the scandium metal center are calculated separately. Two orientations of the pyridine are almost equally favored, both are slightly canted from the perpendicular orientation of the pyridine relative to the metal plane, as introduced in section 4.6 in **Figure 30**. For all practical purposes, both torsional isomers are equivalent and result in basically identical predicted infrared spectra.

8.3 References Chapter 8

1. Johnson, M. K., Cannon, R. D. & Powell, D. B. Vibrational spectra of carboxylato complexes—IV. Mixed-metal and mixed-valence oxo-trinuclear complexes. *Spectrochimica Acta Part A: Molecular Spectroscopy* **38**, 307-315 (1982).
2. Maragh, P. T., Thomas, S. E. & Dasgupta, T. P. Kinetics and mechanism of the aquation of the trinuclear cation, $[\mu_3\text{-oxo-triaqua-hexakis}(\text{acetato})\text{tris}(\text{iron}(\text{III}))]^{+}$ in perchloric acid media. *Inorganica Chimica Acta* **358**, 3610-3616 (2005).
3. Royer, A. C., Russell, K., Belmore, K. & Vincent, J. B. Formation of oxo-centered trinuclear chromium carboxylate complexes and hydrolysis of Cr³⁺ as established by paramagnetic ²H NMR spectroscopy. *Journal of Inorganic Biochemistry* **131**, 12-20 (2014).
4. Døssing, A. & Ders. Recent advances in the coordination chemistry of hydroxo-bridged complexes of chromium(III). *Coordination Chemistry Reviews* **280**, 38-53 (2014).
5. Springborg, J. *et al.* Inter- and Intramolecular Reactions of Binuclear Chromium(III) Amine Complexes with Bridging and Terminally Coordinated Carboxylate. *Acta Chemica Scandinavica* **46**, 1047-1054 (1992).
6. Lawrence, M. A. W., Maragh, P. T. & Dasgupta, T. P. Kinetics and mechanism of the aquation of a series of mixed-metal oxo-centered trinuclear cations, $3\text{-oxo-triaqua-hexakis}(\text{carboxylato})\text{bis}(\text{chromium}(\text{III})\text{iron}(\text{III}))^{+}$, $[\text{Cr}(\text{III})_2\text{Fe}(\text{III})\text{O}(\text{RCOO})_6(\text{H}_2\text{O})_3]^{+}$, (R=H, CH₃, and (CH₃)₂CH) in perchloric acid media. *Journal of Coordination Chemistry* **63**, 2517-2527 (2010).
7. Fujihara, T. *et al.* Kinetic Study on the Substitution of Dimethylacetamide for the Terminal Aqua Ligands in the Trinuclear Chromium(III) Complexes $[\text{Cr}_3(\mu_3\text{-O})(\mu\text{-RCO}_2)_6(\text{H}_2\text{O})_3]^{+}$ (R = H, CH₃, CH₃CH₂, CH₂Cl, CHCl₂, CH₃OCH₂, (CH₃)₃C, CH₂ClCH₂, (C. *Inorganic Chemistry* **37**, 3779-3784 (1998).
8. Fujihara, T., Abe, Y. & Kaizaki, S. Base hydrolysis in homometallic dinuclear chromium(III) complexes bridged by hydroxide and carboxylate. *Journal of the Chemical Society, Dalton Transactions* 1823-1831 (1995). doi:10.1039/DT9950001823
9. Lin, J., Neoh, K. G. & Teo, W. koon. Thermogravimetry–FTIR study of the surface formate decomposition on Cu, CuCl, Cu₂O and CuO. Correlations between reaction selectivity and structural properties. *J. Chem. Soc., Faraday Trans.* **90**, 355-362 (1994).
10. Deacon, G. & Phillips, R. J. Relationships between the carbon-oxygen stretching frequencies of carboxylato complexes and the type of carboxylate coordination. *Coordination Chemistry Reviews* **33**, 227-250 (1980).
11. Ferey, G. A Chromium Terephthalate-Based Solid with Unusually Large Pore Volumes and Surface Area. *Science* **309**, 2040-2042 (2005).
12. Low, J. J., Jakubczak, P., Abrahamian, J. F., Faheem, S. A. & Willis, R. R. Virtual High Throughput Screening Confirmed Experimentally: Porous Coordination Polymer Hydration. 15834-15842 (2009). doi:10.1021/ja9061344
13. Lee, Y. J., Chang, Y. J., Lee, D. J. & Hsu, J. P. Water stable metal-organic framework as adsorbent from aqueous solution: A mini-review. *Journal of the Taiwan Institute of Chemical Engineers* **0**, 1-8 (2018).
14. Hong, K., Bak, W., Moon, D. & Chun, H. Bistable and porous metal-organic frameworks with charge-neutral acs net based on heterometallic M₃O(CO₂)₆ building blocks. *Crystal Growth and Design* **13**, 4066-4070 (2013).
15. Kongpatpanich, K. *et al.* Synthesis and Porous Properties of Chromium Azolate Porous Coordination Polymers. *Inorganic Chemistry* **53**, 9870-9875 (2014).

9 Summary and Outlook

9.1 Summary

Inverse coordination complexes, of which the complex class discussed in this thesis is a notable example, are introduced in chapter 1. Many examples are shown, highlighting the huge range of variations of the participating metals, the bridging and external ligands, including notable properties.

The experimental and theoretical methods used in this thesis are briefly introduced in chapter 2. The working principles of the used ion trap mass spectrometers, the ESI ion source, the tunable IR laser system, and the CID method are introduced. The studied complexes show behavior that necessitates the use of multi component logistic functions in the treatment of the CID spectra, and fragment channel specific treatment of the IRMPD data. In addition, the general idea of DFT calculations, needed for the interpretation of the obtained spectra, is explained.

The infrared spectra of the different ligands are introduced in a brief literature review in chapter 3; both the axial ligand pyridine and the bridging carboxylate ligands, formate and acetate. Their changes in different environments or different bonding situations are discussed and visualized, especially the interplay between fundamental-, overtone-, and combination bands, as well as Fermi resonances between them.

A broad range of DFT calculations are shown in chapter 4. They are used to simulate the geometry, the bonding situation, relative stability and flexibility of the discussed complexes, and to specify the observed trends. Changes in the total electronic energy and possible cooperative effects are investigated by applying the differential many body cooperativity (DMBC) formalism. Moderate cooperative effects upon metal exchange are reported.

The synthesis and the mass spectra, as well as the typical fragmentation patterns of the basic carboxylates, are shown in chapter 5. In that chapter, the CID fragmentation spectra and gas phase IRMPD infrared spectra of a systematic group of transition metal complexes are shown and discussed: the trimetallic oxo-centered homo- and heterometallic complexes of trivalent chromium and iron, with formate and acetate bridging ligands, and pyridine as axial ligands. The stability of the complexes, as predicted by appropriate *ab initio* simulations, is shown to agree with collision induced dissociation (CID) measurements. These simulations also correctly predict the trends in the band splitting of the symmetric and asymmetric carboxylate stretch modes, but fail to account for anharmonic effects observed specifically in the mid IR range.

A new variation on the infrared multi photon dissociation (IRMPD) spectroscopy method is introduced and evaluated. In addition to the commonly considered total fragment yield, the cumulative fragment yield can be used to plot the wavelength dependent relative abundance of different fragmentation products. This is shown to include valuable additional information on the excited chromophors and their coupling to specific fragmentation channels.

In chapter 6, high quality homo- and heterometallic IRMPD spectra of oxo centered carboxylate complexes of chromium and iron show the impacts of the influencing factors: the metal centers, the bridging ligands, their carboxylate stretch modes and CH bend modes, and the terminal ligands. Additional spectra can be found in the Appendix B. The DMBC formalism is applied to the band splitting of the carboxylate stretch modes, small cooperative effects can be seen.

In chapter 7, the CH stretch modes are discussed. In all four formate spectra, anharmonic effects are necessary to explain the observed spectra: combination bands of both carboxylate stretch modes and a Fermi resonance of the fundamental of the CH stretch mode, and a combination band of the asymmetric carboxylate stretch mode with the CH bend mode of the formate bridging ligand.

In chapter 8, for the water adduct species, mixed pyridine water complexes, and the heterotrimetallic ScCrFe complexes, partial hydrolysis is proposed to account for the changes in the observed carboxylic stretch modes. This has potential importance in the understanding or designing the stability and activity of metal organic frameworks based on the basic carboxylates.

9.2 Outlook and Ongoing Work

9.2.1 Synthesis of Interesting Complexes

The pool of interesting transition metals with relevant magnetic, optical, and chemical properties, is obviously not exhausted with cobalt, chromium, iron, or scandium.

For tuning the ligand strength and modifying band positions, fluoroformate¹ and deuterio-formate², as well as halogenated acetates³ (such as trifluoroacetate⁴ and tribromoacetate⁵), can help identify and experimentally verify band assignments. This can happen by suppressing interfering bands, as well as by tuning the properties of the metal core and of spectroscopic features.

Another idea is the substitution⁶ of one of the carboxylate bridging ligands by a zwitterionic carboxylate, such as betaine⁷, to make the neutral mixed valence complexes accessible by mass spectrometry. However, the strong dipole moment of these ligands would definitely influence the metal core, and the methyl groups might have interfering bands in both the CO and CH spectral regions.

Furthermore, it will be interesting to study coupled complexes like the oxoFeFe mixed valence compound, with four iron(III) formate species coupled by a central iron(II) complex.

Another high priority group of species on the to do list are the deuterio-formate complexes, with iron deuterio-formate being the most pressing candidate; as deuterated formate has been shown to exhibit even stronger anharmonic behavior than already observed in the CH spectral region. By removing the interfering CH bands, it may be possible to further support the hypothesis that the broad band observed for the acetate and formate complexes (at 2750 - 3000 cm⁻¹) is a combination band that includes metal core vibrational modes.

9.2.2 IR Measurements

9.2.2.1 Standard and Cold IRMPD

IRMPD spectroscopy¹² in our ICR mass spectrometer has the benefit of immensely improved vacuum quality, as compared to the quadrupole ion traps used in this thesis. Therefore, the problem of in-trap water adduction is mitigated. This is very limiting, especially for the chromium species. Simultaneously, by using the cryostat of the instrument, the resolution of the spectra under cold conditions can be improved greatly by reducing thermal broadening.

Additionally, this allows for the study of very weakly coordinating ligands, like nitrogen¹³, or similarly lightly bound ligands, that would not be stable at elevated temperatures. A good example on the benefits of lowering the ion temperature can be seen in Maćzka et al.¹⁴. The water spectra, as discussed in section 8.1, show hints at either overtones or hydrolysis¹⁵ in the CO spectral range that should be investigated further in this instrument.

For all open questions, two color IRMPD spectroscopy¹⁶ may be of use. It has the potential to gather further evidence on the nature of the anharmonic bands seen in the CH region of the formate complexes. This applies to both modes; the one that was identified as the combination band of the symmetric and asymmetric carboxylate band, and the other combination bands. For previously missing or weak features, it can improve signal intensity by pumping energy into another mode, up to levels slightly under the fragmentation threshold. This amplifies the fragmentation response of weak bands at the wavelength the probe laser is scanning⁸.

The indications on possible hydrolysis of the carboxylate bridge (see **Figure 65**), as modified by terminal ligands, ought to be investigated this way.

Given the current data set, mixed ligand formate spectra with pyridine and water seem to be promising, especially for the chromium formate. It is relatively stable by itself, but as witnessed with the replacement series of Cr to Fe, Cr₃ formate should be right on the verge to be susceptible to hydrolysis through modifying its stability by pyridine coordination.

9.2.2.2 Other Frequency Ranges

The $\nu(\text{M}_3\text{O})_{\text{as}}$ ¹⁷⁻¹⁹ at about 600 - 650 cm⁻¹ and additional bands in that region will give direct insight into the gas phase structure of the complexes. They have the potential to aid in identifying constituent bands of combination and overtone bands, in the observed spectral ranges. The carboxylate bands studied in this thesis only provide indirect information on the metal core. Such gas phase experiments are possible at free electron laser (FEL) facilities. For the condensed phase, the sensitivity of these bands on changes in the mixed valence iron carboxylates is shown by Cannon et al.²⁰.

9.2.3 Kinetics

There seem to be hints for gas phase interconversions between different regio-isomers of heterometallic carboxylates when the isomer population from the ion source or a fragmentation step is not at thermodynamic equilibrium. Further studies are needed to confirm and observe. However, in solution, this has been studied previously^{15,21,22}. The possible gas phase hydrolysis of the formates warrants further attention as well.

A promising two-color experiment may be the time dependent observation of the IVR energy transfer between deuterated/non-deuterated pyridine ligands, as observed in 5.6.1. Energy can be pumped into one chromophore, and delay-dependent changes in the fragmentation intensity of the other ligands by the probe laser should be observed. This is only possible if the timescale is slow enough to be observed with the pulse lengths of our laser. However, this might not be achievable, as very short time scales (ps-ns) have been observed previously²³, although for smaller systems than found in this work.

9.2.4 UV-Vis

The spectra taken by Blake et al.^{24,25} already show compelling behavior in the chromium iron homo- and heterometallic acetates. Therefore, taking gas phase UV-Vis measurements would be extremely interesting. Such measurements are another window into the interaction of different metal centers with each other and their ligands. The spectra we took in solution (section 11.9, **Figure 108**) already show a strong solvatochromic effect, stressing the need for measurements in isolation.

9.2.5 X-ray Magnetic Circular Dichroism (XMCD)

Presently, our group is conducting a long term characterization effort of the intrinsic magnetism in the $[\text{Fe}_3\text{O}(\text{OAc})_6(\text{Py})_n]^+$ complexes by x-ray ionization analysis, as published for other transition metal clusters before⁸⁻¹⁰. The predicted couplings from our joint paper¹¹ in chapter 10 have already been confirmed in yet unpublished results. The next step will be utilizing the higher mass resolution of an ICR setup at the Paul Scherrer Institute (PSI) for future XMCD measurements, as currently in preparation. This resolution is crucial when mixed metal species cannot be synthesized in sufficient purity and are obtained as stochastic mixtures. Depending on the metal combination, the isolation can be quite challenging for simple separation mechanisms, like medium resolution quadrupole mass filters.

9.2.6 Future DFT Studies

Differential many body cooperativity (DMBC) calculations (as done on a Pd_3 complex²⁶) are suggested for non-oxo-centered ($\text{Pd}_{3-n}\text{Pt}_n$), $n = 0 - 3$, hexa-acetate complexes²⁷⁻³² in section 4.7. This will help to bridge the gap between the oxo-centered carboxylates and other trinuclear 3-MET complexes, as well as to study the influence of the central oxo-group on the cooperativity between metal centers.

The overtones and anharmonicities of the formate group are good candidates for anharmonic calculations using methods like VSCF-PT2³³.

Furthermore, investigating possible reaction pathways of the suggested carboxylate hydrolysis, analogous to **Figure 65**, will be helpful. Together with the IR spectra, simulations of the different intermediates are needed to correlate the observed spectra to the relative progression of the reaction. This will help to narrow down a correct description of the situation.

9.2.7 Trapped Ion Mobility Spectrometry (TIMS)

The CID measurements discussed in section 5.3 suggest the existence of a variety of regio-isomers. Often isolating a specific isomer is of interest, especially when they are used as the tuning factor for properties of a specific metal center or the metal interaction. As suggested in our 3-MET proposal for the final funding period, ion mobility, specifically trapped ion mobility spectrometry (TIMS), can be a method of separating isomers by keeping ions of the same collisional cross section (CCS) stationary in a constant gas flow. An attractive potential difference is balanced with drag induced by collisions with the background gas flow; given a sufficient difference of the CCS, isomers can be separated.

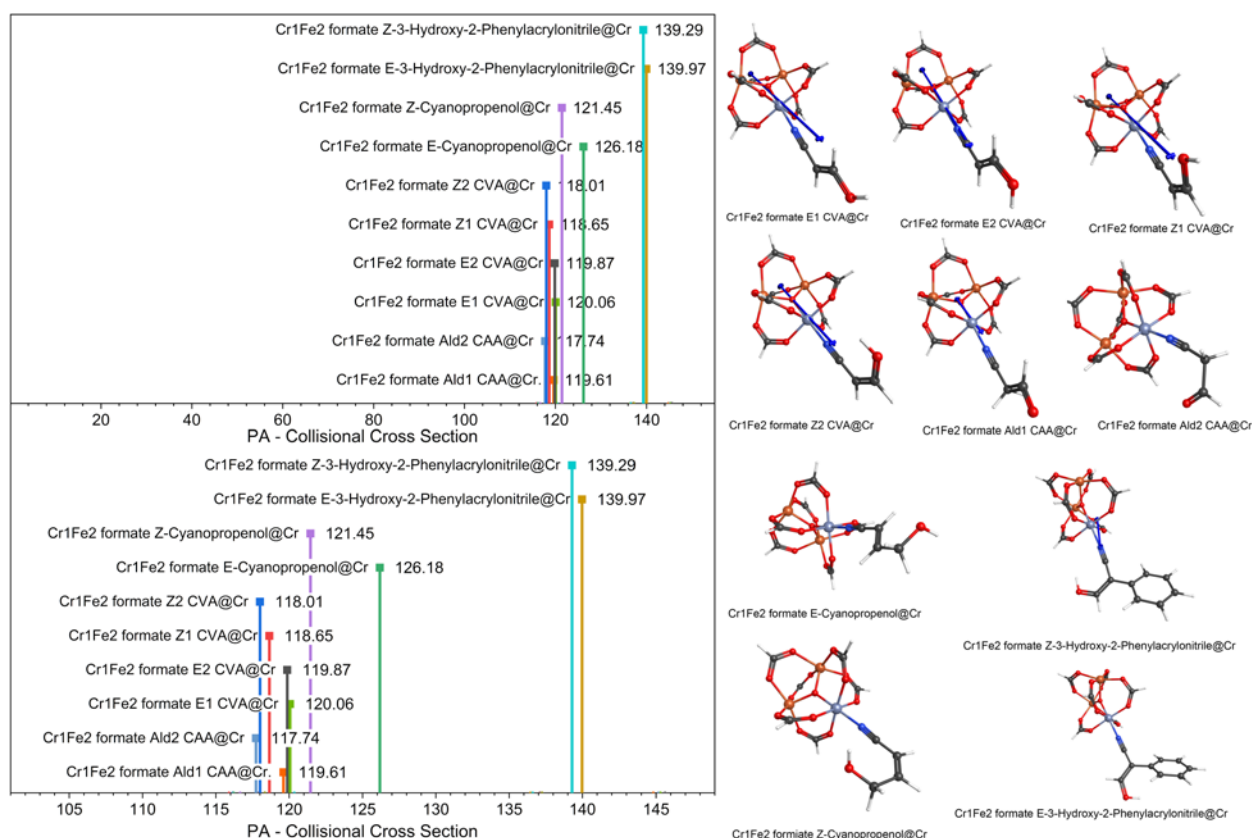


Figure 68 Predicted collisional cross sections (CCS) of several complexes for separation by TIMS (trapped ion mobility spectrometry), calculations done by Patrick Weis, KIT.

Preliminary calculations suggest that regio-isomers of pyridine at different metal centers are too similar in their cross section to isolate with typical TIMS resolutions. However, ligand isomer differentiation may be possible. This still gives us the ability to create a considerable zoo of complexes in a controlled fashion; each with slightly different properties. For example, the different dipole moments of E/Z isomers of cyanopropenole ligands are promising candidates.

9.3 References Chapter 9

- Schloter, K., Nagel, U. & Beck, W. Structure, stability and vibrational spectrum of the fluoroformate anion. *Chemische Berichte* **113**, 3775-3782 (1980).
- Gerardi, H. K. *et al.* Unraveling the Anomalous Solvatochromic Response of the Formate Ion Vibrational Spectrum: An Infrared, Ar-Tagging Study of the HCO_2^- , DCO_2^- , and $\text{HCO}_2^- \cdot \text{H}_2\text{O}$ Ions. *The Journal of Physical Chemistry Letters* **2**, 2437-2441 (2011).
- Schloter, K., Nagel, U. & Beck, W. Experimental and theoretical characterization of Fe_2Cr trinuclear-oxo-centered complex with a $\text{CF}_2\text{CICOO}-$ bridge. *Chemische Berichte* **113**, 3775-3782 (1980).
- Puri, M. & Verma, R. D. Trinuclear metal(III) trifluoroacetates. *Monatshefte für Chemie Chemical Monthly* **115**, 533-539 (1984).
- Mukherjee, R. *et al.* Structural and Spectroscopic Evidence for the Formation of Trinuclear and Tetranuclear Vanadium(III)/Carboxylate Complexes of Acetate and Related Derivatives in Aqueous Solution. *Inorganic Chemistry* **46**, 1575-1585 (2007).
- Ikegami, A., Abe, M., Inatomi, A. & Hisaeda, Y. Synthetic Design of Heterometallic Cluster Compounds with Site-Selective and Stepwise Substitution of Bridging Carboxylates. *Chemistry - A European Journal* **16**, 4438-4441 (2010).
- Quagliano, J. V., Kida, S. & Fujita, J. Preparation and Infrared Studies of Metal Complexes Containing the Zwitterion Ligand Betaine, $(\text{CH}_3)_3\text{NCH}_2\text{COO}^-$. *Journal of the American Chemical Society* **84**, 724-729 (1962).
- Hewer, J. M. Magnetic and Structural Characterization of Isolated Gaseous Ions by XMCD and IRMPD Spectroscopy. (TU Kaiserslautern, 2017).
- Meyer, J., Tombers, M., Niedner-Schatteburg, G. & Lau, T. *Magnetic characterization of Single Molecular Magnets (SMM) of the [Fe₄L_n2] type by X-ray Magnetic Circular Dichroism (XMCD)*. (2010).
- Schütz, G., Goering, E. & Stoll, H. Synchrotron Radiation Techniques Based on X-ray Magnetic Circular Dichroism. in *Handbook of Magnetism and Advanced Magnetic Materials* 1312 (John Wiley & Sons, Ltd, 2007). doi:10.1002/9780470022184.hmm304
- Lang, J. *et al.* Magnetostructural correlation in isolated trinuclear iron(III) oxo acetate complexes. *Physical Chemistry Chemical Physics* **20**, 16673-16685 (2018).
- Jašík, J., Žabka, J., Roithová, J. & Gerlich, D. Infrared spectroscopy of trapped molecular dications below 4K. *International Journal of Mass Spectrometry* **354-355**, 204-210 (2013).
- Lang, J., Mohrbach, J., Dillinger, S., Hewer, J. M. & Niedner-Schatteburg, G. Vibrational blue shift of coordinated N_2 in $[\text{Fe}_3\text{O}(\text{OAc})_6(\text{N}_2)_n]^+$: “non-classical” dinitrogen complexes. *Chemical Communications* **53**, 420-423 (2017).
- Mączka, M., Pietraszko, A., Macalik, B. & Hermanowicz, K. Structure, Phonon Properties, and Order–Disorder Transition in the Metal Formate Framework of $[\text{NH}_4][\text{Mg}(\text{HCOO})_3]$. *Inorganic Chemistry* **53**, 787-794 (2014).
- Lawrence, M. A. W., Maragh, P. T. & Dasgupta, T. P. Kinetics and mechanism of the aquation of a series of mixed-metal oxo-centered trinuclear cations, 3-oxo-triaqua-hexakis(carboxylato)bis-(chromium(III)(iron(III)))⁺, $[\text{Cr}^{\text{III}}_2\text{Fe}^{\text{III}}\text{O}(\text{RCOO})_6(\text{H}_2\text{O})_3]^+$, (R=H, CH₃, and (CH₃)₂CH) in perchloric acid media. *Journal of Coordination Chemistry* **63**, 2517-2527 (2010).
- Nosenko, Y., Menges, F., Riehn, C. & Niedner-Schatteburg, G. Investigation by two-color IR dissociation spectroscopy of Hoogsteen-type binding in a metalated nucleobase pair mimic. *Physical Chemistry Chemical Physics* **15**, 8171-8178 (2013).
- Sowrey, F. E. *et al.* Spin frustration and concealed asymmetry: structure and magnetic spectrum of $[\text{Fe}_3\text{O}(\text{O}_2\text{CPh})_6(\text{py})_3]\text{ClO}_4 \cdot \text{py} \cdot \dagger$. *Journal of the Chemical Society, Dalton Transactions* **6**, 862-866 (2001).
- Peng, L. *et al.* Using Predefined $\text{M}_3(\mu_3\text{-O})$ Clusters as Building Blocks for an Isostructural Series of Metal–Organic Frameworks. *ACS Applied Materials and Interfaces* **9**, 23957-23966 (2017).
- Peng, L. *et al.* Supporting Information Using to 3Using Predefined $\text{M}_3(\mu_3\text{-O})$ Clusters as Building Blocks for an Isostructural Series of Metal–Organic Frameworks. *ACS Applied Materials & Interfaces* **9**, 23957-23966 (2017).
- Wu, R. W. *et al.* Electron Transfer Rates in a Trinuclear Mixed-Valence Iron(III,III,II) Molecule: A

- Variable-Temperature Infrared Spectroscopic Study. *Journal of the Chemical Society-Chemical Communications* **30**, 1657-1658 (1994).
21. Maragh, P. T., Thomas, S. E. & Dasgupta, T. P. Kinetics and mechanism of the aquation of the trinuclear cation, $[\mu_3\text{-oxo-triaqua-hexakis}(\text{acetato})\text{tris}(\text{iron}(\text{III}))]^{+}$ in perchloric acid media. *Inorganica Chimica Acta* **358**, 3610-3616 (2005).
 22. Chaudhary, S. & Van Horn, J. D. Breakdown kinetics of the tri-chromium(III) oxo acetate cluster ($[\text{Cr}_3\text{O}(\text{OAc})_6]^{+}$) with some ligands of biological interest. *Journal of Inorganic Biochemistry* **101**, 329-335 (2007).
 23. Nesbitt, D. J. & Field, R. W. Vibrational Energy Flow in Highly Excited Molecules: Role of Intramolecular Vibrational Redistribution. *The Journal of Physical Chemistry* **100**, 12735-12756 (1996).
 24. Blake, A. B., Sinn, E., Yavari, A., Murray, K. S. & Moubaraki, B. Oxo-centred trinuclear acetate complexes containing mixed-metal clusters. Crystal structure of a chromium(III)iron(III)nickel(II) complex and magnetic properties of a dichromium(III)magnesium(II) complex ‡. *Journal of the Chemical Society, Dalton Transactions* 45-50 (1998). doi:10.1039/a705778d
 25. Blake, A. B. & Yavari, A. Heterotrimeric basic acetates containing chromium(III), iron(III), and a divalent metal: spectroscopic consequences of Metal–Metal interactions. *J. Chem. Soc., Chem. Commun.* 1247-1249 (1982). doi:10.1039/C39820001247
 26. Chmela, J. *et al.* Differential Many-Body Cooperativity in Electronic Spectra of Oligonuclear Transition-Metal Complexes. *ChemPhysChem* **17**, 37-45 (2016).
 27. Stephenson, T. A., Morehouse, S. M., Powell, A. R., Heffer, J. P. & Wilkinson, G. 667. Carboxylates of palladium, platinum, and rhodium, and their adducts. *Journal of the Chemical Society (Resumed)* 3632 (1965). doi:10.1039/jr9650003632
 28. Skapski, A. C. & Smart, M. L. The Crystal Structure of Trimeric Palladium(II) Acetate. *Chemical Communications* 658-259 (1970).
 29. Váňa, J. *et al.* The role of trinuclear species in a palladium acetate/trifluoroacetic acid catalytic system. *Dalton Transactions* **46**, 16269-16275 (2017).
 30. Carole, W. A. & Colacot, T. J. Understanding Palladium Acetate from a User Perspective. *Chemistry - A European Journal* **22**, 7686-7695 (2016).
 31. Pakula, R. J. *et al.* Palladium Acetate Revisited: Unusual Ring-Current Effects, One-Electron Reduction, and Metal–Metal Bonding. *Inorganic Chemistry* **57**, 8046-8049 (2018).
 32. Pakula, R. J. *et al.* Supporting Information for “Palladium Acetate Revisited: Unusual Ring-Current Effects, One-Electron Reduction, and Metal–Metal Bonding.” *Inorganic Chemistry* **57**, 8046-8049 (2018).
 33. Roy, T. K., Carrington, T. & Gerber, R. B. Approximate first-principles anharmonic calculations of polyatomic spectra using MP2 and B3LYP potentials: Comparisons with experiment. *Journal of Physical Chemistry A* **118**, 6730-6739 (2014).

10 Appendix A: Magnetostructural Correlation in Isolated Trinuclear Iron(III) Oxo Acetate Complexes

10.1 Preamble

The following chapter is a reprint of our publication in the journal 'Physical Chemistry Chemical Physics'. The supplementary information is also available in section 10.2.

My contribution to this work includes synthesizing a set of deuterated compounds, for which I took additional IRMPD measurements to supply evidence for our band assignments. Additional DFT calculations necessary for the interpretation of the data, as well as to clarify the torsional ambiguity of the pyridine ligands, were performed by me. I recorded supplementary mass spectra to answer ambiguities in the fragmentation behavior of the complexes. I participated in refining the band assignments, the gaussian fits of the deuterated species, and the more in-depth discussion of the spectra.

Full Reference:

Magnetostructural Correlation in Isolated Trinuclear Iron(III) Oxo Acetate Complexes

Johannes Lang, Joachim M. Hoyer, Jonathan Meyer, Jonas Schuchmann, Christoph van Wüllen
and Gereon Niedner-Schatteburg

Phys. Chem. Chem. Phys., 2018, **20**, 16673-16685

<http://dx.doi.org/10.1039/C7CP07549A>

Reprint license

Reproduced by permission of The Royal Society of Chemistry:

The Royal Society of Chemistry (RSC) hereby grants permission for the use of your paper(s) specified below in the printed and microfilm version of your thesis. You may also make available the PDF version of your paper(s) that the RSC sent to the corresponding author(s) of your paper(s) upon publication of the paper(s) in the following ways: in your thesis via any website that your university may have for the deposition of theses, via your university's Intranet or via your own personal website. We are however unable to grant you permission to include the PDF version of the paper(s) on its own in your institutional repository. The Royal Society of Chemistry is a signatory to the STM Guidelines on Permissions (available on request).

<http://pubs.rsc.org/en/content/articlelanding/2018/cp/c7cp07549>



PCCP

PAPER

Magnetostructural correlation in isolated trinuclear iron(III) oxo acetate complexes†

Cite this: *Phys. Chem. Chem. Phys.*, 2018, 20, 16673

Johannes Lang, Joachim M. Hewer, Jonathan Meyer,  Jonas Schuchmann, Christoph van Wüllen and Gereon Niedner-Schatteburg *

We elucidate the correlation between geometric structures and magnetic couplings in trinuclear iron(III) oxo acetate complexes $[\text{Fe}_3\text{O}(\text{OAc})_6(\text{Py})_n]^+$ ($n = 0, 1, 2, 3$) when isolated and trapped as gaseous ions. Structural information arises from Infra Red-Multiple Photon Dissociation (IR-MPD) and Collision Induced Dissociation (CID) experiments in conjunction with Density Functional Theory (DFT) based calculations. We simulate the antiferromagnetic couplings between the Fe^{III} (d^5) centers by employing a Broken Symmetry approach within our DFT calculations, and we extract the associated antiferromagnetic coupling constants. Coordination of one, two or three axial pyridine ligands to the $[\text{Fe}_3\text{O}(\text{OAc})_6]^+$ subunit distorts the geometry of the triangular Fe_3O core. The $\text{Fe}-\text{O}_{\text{central}}$ bond lengths are enlarged or shortened depending on number of coordinated pyridine ligands. This significantly affects the antiferromagnetic coupling constants between the Fe^{III} centers ranging from -62 cm^{-1} to -28 cm^{-1} in $[\text{Fe}_3\text{O}(\text{OAc})_6(\text{Py})_n]^+$ ($n = 0, 1, 2, 3$). A detailed analysis of the associated exchange couplings indicates a switching of magnetic ground states by pyridine coordination. The total spin S_T in the ground states of $[\text{Fe}_3\text{O}(\text{OAc})_6(\text{Py})_n]^+$ raises from $S_T = 1/2$ ($n = 0$) to $3/2$ ($n = 1$) and $5/2$ ($n = 2$). Coordination of the third pyridine ligand ($n = 3$) re-establishes a spin ground state of $S_T = 1/2$. We thus identify a coordination controlled switching of magnetic ground states.

Received 8th November 2017,
Accepted 26th May 2018

DOI: 10.1039/c7cp07549a

rsc.li/pccp

1. Introduction

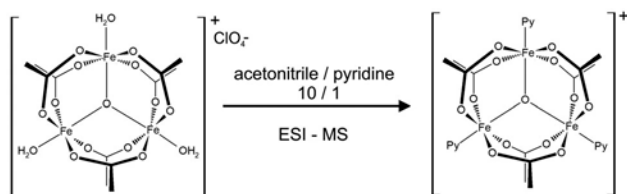
Magnetic properties of polynuclear transition metal complexes relate inextricably to their geometrical structure. It is an active field of research to unravel such magnetostructural correlations^{1–5} since such knowledge is crucial in the rational design of molecular nanomagnets⁶ and in the context of metalloenzymes.⁷ Pairwise distance to coupling correlations are omnipresent, *e.g.* through oxo bridges.⁸ More complex model systems of interest are the oxo-centered trinuclear transition metal (M^{III})₃ acetate complexes of the structural type $[\text{M}_3\text{O}(\text{O}_2\text{R})_6\text{L}_3]^+$ ($\text{L} =$ axial ligands)^{9–13} with $\text{M} = \text{Fe}$ being archetypical. Three Fe ions coordinate around an O_2^- center in a flat triangular arrangement (Fe_3O core). Each of the Fe centers achieves a pseudooctahedral geometry through equatorial coordination with four bridging ligands (O_2R) and axial coordination with an extra monodentate ligand (L). It prevails an antiferromagnetic exchange coupling of the high spin Fe^{III} ions.^{14,15} There is no direct Fe–Fe interaction (distances $> 3 \text{ \AA}$). The electronic ground state is subject of a topological spin frustration: The triangular geometry renders impossible pairwise antiferromagnetic couplings of all three spins.^{16–18}

The electronics of $[\text{M}_3\text{O}(\text{O}_2\text{R})_6\text{L}_3]^+$ complexes are extremely sensitive to intrinsic geometric distortions of the M_3O core¹⁹ induced by the bridging ligands and/or the axial ligands. This was observed before by measurements of the total spin (S_T) in the cases of the symmetrically coordinated $[\text{Fe}_3\text{O}(\text{OAc})_6(\text{H}_2\text{O})_3]\text{NO}_3$ ¹⁵ and the asymmetrically coordinated $[\text{Fe}_3\text{O}(\text{TfEO})_2(\text{O}_2\text{CPh})\text{Cl}_3]$.^{20,21} The former complex revealed a S_T of 1/2 while the latter a S_T of 5/2. All previous experiments have been performed in the condensed phase and external effects such as crystal packing or solvation are assumed to be of minor importance. However, to exclude any external effect it is necessary investigate $[\text{M}_3\text{O}(\text{O}_2\text{R})_6\text{L}_3]^+$ complexes as isolated species in the gas phase.

Electrospray ionization^{20–22} (ESI) enables mass spectrometric investigations of ionic complexes *in vacuo*, and their activation by either photons or collisions. Tandem-MS based methods like Infra Red Multiple Photon dissociation^{23–25} (IR-MPD) and Collision Induced Dissociation^{26–28} (CID) have helped to elucidate molecular structures and vibrations. Both techniques were instrumental under cryogenic conditions^{29–34} and at room temperature.³⁵ The mechanism for molecular dissociation during the IR-MPD process is based on incoherent absorption of multiple photons.^{36,37} The additional energy diffuses into the bath of vibrational background states of the molecule. This process is referred to as intramolecular vibrational redistribution (IVR). Low densities of vibrational states within a molecule may result in an ineffective IVR process, which inhibits molecular dissociation (IVR bottlenecks). In previous

Fachbereich Chemie and Forschungszentrum OPTIMAS, Technische Universität Kaiserslautern, 67663 Kaiserslautern, Germany. E-mail: gns@chemie.uni-kl.de

† Electronic supplementary information (ESI) available. See DOI: 10.1039/c7cp07549a



Scheme 1 The precursor $[\text{Fe}_3\text{O}(\text{OAc})_6(\text{H}_2\text{O})_3]^+$ ($\text{OAc} = \text{CH}_3\text{CO}_2^-$) exchanges in a acetonitrile/pyridine solution (10/1) its three axial H_2O ligands for three stronger bound pyridine ligands. Through ESI/CID we also observe under coordinated species with 0–2 pyridine ligands.

investigations we applied two color IR-MPD schemes to overcome such IVR bottlenecks.³⁸

Experimental results and dedicated *ab initio* calculations have been combined in order to obtain further insight into the structure and intrinsic properties of likely binding motifs.^{39–42} We have previously investigated $[\text{Fe}_3\text{O}(\text{OAc})_6(\text{N}_2)_n]^+$ complexes ($n = 1, 2, 3$) by IR-PD and observed a slight distortion of the triangular Fe_3O core geometry by stepwise N_2 coordination to the Fe centers.⁴³

For this study we exchange the weak binding N_2 ligand with a strong binding pyridine (Py) ligand. The stepwise coordination of 1–3 axial pyridine ligands induces significant geometrical distortions of the Fe_3O core. The main topic in this study is to characterize the geometry distortions and the associated influence on the exchange interactions in the Fe_3O core. We shall provide a description of magnetostructural relationship in isolated $[\text{Fe}_3\text{O}(\text{OAc})_6(\text{Py})_n]^+$ ($n = 0, 1, 2, 3$, cf. Scheme 1). Our gas phase approach excludes bulk or crystal packing effects, and it allows for isolation of under-coordinated molecular ions (e.g. $[\text{Fe}_3\text{O}(\text{OAc})_6]^+$), which would not be accessible in the condensed phases.

We combine experimental CID and IR-MPD investigations of isolated $[\text{Fe}_3\text{O}(\text{OAc})_6(\text{Py})_n]^+$ ($n = 0, 1, 2, 3$) with quantum chemical calculations by broken symmetry Density Functional Theory (DFT) to unravel prevailing magneto structural correlations.

2. Experimental and computational methods

2.1 Collision induced dissociation (CID) and infrared – multiple photon dissociation (IR-MPD) measurements

CID and IR-MPD measurements were performed using a modified Paul-type quadrupole ion trap instrument (AmaZon SL, Bruker Daltonics) at room temperature. The ESI-ion source (Apollo II) was set to positive electrospray ionization mode. Scan speed was $32\,500\text{ m/z s}^{-1}$ (0.3 FWHM/ m/z) with a scan range of 70 to 1200 m/z . Sample solutions of iron(III) oxo acetate perchlorate hydrate ($[\text{Fe}_3\text{O}(\text{OAc})_6(\text{H}_2\text{O})_3(\text{ClO}_4)]$; $\text{OAc} = \text{CH}_3\text{CO}_2^-$; cf. Scheme 1) in a solvent mixture of acetonitrile/pyridine = 100/1 at concentrations of $1 \times 10^{-5}\text{ mol l}^{-1}$ were continuously infused into the ESI chamber by a syringe pump at a flow rate of $2\text{ }\mu\text{L min}^{-1}$. Nitrogen was used as drying gas with a flow rate of 3.0 L min^{-1} at $210\text{ }^\circ\text{C}$. The solutions were sprayed at a nebulizer pressure of 280 mbar (4 psi) and the electrospray needle was held at 4.5 kV. The Paul trap

consists of a ring electrode and two end caps forming a nearly hyperbolic inner profile. The ions enter and exit the trap through pinholes in the end caps. A high voltage RF (radio frequency) potential (781 kHz) is applied to the ring electrode, while the end caps are grounded. The resulting oscillating quadrupolar electric field allows for the accumulation of the ions within the three electrodes. Depending on the amplitude of the RF voltage, the field traps ions within a wide mass range. An auxiliary dipolar voltage is fed to either the exit cap or both end-caps for subsequent ion isolation and fragmentation. A proportional integral derivative (PID) gas controller maintains a partial Helium buffer gas pressure of *ca.* 10^{-3} mbar inside the trap.

CID-appearance and breakdown curves of $[\text{Fe}_3\text{O}(\text{OAc})_6(\text{Py})_n]^+$ ($n = 0, 1, 2$; $\text{OAc} = \text{CH}_3\text{CO}_2^-$; $\text{Py} = \text{pyridine}$) were recorded with varying excitation amplitudes (0.0 V to 1.5 V), which determine the internal energy scale of the mass spectrometer (E_{lab} in Volt). Relative abundances were calculated according to:

$$I_{\text{tot}}^{\text{fr}}(E_{\text{lab}}) = \left(\frac{\sum_i I_i^{\text{fr}}(E_{\text{lab}})}{\sum_i I_i^{\text{fr}}(E_{\text{lab}}) + \sum_i I_i^{\text{p}}(E_{\text{lab}})} \right) \quad (1)$$

where I_i^{fr} = intensity of the fragment ions and I_i^{p} = intensity of the parent ions. Center of mass transferred fragmentation amplitudes (E_{com}) were calculated from internal amplitudes (E_{lab}) by:

$$E_{\text{com}} = \left(\frac{m_{\text{He}}}{m_{\text{He}} + m_{\text{ion}}} \right) \cdot E_{\text{lab}} \quad (2)$$

where m_{ion} stands for the isotopically averaged mass of the molecular ion. Note, that the current application of the CID technique by RF excitation in presence of multiple collisions results in a so called “slow multi collision heating” mode of operation.^{44,45} Fragmentation amplitude dependent CID spectra were modeled and fitted by sigmoid functions of the type

$$I_{\text{fit}}^{\text{fr}}(E_{\text{com}}) = \frac{1}{1 + e^{(E_{\text{com}}^{50} - E_{\text{com}})B}} \quad (3)$$

using a least-squares criterion.

The E_{com}^{50} fit parameter is the amplitude at which the sigmoid function is at half maximum value, whereas B describes the rise of the sigmoid curve. Due to the correlation of fragmentation amplitude and appearance energy, it is feasible to assume, that the appearance curves can be associated to the relative stability of the $[\text{Fe}_3\text{O}(\text{OAc})_6(\text{Py})_n]^+$ complexes.^{46–49}

A KTP/KTA optical parametric oscillator/amplifier (OPO/A, LaserVision) system pumped by a pulsed 10 Hz injection seeded $\text{Nd}^{3+}:\text{YAG}$ laser (PL8000, Continuum) was used as a source of tunable IR radiation ($\delta n = 0.9\text{ cm}^{-1}$, $\delta t = 7\text{ ns}$) for recording vibrational spectra of $[\text{Fe}_3\text{O}(\text{OAc})_6(\text{Py})_n]^+$ ($n = 0, 1, 2, 3$). The OPA idler wave ($\leq 10\text{ mJ}$ per pulse) was used to record spectra within $2600\text{--}3900\text{ cm}^{-1}$. The difference frequency (DF) between the OPA signal and idler waves generated in a AgGaSe_2 crystal ($\leq 2\text{ mJ}$ per pulse) was applied in the range of $1200\text{--}2100\text{ cm}^{-1}$. After passing through the vacuum chamber the IR beam was directed onto a power meter sensor. The idler beam was focused

by a 50 cm CaF₂ lens. The DF radiation was focused tighter, by a 90° off-axis parabolic silver mirror with an effective focal length of 15 cm. The IR spectra were recorded as ion mass chromatograms while continuously scanning the IR wavelength. An experimental IR-MPD spectrum arises from a plot of the fragmentation efficiency as a function of laser frequency (ν). The IR-MPD yield $Y(\nu)$ is defined as:

$$Y(\nu) = \left(\frac{\sum_i I_i^{\text{fr}}(\nu)}{\sum_i I_i^{\text{fr}}(\nu) + \sum_i I_i^{\text{p}}(\nu)} \right) \quad (4)$$

The IR frequency was calibrated using a wave meter (821B-NIR, Bristol instruments). Laser power curves were recorded in parallel to the IR-MPD spectra through digitizing the analog output of the laser power meter by an ample ADC input of the Amazon SL mass spectrometer electronics. Despite the online IR power measurement (laser pulse energies are potted into the background of each IR-MPD spectrum) the recorded spectra were not normalized due to the intrinsically nonlinear power dependence of IR-MPD fragmentation efficiencies.

2.2 Computational methods

Available crystal structure data of $[\text{Fe}_3\text{O}(\text{OAc})_6(\text{Py})_3](\text{FeBr}_4)^{11}$ served as a starting point to calculate minimum energy structures and linear IR absorption spectra of free $[\text{Fe}_3\text{O}(\text{OAc})_6(\text{Py})_n]^+$ ($n = 0, 1, 2, 3$) complexes. We utilized Density Functional Theory (DFT) using the B3LYP_Gaussian^{50,51} functional and cc-pVTZ basis sets⁵² (C, H, N, O) in combination with the ecp-10-mdf⁵³ effective core potential (Fe) as implemented in a local, customized installation of the TURBOMOLE 6.5 program package⁵⁴⁻⁵⁶ and proven suitable in our previous study of $[\text{Fe}_3\text{O}(\text{OAc})_6(\text{N}_2)_n]^+$ ($n = 1, 2, 3$).⁴³ Our custom CANOSSA program serves to investigate antiferromagnetic couplings between the three high spin d⁵ Fe centers by a broken symmetry approach.^{57,58} It permits to localize anti-parallel, unpaired spins separately on the metal centers of the system (e.g. A and B in the most simple case). A broken symmetry state is constructed from a single determinant wavefunction that reflects the antiferromagnetic coupling. Structures with one spin up electron on atom A and one spin down electron on atom B exhibit regions of positive (atom A) and negative (atom B) spin density. The orbitals in the broken symmetry states are optimized by applying the variational principle.

Geometry optimization of all nuclear coordinates yields multiple local minimum structures. As a first step we performed unrestricted DFT calculations with 1–17 unpaired alpha electrons yielding spin multiplicities $2S + 1$ of 2 (doublet) to 18 (18tet). In all cases a spin multiplicity of 16 was most stable (cf. Fig. S11, ESI[†]). This would indicate three ferromagnetically coupled Fe high spin (d⁵) centers. However, we performed geometry optimizations utilizing CANOSSA to simulate 2×5 unpaired alpha electrons and 1×5 unpaired beta electrons on the three Fe centers. This approach yielded more stable

structures in all cases (cf. S7–S10, ESI[†]). This clearly indicates anti ferromagnetically coupled Fe high spin (d⁵) centers – at the expense of spin frustration to discuss.

Harmonic vibrational frequencies of all calculated spectra are scaled with 0.985 to account for prevailing anharmonicity and broadened with gaussian envelope curves (7 cm⁻¹ FWHM). We choose the scaling factor by matching the calculated asymmetric carboxylate stretching vibration frequency of $[\text{Fe}_3\text{O}(\text{OAc})_6]^+$ to the corresponding band position in the IR-MPD spectrum. Standard Gibbs energies of structures, G^0 , of fragmentation free energies, $\Delta_{\text{fr}}G^0$, were calculated at 300 K assuming a rigid rotor model.

Calculations of coupling constants. The identified minimum energy structures of $[\text{Fe}_3\text{O}(\text{OAc})_6(\text{Py})_n]^+$ ($n = 0, 1, 2, 3$) served to calculate single point energies in the four possible broken symmetry configurations (cf. Scheme 2). We used these single point energies to extract three magnetic coupling constants (J_{ij}) per complex as discussed in the following.

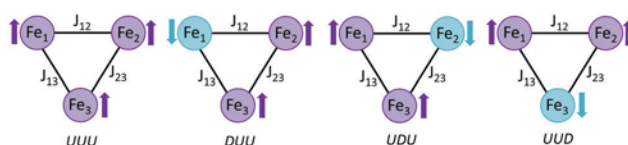
The magnetic coupling between the three spin centers in $[\text{Fe}_3\text{O}(\text{OAc})_6(\text{Py})_n]^+$ ($n = 0, 1, 2, 3$) is governed by the isotropic Heisenberg–Dirac–van Vleck (HDvV) Hamiltonian:⁵⁹

$$\hat{H}_{\text{HDvV}} = - \sum_{i < j} J_{ij} \hat{S}_i \hat{S}_j \quad (5)$$

where J_{ij} are the spin only coupling constants of Fe centers i and j . Ferromagnetic coupling is represented by a positive J value while a negative J value indicates antiferromagnetic coupling. In the case of high spin d⁵ Fe ions in nearly octahedral coordination orbital angular momenta are small, and we are entitled to neglect them in the following. In the case of multiple magnetic centers (as in the present case) it is very difficult to find the eigenfunctions of the HDvV Hamiltonian – even when neglecting orbital momenta. To overcome this issue we make use of an Ising model Hamiltonian^{60,61} in which the total spin operators \hat{S}_i are substituted by the associated z-component $\hat{S}_{z,i}$:

$$\hat{H}_{\text{Ising}} = -2 \sum_{i < j} J_{ij} \hat{S}_{z,i} \hat{S}_{z,j} \quad (6)$$

The eigenvalues of the Ising Hamiltonian and the HDvV Hamiltonian are not identical. However it is possible to extract coupling constants (J_{ij}) from energy differences of appropriate broken symmetry configurations by assuming that all interactions are additive.⁶² Using the Ising Hamiltonian on the four



Scheme 2 Broken symmetry configurations of the triangular Fe₃-core in $[\text{Fe}_3\text{O}(\text{OAc})_6(\text{Py})_n]^+$ ($n = 0, 1, 2, 3$). Purple and turquoise arrows indicate alpha (U) and beta (D) spins, respectively. J_{ij} is the coupling constant between two adjacent Fe-centers. The coordinating ligands are omitted for clarity.

broken symmetry configurations (*cf.* Scheme 2) yields the following eigenvalues:

$$\begin{aligned}\langle \text{UUU} \rangle &= E_0 - 2J_{13}\frac{25}{4} - 2J_{12}\frac{25}{4} - 2J_{23}\frac{25}{4} \\ \langle \text{DUU} \rangle &= E_0 + 2J_{13}\frac{25}{4} + 2J_{12}\frac{25}{4} - 2J_{23}\frac{25}{4} \\ \langle \text{UDU} \rangle &= E_0 - 2J_{13}\frac{25}{4} + 2J_{12}\frac{25}{4} + 2J_{23}\frac{25}{4} \\ \langle \text{UUD} \rangle &= E_0 + 2J_{13}\frac{25}{4} - 2J_{12}\frac{25}{4} + 2J_{23}\frac{25}{4}\end{aligned}\quad (7)$$

By solving this linear system of equations and by the known energies of the four broken symmetry configurations we obtain the three coupling constants J_{12} , J_{13} and J_{23} for $[\text{Fe}_3\text{O}(\text{OAc})_6(\text{Py})_n]^+$ ($n = 0, 1, 2, 3$) – together with an energy offset E_0 – as:

$$\begin{aligned}E_0 &= \frac{1}{4}(\text{UUU} + \text{DUU} + \text{UDU} + \text{UUD}) \\ J_{12} &= \frac{1}{50}(-\text{UUU} + \text{DUU} - \text{UDU} + \text{UUD}) \\ J_{13} &= \frac{1}{50}(-\text{UUU} - \text{DUU} + \text{UDU} + \text{UUD}) \\ J_{23} &= \frac{1}{50}(-\text{UUU} + \text{DUU} + \text{UDU} - \text{UUD})\end{aligned}\quad (8)$$

3. Results and discussion

3.1 CID of $[\text{Fe}_3\text{O}(\text{OAc})_6(\text{Py})_n]^+$ and binding energies of the pyridine ligands

Assignment of mass peaks to molecular species of interest.

Upon electro spraying the above described sample solution and recording mass spectra using the Paul type trap, we observe a series of isotopic peaks at $m/z = 538, 617, 696$ and 775 matching convincingly with simulated isotopic patterns of $[\text{Fe}_3\text{O}(\text{OAc})_6(\text{Py})_n]^+$ ($n = 0, 1, 2, 3$, *cf.* Fig. 1 and Table S1 in the ESI[†]). In solution the axial H_2O ligands of the precursor ion $[\text{Fe}_3\text{O}(\text{OAc})_6(\text{H}_2\text{O})_3]^+$ exchange with the stronger binding pyridine ligand¹¹ (Py, $\text{C}_5\text{H}_5\text{N}$). However, the intensity of the $n = 3$ mass peak is significantly lower than that of $n = 2$. This indicates that $[\text{Fe}_3\text{O}(\text{OAc})_6(\text{Py})_3]^+$ loses one or more pyridine molecules during the ESI and/or trapping process. The decreased resolution of the isotope mass peaks of $[\text{Fe}_3\text{O}(\text{OAc})_6(\text{Py})_3]^+$ at $m/z = 775$ (*cf.* inset of Fig. 1) hints at fragmentation of $[\text{Fe}_3\text{O}(\text{OAc})_6(\text{Py})_3]^+$ during isolation within the Paul trap or the resonance ejection during mass analysis.⁶³ We observe weak mass peaks at 556 , which we assign to $[\text{Fe}_3\text{O}(\text{OAc})_6(\text{H}_2\text{O})]^+$. The satellite peaks at $m/z = 524, 603, 682$ and 761 arise from complexes with a formate group instead of an acetate group in the complex. This exchange likely stems from some impurities of the commercial sample material.

Fragmentation routes and CID curves. CID of the isolated $[\text{Fe}_3\text{O}(\text{OAc})_6(\text{Py})_n]^+$ ($n = 0, 1, 2, 3$) reveal fragment mass peaks (*cf.* Fig. S1–S4, ESI[†]) indicating a cleavage of neutral pyridine ligands. This is the main fragmentation route. Very weak mass

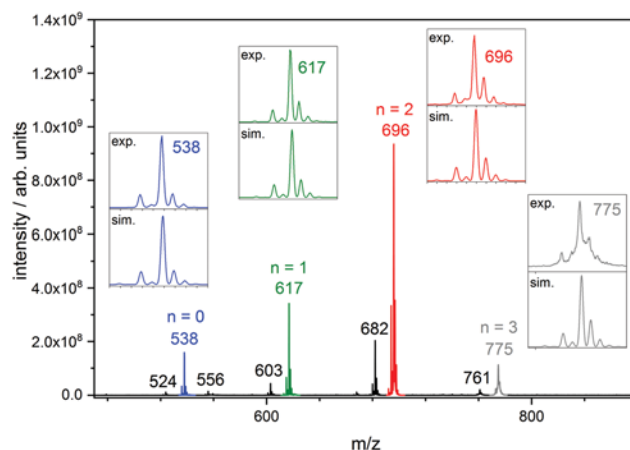
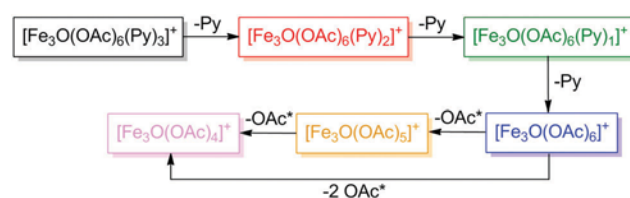


Fig. 1 Cationic mass spectrum of a $[\text{Fe}_3\text{O}(\text{OAc})_6(\text{H}_2\text{O})_3]\text{ClO}_4$ acetonitrile/pyridine = 1/10 solution using the Paul type ion trap. Insets: Experimental and simulated isotopic pattern of $[\text{Fe}_3\text{O}(\text{OAc})_6(\text{Py})_n]^+$ ($n = 0, 1, 2, 3$; OAc = CH_3CO_2^- ; Py = $\text{C}_5\text{H}_5\text{N}$). The mass labeling refers to the most intensive peak.



Scheme 3 CID fragmentation routes of $[\text{Fe}_3\text{O}(\text{OAc})_6(\text{Py})_n]^+$ ($n = 0, 1, 2, 3$). The relative intensities of the fragments depend strongly on the CID amplitude. The subsequent manner of pyridine elimination finds experimental evidence by our CID appearance curves (*cf.* Fig. 2).

peaks at 556 , which we assign to $[\text{Fe}_3\text{O}(\text{OAc})_6(\text{H}_2\text{O})]^+$ indicates H_2O attachment to $[\text{Fe}_3\text{O}(\text{OAc})_6(\text{H}_2\text{O})]^+$ within the ion trap. We observe cleavage of neutral acetoxy radical (OAc^*) – when no pyridine ligands are available (*cf.* Scheme 3).

We elucidate the relative stability of $[\text{Fe}_3\text{O}(\text{OAc})_6(\text{Py})_n]^+$ ($n = 0, 1, 2, 3$) by recording so-called CID breakdown curves of the complexes and CID appearance curves of the associated fragments (*cf.* Fig. 2). In the case of $[\text{Fe}_3\text{O}(\text{OAc})_6(\text{Py})_3]^+$ (*cf.* Fig. 2; $n = 3$; black squares) single pyridine elimination is the primary fragmentation channel as recorded by the fragment peak $[\text{Fe}_3\text{O}(\text{OAc})_6(\text{Py})_2]^+$ (red squares). It prevails to an CID amplitude of $E_{\text{com}} \sim 5$ a.u. (arbitrary units). Higher CID amplitudes reveal additional elimination of the second pyridine ligand ($[\text{Fe}_3\text{O}(\text{OAc})_6(\text{Py})_1]^+$, green squares) which we attribute to secondary fragmentation. The intensity of the double pyridine elimination increases with the CID amplitude while the intensity of single pyridine elimination decreases underlining the subsequent manner of the fragmentation process. We exclude a concurrent elimination process of the first two pyridine ligands. CID amplitudes > 6 a.u. reveal the rising of the next secondary fragment: triple pyridine elimination as recorded fragment peak $[\text{Fe}_3\text{O}(\text{OAc})_6]^+$ (blue squares). Both secondary fragments gain intensity with CID amplitudes with $[\text{Fe}_3\text{O}(\text{OAc})_6(\text{Py})_1]^+$ exhibiting a maximum around $E_{\text{com}} = 7.5$ a.u. We observed no (secondary) elimination of acetoxy (OAc^*) at all applied

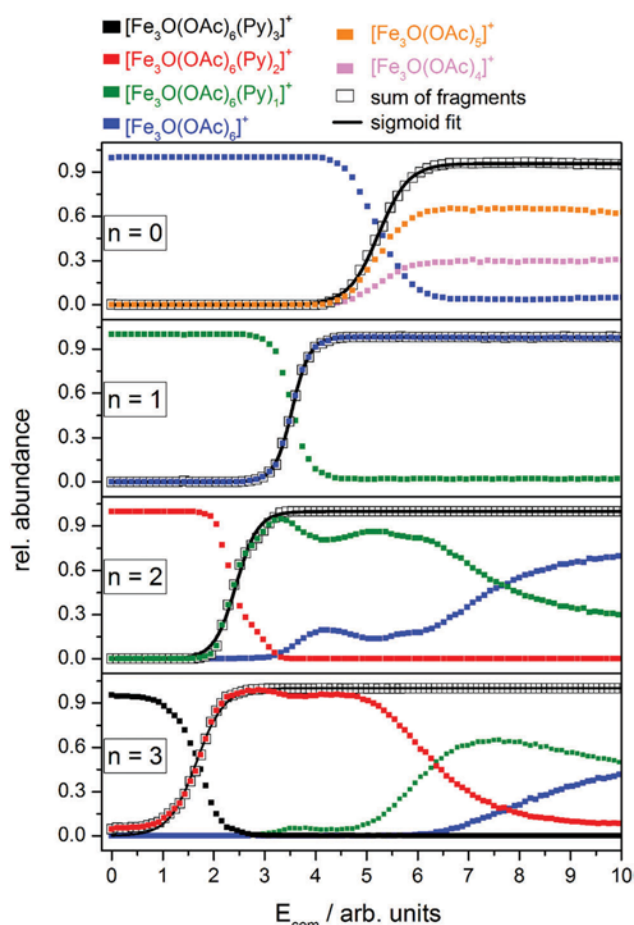


Fig. 2 CID breakdown curves of $[\text{Fe}_3\text{O}(\text{OAc})_6(\text{Py})_n]^+$ ($n = 0, 1, 2, 3$) and appearance curves of the associated fragments.

CID amplitudes. In the case of $[\text{Fe}_3\text{O}(\text{OAc})_6]^+$ (cf. Fig. 2; $n = 0$; blue squares) there is no pyridine ligand available. Accordingly we observe single and double acetoxy (OAc*) elimination ($[\text{Fe}_3\text{O}(\text{OAc})_5]^+$ and $[\text{Fe}_3\text{O}(\text{OAc})_4]^+$) as primary fragments. Both fragment channels gain intensity beyond $E_{\text{com}} = 4.5$ a.u. They reach a constant level at $E_{\text{com}} = 4.5$ a.u. and remain constant throughout the range of applied CID amplitudes.

The fragmentation behavior of $[\text{Fe}_3\text{O}(\text{OAc})_6(\text{Py})_2]^+$ (cf. Fig. 2; $n = 2$; red squares) is similar to $n = 3$ (cf. Fig. 2; $n = 3$; black squares). The primary fragmentation channel in $n = 2$ is single pyridine elimination as recorded by the fragment peak $[\text{Fe}_3\text{O}(\text{OAc})_6(\text{Py})_1]^+$ (green squares). It prevails to an CID amplitude of $E_{\text{com}} = 3.5$ a.u. Higher CID amplitudes reveal additional elimination of the second pyridine ligand (double pyridine elimination) as a secondary fragment ($[\text{Fe}_3\text{O}(\text{OAc})_6]^+$; blue squares). The intensity of the double pyridine elimination increases with the CID amplitude while the intensity of single pyridine elimination decreases. This indicates subsequent elimination of the pyridine ligands. Anti-correlated bumps superimposing both curves are likely artefacts beyond interpretation as of now. We observed no additional secondary elimination of acetoxy (OAc*) at all applied CID amplitudes. The case of $n = 1$ (cf. Fig. 2; $n = 1$; blue squares) is straight forward: Pyridine cleavage as recorded by the fragment

peak $[\text{Fe}_3\text{O}(\text{OAc})_6]^+$, and it prevails at all CID amplitudes. We detected no secondary fragments.

Correlation between E_{com}^{50} CID values and calculated binding energies. In all cases where a pyridine ligand is available ($n = 1, 2, 3$) a single pyridine elimination dominates the sigmoid rise of the fragment appearance curves. This offers an opportunity to investigate the binding energies of the pyridine ligands in $[\text{Fe}_3\text{O}(\text{OAc})_6(\text{Py})_n]^+$ ($n = 1, 2, 3$). By fitting the experimental CID appearance curves (sum of all fragments) we extract E_{com}^{50} values. In doing so we are well aware of the multi collision situation in our ion trap, and we interpret our results in a qualitative way, comparing the obtained E_{com}^{50} to according calculated fragmentation energies $\Delta_{\text{fr}}E_n$ ($n = 1, 2, 3$, energies at 0 K):

$$\Delta_{\text{fr}}E_n = E([\text{Fe}_3\text{O}(\text{OAc})_6(\text{Py})_{n-1}]^+) + E(\text{Py}) - E([\text{Fe}_3\text{O}(\text{OAc})_6(\text{Py})_n]^+)$$

and fragmentation free energies $\Delta_{\text{fr}}G_n^0$ ($n = 1, 2, 3$, free energies at 300 K):

$$\begin{aligned} \Delta_{\text{fr}}G_n^0 &= G^0([\text{Fe}_3\text{O}(\text{OAc})_6(\text{Py})_{n-1}]^+) + G^0(\text{Py}) \\ &\quad - G^0([\text{Fe}_3\text{O}(\text{OAc})_6(\text{Py})_n]^+) \end{aligned}$$

Note, that these calculated fragmentation (free) energies correspond to adiabatic binding (free) energies. Molecular fragmentation might bear an activation barrier on top of the endothermicity of bond breaking.^{64,65} In such cases it would be more appropriate to compare the relative energies of transition state structures to E_{com}^{50} values rather than simple binding energies.^{41,49,66} However, in the presented case we investigate a direct bond cleavage void of any involved structural reorganizations. Such cases are known to lack any activation barrier beyond plain endothermicity of the mere bond breaking,^{67,68} and we are entitled to assume the same for our present case.

The first eliminated pyridine ligand from $[\text{Fe}_3\text{O}(\text{OAc})_6(\text{Py})_3]^+$ (cf. Table 1) has the lowest binding energy ($\Delta_{\text{fr}}E_{n=3}$) of 82 kJ mol⁻¹ ($\Delta_{\text{fr}}G_{n=3}^0 = 20$ kJ mol⁻¹). Accordingly we measure the lowest E_{com}^{50} value of 1.66 a.u. for $[\text{Fe}_3\text{O}(\text{OAc})_6(\text{Py})_3]^+$. The binding energy of the second pyridine molecule to increases to 109 kJ mol⁻¹ ($\Delta_{\text{fr}}G_{n=2}^0 = 35$ kJ mol⁻¹). The associated E_{com}^{50} value of $[\text{Fe}_3\text{O}(\text{OAc})_6(\text{Py})_2]^+$ increases to 2.44 a.u. The last pyridine ligand has the highest binding energy ($\Delta_{\text{fr}}E_{n=1}$) of 134 kJ mol⁻¹ ($\Delta_{\text{fr}}G_{n=1}^0 = 56$ kJ mol⁻¹) and we observe highest E_{com}^{50} value of 3.54 a.u. in the case of $[\text{Fe}_3\text{O}(\text{OAc})_6(\text{Py})_1]^+$.

Both, the calculation as well as the experimental E_{com}^{50} value indicate an obvious trend: the binding energy of pyridine ligands decreases with the number of pyridine ligands coordinated to the $[\text{Fe}_3\text{O}(\text{OAc})_6]^+$ subunit. This hints at significant

Table 1 Calculated fragmentation free energies $\Delta_{\text{fr}}G_n^0$ and fragmentation energies $\Delta_{\text{fr}}E_n$ of $[\text{Fe}_3\text{O}(\text{OAc})_6(\text{Py})_n]^+$ ($n = 1, 2, 3$). The calculations were performed at the B3LYP_Gaussian/cc-pVTZ (H, C, N, O) and ecp-10-mdf (Fe) level of theory and the minimum broken symmetry configuration. The E_{com}^{50} values are extracted from CID appearance curves (cf. Fig. 2)

$[\text{Fe}_3\text{O}(\text{OAc})_6(\text{Py})_n]^+$	$\Delta_{\text{fr}}G_n^0/\text{kJ mol}^{-1}$	$\Delta_{\text{fr}}E_n/\text{kJ mol}^{-1}$	$E_{\text{com}}^{50}/\text{a.u.}$
$n = 3$	20	82	1.66
$n = 2$	35	109	2.44
$n = 1$	56	134	3.54

influences on the structural properties of the $[\text{Fe}_3\text{O}(\text{OAc})_6]^+$ subunit by the coordination of each axial pyridine ligand. We elucidate this influence in the following chapter, by investigating the IR absorptions of $[\text{Fe}_3\text{O}(\text{OAc})_6(\text{Py})_n]^+$ ($n = 0, 1, 2, 3$) via IR-MPD.

3.2 IR-MPD and DFT simulations of $[\text{Fe}_3\text{O}(\text{OAc})_6(\text{Py})_n]^+$

We have recorded IR-MPD spectra of $[\text{Fe}_3\text{O}(\text{OAc})_6(\text{Py})_n]^+$ ($n = 0, 1, 2, 3$) (cf. Fig. 3; red and blue curves) and we have conducted DFT simulations to obtain their linear IR absorption spectra (cf. Fig. 3, black stick spectra and convoluted curves). The DFT

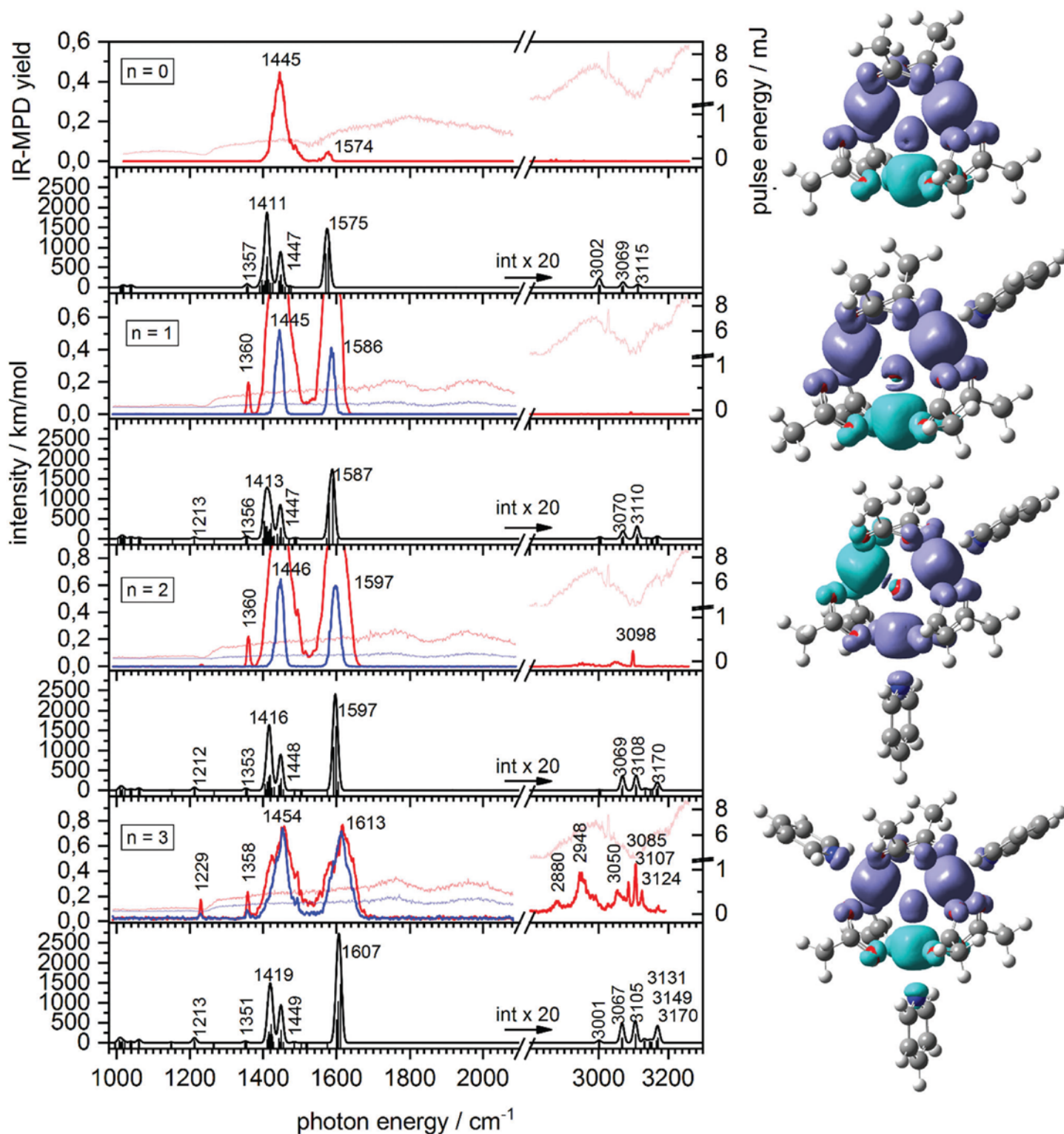


Fig. 3 IR-MPD spectra of $[\text{Fe}_3\text{O}(\text{OAc})_6(\text{Py})_n]^+$ ($n = 0, 1, 2, 3$) (colored curves) and calculated IR absorption spectra (black stick spectra and convoluted curves) in the spectral range of 1000–3300 cm^{-1} . Red curves indicate measurements at maximum photon flux while blue curves show spectra with attenuated pulse energies ($\sim 50\%$). All calculations (geometries, energies and spectra) were performed at the B3LYP/cc-pVTZ (H, C, N, O) and ecp-10-mdf (Fe) level of theory with five unpaired electrons on each Fe center in a UUD ($n = 0, 1, 3$) or DUU ($n = 2$) broken symmetry configuration corresponding to the minimum structures. Spin density iso surfaces indicate unpaired alpha (U, purple) and beta (D, turquoise) spin density. The frequencies are scaled with 0.985 and the stick spectra were convoluted with Gaussian curves (FWHM = 7 cm^{-1}).

calculations reveal minimum structures and spin densities as depicted in Fig. 3. Simulations of antiferromagnetic coupling in $[\text{Fe}_3\text{O}(\text{OAc})_6(\text{Py})_n]^+$ via broken symmetry calculations reveal an energetic stabilization of 19–34 kJ mol⁻¹ relative to the ferromagnetic case (multiplicity of 16, which we call 16tet, cf. Fig. S7–S10 (ESI[†]) for other broken symmetry configurations). This result is in line with the prevailing antiferromagnetic coupling in complexes of the structural type $[\text{M}_3\text{O}(\text{OAc})_6(\text{L})_3]^+$ (M = transition metal, L = ligand) as investigated in the condensed phase.^{9,69,70} Our spin density isosurfaces reveal localized unpaired spin density on the Fe centers with minor delocalization onto the donor atoms of the ligands (oxygen atoms of acetate and nitrogen atoms of pyridine).

Pyridine torsional ambiguity. We have, of course, started to check for the total energy profile along the Py torsional coordinate of the $[\text{Fe}_3\text{O}(\text{OAc})_6(\text{Py})_1]^+$, $n = 1, 2, 3$ complexes, where this coordinate is defined by an axis, that coincides with the N–Fe coordination bond. The according DFT total energy profile (Fig. S17 in the ESI[†]) reveals a clear preference of a single pyridine to orient perpendicular to the Fe₃ plane. A second much shallower and less stable minimum (+4.5 kJ mol⁻¹) arises when the pyridine and Fe₃ planes are parallel. Both orientations are double degenerate and staggered with respect to any of the four proximate Fe–O bonds. At the room temperature – and upon CID excitation much above – conditions of the current experiment the hindered pyridine torsion is thus likely excited, and up to about 20% of all complexes may freely rotate. An exhaustive elucidation of the pyridine torsion in all complexes, $n = 1, 2, 3$ would require further DFT modelling in conjunction with cryogenic IR-MPD experiments. This is beyond the scope of the current study and leaves to be done by a subsequent study (cf. outlook).

IR-MPD and DFT spectra of $[\text{Fe}_3\text{O}(\text{OAc})_6]^+$. DFT modelling reveals weak CH stretching bands of the acetates (2990–3101 cm⁻¹) which do not show in the IR-MPD spectrum. Weak absorption in conjunction with a high fragmentation threshold for OAc* elimination seems to hamper IR-MPD detection in these cases.

The predicted $\nu_s(\text{COO})_{\text{OAc}}$ and $\nu_{\text{as}}(\text{COO})_{\text{OAc}}$ absorption bands at 1411 and 1575 cm⁻¹ find reasonable correspondence in the recorded IR-MPD bands at 1445 and 1574 cm⁻¹ while the slight asymmetry of the 1445 cm⁻¹ IR-MPD band might account for the predicted $\delta(\text{CH}_3)_{\text{OAc}}$ absorption of medium strength at 1447 cm⁻¹. The ratio of the two predicted IR-MPD bands does not match that of the predicted linear IR absorption strengths. Such intensity modulations by mode specific fragmentation efficiencies are well known in action spectroscopy, and e.g. well documented for the cases of symmetric/asymmetric OH stretching bands in single hydrates of many cations (cf. compilation and discussion in ref. 71 and 72). The mechanistic understanding of these H₂O cases may hold in principle for the present COO cases in coordinated OAc as well: vibrations perpendicular to coordination bonds couple less than those parallel to them. For the DFT predictions of further broken symmetry configurations and for an enhanced view onto the spectra the reader may refer to Fig. S7 in the ESI[†].

IR-MPD and DFT spectra of $[\text{Fe}_3\text{O}(\text{OAc})_6(\text{Py})_1]^+$. There is a persisting lack of recordable IR-MPD signal in the CH stretching

mode in this case as well, and likely for the same reasons as in the $n = 0$ case. Coinciding with the measured IR-MPD band at 1586 cm⁻¹, scaled DFT calculations predict two strong proximate $\nu_{\text{as}}(\text{COO})$ stretching bands at 1580 and 1591 cm⁻¹ which are delocalized over those four OAc groups that neighbour the single pyridine ligand. The predicted splitting of 11 cm⁻¹ is not resolved by IR-MPD. It arises from the relative phases of these four COO oscillators. All in phase, they couple to the in plane rocking vibrations of the pyridine, which seems to enhance the IR absorption strength of the 1591 cm⁻¹ band. Pairwise oscillating in opposite phase as by the 1580 cm⁻¹ band they do not couple to the pyridine ligand. The convoluted envelope (7 cm⁻¹ gaussian width) results in a single peak at 1587 cm⁻¹ in agreement with the IR-MPD result at 1586 cm⁻¹.

In the CH₃ wagging mode range of $n = 1$ the picture of the $n = 0$ case repeats void of significant changes. With high photon flux there is another weak IR-MPD band at 1360 cm⁻¹ which might correspond to the predicted IR absorption band at 1356 cm⁻¹. The three predicted bands (at 1356, 1413, and 1447 cm⁻¹) comprise in total of 18 normal modes from various combinations of wagging modes of the six CH₃ groups in the OAc ligands, and a single collective CH bending mode in the pyridine ligand at 1447 cm⁻¹.

Predicted but weak CH absorptions do not yield IR-MPD signals in both cases of $n = 0$ and 1. This indicates a notable lack of anharmonic couplings. For the vibrational DFT predictions of further broken symmetry configurations (which reveal all very similar results) and for an enhanced view onto the spectra the reader may refer to Fig. S8 in the ESI[†].

IR-MPD and DFT spectra of $[\text{Fe}_3\text{O}(\text{OAc})_6(\text{Py})_2]^+$. There is a small amount of IR-MPD signal in the CH stretching mode region, and it comprises of broad bands around 2955 and 3050 cm⁻¹, and a sharp band at 3098 cm⁻¹. None of these coincide exactly with scaled DFT predictions. As the presently chosen scaling optimizes for the fingerprint region, a systematic deviation in the stretching mode region is conceivable. Thus we tentatively assign the two broad IR-MPD bands to the DFT bands at 3069 and 3108 cm⁻¹. Both are six fold degenerate and represent localized and pairwise delocalized CH stretching modes within CH₃ groups of the OAc ligands – in linearly scaled harmonic approximation. It is known since long times that stretch-bend Fermi resonances in CH₃ groups arise through anharmonic couplings,⁷³ and this was recently interpreted by Zwier *et al.* in terms of a model Hamiltonian.⁷⁴ Such couplings persist in a robust way, and they are assumed to be ubiquitous. We agree and conclude that the broadenings of the unresolved IR-MPD bands arise from such stretch bend couplings.

The sharp band of the IR-MPD spectrum at 3098 cm⁻¹ likely corresponds to the twofold degenerate, localized, all in phase CH stretching mode of a pyridine ligand at 3170 cm⁻¹. Void of strong stretch-bend couplings these pyridinic bands are sharp.

IR-MPD and DFT spectra of the $n = 2$ complex in the fingerprint region basically duplicate the $n = 1$ case and need no further discussion. For the vibrational DFT predictions of further broken symmetry configurations and for an enhanced view onto the spectra the reader may refer to Fig. S9 in the ESI[†].

IR-MPD and DFT spectra of $[\text{Fe}_3\text{O}(\text{OAc})_6(\text{Py})_3]^+$. The IR-MPD spectra of the CH stretching mode region reveal broad bands

around 2880, 2948, 3050 and a triplet of sharp bands at 3085, 3107 and 3124 cm^{-1} (cf. Fig. 3). As in the $n = 2$ case, none of these bands coincide exactly with scaled DFT predictions, and a systematic deviation in the stretching mode region prevails. We tentatively assign the three broad IR-MPD bands to the scaled DFT bands at 3001, 3067 and 3105 cm^{-1} . All three bands are six fold degenerate and represent localized and pairwise delocalized CH stretching modes within CH_3 groups of the OAc ligands – the broadening arising from the stretch-bend Fermi couplings as discussed for the $n = 2$ case. The three sharp bands of the IR-MPD spectrum likely correspond to threefold, sixfold, and sixfold degenerate pyridinic CH stretching modes at 3131, 3149, and 3170 cm^{-1} , respectively – lacking strong stretch-bend couplings as discussed in the case of $n = 2$. This assignment is further confirmed by deuteration experiments (see Fig. S18, ESI†).

There are two strong and significantly broadened IR-MPD band peaking around 1454 and 1613 cm^{-1} , and two weak but sharp bands at 1358 and 1229 cm^{-1} . The 1358 cm^{-1} band might correspond to the predicted IR absorption band at 1351 cm^{-1} which comprises of 6 degenerate wagging modes of CH_3 groups from the six OAc ligands, two of which are weakly IR active. The 1229 cm^{-1} band likely corresponds to the scaled DFT prediction at 1213 cm^{-1} which originates from three degenerate pyridinic CH bending modes, two of which are medium IR active.

The 1454 cm^{-1} IR-MPD band is at least 40 cm^{-1} broad and falls into a spectral range where DFT calculations predict three groups of modes. There are twelve asymmetric carboxylic stretching modes of the six OAc ligands in a range of 17 cm^{-1} around 1419 cm^{-1} , nine of which bear high IR activity. Six more such modes fall within 8 cm^{-1} around 1449 cm^{-1} , partially overlapping with three degenerate pyridinic CH bending modes at 1449 cm^{-1} . In effect these 21 modes overlap into two bands peaking at 1419 and 1449 cm^{-1} . Torsional ambiguity, anharmonic couplings and power broadening altogether may account for further broadening as observed in the IR-MPD signal of this case ($n = 3$).

The 1613 cm^{-1} IR-MPD band is predicted to comprise of two strong IR active, almost degenerate, asymmetric carboxylic stretching modes of the six OAc ligands at 1606 and 1610 cm^{-1} , the four more IR inactive symmetric ones occurring 80 cm^{-1} below. Two less strong IR active, degenerate pyridinic CH bending modes at 1601 cm^{-1} are close to the former ones, four more IR inactive modes occurring within 25 cm^{-1} to the red. Note, that the accidental degeneracy of the pyridinic CH bend and carboxylic stretches is highly susceptible to the ferric spin couplings, cf. Fig. S10 in the ESI.† While the UUD, UDU, and UUD configurations yield equivalent patterns, the high spin UUU 16tet configuration is somewhat different. The broad band envelope, however, seems to stay about the same and peaks at 1607 cm^{-1} in any case.

Isotopic substitution studies. The present analysis and the tentative assignments deserve further corroboration as *e.g.* by isotopic substitution experiments. We conducted IR-MPD studies of $[\text{Fe}_3\text{O}(\text{OAcD}_3)_6(\text{Py})_3]^+$, $[\text{Fe}_3\text{O}(\text{OAc})_6(\text{PyD}_5)_3]^+$, and $[\text{Fe}_3\text{O}(\text{OAcD}_3)_6(\text{PyD}_5)_3]^+$ complexes as summarized in the supplement (cf. Fig. S18, ESI†). In the case of $[\text{Fe}_3\text{O}(\text{OAc})_6(\text{PyD}_5)_3]^+$, the three sharp IR-MPD

bands at 3085, 3107 and 3124 cm^{-1} vanish from our observation windows and presumably shift below 2800 cm^{-1} while the broad bands at 2880, 2948, and 3050 cm^{-1} persist in $[\text{Fe}_3\text{O}(\text{OAc})_6(\text{PyD}_5)_3]^+$ but for minor changes in their shape. This supports the above assignments as sharp CH stretching bands of pyridine and broad CH stretching bands of OAc, respectively.

The interpretation of isotopic effects to the broad bands at about 1454 and 1613 cm^{-1} in $[\text{Fe}_3\text{O}(\text{OAc})_6(\text{Py})_3]^+$ is much more involved. We took a look in some depth at the later band, and how it changes upon complete deuteration, $[\text{Fe}_3\text{O}(\text{OAcD}_3)_6(\text{PyD}_5)_3]^+$. The recorded IR-MPD spectra (Fig. S19 and S20, ESI†) reveal, that this band overall redshifts and splits in two. DFT modelling predicts small shifts upon deuteration of the carboxylic stretching modes (mere 9 cm^{-1}) and considerable shifts of the pyridinic CH bending modes (of 38 and 44 cm^{-1}). Either of two conceivable decompositions of the recorded IR-MPD bands into multiple broad Gaussian contributions would be in agreement with a minor shift (by 9 cm^{-1}) amongst the assumed carboxylic bands, and major shifts (of either 31 and 41 cm^{-1} , or 34 and 44 cm^{-1}) in the assumed pyridinic CH bending bands. These interpretations are in line with the assumed assignments (Table S7, ESI†).

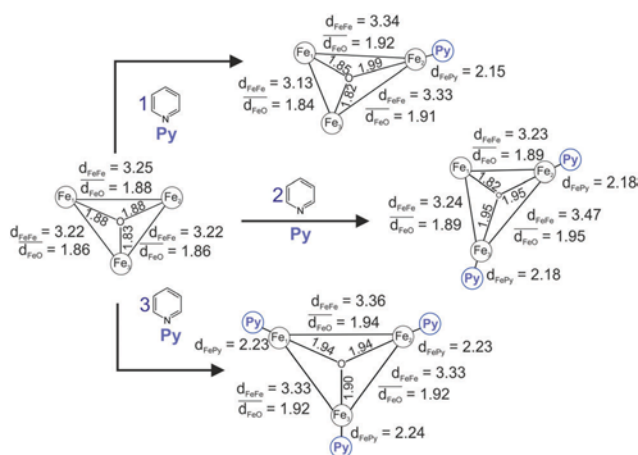
Influence of pyridine coordination on the IR-MPD spectra.

Axial pyridine ligands, coordinated to $[\text{Fe}_3\text{O}(\text{OAc})_6]^+$, modulate the shape, frequency and intensity of the CH_3 bending vibration bands and CO stretching vibration bands. The frequencies of $\delta(\text{CH}_3)$ and $\nu(\text{CO})$ increase with the number of coordinated pyridine ligands n , both in experiments and calculations (cf. Fig. S15, ESI†). The experimental CO stretching vibration bands of $n = 1, 2, 3$ are blue shifted by 12, 23 and 39 cm^{-1} , with respect to $n = 0$. The associated DFT calculated asymmetric carboxylate stretching frequencies – scaled to match the experiment at $n = 0$ – reproduce this blueshift (12, 22 and 32 cm^{-1}). The coordinated carboxylate groups thus sense pyridine coordination through their common Fe centers. Coordination of pyridine ligands lifts the degeneracy of carboxylic CO stretching vibration frequencies ($\nu(\text{CO})$) in the six coordinated acetate ligands – spin frustration acting on top. The calculations predict a splitting of 10 cm^{-1} in the case of $n = 1$ which may be contained within the unresolved recorded IR-MPD bands.

The CH_3 bending vibrations are significantly less affected by pyridine coordination. The experimental $\delta(\text{CH}_3)$ frequencies of $n = 1, 2, 3$ are blue shifted by 0, 1 and 9 cm^{-1} , with respect to $n = 0$. The calculated $\delta(\text{CH}_3)$ frequencies reproduce the less pronounced blue shift (2, 5 and 8 cm^{-1}). In the case of $n = 3$ we record a significantly broadened CO stretching vibration band as well as a broadened CH_3 bending vibration band. The low stability of $[\text{Fe}_3\text{O}(\text{OAc})_6(\text{Py})_3]^+$ seems to result in power broadening even at attenuated photon fluxes. After all of these considerations, we feel able to survey the geometries of the calculated structures of $[\text{Fe}_3\text{O}(\text{OAc})_6(\text{Py})_n]^+$ ($n = 0, 1, 2, 3$) and their influence on the magnetic couplings in some more detail.

3.3 Magnetostructural correlation by DFT

Geometry of $[\text{Fe}_3\text{O}(\text{OAc})_6(\text{Py})_n]^+$ ($n = 0, 1, 2, 3$). All three Fe atoms are coordinated in an pseudooctahedral geometry by four oxygen atoms of the bridging acetate ligands and by the



Scheme 4 Atom distances (Fe–O_{central} distances and mean Fe–O distances $\overline{d_{\text{FeO}}}$, averaged over two adjacent Fe atoms, all in Å) of the Fe₃O-core in $[\text{Fe}_3\text{O}(\text{OAc})_6(\text{Py})_n]^+$ ($n = 0, 1, 2, 3$). The calculations were performed at the B3LYP-Gaussian/cc-pVTZ (H, C, N, O) and ecp-10-mdf (Fe) level of theory with five unpaired electrons on each Fe center and a UUD ($n = 0, 1, 3$) or DUU ($n = 2$) broken symmetry configuration corresponding to the minimum structures.

central O₂[−] di-anion. The nitrogen atoms of the pyridine ligands coordinate in axial position thereby closing the octahedral coordination sphere. A hypothetical equilateral triangular $[\text{Fe}_3\text{O}(\text{OAc})_6(\text{Py})_n]^+$ ($n = 0, 1, 2, 3$) geometry is in fact distorted by two independent effects:

(1) Spin frustration due to antiferromagnetic coupling: a switch of a UUU configuration to a DUU/UDU/UUD configuration results in shortened Fe–O_{central} bond lengths of those bonds which involve a Fe center in D configuration (*cf.* Scheme 4 and Fig. S7–S10, ESI[†]).

(2) Coordination of pyridine ligands: the coordination of a single pyridine enlarges Fe–Fe distances (d_{FeFe}) and Fe–O_{central} bond lengths (d_{FeO}) (by ~ 0.1 Å) of those bonds which involve the pyridine coordinating Fe-center. All the other Fe–Fe distances and Fe–O_{central} bond lengths shorten by ~ 0.1 Å and ~ 0.02 Å respectively.

$[\text{Fe}_3\text{O}(\text{OAc})_6]^+$ exhibits an isosceles Fe–Fe–Fe triangle in C_{2v} symmetry. The coordination of a single pyridine induces a symmetry lowering to a scalene triangle in $[\text{Fe}_3\text{O}(\text{OAc})_6(\text{Py})_1]^+$. On top of the distortion by the spin frustration the coordinated Fe center moves away from the two uncoordinated Fe centers which slightly approach each other. Coordination of a second and a third pyridine molecule distracts each affected Fe site slightly from the other Fe centers in a similar manner. The scalene triangular geometry of $n = 1$ eventually relaxes upon further pyridine coordination (in $n = 2$ and $n = 3$) to isosceles C_{2v} geometries (as upon $n = 0$). The binding distance between the Fe center and the coordinating N atom of the pyridine ligand (*cf.* Table S2, ESI[†]) increases from 2.15 Å ($n = 1$) to 2.24 Å ($n = 3$); such bond weakening indicates a reduction of bond strength, which is in accord with our CID findings.

Determination of antiferromagnetic couplings J_{ij} . Single point calculations of the $[\text{Fe}_3\text{O}(\text{OAc})_6(\text{Py})_n]^+$ minima structures in all possible broken symmetry configurations (UUU, DUU,

Table 2 Magnetic coupling constants (J_{ij} in cm^{-1}) between the Fe centers in $[\text{Fe}_3\text{O}(\text{OAc})_6(\text{Py})_n]^+$ ($n = 0, 1, 2, 3$). The calculations were performed at the B3LYP-Gaussian/cc-pVTZ (H, C, N, O) and ecp-10-mdf (Fe) level of theory with five unpaired electrons on each Fe center

	J_{12}/cm^{-1}	J_{13}/cm^{-1}	J_{23}/cm^{-1}
$n = 0$	−52	−62	−62
$n = 1$	−31	−79	−35
$n = 2$	−48	−48	−21
$n = 3$	−28	−33	−33

UDU and UUD) enable us to extract magnetic coupling constants J_{ij} of the corresponding Fe_{*i*} and Fe_{*j*} centers (*cf.* Table 2).

Through these findings we recognize a correlation of the magnetic coupling with the symmetry/geometry of the triangular Fe₃-core. In order to quantify this magnetostructural correlation we introduce the geometrical parameter $\overline{d_{\text{FeO}}}$, which we define as the average of two Fe–O distances along the shortest superexchange pathway (through the central O₂[−] atom) between two adjacent metal centers ($\overline{d_{\text{FeO}}} = [d(\text{Fe}_{(i)}-\text{O}_{\text{central}}) + (\text{Fe}_{(j)}-\text{O}_{\text{central}})]/2$), as suggested before.³ Since the Fe–Fe distances are longer than 3 Å we expect no direct metal metal interaction.⁸ Elongation of $\overline{d_{\text{FeO}}}$ within the Fe₃O core leads to a significant weakening of antiferromagnetic coupling while shortening of $\overline{d_{\text{FeO}}}$ distances strengthens the same.

In the case of $n = 0$ the triangular Fe₃O core exhibits an isosceles C_{2v} geometry due to small geometry distortions induced by spin frustration effects. This results in two different coupling constants: $J_{12} = J_{23} = -62 \text{ cm}^{-1}$ and $J_{13} = -52 \text{ cm}^{-1}$. Note, that the negative sign of J_{ij} indicates antiferromagnetic coupling. A single pyridine ligand ($n = 1$) lowers the symmetry of the triangular Fe₃-core to a scalene triangular geometry (*cf.* Scheme 4). In the case of $n = 1$ the $\overline{d_{\text{FeO}}}$ parameters of the coordinated Fe center elongates by 0.04 Å and 0.05 Å with respect to $n = 0$ while the $\overline{d_{\text{FeO}}}$ parameter of the non coordinated Fe centers shortens by 0.02 Å. This results in three non identical coupling constants: $J_{12} = -31 \text{ cm}^{-1}$ and $J_{23} = -35 \text{ cm}^{-1}$ (the Fe–O_{central}–Fe coupling weakened due to the enlarged $\overline{d_{\text{FeO}}}$) and $J_{13} = -79 \text{ cm}^{-1}$ (the Fe–O_{central}–Fe coupling strengthened due to the shortened $\overline{d_{\text{FeO}}}$). The distortion of the molecular geometry due to pyridine coordination causes changes in magnetic coupling constants which are significantly larger than the effects of spin frustration.

The Fe₃O core in the $n = 2$ coordination complex relaxes to an isosceles C_{2v} symmetry. This results in two different coupling constants: $J_{12} = J_{13} = -48 \text{ cm}^{-1}$ and $J_{23} = -21 \text{ cm}^{-1}$. In this particular case we observe the weakest antiferromagnetic coupling ($J_{13} = -21 \text{ cm}^{-1}$) due to the large $\overline{d_{\text{FeO}}}$ value. In the case of $n = 3$ all $\overline{d_{\text{FeO}}}$ parameters elongate evenly by 0.06 Å in relation to $n = 0$ leading to an isosceles C_{2v} geometry. We extract two different coupling constants: $J_{13} = J_{23} = -33 \text{ cm}^{-1}$ and $J_{12} = -28 \text{ cm}^{-1}$. Neutron scattering experiments on $[\text{Fe}_3\text{O}(\text{CD}_3\text{CO}_2)_6(\text{Py})_3](\text{NO}_3)$ powder¹⁰ determined two non identical coupling constants ($J_1 = -26.8 \text{ cm}^{-1}$ and $J_2 = -32.9 \text{ cm}^{-1}$) which was attributed to spin frustration.⁷⁵ Our calculated values of J in the $n = 3$ case agree remarkably well with these previous results.

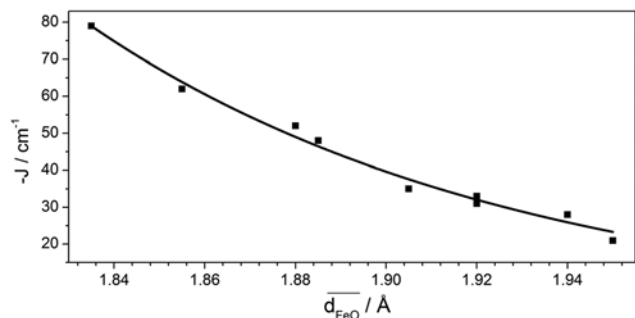


Fig. 4 Correlation between the calculated magnetic coupling constant J and the geometric parameter $\overline{d_{\text{FeO}}}$ in $[\text{Fe}_3\text{O}(\text{OAc})_6(\text{Py})_n]^+$ ($n = 0, 1, 2, 3$). The solid line is a least squares fit with an exponential fit function (eqn (11)). The calculations were performed at the B3LYP-Gaussian/cc-pVTZ (H, C, N, O) and ecp-10-mdf (Fe) level of theory.

We applied the fit function $-J = A \cdot \exp(B \cdot \overline{d_{\text{FeO}}})$ which aims to describe the correlation between the magnetic coupling constants (J_{ij}) and the geometric parameter $\overline{d_{\text{FeO}}}$ (cf. Fig. 4). Such a fit function has been used before³ to correlate experimentally determined coupling constants of oxo-di-iron complexes with the associated geometrical parameters as derived from crystal structures. The exponential form of the analytical expression represents, to a first approximation, the variation of the orbital overlap integral which determines the magnitude of the coupling constant. Our fit parameters $A = 2.2 \times 10^{11} \text{ cm}^{-1}$ and $B = -10.6 \text{ \AA}^{-1}$ are well in line with the previous treatment³ ($A_{\text{lit}} = 8.7 \times 10^{11} \text{ cm}^{-1}$ and $B_{\text{lit}} = -12.663 \text{ \AA}^{-1}$). We thus feel confident that our chosen level of theory describes both the geometrical and magnetic properties of $[\text{Fe}_3\text{O}(\text{OAc})_6(\text{Py})_n]^+$ ($n = 0, 1, 2, 3$) properly.

Spins states of $[\text{Fe}_3\text{O}(\text{OAc})_6(\text{Py})_n]^+$. We established that $[\text{Fe}_3\text{O}(\text{OAc})_6(\text{Py})_n]^+$ ($n = 0, 2, 3$) exhibits an isosceles Fe_3O core geometry with two different coupling constants (cf. Scheme 5). The coupling constant J describes twofold degenerate exchange pathways $\text{Fe}_A\text{-O-Fe}_B$ and $\text{Fe}_A\text{-O-Fe}_C$ while J^* describes the remaining exchange pathway $\text{Fe}_B\text{-O-Fe}_C$. The scalene Fe_3O core geometry in the case of $n = 1$ results in three different coupling constants. However, two of these coupling constants are fairly similar ($J_{12} = -31 \text{ cm}^{-1} \sim J_{23} = -35 \text{ cm}^{-1}$). We define an approximate coupling constant $J = (J_{12} + J_{23})/2 = 33 \text{ cm}^{-1}$. By this approximation the Fe_3O core in the case of $n = 1$ provides a magnetic coupling as depicted in Scheme 5.

We thus evaluate the exchange interactions in $[\text{Fe}_3\text{O}(\text{OAc})_6(\text{Py})_n]^+$ ($n = 0, 1, 2, 3$) by the HDvV Hamiltonian¹⁹

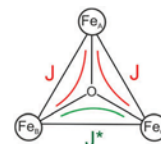
$$\hat{H}_{\text{HDvV}} = -2J(\hat{S}_{\text{FeA}}\hat{S}_{\text{FeB}} + \hat{S}_{\text{FeA}}\hat{S}_{\text{FeC}}) - J^*(\hat{S}_{\text{FeB}}\hat{S}_{\text{FeC}}) \quad (9)$$

By defining a total spin operator \hat{S}_T (eqn (10)) and a partial spin operator \hat{S}_A (eqn (11)) we obtain a descriptive Hamiltonian (eqn (13)):

$$\hat{S}_T = \hat{S}_A + \hat{S}_{\text{FeA}} \quad (10)$$

$$\hat{S}_A = \hat{S}_{\text{FeB}} + \hat{S}_{\text{FeC}} \quad (11)$$

$$\hat{H}_{\text{HDvV}} = -J(\widehat{S}_T^2 - \widehat{S}_A^2 - \widehat{S}_{\text{FeA}}^2) - 0.5J^*(\widehat{S}_A^2 - \widehat{S}_{\text{FeB}}^2 - \widehat{S}_{\text{FeC}}^2) \quad (12)$$



Scheme 5 Magnetic coupling in the Fe_3O core of $[\text{Fe}_3\text{O}(\text{OAc})_6(\text{Py})_n]^+$ ($n = 0, 1, 2, 3$). It is parameterized by two coupling constants J and J^* , which are determined by the geometry of the complexes.

By omitting the three constant single-ion terms $\widehat{S}_{\text{FeA}}^2$, $\widehat{S}_{\text{FeB}}^2$, $\widehat{S}_{\text{FeC}}^2$ we get a simplified HDvV Hamiltonian:

$$\hat{H}_{\text{HDvV}} = -J(\widehat{S}_T^2 - \widehat{S}_A^2) - 0.5J^*(\widehat{S}_A^2) \quad (13)$$

This Hamiltonian yields 27 eigenstates.¹⁹ Depending on the J/J^* ratio, six of these become the ground states of the particular J/J^* ratio (cf. Fig. 5). The higher the J/J^* ratio, the higher the S_A value of the ground state. The total spin (S_T) of these ground states can be 1/2, 3/2 and 5/2—depending on the particular the J/J^* ratio (cf. Table 2 and Scheme 6). Note, that small changes in the J/J^* ratio (e.g. induced by subsequent pyridine coordination) suffice to alter the ground spin state. In summary, the ratio of the coupling constants J and J^* in $[\text{Fe}_3\text{O}(\text{OAc})_6(\text{Py})_n]^+$ ($n = 0, 1, 2, 3$) uniquely determines spin ground states and their effective S_T and S_A values (cf. Fig. 5 and Table 3).

Susceptibility measurements on $[\text{Fe}_3\text{O}(\text{OAc})_6(\text{H}_2\text{O})_3]\text{NO}_3$ at low temperatures¹⁵ have revealed a S_T of 1/2 in agreement with our model calculation. The change of spin states is in $[\text{Fe}_3\text{O}(\text{OAc})_6(\text{Py})_n]^+$ ($n = 0, 1, 2, 3$) in dependence of the Fe_3O core geometry is consistent with previous investigations of asymmetric $[\text{Fe}_3\text{O}(\text{TIEO})_2(\text{O}_2\text{CPh})\text{Cl}_3]$ complexes in the condensed phase by Lippard *et al.*^{76,77} In this case the Fe_3O core geometry is distorted by non equivalent bridging ligands. This results in two non identical coupling constants $J = -8.0 \text{ cm}^{-1}$ and $J^* = -55 \text{ cm}^{-1}$ with a $S_T = 5/2$ ground state ($J/J^* = 0.145$). Note, that in the present case the geometry of the

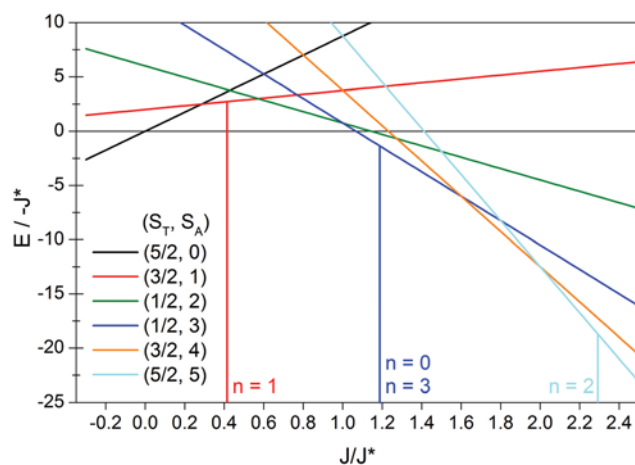
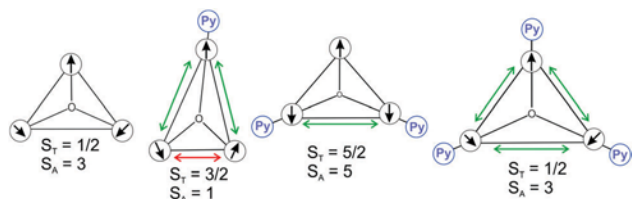


Fig. 5 Eigenvalues of the HDvV Hamiltonian (eqn (13)) for a triangular Fe_3O core in units of J^* in dependence of J/J^* (only ground states indicated). The vertical lines indicate J/J^* ratios and spin states of $[\text{Fe}_3\text{O}(\text{OAc})_6(\text{Py})_n]^+$ ($n = 0, 1, 2, 3$). The spin states are labeled as (S_T, S_A) .



Scheme 6 Effective spins and couplings in the ground states of $[\text{Fe}_3\text{O}(\text{OAc})_6(\text{Py})_n]^+$ ($n = 0, 1, 2, 3$) as extracted from the Hamiltonian in eqn (13).

Table 3 Coupling constants of $[\text{Fe}_3\text{O}(\text{OAc})_6(\text{Py})_n]^+$ ($n = 0, 1, 2, 3$) and their associated spin ground states by Hamiltonian in eqn (13)

n	J/cm^{-1}	J^*/cm^{-1}	J/J^*	$S_T = S_A + S_1$	$S_A = S_2 + S_3$
0	-62	-52	1.19	1/2	3
(1)	(-33) ^a	(-79)	(0.42)	(3/2)	(1)
2	-48	-21	2.29	5/2	5
3	-33	-28	1.18	1/2	3

^a This value is the average of the two actual values, -31 and -35 cm^{-1} .

Fe_3O core is distorted by stepwise coordination of axial pyridine ligands while all bridging ligands are equivalent.

4. Conclusions

We investigated the stability, geometry and magnetic coupling constants of isolated $[\text{Fe}_3\text{O}(\text{OAc})_6(\text{Py})_n]^+$ ($n = 0, 1, 2, 3$) in the gas phase and observed remarkable trends upon coordination of pyridine ligands. CID studies establish the elimination of a single pyridine ligand as the primary fragmentation route. The Fe–Py bond strengths decrease with the number of coordinated pyridine ligands as indicated experimentally by CID appearance curves (E_{com}^{50}) as well as by calculated binding energies ($\Delta_{\text{fr}}G^0$ and $\Delta_{\text{fr}}E$).

Experimental IR-MPD spectra as well as calculated IR absorption spectra reveal significant blue shifts of the asymmetric carboxylic CO stretching vibration frequency upon coordination of pyridine ligands (up to 39 cm^{-1}). This provides spectroscopic evidence for distinct shortenings and elongations of Fe–Fe distances within the triangular Fe_3O core. The geometrical modulation correlates with the magnetic properties of $[\text{Fe}_3\text{O}(\text{OAc})_6(\text{Py})_n]^+$. Broken symmetry based calculations reveal antiferromagnetic magnetic couplings which are crucially affected by the geometric modulation. The isosceles Fe_3O core geometry in the case of $n = 0$ leads to two different identical coupling constants ($J = -62 \text{ cm}^{-1}$ and $J^* = -52 \text{ cm}^{-1}$). The coordination of the first pyridine ligand ($n = 1$) lead to a symmetry lowering and to the formation of a scalene Fe_3O core symmetry. The coordination of the second pyridine ($n = 2$) ligand reintroduces an isosceles Fe_3O core geometry. However, in this case the splitting of the two coupling constants ($J = -42 \text{ cm}^{-1}$ and $J^* = -21 \text{ cm}^{-1}$) is significantly enlarged in relation to the $n = 1$ case. In the case of $n = 3$ we observe an isosceles Fe_3O core geometry with a small splitting of the coupling constants ($J = -33 \text{ cm}^{-1}$ and $J^* = -28 \text{ cm}^{-1}$). The magnitude of the coupling constants offers a wide range (-21 cm^{-1} to -79 cm^{-1}) depending critically on the average distance $\overline{d_{\text{FeO}}}$.

We utilized J/J^* ratios in combination with a model spin Hamiltonian (eqn (13)) to determine the ground spin states of $[\text{Fe}_3\text{O}(\text{OAc})_6(\text{Py})_n]^+$: in the cases of $n = 0$ and 3 the J/J^* ratios of 1.19 and 1.18 respectively indicate a total spins (S_T) of 1/2 in the ground states of the complexes. The J/J^* ratio of 0.42 in the case $n = 1$ indicates a S_T of 3/2. The J/J^* ratio of 2.29 in the case $n = 2$ indicates a S_T of 5/2.

At present we conduct a long term characterization of the intrinsic magnetism in the $[\text{Fe}_3\text{O}(\text{OAc})_6(\text{Py})_n]^+$ complexes by X-ray ionization analysis as conducted for transition metal clusters before,^{78,79} and we have started further investigations by cryo IR spectroscopy at enhanced spectral resolution. We are confident to confirm and possibly refine our current results in the foreseeable future.⁸⁰

Conflicts of interest

There are no conflicts to declare.

Acknowledgements

This work was supported by the German research foundation DFG within the transregional collaborative research center SFB/TRR 88 “Cooperative effects in homo and heterometallic complexes” (3MET) and by the state research center OPTIMAS. We gratefully acknowledge fruitful discussions with Tobias J. Lau. Finally, we thank the reviewers for valuable comments.

References

- 1 S. Bi, C. Liu and H. Hu, *J. Phys. Chem. B*, 2002, **106**, 10786–10792.
- 2 T. Cauchy, E. Ruiz and S. Alvarez, *J. Am. Chem. Soc.*, 2006, **128**, 15722–15727.
- 3 S. M. Gorun and S. J. Lippard, *Inorg. Chem.*, 1991, **30**, 1625–1630.
- 4 L. Gregoli, C. Danieli, A.-L. Barra, P. Neugebauer, G. Pellegrino, G. Poneti, R. Sessoli and A. Cornia, *Chem. – Eur. J.*, 2009, **15**, 6456–6467.
- 5 J. P. S. Walsh, S. Sproules, N. F. Chilton, A.-L. Barra, G. A. Timco, D. Collison, E. J. L. McInnes and R. E. P. Winpenny, *Inorg. Chem.*, 2014, **53**, 8464–8472.
- 6 D. Gatteschi and R. Sessoli, *Angew. Chem., Int. Ed.*, 2003, **42**, 268.
- 7 Y.-W. Lin, *Coord. Chem. Rev.*, 2017, **336**, 1–27.
- 8 R. Werner, S. Ostrovsky, K. Griesar and W. Haase, *Inorg. Chim. Acta*, 2001, **326**, 78–88.
- 9 F. E. Sowrey, C. Tilford, S. Wocadlo, C. E. Anson, A. K. Powell, S. M. Bennington, W. Montfrooij, U. A. Jayasooriya and R. D. Cannon, *J. Chem. Soc., Dalton Trans.*, 2001, 862–866.
- 10 R. D. Cannon, U. A. Jayasooriya, R. Wu, S. K. arapKoske, J. A. Stride, O. F. Nielsen, R. P. White, G. J. Kearley and D. Summerfield, *J. Am. Chem. Soc.*, 1994, **116**, 11869–11874.
- 11 V. Amani, N. Safari and H. R. Khavasi, *Spectrochim. Acta, Part A*, 2012, **85**, 17–24.

- 12 R. Wu, M. Poyraz, F. E. Sowrey, C. E. Anson, S. Wocadlo, A. K. Powell, U. A. Jayasooriya, R. D. Cannon, T. Nakamoto, M. Katada and H. Sano, *Inorg. Chem.*, 1998, **37**, 1913–1921.
- 13 M. K. Johnson, D. B. Powell and R. D. Cannon, *Spectrochim. Acta, Part A*, 1981, **37**, 995–1006.
- 14 A. N. Georgopoulou, Y. Sanakis and A. K. Boudalis, *Dalton Trans.*, 2011, **40**, 6371–6374.
- 15 G. Filoti, J. Bartolome, D. P. E. Dickson, C. Rillo, I. Prisecaru, T. Jovmir, V. Kuncser and C. Turta, *J. Magn. Magn. Mater.*, 1999, **196–197**, 561–563.
- 16 O. Kahn, *Chem. Phys. Lett.*, 1997, **265**, 109–114.
- 17 J. Schnack, *Dalton Trans.*, 2010, **39**, 4677–4686.
- 18 C. T. Dziobkowski, J. T. Wroblewski and D. B. Brown, *Inorg. Chem.*, 1981, **20**, 671–678.
- 19 D. N. Hendrickson, in *Research Frontiers in Magnetochemistry*, ed. C. J. O'Connor, World Scientific Co. Pte. Ltd., Singapore, 1993, pp. 87–108.
- 20 R. Colton, A. D'Agostino and J. C. Traeger, *Mass Spectrom. Rev.*, 1995, **14**, 79–106.
- 21 J. B. Fenn, *Angew. Chem., Int. Ed.*, 2003, **42**, 3871–3894.
- 22 M. Yamashita and J. B. Fenn, *J. Phys. Chem.*, 1984, **88**, 4671–4675.
- 23 N. C. Polfer and J. Oomens, *Mass Spectrom. Rev.*, 2009, **28**, 468–494.
- 24 J. Roithova, *Chem. Soc. Rev.*, 2012, **41**, 547–559.
- 25 N. C. Polfer, *Chem. Soc. Rev.*, 2011, **40**, 2211–2221.
- 26 K. Levsen and H. Schwarz, *Angew. Chem., Int. Ed.*, 1976, **15**, 509–519.
- 27 K. M. Ervin and P. B. Armentrout, *J. Chem. Phys.*, 1987, **86**, 2659–2673.
- 28 A. K. Shukla and J. H. Futrell, *J. Mass Spectrom.*, 2000, **35**, 1069–1090.
- 29 S. Dillinger, J. Mohrbach, J. Hewer, M. Gaffga and G. Niedner-Schatteburg, *Phys. Chem. Chem. Phys.*, 2015, **17**, 10358–10362.
- 30 J. Mohrbach, J. Lang, S. Dillinger, M. Prosenc, P. Braunstein and G. Niedner-Schatteburg, *J. Mol. Spectrosc.*, 2017, **332**, 103–108.
- 31 A. B. Wolk, C. M. Leavitt, E. Garand and M. A. Johnson, *Acc. Chem. Res.*, 2013, **47**, 202–210.
- 32 C. T. Wolke, J. A. Fournier, L. C. Dzugan, M. R. Fagiani, T. T. Odbadrakh, H. Knorke, K. D. Jordan, A. B. McCoy, K. R. Asmis and M. A. Johnson, *Science*, 2016, **354**, 1131–1135.
- 33 J. Jašík, J. Žabka, J. Roithová and D. Gerlich, *Int. J. Mass Spectrom.*, 2013, **354–355**, 204–210.
- 34 J. Seo, W. Hoffmann, S. Warnke, X. Huang, S. Gewinner, W. Schöllkopf, M. T. Bowers, G. von Helden and K. Pagel, *Nat. Chem.*, 2017, **9**, 39–44.
- 35 J. Oomens, J. D. Steill and B. Redlich, *J. Am. Chem. Soc.*, 2009, **131**, 4310–4319.
- 36 J. Oomens, B. G. Sartakov, G. Meijer and G. von Helden, *Int. J. Mass Spectrom.*, 2006, **254**, 1–19.
- 37 A. Simon, C. Joblin, N. Polfer and J. Oomens, *J. Phys. Chem. A*, 2008, **112**, 8551–8560.
- 38 Y. Nosenko, F. Menges, C. Riehn and G. Niedner-Schatteburg, *Phys. Chem. Chem. Phys.*, 2013, **15**, 8171–8178.
- 39 A. Fielicke, G. Meijer and G. von Helden, *Eur. Phys. J. D*, 2003, **24**, 69–72.
- 40 A. M. Ricks, J. M. Bakker, G. E. Douberly and M. A. Duncan, *J. Phys. Chem. A*, 2009, **113**, 4701–4708.
- 41 J. Lang, M. Cayir, S. P. Walg, P. Di Martino-Fumo, W. R. Thiel and G. Niedner-Schatteburg, *Chem. – Eur. J.*, 2016, **22**, 2345–2355.
- 42 N. C. Polfer, J. Oomens, D. T. Moore, G. von Helden, G. Meijer and R. C. Dunbar, *J. Am. Chem. Soc.*, 2006, **128**, 517–525.
- 43 J. Lang, J. Mohrbach, S. Dillinger, J. M. Hewer and G. Niedner-Schatteburg, *Chem. Commun.*, 2017, **53**, 420–423.
- 44 J. Laskin and J. H. Futrell, *Mass Spectrom. Rev.*, 2005, **24**, 135–167.
- 45 S. A. McLuckey and D. E. Goeringer, *J. Mass Spectrom.*, 1997, **32**, 461–474.
- 46 F. Menges, C. Riehn and G. Niedner-Schatteburg, *Z. Phys. Chem.*, 2011, **225**, 595.
- 47 E.-L. Zins, C. Pepe and D. Schröder, *J. Mass Spectrom.*, 2010, **45**, 1253–1260.
- 48 E.-L. Zins, C. Pepe, D. Rondeau, S. Rochut, N. Galland and J.-C. Tabet, *J. Mass Spectrom.*, 2009, **44**, 12–17.
- 49 K. V. Barylyuk, K. Chingin, R. M. Balabin and R. Zenobi, *J. Am. Soc. Mass Spectrom.*, 2010, **21**, 172–177.
- 50 B. Miehlich, A. Savin, H. Stoll and H. Preuss, *Chem. Phys. Lett.*, 1989, **157**, 200–206.
- 51 A. D. Becke, *J. Chem. Phys.*, 1993, **98**, 5648–5652.
- 52 T. H. Dunning, *J. Chem. Phys.*, 1989, **90**, 1007–1023.
- 53 M. Dolg, H. Stoll, H. Preuss and R. M. Pitzer, *J. Phys. Chem.*, 1993, **97**, 5852–5859.
- 54 O. Treutler and R. Ahlrichs, *J. Chem. Phys.*, 1995, **102**, 346–354.
- 55 R. Ahlrichs, M. Bär, M. Häser, H. Horn and C. Kölmel, *Chem. Phys. Lett.*, 1989, **162**, 165–169.
- 56 M. Von Arnim and R. Ahlrichs, *J. Comput. Chem.*, 1998, **19**, 1746–1757.
- 57 E. M. V. Kessler, S. Schmitt and C. van Wüllen, *J. Chem. Phys.*, 2013, **139**, 184110.
- 58 F. Illas, I. P. R. Moreira, C. de Graaf and V. Barone, *Theor. Chem. Acc.*, 2000, **104**, 265–272.
- 59 W. Heisenberg, *Z. Phys.*, 1928, **49**, 619–636.
- 60 E. Ising, *Z. Phys.*, 1925, **31**, 253–258.
- 61 C. N. Yang, *Phys. Rev.*, 1952, **85**, 808–816.
- 62 J. M. Ricart, R. Dovesi, C. Roetti and V. R. Saunders, *Phys. Rev. B: Condens. Matter Mater. Phys.*, 1995, **52**, 2381–2389.
- 63 J. E. McClellan, J. P. Murphy, J. J. Mulholland and R. A. Yost, *Anal. Chem.*, 2002, **74**, 402–412.
- 64 J. Laskin, R. P. W. Kong, T. Song and I. K. Chu, *Int. J. Mass Spectrom.*, 2012, **330–332**, 295–301.
- 65 J. Laskin and Z. B. Yang, *Int. J. Mass Spectrom.*, 2011, **308**, 275–280.
- 66 X.-N. Wu, H.-T. Zhao, J. Li, M. Schlangen and H. Schwarz, *Phys. Chem. Chem. Phys.*, 2014, **16**, 26617–26623.
- 67 P. B. Armentrout and J. Simons, *J. Am. Chem. Soc.*, 1992, **114**, 8627–8633.
- 68 O. W. Wheeler, D. R. Carl, T. E. Hofstetter and P. B. Armentrout, *J. Phys. Chem. A*, 2015, **119**, 3800–3815.
- 69 S. Chaudhary and J. D. Van Horn, *J. Inorg. Biochem.*, 2007, **101**, 329–335.

PCCP

Paper

- 70 A. Figuerola, V. Tangoulis, J. Ribas, H. Hartl, I. Brüdgam, M. Maestro and C. Diaz, *Inorg. Chem.*, 2007, **46**, 11017–11024.
- 71 T. Pankewitz, A. Lagutschenkov, G. Niedner-Schatteburg, S. S. Xantheas and Y. T. Lee, *J. Chem. Phys.*, 2007, **126**, 074307.
- 72 G. Niedner-Schatteburg and V. E. Bondybey, *Chem. Rev.*, 2000, **100**, 4059–4086.
- 73 J. C. Lavalley and N. Sheppard, *Spectrochim. Acta, Part A*, 1972, **28**, 2091–2101.
- 74 E. L. Sibert, D. P. Tabor, N. M. Kidwell, J. C. Dean and T. S. Zwier, *J. Phys. Chem. A*, 2014, **118**, 11272–11281.
- 75 M. L. Baker, G. A. Timco, S. Piligkos, J. S. Mathieson, H. Mutka, F. Tuna, P. Kozłowski, M. Antkowiak, T. Guidi, T. Gupta, H. Rath, R. J. Woolfson, G. Kamieniarz, R. G. Pritchard, H. Weihe, L. Cronin, G. Rajaraman, D. Collison, E. J. L. McInnes and R. E. P. Winpenny, *Proc. Natl. Acad. Sci. U. S. A.*, 2012, **109**, 19113–19118.
- 76 S. M. Gorun, G. C. Papaefthymiou, R. B. Frankel and S. J. Lippard, *J. Am. Chem. Soc.*, 1987, **109**, 4244–4255.
- 77 S. M. Gorun and S. J. Lippard, *J. Am. Chem. Soc.*, 1985, **107**, 4568–4570.
- 78 J. Meyer, M. Tombers, C. v. Wüllen, G. Niedner-Schatteburg, S. Peredkov, W. Eberhardt, M. Neeb, S. Palutke, M. Martins and W. Wurth, *J. Chem. Phys.*, 2015, **143**, 104302.
- 79 A. Langenberg, K. Hirsch, A. Ławicki, V. Zamudio-Bayer, M. Niemeyer, P. Chmiela, B. Langbehn, A. Terasaki, B. v. Issendorff and J. T. Lau, *Phys. Rev. B: Condens. Matter Mater. Phys.*, 2014, **90**, 184420.
- 80 J. Lang, J. M. Hower, M. P. Klein, V. Zamundio-Bayer, B. v. Issendorff and T. Lau, *Preliminary results*, unpublished.

10.2 Supporting Information to ‘Magnetostructural Correlation in Isolated Trinuclear Iron(III) Oxo Acetate Complexes’

Supporting Information to “Magnetostructural correlation in isolated trinuclear iron(III) oxo acetate complexes”

Johannes Lang, Joachim M. Hewer, Jonathan Meyer, Jonas Schuchmann,
Christoph van Wüllen, and Gereon Niedner-Schatteburg

*Fachbereich Chemie and Forschungszentrum OPTIMAS,
Technische Universität Kaiserslautern, 67663 Kaiserslautern, Germany*

Table of Content:

1. Details on the ESI-MS and CID measurements (Bruker AmaZon SL)

Figure S1: Mass spectra of isolated $[\text{Fe}_3\text{O}(\text{OAc})_6]^+$ (top), its CID fragmentation mass spectra of (middle) and simulated mass peaks (FWHM = 0.4).

Figure S2: Mass spectra of isolated $[\text{Fe}_3\text{O}(\text{OAc})_6(\text{Py})_1]^+$ (top), its CID fragmentation mass spectra of (middle) and simulated mass peaks (FWHM = 0.4).

Figure S3: Mass spectra of isolated $[\text{Fe}_3\text{O}(\text{OAc})_6(\text{Py})_2]^+$ (top), its CID fragmentation mass spectra of (middle) and simulated mass peaks (FWHM = 0.4).

Figure S4: Mass spectra of isolated $[\text{Fe}_3\text{O}(\text{OAc})_6(\text{Py})_3]^+$ (top), its CID fragmentation mass spectra of (middle) and simulated mass peaks (FWHM = 0.4).

Figure S5: Mass spectra of isolated $[\text{Fe}_3\text{O}(\text{OAc})_6(\text{Py})_2]^+$ (top), its CID fragmentation (second), subsequent isolation of $[\text{Fe}_3\text{O}(\text{OAc})_6(\text{Py})_1]^+$ (third), its CID fragmentation mass spectra (fourth) and simulated mass peaks (FWHM = 0.4) (bottom).

Table S1: Compilation of ESI-MS data on $[\text{Fe}_3\text{O}(\text{OAc})_6(\text{Py})_n]^+$ ($n = 1,2,3$; $\text{OAc} = \text{CH}_3\text{CO}_2$). The indicated mass labels refer to the most abundant isotope peaks.

Figure S6: Mass spectra of isolated $[\text{Fe}_3\text{O}(\text{OAc})_6(\text{Py})_3]^+$ (**top**), its CID fragmentation (**second**), subsequent isolation of $[\text{Fe}_3\text{O}(\text{OAc})_6(\text{Py})_2]^+$ (**third**), its CID fragmentation mass spectra (**fourth**), isolation of $[\text{Fe}_3\text{O}(\text{OAc})_6(\text{Py})_1]^+$ (**fifth**), its CID fragmentation mass spectra (**sixth**), isolation of $[\text{Fe}_3\text{O}(\text{OAc})_6]^+$ (**seventh**), its CID fragmentation mass spectra (**eighth**) and simulated mass peaks (FWHM = 0.4) (**bottom**).

2. IR-MPD and DFT calculations of $[\text{Fe}_3\text{O}(\text{OAc})_6(\text{Py})_n]^+$ ($n = 0,1,2,3$)

Figure S7: (a) IR-MPD spectrum of $[\text{Fe}_3\text{O}(\text{OAc})_6]^+$ in the spectral range of 1000 – 3300 cm^{-1} . (b-e) Calculated IR absorption spectra of geometry optimized $[\text{Fe}_3\text{O}(\text{OAc})_6]^+$ in the four broken symmetry configurations 16-tet, DUU, UDU and UUD.

Figure S8: (a) IR-MPD spectrum of $[\text{Fe}_3\text{O}(\text{OAc})_6\text{Py}_1]^+$ in the spectral range of 1000 – 3300 cm^{-1} . (b-e) Calculated IR absorption spectra of geometry optimized $[\text{Fe}_3\text{O}(\text{OAc})_6\text{Py}_1]^+$ in the four broken symmetry configurations 16-tet, DUU, UDU and UUD.

Figure S9: (a) IR-MPD spectrum of $[\text{Fe}_3\text{O}(\text{OAc})_6\text{Py}_2]^+$ in the spectral range of 1000 – 3300 cm^{-1} . (b-e) Calculated IR absorption spectra of geometry optimized $[\text{Fe}_3\text{O}(\text{OAc})_6\text{Py}_2]^+$ in the four broken symmetry configurations 16-tet, DUU, UDU and UUD.

Figure S10: (a) IR-MPD spectrum of $[\text{Fe}_3\text{O}(\text{OAc})_6\text{Py}_3]^+$ in the spectral range of 1000 – 3300 cm^{-1} . (b-e) Calculated IR absorption spectra of geometry optimized $[\text{Fe}_3\text{O}(\text{OAc})_6\text{Py}_3]^+$ in the four broken symmetry configurations 16-tet, DUU, UDU and UUD.

Figure S11: Relative energies of $[\text{Fe}_3\text{O}(\text{OAc})_6(\text{Py})_n]^+$ ($n = 0,1,2,3$) as a function of the multiplicity.

Table S2: Calculated fragmentation free energies $\Delta_{fr}G_n^0$ and fragmentation energies $\Delta_{fr}E_n$ of $[\text{Fe}_3\text{O}(\text{OAc})_6(\text{Py})_n]^+$ ($n = 1,2,3$).

Figure S12: Top: IR-MPD spectrum of $[\text{Fe}_3\text{O}(\text{OAc})_6]^+$ in the spectral range of 1000 – 3300 cm^{-1} . **Middle and Bottom:** Calculated IR absorption spectra of geometry optimized $[\text{Fe}_3\text{O}(\text{OAc})_6]^+$ ($S+1 = 16$) without and with dispersion correction (Grimme D3).

Figure S13: Top: IR-MPD spectrum of $[\text{Fe}_3\text{O}(\text{OAc})_6(\text{Py})_1]^+$ in the spectral range of 1000 – 3300 cm^{-1} . **Middle and Bottom:** Calculated IR absorption spectra of geometry optimized $[\text{Fe}_3\text{O}(\text{OAc})_6]^+$ ($S+1 = 16$) without and with dispersion correction (Grimme D3).

Figure S14: Top: IR-MPD spectrum of $[\text{Fe}_3\text{O}(\text{OAc})_6(\text{Py})_2]^+$ in the spectral range of 1000 – 3300 cm^{-1} . **Middle and Bottom:** Calculated IR absorption spectra of geometry optimized $[\text{Fe}_3\text{O}(\text{OAc})_6]^+$ ($S+1 = 16$) without and with dispersion correction (Grimme D3).

Figure S15: Vibrational shifts of the CH_3 bending vibration frequency ($\delta(\text{CH}_3)$) as well as the asymmetric carboxylic CO stretching vibration frequency ($\nu(\text{CO})$) in $[\text{Fe}_3\text{O}(\text{OAc})_6(\text{Py})_n]^+$ ($n = 0,1,2,3$).

Figure S16: Left: Calculated binding energies $\Delta_{fr}E_n$ and free binding energies $\Delta_{fr}G_n^0$ of pyridine ligands in $[\text{Fe}_3\text{O}(\text{OAc})_6(\text{Py})_n]^+$ ($n = 1,2,3$).

Figure S17: Relaxed total energy of the coordinated pyridine torsion around the Fe-N axis in $[\text{Fe}_3\text{O}(\text{OAc})_6(\text{Py})_1]^+$.

3. Monitored m/z values of IRMPD spectra and CID – appearance curves

Table S3: Observed parent and fragment masses of $[\text{Fe}_3\text{O}(\text{OAc})_6]^+$

Table S4: Observed parent and fragment masses of $[\text{Fe}_3\text{O}(\text{OAc})_6(\text{Py})_1]^+$

Table S5: Observed parent and fragment masses of $[\text{Fe}_3\text{O}(\text{OAc})_6(\text{Py})_2]^+$:

Table S6: Observed parent and fragment masses of $[\text{Fe}_3\text{O}(\text{OAc})_6(\text{Py})_3]^+$:

4. Assignments of IR-MPD Bands and isotopic substitution experiments

Figure S18: Isotopic substitution experiments

Figure S19: Isotopic substitution experiments: **(a,b)** IR-MPD spectrum of $[\text{Fe}_3\text{O}(\text{OAc})_6\text{Py}_3]^+$ and $[\text{Fe}_3\text{O}(\text{OAcD}_3)_6(\text{PyD}_5)_3]^+$ in the spectral range of $1500 - 1700\text{cm}^{-1}$, each with a fit of three gaussian functions and their sum. **(c-d)** Calculated IR absorption spectra of geometry optimized $[\text{Fe}_3\text{O}(\text{OAc})_6]^+$ and $[\text{Fe}_3\text{O}(\text{OAcD}_3)_6(\text{PyD}_5)_3]^+$ respectively.

Figure S20: Isotopic substitution experiments: The same as Fig. S18, but with a different decomposition of the experimental spectrum in **(a)**.

Table S7: Assignment of experimentally observed IR-MPD bands to calculated vibrational bands in $[\text{Fe}_3\text{O}(\text{OAc})_6(\text{Py})_n]^+$; $n = 0, 1, 2, 3$.

1. Details on the ESI-MS and CID measurements (Bruker AmaZon SL)

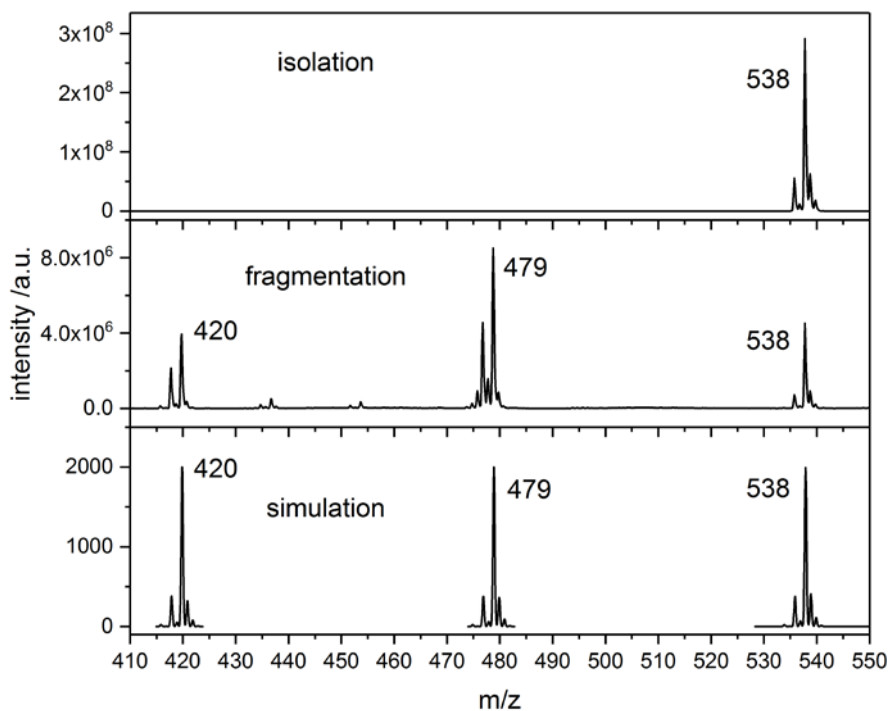


Figure S1: Mass spectra of isolated $[\text{Fe}_3\text{O}(\text{OAc})_6]^+$ (top), its CID fragmentation mass spectra of (middle) and simulated mass peaks (FWHM = 0.4).

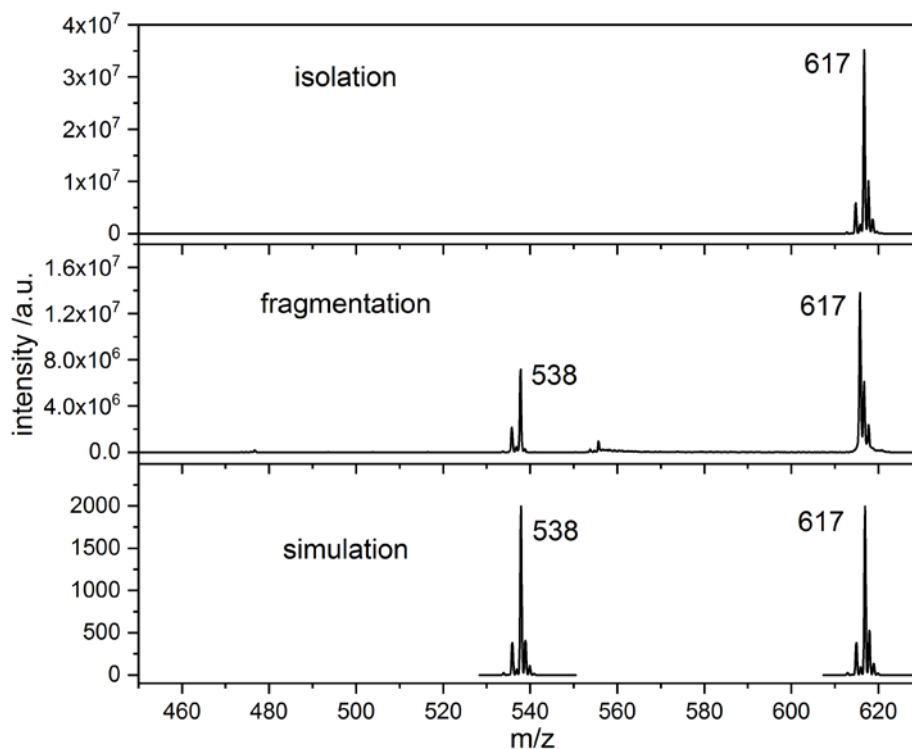


Figure S2: Mass spectra of isolated $[\text{Fe}_3\text{O}(\text{OAc})_6(\text{Py})_1]^+$ (top), its CID fragmentation mass spectra of (middle) and simulated mass peaks (FWHM = 0.4).

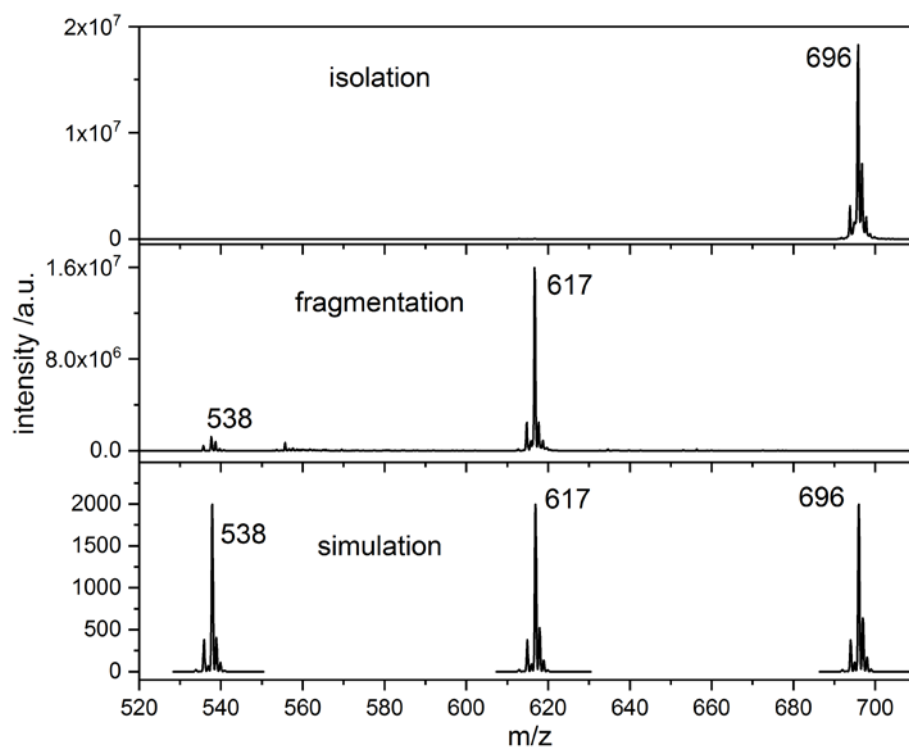


Figure S3: Mass spectra of isolated $[\text{Fe}_3\text{O}(\text{OAc})_6(\text{Py})_2]^+$ (top), its CID fragmentation mass spectra of (middle) and simulated mass peaks (FWHM = 0.4).

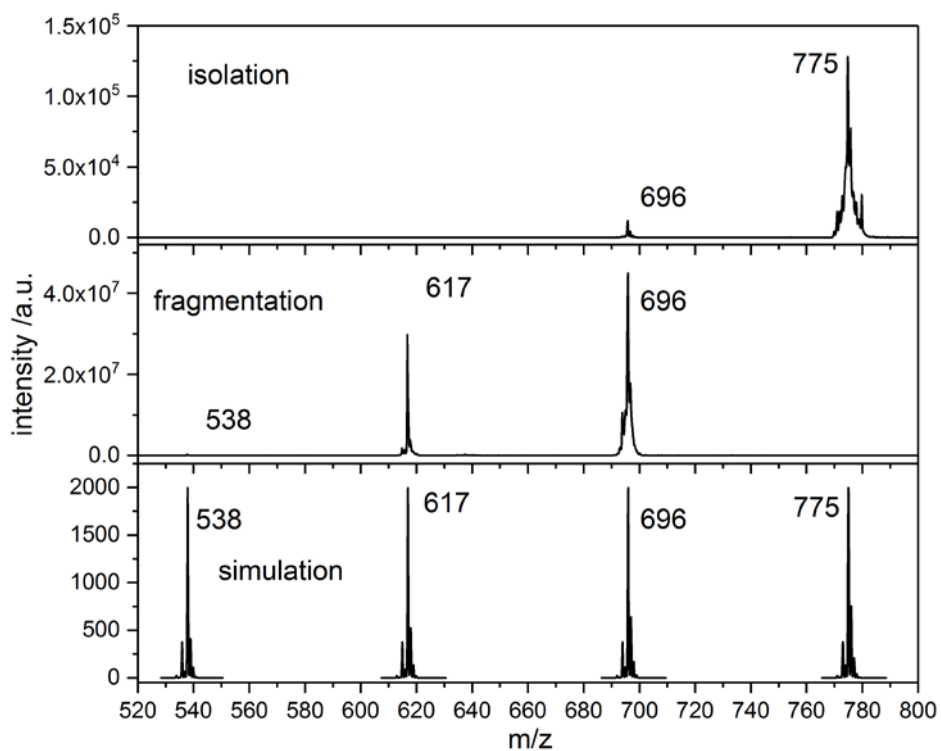


Figure S4: Mass spectra of isolated $[\text{Fe}_3\text{O}(\text{OAc})_6(\text{Py})_3]^+$ (top), its CID fragmentation mass spectra of (middle) and simulated mass peaks (FWHM = 0.4).

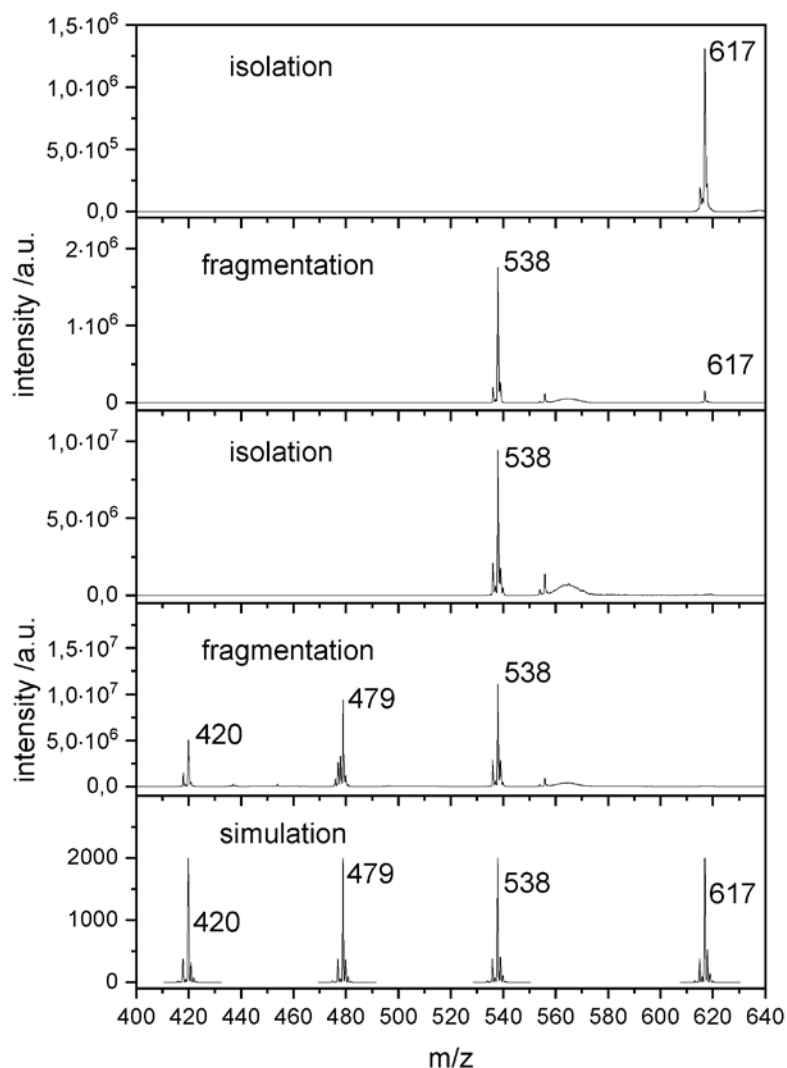


Figure S5: Mass spectra of isolated $[\text{Fe}_3\text{O}(\text{OAc})_6(\text{Py})_2]^+$ (top), its CID fragmentation (second), subsequent isolation of $[\text{Fe}_3\text{O}(\text{OAc})_6(\text{Py})_1]^+$ (third), its CID fragmentation mass spectra (fourth) and simulated mass peaks (FWHM = 0.4) (bottom).

Table S1: Compilation of ESI-MS data on $[\text{Fe}_3\text{O}(\text{OAc})_6(\text{Py})_n]^+$ ($n = 1, 2, 3$; $\text{OAc} = \text{CH}_3\text{CO}_2$). The indicated mass labels refer to the most abundant isotope peaks.

Species	m/z
$[\text{Fe}_3\text{O}(\text{OAc})_4]^+$	420
$[\text{Fe}_3\text{O}(\text{OAc})_5]^+$	479
$[\text{Fe}_3\text{O}(\text{OAc})_6]^+$	538
$[\text{Fe}_3\text{O}(\text{OAc})_6(\text{Py})_1]^+$	617
$[\text{Fe}_3\text{O}(\text{OAc})_6(\text{Py})_2]^+$	696
$[\text{Fe}_3\text{O}(\text{OAc})_6(\text{Py})_3]^+$	775

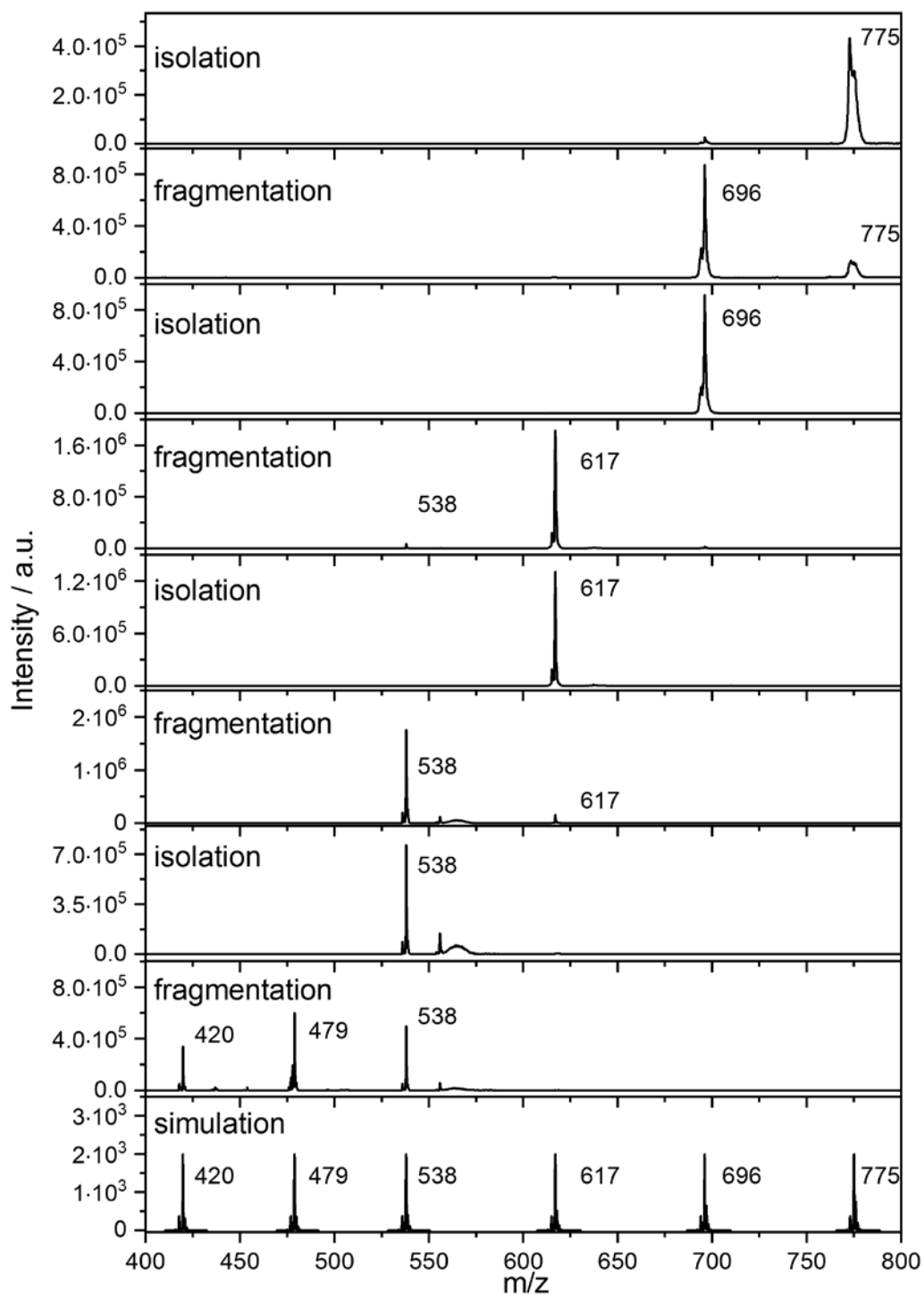


Figure S6: Mass spectra of isolated $[\text{Fe}_3\text{O}(\text{OAc})_6(\text{Py})_3]^+$ (**top**), its CID fragmentation (**second**), subsequent isolation of $[\text{Fe}_3\text{O}(\text{OAc})_6(\text{Py})_2]^+$ (**third**), its CID fragmentation mass spectra (**fourth**), isolation of $[\text{Fe}_3\text{O}(\text{OAc})_6(\text{Py})_1]^+$ (**fifth**), its CID fragmentation mass spectra (**sixth**), isolation of $[\text{Fe}_3\text{O}(\text{OAc})_6]^+$ (**seventh**), its CID fragmentation mass spectra (**eighth**) and simulated mass peaks (FWHM = 0.4) (**bottom**).

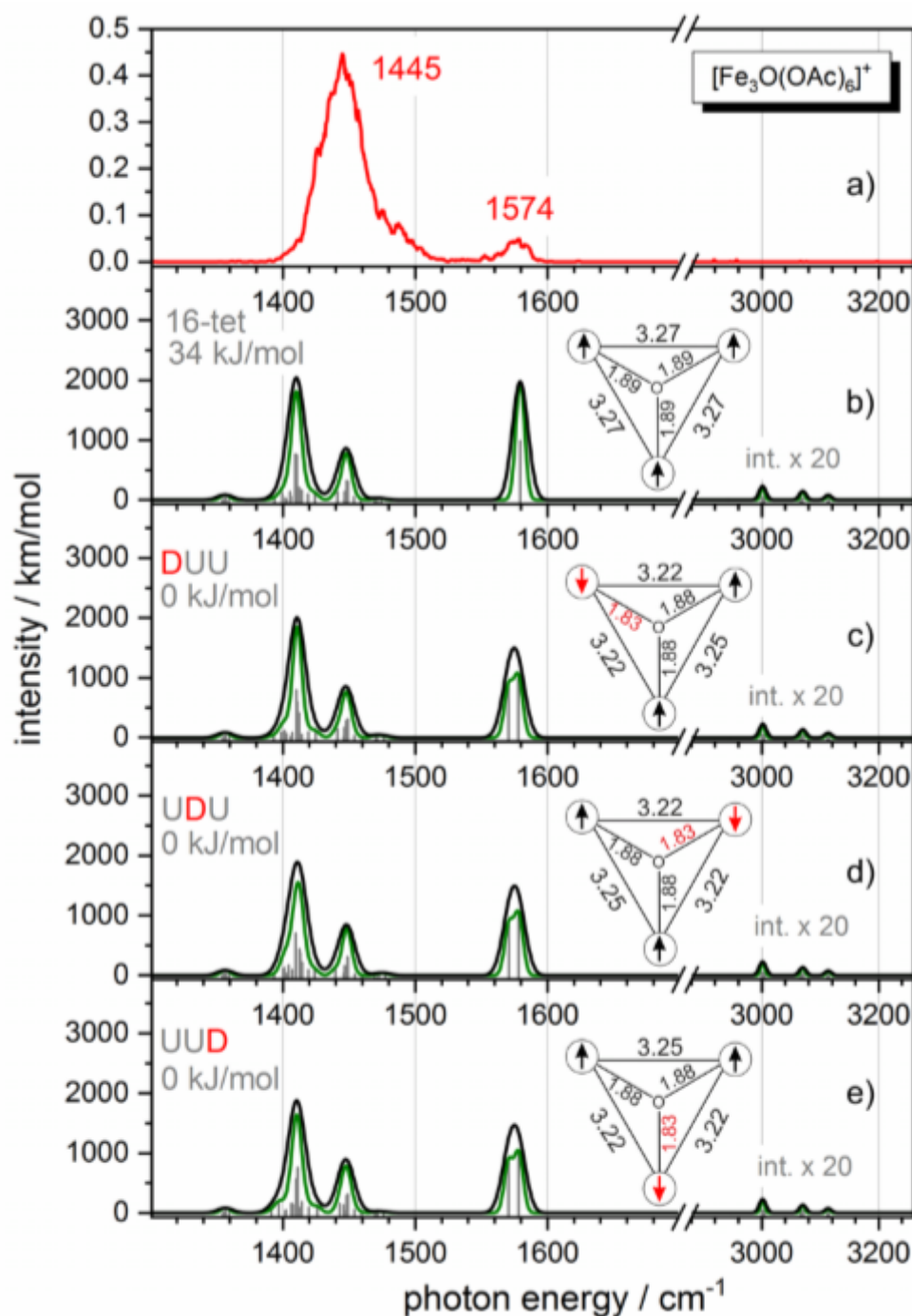
2. IR-MPD and DFT calculations of of $[\text{Fe}_3\text{O}(\text{OAc})_6(\text{Py})_n]^+$ ($n = 0,1,2,3$)

Figure S7: a) IR-MPD spectrum of $[\text{Fe}_3\text{O}(\text{OAc})_6]^+$ in the spectral range of 1000 – 3300 cm^{-1} . (b-e) Calculated IR absorption spectra of geometry optimized $[\text{Fe}_3\text{O}(\text{OAc})_6]^+$ in the four broken symmetry configurations 16-tet, DUU, UDU and UUD. The stick spectra (grey) were broadened with Gaussian envelope curves (FWHM = 7 cm^{-1} (black) and 4 cm^{-1} (green)). The calculations were performed at the B3LYP / cc-pVTZ (H, C, N, O) and ecp-10-mdf (Fe) level of theory. The frequencies are scaled with 0.98. The insets show atomic distances (in Å) within the triangular Fe_3O cores of $[\text{Fe}_3\text{O}(\text{OAc})_6]^+$.

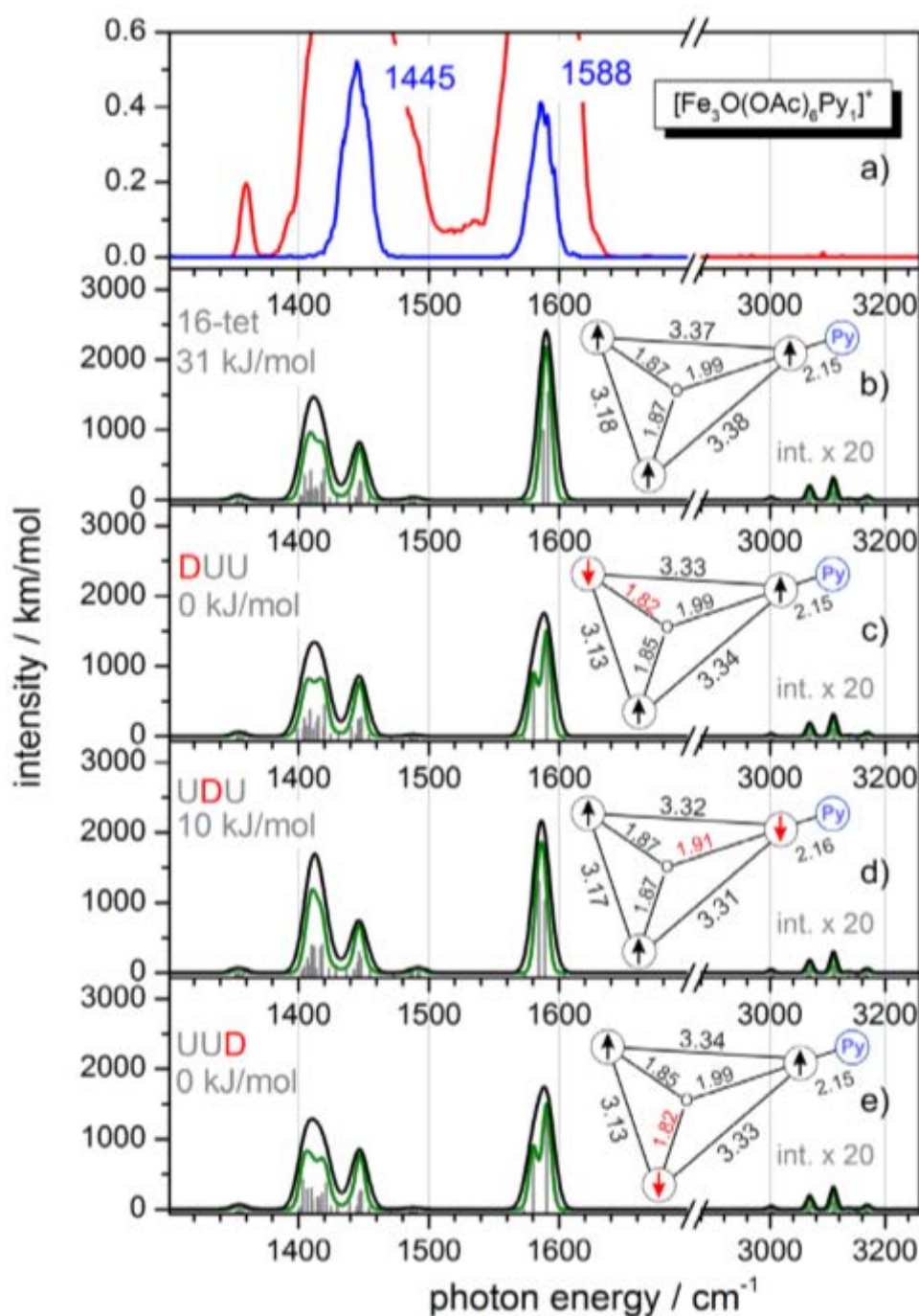


Figure S8: (a) IR-MPD spectrum of $[\text{Fe}_3\text{O}(\text{OAc})_6\text{Py}_1]^+$ in the spectral range of 1000 – 3300 cm^{-1} . Red curves indicate measurements at maximum photon flux while blue curves show spectra with attenuated pulse energies ($\sim 50\%$). (b-e) Calculated IR absorption spectra of geometry optimized $[\text{Fe}_3\text{O}(\text{OAc})_6\text{Py}_1]^+$ in the four broken symmetry configurations 16-tet, DUU, UDU and UUD. The stick spectra (grey) were broadened with Gaussian envelope curves (FWHM = 7 cm^{-1} (black) and 4 cm^{-1} (green)). The calculations were performed at the B3LYP / cc-pVTZ (H, C, N, O) and ecp-10-mdf (Fe) level of theory. The frequencies are scaled with 0.98. The insets show atomic distances (in Å) within the triangular Fe_3O cores of $[\text{Fe}_3\text{O}(\text{OAc})_6\text{Py}_1]^+$.

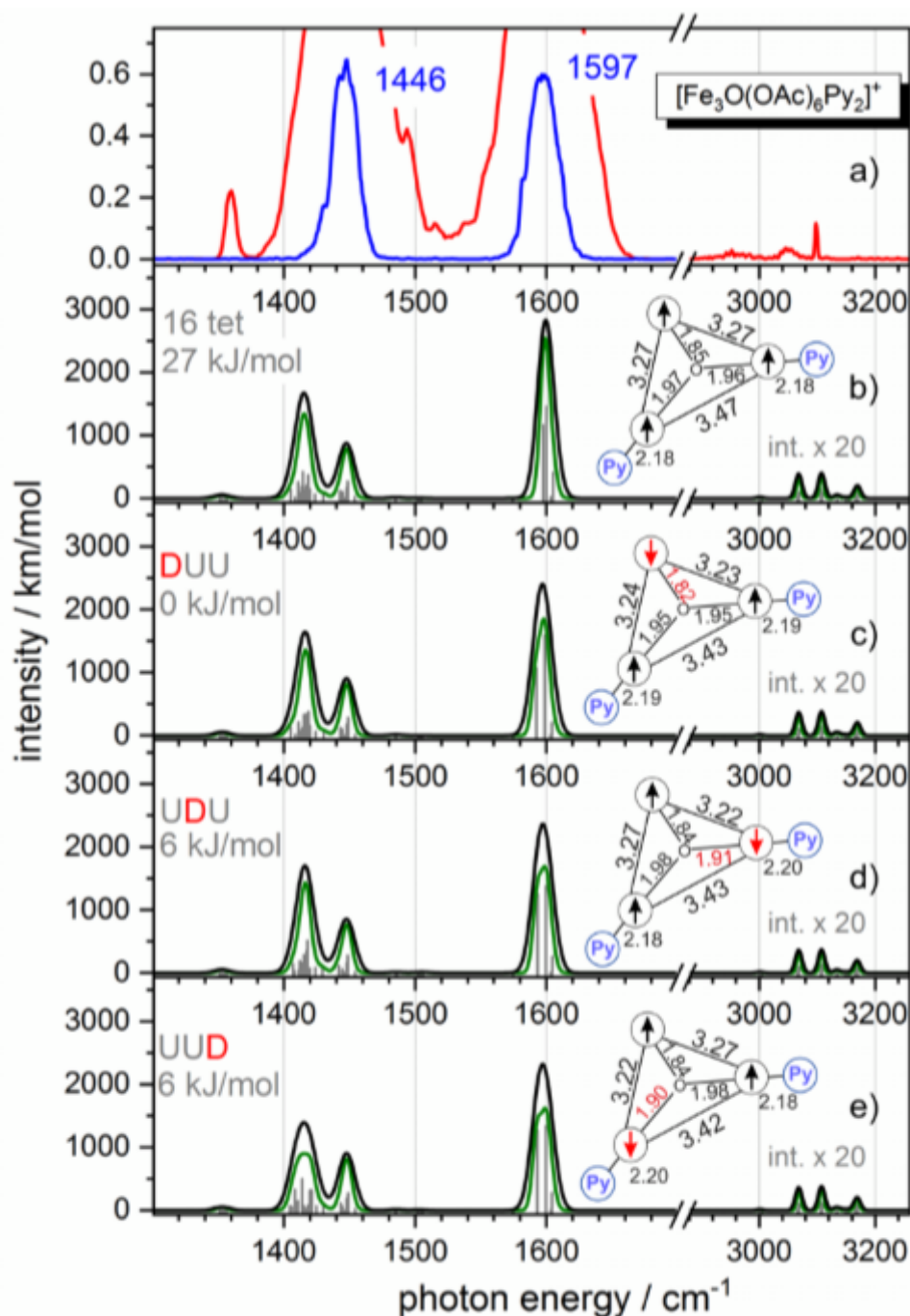


Figure S9: (a) IR-MPD spectrum of $[\text{Fe}_3\text{O}(\text{OAc})_6\text{Py}_2]^+$ in the spectral range of 1000 – 3300 cm^{-1} . Red curves indicate measurements at maximum photon flux while blue curves show spectra with attenuated pulse energies ($\sim 50\%$). (b-e) Calculated IR absorption spectra of geometry optimized $[\text{Fe}_3\text{O}(\text{OAc})_6\text{Py}_2]^+$ in the four broken symmetry configurations 16-tet, DUU, UDU and UUD. The stick spectra (grey) were broadened with Gaussian envelope curves (FWHM = 7 cm^{-1} (black) and 4 cm^{-1} (green)). The calculations were performed at the B3LYP/cc-pVTZ (H, C, N, O) and ecp-10-mdf (Fe) level of theory. The frequencies are scaled with 0.98. The insets show atomic distances (in Å) within the triangular Fe_3O cores of $[\text{Fe}_3\text{O}(\text{OAc})_6\text{Py}_2]^+$.

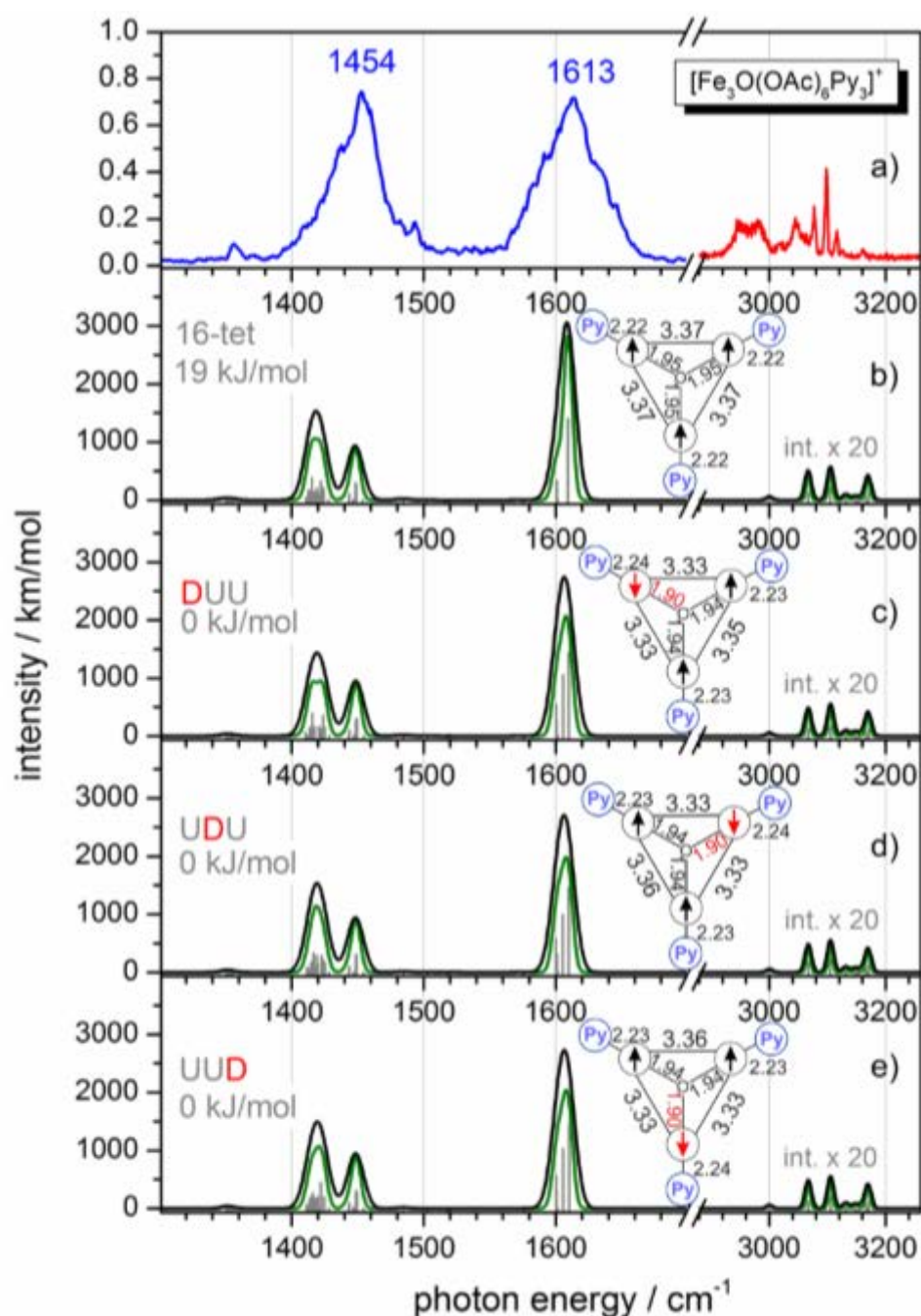


Figure S10: IR-MPD spectrum of $[\text{Fe}_3\text{O}(\text{OAc})_6\text{Py}_3]^+$ in the spectral range of 1000 – 3300 cm^{-1} . Red curves indicate measurements at maximum photon flux while blue curves show spectra with attenuated pulse energies ($\sim 50\%$). **b-e)** Calculated IR absorption spectra of geometry optimized $[\text{Fe}_3\text{O}(\text{OAc})_6\text{Py}_3]^+$ in the four broken symmetry configurations 16-tet, DUU, UDU and UUD. The stick spectra (grey) were broadened with Gaussian envelope curves (FWHM = 7 cm^{-1} (black) and 4 cm^{-1} (green)). The calculations were performed at the B3LYP_Gaussian / cc-pVTZ (H, C, N, O) and ecp-10-mdf (Fe) level of theory. The frequencies are scaled with 0.98. The insets show atomic distances (in Å) within the triangular Fe_3O cores of $[\text{Fe}_3\text{O}(\text{OAc})_6\text{Py}_3]^+$.

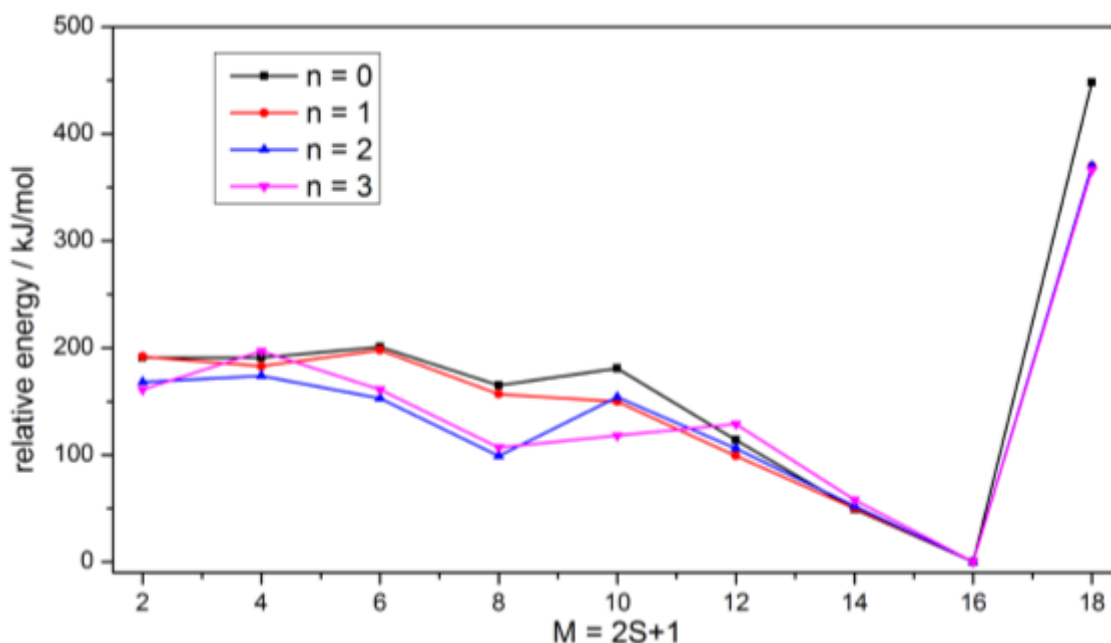


Figure S11: Relative energies of $[\text{Fe}_3\text{O}(\text{OAc})_6(\text{Py})_n]^+$ ($n = 0, 1, 2, 3$) as a function of the multiplicity. The geometry was fully optimized for each multiplicity. The calculations were performed at the B3LYP_Gaussian / cc-pVTZ (H, C, N, O) and ecp-10-mdf (Fe) level of theory

Table S2: Calculated fragmentation free energies $\Delta_{fr}G_n^0$ and fragmentation energies $\Delta_{fr}E_n$ of $[\text{Fe}_3\text{O}(\text{OAc})_6(\text{Py})_n]^+$ ($n = 1, 2, 3$). The multiplicity is $S+1 = 16$. The calculations were performed at the B3LYP/cc-pVTZ (H,C,N,O) and Stuttgart 1997 ECP (Fe) level of theory as implemented in the Gaussian 09 program package. BSSE correction was performed using the counterpoise routine.

$[\text{Fe}_3\text{O}(\text{OAc})_6(\text{Py})_n]^+$	$\Delta_{fr}G_n^0 /$ kJ/mol	$\Delta_{fr}G_n^0$ (BSSE corr.)/ kJ/mol	$\Delta_{fr}E_n /$ kJ/mol	$\Delta_{fr}E_{n=1}$ (BSSE corr.) / kJ/mol
n = 3	28	19	90	81
n = 2	55	46	113	104
n = 1	82	73	136	127

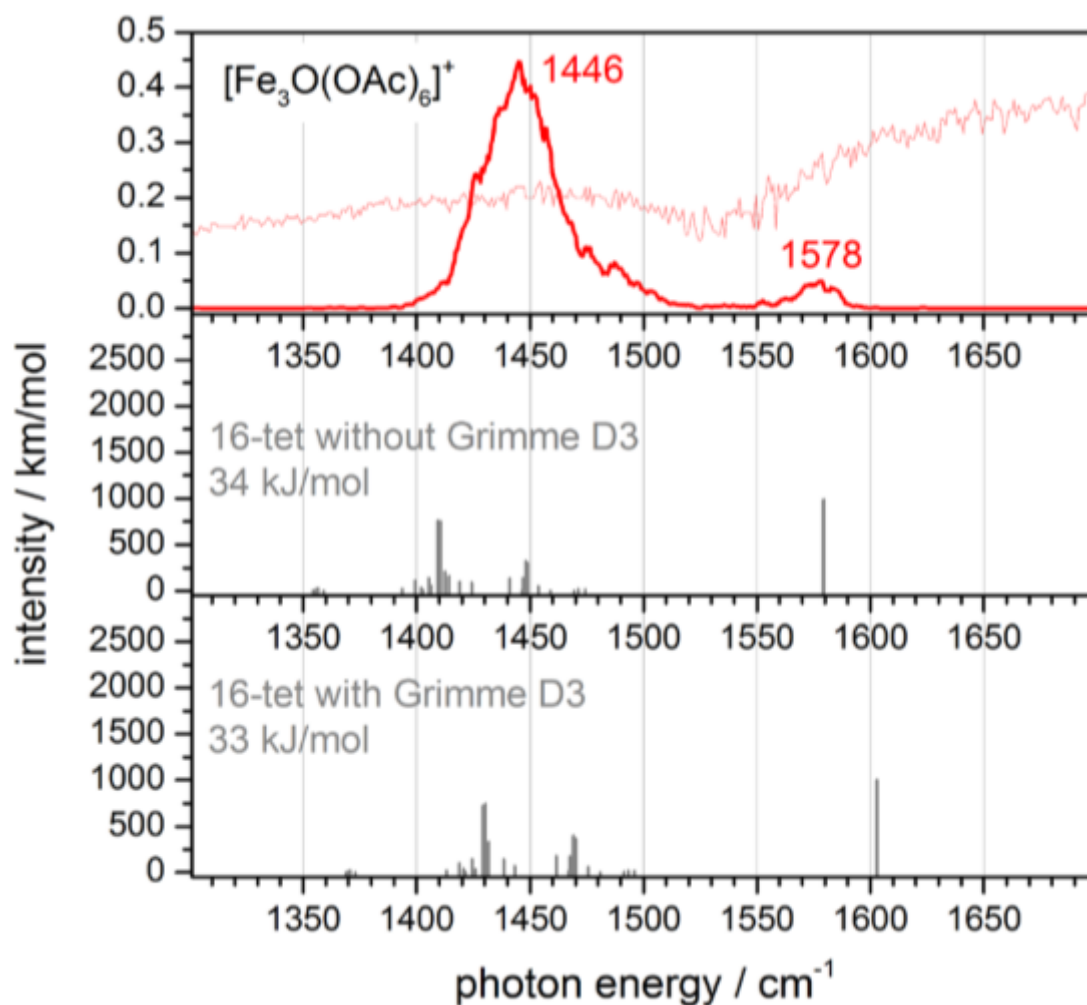


Figure S12: Top: IR-MPD spectrum of $[\text{Fe}_3\text{O}(\text{OAc})_6]^+$ in the spectral range of 1000 – 3300 cm⁻¹. Middle and Bottom: Calculated IR absorption spectra of geometry optimized $[\text{Fe}_3\text{O}(\text{OAc})_6]^+$ ($S+1 = 16$) without and with dispersion correction (Grimme D3). The calculations were performed at the B3LYP/ cc-pVTZ (H, C, N, O) and ecp-10-mdf (Fe) level of theory. The frequencies are scaled with 0.98.

Ref.: S. Grimme, J. Antony, S. Ehrlich and H. Krieg, *J. Chem. Phys.*, 2010, 132, 154104.

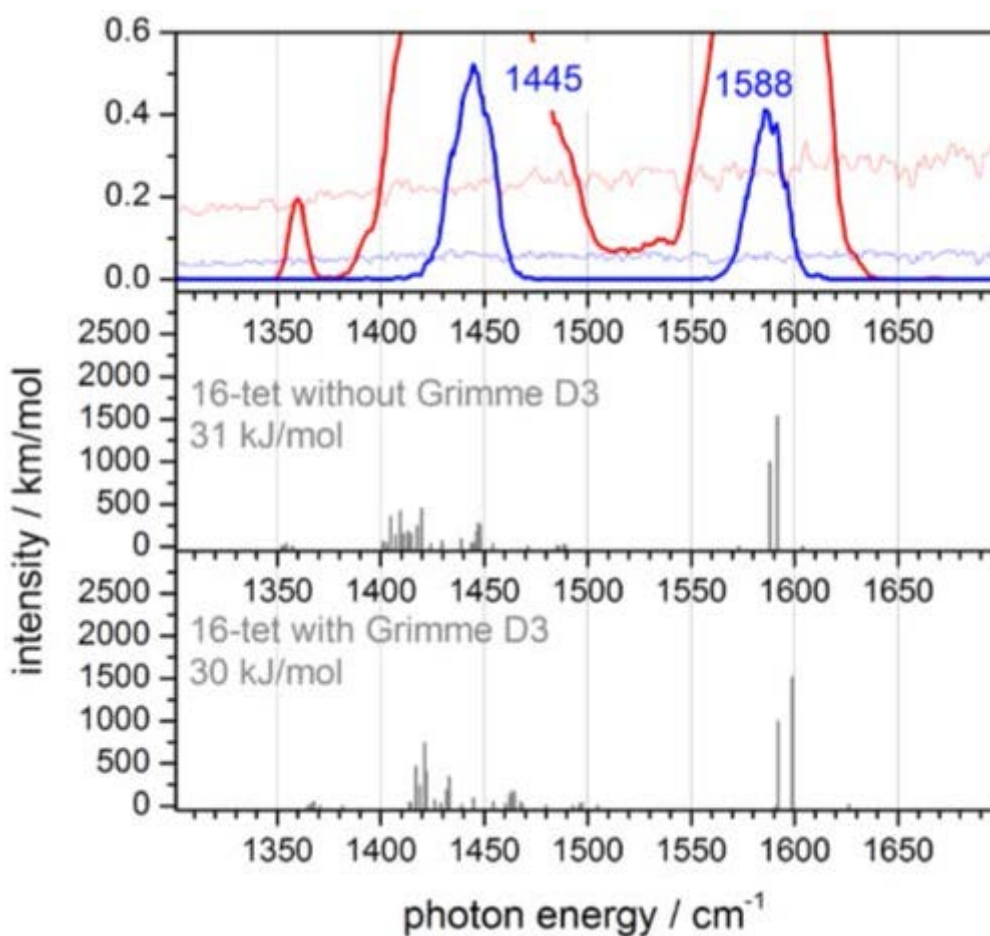


Figure S13: Top: IR-MPD spectrum of $[\text{Fe}_3\text{O}(\text{OAc})_6(\text{Py})_1]^+$ in the spectral range of 1000 – 3300 cm^{-1} . Red curves indicate measurements at maximum photon flux while blue curves show spectra with attenuated pulse energies ($\sim 50\%$). **Middle and Bottom:** Calculated IR absorption spectra of geometry optimized $[\text{Fe}_3\text{O}(\text{OAc})_6]^+$ ($S+1 = 16$) without and with dispersion correction (Grimme D3). The calculations were performed at the B3LYP/ cc-pVTZ (H, C, N, O) and ecp-10-mdf (Fe) level of theory. The frequencies are scaled with 0.98.

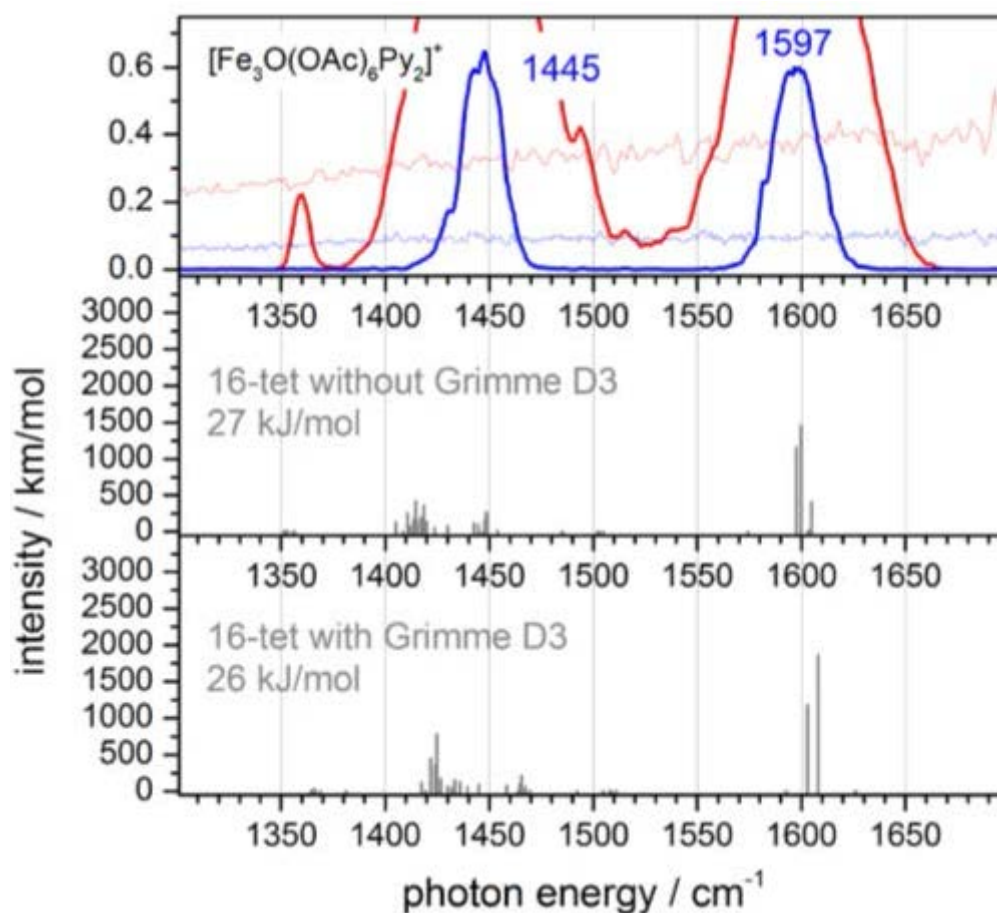


Figure S14: Top: IR-MPD spectrum of $[\text{Fe}_3\text{O}(\text{OAc})_6(\text{Py})_2]^+$ in the spectral range of $1000 - 3300 \text{ cm}^{-1}$. Red curves indicate measurements at maximum photon flux while blue curves show spectra with attenuated pulse energies ($\sim 50\%$). **Middle and Bottom:** Calculated IR absorption spectra of geometry optimized $[\text{Fe}_3\text{O}(\text{OAc})_6]^+$ ($S+1 = 16$) without and with dispersion correction (Grimme D3). The calculations were performed at the B3LYP/ cc-pVTZ (H, C, N, O) and ecp-10-mdf (Fe) level of theory. The frequencies are scaled with 0.98.

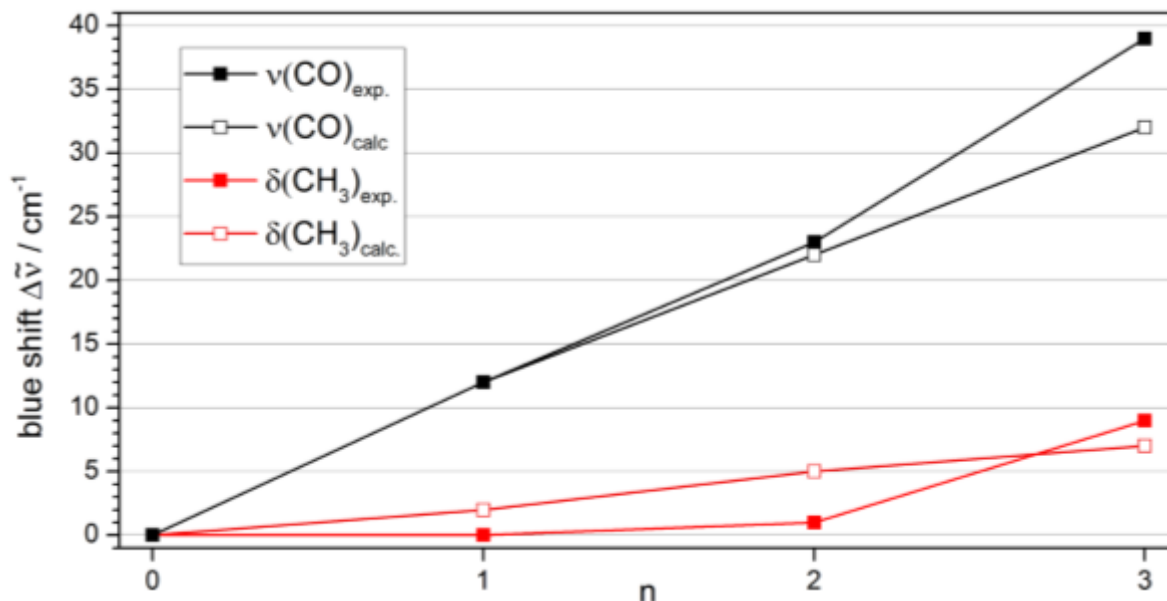


Figure S15: Vibrational shifts of the CH_3 bending vibration frequency ($\delta(\text{CH}_3)$) as well as the asymmetric carboxylic CO stretching vibration frequency ($\nu(\text{CO})$) in $[\text{Fe}_3\text{O}(\text{OAc})_6(\text{Py})_n]^+$ ($n = 0, 1, 2, 3$). The calculations were performed at the B3LYP/cc-pVTZ (H, C, N, O) and ecp-10-mdf (Fe) level of theory with five unpaired electrons on each Fe center and a UUD ($n = 0, 1, 3$) or DUU ($n = 2$) symmetry configuration corresponding to the minimum structures. All frequencies are scaled with 0.98.

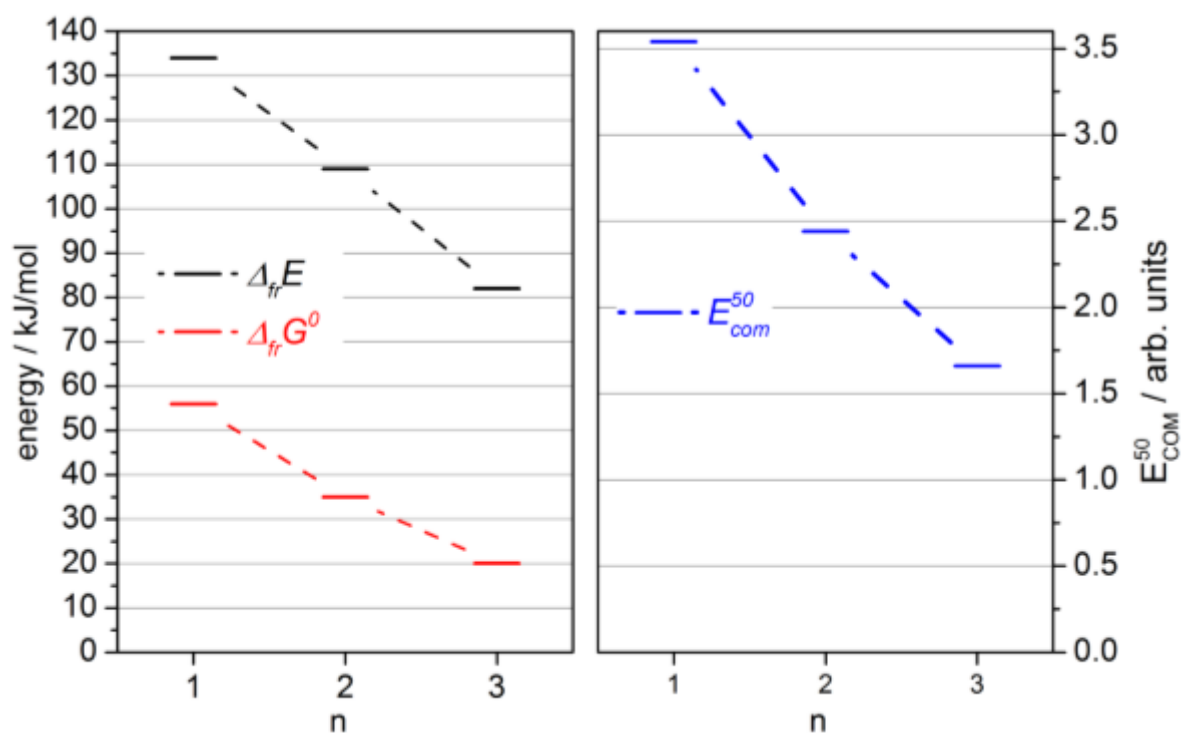


Figure S16: Left: Calculated binding energies $\Delta_{fr}E_n$ and free binding energies $\Delta_{fr}G_n^0$ of pyridine ligands in $[\text{Fe}_3\text{O}(\text{OAc})_6(\text{Py})_n]^+$ ($n = 1, 2, 3$). The calculations were performed at the B3LYP_Gaussian / cc pVTZ (H, C, N, O) and ecp-10-mdf (Fe) level of theory. Right: E_{COM}^{50} values extracted from CID appearance curves (cf. Fig. 2).

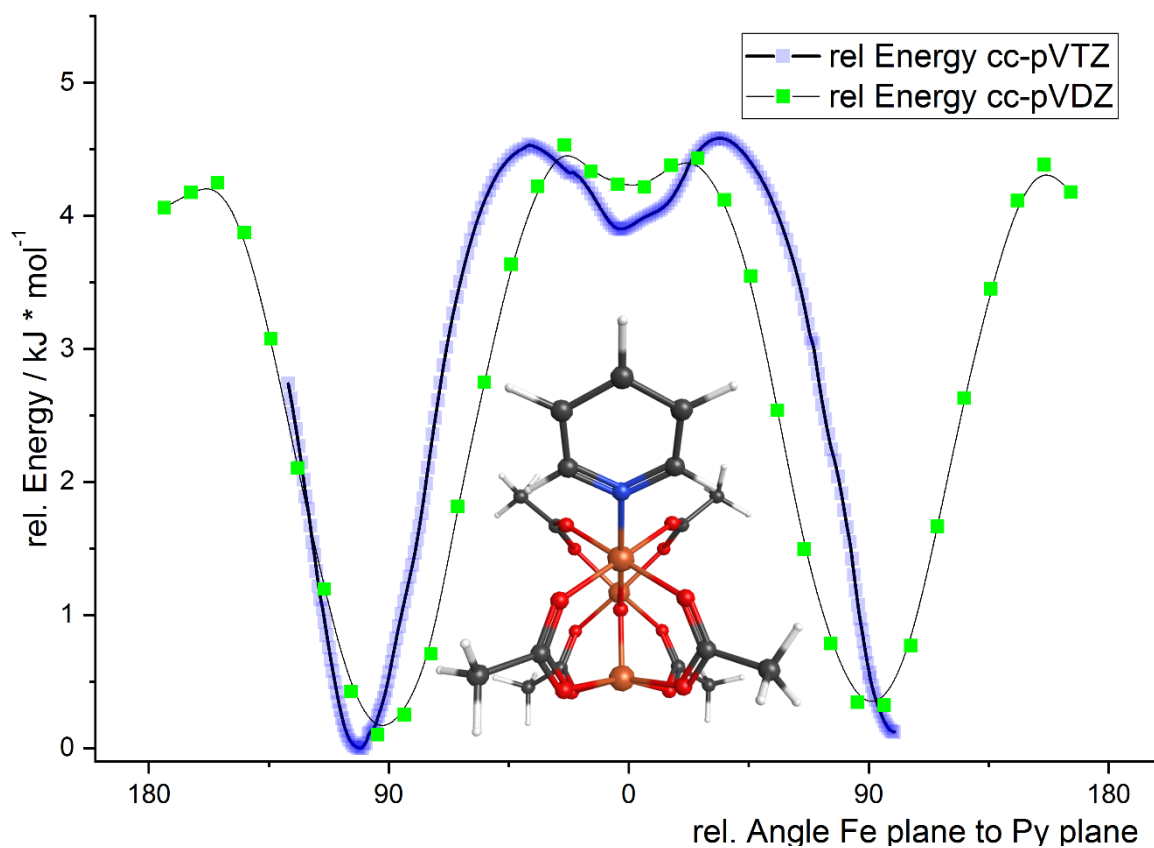


Figure S17: Relaxed total energy of the coordinated pyridine torsion around the Fe-N axis in $[\text{Fe}_3\text{O}(\text{OAc})_6(\text{Py})_1]^+$. Calculation performed at B3LYP / cc-pVDZ (green) and cc-pVTZ (blue) (H, C, N, O) and ecp-10-mdf (Fe) level of theory. The given angle is that of the pyridine plane relative to the plane through all three Fe atoms.

5. Monitored m/z values of IR-MPD spectra and of CID – appearance curves

Table S3: Observed parent and fragment masses of $[\text{Fe}_3\text{O}(\text{OAc})_6]^+$

Parent $[\text{Fe}_3\text{O}(\text{OAc})_6]^+$	Fragment 1 $[\text{Fe}_3\text{O}(\text{OAc})_5]^+$	Fragment 2 $[\text{Fe}_3\text{O}(\text{OAc})_4]^+$
535.8	476.7	417.7
536.8	477.8	418.8
537.8	478.7	419.7
538.7	479.8	420.8
553.7		

Table S4: Observed parent and fragment masses of $[\text{Fe}_3\text{O}(\text{OAc})_6(\text{Py})_1]^+$

Parent $[\text{Fe}_3\text{O}(\text{OAc})_6(\text{Py})_1]^+$	Fragment $[\text{Fe}_3\text{O}(\text{OAc})_6]^+$
614.8	535.8
615.8	536.8
616.8	537.8
617.7	538.7
618.9	553.7

Table S5: Observed parent and fragment masses of $[\text{Fe}_3\text{O}(\text{OAc})_6(\text{Py})_2]^+$

Parent $[\text{Fe}_3\text{O}(\text{OAc})_6(\text{Py})_2]^+$	Fragment 1 $[\text{Fe}_3\text{O}(\text{OAc})_6(\text{Py})_1]^+$	Fragment 2 $[\text{Fe}_3\text{O}(\text{OAc})_6]^+$
693.8	614.8	535.8
694.9	615.8	536.8
695.8	616.8	537.8
696.8	617.7	538.7
698.9	618.9	553.7

Table S6: Observed parent and fragment masses of $[\text{Fe}_3\text{O}(\text{OAc})_6(\text{Py})_3]^+$

Parent $[\text{Fe}_3\text{O}(\text{OAc})_6(\text{Py})_3]^+$	Fragment 1 $[\text{Fe}_3\text{O}(\text{OAc})_6(\text{Py})_2]^+$	Fragment 2 $[\text{Fe}_3\text{O}(\text{OAc})_6(\text{Py})_1]^+$	Fragment 3 $[\text{Fe}_3\text{O}(\text{OAc})_6]^+$
772.9	693.8	614.8	535.8
773.9	694.9	615.8	536.8
775	695.8	616.8	537.8
776	696.8	617.7	538.7
	698.9	618.9	553.7

6. Assignments of IR-MPD Bands and isotopic substitution experiments

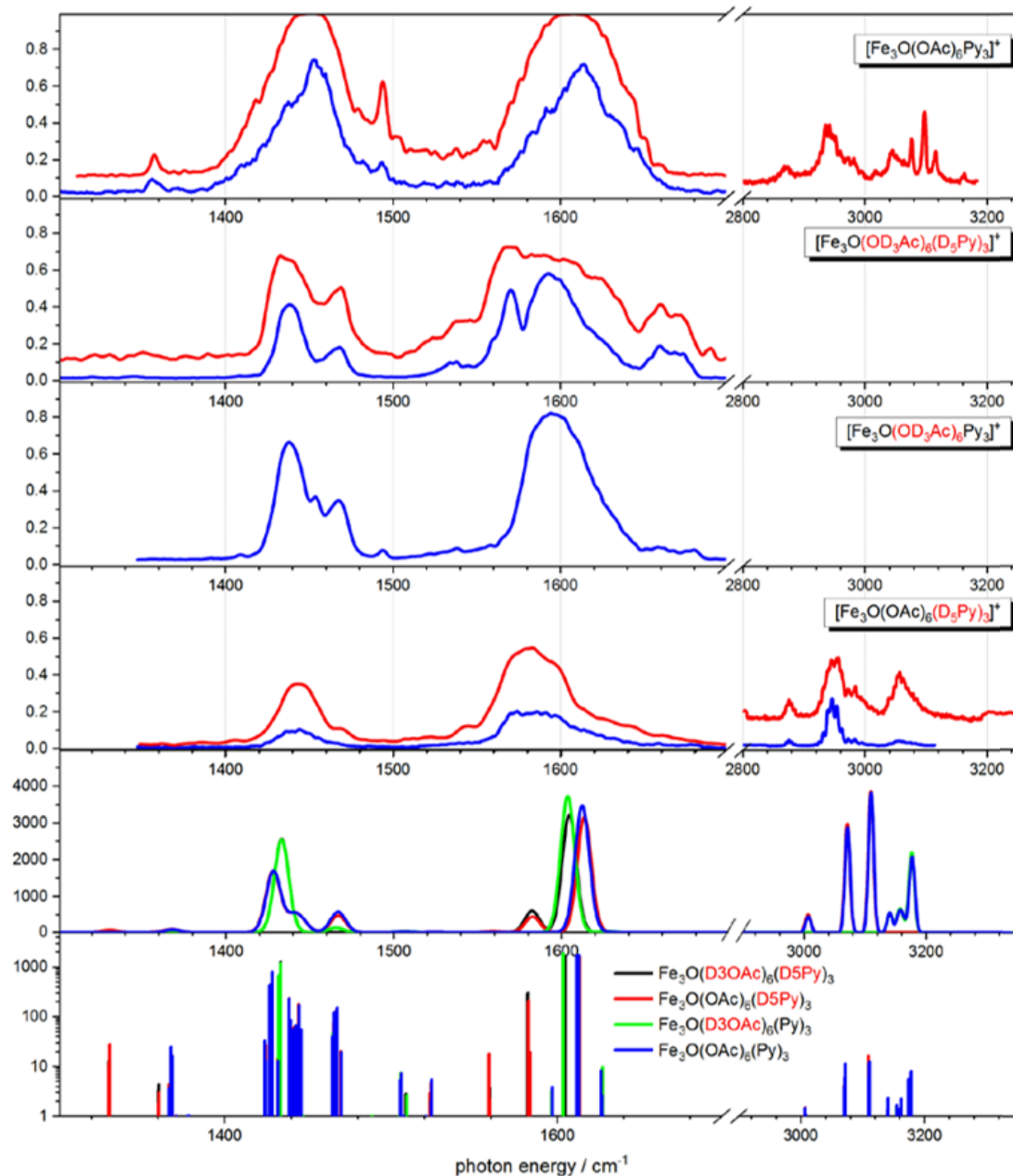


Figure S18: Overview of the isotopic substitution experiments IR-MPD spectra of $[\text{Fe}_3\text{O}(\text{OAc})_6\text{Py}_3]^+$, $[\text{Fe}_3\text{O}(\text{OAcD}_3)_6(\text{PyD}_5)_3]^+$, $[\text{Fe}_3\text{O}(\text{OAcD}_3)_6\text{Py}_3]^+$, $[\text{Fe}_3\text{O}(\text{OAc})_6(\text{PyD}_5)_3]^+$. The red curves are recorded with enhanced photon flux. Note that the three sharp bands above 3000 cm^{-1} in $[\text{Fe}_3\text{O}(\text{OAc})_6\text{Py}_3]^+$ vanish in $[\text{Fe}_3\text{O}(\text{OAc})_6(\text{PyD}_5)_3]^+$ while the three broad bands to the red persist in both cases. The two bottom graphs depict DFT calculations of $[\text{Fe}_3\text{O}(\text{OAc})_6(\text{PyD}_5)_3]^+$ (convoluted, second from bottom) and of all other isotopomers (sticks spectra, bottom graph) at the B3LYP / cc-pVTZ (H, C, N, O) and ecp-10-mdf (Fe) level of theory. These results fully support the assignments of the manuscript. For further interpretation refer to Figs S19 and S20, and to the discussion in the text of the paper.

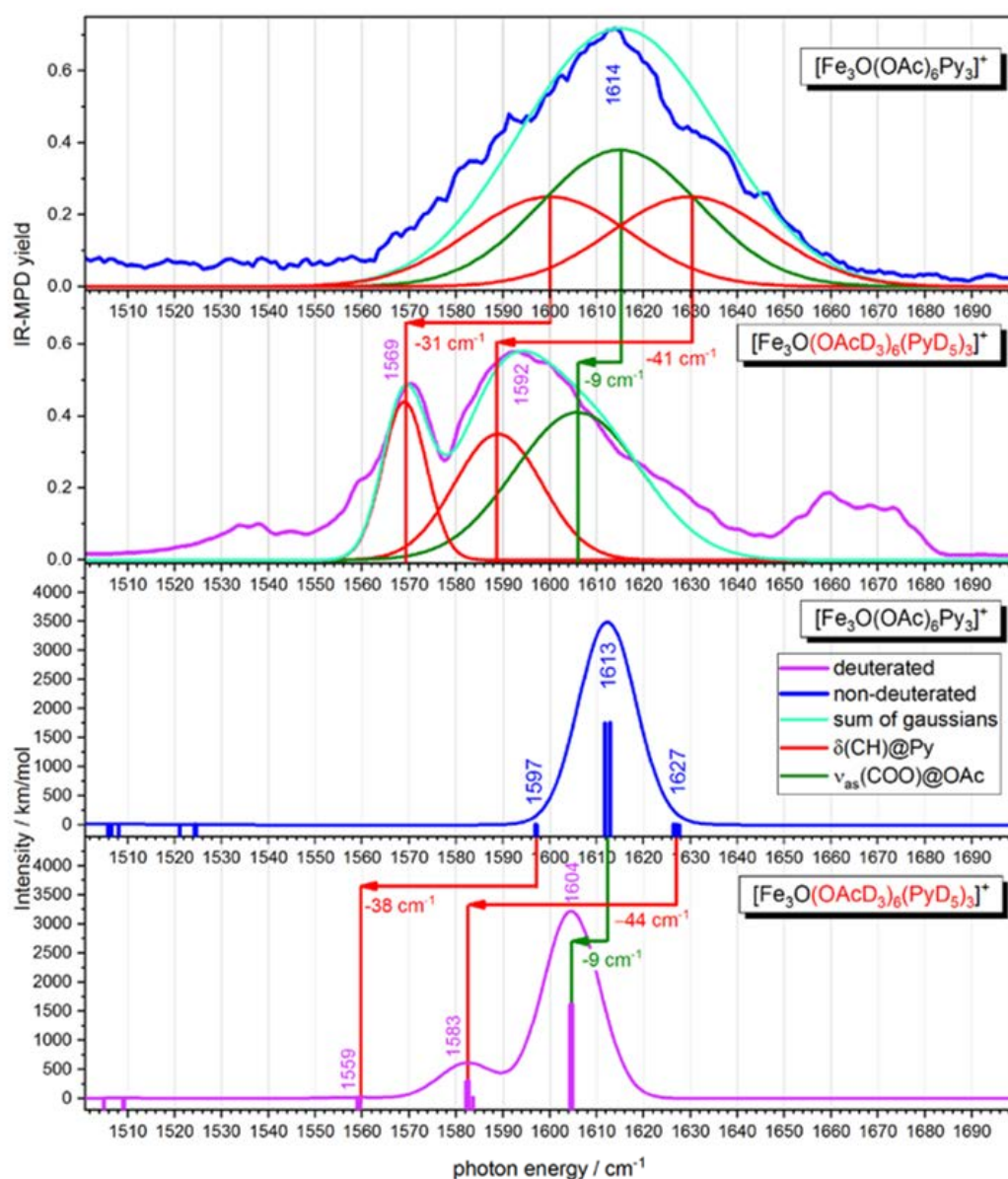


Figure S19: Isotopic substitution experiments: **(a,b)** IR-MPD spectrum of $[\text{Fe}_3\text{O}(\text{OAc})_6\text{Py}_3]^+$ and $[\text{Fe}_3\text{O}(\text{OAcD}_3)_6(\text{PyD}_5)_3]^+$ in the spectral range of 1500 – 1700 cm^{-1} , each with a fit of three gaussian functions and their sum. In graph **(b)** two additional gaussians are added to approximate a new band around 1660, presumably a combination band. **(c-d)** Calculated IR absorption spectra of geometry optimized $[\text{Fe}_3\text{O}(\text{OAc})_6]^+$ and $[\text{Fe}_3\text{O}(\text{OAcD}_3)_6(\text{PyD}_5)_3]^+$ respectively. The stick spectra (blue, pink) were broadened with Gaussian envelope curves (FWHM = 14 cm^{-1} (black)). The calculations were performed at the B3LYP / cc-pVTZ (H, C, N, O) and ecp-10-mdf (Fe) level of theory. The frequencies are scaled with 0.986. Additional experimental bands at 1535 and 1659 cm^{-1} and beyond are likely hot bands and combination bands, respectively.

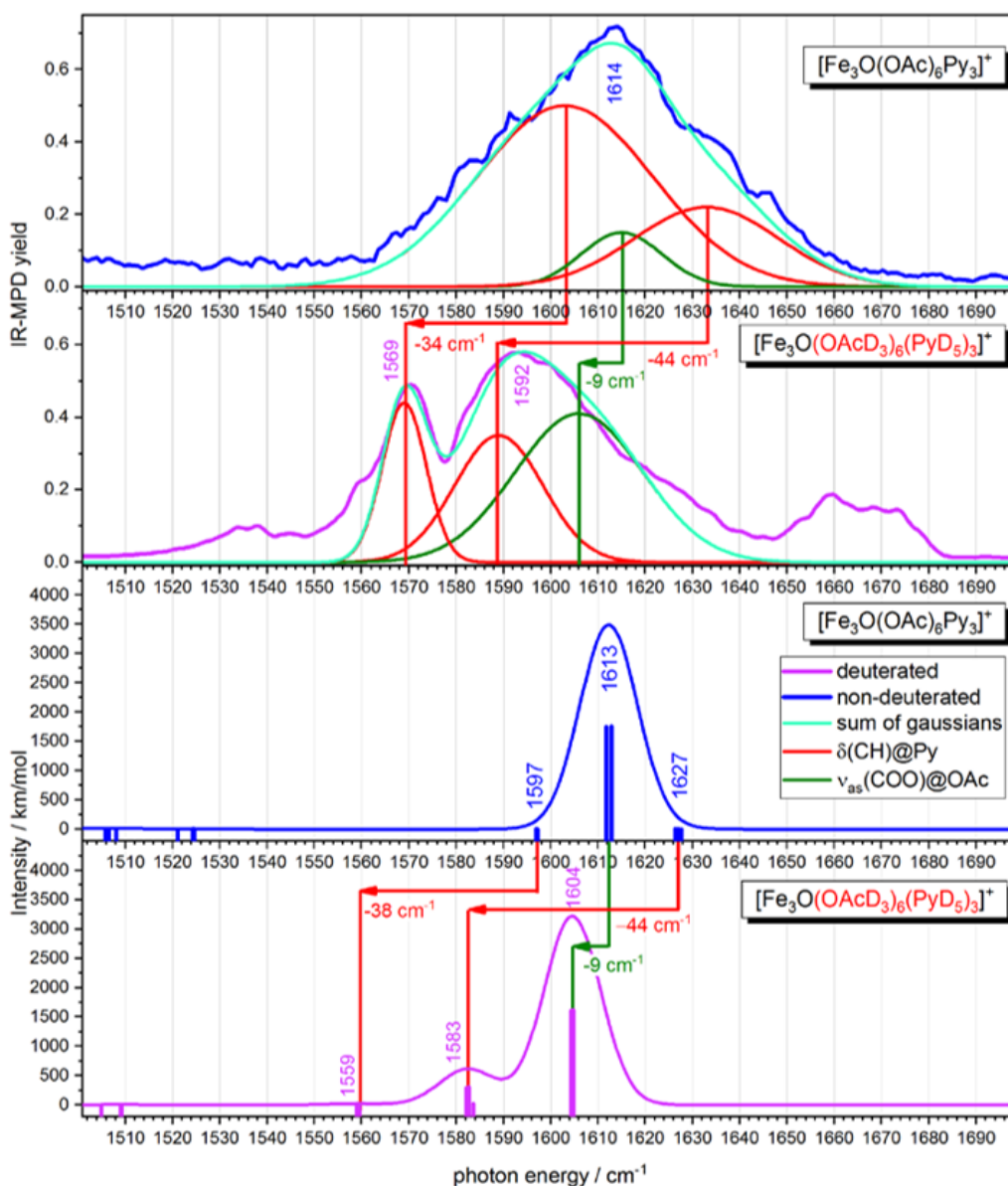


Figure S20: Isotopic substitution experiments: The same as Fig. S18, but with an alternative decomposition of the experimental spectrum in (a). Obviously, the broad band consists of at least three contributions which cannot be determined unambiguously. In any case the experimental IR-MPD observations are well in line with DFT predictions for the linear IR absorptions when considering that mode specific fragmentation likely modulates the intensities in the IR-MPD experiment.

Table S7: Assignment of experimentally observed IR-MPD bands to calculated vibrational bands in $[\text{Fe}_3\text{O}(\text{OAc})_6(\text{Py})_n]^+$; $n = 0, 1, 2, 3$. Calculations are on the B3LYP_Gaussian/cc-pVTZ(H, C, N, O);ecp-10-mdf (Fe) level of theory. Predicted line strengths are indicated by s (strong), m (medium), and w (weak).

	calc. band	IR-MPD	Assignment
n=0	1357 w	-	$\gamma(\text{CH}_3)_{\text{OAc}}$
	1411* s	1445	$\nu_s(\text{COO})_{\text{OAc}}$
	1447 m	1490**	$\gamma(\text{CH}_3)_{\text{OAc}}$
	1575* s	1574	$\nu_{\text{as}}(\text{COO})_{\text{OAc}}$
	3002 w	-	$\nu(\text{CH})_{\text{OAc}}$
	3069 w	-	$\nu(\text{CH})_{\text{OAc}}$
	3115 w	-	$\nu(\text{CH})_{\text{OAc}}$
n=1	1213 w	-	$\delta(\text{CH})_{\text{Py}}$
	1356 w	1360	$\gamma(\text{CH}_3)_{\text{OAc}}$
	1413* s	1445	$\nu_s(\text{COO})_{\text{OAc}}$ $\gamma(\text{CH}_3)_{\text{OAc}}$
	1447 m	-	$\gamma(\text{CH}_3)_{\text{OAc}}$
	1587* s	1586	$\nu_{\text{as}}(\text{COO})_{\text{OAc}}$ $\delta(\text{CH})_{\text{Py}}$
	3070 w	-	$\nu(\text{CH})_{\text{OAc}}$
	3110 w	-	$\nu(\text{CH})_{\text{OAc}}$
	3170 w	3090	$\nu(\text{CH})_{\text{Py}}$
n=2	1212 w	-	$\delta(\text{CH})_{\text{Py}}$
	1353 w	1360	$\gamma(\text{CH}_3)_{\text{OAc}}$
	1416* s	1446	$\nu_s(\text{COO})_{\text{OAc}}$ $\gamma(\text{CH}_3)_{\text{OAc}}$
	1448 m	-	$\gamma(\text{CH}_3)_{\text{OAc}}$
	1597* s	1597	$\nu_{\text{as}}(\text{COO})_{\text{OAc}}$ $\delta(\text{CH})_{\text{Py}}$
	3069 m	2955 b	$\nu(\text{CH})_{\text{OAc}}$
	3108 m	3055 b	$\nu(\text{CH})_{\text{OAc}}$
	3170 w	3098	$\nu(\text{CH})_{\text{Py}}$
n=3	1213 w	1229	$\delta(\text{CH})_{\text{Py}}$
	1351 w	1358	$\gamma(\text{CH}_3)_{\text{OAc}}$
	1419* s	1454 b	$\nu_s(\text{COO})_{\text{OAc}}$ $\gamma(\text{CH}_3)_{\text{OAc}}$
	1449 m	1493**	$\gamma(\text{CH}_3)_{\text{OAc}}$
	1607* s	1613 b	$\nu_{\text{as}}(\text{COO})_{\text{OAc}}$ $\delta(\text{CH})_{\text{Py}}$
	3001 w	2880 b	$\nu(\text{CH}_3)_{\text{OAc}}$
	3067 m	2948 b	$\nu(\text{CH}_3)_{\text{OAc}}$
	3105 m	3050 b	$\nu(\text{CH}_3)_{\text{OAc}}$
	3131 w	3085	$\nu(\text{CH})_{\text{Py}}$
	3149 w	3107	$\nu(\text{CH})_{\text{Py}}$
	3170 m	3124	$\nu(\text{CH})_{\text{Py}}$

* Center of gravity of several near degenerate bands from multiple, equivalent chromophores.

** unresolved shoulder; b indicates significant broadening

11 Appendix B: Additional Figures and Tables

11.1 DFT Simulated Geometries of Homo- and Heterometallic Carboxylate Complexes

These tables include the extracted geometry data from a long series of geometry optimized DFT calculations of the different pyridine complexes discussed in this thesis. The results are summarized in **Figure 27** ff.

11.1.1 Comparison of the $[\text{Fe}_3\text{O}(\text{RCOO})_6\text{Py}_m]^+$ ($m = 3, 2, 1, 0$; $\text{R} = \text{H}, \text{CH}_3$) Complexes

Table 4 Intramolecular distances in $[\text{Fe}_3\text{O}(\text{HCOO})_6\text{Py}_m]^+$ ($m = 3, 2, 1, 0$) complexes, based on B3LYP DFT calculations with a cc-pVTZ basis set and ECP potentials on the Cr and Fe centers.

Formate		Distance (Angstrom)									
Calc #	M1,M2,M3		M1-O	M1-Py	M2-O	M2-Py	M3-O	M3-Py	M1-M2	M2-M3	M3-M1
4319	Py, Py, Py	xxx	1.954	2.202	1.953	2.202	1.953	2.201	3.382	3.384	3.383
4350	Fe, Py, Py	yxx	1.847	---	1.979	2.158	1.979	2.158	3.279	3.494	3.279
4320	Py, Fe, Py	xyx	1.979	2.158	1.847	---	1.979	2.158	3.279	3.279	3.494
4321	Py, Py, Fe	xxxy	1.979	2.158	1.979	2.158	1.847	---	3.494	3.279	3.279
4324	Fe, Fe, Py	yyx	1.869	---	1.869	---	2.010	2.126	3.181	3.388	3.388
4323	Fe,Py, Fe	yxy	1.869	---	2.010	2.126	1.869	---	3.388	3.388	3.181
4322	Py, Fe, Fe	xyy	2.010	2.126	1.869	---	1.869	---	3.388	3.181	3.388
4326	Fe, Fe, Fe	yyy	1.894	---	1.895	---	1.894	---	3.281	3.281	3.282

Formate		average Distance (Angstrom)						
Calc #	M1,M2,M3		Py Fe-O	Py Fe-Py	Fe-O	Py Fe-Py Fe	Py Fe-Fe	Fe-Fe
4319	Py, Py, Py	xxx	1.953	2.202	---	3.383	---	---
4350	Fe, Py, Py	yxx	---	---	---	---	---	---
4320	Py, Fe, Py	xyx	1.979	2.158	1.847	3.494	3.279	---
4321	Py, Py, Fe	xxxy	---	---	---	---	---	---
4324	Fe, Fe, Py	yyx	---	---	---	---	---	---
4323	Fe,Py, Fe	yxy	2.010	2.126	1.869	---	3.388	3.181
4322	Py, Fe, Fe	xyy	---	---	---	---	---	---
4326	Fe, Fe, Fe	yyy	---	---	1.894	---	---	3.281

Formate		average differential Distance (Angstrom)						
Calc #	M1,M2,M3		Py Fe-O	Py Fe-Py	Fe-O	Fe-Fe	Fe-Cr	Cr-Cr
4319	Py, Py, Py	xxx	0.000	0.000	---	0.000	---	---
4350	Fe, Py, Py	yxx	---	---	---	---	---	---
4320	Py, Fe, Py	xyx	0.026	-0.044	0.000	0.111	-0.104	---
4321	Py, Py, Fe	xxxy	---	---	---	---	---	---
4324	Fe, Fe, Py	yyx	---	---	---	---	---	---
4323	Fe,Py, Fe	yxy	0.057	-0.076	0.022	---	0.005	-0.202
4322	Py, Fe, Fe	xyy	---	---	---	---	---	---
4326	Fe, Fe, Fe	yyy	---	---	0.047	---	---	-0.102

Table 5 Intramolecular distances in $[\text{Fe}_3\text{O}(\text{CH}_3\text{COO})_6\text{Py}_m]^+$ ($m = 3, 2, 1, 0$) complexes, based on B3LYP DFT calculations with a cc-pVTZ basis set and ECP potentials on the Cr and Fe centers.

Acetate		Distance (Angstrom)									
Calc #	M1,M2,M3		M1-O	M1-Py	M2-O	M2-Py	M3-O	M3-Py	M1-M2	M2-M3	M3-M1
4278	Py, Py, Py	xxx	1.943	2.228	1.941	2.219	1.941	2.219	3.365	3.360	3.364
4311	Fe, Py, Py	yxx	1.846	---	1.961	2.178	1.962	2.178	3.264	3.464	3.265
4312	Py, Fe, Py	xyx	1.961	2.178	1.846	---	1.962	2.178	3.264	3.265	3.464
4313	Py, Py, Fe	xyx	1.962	2.178	1.962	2.178	1.846	---	3.465	3.264	3.264
4351	Fe, Fe, Py	yyx	1.866	---	1.866	---	1.984	2.148	3.174	3.363	3.363
4315	Fe,Py, Fe	yxy	1.866	---	1.984	2.148	1.866	---	3.363	3.363	3.174
4314	Py, Fe, Fe	xyy	1.984	2.148	1.866	---	1.866	---	3.363	3.174	3.363
4334	Fe, Fe, Fe	yyy	1.885	---	1.886	---	1.885	---	3.265	3.265	3.268

Acetate		average Distance (Angstrom)						
Calc #	M1,M2,M3		Py Fe-O	Py Fe-Py	Fe-O	Py Fe-Py Fe	Py Fe-Fe	Fe-Fe
4278	Py, Py, Py	xxx	1.942	2.222	---	3.363	---	---
4311	Fe, Py, Py	yxx	---	---	---	---	---	---
4312	Py, Fe, Py	xyx	1.962	2.178	1.846	3.464	3.264	---
4313	Py, Py, Fe	xyx	---	---	---	---	---	---
4351	Fe, Fe, Py	yyx	---	---	---	---	---	---
4315	Fe,Py, Fe	yxy	1.984	2.148	1.866	---	3.363	3.174
4314	Py, Fe, Fe	xyy	---	---	---	---	---	---
4334	Fe, Fe, Fe	yyy	---	---	1.885	---	---	3.266

Acetate		average differential Distance (Angstrom)						
Calc #	M1,M2,M3		Py Fe-O	Py Fe-Py	Fe-O	Py Fe-Py Fe	Py Fe-Fe	Fe-Fe
4278	Py, Py, Py	xxx	0.000	0.000	---	0.000	---	---
4311	Fe, Py, Py	yxx	---	---	---	---	---	---
4312	Py, Fe, Py	xyx	0.020	-0.044	-0.039	0.101	-0.099	---
4313	Py, Py, Fe	xyx	---	---	---	---	---	---
4351	Fe, Fe, Py	yyx	---	---	---	---	---	---
4315	Fe,Py, Fe	yxy	0.042	-0.074	-0.019	---	0.000	-0.189
4314	Py, Fe, Fe	xyy	---	---	---	---	---	---
4334	Fe, Fe, Fe	yyy	---	---	0.000	---	---	-0.097

11.1.2 Homo- and Heterometallic Tri-pyridine Complexes

Table 6 Intramolecular distances $[\text{Fe}_{3-n}\text{Cr}_n\text{O}(\text{HCOO})_6\text{Py}_3]^+$ ($n = 3, 2, 1, 0$) complexes based on B3LYP DFT calculations with a cc-pVTZ basis set and ECP potentials on the Cr and Fe centers.

Formate		Distance (Angstrom)								
Calc #	M1,M2,M3	M1-O	M1-Py	M2-O	M2-Py	M3-O	M3-Py	M1-M2	M2-M3	M3-M1
4269	Fe, Fe, Fe xxx	1.954	2.202	1.953	2.201	1.953	2.202	3.382	3.384	3.383
4268	Cr, Fe, Fe yxx	1.963	2.137	1.938	2.209	1.938	2.209	3.385	3.344	3.385
4267	Fe, Cr, Fe yxy	1.938	2.209	1.963	2.137	1.938	2.209	3.385	3.385	3.344
4266	Fe, Fe, Cr xxy	1.938	2.209	1.938	2.209	1.963	2.137	3.344	3.385	3.385
4265	Cr, Cr, Fe yyx	1.950	2.145	1.951	2.145	1.917	2.220	3.384	3.348	3.346
4264	Cr, Fe, Cr yxy	1.951	2.145	1.917	2.220	1.951	2.145	3.348	3.347	3.383
4263	Fe, Cr, Cr xyy	1.917	2.220	1.951	2.145	1.950	2.145	3.348	3.383	3.347
4262	Cr, Cr, Cr yyy	1.934	2.155	1.935	2.155	1.934	2.155	3.351	3.351	3.350

		average Distance (Angstrom)							
Calc #	M1,M2,M3	Fe-O	Fe-Py	Cr-O	Cr-Py	Fe-Fe	Fe-Cr	Cr-Cr	
4269	Fe, Fe, Fe xxx	1.953	2.202	---	---	3.383	---	---	
4268	Cr, Fe, Fe yxx	1.938	2.209	1.963	2.137	3.344	3.385	---	
4267	Fe, Cr, Fe yxy	1.938	2.209	1.963	2.137	3.344	3.385	---	
4266	Fe, Fe, Cr xxy	1.938	2.209	1.963	2.137	3.344	3.385	---	
4265	Cr, Cr, Fe yyx	1.950	2.145	1.951	2.145	1.917	2.220	3.384	3.348
4264	Cr, Fe, Cr yxy	1.951	2.145	1.917	2.220	1.951	2.145	3.348	3.347
4263	Fe, Cr, Cr xyy	1.917	2.220	1.951	2.145	1.950	2.145	3.348	3.383
4262	Cr, Cr, Cr yyy	1.934	2.155	1.935	2.155	1.934	2.155	3.351	3.350

		average differential Distance (Angstrom)							
Calc #	M1,M2,M3	Fe-O	Fe-Py	Cr-O	Cr-Py	Fe-Fe	Fe-Cr	Cr-Cr	
4269	Fe, Fe, Fe xxx	0.000	0.000	---	---	0.000	---	---	
4268	Cr, Fe, Fe yxx	-0.015	0.007	0.029	-0.018	-0.039	0.002	---	
4267	Fe, Cr, Fe yxy	-0.015	0.007	0.029	-0.018	-0.039	0.002	---	
4266	Fe, Fe, Cr xxy	-0.015	0.007	0.029	-0.018	-0.039	0.002	---	
4265	Cr, Cr, Fe yyx	-0.036	0.018	0.016	-0.010	---	-0.036	0.000	
4264	Cr, Fe, Cr yxy	-0.036	0.018	0.016	-0.010	---	-0.036	0.000	
4263	Fe, Cr, Cr xyy	-0.015	0.007	0.029	-0.018	-0.039	0.002	---	
4262	Cr, Cr, Cr yyy	---	---	0.000	0.000	---	---	-0.032	

Table 7 Intramolecular distances $[\text{Fe}_{3-n}\text{Cr}_n\text{O}(\text{CH}_3\text{COO})_6\text{Py}_3]^+$ ($n = 3, 2, 1, 0$) complexes based on B3LYP DFT calculations with a cc-pVTZ basis set and ECP potentials on the Cr and Fe centers.

Acetate		Distance (Angstrom)								
Calc #	M1,M2,M3	M1-O	M1-Py	M2-O	M2-Py	M3-O	M3-Py	M1-M2	M2-M3	M3-M1
4286	Fe, Fe, Fe xxx	1.942	2.219	1.941	2.219	1.942	2.219	3.363	3.361	3.363
4344	Cr, Fe, Fe yxx	1.947	2.151	1.927	2.226	1.927	2.226	3.362	3.324	3.363
4355	Fe, Cr, Fe yxy	1.928	2.226	1.947	2.15	1.927	2.227	3.365	3.362	3.322
4356	Fe, Fe, Cr xxy	1.928	2.226	1.927	2.226	1.947	2.151	3.324	3.362	3.363
4359	Cr, Cr, Fe yyx	1.936	2.162	1.934	2.16	1.913	2.231	3.35	3.331	3.334
4357	Cr, Fe, Cr yxy	1.936	2.158	1.909	2.236	1.936	2.159	3.327	3.327	3.357
4358	Fe, Cr, Cr xyy	1.909	2.237	1.936	2.158	1.936	2.159	3.328	3.359	3.326
4360	Cr, Cr, Cr yyy	1.92	2.168	1.922	2.164	1.921	2.17	3.329	3.331	3.321

		average Distance (Angstrom)							
Calc #	M1,M2,M3	Fe-O	Fe-Py	Cr-O	Cr-Py	Fe-Fe	Fe-Cr	Cr-Cr	
4286	Fe, Fe, Fe xxx	1.942	2.219	---	---	3.362	---	---	
4344	Cr, Fe, Fe yxx	1.927	2.226	1.947	2.151	3.323	3.363	---	
4355	Fe, Cr, Fe yxy	1.927	2.226	1.947	2.151	3.323	3.363	---	
4356	Fe, Fe, Cr xxy	1.927	2.226	1.947	2.151	3.323	3.363	---	
4359	Cr, Cr, Fe yyx	1.910	2.235	1.936	2.159	---	3.329	3.355	
4357	Cr, Fe, Cr yxy	1.910	2.235	1.936	2.159	---	3.329	3.355	
4358	Fe, Cr, Cr xyy	1.909	2.237	1.936	2.158	1.936	2.159	3.328	3.359
4360	Cr, Cr, Cr yyy	---	---	1.921	2.167	---	---	3.327	

11.1.3 Dipyridine Complexes

Table 8 Intramolecular distances as well as absolute and relative energies of $[\text{Fe}_{3-n}\text{Cr}_n\text{O}(\text{HCOO})_6\text{Py}_2]^+$ ($n = 3, 2, 1, 0$) complexes based on B3LYP DFT calculations with a cc-pVTZ basis set and ECP potentials on the Cr and Fe centers.

Formate	CrxFexPy2			rel. Energy	Distance (Angstrom)									UB3LYP Energy	
	Calc #	M1,M2,M3	L1,L2,L3		het/hom H	kJ/mol	M1-O	M1-Py	M2-O	M2-Py	M3-O	M3-Py	M1-M2	M2-M3	M3-M1
	2368	Fe, Fe, Fe	X, Py, Py			1.847	---	1.978	2.158	1.978	2.158	3.279	3.494	3.279	-2079.42873
	2372	Cr, Fe, Fe	X, Py, Py	hom L	31.98	1.867	---	1.964	2.176	1.964	2.176	3.307	3.427	3.307	-2042.56202
	2423	Fe, Cr, Fe	X, Py, Py	het L	0.00	1.839	---	1.960	2.113	1.975	2.159	3.266	3.476	3.259	-2042.5742
	3207	Fe, Fe, Cr	X, Py, Py	het L	0.02	1.976	2.159	1.839	---	1.959	2.119	3.258	3.266	3.477	-2042.57419
	3200	Cr, Cr, Fe	Py, X, Py	het L	31.16	1.955	2.126	1.859	---	1.956	2.189	3.287	3.284	3.424	-2005.70836
	2420	Cr, Fe, Cr	Py, X, Py	hom L	0.00	1.955	2.115	1.831	---	1.954	2.115	3.248	3.249	3.447	-2005.72023
	3198	Fe, Cr, Cr	Py, X, Py	het L	31.13	1.955	2.179	1.859	---	1.954	2.132	3.282	3.288	3.422	-2005.70837
	2389	Cr, Cr, Cr	X, Py, Py			1.848	---	1.947	2.128	1.947	2.128	3.267	3.412	3.267	-1968.85483

Table 9 Intramolecular distances as well as absolute and relative energies of $[\text{Fe}_{3-n}\text{Cr}_n\text{O}(\text{CH}_3\text{COO})_6\text{Py}_2]^+$ ($n = 3, 2, 1, 0$) complexes based on B3LYP DFT calculations with a cc-pVTZ basis set and ECP potentials on the Cr and Fe centers.

Acetate	CrxFexPy2			rel. Energy	Distance (Angstrom)									UB3LYP Energy	
	Calc #	M1,M2,M3	L1,L2,L3		het/hom H	kJ/mol	M1-O	M1-Py	M2-O	M2-Py	M3-O	M3-Py	M1-M2	M2-M3	M3-M1
	1920	Fe, Fe, Fe	X, Py, Py			1.847	---	1.962	2.179	1.961	2.179	3.267	3.464	3.265	-2315.47391
	1898	Cr, Fe, Fe	Py, Py, X	het L	0.08	1.839	---	1.958	2.181	1.943	2.129	3.243	3.447	3.254	-2278.61928
	1899	Fe, Cr, Fe	Py, Py, X	het L	0.00	1.839	---	1.943	2.129	1.959	2.180	3.252	3.447	3.246	-2278.61931
	1900	Fe, Fe, Cr	Py, Py, X	hom L	30.24	1.863	---	1.949	2.196	1.951	2.196	3.288	3.401	3.291	-2278.60779
	1906	Cr, Cr, Fe	X, Py, Py	het L	29.25	1.855	---	1.938	2.142	1.942	2.199	3.269	3.397	3.367	-2241.75389
	1907	Cr, Fe, Cr	X, Py, Py	het L	29.32	1.855	---	1.940	2.200	1.939	2.142	3.264	3.397	3.270	-2241.75386
	1908	Fe, Cr, Cr	X, Py, Py	hom L	0.00	1.832	---	1.939	2.132	1.939	2.131	3.234	3.418	3.236	-2241.76503
	1734	Cr, Cr, Cr	Py, Py, X			1.931	2.144	1.932	2.143	1.845	---	3.386	3.252	3.250	-2204.89999

11.1.4 Monopyridine Complexes

Table 10 Intramolecular distances as well as absolute and relative energies of $[\text{Fe}_{3-n}\text{Cr}_n\text{O}(\text{HCOO})_6\text{Py}_1]^+$ ($n = 3, 2, 1, 0$) complexes based on B3LYP DFT calculations with a cc-pVTZ basis set and ECP potentials on the Cr and Fe centers.

Formate	CrxFexPy1			rel. Energy	Distance (Angstrom)									UB3LYP Energy	
	Calc #	M1,M2,M3	L1,L2,L3		het/hom H	kJ/mol	M1-O	M1-Py	M2-O	M2-Py	M3-O	M3-Py	M1-M2	M2-M3	M3-M1
	2369	Fe, Fe, Fe	Py, X, Py			1.869	---	2.009	2.126	1.869	---	3.388	3.388	3.181	-1831.00551
	2375	Cr, Fe, Fe	X, X, Py	het H	22.13	1.869	---	1.855	---	2.009	2.134	3.188	3.338	3.405	-1794.14227
	2376	Fe, Cr, Fe	X, X, Py	het H	22.14	1.855	---	1.868	---	2.010	2.134	3.187	3.405	3.339	-1794.14227
	2377	Fe, Fe, Cr	X, X, Py	hom H	0.00	1.869	---	1.869	---	1.965	2.092	3.175	3.351	3.351	-1794.1507
	2385	Cr, Cr, Fe	X, X, Py	hom H	23.55	1.860	---	1.860	---	2.000	2.144	3.192	3.359	3.359	-1757.2795
	2384	Cr, Fe, Cr	X, X, Py	het H	0.00	1.866	---	1.855	---	1.964	2.098	3.181	3.312	3.354	-1757.28847
	2383	Fe, Cr, Cr	X, X, Py	het H	0.00	1.855	---	1.866	---	1.964	2.098	3.181	3.354	3.312	-1757.28847
	2390	Cr, Cr, Cr	Py, X, Py			1.856	---	1.964	2.103	1.856	---	3.325	3.325	3.182	-1720.42583

Table 11 Intramolecular distances as well as absolute and relative energies of $[\text{Fe}_{3-n}\text{Cr}_n\text{O}(\text{CH}_3\text{COO})_6\text{Py}_1]^+$ ($n = 3, 2, 1, 0$) complexes based on B3LYP DFT calculations with a cc-pVTZ basis set and ECP potentials on the Cr and Fe centers.

Acetate	CrxFexPy1			rel. Energy	Distance (Angstrom)									UB3LYP Energy	
	Calc #	M1,M2,M3	L1,L2,L3		het/hom H	kJ/mol	M1-O	M1-Py	M2-O	M2-Py	M3-O	M3-Py	M1-M2	M2-M3	M3-M1
	1921	Fe, Fe, Fe	X, X, Py			1.866	---	1.867	---	1.981	2.147	3.172	3.363	3.363	-2067.0581
	1903	Cr, Fe, Fe	X, X, Py	het H	22.10	1.862	---	1.853	---	1.983	2.155	3.176	3.317	3.377	-2030.19488
	1902	Fe, Cr, Fe	X, X, Py	het H	21.97	1.853	---	1.862	---	1.983	2.155	3.177	3.377	3.317	-2030.19493
	1901	Fe, Fe, Cr	X, X, Py	hom H	0.00	1.865	---	1.865	---	1.944	2.109	3.161	3.333	3.332	-2030.2033
	1909	Cr, Cr, Fe	X, X, Py	hom H	22.80	1.854	---	1.854	---	1.976	2.166	3.177	3.335	3.335	-1993.33226
	1911	Cr, Fe, Cr	X, X, Py	het H	0.04	1.859	---	1.852	---	1.943	2.116	3.167	3.297	3.330	-1993.34093
	1912	Fe, Cr, Cr	X, X, Py	het H	0.00	1.852	---	1.859	---	1.944	2.115	3.167	3.331	3.296	-1993.34094
	1917	Cr, Cr, Cr	X, X, Py			1.850	---	1.850	---	1.944	2.120	3.167	3.305	3.305	-1956.47827

11.1.5 Bare Complexes

Table 12 Intramolecular distances as well as absolute and relative energies of $[\text{Fe}_{3-n}\text{Cr}_n\text{O}(\text{HCOO})_6]^+$ ($n = 3, 2, 1, 0$) complexes based on B3LYP DFT calculations with a cc-pVTZ basis set and ECP potentials on the Cr and Fe centers.

Formate	no ligands		Distance (Angstrom)					
Calc #	M1,M2,M3		M1-O	M2-O	M3-O	M1-M2	M2-M3	M3-M1
4326	Fe, Fe, Fe	xxx	1.894	1.895	1.894	3.281	3.281	3.282
4327	Cr, Fe, Fe	yxx	1.873	1.891	1.892	3.276	3.246	3.274
4328	Fe, Cr, Fe	xyx	1.891	1.874	1.891	3.273	3.274	3.248
4329	Fe, Fe, Cr	xxy	1.892	1.891	1.873	3.246	3.276	3.274
4330	Cr, Cr, Fe	yyx	1.871	1.871	1.885	3.258	3.242	3.243
4331	Cr, Fe, Cr	yxy	1.871	1.885	1.871	3.243	3.243	3.258
4332	Fe, Cr, Cr	xyy	1.885	1.871	1.871	3.243	3.258	3.243
4333	Cr, Cr, Cr	yyy	1.867	1.867	1.867	3.233	3.234	3.234
average Distance (Angstrom)								
Calc #	M1,M2,M3		Fe-O	Cr-O	Fe-Fe	Fe-Cr	Cr-Cr	
4326	Fe, Fe, Fe	xxx	1.894	---	3.281	---	---	
4327	Cr, Fe, Fe	yxx					---	
4328	Fe, Cr, Fe	xyx	1.891	1.873	3.247	3.275		
4329	Fe, Fe, Cr	xxy						
4330	Cr, Cr, Fe	yyx			---			
4331	Cr, Fe, Cr	yxy	1.885	1.871		3.243	3.258	
4332	Fe, Cr, Cr	xyy						
4333	Cr, Cr, Cr	yyy	---	1.867	---	---	3.234	
average differential Distance (Angstrom)								
Calc #	M1,M2,M3		Fe-O	Cr-O	Fe-Fe	Fe-Cr	Cr-Cr	
4326	Fe, Fe, Fe	xxx	0.003	---	0.000	---	---	
4327	Cr, Fe, Fe	yxx					---	
4328	Fe, Cr, Fe	xyx	0.000	1.873	-0.035	-0.007		
4329	Fe, Fe, Cr	xxy						
4330	Cr, Cr, Fe	yyx			---			
4331	Cr, Fe, Cr	yxy	-0.006	1.871		-0.039	-0.023	
4332	Fe, Cr, Cr	xyy						
4333	Cr, Cr, Cr	yyy	---	1.867	---	---	-0.048	

Table 13 Intramolecular distances as well as absolute and relative energies of $[\text{Fe}_{3-n}\text{Cr}_n\text{O}(\text{CH}_3\text{COO})_6]^+$ ($n = 3, 2, 1, 0$) complexes based on B3LYP DFT calculations with a cc-pVTZ basis set and ECP potentials on the Cr and Fe centers.

Acetate			Distance (Angstrom)					
Calc #	no ligands		M1-O	M2-O	M3-O	M1-M2	M2-M3	M3-M1
4334	Fe, Fe, Fe	xxx	1.885	1.886	1.885	3.265	3.265	3.268
4354	Cr, Fe, Fe	yxx	1.863	1.883	1.883	3.257	3.233	3.258
4336	Fe, Cr, Fe	xyx	1.882	1.864	1.882	3.257	3.257	3.234
4337	Fe, Fe, Cr	xxy	1.882	1.883	1.864	3.233	3.257	3.258
4353	Cr, Cr, Fe	yyx	1.861	1.861	1.877	3.239	3.230	3.229
4339	Cr, Fe, Cr	yxy	1.861	1.877	1.861	3.229	3.230	3.240
4352	Fe, Cr, Cr	xyy	1.877	1.861	1.861	3.230	3.239	3.229
4341	Cr, Cr, Cr	yyy	1.858	1.858	1.858	3.217	3.218	3.220
			average Distance (Angstrom)					
Calc #	M1,M2,M3		Fe-O	Cr-O	Fe-Fe	Fe-Cr	Cr-Cr	
4334	Fe, Fe, Fe	xxx	1.885	---	3.266	---	---	
4354	Cr, Fe, Fe	yxx					---	
4336	Fe, Cr, Fe	xyx	1.883	1.864	3.233	3.257		
4337	Fe, Fe, Cr	xxy						
4353	Cr, Cr, Fe	yyx			---		3.239	
4339	Cr, Fe, Cr	yxy	1.877	1.861		3.230		
4352	Fe, Cr, Cr	xyy						
4341	Cr, Cr, Cr	yyy	---	1.858	---	---		3.218
			average differential Distance (Angstrom)					
Calc #	M1,M2,M3		Fe-O	Cr-O	Fe-Fe	Fe-Cr	Cr-Cr	
4334	Fe, Fe, Fe	xxx	0.000	---	0.000	---	---	
4354	Cr, Fe, Fe	yxx					---	
4336	Fe, Cr, Fe	xyx	-0.003	0.006	-0.033	-0.009		
4337	Fe, Fe, Cr	xxy						
4353	Cr, Cr, Fe	yyx			---		-0.027	
4339	Cr, Fe, Cr	yxy	-0.008	0.003		-0.037		
4352	Fe, Cr, Cr	xyy						
4341	Cr, Cr, Cr	yyy	---	0.000	---	---		-0.048

11.2 Geometry Changes on Metal or Ligand Exchange

Table 14 Geometry change depending on metal exchange in $[\text{Fe}_{3-n}\text{Cr}_n\text{O}(\text{Fo})_6\text{Py}_m]^+$, ($n = 3, 2, 1, 0$; $m = 0, 1, 2, 3$) complexes, based on B3LYP DFT calculations with a cc-pVTZ basis set and ECP potentials on the Cr and Fe centers.

Formate Ligand	Metal core	Fe-Py	Cr-Py	Fe-O @Py	Cr-O @Py	Fe-O no Py	Cr-O no Py	Type	rel. Energy kJ/mol
		Angstrom							
Py3	Fe3	2.202	---	1.953	---	---	---		
Py3	CrFe2	2.209	2.137	1.938	1.963	---	---		
Py3	Cr2Fe	2.220	2.145	1.917	1.951	---	---		
Py3	Cr3	---	2.155	---	1.934	---	---		
Py2	Fe3	2.158	---	1.978	---	1.847	---		
Py2	CrFe2	2.176	---	1.964	---	---	1.867	hom-L	31.98
Py2	CrFe2	2.159	2.113	1.975	1.960	1.839	---	het-L	0.00
Py2	Cr2Fe	2.189	2.126	1.956	1.955	---	1.859	het-L	31.16
Py2	Cr2Fe	---	2.115	---	1.955	1.831	---	hom-L	0.00
Py2	Cr3	---	2.128	---	1.947	---	1.848		
Py1	Fe3	2.126	---	2.009	---	1.869	---		
Py1	CrFe2	2.134	---	2.010	---	1.855	1.868	het-H	22.13
Py1	CrFe2	---	2.092	---	1.965	1.869	---	hom-H	0.00
Py1	Cr2Fe	---	2.098	2.000	---	1.860	---	hom-H	23.55
Py1	Cr2Fe	---	2.098	---	1.964	1.855	1.866	het-H	0.00
Py1	Cr3	---	2.103	---	1.964	---	1.856		
no Py	Fe3	---	---	---	---	1.894	---	--	
no Py	CrFe2	---	---	---	---	1.891	1.873		
no Py	Cr2Fe	---	---	---	---	1.885	1.871		
no Py	Cr3	---	---	---	---	---	1.867		

Table 15 Geometry change depending on ligand exchange in $[\text{Fe}_{3-n}\text{Cr}_n\text{O}(\text{Fo})_6\text{Py}_m]^+$, ($n = 3, 2, 1, 0$; $m = 0, 1, 2, 3$) complexes, based on B3LYP DFT calculations with a cc-pVTZ basis set and ECP potentials on the Cr and Fe centers.

Formate Metal core	Ligand	Fe-Py	Cr-Py	Fe-O @Py	Cr-O @Py	Fe-O no Py	Cr-O no Py	Type	rel. Energy kJ/mol
		Angstrom							
Fe3	Py3	2.202	---	1.953	---	---	---		
Fe3	Py2	2.158	---	1.978	---	1.847	---		
Fe3	Py1	2.126	---	2.009	---	1.869	---		
Fe3	no Py	---	---	---	---	1.894	---	--	
CrFe2	Py3	2.209	2.137	1.938	1.963	---	---		
CrFe2	Py2	2.176	---	1.964	---	---	1.867	hom-L	31.98
CrFe2	Py2	2.159	2.113	1.975	1.960	1.839	---	het-L	0.00
CrFe2	Py1	2.134	---	2.010	---	1.855	1.868	het-H	22.13
CrFe2	Py1	---	2.092	---	1.965	1.869	---	hom-H	0.00
CrFe2	no Py	---	---	---	---	1.891	1.873		
Cr2Fe	Py3	2.220	2.145	1.917	1.951	---	---		
Cr2Fe	Py2	2.189	2.126	1.956	1.955	---	1.859	het-L	31.16
Cr2Fe	Py2	---	2.115	---	1.955	1.831	---	hom-L	0.00
Cr2Fe	Py1	---	2.098	2.000	---	1.860	---	hom-H	23.55
Cr2Fe	Py1	---	2.098	---	1.964	1.855	1.866	het-H	0.00
Cr2Fe	no Py	---	---	---	---	1.885	1.871		
Cr3	Py3	---	2.155	---	1.934	---	---		
Cr3	Py2	---	2.128	---	1.947	---	1.848		
Cr3	Py1	---	2.103	---	1.964	---	1.856		
Cr3	no Py	---	---	---	---	---	1.867		

Table 16 Geometry change depending on metal exchange in $[\text{Fe}_{3-n}\text{Cr}_n\text{O}(\text{OAc})_6\text{Py}_m]^+$, ($n = 3, 2, 1, 0$; $m = 0, 1, 2, 3$) complexes, based on B3LYP DFT calculations with a cc-pVTZ basis set and ECP potentials on the Cr and Fe centers.

Acetate Ligand	Metal core	Fe-Py	Cr-Py	Fe-O @Py	Cr-O @Py	Fe-O no Py	Cr-O no Py	Type	rel. Energy kJ/mol
		Angstrom							
Py3	Fe3	2.219	---	1.942	---	---	---		
Py3	CrFe2	2.226	2.151	1.977	1.947	---	---		
Py3	Cr2Fe	2.235	2.159	1.910	1.936	---	---		
Py3	Cr3	---	2.167	---	1.921	---	---		
Py2	Fe3	2.179	---	1.962	---	1.847	---		
Py2	CrFe2	2.180	2.129	1.959	1.943	1.839	1.839	hom-L	30.24
Py2	CrFe2	2.181	2.129	1.958	1.943	1.839	---	het-L	0.00
Py2	Cr2Fe	2.199	2.142	1.942	1.938	---	1.855	het-L	29.25
Py2	Cr2Fe	---	2.132	---	1.939	1.832	---	hom-L	0.00
Py2	Cr3	---	2.144	---	1.932	---	1.845		
Py1	Fe3	2.147	---	1.981	---	1.866	---		
Py1	CrFe2	2.155	---	1.983	---	1.853	1.862	het-H	22.00
Py1	CrFe2	---	2.109	---	1.944	1.865	---	hom-H	0.00
Py1	Cr2Fe	2.166	---	1.976	---	---	1.854	hom-H	22.80
Py1	Cr2Fe	---	2.166	---	1.944	1.940	1.855	het-H	0.00
Py1	Cr3	---	2.120	---	1.944	---	1.850		
no Py	Fe3	---	---	---	---	1.885	---	--	
no Py	CrFe2	---	---	---	---	1.883	1.864		
no Py	Cr2Fe	---	---	---	---	1.877	1.861		
no Py	Cr3	---	---	---	---	---	1.858		

Table 17 Geometry change depending on ligand exchange in $[\text{Fe}_{3-n}\text{Cr}_n\text{O}(\text{OAc})_6\text{Py}_m]^+$, ($n = 3, 2, 1, 0$; $m = 0, 1, 2, 3$) complexes, based on B3LYP DFT calculations with a cc-pVTZ basis set and ECP potentials on the Cr and Fe centers.

Acetate Metal core	Ligand	Fe-Py	Cr-Py	Fe-O @Py	Cr-O @Py	Fe-O no Py	Cr-O no Py	Type	rel. Energy kJ/mol
		Angstrom							
Fe3	Py3	2.219	---	1.942	---	---	---		
Fe3	Py2	2.179	---	1.962	---	1.847	---		
Fe3	Py1	2.147	---	1.981	---	1.866	---		
Fe3	no Py	---	---	---	---	1.885	---		
CrFe2	Py3	2.226	2.151	1.977	1.947	---	---		
CrFe2	Py2	2.180	2.129	1.959	1.943	1.839	1.839	hom-L	30.24
CrFe2	Py2	2.181	2.129	1.958	1.943	1.839	---	het-L	0.00
CrFe2	Py1	2.155	---	1.983	---	1.853	1.862	het-H	22.00
CrFe2	Py1	---	2.109	---	1.944	1.865	---	hom-H	0.00
CrFe2	no Py	---	---	---	---	1.883	1.864		
Cr2Fe	Py3	2.235	2.159	1.910	1.936	---	---		
Cr2Fe	Py2	2.199	2.142	1.942	1.938	---	1.855	het-L	29.25
Cr2Fe	Py2	---	2.132	---	1.939	1.832	---	hom-L	0.00
Cr2Fe	Py1	2.166	---	1.976	---	---	1.854	hom-H	22.80
Cr2Fe	Py1	---	2.166	---	1.944	1.940	1.855	het-H	0.00
Cr2Fe	no Py	---	---	---	---	1.877	1.861		
Cr3	Py3	---	2.167	---	1.921	---	---		
Cr3	Py2	---	2.144	---	1.932	---	1.845		
Cr3	Py1	---	2.120	---	1.944	---	1.850		
Cr3	no Py	---	---	---	---	---	1.858		

11.3 Tables of Calculations for Differential Many Body Cooperativity (DMBC)

These tables include all information necessary to apply the DMBC formalism as introduced in section 2.7. As shown in **Figure 16**, for the hetero-metallic or partially coordinated cases, the energies are degenerate, the minor differences in the list here are in the margin of error for the DFT calculations employed here...

11.3.1 Acetate

Table 18 Differential many body cooperativity for Fe to Cr exchange in $[\text{Fe}_{3-n}\text{Cr}_n\text{O}(\text{OAc})_6\text{Py}_m]^+$, $n = 3, 2, 1, 0$; $m = 0, 3$ and Ligand to no Ligand exchange in $[\text{Fe}_3\text{O}(\text{OAc})_6\text{Py}_n]$, ($n = 3, 2, 1, 0$) based on B3LYP DFT calculations with a cc-pVTZ basis set and ECP potentials on the Cr and Fe centers.

Differential many body cooperativity Acetate, Fe → Cr									
Cr _x /Fe _x Acetate Py ₃ single point									
Calc #	x=M, y=M' M=Fe, M'=Cr	Property	Total electronic energy		P1(1)	P2(1)	P3(1)	dP(1)/10 ³	dP(1)
			(kJ/mol)	(Hartree)	96771.89	96771.63	96771.75	2903.15	290315.27
4278	Fe, Fe, Fe	xxx	-6731469.79638647	-2563.88108794					
4279	Cr, Fe, Fe	yxx	-6634697.90955145	-2527.02262790	P12(2)	P13(2)	P23(2)	dP(2)	
4280	Fe, Cr, Fe	xyx	-6634698.16524890	-2527.02272529	-1.60	-1.55	-1.70	-4.85	
4281	Fe, Fe, Cr	xxy	-6634698.04518478	-2527.02267956					
4282	Cr, Cr, Fe	yyx	-6537927.88109784	-2490.16487568				dP(3)	
4283	Cr, Fe, Cr	yxy	-6537927.70513683	-2490.16480866				1.38	
4284	Fe, Cr, Cr	xyy	-6537928.11453105	-2490.16496459					
4285	Cr, Cr, Cr	yyy	-6441157.99300346	-2453.30717692					
Cr _x /Fe _x Acetate Py ₃ geometry optimized									
Calc #	x=M, y=M' M=Fe, M'=Cr	Property	Total electronic energy		P1(1)	P2(1)	P3(1)	dP(1)/10 ³	dP(1)
			(kJ/mol)	(Hartree)	96764.89	96764.79	96764.82	2902.95	290294.50
4286	Fe, Fe, Fe	xxx	-6731469.85188954	-2563.88110908					
4344	Cr, Fe, Fe	yxx	-6634704.95925525	-2527.02531299	P12(2)	P13(2)	P23(2)	dP(2)	
4361	Fe, Cr, Fe	xyx	-6634705.05894548	-2527.02535096	-1.62	-1.77	-1.68	-5.07	
4356	Fe, Fe, Cr	xxy	-6634705.03439705	-2527.02534161					
4359	Cr, Cr, Fe	yyx	-6537941.78608715	-2490.17017181				dP(3)	
4405	Cr, Fe, Cr	yxy	-6537941.91153355	-2490.17021959				1.28	
4362	Fe, Cr, Cr	xyy	-6537941.92452977	-2490.17022454					
4404	Cr, Cr, Cr	yyy	-6441179.14308628	-2453.31523256					
Cr _x /Fe _x Acetate no Ligand geometry optimized									
Calc #	x=M, y=M' M=Fe, M'=Cr	Property	Total electronic energy		P1(1)	P2(1)	P3(1)	dP(1)/10 ³	dP(1)
			(kJ/mol)	(Hartree)	96780.33	96780.35	96780.25	2903.41	290340.94
4334	Fe, Fe, Fe	xxx	-4774821.73770913	-1818.63330326					
4354	Cr, Fe, Fe	yxx	-4678041.40847384	-1781.77162768	P12(2)	P13(2)	P23(2)	dP(2)	
4336	Fe, Cr, Fe	xyx	-4678041.38634088	-1781.77161925	-2.84	-2.41	-2.78	-8.03	
4337	Fe, Fe, Cr	xxy	-4678041.48324808	-1781.77165616					
4353	Cr, Cr, Fe	yyx	-4581263.89697766	-1744.91102532				dP(3)	
4339	Cr, Fe, Cr	yxy	-4581263.56356542	-1744.91089833				6.17	
4352	Fe, Cr, Cr	xyy	-4581263.90845110	-1744.91102969					
4341	Cr, Cr, Cr	yyy	-4484482.65477725	-1708.04900201					
Fe ₃ Acetate Py/noPy									
Calc #	x=Py at Fe y=bare Fe	Property	Total electronic energy		P1(1)	P2(1)	P3(1)	dP(1)/10 ³	dP(1)
			(kJ/mol)	(Hartree)	652193.07	652193.07	652193.06	19565.79	1956579.20
4286	Py, Py, Py	xxx	-6731469.85188954	-2563.881109					
4311	Fe, Py, Py	yxx	-6079276.78042566	-2315.473921	P12(2)	P13(2)	P23(2)	dP(2)	
4312	Py, Fe, Py	xyx	-6079276.78066195	-2315.473921	22.90	22.91	22.91	68.71	
4313	Py, Py, Fe	xxy	-6079276.79042882	-2315.473925					
4351	Fe, Fe, Py	yyx	-5427060.81192377	-2067.058013				dP(3)	
4315	Fe, Py, Fe	yxy	-5427060.81189751	-2067.058013				0.20	
4314	Py, Fe, Fe	xxy	-5427060.81189751	-2067.058013					
4334	Fe, Fe, Fe	yyy	-4774821.73770913	-1818.633303					
Cr _x /Fe _x Acetate no Ligand geometry optimized, one per group of energetically degenerate isomers									
Calc #	x=M, y=M' M=Fe, M'=Cr	Property	Total electronic energy		P1(1)	P2(1)	P3(1)	dP(1)/10 ³	dP(1)
			(kJ/mol)	(Hartree)	96780.33	96780.33	96780.33	2903.41	290340.99
4334	Fe, Fe, Fe	xxx	-4774821.73770913	-1818.63330326					
4354	Cr, Fe, Fe	yxx	-4678041.40847384	-1781.77162768	P12(2)	P13(2)	P23(2)	dP(2)	
4354	Cr, Fe, Fe	yxx	-4678041.40847384	-1781.77162768	-2.82	-2.82	-2.82	-8.45	
4354	Cr, Fe, Fe	yxx	-4678041.40847384	-1781.77162768					
4353	Cr, Cr, Fe	yyx	-4581263.89697766	-1744.91102532				dP(3)	
4353	Cr, Cr, Fe	yyx	-4581263.89697766	-1744.91102532				6.55	
4353	Cr, Cr, Fe	yyx	-4581263.89697766	-1744.91102532					
4341	Cr, Cr, Cr	yyy	-4484482.65477725	-1708.04900201					

... The implementation used here is including all cases necessary, even in complexes of lower symmetry like linear or t-shaped arrangements, where the different metal positions have more distinct energy differences.

Table 19 Differential many body cooperativity for Cr to Fe exchange in $[\text{Fe}_{3-n}\text{Cr}_n\text{O}(\text{OAc})_6\text{Py}_m]$, ($n = 3, 2, 1, 0$; $m = 0, 3$) and no Ligand to Ligand exchange in $[\text{Fe}_3\text{O}(\text{OAc})_6\text{Py}_n]^+$, $n = 3, 2, 1, 0$ based on B3LYP DFT calculations with a cc-pVTZ basis set and ECP potentials on the Cr and Fe centers.

Differential many body cooperativity Acetate, Cr → Fe									
Crx/Fex Acetate Py3 single point									
Calc #	x=Fe, y=Cr M=Fe, M'=Cr	Property	Total electronic energy		P1(1)	P2(1)	P3(1)	dP(1)/10 ³	dP(1)
			(kJ/mol)	(Hartree)	-96770.12	-96769.71	-96769.89	-2903.10	-290309.72
4285	Cr, Cr, Cr	yyy	-6441157.99300346	-2453.30717692					
4284	Fe, Cr, Cr	xyy	-6537928.11453105	-2490.16496459	P12(2)	P13(2)	P23(2)	dP(2)	
4283	Cr, Fe, Cr	xyx	-6537927.70513683	-2490.16480866	-0.22	-0.16	-0.32	-0.70	
4282	Cr, Cr, Fe	yyx	-6537927.88109784	-2490.16487568					
4281	Fe, Fe, Cr	xxxy	-6634698.04518478	-2527.02267956				dP(3)	
4280	Cr, Cr, Fe	xyx	-6634698.16524890	-2527.02272529				-1.38	
4279	Cr, Fe, Fe	yxx	-6634697.90955145	-2527.02262790					
4278	Fe, Fe, Fe	xxx	-6731469.79638647	-2563.88108794					
Crx/Fex Acetate Py3 geometry optimized									
Calc #	x=Fe, y=Cr M=Fe, M'=Cr	Property	Total electronic energy		P1(1)	P2(1)	P3(1)	dP(1)/10 ³	dP(1)
			(kJ/mol)	(Hartree)	-96762.78	-96762.77	-96762.64	-2902.88	-290288.19
4404	Cr, Cr, Cr	yyy	-6441179.14308628	-2453.31523256					
4362	Fe, Cr, Cr	xyy	-6537941.92452977	-2490.17022454	P12(2)	P13(2)	P23(2)	dP(2)	
4405	Cr, Fe, Cr	xyx	-6537941.91153355	-2490.17021959	-0.34	-0.49	-0.40	-1.24	
4359	Cr, Cr, Fe	yyx	-6537941.78608715	-2490.17017181					
4356	Fe, Fe, Cr	xxxy	-6634705.03439705	-2527.02534161				dP(3)	
4361	Cr, Cr, Fe	xyx	-6634705.05894548	-2527.02535096				-1.28	
4344	Cr, Fe, Fe	yxx	-6634704.95925525	-2527.02531299					
4286	Fe, Fe, Fe	xxx	-6731469.85188954	-2563.88110908					
Crx/Fex Acetate no Ligand geometry optimized									
Calc #	x=Fe, y=Cr M=Fe, M'=Cr	Property	Total electronic energy		P1(1)	P2(1)	P3(1)	dP(1)/10 ³	dP(1)
			(kJ/mol)	(Hartree)	-96781.25	-96780.91	-96781.24	-2903.43	-290343.40
4341	Cr, Cr, Cr	yyy	-4484482.65477725	-1708.04900201					
4352	Fe, Cr, Cr	xyy	-4581263.90845110	-1744.91102969	P12(2)	P13(2)	P23(2)	dP(2)	
4339	Cr, Fe, Cr	xyx	-4581263.56356542	-1744.91089833	3.33	3.76	3.40	10.50	
4353	Cr, Cr, Fe	yyx	-4581263.89697766	-1744.91102532					
4337	Fe, Fe, Cr	xxxy	-4678041.48324808	-1781.77165616				dP(3)	
4336	Cr, Cr, Fe	xyx	-4678041.38634088	-1781.77161925				-6.17	
4354	Cr, Fe, Fe	yxx	-4678041.40847384	-1781.77162768					
4334	Fe, Fe, Fe	xxx	-4774821.73770913	-1818.63330326					
Fe3 Acetate Py/noPy									
Calc #	x=Py at Fe y=bare Fe	Property	Total electronic energy		P1(1)	P2(1)	P3(1)	dP(1)/10 ³	dP(1)
			(kJ/mol)	(Hartree)	-652239.07	-652239.07	-652239.07	-19567.17	-1956717.22
4334	Fe, Fe, Fe	yyy	-4774821.73770913	-1818.63330326					
4314	Py, Fe, Fe	xyy	-5427060.81189751	-2067.05801253	P12(2)	P13(2)	P23(2)	dP(2)	
4315	Fe, Py, Fe	xyx	-5427060.81189751	-2067.05801253	23.10	23.11	23.11	69.31	
4351	Fe, Fe, Py	yyx	-5427060.81192377	-2067.05801254					
4313	Py, Py, Fe	xxxy	-6079276.79042882	-2315.47392513				dP(3)	
4312	Py, Fe, Py	xyx	-6079276.78066195	-2315.47392141				-0.20	
4311	Fe, Py, Py	yxx	-6079276.78042566	-2315.47392132					
4286	Py, Py, Py	xxx	-6731469.85188954	-2563.88110908					
Crx/Fex Acetate no Ligand geometry optimized, one per group of energetically degenerate isomers									
Calc #	x=M, y=M' M=Cr, M'=Fe	Property	Total electronic energy		P1(1)	P2(1)	P3(1)	dP(1)/10 ³	dP(1)
			(kJ/mol)	(Hartree)	-96781.24	-96781.24	-96781.24	-2903.44	-290343.73
4341	Cr, Cr, Cr	yyy	-4484482.65477725	-1708.04900201					
4353	Cr, Cr, Fe	xyy	-4581263.89697766	-1744.91102532	P12(2)	P13(2)	P23(2)	dP(2)	
4353	Cr, Cr, Fe	yyx	-4581263.89697766	-1744.91102532	3.73	3.73	3.73	11.19	
4353	Cr, Cr, Fe	yyx	-4581263.89697766	-1744.91102532					
4354	Cr, Fe, Fe	yxx	-4678041.40847384	-1781.77162768				dP(3)	
4354	Cr, Fe, Fe	yxx	-4678041.40847384	-1781.77162768				-6.55	
4354	Cr, Fe, Fe	yxx	-4678041.40847384	-1781.77162768					
4334	Fe, Fe, Fe	xxx	-4774821.73770913	-1818.63330326					

11.3.2 Formate

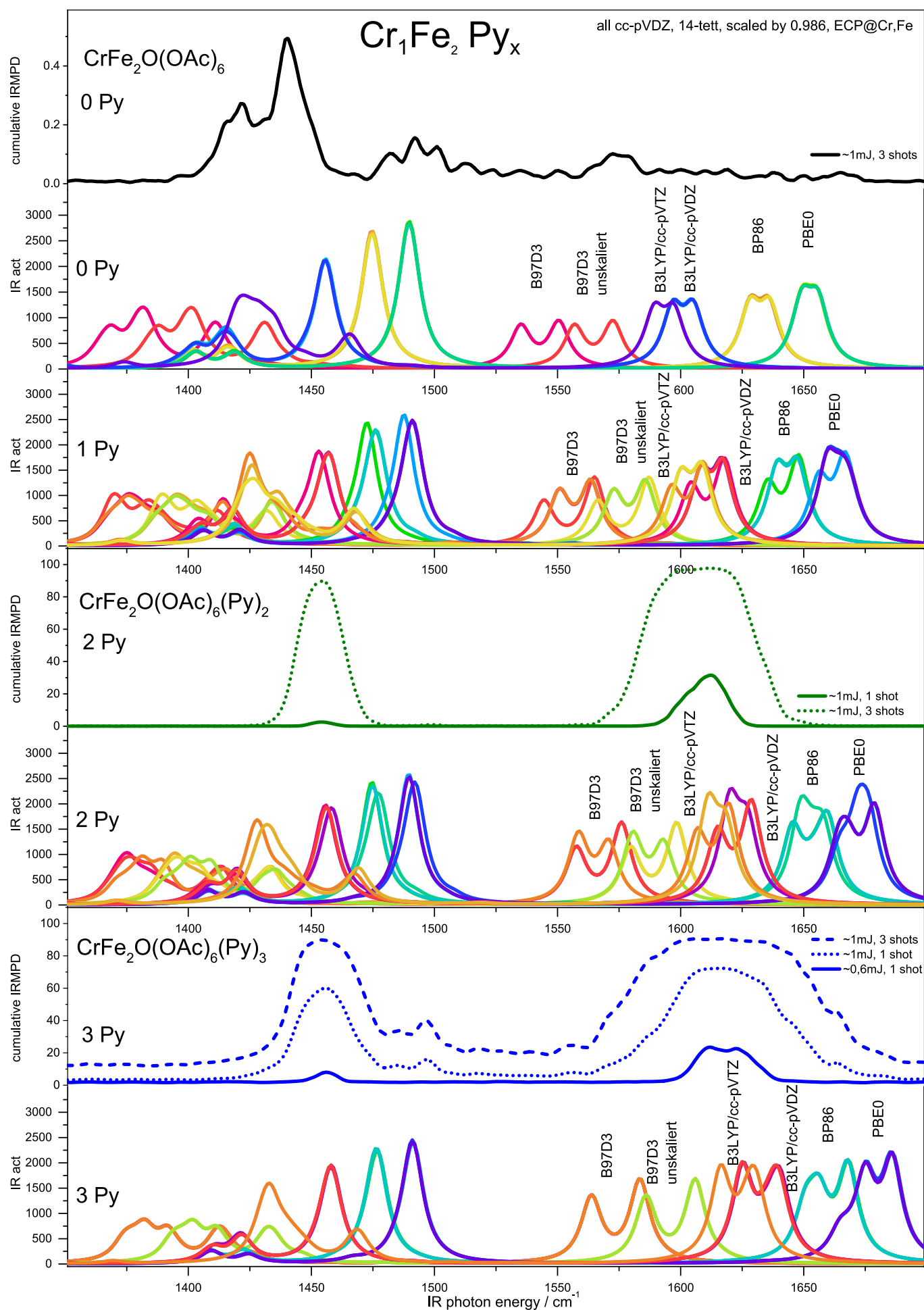
Table 20 Differential many body cooperativity for Fe to Cr exchange in $[\text{Fe}_{3-n}\text{Cr}_n\text{O}(\text{Fo})_6\text{Py}_m]^+$, ($n = 3, 2, 1, 0$; $m = 0, 3$) and Ligand to no Ligand exchange in $[\text{Fe}_3\text{O}(\text{Fo})_6\text{Py}_n]^+$, ($n = 3, 2, 1, 0$) based on B3LYP DFT calculations with a cc-pVTZ basis set and ECP potentials on the Cr and Fe centers.

Differential many body cooperativity Formate, Fe → Cr									
Crx/Fex Formate Py3 single point					(kJ/mol)				
Calc #	x=M, y=M'	Property	Total electronic energy		P1(1)	P2(1)	P3(1)	dP(1)/10 ³	dP(1)
	M=Fe, M'=Cr		(kJ/mol)	(Hartree)	96756.61	96756.58	96756.60	2902.70	290269.78
4277	Fe, Fe, Fe	xxx	6111725.57093186	2327.83301121					
4276	Cr, Fe, Fe	yxx	6014968.96046356	2290.98036963	P12(2)	P13(2)	P23(2)	dP(2)	
4275	Fe, Cr, Fe	xyx	6014968.99548773	2290.98038297	-1.19	-1.47	-1.25	-3.91	
4274	Fe, Fe, Cr	xxy	6014968.97537640	2290.98037531					
4273	Cr, Cr, Fe	yyx	5918213.57387210	2254.12819420				dP(3)	
4272	Cr, Fe, Cr	yxy	5918213.83264138	2254.12829276				1.17	
4271	Fe, Cr, Cr	xyy	5918213.65373981	2254.12822462					
4270	Cr, Cr, Cr	yyy	5821458.53258639	2217.27615029					
Crx/Fex Formate Py3 geometry optimized					(kJ/mol)				
Calc #	x=M, y=M'	Property	Total electronic energy		P1(1)	P2(1)	P3(1)	dP(1)/10 ³	dP(1)
	M=Fe, M'=Cr		(kJ/mol)	(Hartree)	96763.71	96763.72	96763.72	2902.91	290291.15
4269	Fe, Fe, Fe	xxx	6111747.31800087	2327.84129423					
4268	Cr, Fe, Fe	yxx	6014983.60313961	2290.98594673	P12(2)	P13(2)	P23(2)	dP(2)	
4267	Fe, Cr, Fe	xyx	6014983.60298209	2290.98594667	-1.15	-1.15	-1.15	-3.44	
4266	Fe, Fe, Cr	xxy	6014983.60279830	2290.98594660					
4265	Cr, Cr, Fe	yyx	5918221.03654079	2254.13103658				dP(3)	
4264	Cr, Fe, Cr	yxy	5918221.03465043	2254.13103586				1.08	
4263	Fe, Cr, Cr	xyy	5918221.03441413	2254.13103577					
4262	Cr, Cr, Cr	yyy	5821458.53271767	2217.27615034					
Crx/Fex Formate no Ligand geometry optimized					(kJ/mol)				
Calc #	x=M, y=M'	Property	Total electronic energy		P1(1)	P2(1)	P3(1)	dP(1)/10 ³	dP(1)
	M=Fe, M'=Cr		(kJ/mol)	(Hartree)	96779.77	96779.94	96779.77	2903.39	290339.48
4326	Fe, Fe, Fe	xxx	4155041.32790232	1582.5714446400					
4327	Cr, Fe, Fe	yxx	4058261.55671706	1545.7099816100	P12(2)	P13(2)	P23(2)	dP(2)	
4328	Fe, Cr, Fe	xyx	4058261.39136306	1545.7099186300	-2.33	-2.16	-2.33	-6.82	
4329	Fe, Fe, Cr	xxy	4058261.55884371	1545.7099824200					
4330	Cr, Cr, Fe	yyx	3961483.95159554	1508.8493435900				dP(3)	
4331	Cr, Fe, Cr	yxy	3961483.95151678	1508.8493435600				4.69	
4332	Fe, Cr, Cr	xyy	3961483.95159554	1508.8493435900					
4333	Cr, Cr, Cr	yyy	3864703.98951018	1471.9878078500					
Fe3 Formate Py/noPy					(kJ/mol)				
Calc #	x=Py at Fe	Property	Total electronic energy		P1(1)	P2(1)	P3(1)	dP(1)/10 ³	dP(1)
	y=bare Fe		(kJ/mol)	(Hartree)	652207.19	652207.19	652207.19	19566.22	1956621.57
4319	Py, Py, Py	xxx	6111747.31805337	2327.8412942500					
4350	Fe, Py, Py	yxx	5459540.12932850	2079.4287295100	P12(2)	P13(2)	P23(2)	dP(2)	
4320	Py, Fe, Py	xyx	5459540.12932850	2079.4287295100	27.96	27.96	27.96	83.89	
4321	Py, Py, Fe	xxy	5459540.12932850	2079.4287295100					
4322	Fe, Fe, Py	yyx	4807304.97708577	1831.0055140300				dP(3)	
4323	Fe,Py, Fe	yxy	4807304.97708577	1831.0055140300				0.53	
4324	Py, Fe, Fe	xyy	4807304.97708577	1831.0055140300					
4326	Fe, Fe, Fe	yyy	4155041.32790232	1582.5714446400					
Crx/Fex Formate no Ligand geometry optimized one per group of energetically degenerate isomers					(kJ/mol)				
Calc #	x=M, y=M'	Property	Total electronic energy		P1(1)	P2(1)	P3(1)	dP(1)/10 ³	dP(1)
	M=Fe, M'=Cr		(kJ/mol)	(Hartree)	96779.77	96779.77	96779.77	2903.39	290339.31
4326	Fe, Fe, Fe	xxx	-4155041.32790232	-1582.5714446400					
4327	Cr, Fe, Fe	yxx	-4058261.55671706	-1545.7099816100	P12(2)	P13(2)	P23(2)	dP(2)	
4327	Cr, Fe, Fe	yxx	-4058261.55671706	-1545.7099816100	-2.17	-2.17	-2.17	-6.50	
4327	Cr, Fe, Fe	yxx	-4058261.55671706	-1545.7099816100					
4330	Cr, Cr, Fe	yyx	-3961483.95159554	-1508.8493435900				dP(3)	
4330	Cr, Cr, Fe	yyx	-3961483.95159554	-1508.8493435900				4.52	
4330	Cr, Cr, Fe	yyx	-3961483.95159554	-1508.8493435900					
4333	Cr, Cr, Cr	yyy	-3864703.98951018	-1471.9878078500					

Table 21 Differential many body cooperativity for Cr to Fe exchange in $[\text{Fe}_{3-n}\text{Cr}_n\text{O}(\text{Fo})_6\text{Py}_m]^+$, ($n = 3, 2, 1, 0$; $m = 0, 3$) and no Ligand to Ligand exchange in $[\text{Fe}_3\text{O}(\text{Fo})_6\text{Py}_n]^+$, $n = 3, 2, 1, 0$ based on B3LYP DFT calculations with a cc-pVTZ basis set and ECP potentials on the Cr and Fe centers.

Differential many body cooperativity Formate, Cr → Fe									
Crx/Fex Formate Py3 single point									
				(kJ/mol)					
Calc #	x=M, y=M' M=Cr, M'=Fe	Property	Total electronic energy		P1(1)	P2(1)	P3(1)	dP(1)/10 ³	dP(1)
			(kJ/mol)	(Hartree)	-96755.12	-96755.30	-96755.04	-2902.65	-290265.46
4270	Cr, Cr, Cr	yyy	-5821458.53258639	-2217.27615029					
4271	Fe, Cr, Cr	xyy	-5918213.65373981	-2254.12822462	P12(2)	P13(2)	P23(2)	dP(2)	
4272	Cr, Fe, Cr	xyx	-5918213.83264138	-2254.12829276	-0.02	-0.30	-0.09	-0.41	
4273	Cr, Cr, Fe	yyx	-5918213.57387210	-2254.12819420					
4274	Fe, Fe, Cr	xxxy	-6014968.97537640	-2290.98037531				dP(3)	
4275	Fe, Cr, Fe	xyx	-6014968.99548773	-2290.98038297				-1.17	
4276	Cr, Fe, Fe	yxx	-6014968.96046356	-2290.98036963					
4277	Fe, Fe, Fe	xxx	-6111725.57093186	-2327.83301121					
Crx/Fex Formate Py3 geometry optimized									
				(kJ/mol)					
Calc #	x=M, y=M' M=Cr, M'=Fe	Property	Total electronic energy		P1(1)	P2(1)	P3(1)	dP(1)/10 ³	dP(1)
			(kJ/mol)	(Hartree)	-96762.50	-96762.50	-96762.50	-2902.88	-290287.51
4262	Cr, Cr, Cr	yyy	-5821458.53271767	-2217.27615034					
4263	Fe, Cr, Cr	xyy	-5918221.03441413	-2254.13103577	P12(2)	P13(2)	P23(2)	dP(2)	
4264	Cr, Fe, Cr	xyx	-5918221.03465043	-2254.13103586	-0.07	-0.06	-0.06	-0.20	
4265	Cr, Cr, Fe	yyx	-5918221.03654079	-2254.13103658					
4266	Fe, Fe, Cr	xxxy	-6014983.60279830	-2290.98594660				dP(3)	
4267	Fe, Cr, Fe	xyx	-6014983.60298209	-2290.98594667				-1.08	
4268	Cr, Fe, Fe	yxx	-6014983.60313961	-2290.98594673					
4269	Fe, Fe, Fe	xxx	-6111747.31800087	-2327.84129423					
Crx/Fex Formate no Ligand geometry optimized									
				(kJ/mol)					
Calc #	x=M, y=M' M=Cr, M'=Fe	Property	Total electronic energy		P1(1)	P2(1)	P3(1)	dP(1)/10 ³	dP(1)
			(kJ/mol)	(Hartree)	-96779.96	-96779.96	-96779.96	-2903.40	-290339.89
4333	Cr, Cr, Cr	yyy	-3864703.98951018	-1471.9878078500					
4332	Fe, Cr, Cr	xyy	-3961483.95159554	-1508.8493435900	P12(2)	P13(2)	P23(2)	dP(2)	
4331	Cr, Fe, Cr	xyx	-3961483.95151678	-1508.8493435600	2.35	2.52	2.36	7.23	
4330	Cr, Cr, Fe	yyx	-3961483.95159554	-1508.8493435900					
4329	Fe, Fe, Cr	xxxy	-4058261.55884371	-1545.7099824200				dP(3)	
4328	Fe, Cr, Fe	xyx	-4058261.39136306	-1545.7099186300				-4.69	
4327	Cr, Fe, Fe	yxx	-4058261.55671706	-1545.7099816100					
4326	Fe, Fe, Fe	xxx	-4155041.32790232	-1582.5714446400					
Fe3 Formate Py/noPy									
				(kJ/mol)					
Calc #	x=Py at Fe y=bare Fe	Property	Total electronic energy		P1(1)	P2(1)	P3(1)	dP(1)/10 ³	dP(1)
			(kJ/mol)	(Hartree)	-652263.65	-652263.65	-652263.65	-19567.91	#####
4326	Fe, Fe, Fe	yyy	-4155041.32790232	-1582.5714446400					
4324	Py, Fe, Fe	xyy	-4807304.97708577	-1831.0055140300	P12(2)	P13(2)	P23(2)	dP(2)	
4323	Fe, Py, Fe	xyx	-4807304.97708577	-1831.0055140300	28.50	28.50	28.50	85.49	
4322	Fe, Fe, Py	yyx	-4807304.97708577	-1831.0055140300					
4321	Py, Py, Fe	xxxy	-5459540.12932850	-2079.4287295100				dP(3)	
4320	Py, Fe, Py	xyx	-5459540.12932850	-2079.4287295100				-0.53	
4350	Fe, Py, Py	yxx	-5459540.12932850	-2079.4287295100					
4319	Py, Py, Py	xxx	-6111747.31805337	-2327.8412942500					
Crx/Fex Formate no Ligand geometry optimized one per group of energetically degenerate isomers									
				(kJ/mol)					
Calc #	x=M, y=M' M=Cr, M'=Fe	Property	Total electronic energy		P1(1)	P2(1)	P3(1)	dP(1)/10 ³	dP(1)
			(kJ/mol)	(Hartree)	-96779.96	-96779.96	-96779.96	-2903.40	-290339.89
4333	Cr, Cr, Cr	yyy	-3864703.98951018	-1471.9878078500					
4330	Cr, Cr, Fe	yyx	-3961483.95159554	-1508.8493435900	P12(2)	P13(2)	P23(2)	dP(2)	
4330	Cr, Cr, Fe	yyx	-3961483.95159554	-1508.8493435900	2.36	2.36	2.36	7.07	
4330	Cr, Cr, Fe	yyx	-3961483.95159554	-1508.8493435900					
4327	Cr, Fe, Fe	yxx	-4058261.55671706	-1545.7099816100				dP(3)	
4327	Cr, Fe, Fe	yxx	-4058261.55671706	-1545.7099816100				-4.52	
4327	Cr, Fe, Fe	yxx	-4058261.55671706	-1545.7099816100					
4326	Fe, Fe, Fe	xxx	-4155041.32790232	-1582.5714446400					

11.4 Additional DFT Graphs to Chapter 4.2

Figure 69 Full series of hybrid functional calculations on [CrFe₂O(OAc)₆(Py)_{3.0}]⁺ ions.

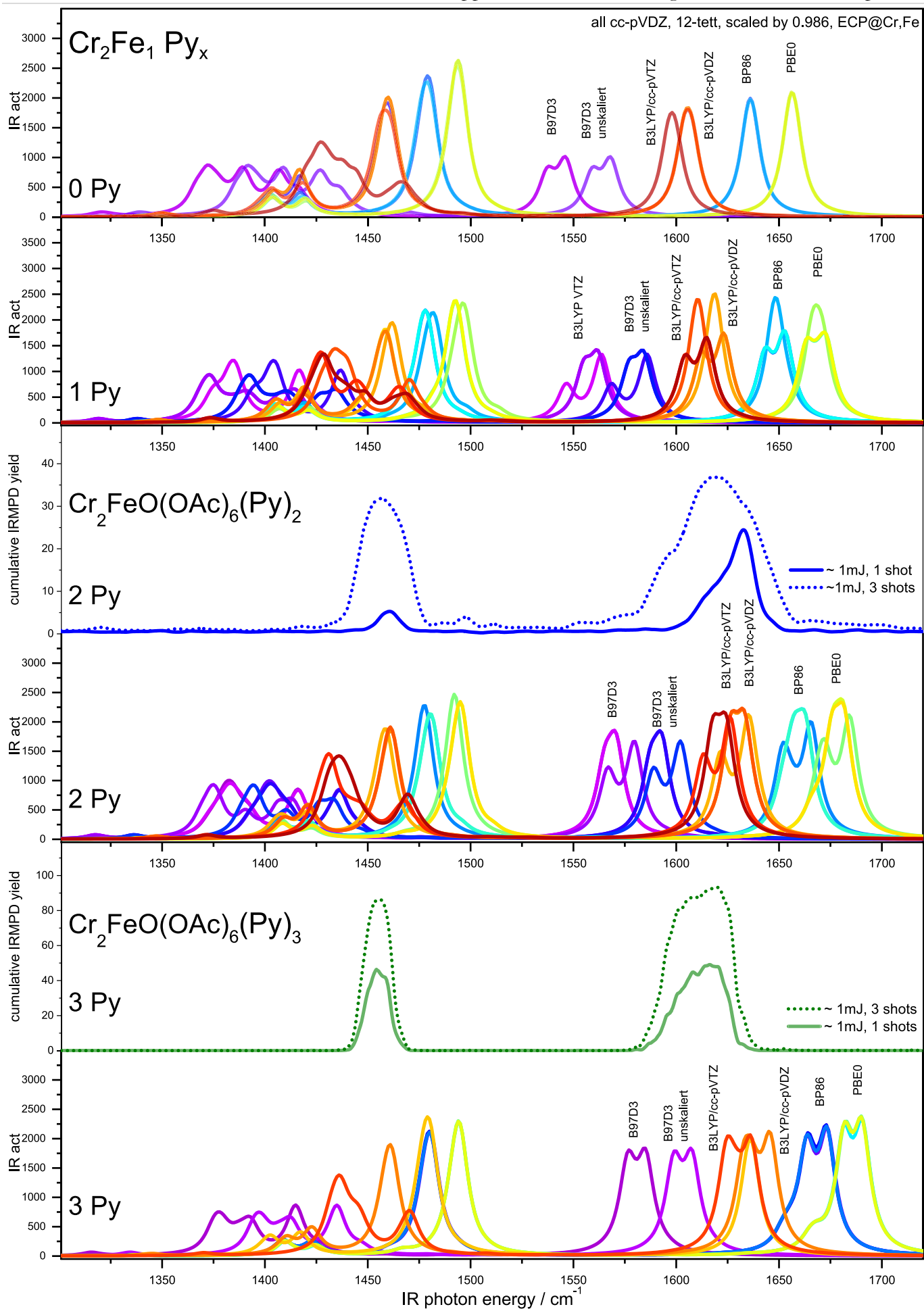


Figure 70 Full series of hybrid functional calculations on $[\text{Cr}_2\text{FeO}(\text{OAc})_6(\text{Py})_{3.0}]^+$ ions.

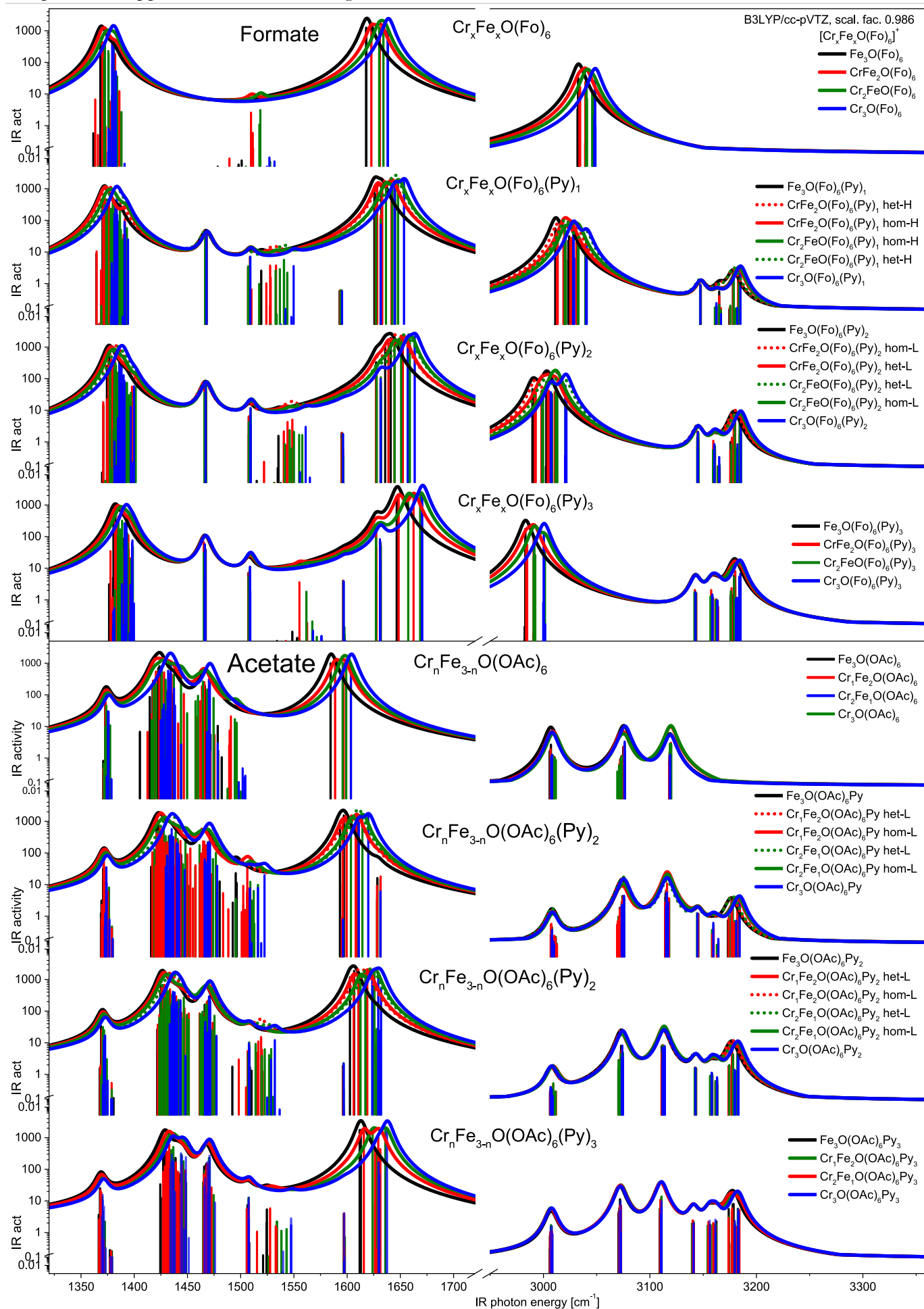


Figure 71 Systematic overview of all DFT simulated IR spectra calculated using a cc-pVTZ basis set and the B3LYP functional.

11.5 Additional CID Graphs to Chapter 5.3

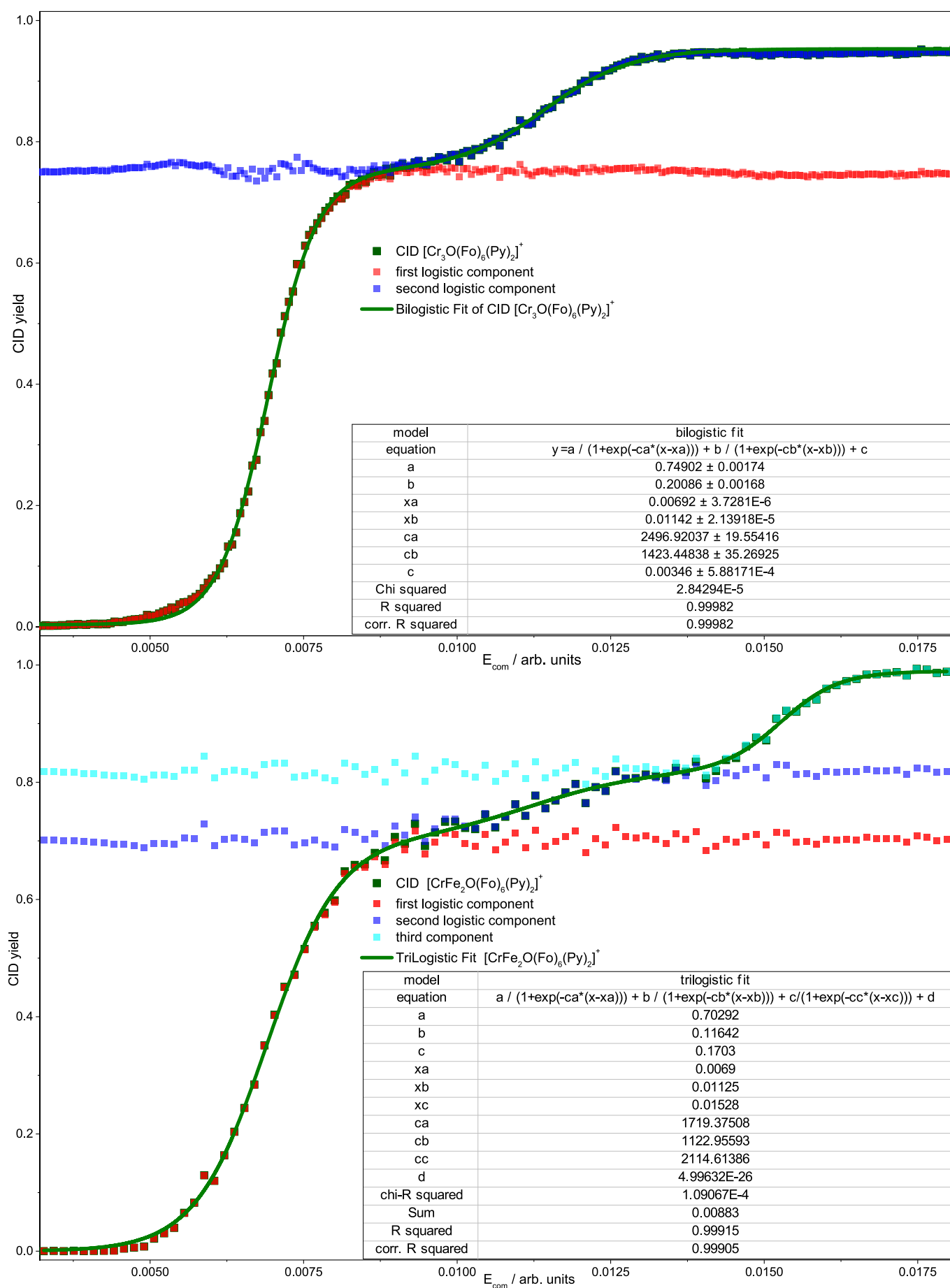


Figure 72 Bi-logistic fit of $[\text{Cr}_3\text{O}(\text{Fo})_6(\text{Py})_2]^+$ complexes and Tri-logistic fit of $[\text{CrFe}_2\text{O}(\text{Fo})_6(\text{Py})_2]^+$ complexes where dual pyridine loss competes with single pyridine loss. See **Figure 73**.

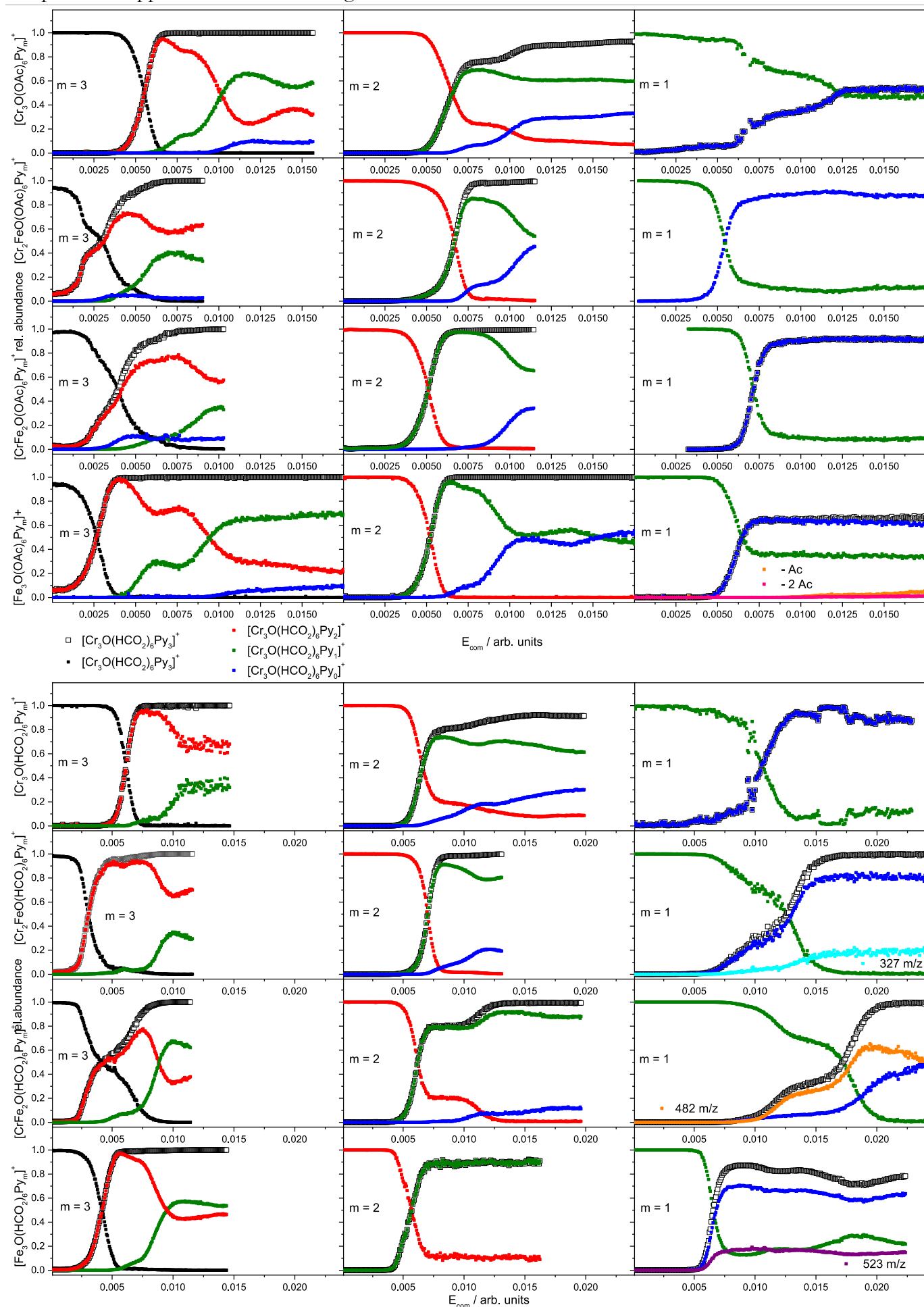


Figure 73 CID spectra of all Cr_xFe_xPy_x Formate and Acetate complexes, derived from the data featured in J. Krüger's bachelor thesis¹.

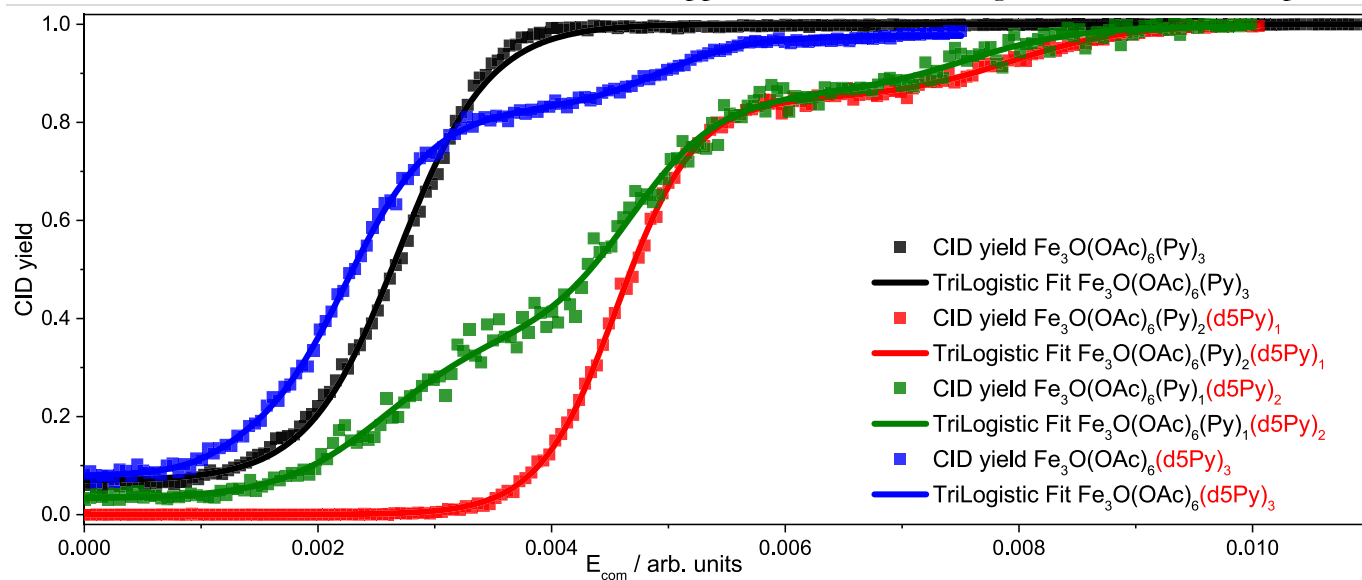


Figure 74 CID spectra of mixed Py/ D_5 Py complexes $[Fe_3O(OAc)_6(Py)_m(D_5Py)_{3-n}]^+$ for $n = 0 - 3$.

Table 22 Calculated BSSE²⁻⁴ corrected (see 0) fragmentation energies $\Delta_{fr}E_m$ and E_{COM}^{50} values for various species $[Cr_nFe_{3-n}O(OAc)_6Py_m]^+$ ($n, m = 1, 2, 3$) set in correlation. (n.a.p = no assignment possible). Green highlighted are the fragmentation energies which have been assigned to the first E_{COM}^{50} value. Already featured in J.Krüger's bachelor thesis¹.

<i>Species</i>	$\Delta_{fr}E_m$	E_{COM}^{50}	$\Delta_{fr}E_m$	E_{COM}^{50}
	<i>kJ/mol</i>	<i>a.u.</i>	<i>kJ/mol</i>	<i>a.u.</i>
	<i>Fe-Py</i>	<i>level 1</i>	<i>Cr-Py</i>	<i>level 2</i>
$[Cr_3O(OAc)_6Py_3]^+$		5.5	122	
$[Cr_3O(OAc)_6Py_2]^+$		6.2	139	
$[Cr_3O(OAc)_6Py_1]^+$		8.2	158	
$[Cr_2FeO(OAc)_6Py_3]^+$	99	1.7	126	n.a.p
$[Cr_2FeO(OAc)_6Py_2]^+$	119	5.76	145	6.78
$[Cr_2FeO(OAc)_6Py_1]^+$	141	5.34	160	n.a.p
$[CrFe_2O(OAc)_6Py_3]^+$	103	2.45	130	n.a.p
$[CrFe_2O(OAc)_6Py_2]^+$	128	5.06	146	n.a.p
$[CrFe_2O(OAc)_6Py_1]^+$	147	7.01	164	n.a.p
$[Fe_3O(OAc)_6Py_3]^+$	107	2.69		
$[Fe_3O(OAc)_6Py_2]^+$	129	5.19		
$[Fe_3O(OAc)_6Py_1]^+$	151	6.04		

Table 23 Calculated BSSE²⁻⁴ corrected (see 0) fragmentation energies $\Delta_{fr}E_m$ and E_{COM}^{50} values for various species $[Cr_nFe_{3-n}O(Fo)_6Py_m]^+$ ($n, m = 1, 2, 3$) set in correlation. (n.a.p = no assignment possible). Green highlighted are the fragmentation energies which have been assigned to the first E_{COM}^{50} value. Already featured in J.Krüger's bachelor thesis¹.

<i>Species</i>	$\Delta_{fr}E_m$ <i>kJ/mol</i> <i>Fe-Py</i>	E_{COM}^{50} <i>a.u.</i> <i>level 1</i>	$\Delta_{fr}E_m$ <i>kJ/mol</i> <i>Cr-Py</i>	E_{COM}^{50} <i>a.u.</i> <i>level 2</i>
$[Cr_3O(Fo)_6Py_3]^+$		6.14	138	
$[Cr_3O(Fo)_6Py_2]^+$		6.38	159	
$[Cr_3O(Fo)_6Py_1]^+$		10.45	183	
$[Cr_2FeO(Fo)_6Py_3]^+$	115	3.02	143	5.11
$[Cr_2FeO(Fo)_6Py_2]^+$	139	7	166	11.79
$[Cr_2FeO(Fo)_6Py_1]^+$	167	n.a.p	186	n.a.p
$[CrFe_2O(Fo)_6Py_3]^+$	120	2.96	147	6.55
$[CrFe_2O(Fo)_6Py_2]^+$	149	6.13	167	11.23
$[CrFe_2O(Fo)_6Py_1]^+$	190	n.a.p	173	n.a.p
$[Fe_3O(Fo)_6Py_3]^+$	123	4.15		
$[Fe_3O(Fo)_6Py_2]^+$	150	5.54		
$[Fe_3O(Fo)_6Py_1]^+$	178	n.a.p		

11.6 Additional IRMPD Graphs

The cumulative IRMPD graphs shown in the main section of this thesis frequently only show one example of typically several IRMPD measurements taken at different laser fluences and or shot sizes. The complete set of results is presented here.

11.6.1 Additional IRMPD Graphs of Acetate Pyridine Complexes

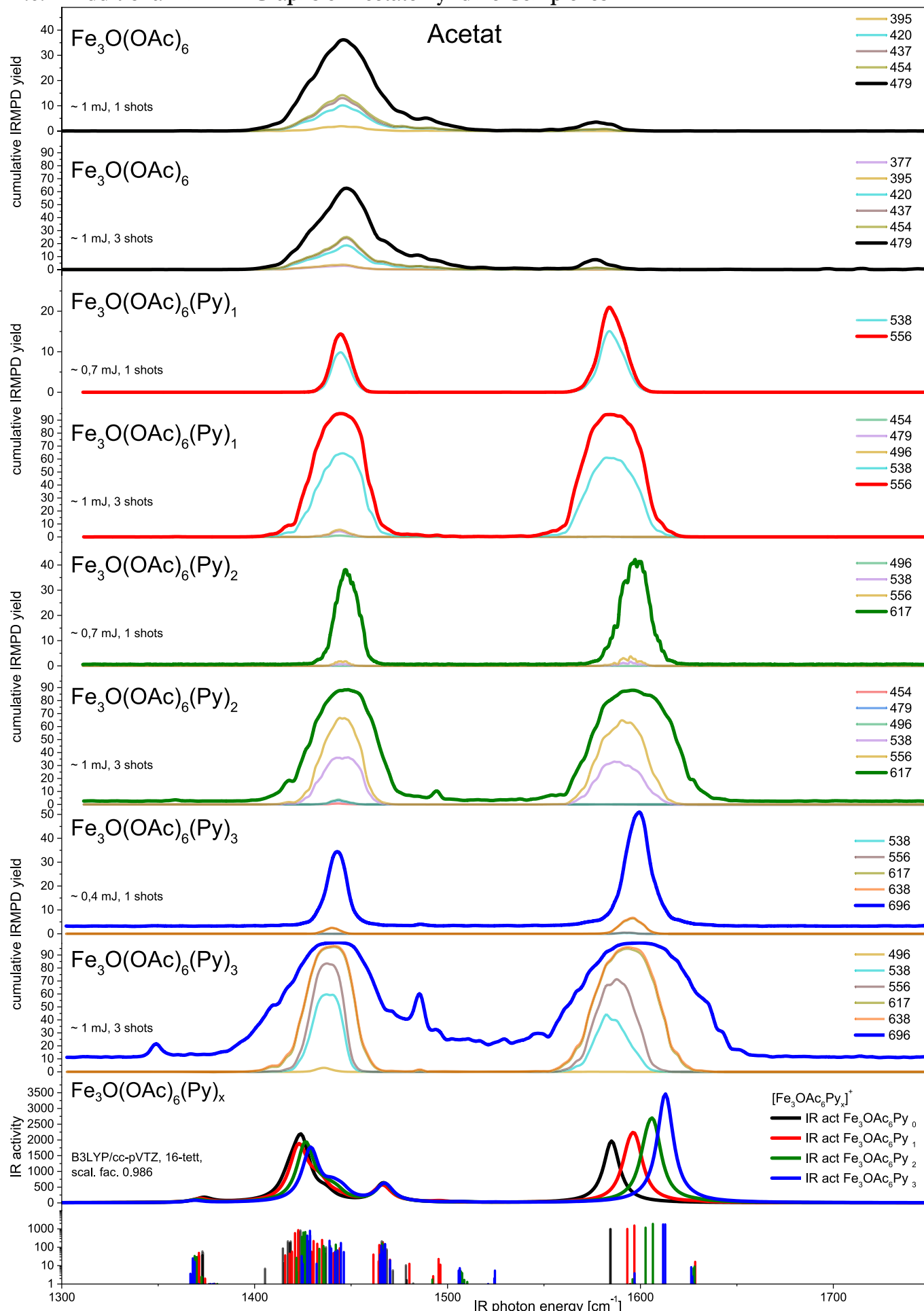


Figure 75 IRMPD spectra in the CO region of the $[\text{Fe}_3\text{O}(\text{OAc})_6\text{Py}_n]^+$ $n = 0, 1, 2, 3$ species, cumulative fragment trace labels in m/z .

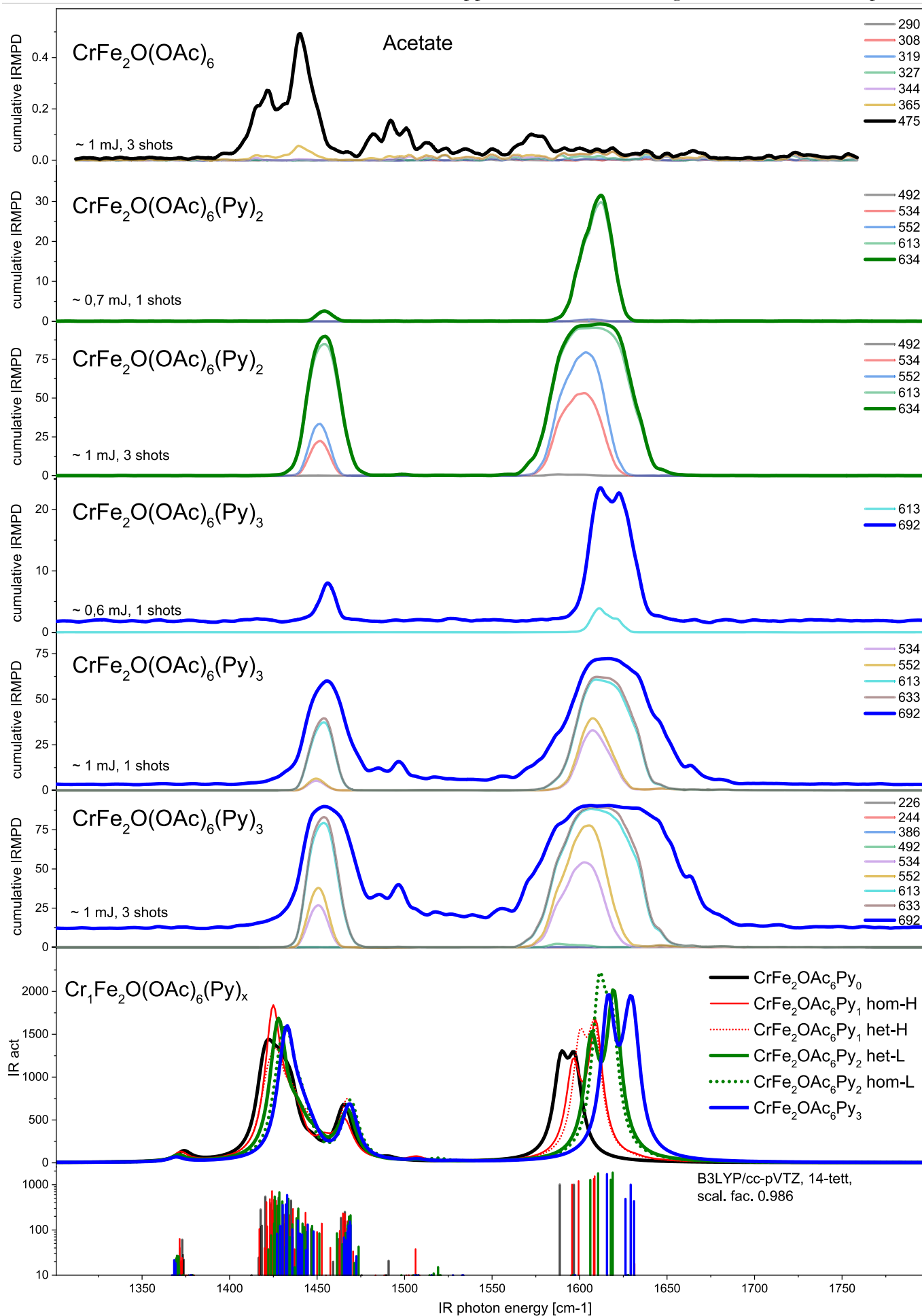


Figure 76 IRMPD spectra in the CO region of the [CrFe₂O(OAc)₆Py_n]⁺ n = 0, 2, 3 species, cumulative fragment trace labels in m/z.

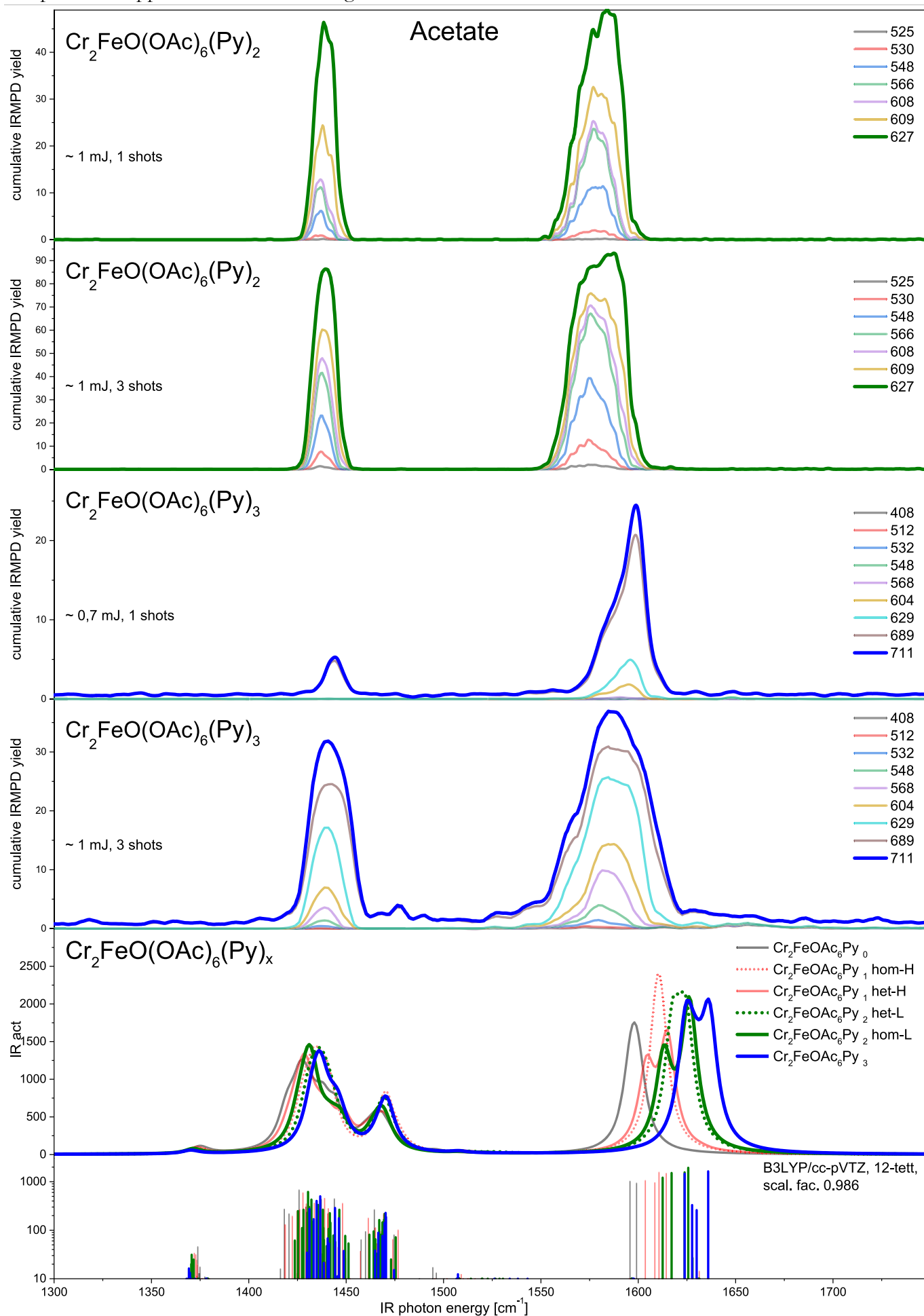


Figure 77 IRMPD spectra in the CO region of the $[\text{Cr}_2\text{FeO}(\text{OAc})_6(\text{Py})_n]^+$ $n = 2, 3$ species, cumulative fragment trace labels in m/z .

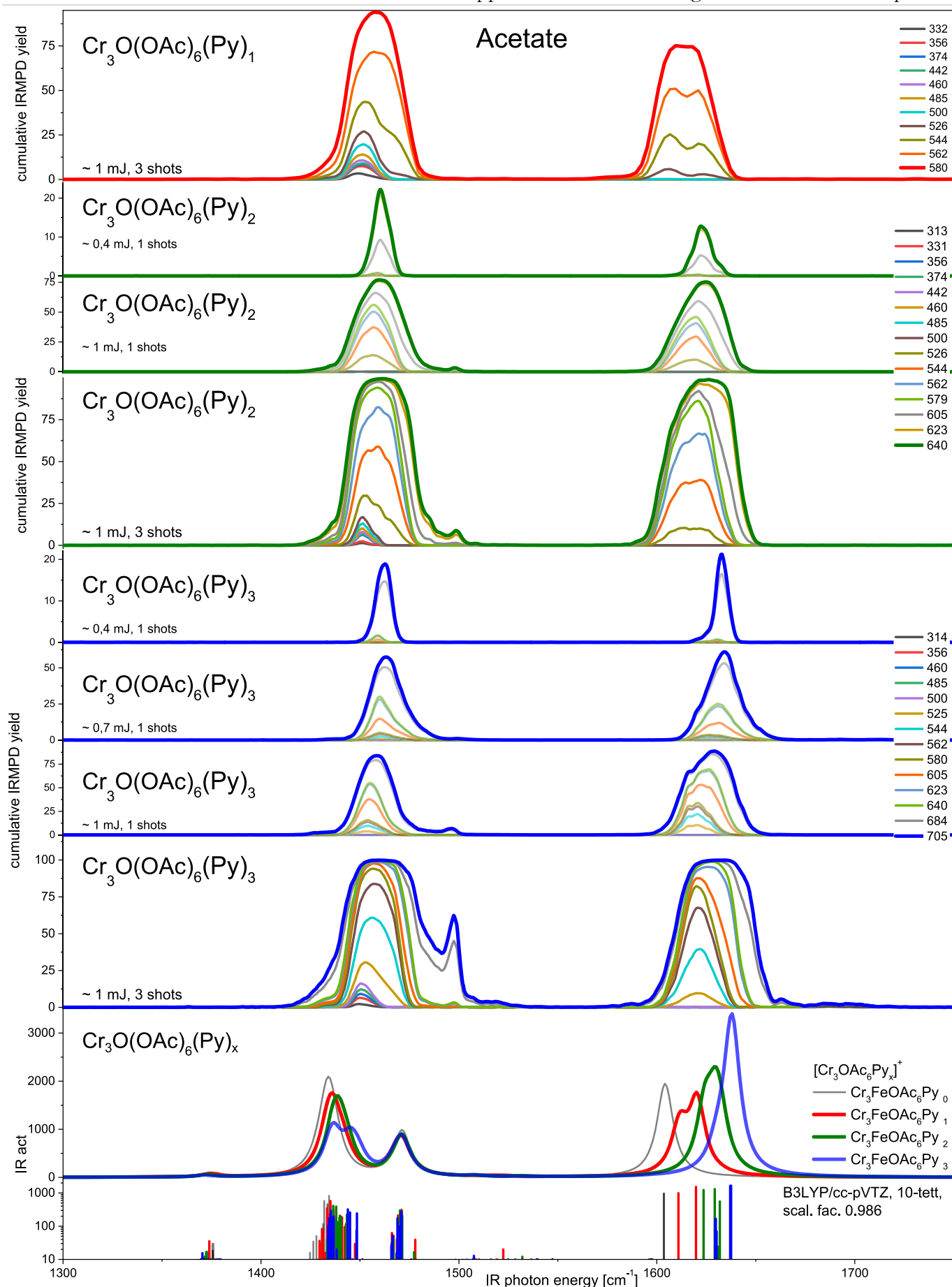


Figure 78 IRMPD spectra in the CO region of the $[\text{Cr}_3\text{O}(\text{OAc})_6\text{Py}_n]^+$ $n = 1, 2, 3$ species, cumulative fragment trace labels in m/z.

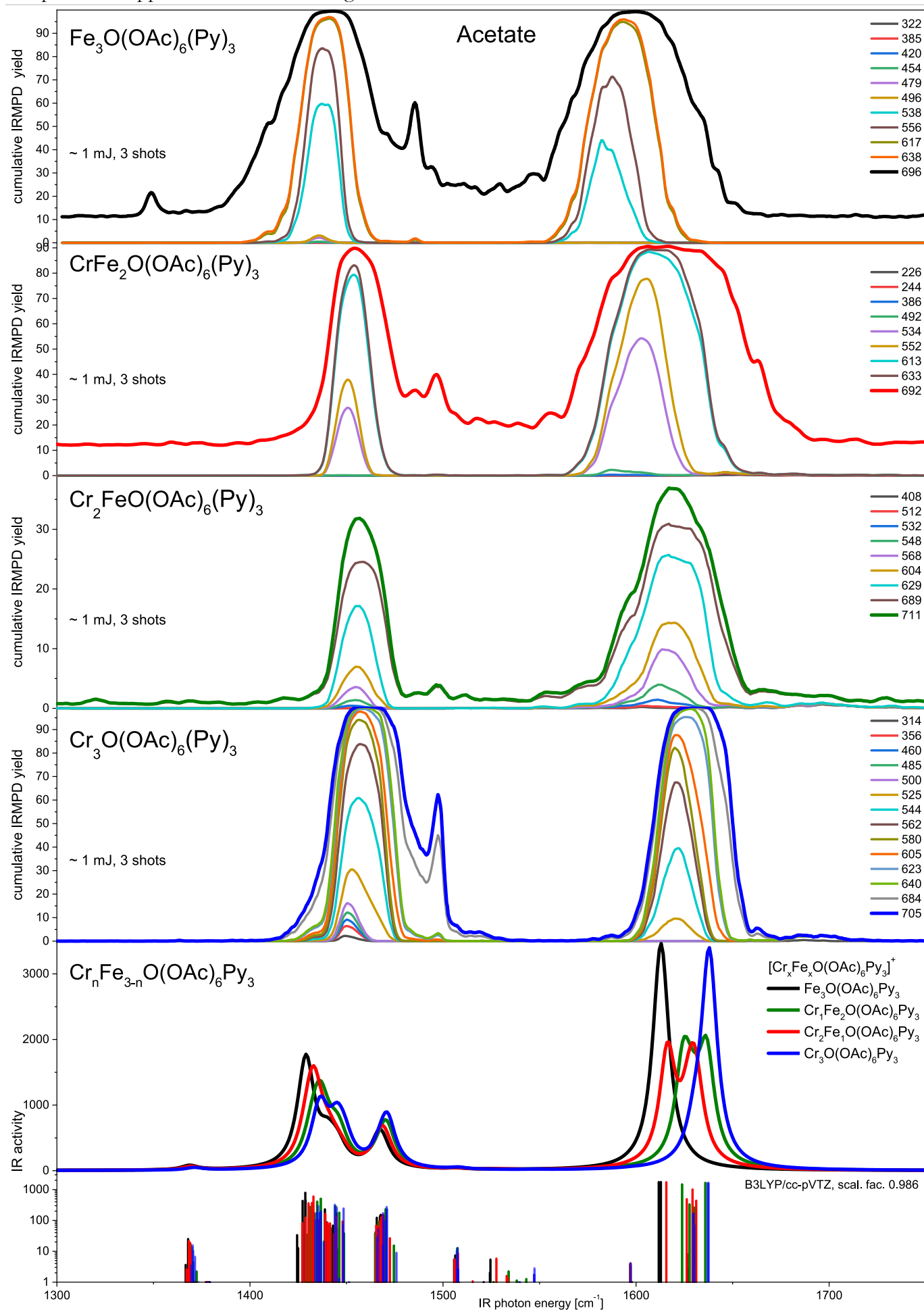


Figure 79 IRMPD spectra of $[\text{Cr}_n\text{Fe}_{3-n}\text{O}(\text{OAc})_6(\text{Py})_3]^+$ in the CO region, cumulative fragment trace labels in m/z .

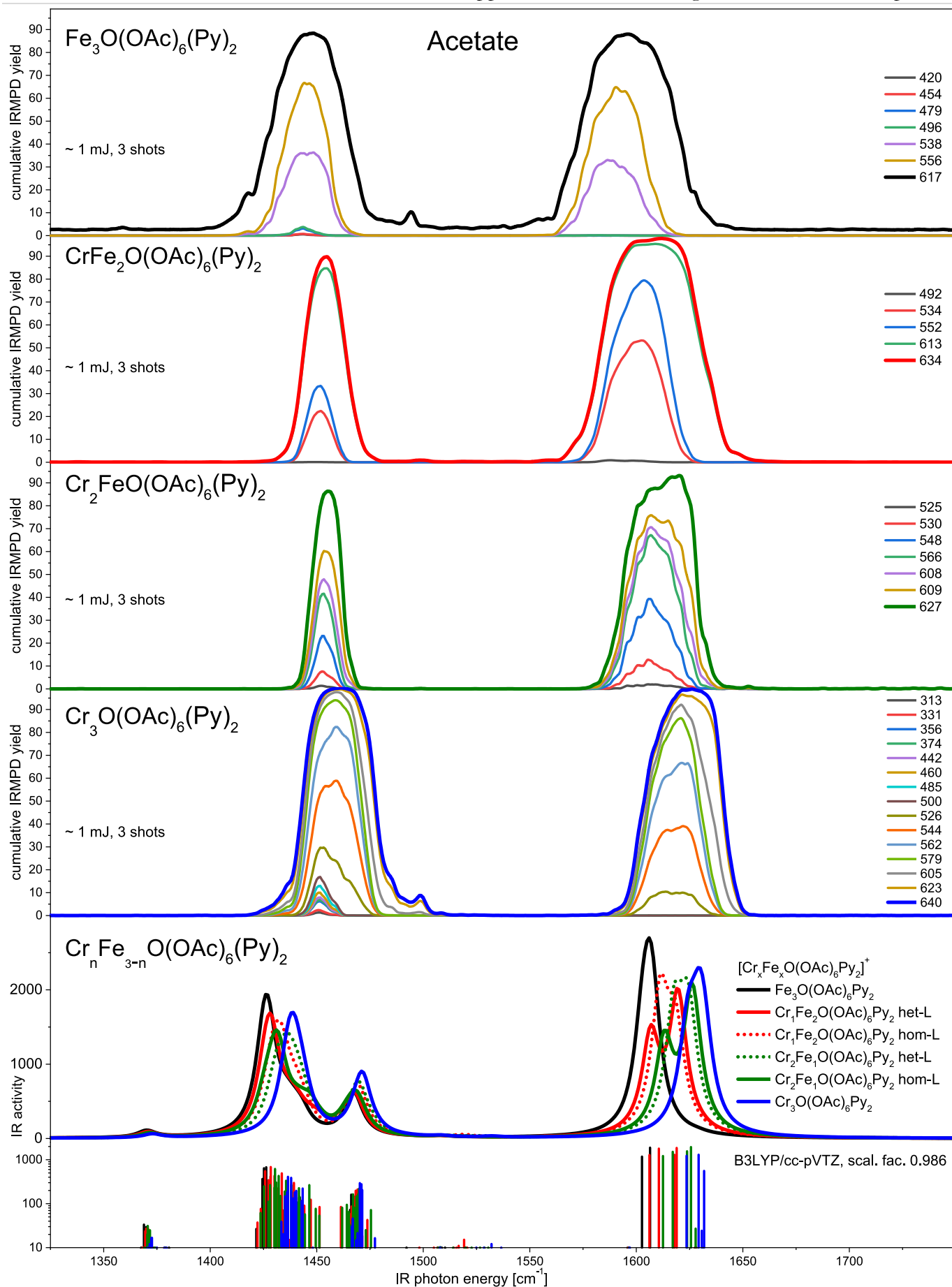


Figure 80 IRMPD spectra of $[\text{Cr}_n\text{Fe}_{3-n}\text{O}(\text{OAc})_6(\text{Py})_2]^+$ in the CO region, cumulative fragment trace labels in m/z .

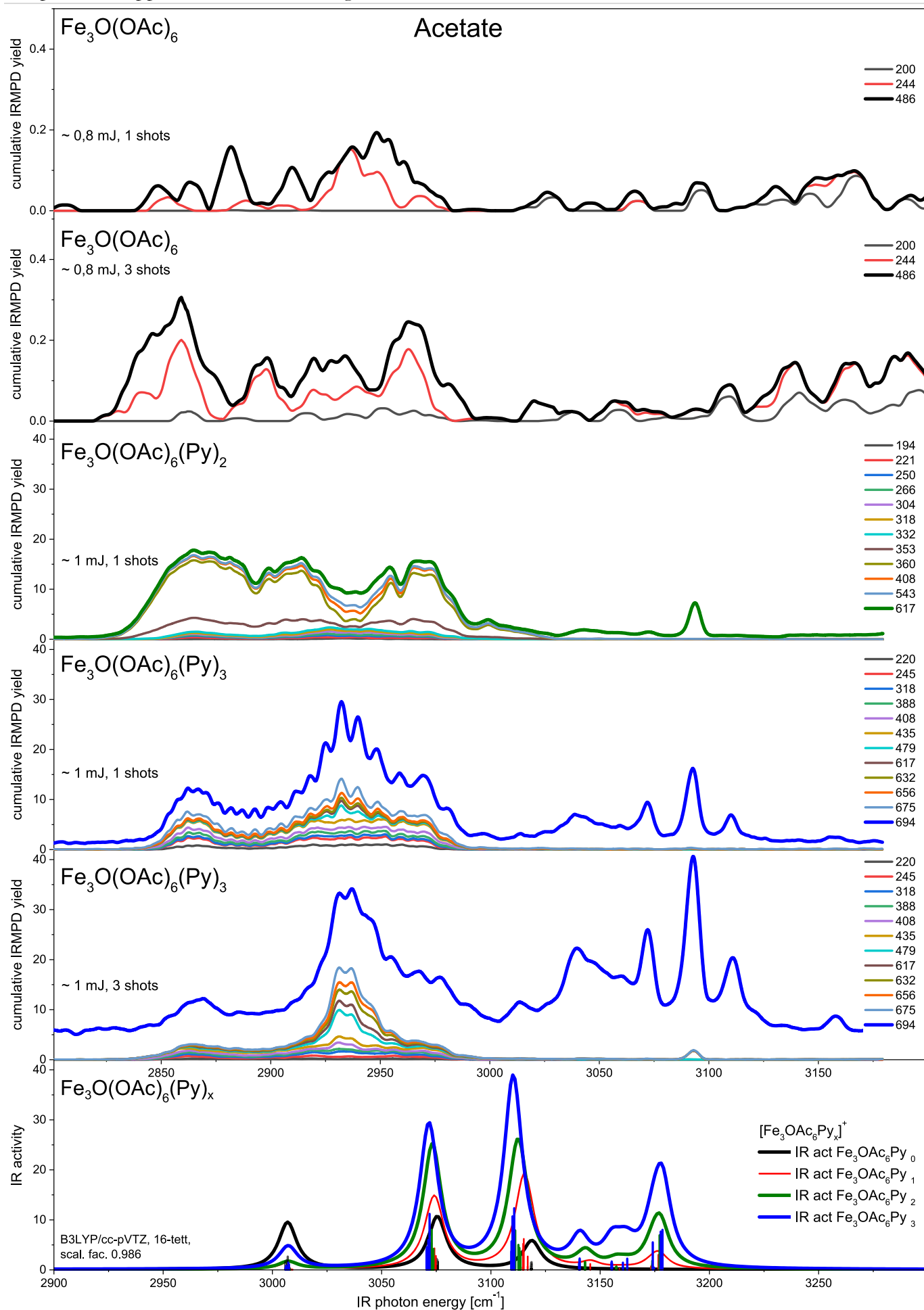


Figure 81 IRMPD spectra of $[\text{Fe}_3\text{O}(\text{OAc})_6(\text{Py})_n]^+$ at different laser fluences/shot counts in the CH region, cumulative fragment trace labels in m/z.

11.6.1.1 Acetate Complexes with Axial Ligand Pyridine, Isotope Exchange

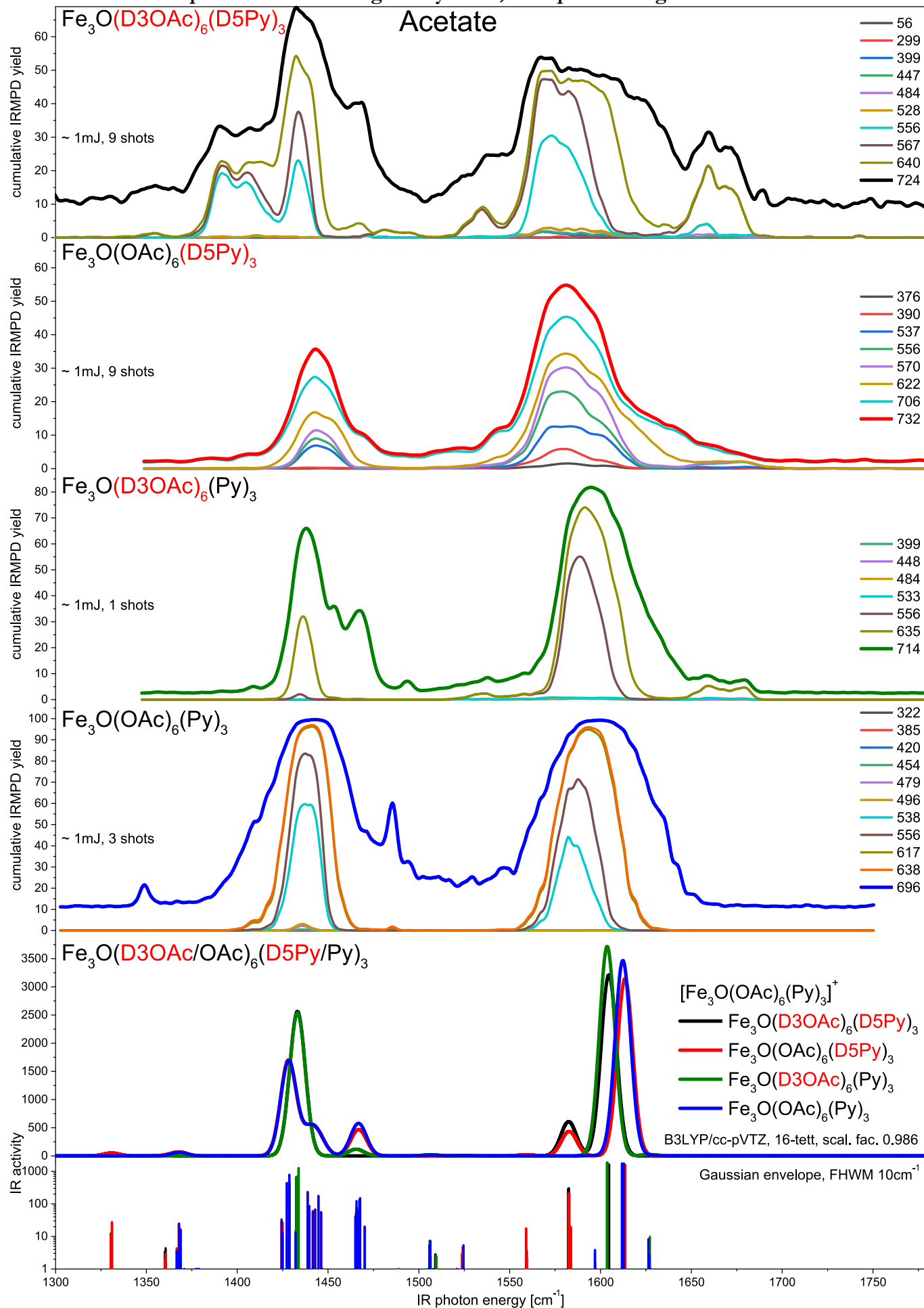


Figure 82 Successive deuterated pyridine ligand coordination of $[\text{Fe}_3\text{O}(\text{OAc})_6(\text{D}_5\text{Py})_n]^+$ spectra in the CO spectral region, cumulative fragment trace labels in m/z .

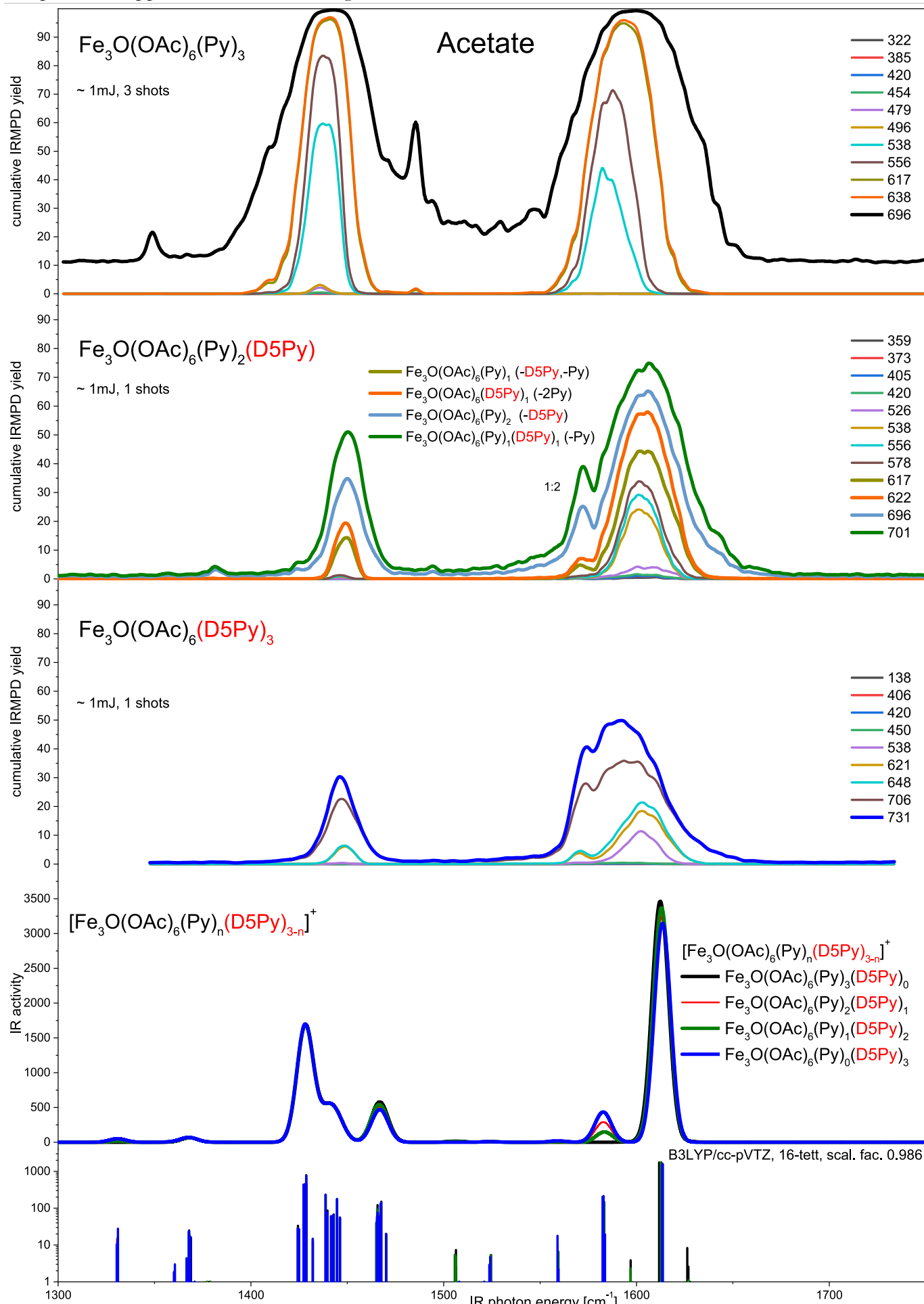


Figure 83 IRMPD spectra of mixed ligand $[\text{Fe}_3\text{O}(\text{OAc})_6(\text{Py})_n(\text{D5Py})_m]^+$ in the CO region. Refer to 5.6.1 for a discussion on the energy transfer from the **D5Py** Ligand absorbing at 1590 cm^{-1} to the Py ligands, witnessed by the fragmentation pattern, cumulative fragment trace labels in m/z .

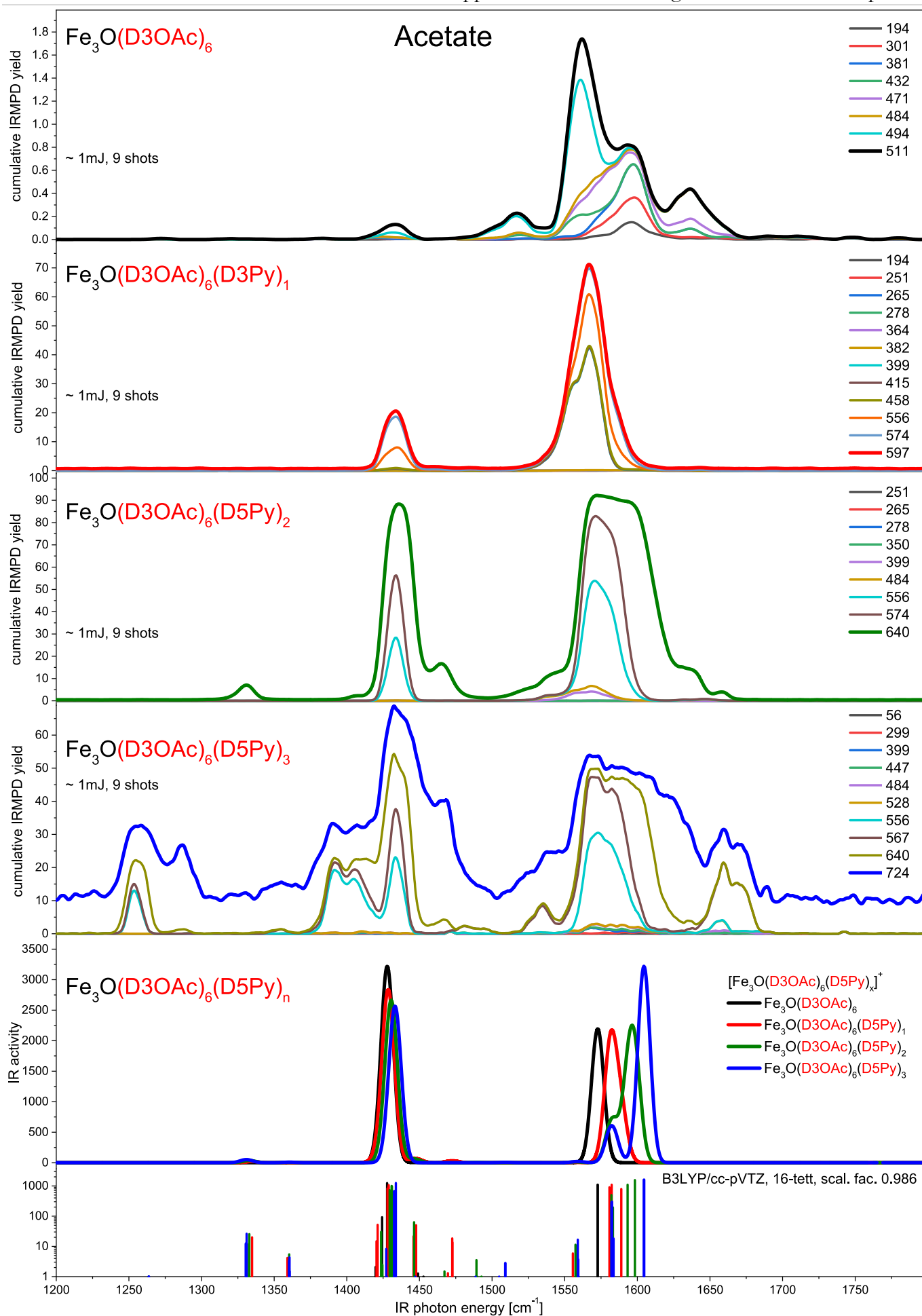


Figure 84 Successive deuterated pyridine ligand coordination of $[\text{Fe}_3\text{O}(\text{D}_3\text{OAc})_6(\text{D}_5\text{Py})_n]^+$ spectra in the CO spectral region, cumulative fragment trace labels in m/z .

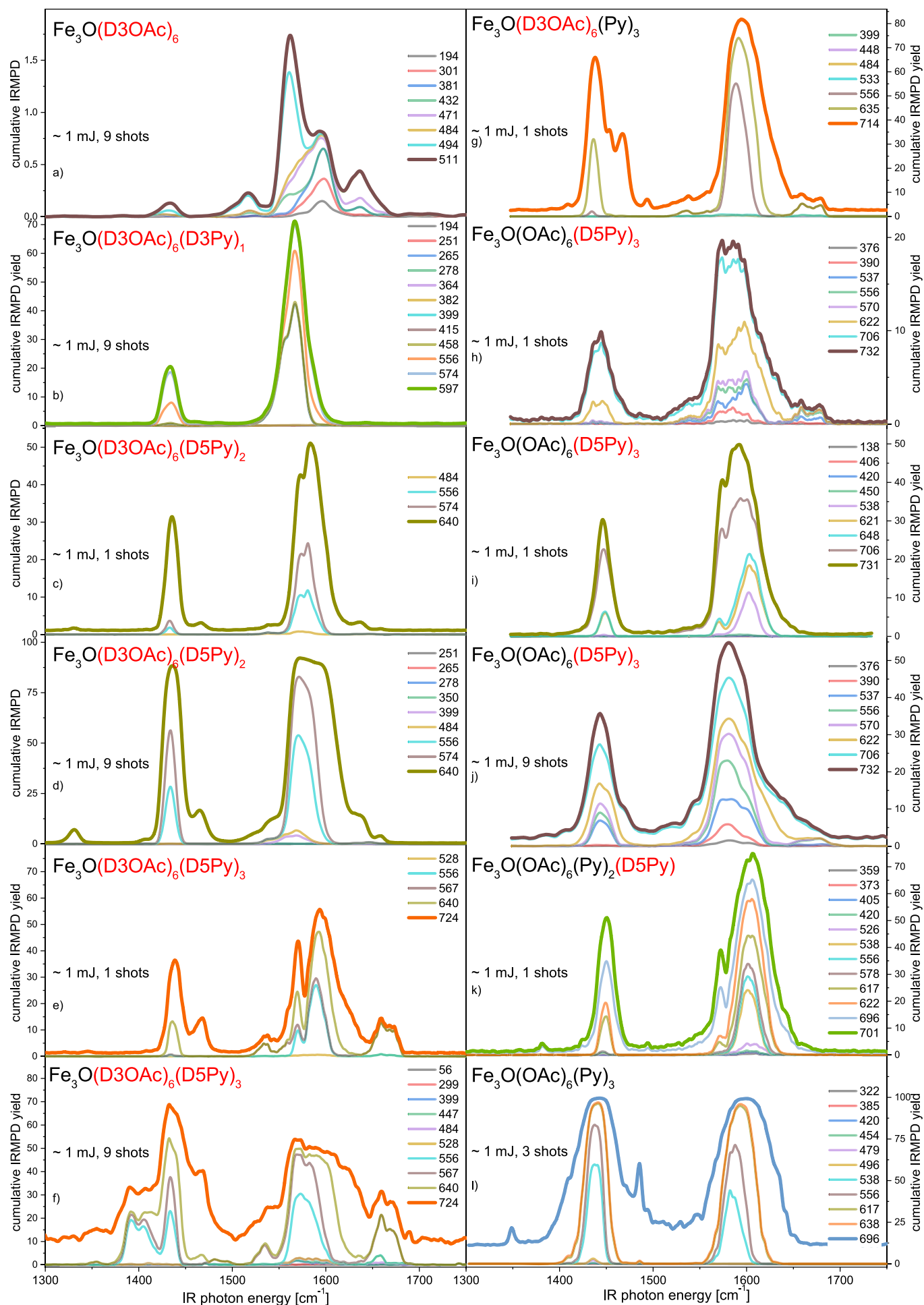


Figure 85 All different IRMPD spectra of all measured $[\text{Fe}_3\text{O}(\text{OAc}/\text{D}_3\text{OAc})_6(\text{Py})_n(\text{D}_5\text{Py})_m]^+$ spectra in the CO region, cumulative fragment trace labels in m/z.

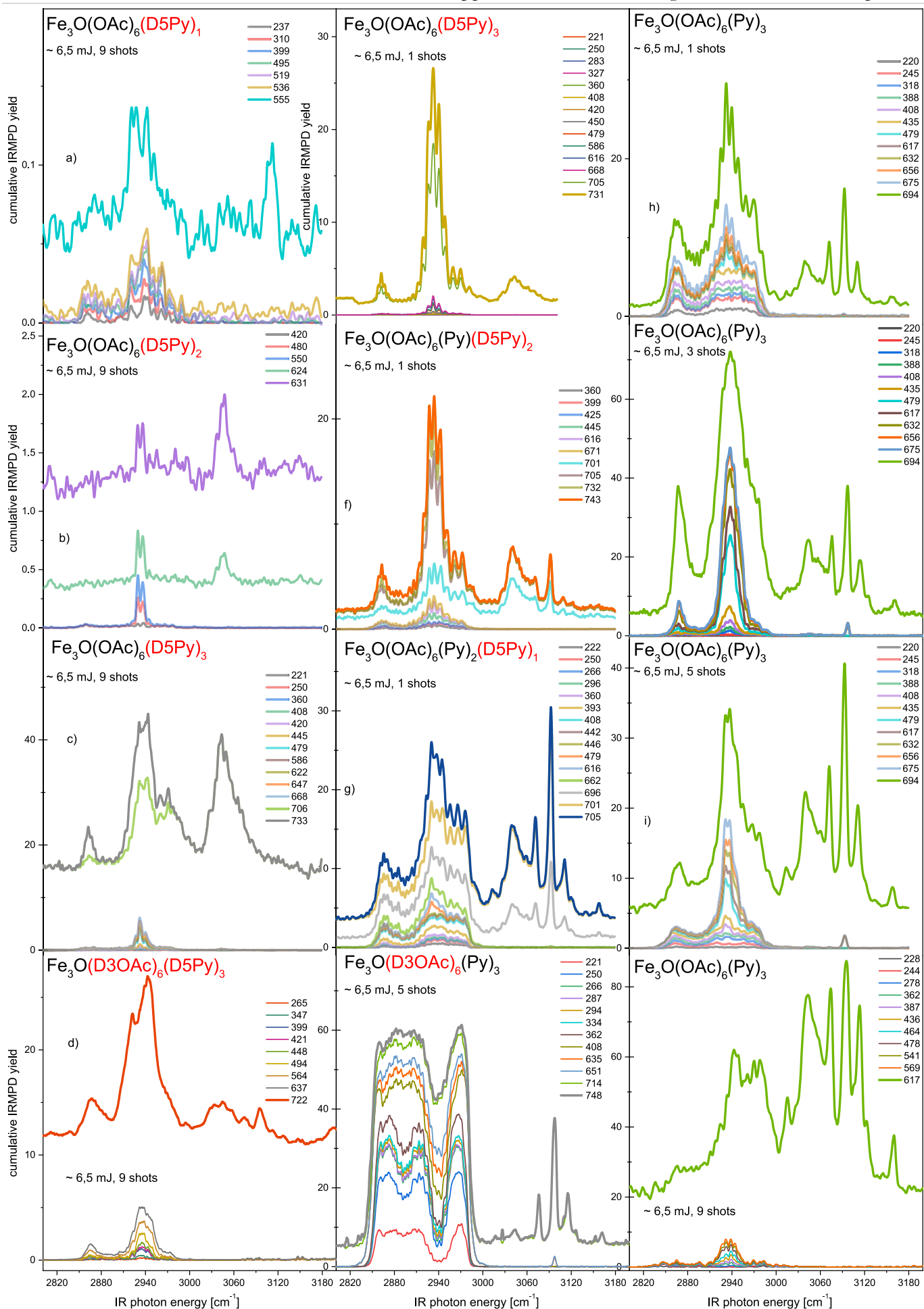


Figure 86 IRMPD spectra in the CH region of all $[\text{Fe}_3\text{O}(\text{OAc})_6(\text{Py})_3]^+$ and $[\text{Fe}_3\text{O}(\text{OAc}/\text{D}_3\text{OAc})_6(\text{Py})_n(\text{D}_5\text{Py})_m]^+$ in the CH region, cumulative fragment trace labels in m/z.

Acetate, Axial Ligand Water

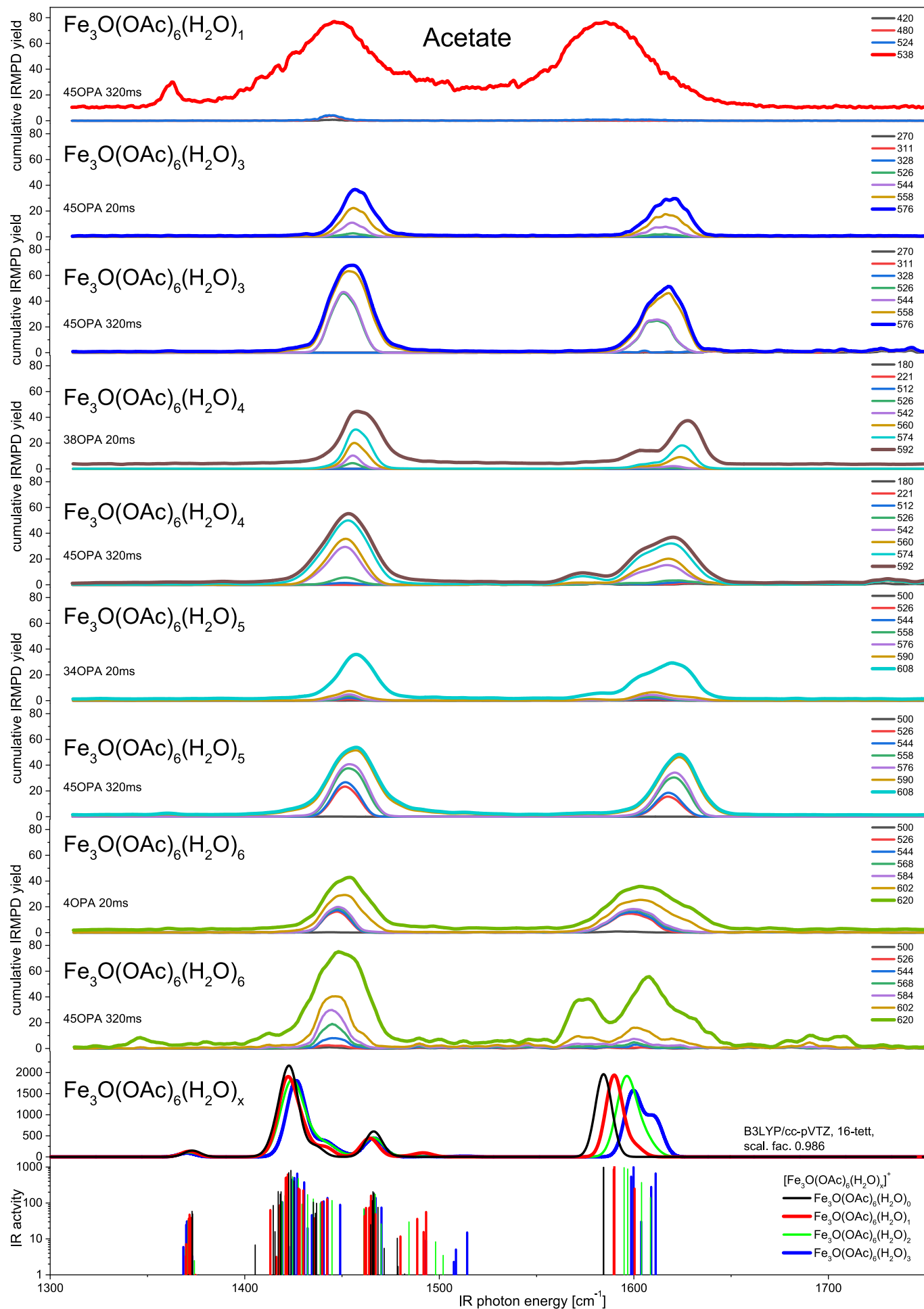


Figure 87 IRMPD spectra of $[\text{Fe}_3\text{O}(\text{OAc})_6(\text{H}_2\text{O})_n]^+$ with $n = 1, 3 - 6$ at different laser fluences/shot counts in the CO region, cumulative fragment trace labels in m/z .

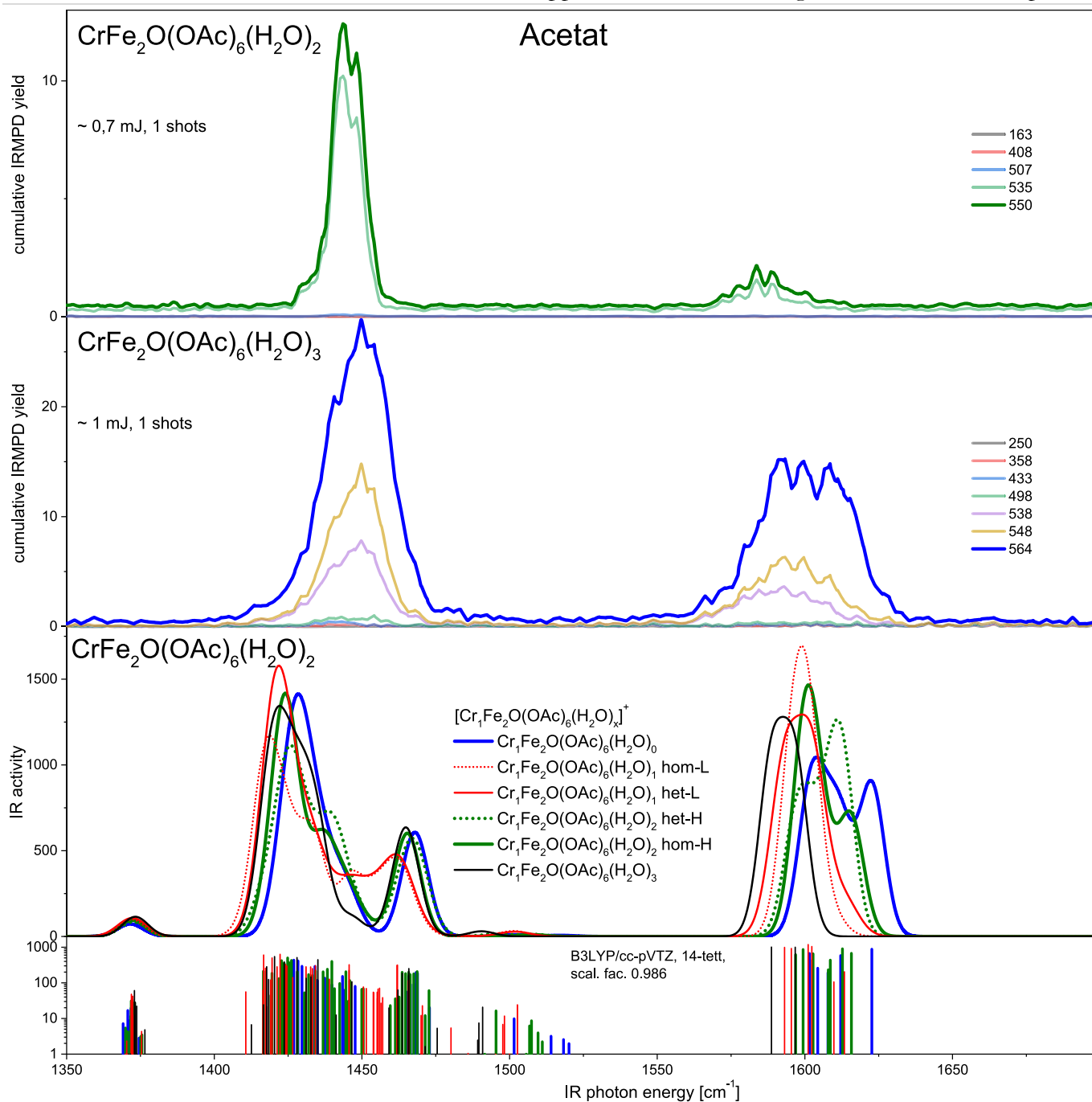


Figure 88 IRMPD spectra of $[\text{CrFe}_2\text{O}(\text{Fo})_6(\text{H}_2\text{O})_n]^+$ with $n = 2, 3$ in the CO region, cumulative fragment trace labels in m/z .

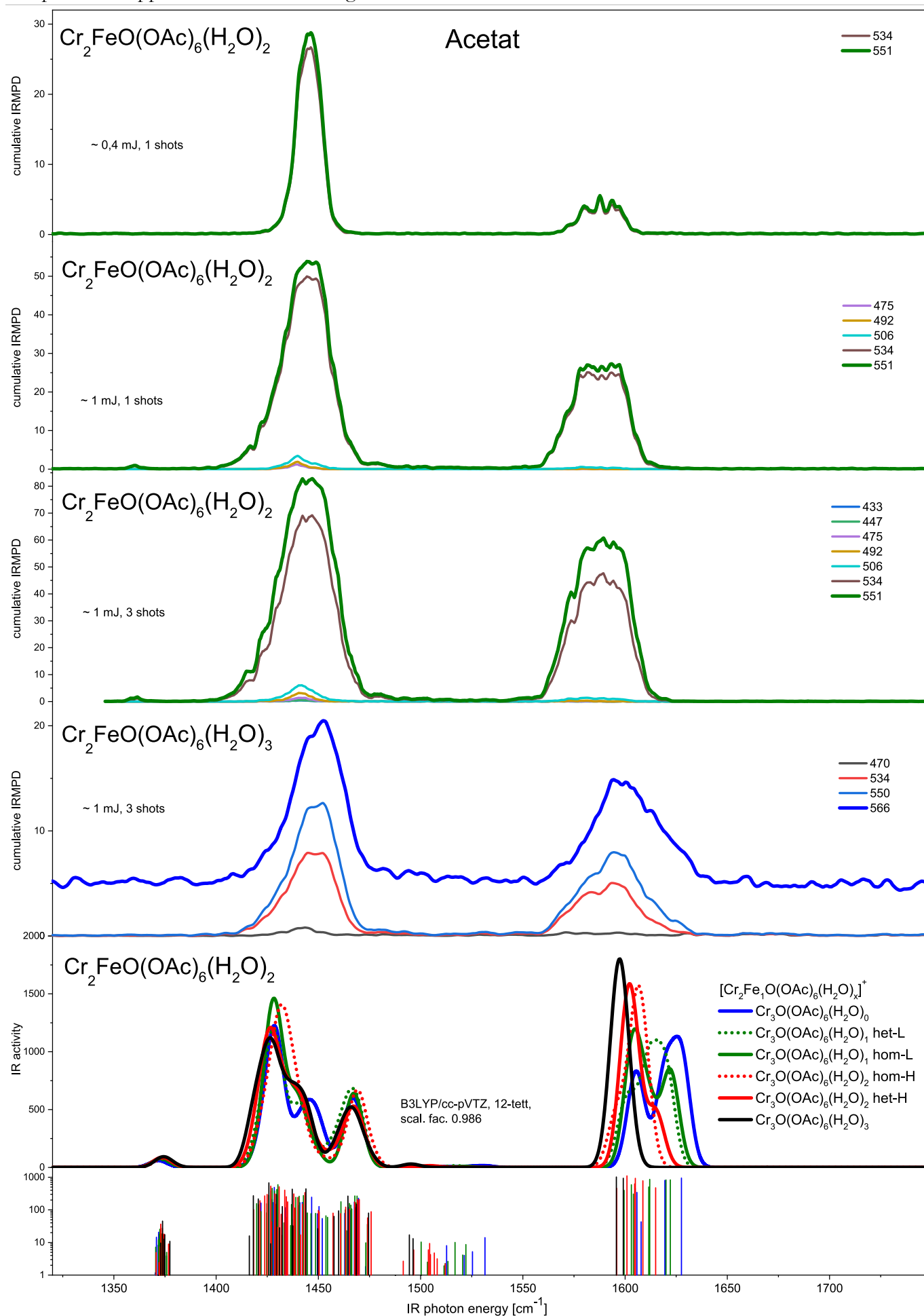


Figure 89 IRMPD spectra of $[\text{Cr}_2\text{FeO}(\text{OAc})_6(\text{H}_2\text{O})_n]^+$ with $n = 2, 3$ in the CO region, cumulative fragment trace labels in m/z .

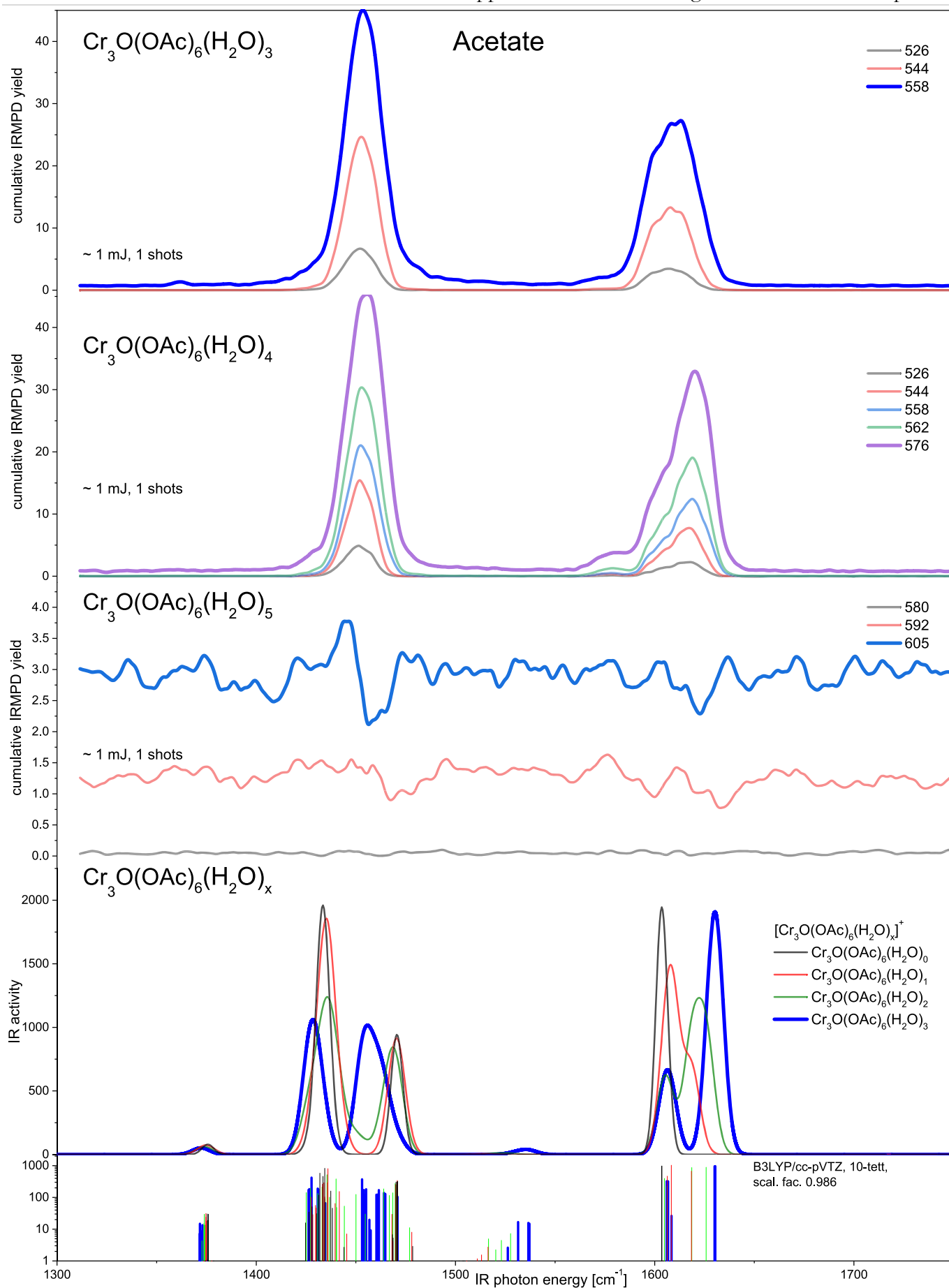


Figure 90 IRMPD spectra of $[\text{Cr}_3\text{O}(\text{Fo})_6(\text{H}_2\text{O})_n]^+$ with $n = 3, 4, 5$ in the CO region, cumulative fragment trace labels in m/z .

11.6.1.2 Acetate DMF, DMSO, THF

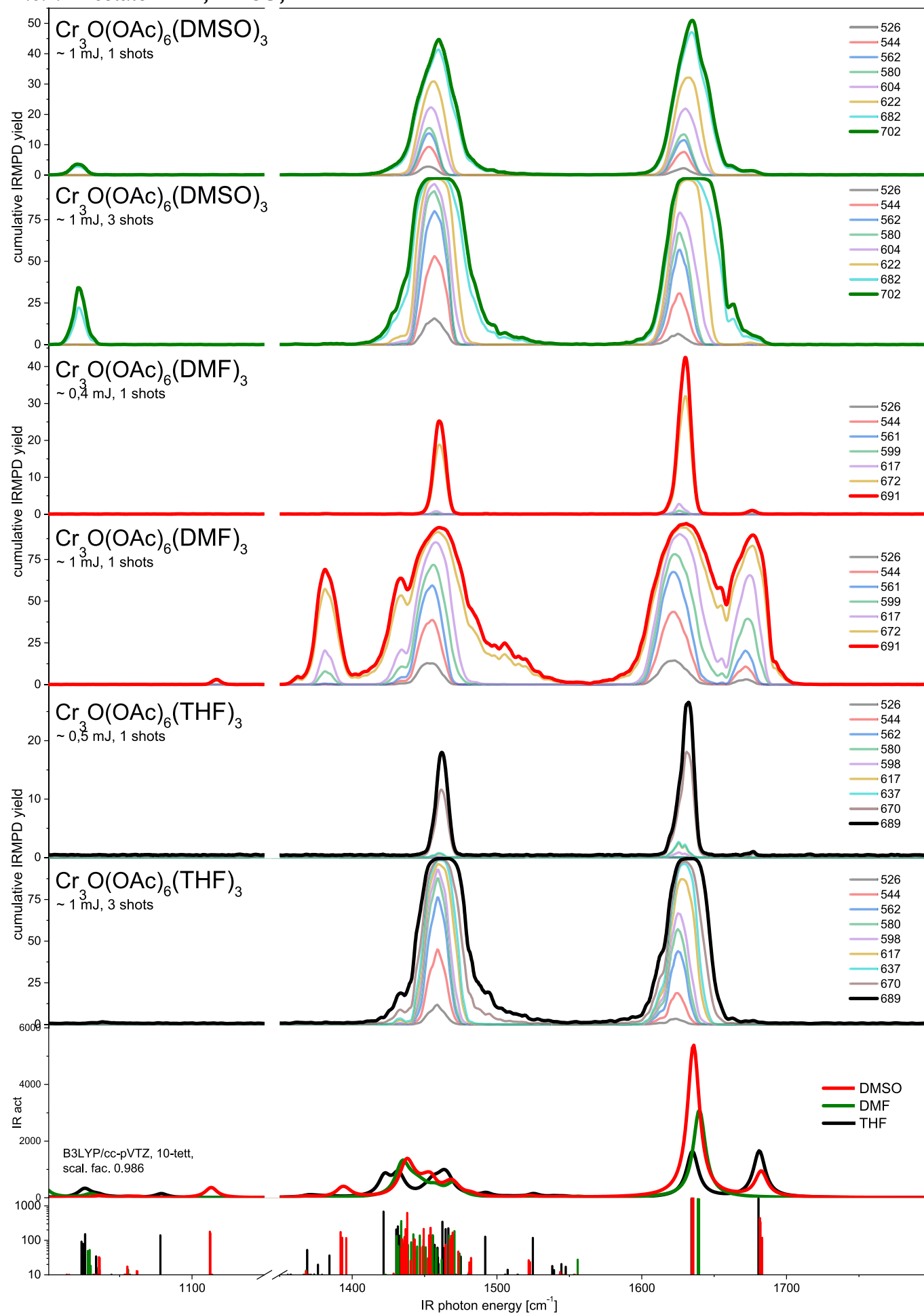


Figure 91 IRMPD spectra of $[\text{Cr}_3\text{O}(\text{OAc})_6(\text{L})_3]^+$ with $\text{L} = \text{THF}, \text{DMSO}, \text{DMF}$ at different laser fluences/shot counts in the CO region, cumulative fragment trace labels in m/z .

11.6.1.3 Formate, Axial Ligand Pyridine, Ligand Variation

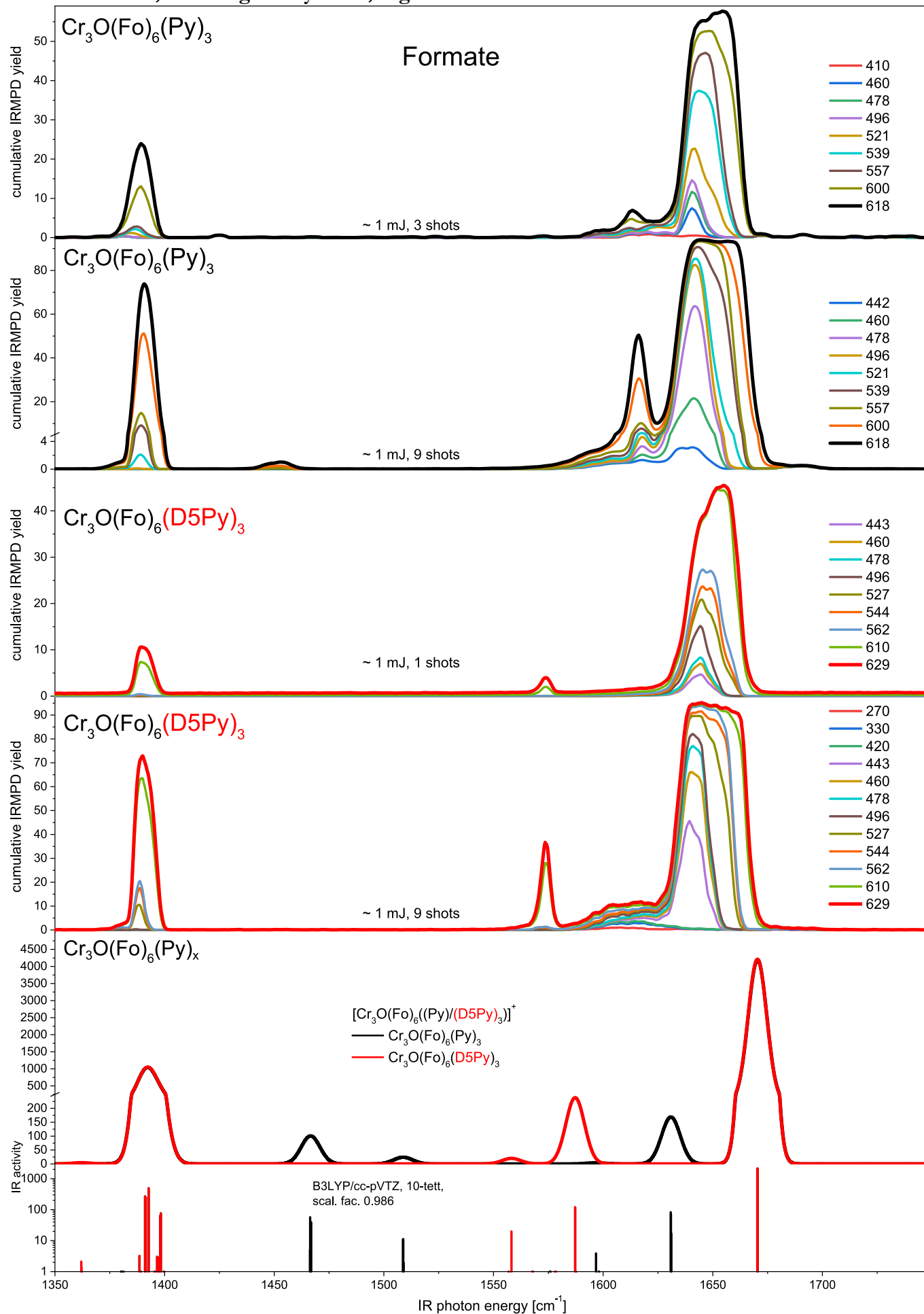


Figure 92 IRMPD spectra of formate $[\text{Cr}_3\text{O}(\text{Fo})_6(\text{L})_3]^+$ with $\text{L} = (\text{Py}_3 \text{ and } \text{D}_5\text{Py}_3)$ in the CO spectral region, cumulative fragment trace labels in m/z .

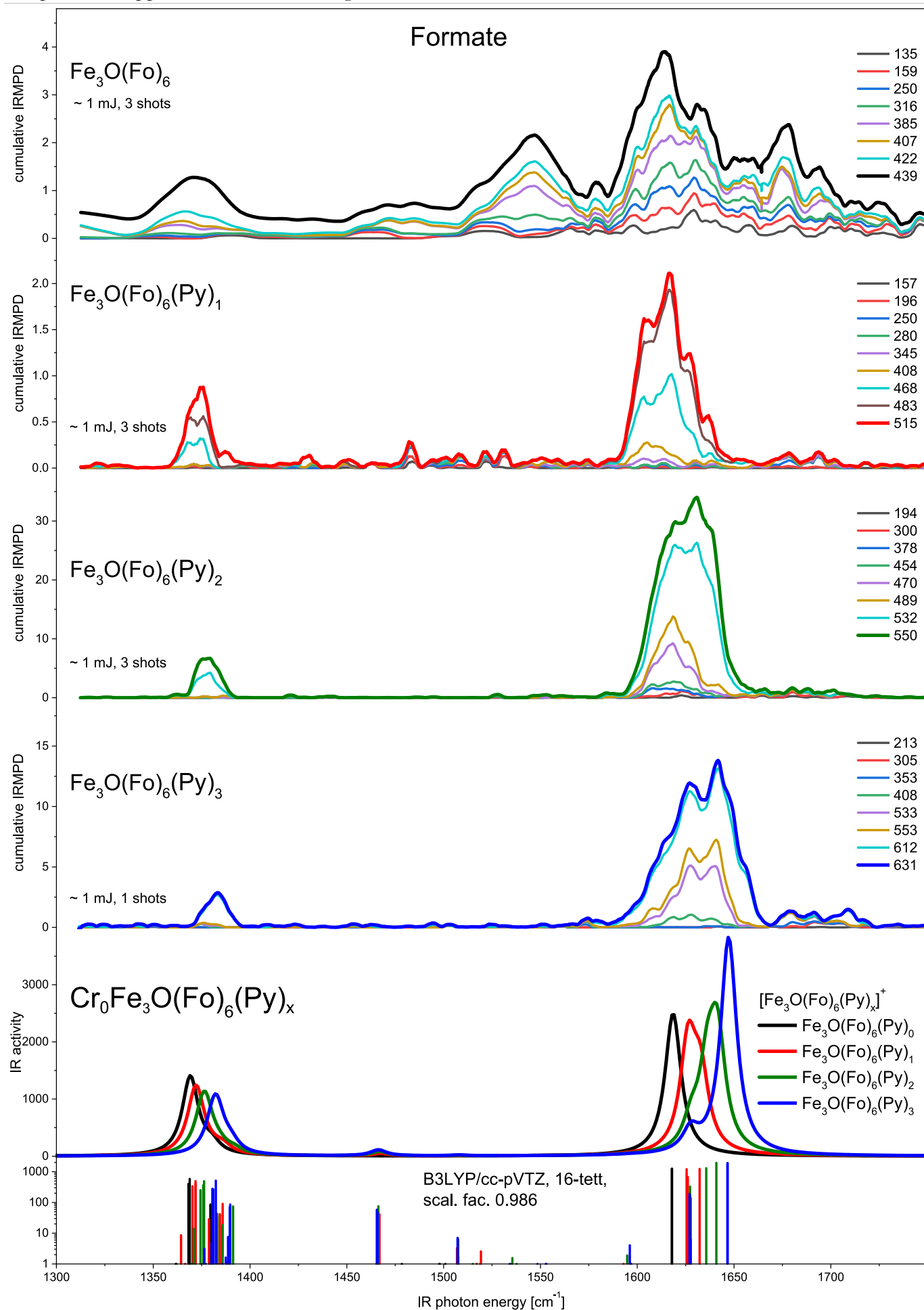


Figure 93 IRMPD spectra of formate $[\text{Fe}_3\text{O}(\text{Fo})_6(\text{Py})_n]^+$ with $n = 0 - 3$ in the CO spectral region, ligand variation, cumulative fragment trace labels in m/z .

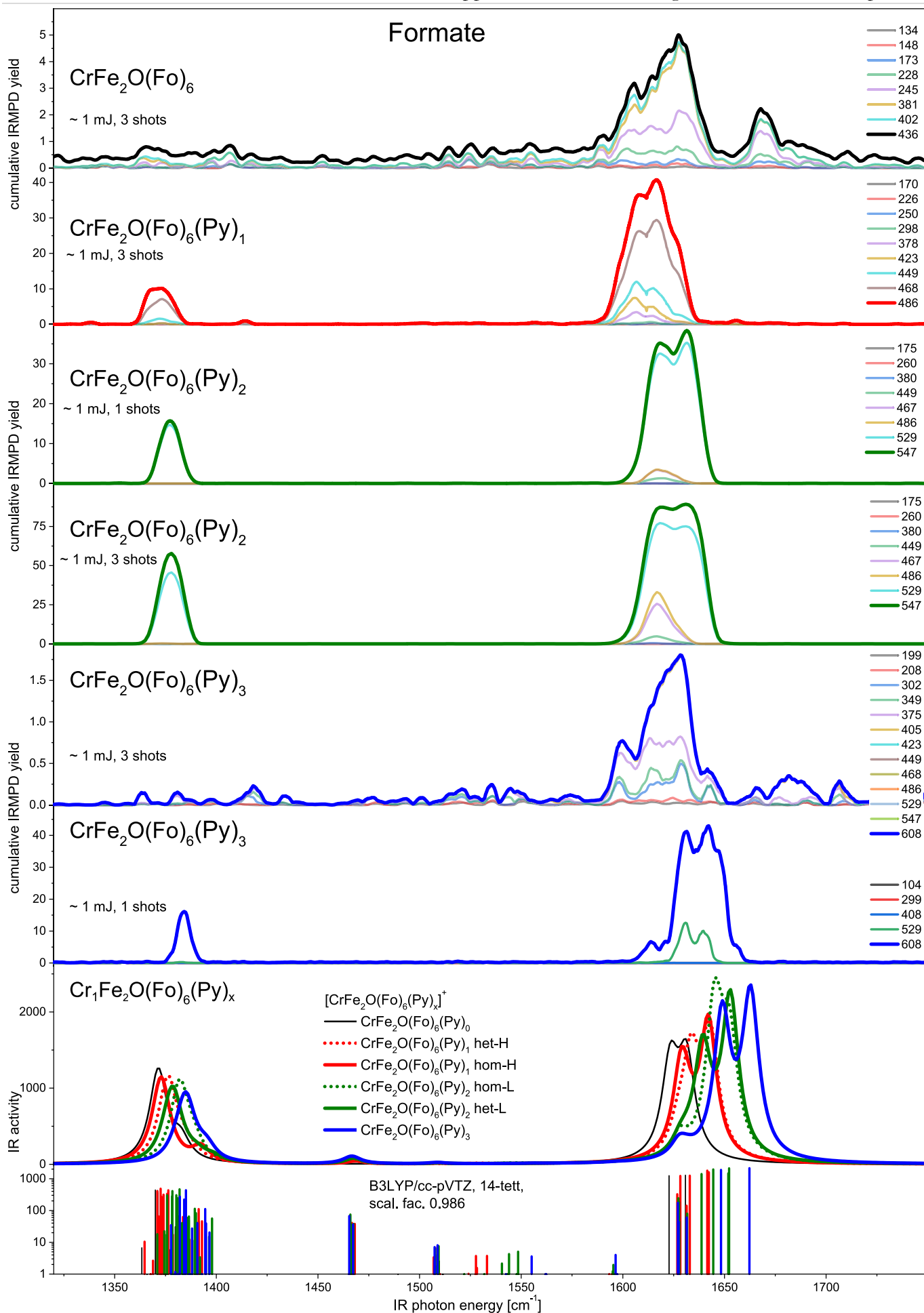


Figure 94 IRMPD spectra of formate $[\text{Cr}_1\text{Fe}_2\text{O}(\text{Fo})_6(\text{Py})_n]^+$ with $n = 0 - 3$ in the CO spectral region, ligand variation, cumulative fragment trace labels in m/z .

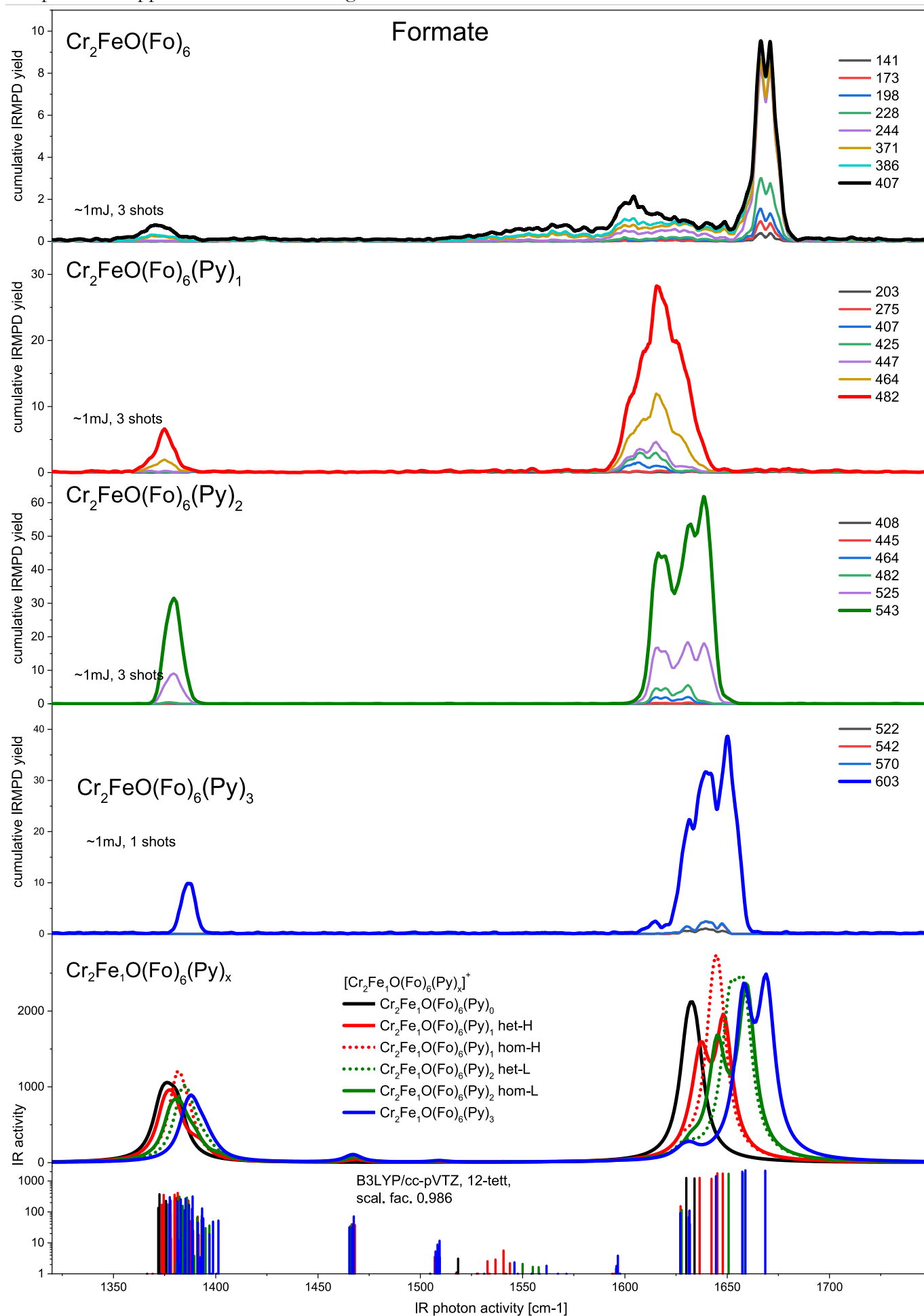


Figure 95 IRMPD spectra of formate $[\text{Cr}_2\text{Fe}_1\text{O}(\text{Fo})_6(\text{Py})_n]^+$ with $n = 0 - 3$ in the CO spectral region, ligand variation, cumulative fragment trace labels in m/z .

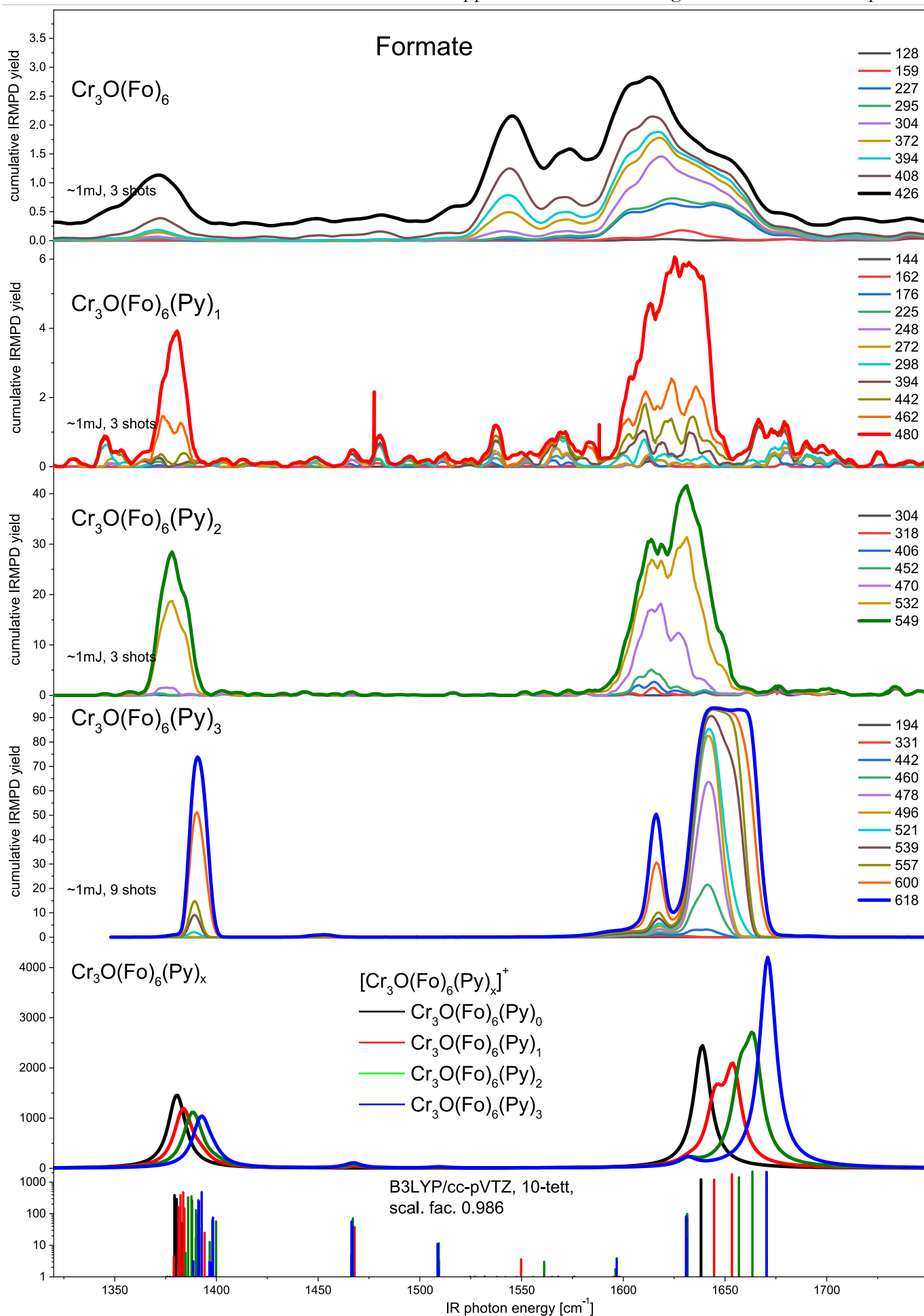


Figure 96 IRMPD spectra of formate $[\text{Cr}_3\text{O}(\text{Fo})_6(\text{Py})_n]^+$ with $n = 0 - 3$ in the CO spectral region, ligand variation, cumulative fragment trace labels in m/z .

11.6.1.4 Formate, Axial Ligand Pyridine, Metal Variation

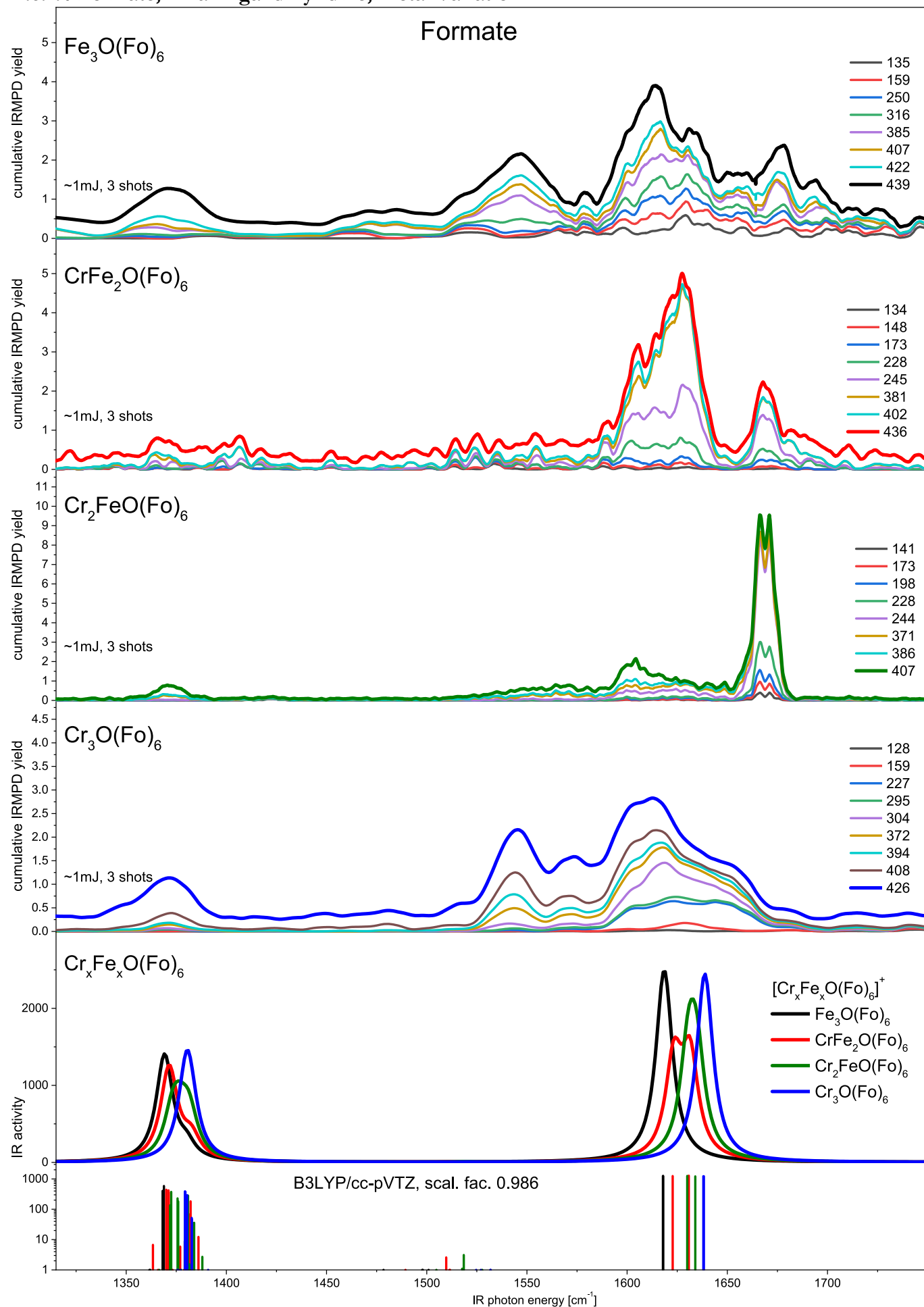


Figure 97 IRMPD spectra of formate $[\text{Cr}_n\text{Fe}_{3-n}\text{O}(\text{Fo})_6]^+$ with $n = 0 - 3$ in the CO spectral region, metal variation, cumulative fragment trace labels in m/z .

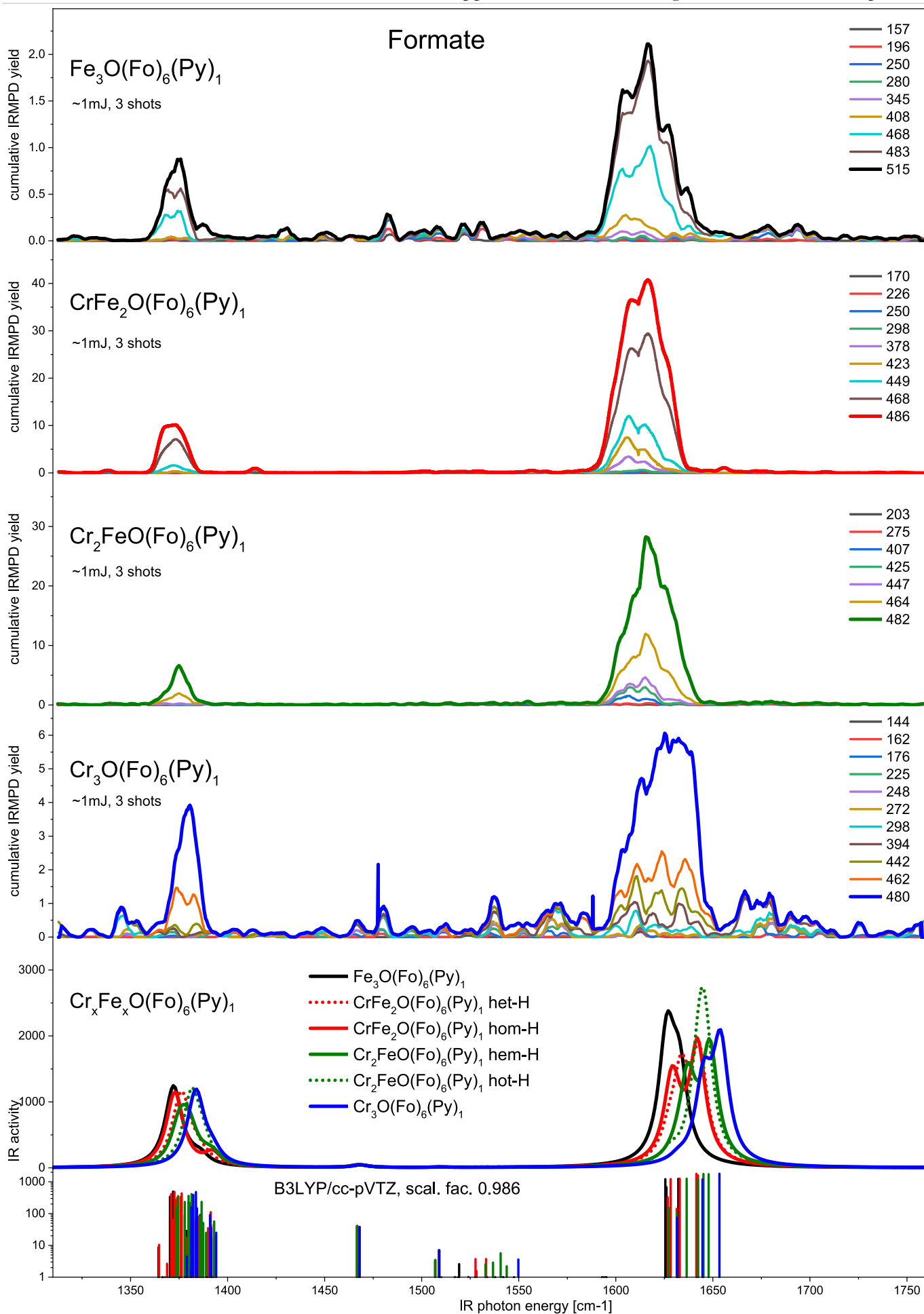


Figure 98 IRMPD spectra of formate $[\text{Cr}_n\text{Fe}_{3-n}\text{O}(\text{Fo})_6(\text{Py})_1]^+$ with $n = 0 - 3$ in the CO spectral region, metal variation, cumulative fragment trace labels in m/z .

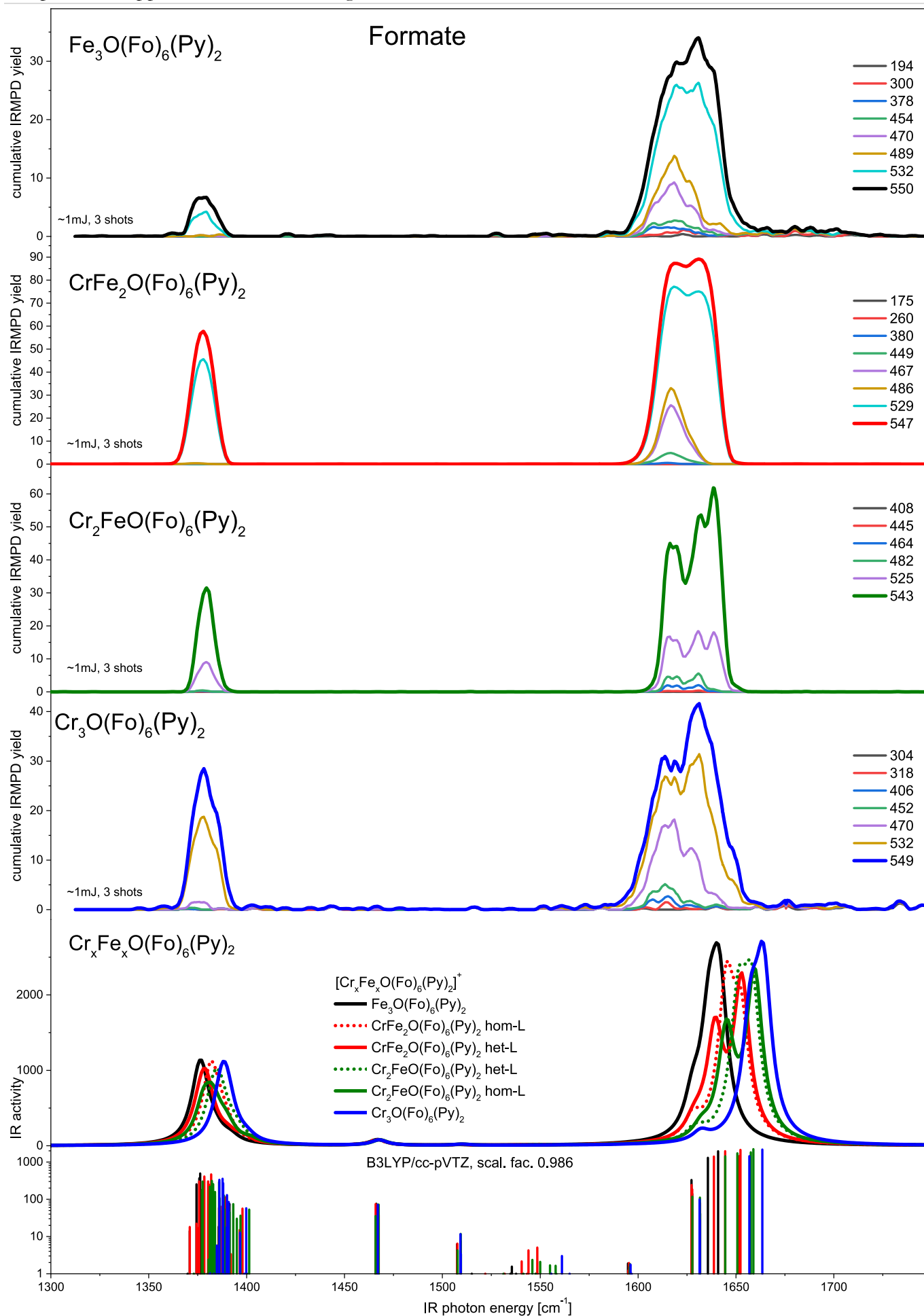


Figure 99 IRMPD spectra of formate $[\text{Cr}_n\text{Fe}_{3-n}\text{O}(\text{Fo})_6(\text{Py})_2]^+$ with $n = 0 - 3$ in the CO spectral region, metal variation, cumulative fragment trace labels in m/z .

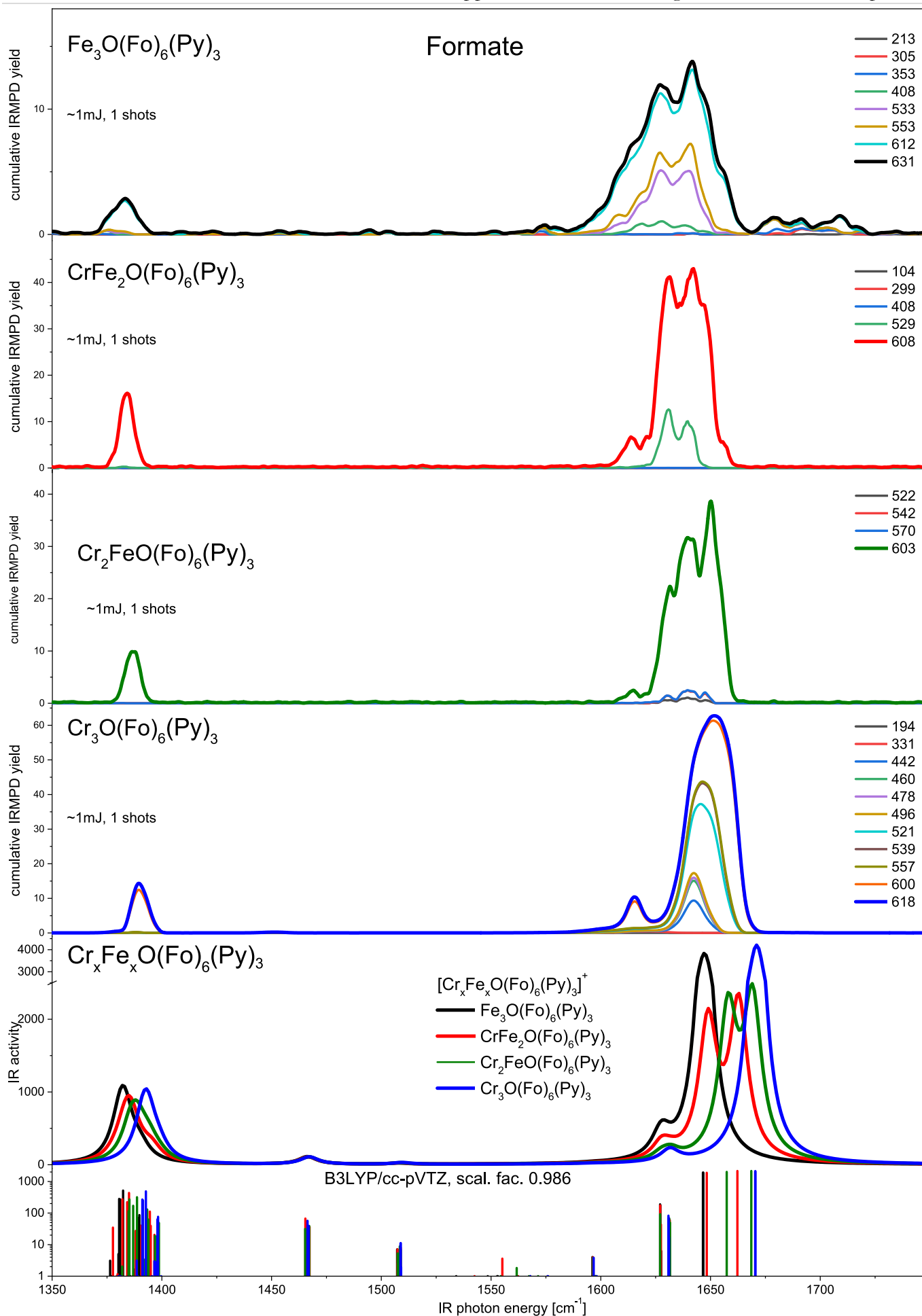


Figure 100 IRMPD spectra of formate $[\text{Cr}_n\text{Fe}_{3-n}\text{O}(\text{Fo})_6(\text{Py})_3]^+$ with $n = 0 - 3$ in the CO spectral region, metal variation, cumulative fragment trace labels in m/z .

11.6.1.5 Formate, Axial Ligand Water

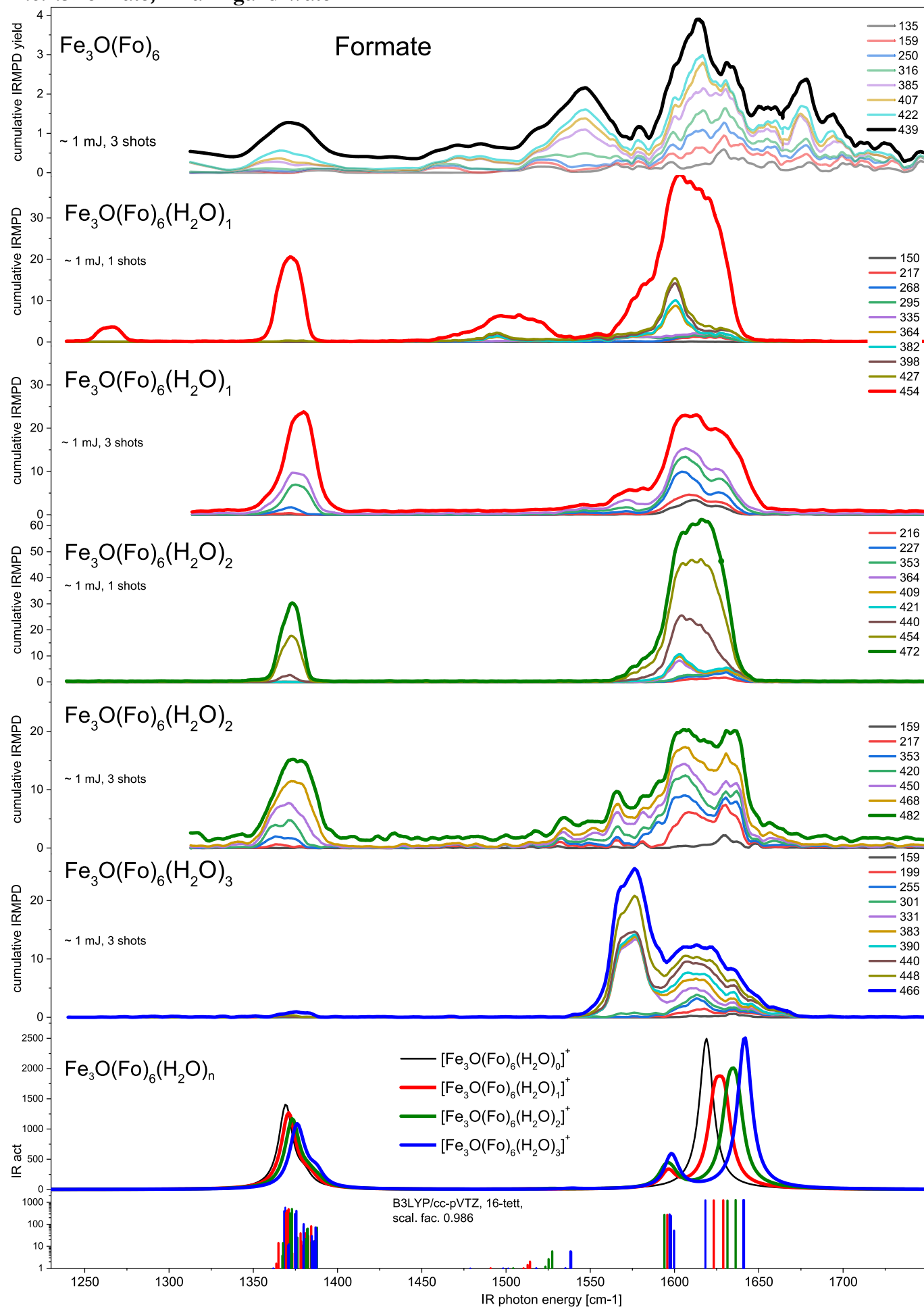


Figure 101 IRMPD spectra of formate $[\text{Fe}_3\text{O}(\text{Fo})_6(\text{H}_2\text{O})_n]^+$ with $n = 1 - 3$ in the CO spectral region. Cumulative fragment trace labels in m/z .

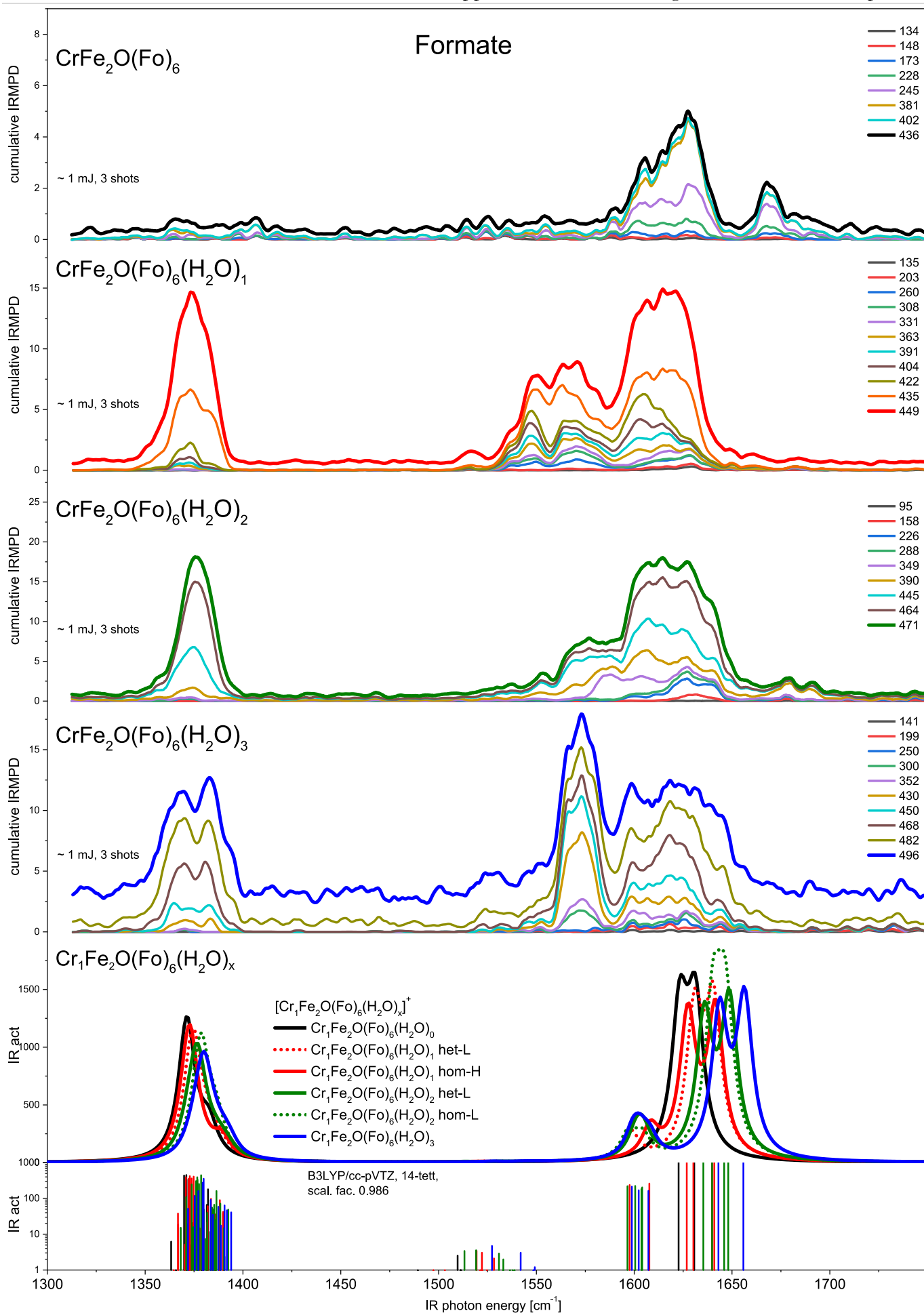


Figure 102 IRMPD spectra of formate $[\text{CrFe}_2\text{O}(\text{Fo})_6(\text{H}_2\text{O})_n]^+$ with $n = 0 - 3$ in the CO spectral region, cumulative fragment trace labels in m/z .

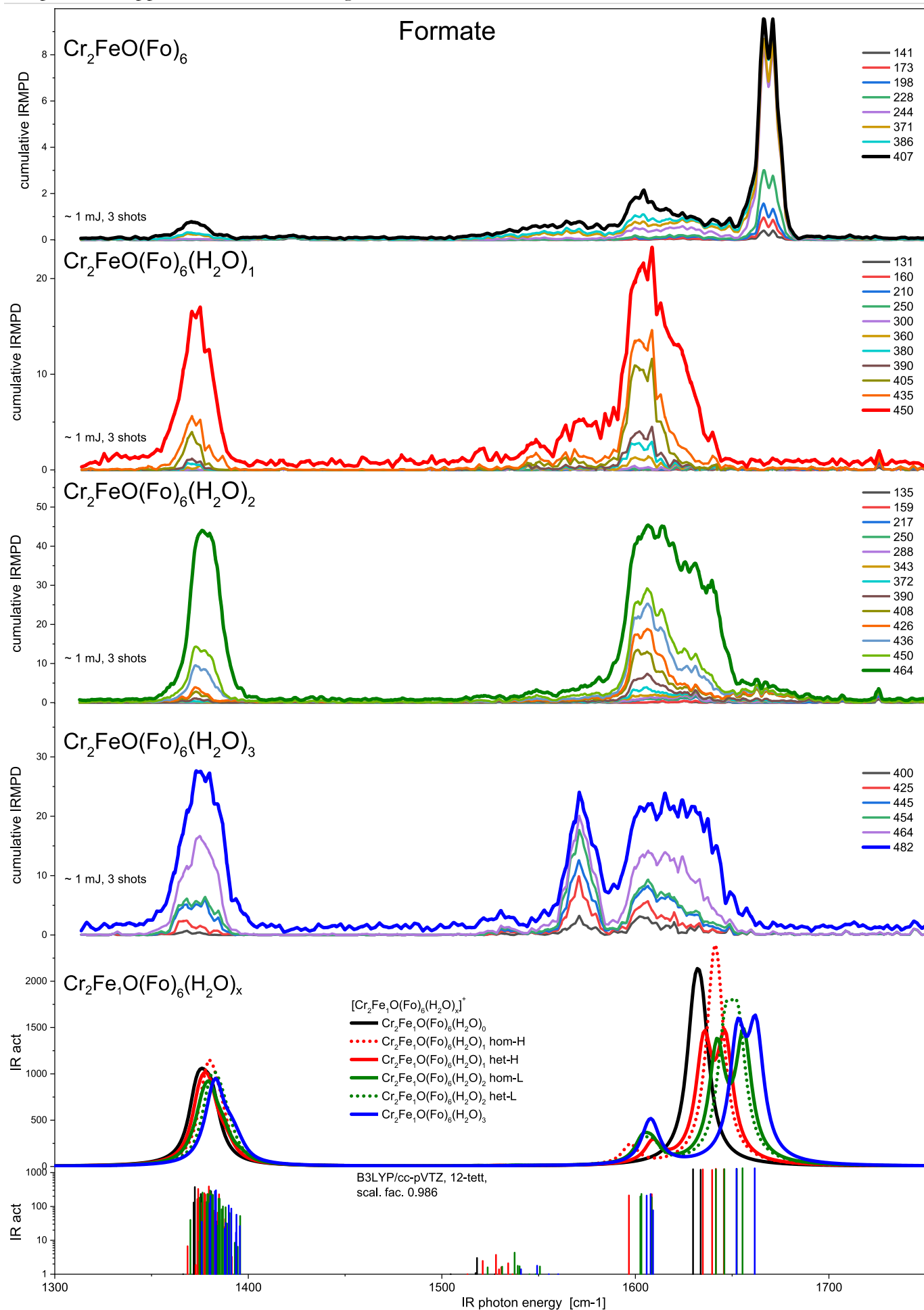


Figure 103 IRMPD spectra of formate $[\text{Cr}_2\text{FeO}(\text{Fo})_6(\text{H}_2\text{O})_n]^+$ with $n = 0 - 3$ in the CO spectral region, cumulative fragment trace labels in m/z .

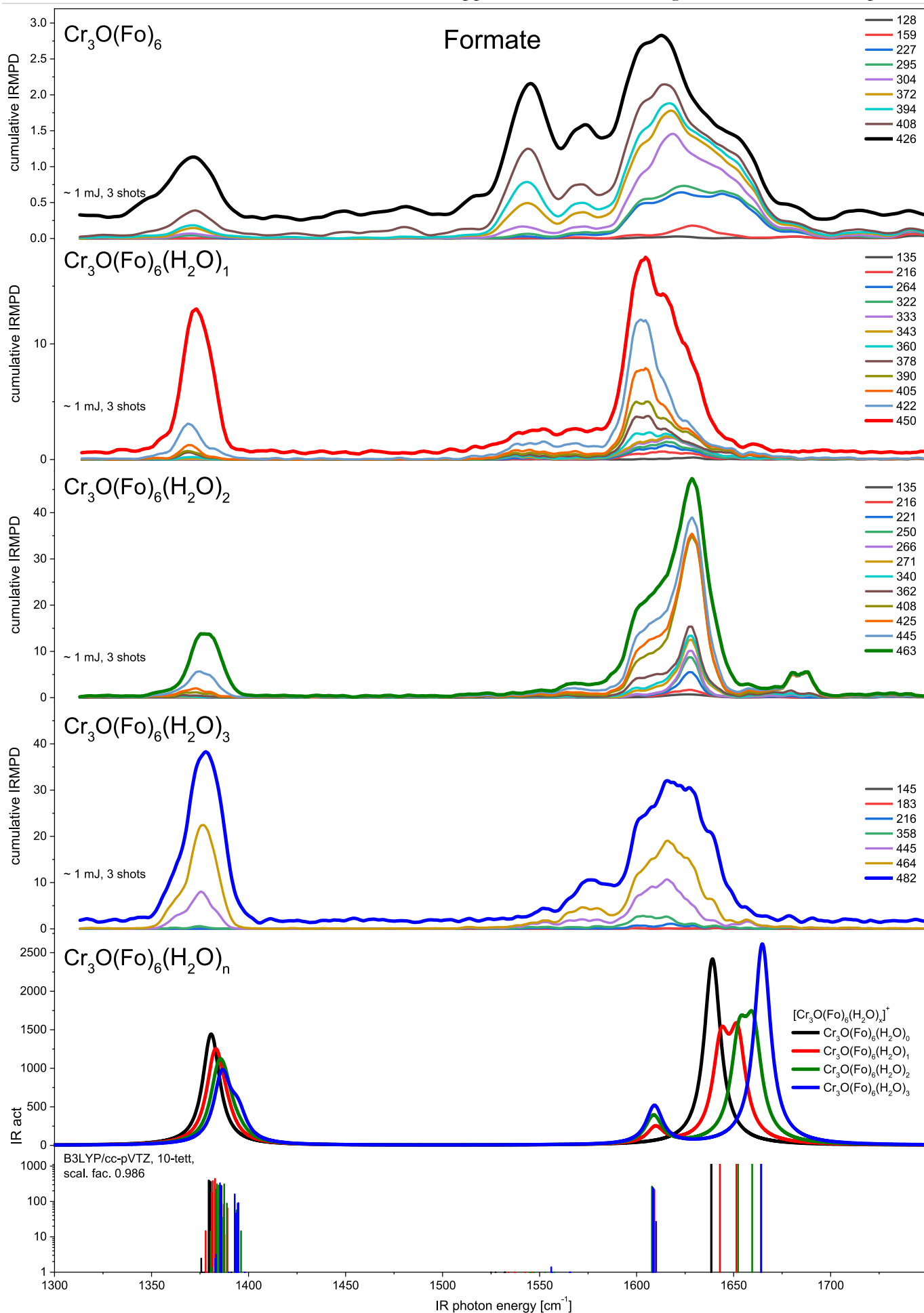


Figure 104 IRMPD spectra of formate $[\text{Cr}_3\text{O}(\text{Fo})_6(\text{H}_2\text{O})_n]^+$ with $n = 0 - 3$ in the CO spectral region, cumulative fragment trace labels in m/z .

11.6.2 Additional IRMPD Spectra of the ScCrFe Acetate and Formate Complexes

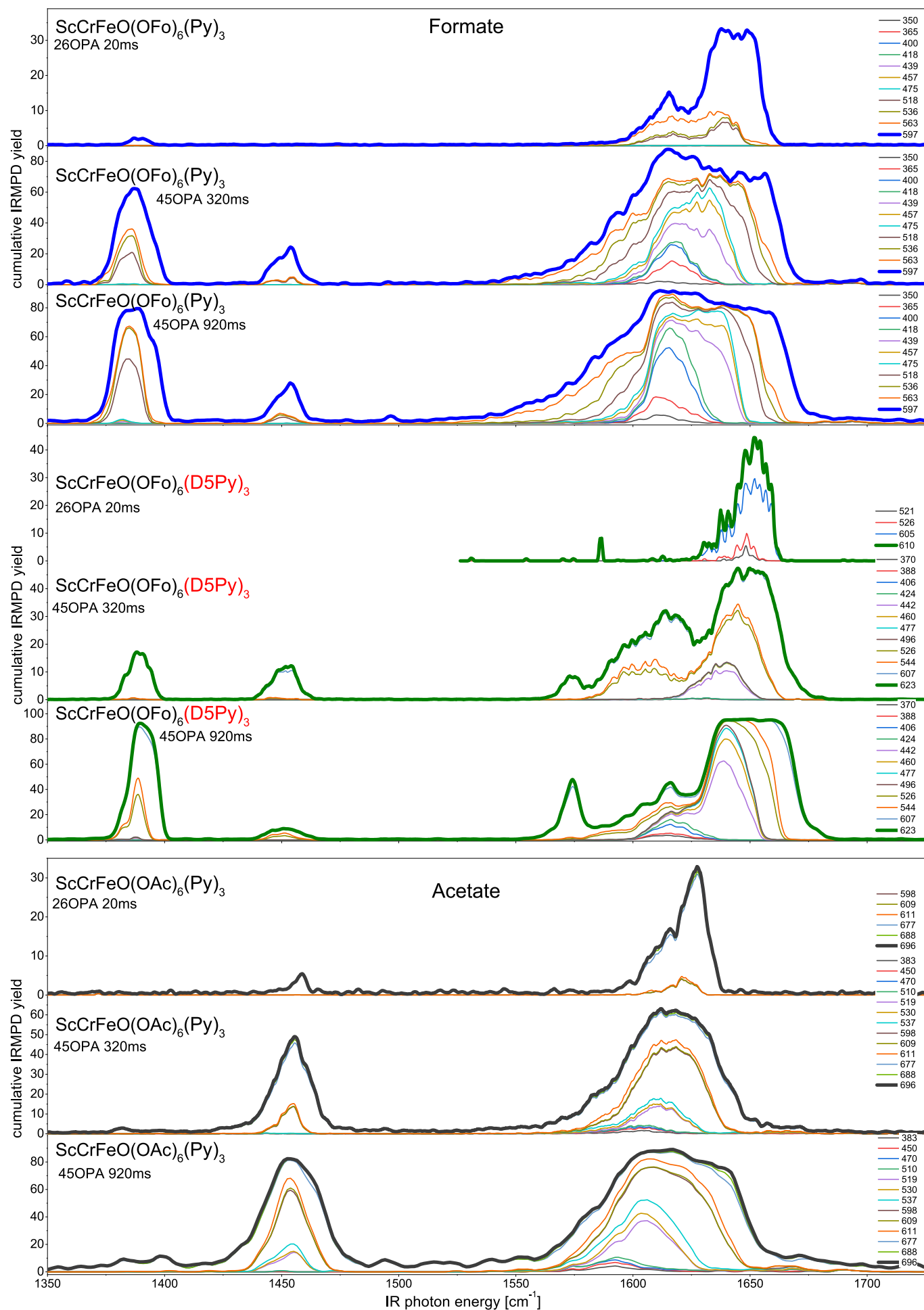


Figure 105 IRMPD spectra of $[\text{ScCrFeO}(\text{B})_6(\text{Py})_3]^+$ (with B = formate and acetate) in the CO spectral region at different laser fluences/shot counts, cumulative fragment trace labels in m/z .

11.7 Gaussian Fits on all Pyridine Spectra

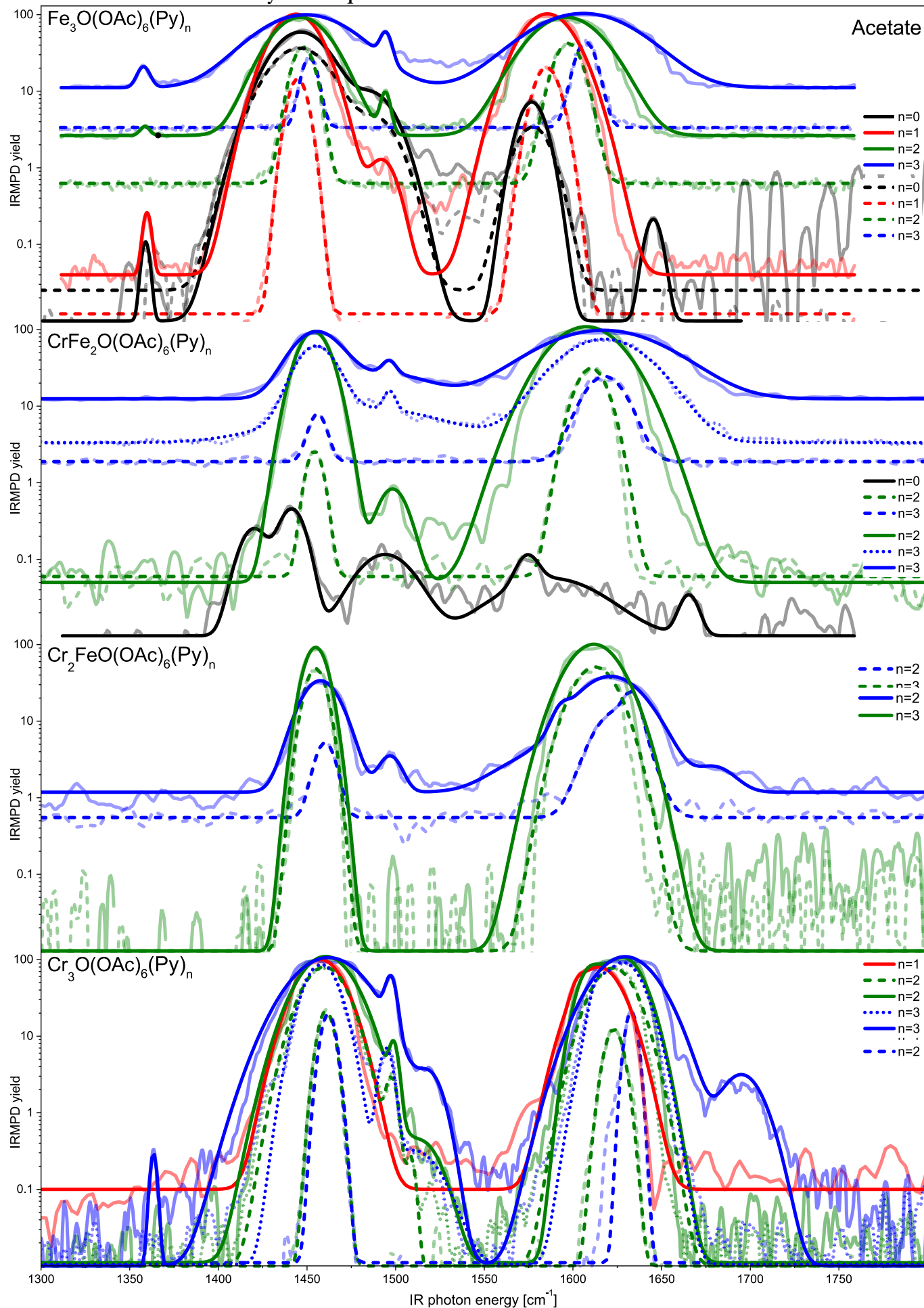


Figure 106 Cumulative sum of all gaussian fits for the acetate species used for the trend discussion in chapter 6.4. An example for the used functions can be seen in **Figure 55**. The original spectra are shown slightly transparent behind the fit curves in the same colors, cumulative fragment trace labels in m/z.

11.8 Additional Tables of IR Band Position and the DMBC Formalism

Table 24 Table of band positions of the symmetric $\nu(\text{COO})_s$ and asymmetric $\nu(\text{COO})_{as}$ carboxylate vibration and the corresponding band splitting $\Delta\nu$ for the Acetate spectra as determined by the gaussian fits shown as their cumulative sum in **Figure 106**, more detail in **Table 31**.

Acetate	$\nu(\text{sym})$	$\nu(\text{sym})$	$\nu(\text{sym})$	$\nu(\text{sym})$
m	0	1	2	3
0	1445.98392	1441.42958		
1	1444.30413			1457.32643
2	1447.01633	1454.05345	1454.867525	1460.36086
3	1450.30309	1455.33141	1458.885825	1460.697217
m	$\nu(\text{asym})$	$\nu(\text{asym})$	$\nu(\text{asym})$	$\nu(\text{asym})$
	0	1	2	3
0	1577.087015	1574.30416		
1	1585.373875			1614.5218
2	1596.67761	1608.90274	1612.1556	1624.6516
3	1606.5914	1617.48703	1623.2316	1630.1494
m	$\Delta\nu$	$\Delta\nu$	$\Delta\nu$	$\Delta\nu$
	0	1	2	3
0	131.10	132.87		
1	141.07			157.20
2	149.66	154.85	157.29	164.29
3	156.29	162.16	164.35	169.45

Table 25 Table of band positions of the symmetric $\nu(\text{COO})_s$ and asymmetric $\nu(\text{COO})_{as}$ carboxylate vibration and the corresponding band splitting $\Delta\nu$ for the formate spectra determined by the gaussian fits shown as their cumulative sum in **Figure 106**, more detail in **Table 30**.

Formate	$\nu(\text{sym})$	$\nu(\text{sym})$	$\nu(\text{sym})$	$\nu(\text{sym})$
m	0	1	2	3
0	1368.58	1373.61	1378.04	1382.60
1	1368.58	1371.83	1377.69	1384.01
2	1371.76	1375.02	1379.21	1386.73
3	1370.19	1379.08	1378.78	1389.90
m	$\nu(\text{asym})$	$\nu(\text{asym})$	$\nu(\text{asym})$	$\nu(\text{asym})$
	0	1	2	3
0	1608.45	1615.78	1628.63	1635.15
1	1604.27	1615.10	1625.16	1638.07
2	1603.08	1617.59	1635.39	1644.33
3	1610.32	1628.94	1631.87	1650.57
m	$\Delta\nu$	$\Delta\nu$	$\Delta\nu$	$\Delta\nu$
	0	1	2	3
0	239.87	242.17	250.60	252.56
1	235.69	243.27	247.47	254.06
2	231.32	242.56	256.18	257.59
3	240.13	249.86	253.10	260.67

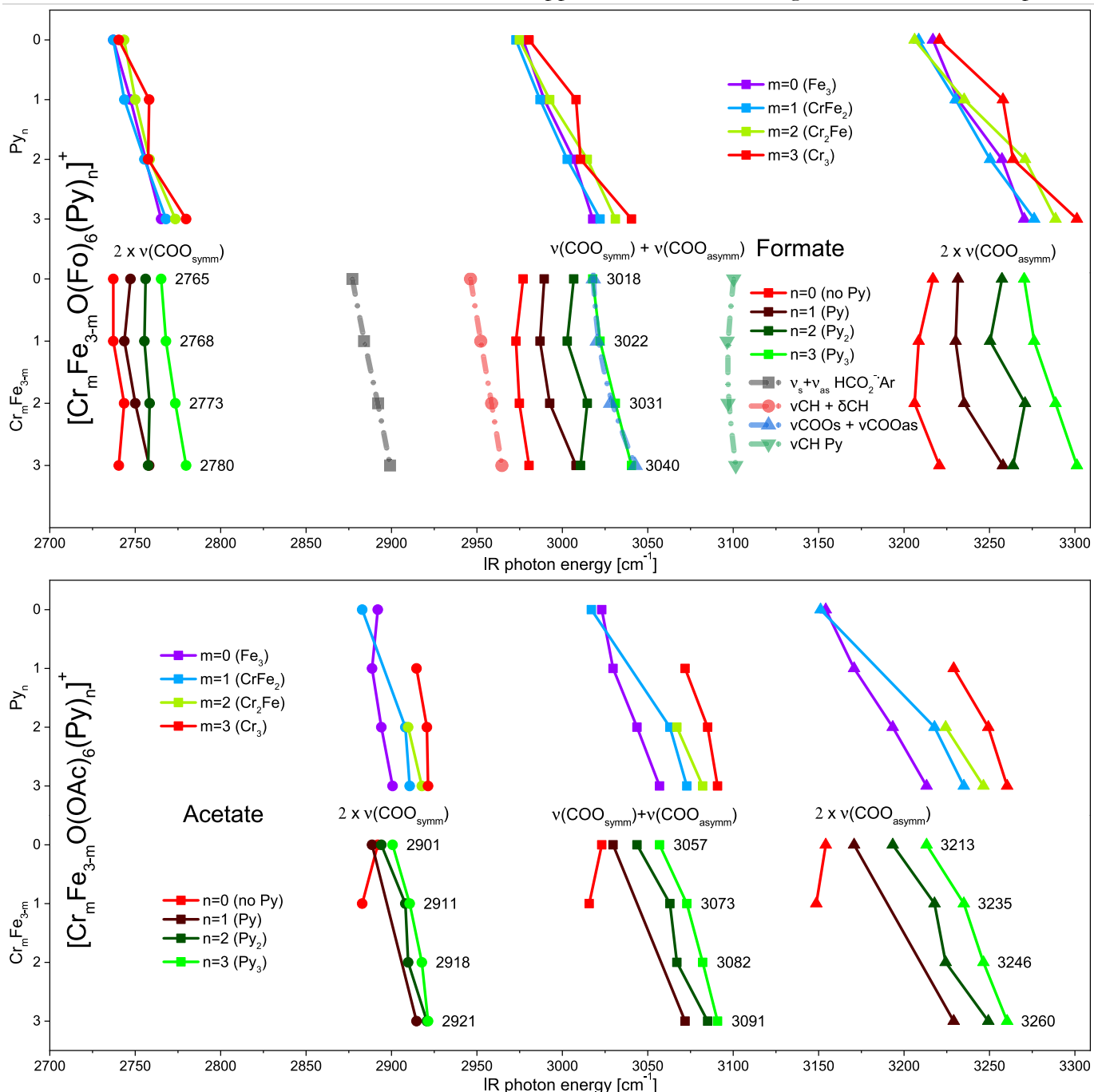


Figure 107 The sum of the symmetric $\nu(\text{COO})_s$ and asymmetric $\nu(\text{COO})_{as}$ carboxylate vibration as well as the double of the symmetric $\nu(\text{COO})_s$ and asymmetric $\nu(\text{COO})_{as}$ vibration mode for both the formate (top graph) as well as the acetate (bottom graph) species. For the formates, the observed values for the fully pyridine coordinated formates are also plotted.

Table 26 Compiled experimental and theoretical fundamental vibrational transitions of formate, partly based on the tables in the literature⁵⁻⁷ but expanded considerably.

			Fundamentals													
			Mode		v CH		v COa		v IP		v COs		v OOP		v OCO b	
			symmetry type		v1	a1	v4	b1	v5	b1	v2	a1	v6	b2	v3	a1
			Isotopomer at CH/CD		H	D	H	D	H	D	H	D	H	D	H	D
			type of motion		C-H stretching		C-O asym stretching		COO rocking		OCO sym stretching		COO rocking		COO deformation	
Method/Source	Author		Species						(C-H δ out-of-plane)				(C-H δ out-of-plane)			
Ne Matrix	Jacox ⁸	[2]	HCO ₂ ⁻		2455.7	1844.6	1628.9	1625	---		1323	1309.1	---		744.1	736.9
Ar Prediss.	Johnson ⁷	[1]	HCO ₂ ⁻		2449	1842	1622	1622	---		1314	1297	---		---	
Theory	Botschwina, Krekeler ⁹	[7]	HCO ₂ ⁻		2441.2	1835.8	1619.1	1616.5	1340.7	988.8	1316.4	1303.7	1030.3	894.4	738	731
H2 Matrix	Yuan Pern Lee ¹⁰	[8]	HSO ₂ ⁻		2875.7				1249.9				1003.2		814.3	
IR	Kidd/Mantsch ¹¹	[9]	Polycrystalline NaHCO ₂		2830.2	2131.2	1607.3	1588.5	1367.2	1013.4	1360.6	1331.3	1068.4	914.9	774.6	766.9
IR	Ito/Bernstein ¹²	[3]	Aqueous KHCO ₂		2803		1585		1383		1351		1069		760	
IR	Hammaker ^{13,14}	[10]	Aqueous NaHCO ₂		2813		1592		1384		1353		---		767	
Raman	Bartholomew ^{15,16}	[11]	Aqueous NaHCO ₂		2819	2113	1597	1587	1381	1025	1350	1324	1063	915	764	759
IR	Mentzen ¹⁷⁻¹⁹	[12]	Crystalline Th(HCOO) ₄ α		2870		1570		1383		1374		1128		771	
IR	Mentzen ¹⁷⁻¹⁹	[12]	Crystalline Th(HCOO) ₄ γ		2875		1570		1370				1065		783	
EELS	Dubois ²⁰	[13]	HCO ₂ ⁻ @ Cu(100) surface		2870		--		1325						760	
EELS	Sexton ^{21,22}	[14]	HCO ₂ ⁻ @ Cu(100) surface		2840		1640				1360				790	
Raman	Spinner ²³⁻²⁵	[15]	Aqueous Na HCO ₂ ⁻		2820	2118	1593	1583	1386	1024	1355	1328	1067	916	771	761
IR	Calatayud ²⁶	[16]	HCO ₂ ⁻ @ β-Ga2O3 surface		2915		1580		1385		1369					
IR	Li ^{27,28}	[17]	HCO ₂ ⁻ @ Ceria (CeO2) surface		2845		1553		1371		1362		995		777	
Raman	Galzerani ²⁹	[18]	LiHCO ₂ *H ₂ O		2859		1585		1371		1355		1068		784	
IR	Liu ³⁰	[19]	Ba(COOH) ₂		2864		1600		1400		1361		1076		768	
IR	Cannon ³¹	[6]	Cr ₃ O(OOCH) ₆ (Py) ₃ ClO ₃		2896		1653		1390		1377		--		770	
Raman	Cannon ³¹	[6]	Cr ₃ O(OOCH) ₆ (H ₂ O)HCO ₂		2898		1644		1390		1374		1040		771	
Raman	Cannon ³¹	[6]	Fe ₃ O(OOCH) ₆ (H ₂ O) ₃ Cl		2882		1620		1394		1369		1066		755	
IR	Cannon ³¹	[6]	Cr ₃ O(OOCH) ₆ (H ₂ O) ₃ Br		2896		1652		1397		1378		1040		773	
IR	Cannon ³¹	[6]	Fe ₃ O(OOCH) ₆ (H ₂ O) ₃ Cl		2953		1635		1394		1369		1052		759	
IR	Kiana ³²	[23]	Fe3O(OOCH)6(H2O)3NO3		2868		1635				1369		1046		755	
IR	Kiana ³²	[23]	Fe3O(OOCH)6(H2O)3OOCH		2881		1635		1399		1371		1053		760	
IR	Kiana ³²	[23]	Cr3O(OOCH)6(H2O)3NO3		2899		1654		1401		1378		1042		765	
IR	Kiana ³²	[23]	Cr3O(OOCH)6(H2O)3OOCH		2894		1653		1396		1378				771	
Raman	Chiupa ³³	[20]	oxoFeFe		2876		1657		1391		1377		1051		788	
IR	Chiupa ³³	[20]	oxoFeFe		2873		1642		1395		1374		1051		786	
IR	Maczka ^{34,35}	[21]	Y(HCOO)		2856		1616		1398		1373		1074		792	
Raman	Moura ³⁶	[22]	CuNi(HCOO)2		2879		1573		1397		1371		1072		766	

Table 27 Compiled list of combination and overtone vibrational transitions of formate, partly based on the tables in in the literature⁵⁻⁷ albeit expanded considerably.

Method/ Source	Author	Ref	Species	Combinations/Overtones											
				v(comb)		assign	v''(comb)		assign	v'''(comb)		assign	ΔvCOO	2v4	vCOsa+ vCHip
Ne Matrix	Jacox ⁸	[2]	HCO ₂ ⁻	n.o.			n.o.						305.9		
Ar Prediss.	Johnson ⁷	[1]	HCO ₂ ⁻	2675	1976	2vH/DIP	1769		2vδOOP	2928	2900	vCOs + vCOa	308		
Theory	Botschwina, Krekeler ⁹	[7]	HCO ₂ ⁻	2677	1976		2050.6	1771	2vδOOP	2923	2906		302.7	2681.4	2959.8
H2 Matrix	Yuan Pern Lee ¹⁰	[8]	HSO ₂ ⁻												1249.9
IR	Kidd/ Mantsch ¹¹	[9]	Polycrystalline NaHCO ₂	2718.3			n.o.			2945				2734.4	2974.5
IR	Ito/ Bernstein ¹²	[3]	Aqueous KHCO ₂	2728		v2+v5	n.o.	2415	v2+v6	2974		v4+v5	234	2766	2968
IR	Hammaker ^{13,14}	[10]	Aqueous NaHCO ₂	n.o.			n.o.						239	2768	2976
Raman	Bartholo- mew ^{15,16}	[11]	Aqueous NaHCO ₂	2733	2028	2vH/DIP	n.o.						247	2762	2978
IR	Mentzen ¹⁷⁻¹⁹	[12]	Crystalline Th(HCOO) ₄ α	2750		2vs(CO)	2930		n.a.	3030		vCOs + vCOa	196	2766	2953
IR	Mentzen ¹⁷⁻¹⁹	[12]	Crystalline Th(HCOO) ₄ γ	2740		n.a.	2960		vCOs + vCOa					2740	2940
EELS	Dubois ²⁰	[13]	HCO ₂ ⁻ @Cu(100) surface				2930		vCOsa+ vCHip					2650	
EELS	Sexton ^{21,22}	[14]	HCO ₂ ⁻ @Cu(100) surface				2910						280		
Raman	Spinner ²³⁻²⁵	[15]	Aqueous Na HCO ₂ ⁻	2732	2030	2vH/DIP	2973	--	vCOsa+ vCHip				238	2772	2979
IR	Calatayud ²⁶	[16]	HCO ₂ ⁻ @ β-Ga2O3 surface				~3000		vCOsa+ vCHip				211	2770	2965
IR	Li ^{27,28}	[17]	HCO ₂ ⁻ @ Ceria (CeO2) surface	2723			2933		vCOsa+ vCHip				191	2742	2924
Raman	Galzerani ²⁹	[18]	LiHCO ₂ *H ₂ O	2751		vs(CO)+vHIP							230	2742	2956
IR	Liu ³⁰	[19]	Ba(COOH) ₂	2746		2vHIP	2912		vCOsa+ vCHip	2976		vCOs + vCOa	239	2800	3000
IR	Cannon ³¹	[6]	Cr ₃ O(OOCH) ₆ (Py) ₃ ClO ₃				2972		n.a.				276	2780	3043
Raman	Cannon ³¹	[6]	Cr ₃ O(OOCH) ₆ (H ₂ O)HCO ₂				2975		n.a.				270	2780	3034
Raman	Cannon ³¹	[6]	Fe ₃ O(OOCH) ₆ (H ₂ O) ₃ Cl				2961		n.a.				251	2788	3014
IR	Cannon ³¹	[6]	Cr ₃ O(OOCH) ₆ (H ₂ O) ₃ Br				2965		n.a.				274	2794	3049
IR	Cannon ³¹	[6]	Fe ₃ O(OOCH) ₆ (H ₂ O) ₃ Cl				2975		n.a.				266	2788	3029
IR	Kiana ³²	[23]	Fe3O(OOCH)6(H2O)3NO3				2950						266		
IR	Kiana ³²	[23]	Fe3O(OOCH)6(H2O)3NO3				2955						264		
IR	Kiana ³²	[23]	Cr3O(OOCH)6(H2O)3NO3				2963						276		
IR	Kiana ³²	[23]	Cr3O(OOCH)6(H2O)3OOCH										275		
Raman	Chiupa ³³	[20]	oxoFeFe	2773			2970			3036			280		
IR	Chiupa ³³	[20]	oxoFeFe	2772			2959						268		
IR	Maczka ^{34,35}	[21]	Y(HCOO)	2780			2926			2964			243		
Raman	Moura ³⁶	[22]	CuNi(HCOO)2	2740			2904			2976			202		

Table 28 Literature references for the formate band positions referenced in **Figure 58**.

Formate	Source	Method	$\nu(\text{COO})_s$	$\nu(\text{COO})_{as}$	$\Delta\nu$
HCOO-	Geradi 2011 ⁷	Gas Ar tag PF	1314	1622	308
HCOO-	Jacox 2003 ⁸	Ne matrix IR	1323	1629	306
HCOONa	Ito 1956 ¹²	IR	1349	1567	218
HCOONa	Newman 1952 ³⁷	IR polarized	1365	1620	255
HCOONa	Fonteyne 1943 ³⁸	Raman	1386	1584	198
Cr3 HCOO Py3 ClO4-	Cannon 1981 ³⁹	IR	1377	1635	258
Cr3 HCOO Aq3 Cl-	Cannon 1981 ³⁹	IR	1367	1639	272
Fe3 HCOO Aq3 Cl-	Cannon 1981 ³⁹	IR	1369	1635	266

Table 29 Literature references for the acetate band positions referenced in **Figure 58**.

Acetate	Source	Method	$\nu(\text{COO})_s$	$\nu(\text{COO})_{as}$	$\Delta\nu$
Fe3 F3CCOO	Puri 1984 ⁴⁰	IR	1440	1625	185
Cr3 F3CCOO	Puri 1984 ⁴⁰	IR	1435	1650	215
Mn3 F3CCOO	Puri 1984 ⁴⁰	IR	1450	1660	210
CH3COONa	Kotov 1968 ⁴¹	IR	1443	1578	135
CH3COONa	Deacon 1980 ⁴²	IR	1414	1578	164
CH3COO- aq	Rudolph 2014 ⁴³	IR aq + Raman	1413	1556	142
Br3CCOO-	Rudolph 2011 ⁴⁴	IR aq + Raman	1332	1651	319
CH3COO- aq	Ito 1956 ¹²	IR aq	1413	1556	143
Cr3 H3CCOO Py3 Cl-	Cannon 1981 ³⁹	IR liq. N2	1455	1610	155
Cr3 H3CCOO Aq3 Cl-	Cannon 1981 ³⁹	IR liq. N2	1454	1610	156
Fe3 H3CCOO Py3 NO3	Cannon 1981 ³⁹	IR liq. N2	1440	1590	150
Fe3 H3CCOO Aq3 NO3	Cannon 1981 ³⁹	IR liq. N2	1444	1585	141
Fe3 H3CCOO Py3 NO3	Fernandes 1996 ⁴⁵	IR	1450	1600	150
Fe3 H3CCOO Aq3 NO3	Fernandes 1996 ⁴⁵	IR	1430	1580	150
Fe3 H3CCOO Py3 FeBr4	Amani 2012 ⁴⁶	IR	1443	1601	158
Fe3 H3CCOO Aq3 Cl	Amani 2012 ⁴⁶	IR	1445	1592	147

Table 30 Table of band positions of the symmetric $\nu(\text{COO})_s$ and asymmetric $\nu(\text{COO})_{as}$ carboxylate vibration, the corresponding band splitting $\Delta\nu$, the $\delta(\text{Py-CH})$, hot bands and combination bands for the formate spectra, as determined by the gaussian fits shown as their cumulative sum in **Figure 106**.

Formate (n;m)	$\nu(\text{COO})_s$	$\nu(\text{COO})_{as}$	$\nu(\text{COO})_{as}-\nu(\text{COO})_s$	$\nu(\text{COO})_{as}+\nu(\text{COO})_s$	$\delta(\text{Py-CH})$	ν'	ν^*	$\nu^\#$	$\nu^\#\prime$	$\nu\sim$
0;0	1368.58	1608.45	239.87	2977.03		1480.84	1546.41	1623.99	1676.11	
0;1	1373.61	1615.78	242.17	2989.39	1602.40		1510.15	1682.67		
0;2	1378.04	1628.63	250.60	3006.67	1610.56		1590.00	1687.72		
0;3	1382.60	1635.15	252.56	3017.75	1610.19		1577.00	1699.32		
1;0	1368.58	1604.27	235.69	2972.85		1403.66	1574.27	1625.52	1669.67	
1;1	1371.83	1615.10	243.27	2986.92	1602.74	1414.21	1537.61	1655.84		1338.0628
1;2	1377.69	1625.16	247.47	3002.86						
1;3	1384.01	1638.07	254.06	3022.08	1612.42					
2;0	1371.76	1603.08	231.32	2974.83		1421.90	1558.22	1668.70		1624.5559
2;1	1375.02	1617.59	242.56	2992.61	1617.59	1400.00	1523.61	1678.15		1345
2;2	1379.21	1635.39	256.18	3014.59	1617.81					
2;3	1386.73	1644.33	257.59	3031.06	1613.15	1452.28				1494.14
3;0	1370.19	1610.32	240.13	2980.51			1546.07	1654.07		
3;1	1379.08	1628.94	249.86	3008.02	1608.88		1555.77	1676.30		
3;2	1378.78	1631.87	253.10	3010.65	1610.73			1677.90		
3;3	1389.90	1650.57	260.67	3040.47	1615.47		1615.47	1679.00		1451.00

Table 31 Table of band positions of the symmetric $\nu(\text{COO})_s$ and asymmetric $\nu(\text{COO})_{as}$ carboxylate vibration, the corresponding band splitting $\Delta\nu$ and the $\delta(\text{CH}_3)$ band for the Acetate spectra as determined by the gaussian fits shown as their cumulative sum in **Figure 106**.

m	Acetate (m;n)	laser energy	$\nu(\text{COO})_s$	$\nu(\text{COO})_a$	$\Delta\nu(\text{COO})_{as-s}$	$\delta(\text{CH}_3)_{as}$	$\delta(\text{CH}_3)_s$	ν'	ν''	ν'''
0	0;0	low	1445.60	1577.38	131.78	1489.26				
0	0;1	low	1444.80	1585.19	140.39					
0	0;2	low	1447.85	1597.22	149.36					
0	0;3	low	1451.43	1607.20	155.78					
0	0;0	high	1446.37	1576.80	130.43	1487.44	1358.95			1645.33
0	0;1	high	1443.81	1585.56	141.75	1492.29	1359.77			
0	0;2	high	1446.18	1596.14	149.96	1494.25	1358.62			
0	0;3	high	1449.18	1605.98	156.80	1494.41	1357.67			
1	1;0	med	1441.43	1574.30	132.87	1494.05		1420.02	1587.22	1665.39
1	1;2	low	1454.26	1610.28	156.02					
1	1;3	low	1455.93	1617.81	161.88					
1	1;2	high	1453.85	1607.53	153.68	1499.05				
1	1;3	med	1454.97	1617.70	162.73	1496.60				
1	1;3	high	1455.09	1616.95	161.86	1496.25				
2	2;2	low	1454.87	1612.47	157.60					
2	2;3	low	1460.20	1625.07	164.87					1633.37
2	2;2	high	1454.87	1611.85	156.98					
2	2;3	high	1457.57	1621.39	163.82	1496.86		1578.53	1593.30	1680.00
3	3;1	med	1457.33	1614.52	157.20				1602.97	
3	3;2	low	1460.75	1623.13	162.39					
3	3;3	low	1462.00	1632.88	170.87					
3	3;2	med	1459.77	1622.62	162.85	1497.66		1508.49		
3	3;3	med	1458.06	1628.13	170.07	1494.66		1510.00	1613.74	
3	3;2	high	1460.57	1628.20	167.64	1498.90		1514.31	1609.23	
3	3;3	high	1462.03	1629.44	167.41	1497.26	1363.42	1519.11		1695.10

Table 32 Table of averaged band positions for the different shot counts and laser power settings of the symmetric $\nu(\text{COO})_s$ and asymmetric $\nu(\text{COO})_{as}$ carboxylate vibration, the corresponding band splitting $\Delta\nu$ and the $\delta(\text{CH}_3)$ band for the Acetate spectra as determined by the gaussian fits shown as their cumulative sum in **Figure 106**.

m	Acetate	$\nu(\text{COO})_s$	$\nu(\text{COO})_{as}$	$\nu(\text{COO})_{as}-\nu(\text{COO})_s$	$\nu(\text{COO})_{as}+\nu(\text{COO})_s$	$\delta(\text{CH}_3)$
0	0;0	1445.98	1577.09	131.10	3023.07	1488.35
0	0;1	1444.30	1585.37	141.07	3029.68	1492.29
0	0;2	1447.02	1596.68	149.66	3043.69	1494.25
0	0;3	1450.30	1606.59	156.29	3056.89	1494.41
1	1;0	1441.43	1575.55	131.65	3016.98	1490.75
1	1;1					
1	1;2	1454.05	1608.90	154.85	3062.96	1499.05
1	1;3	1455.33	1617.49	162.16	3072.82	1496.42
2	2;0					
2	2;1					
2	2;2	1454.87	1612.16	157.29	3067.02	
2	2;3	1458.89	1623.23	164.35	3082.12	
3	3;0					
3	3;1	1457.33	1614.52	157.20	3071.85	
3	3;2	1460.36	1624.65	164.29	3085.01	1498.28
3	3;3	1460.70	1630.15	169.45	3090.85	1495.96

Table 33 Application of the DMBC formalism on the band splitting band splitting $\Delta\nu$ of the symmetric $\nu(\text{COO})_s$ and asymmetric $\nu(\text{COO})_{as}$ carboxylate vibration for successive Fe to Cr substitution or Py ligand coordination.

Differential many body cooperativity IRMPD Formate , Fe \rightarrow Cr							
		Cr _x /Fe _x no Py			cm ⁻¹		
x=M, y=M'	Property	Wavenumber		P1(1)	P2(1)	P3(1)	dP(1)
M=Fe, M'=Cr		cm ⁻¹	cm ⁻¹	2.30	2.30	2.30	6.90
Fe, Fe, Fe	xxx	239.86687000	239.86687000				
Cr, Fe, Fe	yxx	242.16578000		P12(2)	P13(2)	P23(2)	dP(2)
Fe, Cr, Fe	yx	242.16578000	242.16578000	6.13	6.13	6.13	18.40
Fe, Fe, Cr	xy	242.16578000					
Cr, Cr, Fe	yyx	250.59741000					dP(3)
Cr, Fe, Cr	xy	250.59741000	250.59741000				-12.60
Fe, Cr, Cr	xy	250.59741000					
Cr, Cr, Cr	yyy	252.55755000	252.55755000				

Differential many body cooperativity IRMPD Formate , Fe \rightarrow Cr							
		Cr _x /Fe _x Py ₃			cm ⁻¹		
x=M, y=M'	Property	Wavenumber		P1(1)	P2(1)	P3(1)	dP(1)
M=Fe, M'=Cr		cm ⁻¹	cm ⁻¹	9.73	9.73	9.73	29.19
Fe, Fe, Fe	xxx	240.12970000	240.12970000				
Cr, Fe, Fe	yxx	249.85960000		P12(2)	P13(2)	P23(2)	dP(2)
Fe, Cr, Fe	yx	249.85960000	249.85960000	-6.49	-6.49	-6.49	-19.48
Fe, Fe, Cr	xy	249.85960000					
Cr, Cr, Fe	yyx	253.09728000					dP(3)
Cr, Fe, Cr	xy	253.09728000	253.09728000				10.83
Fe, Cr, Cr	xy	253.09728000					
Cr, Cr, Cr	yyy	260.67246000	260.67246000				

Differential many body cooperativity IRMPD Acetate , Fe \rightarrow Cr							
		Cr _x /Fe _x Py ₃			cm ⁻¹		
x=M, y=M'	Property	Wavenumber		P1(1)	P2(1)	P3(1)	dP(1)
M=Fe, M'=Cr		cm ⁻¹	cm ⁻¹	5.87	5.87	5.87	17.60
Fe, Fe, Fe	xxx	156.28831000	156.28831000				
Cr, Fe, Fe	yxx	162.15562000		P12(2)	P13(2)	P23(2)	dP(2)
Fe, Cr, Fe	yx	162.15562000	162.15562000	-3.68	-3.68	-3.68	-11.03
Fe, Fe, Cr	xy	162.15562000					
Cr, Cr, Fe	yyx	164.34577500					dP(3)
Cr, Fe, Cr	xy	164.34577500	164.34577500				6.59
Fe, Cr, Cr	xy	164.34577500					
Cr, Cr, Cr	yyy	169.45218667	169.45218667				

Differential many body cooperativity IRMPD Acetate , Fe ₃ no Py \rightarrow 3Py							
		Fe ₃ Py _{0.3}			cm ⁻¹		
x=M, y=M'	Property	Wavenumber		P1(1)	P2(1)	P3(1)	dP(1)
M=Fe, M'=Cr		cm ⁻¹	cm ⁻¹	9.97	9.97	9.97	29.90
Fe, Fe, Fe	xxx	131.10310000	131.10310000				
Cr, Fe, Fe	yxx	141.06974500		P12(2)	P13(2)	P23(2)	dP(2)
Fe, Cr, Fe	yx	141.06974500	141.06974500	-1.38	-1.38	-1.38	-4.13
Fe, Fe, Cr	xy	141.06974500					
Cr, Cr, Fe	yyx	149.66128000					dP(3)
Cr, Fe, Cr	xy	149.66128000	149.66128000				-0.59
Fe, Cr, Cr	xy	149.66128000					
Cr, Cr, Cr	yyy	156.28831000	156.28831000				

Differential many body cooperativity IRMPD Formate , Fe ₃ no Py \rightarrow 3Py							
		Fe ₃ Py _{0.3}			cm ⁻¹		
x=M, y=M'	Property	Wavenumber		P1(1)	P2(1)	P3(1)	dP(1)
M=Fe, M'=Cr		cm ⁻¹	cm ⁻¹	-4.17	-4.17	-4.17	-12.52
Fe, Fe, Fe	xxx	239.86687000	239.86687000				
Cr, Fe, Fe	yxx	235.69342000		P12(2)	P13(2)	P23(2)	dP(2)
Fe, Cr, Fe	yx	235.69342000	235.69342000	-0.20	-0.20	-0.20	-0.60
Fe, Fe, Cr	xy	235.69342000					
Cr, Cr, Fe	yyx	231.32163000					dP(3)
Cr, Fe, Cr	xy	231.32163000	231.32163000				13.38
Fe, Cr, Cr	xy	231.32163000					
Cr, Cr, Cr	yyy	240.12970000	240.12970000				

Table 34 Application of the DMBC formalism on the band splitting band splitting $\Delta\nu$ of the symmetric $\nu(\text{COO})_s$ and asymmetric $\nu(\text{COO})_{as}$ carboxylate vibration for successive Cr to Fe substitution or Py ligand removal.

Differential many body cooperativity IRMPD Formate , Cr \rightarrow Fe							
		Cr _x /Fe _x no Py			cm ⁻¹		
x=Fe, y=Cr	Property	Wavenumber		P1(1)	P2(1)	P3(1)	dP(1)
M=Fe, M'=Cr		cm ⁻¹	cm ⁻¹	-1.96	-1.96	-1.96	-5.88
Cr, Cr, Cr	yyy	252.55755000	252.55755000				
Fe, Cr, Cr	xyy	250.59741000		P12(2)	P13(2)	P23(2)	dP(2)
Cr, Fe, Cr	yxy	250.59741000	250.59741000	-6.47	-6.47	-6.47	-19.41
Cr, Cr, Fe	yyx	250.59741000					
Fe, Fe, Cr	xxy	242.16578000					dP(3)
Fe, Cr, Fe	xyx	242.16578000	242.16578000				12.60
Cr, Fe, Fe	yxx	242.16578000					
Fe, Fe, Fe	xxx	239.86687000	239.86687000				

Differential many body cooperativity IRMPD Formate , Cr \rightarrow Fe							
		Cr _x /Fe _x Py ₃			cm ⁻¹		
x=Fe, y=Cr	Property	Wavenumber		P1(1)	P2(1)	P3(1)	dP(1)
M=Fe, M'=Cr		cm ⁻¹	cm ⁻¹	-7.58	-7.58	-7.58	-22.73
Cr, Cr, Cr	yyy	260.67246000	260.67246000				
Fe, Cr, Cr	xyy	253.09728000		P12(2)	P13(2)	P23(2)	dP(2)
Cr, Fe, Cr	yxy	253.09728000	253.09728000	4.34	4.34	4.34	13.01
Cr, Cr, Fe	yyx	253.09728000					
Fe, Fe, Cr	xxy	249.85960000					dP(3)
Fe, Cr, Fe	xyx	249.85960000	249.85960000				-10.83
Cr, Fe, Fe	yxx	249.85960000					
Fe, Fe, Fe	xxx	240.12970000	240.12970000				

Differential many body cooperativity IRMPD Acetate , Cr \rightarrow Fe							
		Cr _x /Fe _x Py ₃			cm ⁻¹		
x=Fe, y=Cr	Property	Wavenumber		P1(1)	P2(1)	P3(1)	dP(1)
M=Fe, M'=Cr		cm ⁻¹	cm ⁻¹	-5.11	-5.11	-5.11	-15.32
Cr, Cr, Cr	yyy	169.45218667	169.45218667				
Fe, Cr, Cr	xyy	164.34577500		P12(2)	P13(2)	P23(2)	dP(2)
Cr, Fe, Cr	yxy	164.34577500	164.34577500	2.92	2.92	2.92	8.75
Cr, Cr, Fe	yyx	164.34577500					
Fe, Fe, Cr	xxy	162.15562000					dP(3)
Fe, Cr, Fe	xyx	162.15562000	162.15562000				-6.59
Cr, Fe, Fe	yxx	162.15562000					
Fe, Fe, Fe	xxx	156.28831000	156.28831000				

Differential many body cooperativity IRMPD Acetate , Fe ₃ 3 Py \rightarrow no Py							
		Cr _x /Fe _x Acetate Py ₃			cm ⁻¹		
x=Fe, y=Cr	Property	Wavenumber		P1(1)	P2(1)	P3(1)	dP(1)
M=Fe, M'=Cr		cm ⁻¹	cm ⁻¹	-6.63	-6.63	-6.63	-19.88
Cr, Cr, Cr	yyy	156.28831000	156.28831000				
Fe, Cr, Cr	xyy	149.66128000		P12(2)	P13(2)	P23(2)	dP(2)
Cr, Fe, Cr	yxy	149.66128000	149.66128000	-1.96	-1.96	-1.96	-5.89
Cr, Cr, Fe	yyx	149.66128000					
Fe, Fe, Cr	xxy	141.06974500					dP(3)
Fe, Cr, Fe	xyx	141.06974500	141.06974500				0.59
Cr, Fe, Fe	yxx	141.06974500					
Fe, Fe, Fe	xxx	131.10310000	131.10310000				

Differential many body cooperativity IRMPD Formate , Fe ₃ 3 Py \rightarrow no Py							
		Cr _x /Fe _x Acetate Py ₃			cm ⁻¹		
x=Fe, y=Cr	Property	Wavenumber		P1(1)	P2(1)	P3(1)	dP(1)
M=Fe, M'=Cr		cm ⁻¹	cm ⁻¹	-8.81	-8.81	-8.81	-26.42
Cr, Cr, Cr	yyy	240.12970000	240.12970000				
Fe, Cr, Cr	xyy	231.32163000		P12(2)	P13(2)	P23(2)	dP(2)
Cr, Fe, Cr	yxy	231.32163000	231.32163000	13.18	13.18	13.18	39.54
Cr, Cr, Fe	yyx	231.32163000					
Fe, Fe, Cr	xxy	235.69342000					dP(3)
Fe, Cr, Fe	xyx	235.69342000	235.69342000				-13.38
Cr, Fe, Fe	yxx	235.69342000					
Fe, Fe, Fe	xxx	239.86687000	239.86687000				

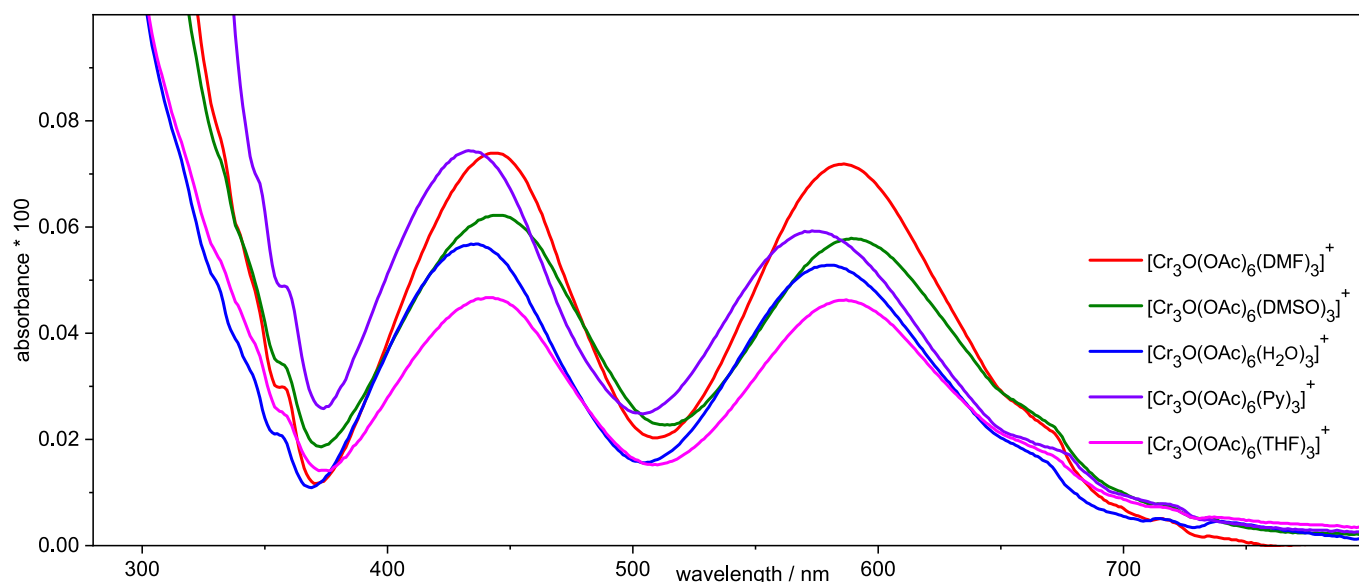
11.9 UV VIS-, ATR Spectra of several $\text{Cr}_3\text{O}(\text{OAc})_6\text{L}_3$ Complexes

Figure 108 UV VIS transmission spectra of $[\text{Cr}_3\text{O}(\text{OAc})_6(\text{L})_3]^+$ salt in different solvents, DMF, DMSO, water, pyridine and THF, as reference to the spectra reported by Blake et al.⁴⁷⁻⁴⁹.

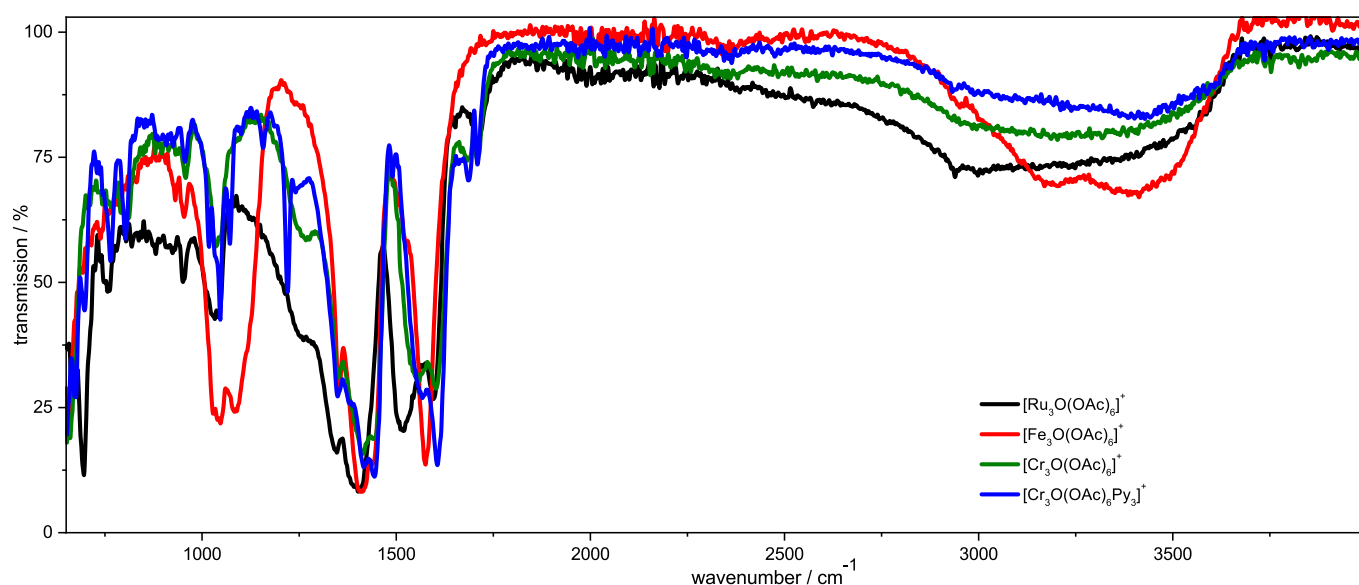


Figure 109 ATR spectra of different M_3O acetate species.

11.10 References for the Appendix B

1. Krüger, J. S. Regioselective fragmentation of trimeric iron and chromium carboxylates. (TU Kaiserslautern, 2018).
2. Sherrill, C. Counterpoise Correction and Basis Set Superposition Error. *Vergil.Chemistry.Gatech.Edu* 1-5 (2010). Available at: <http://vergil.chemistry.gatech.edu/notes/cp.pdf>.
3. Buldakov, M. A., Cherepanov, V. N., Kalugina, Y. N., Zvereva-Loëte, N. & Boudon, V. Static polarizability surfaces of the van der Waals complex $\text{CH}_4\text{-N}_2$. *The Journal of Chemical Physics* **132**, 164304 (2010).
4. Kalugina, Y. N., Cherepanov, V. N., Buldakov, M. A., Zvereva-Loëte, N. & Boudon, V. Theoretical investigation of the potential energy surface of the van der Waals complex $\text{CH}_4\text{-N}_2$. *The Journal of Chemical Physics* **131**, 134304 (2009).
5. Gerardi, H. K. *et al.* Supporting information to “Unraveling the Anomalous Solvatochromic Response of the Formate Ion Vibrational Spectrum: An Infrared, Ar-Tagging Study of the HCO_2^- , DCO_2^- , and $\text{HCO}_2^- \cdot \text{H}_2\text{O}$ Ions.” *The Journal of Physical Chemistry Letters* **2**, 2437-2441 (2011).
6. Ito, K. & Bernstein, H. J. The vibrational spectra of the formate, acetate and oxalate ions. *Canadian Journal of*

- Chemistry* **34**, 170-178 (1956).
7. Gerardi, H. K. *et al.* Unraveling the Anomalous Solvatochromic Response of the Formate Ion Vibrational Spectrum: An Infrared, Ar-Tagging Study of the HCO_2^- , DCO_2^- , and $\text{HCO}_2^- \cdot \text{H}_2\text{O}$ Ions. *The Journal of Physical Chemistry Letters* **2**, 2437-2441 (2011).
 8. Forney, D., Jacox, M. E. & Thompson, W. E. Infrared spectra of trans -HOCO, HCOOH^+ , and HCO_2^- trapped in solid neon. *The Journal of Chemical Physics* **119**, 10814-10823 (2003).
 9. Krekeler, C., Mladenovic, M. & Botschwina, P. A theoretical investigation of the vibrational states of HCO_2^- and its isotopomers. *Physical Chemistry Chemical Physics* **7**, 882 (2005).
 10. Tsuge, M. & Lee, Y.-P. Infrared spectra of HSCS^+ , c-HSCS, and HCS_2^- produced on electron bombardment of CS_2 in solid para-hydrogen. *Physical Chemistry Chemical Physics* **19**, 9641-9653 (2017).
 11. Kidd, K. G. & Mantsch, H. H. Formate anion: The physical force field. *Journal of Molecular Spectroscopy* **85**, 375-389 (1981).
 12. Ito, K. & Bernstein, H. J. The vibrational spectra of the formate, acetate, and oxalate ions. *Canadian Journal of Chemistry* **34**, 170-178 (1956).
 13. Hammaker, R. M. & Walters, J. P. The infrared spectra of C-13 enriched sodium formate. *Spectrochimica Acta* **20**, 1311-1317 (1964).
 14. Rook, S. L. & Hammaker, R. M. Correlation of the C-H stretching frequency and ^{13}C -H coupling constant for substituted aldehydes. *Spectrochimica Acta Part A: Molecular Spectroscopy* **27**, 1899-1907 (1971).
 15. Bartholomew, R. J. & Irish, D. E. Raman spectral studies of solutions at elevated temperatures and pressures. 13. Sodium formate – water. *Canadian Journal of Chemistry* **71**, 1728-1733 (1993).
 16. Bartholomew, R. J., Stevenson, W. J. & Irish, D. E. A Raman spectral study of the kinetics of deuterium-hydrogen exchange on the formate anion at elevated temperatures and pressures. *Spectrochimica Acta Part A: Molecular and Biomolecular Spectroscopy* **52**, 1695-1701 (1996).
 17. Mentzen, B. F. & Comel, C. Study of the polymorphism of strontium and calcium formates by infrared spectroscopy. *Spectrochimica Acta Part A: Molecular Spectroscopy* **30**, 1263-1270 (1974).
 18. Mentzen, B. F. The infrared absorption of crystalline thorium tetraformates. I. Characterization of thorium tetraformates in the solid state by infrared spectroscopy. *Journal of Solid State Chemistry* **3**, 12-19 (1971).
 19. Bagnall, K. W. Thorium Formiate. in *Gmelin Handbook of Inorganic Chemistry* (ed. Fluck, E.) 37-40 doi:10.1007/978-3-662-08315-6
 20. Dubois, L. H., Ellis, T. H., Zegarski, B. R. & Kevan, S. D. New insights into the kinetics of formic acid decomposition on copper surfaces. *Surface Science* **172**, 385-397 (1986).
 21. Sexton, B. A. Observation of formate species on a copper (100) surface by high resolution electron energy loss spectroscopy. *Surface Science* **88**, 319-330 (1979).
 22. Sexton, B. A. Summary Abstract: Vibrational spectra of formate and acetate species on copper (100). *Journal of Vacuum Science and Technology* **17**, 141-142 (1980).
 23. Spinner, E. Further Studies of Depolarization Ratios in the Raman Spectrum of Aqueous Formate Ion. *Australian Journal of Chemistry* **38**, 47 (1985).
 24. Spinner, E. The effect of disc pressing on the infrared spectrum of potassium formate. Two modifications of HCO_2K and DCO_2K . *Spectrochimica Acta Part A: Molecular Spectroscopy* **31**, 1545-1546 (1975).
 25. Spinner, E. Vibration-spectral studies of carboxylate ions. Part III. Sodium formate, HCO_2Na and DCO_2Na ; Raman-spectral depolarisation ratios in aqueous solution, and band splitting in the solid-state infrared spectrum. *Journal of the Chemical Society B: Physical Organic* 879 (1967). doi:10.1039/j29670000879
 26. Calatayud, M., Collins, S. E., Baltanás, M. A. & Bonivardi, A. L. Stability of formate species on $\beta\text{-Ga}_2\text{O}_3$. *Physical Chemistry Chemical Physics* **11**, 1397 (2009).
 27. Li, C. *et al.* Adsorption of carbon monoxide and carbon dioxide on cerium oxide studied by Fourier-transform infrared spectroscopy. Part 2.—Formation of formate species on partially reduced CeO_2 at room temperature. *Journal of the Chemical Society, Faraday Transactions 1: Physical Chemistry in Condensed Phases* **85**, 1451 (1989).
 28. Vayssilov, G. N., Mihaylov, M., Petkov, P. S., Hadjiivanov, K. I. & Neyman, K. M. Reassignment of the Vibrational Spectra of Carbonates, Formates, and Related Surface Species on Ceria: A Combined Density Functional and Infrared Spectroscopy Investigation. *The Journal of Physical Chemistry C* **115**, 23435-23454 (2011).
 29. Galzerani, J. C., Srivastava, R., Katiyar, R. S. & Porto, S. P. S. Temperature-dependent Raman study of H-bonds and possible phase-transition in $\text{LiHCOO} \cdot \text{H}_2\text{O}$. *Journal of Raman Spectroscopy* **6**, 174-182 (1977).
 30. Liu, J., Wang, Y., Lan, G. & Zheng, J. Vibrational spectra of barium formate crystal. *Journal of Raman Spectroscopy*

- 32**, 1000-1003 (2001).
31. Johnson, M. K., Powell, D. B. & Cannon, R. D. Vibrational spectra of carboxylato complexes—III. Trinuclear ‘basic’ acetates and formates of chromium(III), iron(III) and other transition metals. *Spectrochimica Acta Part A: Molecular Spectroscopy* **37**, 995-1006 (1981).
 32. Kiana, S., Yazdanbakhsh, M., Jamialahmadi, M. & Tayyari, S. F. Vibrational assignment and structure of trinuclear oxo-centered of basic formate iron(III) and chromium(III) complexes: A density functional theory study. *Spectrochimica Acta Part A: Molecular and Biomolecular Spectroscopy* **130**, 287-294 (2014).
 33. Ciupa, A., Trzebiatowska-Gusowska, M. & Ptak, M. Vibrational properties of the mixed-valence iron oxo-complex. *Vibrational Spectroscopy* **86**, 218-222 (2016).
 34. Maczka, M., Hanuza, J. & Kaminski, A. A. Polarized IR, spontaneous and stimulated Raman spectra of Y(HCOO) 3·2H2O single crystal - A new Raman laser material. *Journal of Raman Spectroscopy* **37**, 1257-1264 (2006).
 35. Maćzka, M., Pietraszko, A., Macalik, B. & Hermanowicz, K. Structure, Phonon Properties, and Order–Disorder Transition in the Metal Formate Framework of [NH 4][Mg(HCOO) 3]. *Inorganic Chemistry* **53**, 787-794 (2014).
 36. Moura, M. R. *et al.* Phonons in isostructural compounds CuxM1-x(HCOO)2·2H2O (M = Mn, Co, Ni, Zn, and Cd): a Raman scattering study. *Journal of Raman Spectroscopy* **33**, 273-277 (2002).
 37. Newman, R. Polarized Infrared Spectrum of Sodium Nitrite. *The Journal of Chemical Physics* **20**, 444-446 (1952).
 38. Fonteyne, R. Zur Kenntnis des “A-Effektes.” *Die Naturwissenschaften* **31**, 441-442 (1943).
 39. Powell, D. B. & Cannon, R. D. Vibrational spectra of carboxylato complexes- III. Trinuclear ‘basic’ acetates and formates of chromium(III), iron(III) and other transition metals*. *East* **37**, 995-1006 (1981).
 40. Puri, M. & Verma, R. D. Trinuclear metal(III) trifluoroacetates. *Monatshefte für Chemie Chemical Monthly* **115**, 533-539 (1984).
 41. Kotov, A. V & Gribov, L. A. Interpretation of the vibrational spectrum of acetic acid and its ion. *Zhurnal Prikladnoi Spektroskopii* **9**, 1247-1251 (1968).
 42. Deacon, G. & Phillips, R. J. Relationships between the carbon-oxygen stretching frequencies of carboxylato complexes and the type of carboxylate coordination. *Coordination Chemistry Reviews* **33**, 227-250 (1980).
 43. Rudolph, W. W., Fischer, D. & Irmer, G. Vibrational spectroscopic studies and DFT calculations on NaCH 3 CO 2 (aq) and CH 3 COOH(aq). *Dalton Trans.* **43**, 3174-3185 (2014).
 44. Rudolph, W. W. & Irmer, G. Raman spectroscopic studies and DFT calculations on tribromoacetic acid and tribromoacetic acid-d. *Spectrochimica Acta - Part A: Molecular and Biomolecular Spectroscopy* **90**, 165-172 (2012).
 45. Fernandes, C., Stadler, E., Drago, V., Jorge da Cunha, C. & Hiroko Kuwabara, I. Mössbauer, vibrational and electronic spectroscopy of trinuclear μ -oxo iron(III) acetate clusters with pyridine and derivatives as ligands. *Spectrochimica Acta Part A: Molecular and Biomolecular Spectroscopy* **52**, 1815-1821 (1996).
 46. Amani, V., Safari, N. & Khavasi, H. R. Solution and solid state characterization of oxo-centered trinuclear iron(III) acetate complexes [Fe3(μ 3-O)(μ -OAc)6(L)3]+. *Spectrochimica Acta - Part A: Molecular and Biomolecular Spectroscopy* **85**, 17-24 (2012).
 47. Blake, A. B., Yavari, A., Hatfield, W. E. & Sethulekshmi, C. N. Magnetic and spectroscopic properties of some heterotrinuclear basic acetates of chromium(III), iron(III), and divalent metal ions. *Journal of the Chemical Society, Dalton Transactions* 2509 (1985). doi:10.1039/dt9850002509
 48. Blake, A. B. & Yavari, A. Heterotrinuclear basic acetates containing chromium(III), iron(III), and a divalent metal: spectroscopic consequences of Metal–Metal interactions. *J. Chem. Soc., Chem. Commun.* 1247-1249 (1982). doi:10.1039/C39820001247
 49. Blake, A. B., Yavari, A. & Kubicki, H. Exchange interactions in a series of novel heteronuclear basic carboxylate complexes containing two iron(III) ions and a divalent metal ion. *Journal of the Chemical Society, Chemical Communications* 796-797 (1981). doi:10.1039/C39810000796

11.11 Abbreviations

ATR-IR	attenuated total reflection infrared spectroscopy	HREELS	high resolution electron energy loss spectroscopy
B	bridging ligand	IE-Modell	ion evaporation model
B3LYP	Becke, 3-parameter, Lee-Yang-Parr	IRMPD	infrared multiphoton dissociation
BSSE	basis set superposition error	IVR	internal vibrational redistribution)
c	concentration	KTA	potassium titanyl arsenate
cc-pVDZ	double-zeta correlation consistent basis set	KTP	potassium titanyl phosphate
cc-pVTZ	triple-zeta correlation consistent basis set	L	ligand
CID	collision induced dissociation	m/z	mass to charge ratio
COM	center of mass	MeCN	acetonitrile
Cr	chromium	MOF	metal-organic framework
CR-Modell	charge residue model	n.a.p	no assignment possible
DC	direct current	OAc	acetate (CH ₃ COO)-
DCV	direct current voltage	OPA	optical parametric amplifier
DFM	difference frequency mixing	OPO	optical parametric oscillator
DFT	density functional theory	POP	porous coordination polymer
DMBC	differential many body cooperativity	Py	pyridine (C ₅ H ₅ N)
DME	dimethyl ether	RF	radio frequency
ECP	effective core potentials	SHG	second harmonic generation
EPR	electron paramagnetic resonance	sim.	Simulated
ESI	electrospray ionization	TIMS	travelling ion mobility spectroscopy
ETD	electron transfer dissociation	TM	transition metal
exp.	experimental	UV-Vis	ultraviolet visible spectroscopy
Fe	iron	VBS	Visual Basic Scripting
FEL	free electron laser	VSCF	vibrational self-consistent field
FHWM	full width at half maximum	XMCD	X-ray magnetic circular dichroism
Fo	formate	YAG	Yttrium-Aluminum-Granat
FT-IR	Fourier transform infrared spectroscopy		

Danksagung

Ich danke Herrn Prof. Dr. Gereon Niedner-Schatteburg für die Betreuung meiner Promotion, die gute Zusammenarbeit und vor allem für den mir eingeräumten Freiraum in meiner wissenschaftlichen Arbeit.

Herrn Prof. Dr. Gerhards danke ich für die Übernahme des Zweitgutachtens und die stetige freundliche Unterstützung. Herrn Prof. Dr. Thiel danke ich für die Übernahme des Prüfungsvorsitzes und für die Unterstützung seiner Gruppe bei unseren Synthesearbeiten.

Ich möchte vielen alten Gruppenmitgliedern, Fabian Menges, Lars Barzen, Heinrich Kampschulte, Christine Merkert, Jennifer Meyer und Matthias Tombers für die Hilfen beim Einstieg in den Arbeitskreis danken.

Für die Unterstützung meiner Arbeit danke ich allen Vertiefungspraktikanten, Diplomanden und Bacheloranden, die ich betreuen durfte: Mike Lembach, Max Luczak, Kevin Weffling, Jonas Schuchmann, Jonas Krüger und einigen mehr. Meinen Kollegen Matthias Tombers, Joachim Hewer und Johannes Lang danke ich für die Einarbeitung und die Zusammenarbeit während der Nachtschichten am BESSY in Berlin.

Thomas Kolling und Yevgeniy Nosenko danke ich für die technische Unterstützung bei Problemen jeglicher Art während meiner Doktorarbeit.

Herrn PD Dr. Christoph Riehn danke ich für die stete Diskussionsbereitschaft und die Zusammenarbeit bei den Anfängerpraktika.

Ich danke allen PC'lern, Theoretikern und dem AK Patureau, die super Zusammenarbeit bei den Anfängerpraktika und die gute Atmosphäre im Kaffezimmer und den Seminaren.

Ein besonderer Dank geht an Hilde Seelos, Sybille Heieck, Petra Wetzels und Birgit Harrison-Weber für moralische und praktische Unterstützung bei jeglichen Herausforderungen in der Bürokratie und anderen Lebensfragen.

Meiner Familie, allen voran meiner Mutter Eva in stillem Andenken, meinem Vater Andreas und meinen Geschwistern Mijanu, Johannes, Joscha und Michael sei Dank für ihre stete Unterstützung und Hilfe, praktisch, moralisch und durch die Gewissheit das ihr immer für mich da seid.

Meinem Bruder Johannes, Mike Lembach und Natasha besonderen Dank für die Hilfe beim Korrekturlesen meiner Arbeit.

Meiner neuen kleinen Familie mit Natasha und Joschua, ihr seid mir auch unheimlich wertvoll und seid alle Anstrengungen wert, in dieser Promotion und sonst in meinem Leben! Danke, dass ihr da seid!

Thank you, Tasha, for being there for me while I was working on this thesis, for proofreading, and for being an awesome mom and partner.

Eidesstattliche Erklärung

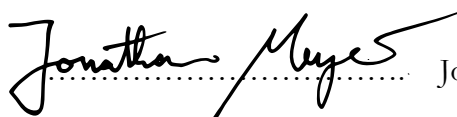
Hiermit bestätige ich, Jonathan Ruben Meyer, dass die vorliegende Arbeit mit dem Titel

‘Fragmentation and Infrared Spectroscopy of oxo-centered Homo- and Heterotrimetallic Carboxylate
Bridged Transition Metal Complexes’

gemäß der Promotionsordnung des Fachbereichs Chemie der Technischen Universität Kaiserslautern selbstständig und mit keinen anderen als den hier angegebenen Quellen und Hilfsmitteln angefertigt wurde.

Alle Stellen der Arbeit, die wörtlich oder sinngemäß aus Veröffentlichungen oder aus anderen fremden Quellen entnommen wurden, sind als solche einzeln kenntlich gemacht.

Kaiserslautern, Dezember 2018



Jonathan Ruben Meyer

Curriculum Vitae

Personal Information

Name Jonathan Ruben Meyer

School Education

09/2000 - 03/2009 Gymnasium Kusel, Abitur

University Education

10/2006 - 09/2012
Studies in Chemistry at the University of Kaiserslautern
Specialization: Physical Chemistry
Diploma of chemistry in the group of Prof. Dr. Niedner-Schatteburg,
Title of the thesis 'Laser desorption proton transfer reaction mass spectrometry (LD-PTR-MS) and characterization of simple carbohydrates'

10/2012 - 12/2018
PhD student in the group of Prof. Dr. Niedner-Schatteburg,
Dissertation in Physical Chemistry
Title of the thesis: 'Fragmentation and Infrared Spectroscopy of oxo-centered Homo- and Heterotrimetallic Carboxylate Bridged Transition Metal Complexes'

Foreign Languages

English

Chinese

Awards

Freshmen scholarship TU Kaiserslautern

Poster Prize, 11th Asian International Seminar on Atomic and Molecular Physics (AISAMP11), 2015, Sendai

Contribution to Conferences: Oral Presentations

112th Bunsentagung, Karlsruhe, 10.05.2013.

One and two color IRMPD-Spectra of cold tetranuclear cobalt cluster complexes with carbonyl and bis(diphenylphosphino)amino ligands

Tohoku University, Sendai, Japan 12.-17.10.2014.

Guest scientist exchange, Prof. F. Misaizu, Dept. of Chemistry, seminar presentation: velocity map imaging, magnetron sputtering, cryo-spectroscopy, ion mobility

Contribution to Conferences: Poster Presentations

DPG Frühjahrstagung, Heidelberg, 24.-26.4.2014.

Jonathan Meyer, Thomas Kolling, Gereon Niedner-Schatteburg, 'Versatile concepts in cryo spectroscopy of isolated metal clusters and complexes'

11th Asian Intern. Seminar on Atomic and Molecular Physics, Sendai, Japan, 05.-10.10.2014

Jonathan Meyer, Matthias Tombers, Jennifer Meyer, Gereon Niedner-Schatteburg, Annie K. Powell, Valeriu Mereacre, Arkadiusz Lawicki, Tobias Lau, Bernd von Issendorff, Akira Terasaki, Thomas Schlathölter, 'Magnetic characterization of Single Molecular Magnets (SMM) of the [Fe₄Ln₂] type by X-ray Magnetic Circular Dichroism (XMCD)', best poster award

116th Bunsentagung, Kaiserslautern, 25.-27.05.2017.

Jonathan Meyer, Michael Lembach, Pol Boden, Gereon Niedner-Schatteburg, 'Activation of small organic molecules by size selected transition metal clusters (n = 2 - 8) in the gas phase'

FT-MS Tagung, Kaiserslautern, 21.-22.09.2017.

Sebastian Dillinger, Jennifer Mohrbach, Jonathan Meyer and Gereon Niedner-Schatteburg, 'Rough and Smooth Surfaces of Cationic Nickel Clusters probed by Cryo Kinetics and Spectroscopy'

Clustertreffen 2017, Bacharach, 25.-29.09.2017.

Sebastian Dillinger, Jennifer Mohrbach, Jonathan Meyer and Gereon Niedner-Schatteburg, 'Probing Cluster Surface Morphology by Cryo Kinetics and Spectroscopy of N₂ on Cationic Nickel Clusters'

Publications

X-ray magnetic circular dichroism (XMCD) spectroscopy of gaseous [Mn₁₂Ac]⁺

Matthias Tombers, Jennifer Meyer, Jonathan Meyer, Arkadiusz Lawicki, Vicente Zamudio-Bayer, Tobias Lau, Eva Kessler, Christoph van Wüllen and Gereon Niedner-Schatteburg

In preparation

Magnetostructural Correlation in Isolated Trinuclear Iron(III) Oxo Acetate Complexes

Johannes Lang, Joachim M. Hewer, Jonathan Meyer, Jonas Schuchmann, Christoph van Wüllen and Gereon Niedner-Schatteburg

Phys. Chem. Chem. Phys., 2018, 20, 16673-16685

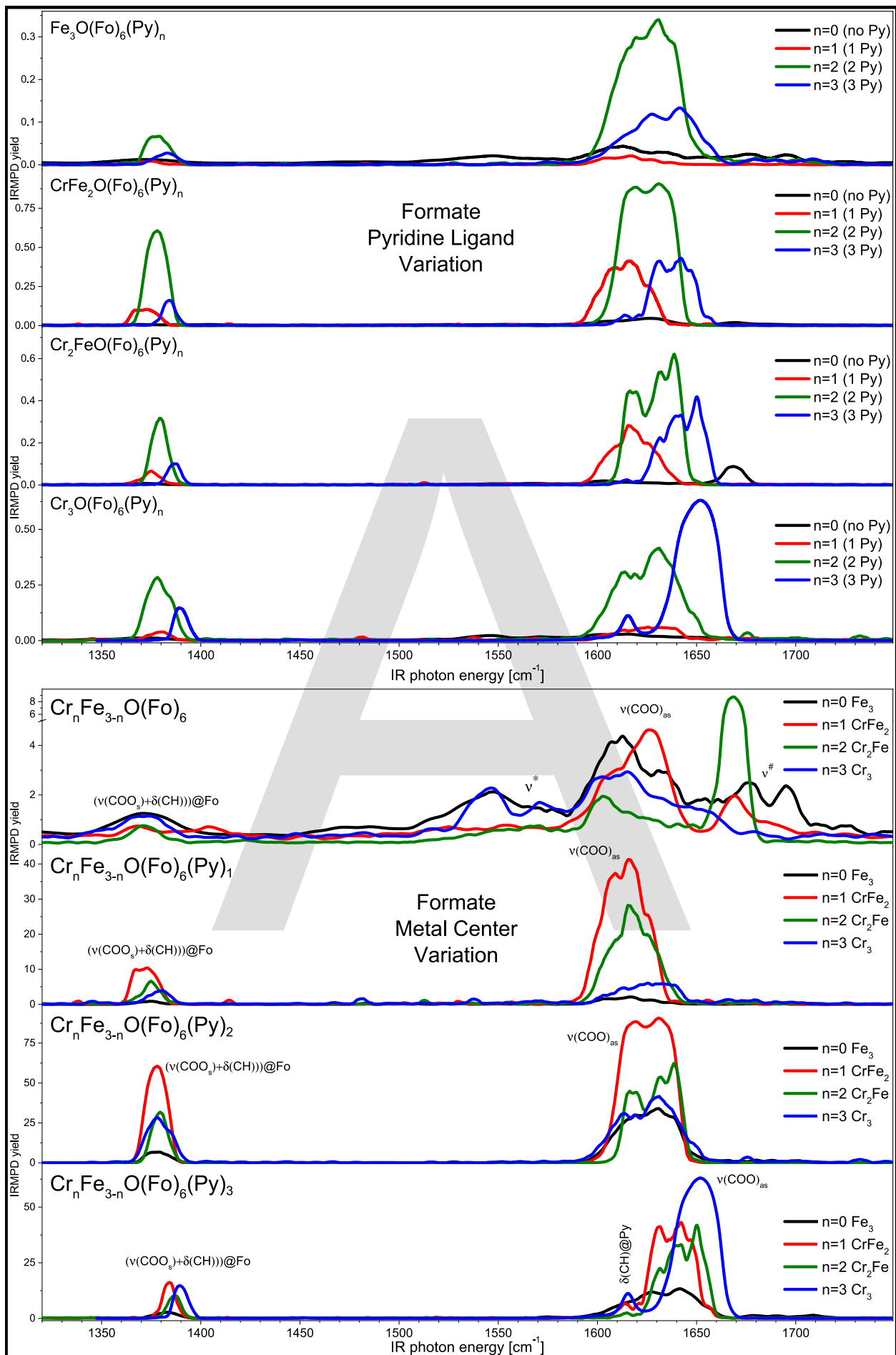


Figure 50 A Pyridine ligand and metal exchange induced changes in the IRMPD spectra of the $[\text{Cr}_n\text{Fe}_{3-n}\text{O}(\text{Fo})_6(\text{Py})_m]^+$ complexes with $n, m = 0 - 3$, cumulative fragment trace labels in m/z .

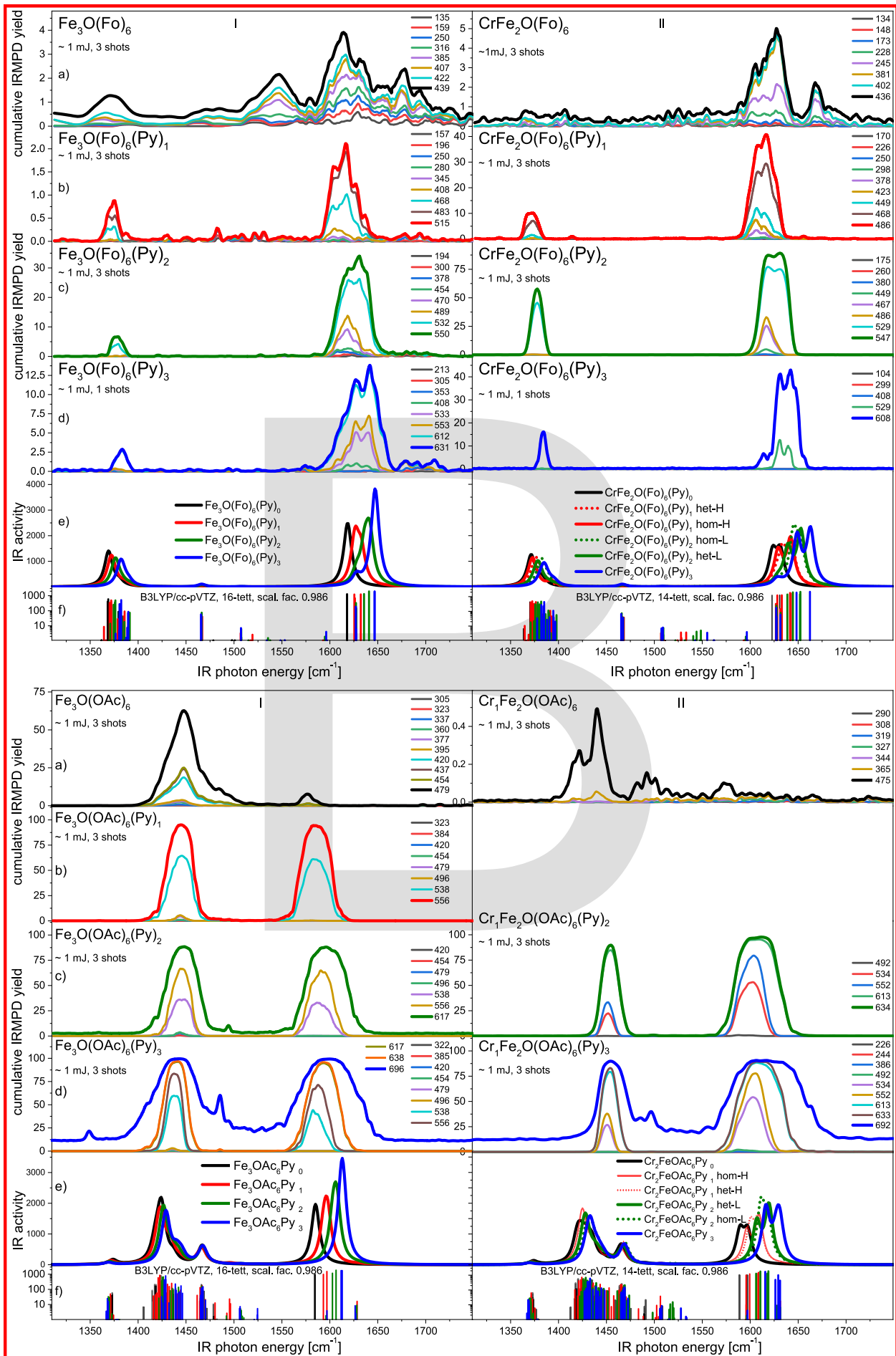


Figure 51 B Pyridine ligand induced changes in the IRMPD spectra of $[\text{Cr}_n\text{Fe}_{3-n}\text{O}(\text{Fo})_6(\text{Py})_m]^+$ and $[\text{Cr}_n\text{Fe}_{3-n}\text{O}(\text{OAc})_6(\text{Py})_m]^+$ complexes with $n = 0, 1; m = 0 - 3$, cumulative fragment trace labels in m/z .

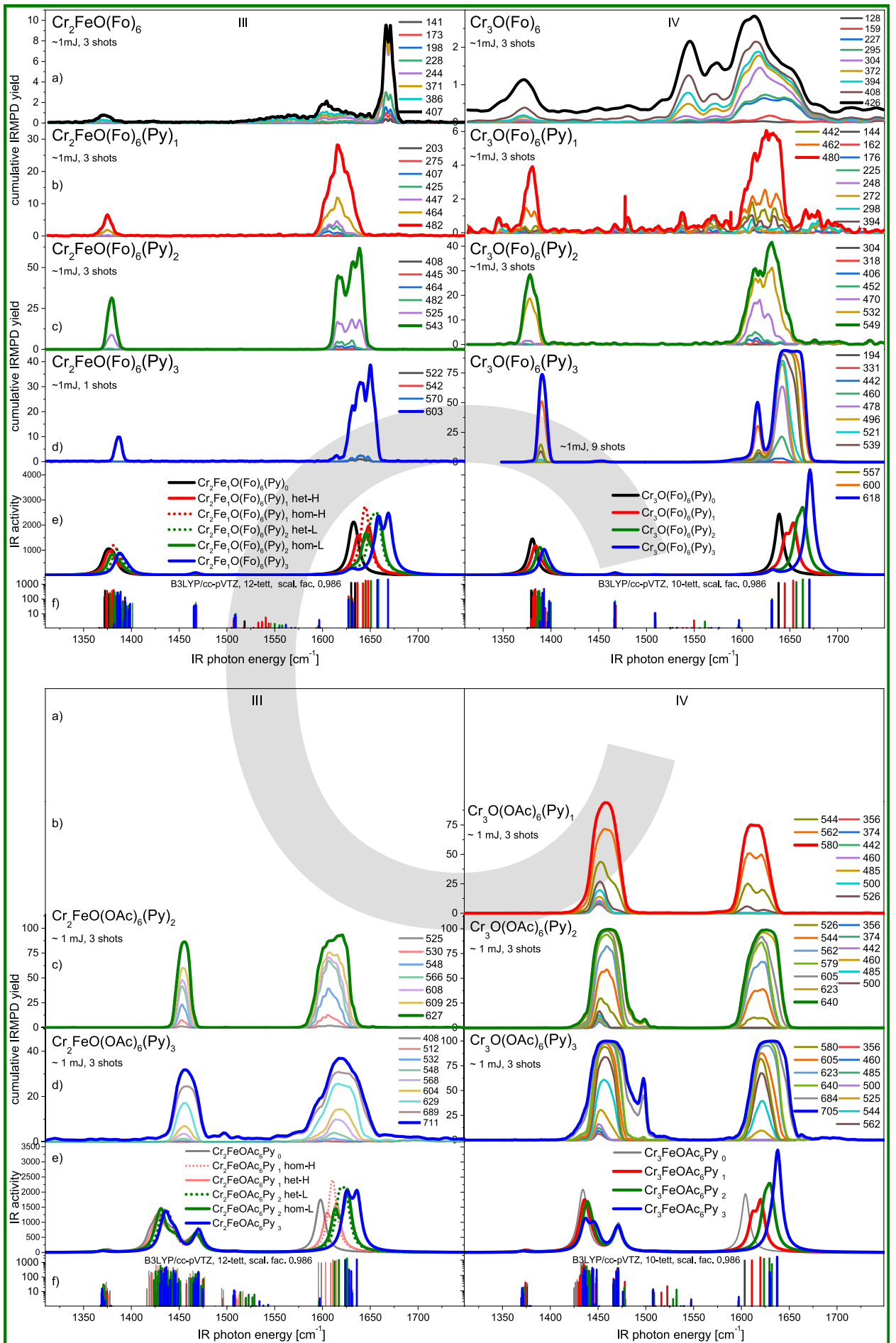


Figure 52 C Pyridine ligand induced changes in the IRMPD spectra of $[\text{Cr}_n\text{Fe}_{3-n}\text{O}(\text{Fo})_6(\text{Py})_m]^+$ and $[\text{Cr}_n\text{Fe}_{3-n}\text{O}(\text{OAc})_6(\text{Py})_m]^+$ complexes with $n = 2, 3$; $m = 0 - 3$, cumulative fragment trace labels in m/z .

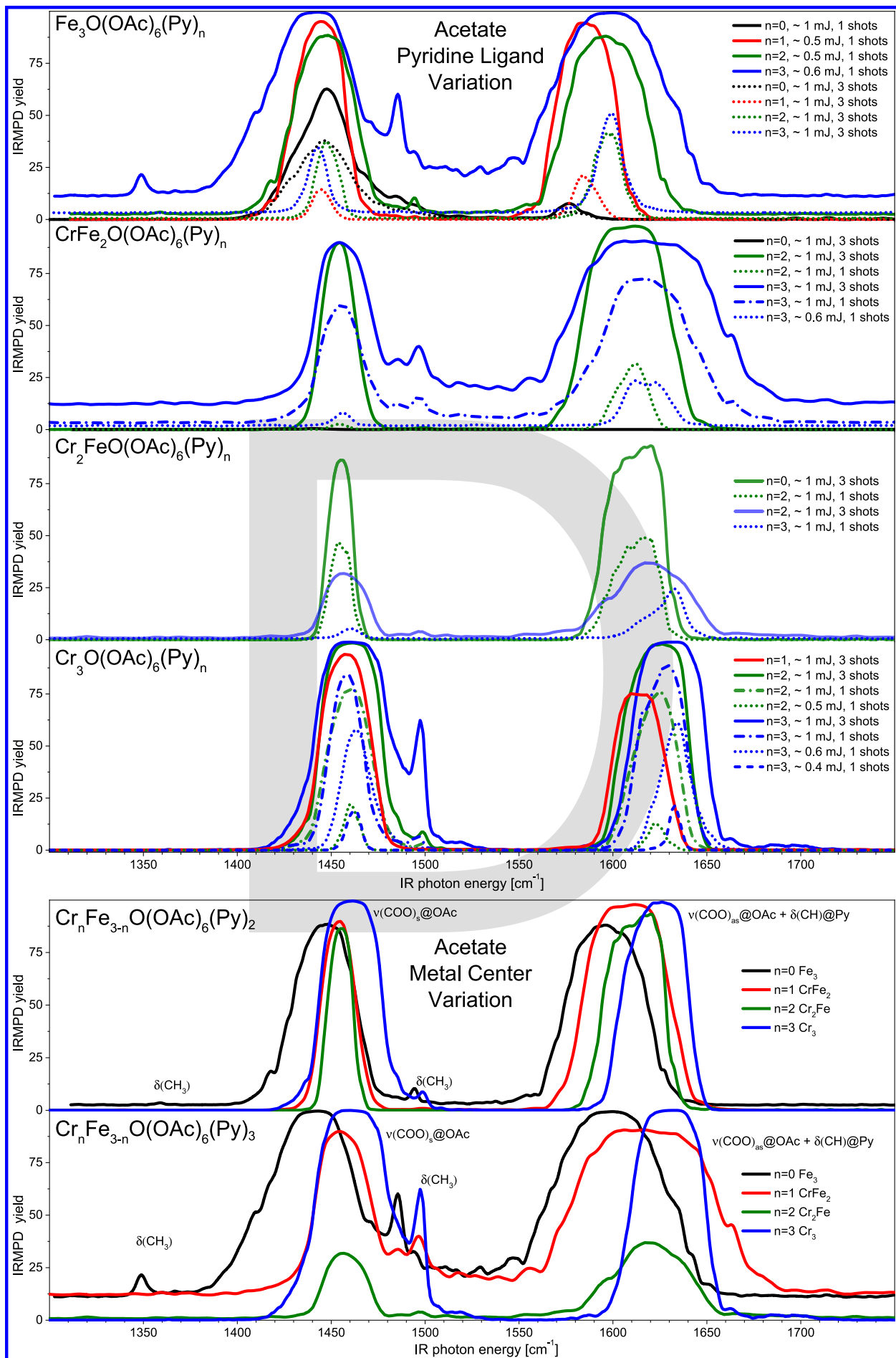


Figure 53 D Pyridine ligand and metal exchange induced changes in the IRMPD spectra of the $[\text{Cr}_n\text{Fe}_{3-n}\text{O}(\text{OAc})_6(\text{Py})_m]^+$ complexes with $n, m = 0 - 3$, cumulative fragment trace labels in m/z .

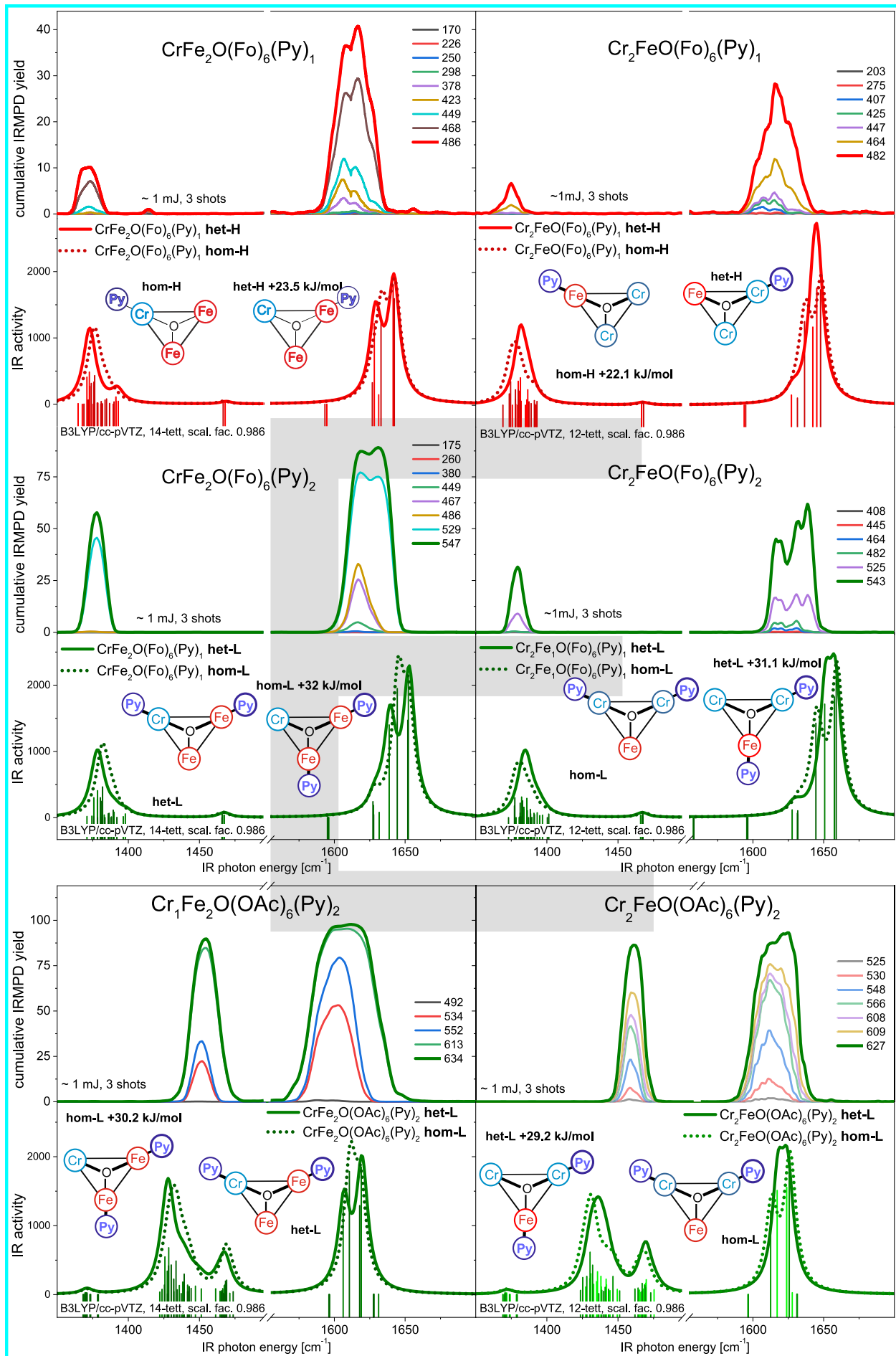


Figure 54 E hom/het-H and hom/het-L predicted and measured IRMPD/IR spectra of all heterometallic $\text{Cr}_n\text{Fe}_{3-n}$ species of all measured formate and acetate bridged complexes for $n = 1, 2$, cumulative fragment trace labels in m/z .

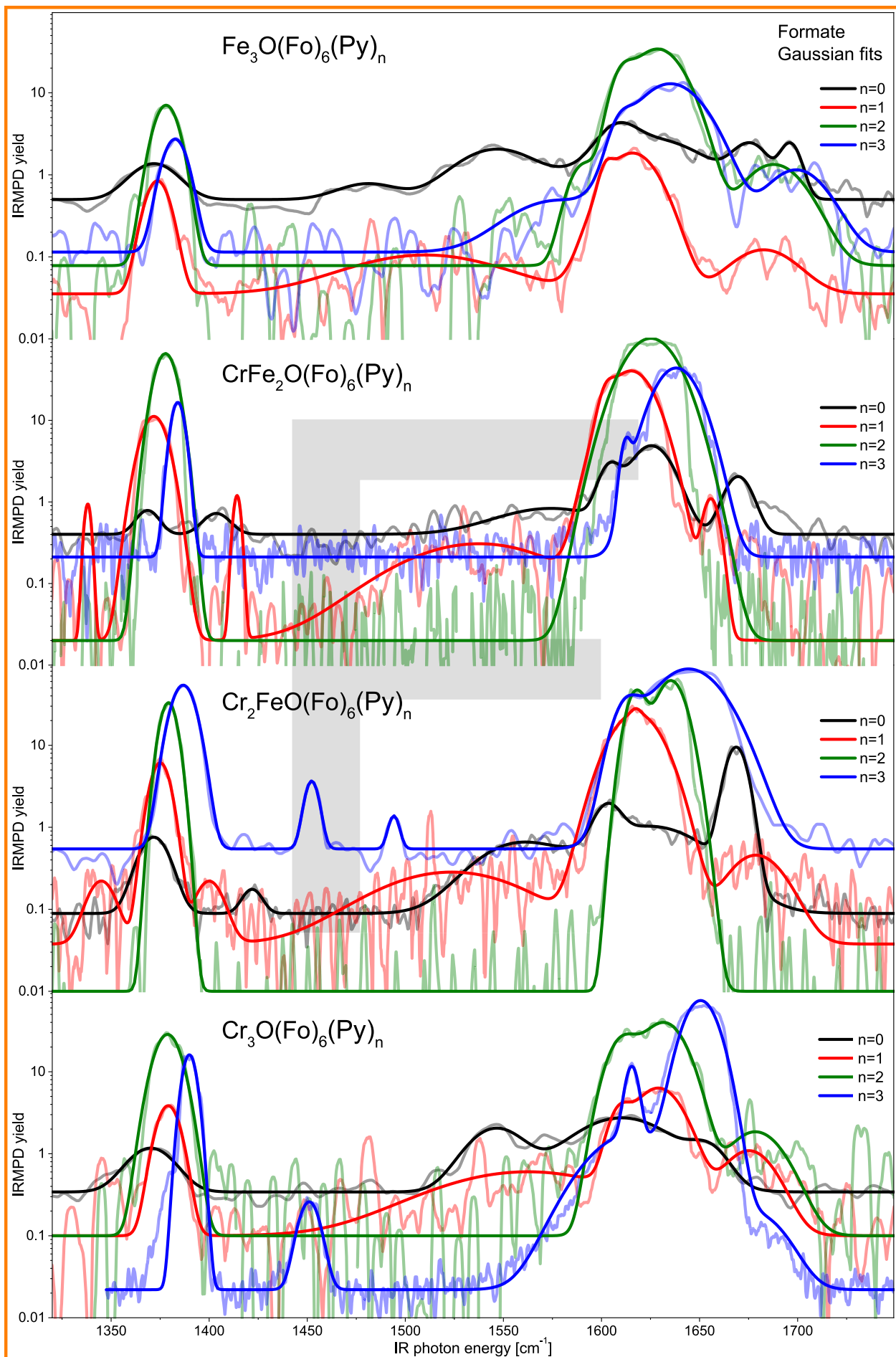


Figure 56 F Gaussian curve fits of the IRMPD spectra shown in a semilogarithmic scale in the CO region of the $[\text{Fe}_n\text{Cr}_{3-n}\text{O}(\text{Fo})_6\text{Py}_m]^+$ complexes with $n, m = 0, 1, 2, 3$ species. Refer to **Table 31** for the formate band positions determined by the fits.

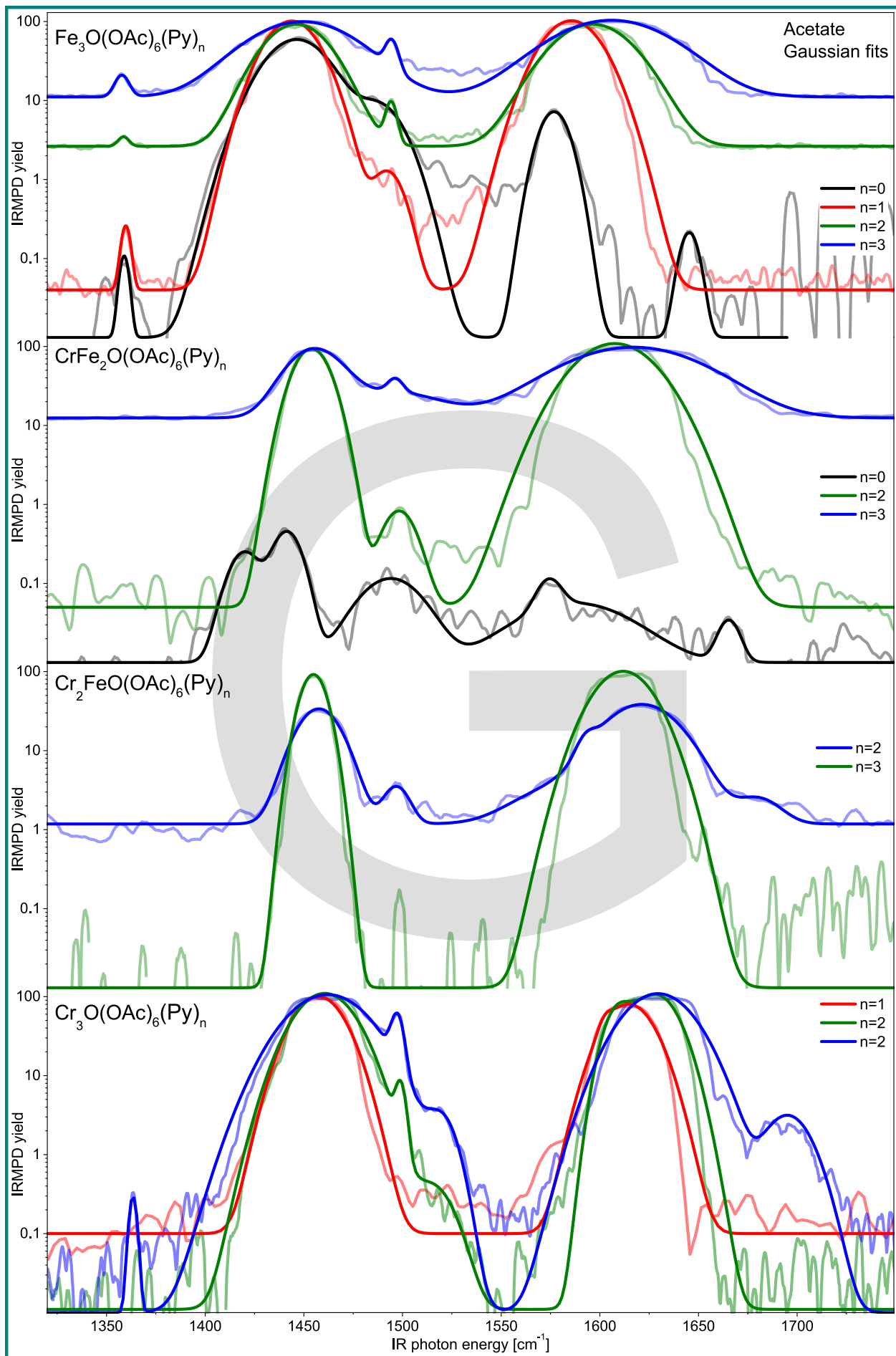


Figure 57 G Gaussian curve fits of the IRMPD spectra shown in a semilogarithmic scale in the CO region of the $[\text{Fe}_n\text{Cr}_{3-n}\text{O}(\text{OAc})_6(\text{Py})_m]^+$ complexes with $n, m = 0, 1, 2, 3$ species. Refer to **Figure 106** for all Gaussian fits and **Table 31** for the acetate band positions determined by the fits.

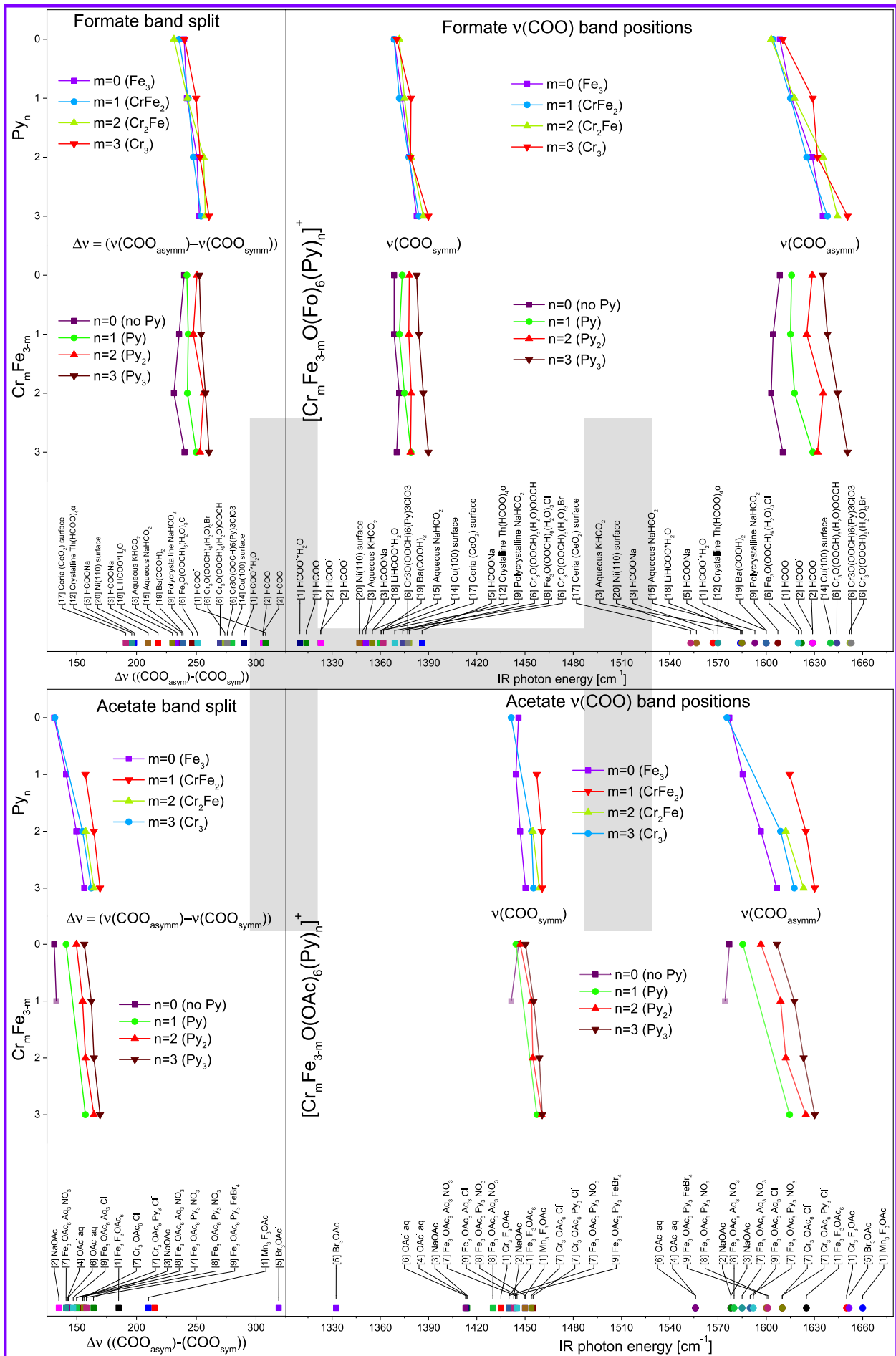


Figure 58 H Trends of $v(\text{COO})_s$, $v(\text{COO})_{as}$ and Δv . The literature references refer to **Table 28** for the formate and **Table 29** for the acetate species. The peaks are fitted with a gaussian function as shown in **Figure 57** and **Figure 106**.